

**UNIVERSITY OF CRETE**

**Department of Chemistry**

**LABORATORY OF BIOINORGANIC CHEMISTRY**



**Doctoral Thesis**

**Light harvesting Applications of Self-Assembled and  
Surface-Anchored Porphyrin Chromophores**

**EMMANOUIL N. NIKOLOUDAKIS**

**Thesis Supervisor: Athanassios G. Coutsolelos**

**Heraklion 2022**

**ΠΑΝΕΠΙΣΤΗΜΙΟ ΚΡΗΤΗΣ**

**Τμήμα Χημείας**

**ΕΡΓΑΣΤΗΡΙΟ ΒΙΟΑΝΟΡΓΑΝΗΣ ΧΗΜΕΙΑΣ**



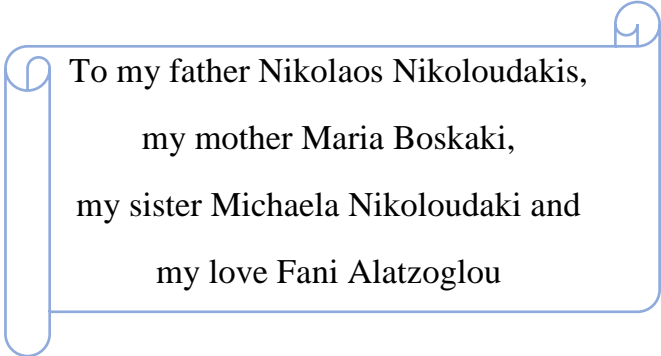
**Διδακτορική Διατριβή**

**Εφαρμογές Αξιοποίησης Ηλιακής Ακτινοβολίας με τη  
Χρήση Αυτο-οργανωμένων και Προσροφημένων σε  
Επιφάνεια Πορφυρινικών Χρωμοφόρων.**

**ΕΜΜΑΝΟΥΗΛ Ν. ΝΙΚΟΛΟΥΔΑΚΗΣ**

**Υπεύθυνος Καθηγητής: Αθανάσιος Γ. Κουτσολέλος**

**Ηράκλειο 2022**



To my father Nikolaos Nikoloudakis,  
my mother Maria Boskaki,  
my sister Michaela Nikoloudaki and  
my love Fani Alatzoglou

## **Εξεταστική Επιτροπή (αλφαβητικά)**

**Κουτσολέλος Γ. Αθανάσιος (Επιβλέπων)**

*Καθηγητής, Τμήμα Χημείας, Πανεπιστήμιο Κρήτης*

**Βασιλικογιαννάκης Γεώργιος**

*Καθηγητής, Τμήμα Χημείας, Πανεπιστήμιο Κρήτης*

**Κιτσόπουλος Θεοφάνης**

*Καθηγητής, Τμήμα Χημείας, Πανεπιστήμιο Κρήτης*

**Μητράκη Άννα**

*Καθηγήτρια, Τμήμα Επιστήμης και Τεχνολογίας Υλικών, Πανεπιστήμιο Κρήτης*

**Odobel Fabrice**

*Research Director at CNRS, Chimie Et Interdisciplinarité, Synthèse, Analyse, Modélisation (CEISAM), University of Nantes, France*

**Ταβερναράκης Νεκτάριος**

*Καθηγητής, Τμήμα Ιατρικής, Πανεπιστήμιο Κρήτης*

**Ταγματάρχης Νίκος**

*Διευθυντής Ερευνών, Ινστιτούτο Θεωρητικής και Φυσικής Χημείας, Εθνικό Ίδρυμα Ερευνών*



## **Acknowledgments**

*First of all, I would like to thank my supervisor, professor Athanassios G. Coutsolelos, who gave me the opportunity to conduct my PhD research in his group and for the trust he showed in me. I am very thankful for the finest working environment he provided in the Laboratory of Bio-Inorganic Chemistry (LBIC). I am proud of being a member of LBIC since I was able to work as part of an inspiring research team that allowed everyone's talents to grow. A passionate work environment that was very engaging in personal but professional level as well. My supervisor's guidance throughout these years was really helpful and crucial for the accomplishment of all the work described in this thesis.*

*I would also like to thank prof. Anna Mitraki for her useful advice and for the self-assembling experiments I performed in her laboratory, along with her students Marita Vasila, Konstandina Mitropoulou and Chrysanthi Apostolidou. I am very grateful to prof. Fabrice Odobel for accepting me as an Erasmus student, let me work in his laboratory and helped me acquire essential knowledge and skills for my future career. I learned many things while working alongside him. I would like to express my sincere gratitude to the rest of my committee members, prof. Georgios Vassilikogiannakis, prof. Theofanis Kitsopoulos, prof. Nektarios Tavernarakis and Dr. Nikos Tagmatarchis for accepting to evaluate this doctoral thesis.*

*I want to express my genuine appreciation to prof. Francis D'Souza who accepted me to work in his laboratory as a visiting research student. He gave me the opportunity to obtain useful new knowledge and new skills.*

*In addition, I am also very grateful to prof. Haralambos Katerinopoulos for writing numerous recommendation letters on my behalf and for trusting me in being a graduate teaching assistant for his organic chemistry course.*

*I would like to thank as well our collaborator, prof. Xuehai Yan for the photodynamic therapy experiments.*

*I am obliged to all the past and current members of LBIC group, Dr. Nikolaou Vasilis, Dr. Charisiadis Asterios, Dr. Ladomenou Kalliopi, Dr. Karikis Kostas, Dr. Gannoudis Emmanouil, Dr. Landrou Georgios, Dr. Trapali Adelaida, M.Sc. Papadakis*

*Michael, M.Sc. Panagiotakis Stelios, M.Sc. Aspasia Stoumpidi, M.Sc. Eleni Agapaki, Emmanouil Orfanos, Magda Topouza, M.Sc. Maria Kandyli, M.Sc. Glymenaki Eleni, M.Sc. Pigiaki Maria for the friendly, supportive and cooperative work environment we had in the lab. I am very grateful to all of them.*

*I absolutely owe a big thank you to Dr. Georgios Charalambidis for his support, guidance and general help in our research and for being my friend inside and outside the lab. I feel very lucky that I worked alongside him.*

*I want to express my sincere appreciation to the Fulbright Foundation for the visiting researcher scholarship, enabling my visit in the University of North Texas in Denton, TX, US. This funding gave me the opportunity to live and work overseas, meet new people, cultures and acquire new knowledge, techniques and skills.*

*Ms. Aleka Manousaki and Mr Stefanos Papadakis are gratefully thanked for expert technical assistance with Scanning Electron Microscopy experiments.*

*I would also like to thank the European Union and Greek national funds through the Regional Operational Program “Crete 2014-2020,” project code OPS:5029187, for the financial support.*

*The biggest thank you is something I owe to my family and my partner, who always support me with everything I do in my life!*

# Curriculum Vitae

## Personal Details

---

**Name:** Emmanouil N. Nikoloudakis  
**Address:** 2 Valentinou Bogiatzidou, Heraklion, Crete, 71305, Greece.  
**Date of birth:** 06 April 1995  
**Place of birth:** Heraklion, Crete, Greece  
**Nationality:** Greek  
**Phone:** +30 6986421584  
**Email:** [nik21man@gmail.com](mailto:nik21man@gmail.com), [chemp1025@edu.chemistry.uoc.gr](mailto:chemp1025@edu.chemistry.uoc.gr)

## Academic Background

---

### 02/2019 – present **PhD Candidate in Inorganic Chemistry:**

Laboratory of Bioinorganic Chemistry, University of Crete,  
Department of Chemistry, Heraklion.

Supervisor: Prof. Athanassios G. Coutsolelos.

### 02/2017 – 02/2019 **Master degree in Inorganic Chemistry:**

Laboratory of Bioinorganic Chemistry, University of Crete,  
Department of Chemistry, Heraklion.

✓ **Master Thesis title:** “*Bio-inspired molecular self-assembly based on organic and inorganic moieties.*”

Supervisor: Prof. Athanassios G. Coutsolelos.

### 09/2013 - 02/2017 **Bachelor in Chemistry (9.47/10)**

University of Crete, Department of Chemistry, Heraklion.

✓ **Undergraduate Thesis title:** Studies on novel catalysts and photosensitizers for photocatalytic hydrogen production.

Courses: Principles of Chemistry, Introduction to Computers Science, Qualitative and Quantitative Analysis, Physics I &II, English for Chemistry I&II, Introduction to Biology, Mathematics I & II, Analytical Chemistry I&II, Organic Chemistry I&II, Inorganic Chemistry I&II, Physical Chemistry I & II,

Environmental Chemistry, Biochemistry I & II, Chemistry of Biomolecules, Bio-inorganic Chemistry, Soft Condensed Matter, Metal Ions in Medicine, Crystal Structure Determination of Biological Macromolecules, Chemistry of Advanced Materials, Inorganic Biomaterials, NMR spectroscopy, Medicinal Chemistry, Computational Chemistry, Atmospheric Chemistry.

Laboratories: General Chemistry, Organic Chemistry I & II, Inorganic Chemistry I & II, Biochemistry, Analytical Chemistry I & II and Physical Chemistry I & II.

### Teaching Experience

---

**06/2021 - 08/2021**

**Graduate Laboratory Assistant**

Student Practice Laboratory of General Chemistry, University of Crete, Department of Chemistry, Heraklion.  
Supervisor: Spyridon Kornilios

**10/2020 - 12/2020**

**Graduate Laboratory Assistant**

Student Practice Laboratory of Inorganic Chemistry, University of Crete, Department of Chemistry, Heraklion.  
Supervisor: Stelios Terzakis

**10/2019 - 01/2020**

**Graduate Teaching Assistant**

Organic Chemistry III course, University of Crete, Department of Chemistry, Heraklion. Supervisor: Prof. Charalambos Katerinopoulos

**10/2019 - 01/2020**

**Graduate Laboratory Assistant**

Student Practice Laboratory of General Chemistry, University of Crete, Department of Chemistry, Heraklion.  
Supervisor: Spyridon Kornilios

**02/2018 - 05/2018**

**Graduate Laboratory Assistant**

Student Practice Laboratory of Inorganic Chemistry, University of Crete, Department of Chemistry, Heraklion.  
Supervisor: Eleftheria Vardalachaki

**02/2017 - 05/2017**      **Graduate Laboratory Assistant**  
Student Practice Laboratory of General Chemistry, University of Crete, Department of Chemistry, Heraklion.  
Supervisor: Spyridon Kornilios

**02/2015 - 05/2015**      **Undergraduate Laboratory Assistant**  
Student Practice Laboratory of General Chemistry, University of Crete, Department of Chemistry, Heraklion.  
Supervisor: Spyridon Kornilios  
✓ Preparation of Chemical Reagents

### Research Experience

---

**08/2021 - 12/2021**      **Fellowship in University of North Texas by the Fulbright Foundation**  
1508 W. Mulberry Street, 76201 **Denton, TX United States.**  
Supervisor: Prof. Francis D'Souza

✓ Purpose of visit: “*Synthesis and photocatalytic investigation of “nickel porphyrin-Ruthenium” dyads for photo-induced water oxidation to produce H<sub>2</sub>.*”

**02/2020 - 03/2020**      **Internship in Nantes University with Erasmus+ program**  
& CEISAM / IMF/ 2 rue de la Houssinière, 44322 **Nantes France.**

**09/2020 - 10/2020**      Supervisor: Prof. Fabrice Odobel  
✓ Purpose of visit: “*Synthesis and study of photoelectrochemical properties of “zinc porphyrin-TEMPO” dyads for alcohol oxidation photocatalysis.*”

**09/2017 - 12/2017**      **Internship in CEA Grenoble with Erasmus+ program**  
CEA / BIG / LCBM / 17 rue des Martyrs 38054 **Grenoble France.**

Supervisor: Prof. Stéphane Torelli  
✓ Purpose of visit: “*Synthesis, characterization and N<sub>2</sub>O reductase activity of Cu<sup>2+</sup> complexes with {Cu<sub>2</sub>S} cores.*”

**06/2015 - 08/2015**      **Traineeship in a physical chemistry laboratory at IESL-FORTH**

Institute of Electronic Structure and LASER / FORTH,  
Heraklion Greece.

Supervisor: Prof. Peter Rakitzis

- ✓ Purpose of visit: “Adsorption studies of  $I_2$  on steel coated with polymeric material by measuring the absorption under high vacuum.”

**Work Experience**

---

**05/2019 - 06/2019**      Research program: “Encapsulation of Chromophores by Self-assembled Hydrogels with Biomedical Applications” (project code: T1EDK-01504) funded by the Operational Program Competitiveness, Entrepreneurship, and Innovation, under the call RESEARCH – CREATE – INNOVATE.

**08/2019 - 03/2022**      Research program: “Synthesis of new materials for the development of photo-electrochemical devices towards  $H_2$  production and  $CO_2$  reduction” (project code OPS: 5029187) funded by Regional Operational Program “Crete 2014-2020”.

**Additional information**

---

- Publications**
1. Nikoloudakis E., Pati P. B., Charalambidis G., Budkina D. S., Diring S., Planchat A., Jacquemin D., Vauthey E., Coutsolelos A.G., Odobel F., “Dye-Sensitized Photoelectrosynthesis Cells for Benzyl Alcohol Oxidation Using a Zinc Porphyrin Sensitizer and TEMPO Catalyst”, *ACS Catal.* **2021**, 11, 19, 12075–12086.
  2. Nikolaou V., Charalambidis G., Landrou G., Nikoloudakis E., Planchat A., Tsalameni R., Junghans K., Kahnt A., Odobel F., Coutsolelos A.G., “Antenna Effect in BODIPY-(Zn)Porphyrin Entities Promotes  $H_2$  Evolution in Dye-Sensitized Photocatalytic Systems”, *ACS Appl. Energy Mater.* **2021**, 4, 9, 10042–10049.
  3. Glymenaki E, Kandyli M, Apostolidou C. P., Kokotidou C., Charalambidis G., Nikoloudakis E., Panagiotakis S.,

- Koutserinaki E., Klontza V., Michail P., Charisiadis A., Mitraki A., Coutsolelos A. G., “ Design and Synthesis of Porphyrin–Nitrilotriacetic Acid Dyads with Potential Applications in Peptide Labeling through Metallochelate Coupling” *ACS Omega* **2022**, 7, 2, 1803–1818.
4. Nikoloudakis E., Charalambidis G., Vasila M., Orfanos E., Angaridis P., Spyroulias G.A., Coutsolelos A.G., “Gadolinium porphyrinate double-deckers for visible light driven H<sub>2</sub> evolution”, *Polyhedron*, **2021**, 208, 115421.
  5. Nikoloudakis E., Pigiaki M., Polychronaki M.N., Margaritopoulou A., Charalambidis G., Serpetzoglou E., Mitraki A., Loukakos P.A., Coutsolelos A.G., “Self-Assembly of Porphyrin Dipeptide Conjugates toward Hydrogen Production”, *ACS Sustain. Chem. Eng.*, **2021**, 9, 7781-7791.
  6. Charisiadis A., Glymenaki E., Planchat A., Margiola S., Lavergne-Bril A., Nikoloudakis E., Nikolaou V., Charalambidis G., Coutsolelos A.G., Odobel F., “Photoelectrochemical properties of dyads composed of porphyrin/ruthenium catalyst grafted on metal oxide semiconductors”, *Dyes Pigm.*, **2021**, 185, 108908.
  7. Ladomenou K., Landrou G., Charalambidis G., Nikoloudakis E. and Coutsolelos A. G., “Carbon dots for photocatalytic H<sub>2</sub> production in aqueous media with molecular Co catalysts”, *Sustain. Energy Fuels*, **2021**, 5, 449-458.
  8. Nikolaou, V., Charalambidis, G., Ladomenou, K., Nikoloudakis, E., Drivas, C., Vamvasakis, I., Panagiotakis, S., Landrou, G., Agapaki, E., Stangel, C., Henkel, C., Joseph, J., Armatas, G., Vasilopoulou, M., Kennou, S., Guldi, D.M. and Coutsolelos, A.G., “Controlling Solar Hydrogen Production by Organizing Porphyrins”, *ChemSusChem*, **2021**, 14, 961-970.
  9. Chang R., Nikoloudakis E., Zou Q., Mitraki A., Coutsolelos A. G., Yan X., “Supramolecular Nanodrugs Constructed by Self-Assembly of Peptide Nucleic Acid-Photosensitizer Conjugates for

- Photodynamic Therapy” *ACS Appl. Bio Mater.*, **2020**, 3(1), 2-9.
10. Nikoloudakis E., Orphanos E., Agapaki E., Nikolaou V., Charisiadis A., Charalambidis G., Mitraki A., Coutsolelos A. G., “Molecular self-assembly of porphyrin and BODIPY chromophores connected with diphenylalanine moieties” *J. Porphyr. Phthalocyanines*, **2020** 24(5-7), 775-785.
  11. Nikoloudakis E., Mitropoulou K., Landrou G., Charalambidis G., Nikolaou V., Mitraki A., Coutsolelos A. G., “Self-Assembly of Aliphatic Dipeptides coupled with porphyrin and BODIPY chromophores”, *Chem. Commun.*, **2019**, 55, 14103-14106.
  12. Nikoloudakis E., Karikis K., Kokotidou C., Charisiadis A., Douvas A. M., Mitraki A., Charalambidis G., Yan X., Coutsolelos A. G., “Self-assembling study of PNA-Porphyrin and PNA-BODIPY Hybrids in Mixed Solvent Systems”, *Nanoscale*, **2019**, 11, 3557-3566.
  13. Nikoloudakis E., Karikis K., Laurans M., Kokotidou C., Solé-Daura A., Carbó J. J., Charisiadis A., Charalambidis G., Izzet G., Mitraki A., Douvas A. M., Poblet J. M., Proust A. and Coutsolelos A. G., “Experimental and theoretical study of nanometric spheres from polyoxometalate-phenylalanine hybrids”, *Dalton Trans.*, **2018**, 47, 6304-6313.
  14. Karikis K., Butkiewicz A., Folias F., Charalambidis G., Kokotidou C., Charisiadis A., Nikolaou V., Nikoloudakis E., Frelek J., Mitraki A., Coutsolelos A. G., “Self-assembly of (Boron-dipyrromethane)-diphenylalanine Conjugates Forming Chiral Supramolecular Materials”, *Nanoscale*, **2018**, 10, 1735-1741.

#### Conferences

1. Nikoloudakis E., “Photocatalytic hydrogen production of self-assembled Porphyrin-Dipeptide hybrids”, International Solar Fuels Conference (ISFC) **2021**, 26 - 29 July 2021, **UK**, poster and oral presentation, *Virtual Conference*.
2. Coutsolelos A.G., Nikoloudakis E., Pigiaki M., Polychronaki



- M.N., Margaritopoulou A., Charalambidis G., Serpetzoglou E., Mitraki A., Loukakos P.A., “Self-assembled porphyrin-dipeptide hybrids produce hydrogen photocatalytically”, 11th International Conference on Porphyrins and Phthalocyanines (**ICPP-11**), 28 June – 3 July **2021, USA, Virtual Meeting**.
3. Nikolaou V., Charalambidis G., Ladomenou K., Nikoloudakis E., Drivas C., Vamvasakis I., Panagiotakis S., Landrou G., Agapaki E., Stangel C., Henkel C., Joseph J., Armatas G., Vasilopoulou M., Kennou S., Guldi D.M., Coutsolelos A.G., “Controlling solar hydrogen production by organizing porphyrins”, 11th International Conference on Porphyrins and Phthalocyanines (**ICPP-11**), 28 June – 3 July **2021, USA, Virtual Meeting**.
  4. Charalambidis G., Nikoloudakis E., Charisiadis A., Nikolaou V., Coutsolelos A.G., “Photocatalytic hydrogen evolving systems based on porphyrin derivatives”, 11th International Conference on Porphyrins and Phthalocyanines (**ICPP-11**), 28 June – 3 July **2021, USA, Virtual Meeting**.
  5. Joint UK Solar Fuels Network (**SFN**) - SuperSolar Early Career Researcher (**ECR**) Meeting 28 April 2021, London **UK, Virtual Meeting**.
  6. Ladomenou K., Landrou G., Charalambidis G., Nikoloudakis E., Coutsolelos A.G., “Carbon dots for photocatalytic H<sub>2</sub> production in aqueous media with molecular Co catalysts”, **ACS Spring Meeting 2021**, 5-16 April 2021, **USA, Virtual Conference**.
  7. Charalambidis G., Charisiadis A., Glymenaki E., Planchat A., Margiola S., Nikoloudakis E., Nikolaou V., Coutsolelos A., Odobel F., “Photoelectrochemical properties of dyads composed of porphyrin/ruthenium catalyst grafted on metal oxide semiconductors”, **ACS Spring Meeting 2021**, 5-16 April 2021, **USA, Virtual Conference**.
  8. 8<sup>th</sup> **UK Solar Fuels Symposium**, online conference, 1 December **2020**.

9. Coutsolelos A. G., Nikoloudakis E., Karikis K., Han J., Kokotidou C., Charisiadis A., Folias F., Mitraki A., Charalambidis G., Yan X., 3rd International Solar Fuels Conference (ISF-3) International Conference on Artificial Photosynthesis-2019 (ICARP2019), **Hiroshima, Japan**, 20-24 November **2019**, poster presentation.
10. Nikolaou V., Nikoloudakis E., Mitropoulou K., Charalambidis G., Landrou G., Mitraki A., Coutsolelos A. G., 3rd International Solar Fuels Conference-YOUNG (ISF3-YOUNG), **Hiroshima, Japan**, 19-20 November, **2019**, poster presentation.
11. Nikoloudakis E., “Light driven H<sub>2</sub> production using self-assembled nanostructures of PNA-Porphyrin and PNA-BODIPY hybrids”, 13<sup>th</sup> DEMSEE conference **Heraklion**, 19-20 September **2019**, oral presentation.
12. Nikoloudakis E., Karikis K., Kokotidou C., Charalambidis G., Charisiadis A., Mitraki A., Coutsolelos A. G., 21<sup>th</sup> Postgraduate Conference, Chemistry Department, University of Crete, **Heraklion** 15-17 May **2019**, poster presentation.
13. International Symposium “Chemistry at the Interface of Biology/Medicine”, University of Crete, **Heraklion**, 21-25 September **2018**.
14. Charalambidis G., Karikis K., Nikoloudakis E., Kokotidou C., Charisiadis A., Nikolaou V., Mitraki A., Coutsolelos A.G. PSA-2018: Peptide Self-Assembly: Biology, Chemistry, Materials and Engineering, **Beijing, China**, 23-25 August, **2018**, poster presentation.
15. Coutsolelos, A.G.; Mitraki, A.; Charalambidis, G.; Kokotidou, C.; Karikis, K.; Nikoloudakis, E.; Charisiadis, A., Peptide Self-Assembly: Biology, Chemistry, Materials and Engineering, **Beijing, China**, August 23-25, **2018**,. oral presentation.

16. Nikoloudakis E., Karikis K., Kokotidou C., Charalambidis G., Douvas A. M., Mitraki A., Coutsolelos A. G., ICPP10, **Munich, Germany**, 1 - 6 July, **2018**, poster and invited oral presentation.
17. Nikoloudakis E., 20<sup>th</sup> Postgraduate Conference, Chemistry Department, University of Crete, **Heraklion** 25-27 June **2018**, (organizing committee), oral presentation.
18. 19<sup>th</sup> Postgraduate Conference, Department of Chemistry, University of Crete, **Heraklion** 2-4 May **2017**.
19. 22<sup>th</sup> Hellenic Chemistry Conference, Association of Greek Chemists, **Thessaloniki**, 2-4 December **2016**.
20. International Symposium “Chemistry at the Interface of Biology / Medicine”, University of Crete, **Heraklion**, 23-26 September **2016**.
21. 18<sup>th</sup> Postgraduate Conference, Department of Chemistry, University of Crete, **Heraklion** 26-27 March **2016**.

#### Seminars

1. 4<sup>th</sup> Microscopy *online* seminar, IIN “Demokritos”, 03/2021.
2. *Laboratory Safety* Seminar, IMBB-ITE, **Heraklion**, Crete, 03/2018.
3. *Scientific Writing* workshop, UoC, **Heraklion**, 1/03/2018-26/04/2018.
4. 4<sup>th</sup> Mathematical Summer School, **Leptokaria, Pieria**, Greece, (7/2010).
5. English language course, in **Colchester, England**, 22 – 28 July 2009.

#### Scholarships

- Fellowship from **Fulbright Foundation**, to travel as a visiting research student in the University of North Texas, Denton, TX, US, 08/2021 – 12/2021.
- Scholarship from **ELKE, University of Crete**, as a teaching assistant in undergraduate laboratory courses, 06/2021 – 08/2021.
- Scholarship from **IPTO (AΔMHE) company**, for his graduate research related to energy and environment, 10/2019 - 9/2020.

- Scholarship from **Onassis Foundation**, for his graduate studies to obtain a master degree in Chemistry, 10/2017 - 2/2019.
- Fellowship from “**Maria Michail Manasaki**” Bequest, for his graduate studies to obtain a master degree in Chemistry, 3/2017 - 9/2017.
- Fellowship from “**Chrisanthou and Anastasia Karidi**” Bequest, for entering the chemistry department with the highest score in entrance-exams 7/2014.

- Language skills**
- Greek:** Native language
  - English:** [Michigan Certificate of Proficiency in English & Edexcel level 5]
  - German:** [Goethe-Zertifikat B2 & Greek State certificate for German Level B2]
  - French:** [Level A1]
- Computer skills** → KeyCERT IT Basic Plus, Knowledge of use of *Microsoft Office*™, *Open Office*™, *Origin*, *Chemdraw*, *Topspin*, *ChemSketch*, *Avogardo*, *Mercury*, *TeamViewer*, *Neofox viewer*, *EC-lab*, *Spectragryph*, *Endnote* and *Mendeley* programs.
- Technical skills**
- Synthesis, purification and characterization of chromophores. Synthesis under anaerobic conditions.
  - Photocatalytic and Photoelectrochemical experiments.
  - NMR, UV-Vis, FT-IR and Fluorescence spectroscopies, GC and MALDI-TOF spectrometries, Cyclic and SW voltammetry.
  - Driving license: B
- Memberships**
- Society of Porphyrins & Phthalocyanines, 2018 - today
  - Association of Greek Chemists, 2017 - today
- School Awards**
1. **Praise** from the Association of Greek Chemists – Peripheral Department of Crete, 27<sup>th</sup> National Student Chemistry Competition, (March 2013).

2. **Praise** from the Association of Greek Chemists – Peripheral Department of Crete, 26<sup>th</sup> National Student Chemistry Competition, (March 2012).
3. **Appraising Diploma** and **Bronze Medal** from the Greek Mathematical Society, 29<sup>th</sup> National Mathematical Olympiad, School Year 2011-2012.
4. **Appraising Diploma** and **Bronze Medal** from the Greek Mathematical Society, 29<sup>th</sup> National Mathematical Olympiad, School Year 2009-2010.
5. **Excellence Awards** from the Greek Mathematical Society for my performance at the National Mathematical Competition "Archimidis" March 2012 and March 2010.
6. **Awards** from the Greek Mathematical Society for the National Mathematical Competition "Euclidis", school years 2011-2012, 2010-2011, 2009-2010.
7. **Praises** from the Greek Mathematical Society for my performance at the National Mathematical Competition "Thalis", school years 2012-2013, 2011-2012, 2010-2011, 2009-2010, 2008-2009.
8. **Excellence and Progress Awards** from School, school years 2012-2013 (degree 19/20), 2011-2012 (degree 19,6/20), 2010-2011 (degree 19,7/20), 2009-2010 (degree 19,85/20), 2008-2009 (degree 19,85/20), 2007-2008 (degree 19,85/20).

## Βιογραφικό Σημείωμα

### Προσωπικές πληροφορίες

---

**Όνομα:** Εμμανουήλ Ν. Νικολουδάκης  
**Διεύθυνση:** 2 Βαλεντίνου Μπογιατζίδου, Ηράκλειο, Κρήτη, 71305, Ελλάδα.  
**Ημερομηνία γέννησης:** 06 Απριλίου 1995  
**Τόπος γέννησης:** Ηράκλειο Κρήτης, Ελλάδα  
**Εθνικότητα:** Ελληνική  
**Τηλέφωνο:** +30 6986421584  
**Email:** [nik21man@gmail.com](mailto:nik21man@gmail.com), [chemp1025@edu.chemistry.uoc.gr](mailto:chemp1025@edu.chemistry.uoc.gr)

### Εκπαίδευση

---

- 02/2019 – παρόν Υποψήφιος διδάκτορας στην Ανόργανη Χημεία:**  
Εργαστήριο Βιοανόργανης Χημείας, Πανεπιστήμιο Κρήτης,  
Τμήμα Χημείας, Πανεπιστημιούπολη Βουτών, Ηράκλειο.  
Υπ. Καθ. Αθανάσιος Κουτσολέλος.
- 02/2017 – 02/2019 Μεταπτυχιακό δίπλωμα ειδίκευσης στην Ανόργανη Χημεία:**  
Εργαστήριο Βιοανόργανης Χημείας, Πανεπιστήμιο Κρήτης,  
Τμήμα Χημείας, Πανεπιστημιούπολη Βουτών, Ηράκλειο.  
✓ **Τίτλος εργασίας:** Βιο-εμπνευσμένη μοριακή αυτο-  
οργάνωση βασισμένη σε οργανικές και ανόργανες οντότητες.  
Υπ. Καθ. Αθανάσιος Κουτσολέλος.
- 09/2013 - 02/2017 Πτυχίο Χημείας (9.47/10)**  
Πανεπιστήμιο Κρήτης, Τμήμα Χημείας, Πανεπιστημιούπολη  
Βουτών, Ηράκλειο.  
✓ **Τίτλος εργασίας:** Μελέτες νέων καταλυτών και  
φωτοευαισθητοποιητών για φωτοκαταλυτική παραγωγή  
υδρογόνου.  
Μαθήματα: Αρχές Χημείας, Εισαγωγή στην Επιστήμη  
Υπολογιστών, Ποιοτική και Ποσοτική Ανάλυση, Φυσική I & II,  
Αγγλικά για Χημεία I&II, Εισαγωγή στη Βιολογία, Μαθηματικά I

& II, Αναλυτική Χημεία I&II, Οργανική Χημεία I & II, Ανόργανη Χημεία I & II, Φυσικοχημεία I & II, Περιβαλλοντική Χημεία, Βιοχημεία I & II, Χημεία Βιομορίων, Βιοανόργανη Χημεία, Δομή και Ιδιότητες Χαλαρής Συμπυκνωμένης Ύλης, Μεταλλικά Ιόντα στην Ιατρική, Κρυσταλλογραφική Ανάλυση Βιολογικών Μακρομορίων, Χημεία Προηγμένων Υλικών, Ανόργανα Βιοϋλικά, Φασματοσκοπία NMR, Φαρμακευτική Χημεία, Υπολογιστική Χημεία I, Ατμοσφαιρική Χημεία.

Εργαστήρια: Γενικής Χημείας, Οργανικής Χημείας I & II, Ανόργανης Χημείας I & II, Βιοχημείας, Αναλυτικής Χημείας I & II and Φυσικοχημείας I & II.

#### Διδακτική εμπειρία

---

- 06/2021 - 08/2021** **Μεταπτυχιακός Βοηθός Εργαστηρίου**  
Εργαστήριο Γενικής Χημείας, Πανεπιστήμιο Κρήτης, Τμήμα Χημείας, Πανεπιστημιούπολη Βουτών, Ηράκλειο. Υπ. Κορνήλιος Σπυρίδων.
- 10/2020 - 12/2020** **Μεταπτυχιακός Βοηθός Εργαστηρίου**  
Εργαστήριο Ανόργανης Χημείας, Πανεπιστήμιο Κρήτης, Τμήμα Χημείας, Πανεπιστημιούπολη Βουτών, Ηράκλειο. Υπ. Στέλιος Τερζάκης.
- 10/2019 - 01/2020** **Μεταπτυχιακός Βοηθός Μαθήματος**  
Οργανική Χημεία III, Πανεπιστήμιο Κρήτης, Τμήμα Χημείας, Ηράκλειο, Υπ. Καθ. Χαράλαμπος Κατερινόπουλος
- 10/2019 - 01/2020** **Μεταπτυχιακός Βοηθός Εργαστηρίου**  
Εργαστήριο Γενικής Χημείας, Πανεπιστήμιο Κρήτης, Τμήμα Χημείας, Πανεπιστημιούπολη Βουτών, Ηράκλειο. Υπ. Κορνήλιος Σπυρίδων.
- 02/2018 - 05/2018** **Μεταπτυχιακός Βοηθός Εργαστηρίου**  
Εργαστήριο Ανόργανης Χημείας, Πανεπιστήμιο Κρήτης, Τμήμα Χημείας, Πανεπιστημιούπολη Βουτών, Ηράκλειο. Υπ. Ελευθερία Βαρδαλαχάκη.

**02/2017 - 05/2017**      **Μεταπτυχιακός Βοηθός Εργαστηρίου**  
Εργαστήριο Γενικής Χημείας, Πανεπιστήμιο Κρήτης, Τμήμα Χημείας, Πανεπιστημιούπολη Βουτών, Ηράκλειο. Υπ. Κορνήλιος Σπυρίδων.

**02/2015 - 05/2015**      **Προπτυχιακός Βοηθός Εργαστηρίου**  
Εργαστήριο Γενικής Χημείας, Πανεπιστήμιο Κρήτης, Τμήμα Χημείας, Πανεπιστημιούπολη Βουτών, Ηράκλειο. Υπ. Κορνήλιος Σπυρίδων.

✓ Παρασκευή Χημικών Αντιδραστηρίων

### **Ερευνητική Εμπειρία**

---

**08/2021 - 12/2021**      **Ερευνητική υποτροφία στο University of North Texas από το ίδρυμα Fulbright**

1508 W. Mulberry Street, 76201 **Denton, TX United States.**

Supervisor: Prof. Francis D'Souza

✓ Σκοπός επίσκεψης: «*Σύνθεση και φωτοκαταλυτικές μελέτες δυάδων πορφυρινών νικελίου - ρουθηνίου για φωτοεπαγόμενη οξείδωση τυ νερού προς παραγωγή υδρογόνου.*»

**02/2020 - 03/2020**      **Πρακτική άσκηση στο Nantes University με το πρόγραμμα Erasmus+**

**&**

CEISAM / IMF/ 2 rue de la Houssinière, 44322 **Nantes France.**

**09/2020 - 10/2020**      Supervisor: Prof. Fabrice Odobel

✓ Σκοπός επίσκεψης: «*Σύνθεση και μελέτη φωτοηλεκτροχημικών ιδιοτήτων σε δυάδες πορφυρινών-TEMPO για οξείδωση αλκοολών.*»

**09/2017 - 12/2017**      **Πρακτική άσκηση στο CEA στη Grenoble με το πρόγραμμα Erasmus+**

CEA / BIG / LCBM / 17 rue des Martyrs 38054 **Grenoble France.**



Supervisor: Prof. Stéphane Torelli

- ✓ Σκοπός επίσκεψης: «*Σύνθεση, χαρακτηρισμός συμπλόκων του χαλκού με πυρήνα {Cu<sub>2</sub>S} ως μοντέλο N<sub>2</sub>O-αναγωγής.*»

**06/2015 - 08/2015**

### **Μαθητεία σε Εργαστήριο του ΙΤΕ**

Ινστιτούτο ηλεκτρονικής δομής και LASER , Ίδρυμα Τεχνολογίας και Έρευνας, Ελλάδα, Ηράκλειο Κρήτης.

Υπ. Καθ. Πέτρος Ρακιτζής.

- ✓ Σκοπός επίσκεψης: «*Μελέτη προσρόφησης του I<sub>2</sub> σε επικαλυμμένα με πολυμερές τοιχώματα από ασόλι, με μέτρηση της απορρόφησης σε συνθήκες υψηλού κενού.*»

### **Εργασιακή Εμπειρία**

---

**05/2019 - 06/2019**

Ερευνητικό πρόγραμμα: “Encapsulation of Chromophores by Self-assembled Hydrogels with Biomedical Applications” (κωδικός έργου: T1EDK-01504) χρηματοδοτούμενο από το επιχειρησιακό πρόγραμμα Ανταγωνιστικότητα, Επιχειρηματικότητα και Καινοτομία της δράσης ΕΡΕΥΝΩ – ΔΗΜΙΟΥΡΓΩ – ΚΑΙΝΟΤΟΜΩ.

**08/2019 - 03/2022**

Ερευνητικό πρόγραμμα: “Synthesis of new materials for the development of photo-electrochemical devices towards H<sub>2</sub> production and CO<sub>2</sub> reduction” (project code OPS: 5029187) χρηματοδοτούμενο από το περιφερειακό επιχειρησιακό πρόγραμμα “Crete 2014-2020”.

### **Πρόσθετες πληροφορίες**

---

#### **Δημοσιεύσεις**

1. Nikoloudakis E., Pati P. B., Charalambidis G., Budkina D. S., Diring S., Planchat A., Jacquemin D., Vauthey E., Coutsolelos A.G., Odobel F., “Dye-Sensitized Photoelectrosynthesis Cells for Benzyl Alcohol Oxidation Using a Zinc Porphyrin Sensitizer and TEMPO Catalyst”, *ACS Catal.* **2021**, 11, 19, 12075–12086.
2. Nikolaou V., Charalambidis G., Landrou G., Nikoloudakis E., Planchat A., Tsalameni R., Junghans K., Kahnt A., Odobel F., Coutsolelos A.G., “Antenna Effect in BODIPY-(Zn)Porphyrin

- Entities Promotes H<sub>2</sub> Evolution in Dye-Sensitized Photocatalytic Systems”, *ACS Appl. Energy Mater.* **2021**, 4, 9, 10042–10049.
3. Glymenaki E, Kandyli M, Apostolidou C. P., Kokotidou C., Charalambidis G., Nikoloudakis E., Panagiotakis S., Koutserinaki E., Klontza V., Michail P., Charisiadis A., Mitraki A., Coutsolelos A. G., *ACS Omega* **2022**, 7, 2, 1803–1818.
  4. Nikoloudakis E., Charalambidis G., Vasila M., Orfanos E., Angaridis P., Spyroulias G.A., Coutsolelos A.G., “Gadolinium porphyrinate double-deckers for visible light driven H<sub>2</sub> evolution”, *Polyhedron*, **2021**, 208, 115421.
  5. Nikoloudakis E., Pigiaki M., Polychronaki M.N., Margaritopoulou A., Charalambidis G., Serpetzoglou E., Mitraki A., Loukakos P.A., Coutsolelos A.G., “Self-Assembly of Porphyrin Dipeptide Conjugates toward Hydrogen Production”, *ACS Sustain. Chem. Eng.*, **2021**, 9, 7781-7791.
  6. Charisiadis A., Glymenaki E., Planchat A., Margiola S., Lavergne-Bril A., Nikoloudakis E., Nikolaou V., Charalambidis G., Coutsolelos A.G., Odobel F., “Photoelectrochemical properties of dyads composed of porphyrin/ruthenium catalyst grafted on metal oxide semiconductors”, *Dyes Pigm.*, **2021**, 185, 108908.
  7. Ladomenou K., Landrou G., Charalambidis G., Nikoloudakis E. and Coutsolelos A. G., “Carbon dots for photocatalytic H<sub>2</sub> production in aqueous media with molecular Co catalysts”, *Sustain. Energy Fuels*, **2021**, 5, 449-458.
  8. Nikolaou, V., Charalambidis, G., Ladomenou, K., Nikoloudakis, E., Drivas, C., Vamvasakis, I., Panagiotakis, S., Landrou, G., Agapaki, E., Stangel, C., Henkel, C., Joseph, J., Armatas, G., Vasilopoulou, M., Kennou, S., Guldi, D.M. and Coutsolelos, A.G., “Controlling Solar Hydrogen Production by Organizing Porphyrins”, *ChemSusChem*, **2021**, 14, 961-970.
  9. Chang R., Nikoloudakis E., Zou Q., Mitraki A., Coutsolelos A. G.,

- Yan X., “Supramolecular Nanodrugs Constructed by Self-Assembly of Peptide Nucleic Acid-Photosensitizer Conjugates for Photodynamic Therapy” *ACS Appl. Bio Mater.*, **2020**, 3, 1, 2-9.
10. Nikoloudakis E., Orphanos E., Agapaki E., Nikolaou V., Charisiadis A., Charalambidis G., Mitraki A., Coutsolelos A. G., “Molecular self-assembly of porphyrin and BODIPY chromophores connected with diphenylalanine moieties” *J. Porphyr. Phthalocyanines*, **2020** 24(5-7), 775-785.
  11. Nikoloudakis E., Mitropoulou K., Landrou G., Charalambidis G., Nikolaou V., Mitraki A., Coutsolelos A. G., “Self-Assembly of Aliphatic Dipeptides coupled with porphyrin and BODIPY chromophores”, *Chem. Commun.*, **2019**, 55, 14103-14106.
  12. Nikoloudakis E., Karikis K., Kokotidou C., Charisiadis A., Douvas A. M., Mitraki A., Charalambidis G., Yan X., Coutsolelos A. G., “Self-assembling study of PNA-Porphyrin and PNA-BODIPY Hybrids in Mixed Solvent Systems”, *Nanoscale*, **2019**, 11, 3557-3566.
  13. Nikoloudakis E., Karikis K., Laurans M., Kokotidou C., Solé-Daura A., Carbó J. J., Charisiadis A., Charalambidis G., Izzet G., Mitraki A., Douvas A. M., Poblet J. M., Proust A. and Coutsolelos A. G., “Experimental and theoretical study of nanometric spheres from polyoxometalate-phenylalanine hybrids”, *Dalton Trans.*, **2018**, 47, 6304-6313.
  14. Karikis K., Butkiewicz A., Folias F., Charalambidis G., Kokotidou C., Charisiadis A., Nikolaou V., Nikoloudakis E., Frelek J., Mitraki A., Coutsolelos A. G., “Self-assembly of (Boron-dipyrromethane)-diphenylalanine Conjugates Forming Chiral Supramolecular Materials”, *Nanoscale*, **2018**, 10, 1735-1741.
- Συνέδρια**
1. Nikoloudakis E., “Photocatalytic hydrogen production of self-assembled Porphyrin-Dipeptide hybrids”, International Solar Fuels Conference (ISFC) **2021**, 26 - 29 July 2021, **UK**, poster and oral presentation, *Virtual Conference*.

2. Coutsolelos A.G., Nikoloudakis E., Pigiaki M., Polychronaki M.N., Margaritopoulou A., Charalambidis G., Serpetzoglou E., Mitraki A., Loukakos P.A., “Self-assembled porphyrin-dipeptide hybrids produce hydrogen photocatalytically”, 11th International Conference on Porphyrins and Phthalocyanines (**ICPP-11**), 28 June – 3 July **2021, USA, Virtual Meeting**.
3. Nikolaou V., Charalambidis G., Ladomenou K., Nikoloudakis E., Drivas C., Vamvasakis I., Panagiotakis S., Landrou G., Agapaki E., Stangel C., Henkel C., Joseph J., Armatas G., Vasilopoulou M., Kennou S., Guldi D.M., Coutsolelos A.G., “Controlling solar hydrogen production by organizing porphyrins”, 11th International Conference on Porphyrins and Phthalocyanines (**ICPP-11**), 28 June – 3 July **2021, USA, Virtual Meeting**.
4. Charalambidis G., Nikoloudakis E., Charisiadis A., Nikolaou V., Coutsolelos A.G., “Photocatalytic hydrogen evolving systems based on porphyrin derivatives”, 11th International Conference on Porphyrins and Phthalocyanines (**ICPP-11**), 28 June – 3 July **2021, USA, Virtual Meeting**.
5. Joint UK Solar Fuels Network (**SFN**) - SuperSolar Early Career Researcher (**ECR**) Meeting 28 April 2021, London **UK, Virtual Meeting**.
6. Ladomenou K., Landrou G., Charalambidis G., Nikoloudakis E., Coutsolelos A.G., “Carbon dots for photocatalytic H<sub>2</sub> production in aqueous media with molecular Co catalysts”, **ACS Spring Meeting 2021**, 5-16 April 2021, **USA, Virtual Conference**.
7. Charalambidis G., Charisiadis A., Glymenaki E., Planchat A., Margiola S., Nikoloudakis E., Nikolaou V., Coutsolelos A., Odobel F., “Photoelectrochemical properties of dyads composed of porphyrin/ruthenium catalyst grafted on metal oxide semiconductors”, **ACS Spring Meeting 2021**, 5-16 April 2021, **USA, Virtual Conference**.

8. 8<sup>th</sup> UK Solar Fuels Symposium, online conference, 1 December **2020**.
9. Coutsolelos A. G., Nikoloudakis E., Karikis K., Han J., Kokotidou C., Charisiadis A., Folias F., Mitraki A., Charalambidis G., Yan X., 3rd International Solar Fuels Conference (ISF-3) International Conference on Artificial Photosynthesis-2019 (ICARP2019), **Hiroshima, Japan**, 20-24 November **2019**, poster presentation.
10. Nikolaou V., Nikoloudakis E., Mitropoulou K., Charalambidis G., Landrou G., Mitraki A., Coutsolelos A. G., 3rd International Solar Fuels Conference-YOUNG (ISF3-YOUNG), **Hiroshima, Japan**, 19-20 November, **2019**, poster presentation.
11. Nikoloudakis E., “Light driven H<sub>2</sub> production using self-assembled nanostructures of PNA-Porphyrin and PNA-BODIPY hybrids”, 13<sup>th</sup> DEMSEE conference **Heraklion**, 19-20 September **2019**, oral presentation.
12. Nikoloudakis E., Karikis K., Kokotidou C., Charalambidis G., Charisiadis A., Mitraki A., Coutsolelos A. G., 21<sup>th</sup> Postgraduate Conference, Chemistry Department, University of Crete, **Heraklion** 15-17 May **2019**, poster presentation.
13. International Symposium “Chemistry at the Interface of Biology/Medicine”, University of Crete, **Heraklion**, 21-25 September **2018**.
14. Charalambidis G., Karikis K., Nikoloudakis E., Kokotidou C., Charisiadis A., Nikolaou V., Mitraki A., Coutsolelos A.G. PSA-2018: Peptide Self-Assembly: Biology, Chemistry, Materials and Engineering, **Beijing, China**, 23-25 August, **2018**, poster presentation.
15. Coutsolelos, A.G.; Mitraki, A.; Charalambidis, G.; Kokotidou, C.; Karikis, K.; Nikoloudakis, E.; Charisiadis, A., Peptide Self-Assembly: Biology, Chemistry, Materials and Engineering, **Beijing, China**, August 23-25, **2018**,. oral presentation.

16. Nikoloudakis E., Karikis K., Kokotidou C., Charalambidis G., Douvas A. M., Mitraki A., Coutsolelos A. G., ICPP10, **Munich, Germany**, 1 - 6 July, **2018**, poster and invited oral presentation.
17. Nikoloudakis E., 20<sup>th</sup> Postgraduate Conference, Chemistry Department, University of Crete, **Heraklion** 25-27 June **2018**, (organizing committee), oral presentation.
18. 19<sup>th</sup> Postgraduate Conference, Department of Chemistry, University of Crete, **Heraklion** 2-4 May **2017**.
19. 22<sup>th</sup> Hellenic Chemistry Conference, Association of Greek Chemists, **Thessaloniki**, 2-4 December **2016**.
20. International Symposium “Chemistry at the Interface of Biology / Medicine”, University of Crete, **Heraklion**, 23-26 September **2016**.
21. 18<sup>th</sup> Postgraduate Conference, Department of Chemistry, University of Crete, **Heraklion** 26-27 March **2016**.

#### Σεμινάρια

1. 4<sup>th</sup> Microscopy *online* seminar, IIN “Demokritos”, 03/2021.
2. Σεμινάριο *Ασφάλεια Εργαστηρίου* IMBB-ITE, 3/2018, Ηράκλειο
3. *Scientific Writing* workshop, Τμήμα Χημείας, Ηράκλειο, Εαρινό 2018.
4. 4<sup>ο</sup> Μαθηματικό Καλοκαιρινό Σχολείο από 25-31 Ιουλίου 2010, Λεπτοκαρυά Πιερίας, Ελλάδα.
5. English language course, in **Colchester, England**, 22 – 28 July 2009.

#### Υποτροφίες

- Υποτροφία από το ίδρυμα **Fulbright**, για το ταξίδι ως επισκέπτης ερευνητής στο Πανεπιστήμιο University of North Texas, Denton, TX, US, 08/2021 – 12/2021.
- Υποτροφία από τον **ΕΛΚΕ** του **Πανεπιστημίου Κρήτης** για παροχή επικουρικού διδακτικού έργου σε προπτυχιακό εργαστήριο, 06/2021 – 08/2021.
- Υποτροφία από την εταιρία **ΑΔΜΗΕ**, για την μεταπτυχιακή έρευνα σχετιζόμενη με ενέργεια και περιβάλλον, 10/2019 - 9/2020.

- Υποτροφία από το ίδρυμα Ωνάση, Οκτώβριος 2017 για τις μεταπτυχιακές του σπουδές, 10/2017 - 2/2019.
- Υποτροφία κληροδοτήματος “Μαρίας Μιχαήλ Μανασάκη”, για τις μεταπτυχιακές του σπουδές, 3/2017 - 9/2017.
- Υποτροφία κληροδοτήματος “Χρυσάνθου και Αναστασίας Καρύδη” για την επίδοση στις εισαγωγικές πανελλήνιες εξετάσεις 7/2014.

**Γλωσσικές**

**Ελληνικά:** Μητρική γλώσσα

**Δεξιότητες**

**Αγγλικά:** [Michigan Certificate of Proficiency in English & Edexcel level 5]

**Γερμανικά:** [Goethe-Zertifikat B2 & Ελληνικό πιστοποιητικό γλωσσομάθειας Γερμανικά Επίπεδο B2]

**Γαλλικά:** [Level A1]

**Δεξιότητες**

**Πληροφορικής**

- KeyCERT IT Basic Plus, Knowledge of use of *Microsoft Office*™, *Open Office*™, *Origin*, *Chemdraw*, *Topspin*, *ChemSketch*, *Avogardo*, *Mercury*, *TeamViewer*, *Neofox viewer*, *EC-lab*, *Spectragryph*, *Endnote* and *Mendeley* programs.

**Τεχνικές**

**δεξιότητες**

- Σύνθεση, καθαρισμός και χαρακτηρισμός χρωμοφόρων.  
Σύνθεση κάτω από αναερόβιες συνθήκες.
- Φωτοκαταλυτικά και φωτοηλεκτροκαταλυτικά πειράματα.
- Φασματοσκοπίες NMR, UV-Vis, FT-IR και Φθορισμού, GC και MALDI-TOF φασματομετρίας, Κυκλική βολταμετρία.
- Δίπλωμα οδήγησης: B

**Memberships**

- Society of Porphyrins & Phthalocyanines, 2018 – σήμερα.
- Ένωση Ελλήνων Χημικών, 2017 – σήμερα.

**Τιμητικές διακρίσεις και βραβεία**

1. Έπαινος από την Ένωση Ελλήνων Χημικών-Περιφερειακό Τμήμα Κρήτης για τη διάκριση στον 27<sup>ο</sup> Πανελλήνιο Μαθητικό Διαγωνισμό Χημείας (3/2013).
2. Έπαινος από την Ένωση Ελλήνων Χημικών-Περιφερειακό Τμήμα Κρήτης για τη διάκριση στον 26<sup>ο</sup> Πανελλήνιο Μαθητικό Διαγωνισμό Χημείας (3/2012).

**3. Τιμητικό Δίπλωμα και Χάλκινο Μετάλλιο** από την Ελληνική Μαθηματική Εταιρία για την επίδοση στην 29<sup>η</sup> Εθνική Μαθηματική Ολυμπιάδα "Αρχιμήδης" κατά το σχολικό έτος 2011-2012.

**4. Τιμητικό Δίπλωμα και Χάλκινο Μετάλλιο** από την Ελληνική Μαθηματική Εταιρία για την επίδοση στην 27<sup>η</sup> Εθνική Μαθηματική Ολυμπιάδα "Αρχιμήδης" κατά το σχολικό έτος 2009-2010.

**5. Αριστείο** από την Ελληνική Μαθηματική Εταιρία για την επίδοση στον Πανελλήνιο Μαθηματικό διαγωνισμό "Αρχιμήδης", Μάρτιος 2012 και 2010.

**6. Βραβείο** από την Ελληνική Μαθηματική Εταιρία για την επίδοση στον Πανελλήνιο Μαθηματικό διαγωνισμό "Ευκλείδης", σχολικά έτη 2011-2012, 2010-2011, 2009-2010.

**7. Έπαινος** από την Ελληνική Μαθηματική Εταιρία για την επίδοση στον Πανελλήνιο Μαθηματικό διαγωνισμό "Θαλής", σχολικά έτη 2012-2013, 2011-2012, 2010-2011, 2009-2010, 2008-2009.

**8. Αριστείο και Βραβείο** προόδου από το σχολείο, 2012-2013 (βαθμός 19/20), 2011-2012 (βαθμός 19,6/20), 2010-2011 (βαθμός 19,7/20), 2009-2010 (βαθμός 19,85/20), 2008-2009 (βαθμός 19,85/20), 2007-2008 (βαθμός 19,85/20).



## **Abstract**

The present PhD dissertation describes the synthesis of new porphyrin-based hybrid molecules and their utilization in light harvesting applications. The synthesized porphyrin conjugates were modified with functional groups or connected with other entities depending on their target application.

The first aim of this work was the development of well-organized assemblies by covalently connecting a molecular self-assembly inducer to a porphyrinoid chromophore. This approach aims to construct materials with enhanced properties in the self-assembly state. The resulting hybrids possessed both light harvesting and self-assembling properties and were further investigated in applications such as photocatalytic H<sub>2</sub> production and photodynamic therapy. Regarding the self-assembly part, we synthesized and investigated hybrid chromophore conjugates connected with peptide-based molecules. In detail, we utilized aromatic and aliphatic dipeptides as well as peptide nucleic acids (PNAs), bearing various protecting groups, and linked them with porphyrin and boron-dipyrromethene chromophores. From the synthesized hybrids, those coupled with a peptide nucleic acid, were applied in photodynamic therapy *in vitro* after their self-assembly in spherical nanoparticles.

Concerning the photocatalytic hydrogen (H<sub>2</sub>) evolution using self-assembled nanostructures, we covalently attached the diphenylalanine dipeptide to a tripyridyl porphyrin macrocycle, and the resulting hybrid was able to form self-assembling nanostructures. This hybrid was metallated with non-noble metals, Zn and Sn, and investigated towards photo-induced H<sub>2</sub> production. The Sn derivative was able to produce hydrogen photocatalytically in the presence of a cobaloxime catalyst and TEOA as sacrificial electron donor. When the self-assembling nanostructures of the Sn metallated hybrid were employed in the catalysis, the hydrogen production was improved.

The second target investigated herein concerns the development of artificial photosynthetic systems based on porphyrin dyads for light driven oxidation transformations. To that end, several photosensitizer-catalyst dyads were

synthesized, characterized and investigated in dye-sensitized photo-electrochemical (DSPEC) devices for water and alcohol oxidation.

For the photocatalytic water oxidation we synthesized a dyad (NiP-Ru) consisting of a ruthenium tris(bipyridyl),  $[\text{Ru}(\text{bpy})_3]^{2+}$  as photosensitizer, and a nickel porphyrin, as water oxidation catalyst. Photocatalytic experiments in organic solutions demonstrated that the covalently connected dyad exhibited enhanced catalytic activity compared to the non-covalent two-component system. Moreover, a dye sensitized photoelectrochemical cell (PEC) was prepared using the NiP-Ru dyad (bearing appropriate anchoring moiety on the photosensitizer) anchored on  $\text{TiO}_2$  as photoanode and demonstrated its ability to perform water oxidation in aqueous media at neutral pH.

Finally, a series of dyads consisted of a zinc porphyrin (ZnP) sensitizer and a TEMPO organo-catalyst, bearing different anchoring groups on the ZnP, were synthesized.  $\text{TiO}_2$  based dye-sensitized photo-electrochemical (DSPEC) systems were fabricated with these dyads and their catalytic activity in light driven oxidation of methoxybenzyl alcohol into aldehyde was explored. The chemisorbed dyads were proved photocatalytically active towards alcohol oxidation both in aqueous and in organic solutions. The comparison between the intra-molecular dyad system and the intermolecular two-component system revealed that both strategies lead to similar performances. However, the employment dyad is preferable since the recovery of the catalyst is much easier and the quantity of the catalyst involved is much lower.

**Keywords:** Porphyrin, BODIPY, self-assembly, hydrogen production, dye-sensitized photo-electrochemical cells, water oxidation, alcohol oxidation.

## Περίληψη

Η παρούσα διδακτορική διατριβή περιγράφει την σύνθεση νέων πορφυρινικών υβριδικών μορίων και την αξιοποίησή τους σε εφαρμογές δέσμευσης και αξιοποίησης της ηλιακής ακτινοβολίας. Τα συντιθέμενα πορφυρινικά παράγωγα διέθεταν στην περιφέρειά τους κατάλληλες λειτουργικές ομάδες σύμφωνα με την εφαρμογή στην οποία αποσκοπούσαν.

Ο πρώτος στόχος αυτής της εργασίας είναι η κατασκευή καλά οργανωμένων δομών με βελτιωμένες ιδιότητες στην αυτό-οργανωμένη κατάσταση, μέσω της ομοιοπολικής σύνδεσης ενός μορίου που επάγει την αυτό-οργάνωση και ενός πορφυρινικού χρωμοφόρου. Τα υβριδικά μόρια που προέκυψαν είχαν τόσο ικανότητα απορρόφησης της ηλιακής ακτινοβολίας όσο και ικανότητα αυτό-οργάνωσης και μελετήθηκαν σε εφαρμογές όπως η φωτοκαταλυτική παραγωγή υδρογόνου αλλά και η φωτοδυναμική θεραπεία. Σχετικά με το πεδίο της αυτο-οργάνωσης, συνθέσαμε και μελετήσαμε υβριδικά χρωμοφόρα συνδεδεμένα με πεπτίδια ή ανάλογα πεπτιδίων. Πιο συγκεκριμένα αξιοποιήσαμε αρωματικά και αλειφατικά πεπτίδια καθώς και πεπτιδικά νουκλεϊκά οξέα, που έχουν διάφορες προστατευτικές ομάδες, και τα συνδέσαμε με χρωμοφόρα πορφυρινών και βοριο-διπυρρομεθανίων. Τα υβριδικά μόρια έφεραν ένα πεπτιδικό νουκλεϊκό οξύ μελετήθηκαν αρχικά ως προς την ικανότητα αυτο-οργάνωσης και έπειτα εφαρμόστηκαν σε πειράματα φωτοδυναμικής θεραπείας. Έπειτα από ακτινοβόληση αυτές οι αυτό-οργανωμένες δομές αποδείχτηκαν αποδοτικά νανοφάρμακα για φωτοδυναμική θεραπεία *in-vitro*.

Για την αξιοποίηση των αυτο-οργανωμένων νανοδομών στη φωτοκαταλυτική παραγωγή υδρογόνου, συνδέσαμε το διπεπτίδιο της διφαινυλαλανίνης με ένα τριπυρίδυλο πορφυρινικό παράγωγο. Το υβριδικό παράγωγο είχε την ικανότητα να αυτο-οργανώνεται, σχηματίζοντας σφαιρικές νανοδομές. Ο δακτύλιος της πορφυρίνης μεταλλώθηκε με Zn και Sn και τα μεταλλωμένα παράγωγα μελετήθηκαν ως φωτοευαίσθητοποιητές στη φωτοκαταλυτική παραγωγή υδρογόνου. Το μεταλλωμένο με κασσίτερο παράγωγο ήταν σε θέση να παράγει υδρογόνο φωτοκαταλυτικά παρουσία ενός γνωστού καταλύτη κοβαλοξίμης και τριαιθανολαμίνης ως θυσιαστικό δότη ηλεκτρονίων. Όταν οι αυτο-οργανωμένες νανοδομές του μεταλλωμένου με Sn παραγώγου εφαρμόστηκαν στην κατάλυση βελτιώθηκε η απόδοση παραγωγής υδρογόνου.

Ο δεύτερος στόχος που μελετάται στην παρούσα διατριβή σχετίζεται με την ανάπτυξη συστημάτων τεχνητής φωτοσύνθεσης. Πιο συγκεκριμένα, πορφυρινικές δυάδες που έχουν κατάλληλη ομάδα πρόσδεσης, εφαρμόστηκαν σε φωτοκαταλυτικές οξειδωτικές μετατροπές. Για αυτό το σκοπό συντέθηκαν και χαρακτηρίστηκαν διάφορες δυάδες χρωμοφόρου-καταλύτη και μελετήθηκαν σε συσκευές φωτοηλεκτροχημικής οξείδωσης του νερού και αλκοολών.

Για την φωτοκαταλυτική οξείδωση του νερού συντέθηκε μια δυάδα (NiP-Ru) αποτελούμενη από ένα σύμπλοκο του ρουθηνίου  $[Ru(bpy)_3]^{2+}$  ως φωτοευαισθητοποιητή και μια πορφυρίνη του νικελίου ως καταλύτη. Τα φωτοκαταλυτικά πειράματα σε διάλυμα έδειξαν ότι η ομοιοπολικά συνδεδεμένη δυάδα ήταν αποδοτικότερη σε σχέση με το μη ομοιοπολικό σύστημα δύο συστατικών. Κατασκευάστηκε επίσης ένα φωτοηλεκτροχημικό κελί χρησιμοποιώντας τη δυάδα NiP-Ru, μετά την πρόσδεσή της σε ένα ηλεκτρόδιο  $TiO_2$  το οποίο λειτουργεί ως φωτοάνοδος. Οι φωτοκαταλυτικές μελέτες έδειξαν ότι αυτό το σύστημα είναι σε θέση να πραγματοποιεί την οξείδωση του νερού σε ρυθμιστικό διάλυμα με ουδέτερο pH.

Τέλος συντέθηκαν μια σειρά από δυάδες Zn-πορφυρίνης-TEMPO, έχοντας διαφορετικές ομάδες πρόσδεσης πάνω στον πορφυρινικό δακτύλιο, όπου η πορφυρίνη είχε τον ρόλο του φωτοευαισθητοποιητή και το TEMPO ήταν ο οργανοκαταλύτης. Χρησιμοποιώντας αυτές τις δυάδες, κατασκευάστηκαν φωτοηλεκτροχημικά κελιά βασισμένα σε φωτοανόδους  $TiO_2$  και μελετήθηκε η ικανότητά τους να οξειδώνουν την μεθόξυ-βενζυλική αλκοόλη στην αντίστοιχη αλδεΐδη. Οι προσροφημένες δυάδες αποδείχθηκαν φωτοκαταλυτικά δραστικές στην οξείδωση αλκοολών τόσο σε υδατικούς όσο και σε οργανικούς (ακετονιτρίλιο) διαλύτες. Η σύγκριση του ενδομοριακού συστήματος (δυάδα) με ένα διαμοριακό σύστημα δύο συστατικών έδειξε ότι και οι δύο προσεγγίσεις έχουν παραπλήσια απόδοση. Παρόλα αυτά, η χρήση ομοιοπολικά συνδεδεμένων συστημάτων παρουσιάζει μεγαλύτερο ενδιαφέρον καθώς είναι ευκολότερη η ανάκτηση του καταλύτη και παράλληλα απαιτείται λιγότερη ποσότητα από αυτόν.

**Λέξεις κλειδιά:** Πορφυρίνη, BODIPY, αυτό-οργανωση, παραγωγή υδρογόνου, φωτοηλεκτροχημικά κελιά, οξείδωση του νερού, οξείδωση αλκοολών.

## **Table of Contents**

Chapter 1: General Introduction .....	1
1.1 Energy problem .....	1
1.2 Porphyrinoids and their Properties .....	4
1.3 Self-Assembly of chromophores .....	13
1.4 Water splitting: H <sub>2</sub> production and water oxidation.....	17
1.5 Alcohol oxidation .....	20
Chapter 2: Thesis Aims and Structure .....	22
Chapter 3: Self-assembly of chromophores and their applications .....	29
3.1 Synthesis and self-assembling studies.....	32
3.2 Photodynamic therapy systems .....	50
3.3 Photocatalytic H <sub>2</sub> production systems .....	58
3.4 Experimental Section.....	79
Chapter 4: Light driven Oxidation transformations.....	91
4.1 Photocatalytic Water Oxidation .....	91
4.2 Photocatalytic Alcohol Oxidation .....	106
4.3 Experimental Section.....	138
Chapter 5: Conclusions and Perspectives .....	152
Chapter 6: Appendix .....	155

## **Table of Figures in the main text**

<b>Figure 1.1</b> Global energy consumption by source. ....	1
<b>Figure 1.2</b> Global energy potential illustrated by offer per year regarding the renewable energy sources and total reserves for the fossil fuels. ....	2
<b>Figure 1.3</b> Natural photosynthesis in the carbon cycle. ....	3
<b>Figure 1.4</b> Structures of chlorophyll a, heme c, heme b, vitamin B12, cofactor F430. ....	4
<b>Figure 1.5</b> Chemical structure of porphyrin macrocycles along with the number of $\pi$ -electrons implied in aromaticity (depicted in red). ....	5
<b>Figure 1.6</b> Absorption spectra of a free base (black line), a zinc-metallated (blue line) and a tin-metallated (red line) porphyrin. ....	6
<b>Figure 1.7:</b> A simplified Perrin-Jablonski diagram for porphyrin molecules. ....	7
<b>Figure 1.8:</b> Characteristic emission spectra of a free base (black line) and a zinc metallated (red line). ....	7
<b>Figure 1.9</b> Synthesis of the A <sub>2</sub> BC porphyrins. ....	11
<b>Figure 1.10:</b> General structure of BDP derivatives. ....	12
<b>Figure 1.11:</b> Representative absorption and emission spectra of a BDP derivative. ....	12
<b>Figure 1.12:</b> The two synthetic pathways (A and B) for the preparation of BDP dyes. ....	13
<b>Figure 1.13:</b> The self-assembly of bacteriochlorophylls in green sulfur bacteria: a) photosynthetic antenna assembly of chlorosomes, b) chlorosome, c) tubular assemblies of bacteriochlorophylls and d) molecular structure of bacteriochlorophyll-c. ....	14
<b>Figure 1.14:</b> Example of porphyrin self-assembly based on ionic electrostatic interactions. ..	15
<b>Figure 1.15:</b> Schematic illustration the “good-bad” solvent self-assembly protocol. ....	16
<b>Figure 1.16</b> a) Schematic illustration photoelectrochemical water splitting cell, b) tandem dye-sensitized photoelectrochemical cell for water splitting consisting of catalyst-photosensitizer dyads. ....	18
<b>Figure 1.17</b> Schematic illustration of photochemical water splitting cell. ....	18
<b>Figure 1.18</b> Simplified scheme for photocatalytic water oxidation (a) and photocatalytic hydrogen evolution (b). ....	19
<b>Figure 1.19</b> Simplified scheme for photocatalytic alcohol oxidation in a DSPEC device. ....	21
<b>Figure 2.1</b> Graphic illustration of bio-inspired solar energy utilization schemes investigated in the present thesis. ....	22
<b>Figure 2.2</b> Chromophore-peptide based hybrid compounds investigated in this thesis. ....	23
<b>Figure 2.3</b> Chromophore-catalyst dyads for water and alcohol oxidation. ....	24
<b>Figure 2.4</b> Schematic illustration of supramolecular nanoparticles constructed by self-assembly of PNA-photosensitizer conjugates for photodynamic therapy. ....	25
<b>Figure 2.5</b> Schematic illustration of the photocatalytic system for hydrogen production utilizing the supramolecular nanostructures of porphyrin-diphenylalanine hybrids. ....	26
<b>Figure 2.6</b> Schematic illustration of the <b>NiP-Ru</b> DSPEC system for water oxidation. ....	27
<b>Figure 2.7</b> Schematic illustration of the <b>ZnP-TEMPO</b> DSPEC system for alcohol oxidation. ....	28
<b>Figure 3.1.1</b> <b>Fmoc-FF-TPP</b> self-assembles into spheres or fibers depending on the solvent system. ....	30
<b>Figure 3.1.2</b> <b>TPP-G-FF</b> self-assembles into nanodots with high light-to-heat conversion efficiency providing a remote-controlled way to destroy carcinomatous cells and tissues. <sup>19</sup> . ....	30
<b>Figure 3.1.3</b> Chemical structures of Isoleucine-Isoleucine and Alanine-Isoleucine. ....	31
<b>Figure 3.1.4</b> PNA self-assembled nanospheres have properties of photonic crystals. ....	31
<b>Figure 3.1.5</b> The structures and size distributions of the PNA-BDP NPs and PNA-TPP NPs. (a) TEM image and (b) SEM image of the PNA-BDP NPs. (c) DLS profile of the PNA-BDP NPs with a picture of the sample shown in the inset. (d) TEM image and (e) SEM image of the PNA-TPP NPs. (f) DLS profile of the PNA-TPP NPs with a picture of the sample shown in the inset. ....	34
<b>Figure 3.1.6</b> Self-assembly behavior of <b>Py<sub>3</sub>P-FF</b> in (a) DCM-MeOH 2:8, (b) HFIP-MeOH 2:8, (c) DCM-Heptane 2:8, (d) THF-MeOH 2:8. ....	36

<b>Figure 3.1.7</b> Self-assembly behavior of <b>Py<sub>3</sub>P-FF</b> in (a) DCM-MeOH 2:8, (b) HFIP-MeOH 2:8, (c) DCM-Heptane 2:8.....	37
<b>Figure 3.1.8</b> Self-assembly behavior of <b>SnPy<sub>3</sub>P-FF</b> in (a) DCM-MeOH 2:8, (b) HFIP-MeOH 2:8, (c) DCM-Heptane 2:8, (d) THF-MeOH 2:8.....	38
<b>Figure 3.1.9</b> Self-assembly behavior of <b>SnPy<sub>3</sub>P-FF</b> in (a) DCM-MeOH 2:8, (b,c) HFIP-MeOH 2:8, (d) THF-MeOH 2:8, (e) DCM-Heptane 2:8, (f) DCM solution.....	38
<b>Figure 3.1.10</b> Self-assembly behavior of <b>ZnPy<sub>3</sub>P-FF</b> in (a) DCM-MeOH 2:8, (b) HFIP-MeOH 2:8, (c) DCM-Heptane 2:8, (d) THF-MeOH 2:8.....	39
<b>Figure 3.1.11</b> Normalized absorption spectra of <b>Py<sub>3</sub>P-FF</b> (a) and <b>SnPy<sub>3</sub>P-FF</b> (b) in solution (black line) and in self-assembled states.....	39
<b>Figure 3.1.12</b> Normalized emission spectra of <b>Py<sub>3</sub>P-FF</b> (a) and <b>SnPy<sub>3</sub>P-FF</b> (b) in solution (black line) and in self-assembled states.....	40
<b>Figure 3.1.13</b> Normalized absorption (a) and emission (b) spectra of <b>ZnPy<sub>3</sub>P-FF</b> in solution (black line) and in self-assembled states.....	40
<b>Figure 3.1.14</b> Self-assembly behavior of <b>FmocFF-ZnTPP</b> in (a) THF-MeOH 2:8, (b) DCM-Heptane 1:1 and (c) <b>FmocFF-FeTPP</b> in DCM-Heptane 1:1.....	42
<b>Figure 3.1.15</b> SEM images of a) <b>Boc-Ile-Ile-BDP</b> in HFIP-EtOH 2:8, b) <b>Boc-Ile-Ile-BDP</b> in HFIP-MeOH 2:8, c) <b>Boc-Ala-Ile-BDP</b> in HFIP-EtOH 2:8, d) <b>Boc-Ala-Ile-BDP</b> in HFIP-MeOH 2:8.....	45
<b>Figure 3.1.16</b> Self-assembly behavior of (a) <b>Boc-Ala-Ile-BDP</b> in HFIP-H <sub>2</sub> O 2:8, (b) <b>Boc-Ile-Ile-BDP</b> in HFIP-H <sub>2</sub> O 2:8.....	45
<b>Figure 3.1.17</b> Self-assembly behavior of (a) <b>Fmoc-Ile-Ile-BDP</b> in HFIP-MeOH 2:8, (b) <b>Fmoc-Ile-Ile-BDP</b> in HFIP-EtOH 2:8, (c) <b>Fmoc-Ile-Ile-BDP</b> in HFIP-H <sub>2</sub> O 2:8, (d) <b>Fmoc-Ala-Ile-BDP</b> in HFIP-H <sub>2</sub> O 2:8.....	46
<b>Figure 3.1.18</b> Normalized absorbance spectra of <b>Boc-Ile-Ile-BDP</b> (a) and <b>Boc-Ala-Ile-BDP</b> (b) in solution (red line) and in self-assembled state.....	46
<b>Figure 3.1.19</b> Normalized emission spectra of <b>Boc-Ile-Ile-BDP</b> (a) and <b>Boc-Ala-Ile-BDP</b> (b) in solution (red line) and in self-assembled state.....	47
<b>Figure 3.1.20</b> Normalized emission spectra of <b>Fmoc-Ile-Ile-BDP</b> (a) and <b>Fmoc-Ala-Ile-BDP</b> (b) in solution (black line) and in self-assembled states.....	47
<b>Figure 3.1.21</b> Self-assembly behavior of <b>Fmoc-Lys(palmitoyl)-TPP</b> in (a) DCM-MeOH 2:8, (b) DCM-Heptane 2:8, (c) THF-MeOH 2:8, (d) THF-Heptane 2:8.....	49
<b>Figure 3.2.1</b> UV/Vis absorption spectra of (a) the PNA-BDP NPs and molecular PNA-BDP and (b) PNA-TPP NPs and molecular PNA-TPP. DLS size profiles of (c) the PNA-BDP and (d) PNA-TPP NPs under diluted concentrations. DLS size profiles of (e) the PNA-BDP NPs and (f) PNA-TPP NPs dispersed in water and in DMEM showing that the samples are highly stable in the presence of DMEM.....	53
<b>Figure 3.2.2</b> Emission spectra of (a) PNA-BDP NPs versus molecular PNA-BDP in DMSO solution and (b) PNA-TPP NPs versus molecular PNA-TPP in DMSO solution.....	54
<b>Figure 3.2.3</b> CLSM images showing in vitro fluorescence of the PNA-BDP NPs. The cells were incubated with the PNA-BDP NPs and imaged by CLSM at various time points. Scale bars represent 30 μm.....	55
<b>Figure 3.2.4</b> (a) CLSM images of MCF-7 cells that have been incubated with the PNA-TPP NPs for various time periods. Scale bars denote 30 μm. (b) CLSM image of MCF-7 cells incubated with the PNA-TPP NPs for 24 h followed by the staining with both Hoechst 33342 and Alexa 488.....	55
<b>Figure 3.2.5</b> (a) Bright field (left) and CLSM (right) images showing selective PDT effect of the PNA-BDP NPs on MCF-7 cells. (b) Viability of MCF-7 cells incubated with the PNA-BDP NPs and treated with or without light irradiation. (c) Bright field (left) and CLSM (right) images showing selective PDT effect of the PNA-TPP NPs on MCF-7 cells. (d) Viability of MCF-7 cells incubated with the PNA-TPP NPs and treated with or without light irradiation.....	57
<b>Figure 3.3.1</b> Photocatalytic hydrogen production plots of <b>SnPy<sub>3</sub>P-FF</b> in self-assembled states and in solid state. The photocatalytic experiments were conducted in a 1:1 CH <sub>3</sub> CN:H <sub>2</sub> O solvent	

mixture containing 5% (v/v) TEOA at pH=7. The concentrations of the porphyrin PS was $8 \times 10^{-5}$ M and [Co(dmgH) <sub>2</sub> (Cl)(Py)] catalyst was $9.8 \times 10^{-4}$ M. ....	60
<b>Figure 3.3.2</b> TA spectra of <b>SnPy<sub>3</sub>P-FF</b> in water at different delay times ( $t_D$ : -4 ps (green line), 323 ps (black line), 492 ps (red), 696 ps (blue line), 824 ps (magenta line). ....	61
<b>Figure 3.3.3</b> Energy diagram depicting the fundamental photophysical processes of porphyrins following excitation in the Soret band ( $\lambda_{exc} = 395$ nm). Energy values of singlet and triplet states are based on experimental and computational studies. ....	62
<b>Figure 3.3.4</b> Emission spectra of <b>SnPy<sub>3</sub>P-FF</b> in CH <sub>3</sub> CN-H <sub>2</sub> O 1:1 after excitation at Soret (426 nm) and the first Q band (550 nm) where ( $A_{426nm} = A_{550nm} = 0.11$ ). ....	63
<b>Figure 3.3.5</b> Normalized kinetic curves of <b>SnPy<sub>3</sub>P-FF</b> sample (blue line, $4 \times 10^{-5}$ M) and <b>SnPy<sub>3</sub>P-FF</b> –[Co(dmgH) <sub>2</sub> (Cl)(Py)] catalyst ( <b>SnPy<sub>3</sub>P-FF</b> –Co) sample (red line), probing at 450 nm. ....	64
<b>Figure 3.3.6</b> Energy diagram indicating main photophysical processes occurring following excitation of <b>SnPy<sub>3</sub>P-FF</b> –Co at 395 nm. ....	65
<b>Figure 3.3.7</b> <sup>1</sup> H NMR in CD <sub>3</sub> CN of <b>SnPy<sub>3</sub>P-FF</b> before (red line) and after the addition of 10 equivalents of [Co(dmg) <sub>2</sub> CIPy] cobaloxime. ....	66
<b>Figure 3.3.8</b> Structural proposition of the ‘complex’ between the self-assembled tin-porphyrin with cobaloxime. ....	67
<b>Figure 3.3.9</b> Emission spectra of <b>SnPy<sub>3</sub>P-FF</b> in CH <sub>3</sub> CN-H <sub>2</sub> O 1:1 ( $8 \times 10^{-6}$ M) after excitation the first Q band (550 nm) where $A_{550nm} = 0.09$ (blue line), after adding only TEOA (red line, 0.5% v/v), after adding only the cobaloxime catalyst (black line, $9.8 \times 10^{-5}$ M). ....	68
<b>Figure 3.3.10</b> Structures of the gadolinium porphyrin double deckers and monomers that were studied in this work. ....	70
<b>Figure 3.3.11</b> Powder XRD patterns of all studied compounds. The data for TbH(TPP) <sub>2</sub> were obtained from the literature. ....	71
<b>Figure 3.3.12</b> FT-IR spectra of all studied compounds. ....	72
<b>Figure 3.3.13</b> FT-IR spectra of <b>GdH(TPyP)<sub>2</sub></b> , <b>Gd(TPyP)acac</b> , <b>GdH(TPP)<sub>2</sub></b> and <b>Gd(TPP)acac</b> . ....	72
<b>Figure 3.3.14</b> FT-IR spectra of <b>GdH(OBP)<sub>2</sub></b> and <b>Gd(OBP)acac</b> . ....	73
<b>Figure 3.3.15</b> (a) Photocatalytic hydrogen production plots of the gadolinium porphyrin complexes studied herein. The photocatalytic experiments were conducted in a water with ascorbic acid 1 M at pH=4. Each experiment contained 2.5 mg of the porphyrin photosensitizer and 5% w/w of Na <sub>2</sub> PtCl <sub>6</sub> ·6H <sub>2</sub> O as co-catalyst, (b) Cycling runs for the photocatalyzed hydrogen evolution of <b>GdH(TPyP)<sub>2</sub></b> . ....	74
<b>Figure 3.3.16</b> SEM images of (a) <b>GdH(TPyP)<sub>2</sub></b> , (b) <b>Gd(TPP)acac</b> , (c) <b>Gd(TPyP)acac</b> , (d) <b>GdH(TPP)<sub>2</sub></b> , (e) <b>Gd(Br<sub>8</sub>TPP)acac</b> and (f) <b>GdH(Br<sub>8</sub>TPP)<sub>2</sub></b> . ....	76
<b>Figure 3.3.17</b> SEM images of (a) <b>GdH(TPyP)<sub>2</sub></b> in DCM-MeOH 1:1, (b) <b>GdH(TPyP)<sub>2</sub></b> in DCM-Heptane 1:1, (c) <b>Gd(TPP)acac</b> in DCM-MeOH 1:1 and (d) <b>Gd(TPP)acac</b> in DCM-Heptane 1:1. ....	77
<b>Figure 3.3.18</b> SEM images of <b>GdH(TPP)<sub>2</sub></b> (a) in water, (b) in DCM-Heptane 1:1 and (c) in DCM-MeOH 1:1. ....	77
<b>Figure 4.1</b> Oxidation and reduction reactions in photosynthesis and water splitting. ....	91
<b>Figure 4.2</b> Chemical structures of water-soluble nickel porphyrin photocatalysts for water oxidation and [Ru(bpy) <sub>3</sub> ] <sup>2+</sup> photosensitizer. ....	93
<b>Figure 4.3</b> DSPEC for water oxidation utilizing ruthenium based catalyst and photosensitizer. ....	94
<b>Figure 4.4</b> Absorption spectrum of <b>NiP-Ru</b> dyad, <b>NiP</b> and <b>Ru-bpy</b> in DMF. ....	98
<b>Figure 4.5</b> Emission intensity of <b>Ru-bpy</b> (blue line) and <b>NiP-Ru</b> dyad (red line) after excitation at 480 nm, recorded in DMF solutions with a concentration of 0.01 mM of individual compounds. ....	98
<b>Figure 4.6</b> Spectral changes observed during (a) first oxidation of <b>NiP</b> and (b) first reduction of <b>Ru-bpy</b> in benzonitrile containing 0.2 M (TBA)ClO <sub>4</sub> . ....	100
<b>Figure 4.7</b> Femtosecond TA spectra at the indicated delay times of (a) <b>Ru-bpy</b> ( $\lambda_{ex} = 464$ nm), (b) <b>NiP</b> ( $\lambda_{ex} = 424$ nm) and (c) <b>NiP-Ru</b> dyad ( $\lambda_{ex} = 464$ nm) in benzonitrile. ....	100



<b>Figure 4.8</b> a) UV-Vis spectral changes observed during electron pooling experiment. <b>NiP-Ru</b> dyad containing methyl viologen in DMF as a function of irradiation time is shown. A 450 W Xe lamp with a 400 nm filter was used, b) changes of the absorption maxima at 608 nm, attributed to MV <sup>+</sup> , versus the irradiation time for covalently linked <b>NiP-Ru</b> dyad and 1:1 mixture of <b>NiP</b> and <b>Ru-bpy</b> revealing much improved photocatalytic effect by the dyad. ...	102
<b>Figure 4.9</b> a) UV-Vis spectra of <b>NiP</b> and <b>Rubpy</b> photocatalytic system in DMF before and after irradiation with Xenon lamp (in the presence of Methyl Viologen), b) photograph of the UV-Vis cell where the blue color of MV <sup>+</sup> is easily seen. ....	102
<b>Figure 4.10</b> O <sub>2</sub> evolution during photocatalytic H <sub>2</sub> O oxidation after irradiation with a 450 W Xenon lamp (cut-off filter $\lambda > 400$ nm). All solutions besides the <b>NiP-Ru</b> on TiO <sub>2</sub> /FTO (magenta line) contained 50 mM of MV in DMF and 4% H <sub>2</sub> O. ....	103
<b>Figure 4.11</b> a) Photocatalytic O <sub>2</sub> evolution plots versus irradiation time using <b>NiP-Ru</b> dyad under different concentrations, (b) O <sub>2</sub> evolution rate as a function of the dyad concentration. Conditions: 50 mM of MV in DMF and 4% H <sub>2</sub> O. ....	104
<b>Figure 4.12</b> photoelectrochemical performance illustrated by light on and off experiments from TiO <sub>2</sub> (1 cm <sup>2</sup> ) on FTO sensitized with <b>NiP-Ru</b> dyad, and <b>Ru-bpy</b> reference after applying 0 V versus Ag/AgCl reference electrode in phosphate buffer of pH = 7. ....	104
<b>Figure 4.13</b> DSPEC system for alcohol oxidation reported by Meyer and co-workers. ....	108
<b>Figure 4.14</b> Structures of the compounds used in this paragraph. ....	110
<b>Figure 4.15</b> <sup>1</sup> H-NMR spectra which verify the hydrolysis of the phosphoric ester group for the synthesis of <b>PO(OH)<sub>2</sub>-ZnP-TEMPO</b> dyad. ....	113
<b>Figure 4.16</b> UV-Vis absorption spectrum (a) and overlay of the absorption and emission spectra ( $\lambda_{exc} = 430$ nm) (b) of <b>HO<sub>2</sub>C-ZnP-TEMPO</b> in THF. ....	115
<b>Figure 4.17</b> Emission spectra recorded in THF from isoabsorbing solutions at the excitation wavelength with $\lambda_{exc} = 556$ nm of (a) <b>HO<sub>2</sub>C-ZnP</b> and <b>HO<sub>2</sub>C-ZnP-TEMPO</b> and (b) of <b>hyd-ZnP</b> and <b>hyd-ZnP-TEMPO</b> . ....	116
<b>Figure 4.18</b> Overlay of cyclic voltammograms of (a) <b>HO<sub>2</sub>C-ZnP</b> and <b>HO<sub>2</sub>C-ZnP-TEMPO</b> and (b) <b>hyd-ZnP</b> and <b>hyd-ZnP-TEMPO</b> , chemisorbed on meso-ITO and recorded in acetonitrile with LiClO <sub>4</sub> (0.1 M) as supporting electrolyte solutions. ....	117
<b>Figure 4.19</b> Cyclic voltammograms of <b>HO<sub>2</sub>C-ZnP-TEMPO</b> chemisorbed on meso-ITO and recorded in acetonitrile with LiClO <sub>4</sub> (0.1 M) as supporting electrolyte solutions without (red trace) and with methoxybenzyl-alcohol (black trace). Scan rate 50 mV/s. ....	117
<b>Figure 4.20</b> Cyclic voltammograms and square wave spectra of <b>HO<sub>2</sub>C-ZnP-TEMPO</b> and <b>hyd-ZnP-TEMPO</b> in DCM solution. ....	117
<b>Figure 4.21</b> Cyclic voltammograms and square wave spectra of <b>hyd-ZnP</b> and <b>NH<sub>2</sub>-TEMPO</b> in DCM solution. ....	118
<b>Figure 4.22</b> Fs-ps transient absorption spectra recorded at various time delays after 550 nm excitation of TiO <sub>2</sub> films with high (A) and low (B) concentrations of adsorbed <b>hyd-ZnP-TEMPO</b> . The gray line in A represents the stimulated emission spectrum in acetonitrile. The inset in B shows the time evolution of the absorbance of the porphyrin cation band at 405 nm. ....	119
<b>Figure 4.23</b> ns- $\mu$ s transient absorption spectra recorded at various time delays after 532 nm excitation of a TiO <sub>2</sub> film with a low concentration of adsorbed <b>hyd-ZnP-TEMPO</b> . The inset shows the time evolution of the absorbance of the porphyrin cation band at 410 nm. ....	120
<b>Figure 4.24</b> Pictures of the fabricated DSSCs. ....	121
<b>Figure 4.25</b> Pictures of a <b>hyd-ZnP-TEMPO</b> chemisorbed on the nanocrystalline TiO <sub>2</sub> films. ....	123
<b>Figure 4.26</b> Photocurrent density responses during long-term photolysis experiments with TiO <sub>2</sub> photoelectrodes coated with the dyads <b>hyd-ZnP-TEMPO</b> , <b>HOOC-ZnP-TEMPO</b> , <b>H<sub>2</sub>O<sub>3</sub>P-ZnP-TEMPO</b> and <b>hyd-ZnP</b> and <b>HOOC-ZnP</b> reference compounds in 0.1 M borate buffer pH = 9 containing <i>para</i> -methoxybenzyl alcohol (50 mM) and [NaClO <sub>4</sub> ] = 0.1 M. All experiments were recorded under white light with a 400 nm cutoff filter. ....	124
<b>Figure 4.27</b> Chopped light voltammetry measurements recorded at a constant potential of 0 V vs. SCE of TiO <sub>2</sub> photoelectrodes coated with <b>HOOC-ZnP-TEMPO</b> , <b>H<sub>2</sub>O<sub>3</sub>P-ZnP-TEMPO</b> and <b>Py<sub>3</sub>ZnP-TEMPO</b> in 0.1 M borate buffer buffer at pH = 9 containing [ <i>para</i> -methoxybenzyl	

alcohol] = 50 mM, [NaClO <sub>4</sub> ] = 0.1. All experiments were recorded under light with a 400 nm cutoff filter.....	125
<b>Figure 4.28</b> Chopped light linear sweep voltammetry measurements recorded under white light irradiation (white light Zhaner lamp about 350 W/m <sup>2</sup> ) of <b>HOOC-ZnP-TEMPO</b> , <b>H<sub>2</sub>O<sub>3</sub>P-ZnP-TEMPO</b> and <b>Py<sub>3</sub>ZnP-TEMPO</b> on TiO <sub>2</sub> film with 0.1 M borate buffer at pH = 9 containing [ <i>para</i> -methoxybenzyl alcohol] = 50 mM, [NaClO <sub>4</sub> ] = 0.1 M. Scan starts from -0.5 V and ends at 0.3 V vs. SCE with scan rate 5 mV/s.....	125
<b>Figure 4.29</b> Photocurrent density responses during long-term photolysis experiments with TiO <sub>2</sub> photoelectrodes coated with the dyad <b>hyd-ZnP-TEMPO</b> , containing <i>para</i> -methoxybenzyl alcohol (50 mM) in 0.1 M borate buffer (red trace) and 0.1 M carbonate buffer both at pH = 10. ....	126
<b>Figure 4.30</b> Photocurrent density responses during long-term photolysis experiments with TiO <sub>2</sub> photoelectrodes coated with the dyad <b>hyd-ZnP-TEMPO</b> , containing <i>para</i> -methoxybenzyl alcohol (50 mM) in 0.1 M borate buffer (red trace) and 0.1 M carbonate buffer both at pH = 10. ....	126
<b>Figure 4.31</b> Typical photocurrent density responses during long-term photolysis experiments with TiO <sub>2</sub> photoelectrodes coated with hyd-ZnP-TEMPO in 0.1 M borate buffer containing <i>para</i> -methoxybenzyl alcohol (50 mM) and [NaClO <sub>4</sub> ] = 0.1 M at different pHs. All experiments were recorded in the same irradiation conditions: white light (about 100 mW/cm <sup>2</sup> ) with a 400 nm cutoff filter.....	128
<b>Figure 4.32</b> Chopped light linear sweep voltammetry measurements recorded under white light irradiation (white light Zhaner lamp about 350 W/m <sup>2</sup> ) of <b>hyd-ZnP-TEMPO</b> and <b>hyd-ZnP</b> on TiO <sub>2</sub> film with 0.1 M borate buffer at pH = 8 containing [ <i>para</i> -methoxybenzyl alcohol] = 50 mM, [NaClO <sub>4</sub> ] = 0.1 M. Scan starts from -0.5 V and ends at 0.3 V vs. SCE with scan rate 5 mV/s. ....	129
<b>Figure 4.33</b> Chopped light voltammetry measurements of <b>hyd-ZnP-TEMPO</b> recorded at a constant potential of 0 V vs. SCE with (red trace) and without (black trace) <i>para</i> -methoxybenzyl alcohol (10 mM) in the same conditions as above ( <b>Figure 4.32</b> ).....	130
<b>Figure 4.34</b> IPCE spectrum of <b>hyd-ZnP-TEMPO</b> recorded at a constant potential of 0 V vs. SCE in borate buffer at pH = 8 and its and absorption spectrum recorded on thin (4 μm) monocrystalline TiO <sub>2</sub> film without scattering layer. ....	131
<b>Figure 4.35</b> Chopped light voltammetry measurements of <b>hyd-ZnP-TEMPO</b> recorded at a constant potential of 0 V vs. SCE in presence of different concentrations of (A) 2,6-lutidine and (B) N-methyl-imidazole in acetonitrile recorded under white light irradiation (1000 W/m <sup>2</sup> ) with <i>para</i> -methoxybenzyl alcohol (10 mM) and [LiClO <sub>4</sub> ] = 0.1 M.....	132
<b>Figure 4.36</b> Typical photocurrent density responses during long-term photolysis experiments with TiO <sub>2</sub> photoelectrodes recorded in either aqueous 0.1 M borate buffer at pH = 8 with [NaClO <sub>4</sub> ] = 0.1 M or in acetonitrile electrolyte containing [ <b>Me-Imd</b> ] = 0.1 M and [LiClO <sub>4</sub> ] = 0.1 M. ....	133
<b>Figure 4.37</b> Typical photocurrent density responses of <b>hyd-ZnP-TEMPO</b> during long-term photolysis experiments in 0.1 M borate buffer at pH = 8 (left) or in acetonitrile in presence of 0.1 M of Me-Imd (right) with different benzyl alcohol substrates (50 mM). Irradiation conditions: white light (about 100 mW/cm <sup>2</sup> ). ....	134
<b>Figure 4.38</b> Chopped light linear sweep voltammetry measurements recorded under white light irradiation (about 1000 W/m <sup>2</sup> ) at a constant potential of 0 V vs. SCE with of <b>hyd-ZnP</b> on TiO <sub>2</sub> film in acetonitrile containing [ <i>para</i> -methoxybenzyl alcohol] = 50 mM, [LiClO <sub>4</sub> ] = 0.1 M, [MeImd]=0.1 M with increasing concentration of <b>ac-TEMPO</b> .....	136
<b>Figure 5.1</b> Chemical structures of the proposed <b>Fmoc-FF-SnPy<sub>3</sub>P</b> and <b>Fmoc-Ile-Ile-SnPy<sub>3</sub>P</b> hybrids as photosensitizers for photocatalytic H <sub>2</sub> production. ....	152
<b>Figure 5.2</b> Chemical structure of the proposed <b>Fmoc-FH-Co</b> hybrid as catalyst for photocatalytic H <sub>2</sub> production.....	153
<b>Figure 5.3</b> Chemical structure of the proposed <b>NiF<sub>6</sub>P-Ru-CONOH</b> dyad for photocatalytic water oxidation.....	153
<b>Figure 5.4</b> Chemical structure of the proposed <b>hyd-ZnP-BDP(Im)-TEMPO</b> dyad for photocatalytic alcohol oxidation.....	154

## Table of Schemes in the main text

<b>Scheme 1.1</b> Synthesis of 5,10,15,20-tetraphenylporphyrin (TPP) by Rothemund. ....	8
<b>Scheme 1.2</b> Synthesis of 5,10,15,20-tetraphenylporphyrin by Adler, Longo and coworkers... ..	9
<b>Scheme 1.3</b> Synthesis of unsymmetrical porphyrins via mixed condensation reaction of two different aldehydes and pyrrole. ....	9
<b>Scheme 1.4</b> Lindsey's method for the preparation of TPP. ....	10
<b>Scheme 1.5</b> Lindsey's method for the preparation of dipyrromethanes. ....	11
<b>Scheme 3.1.1</b> Synthesis of <b>PNA-TPP</b> and <b>PNA-BDP</b> . ....	33
<b>Scheme 3.1.2</b> Synthesis of <b>Py<sub>3</sub>P-FF</b> , <b>SnPy<sub>3</sub>P-FF</b> and <b>ZnPy<sub>3</sub>P-FF</b> . ....	35
<b>Scheme 3.1.3</b> Synthesis of <b>FmocFF-ZnTPP</b> , <b>FmocFF-FeTPP</b> . ....	41
<b>Scheme 3.1.4</b> Concept for the study of the dipeptide-BDP hybrids. ....	43
<b>Scheme 3.1.5</b> Synthetic approach for the synthesis of <b>Boc-Ala-Ile-BDP</b> and <b>Boc-Ile-Ile-BDP</b> . ....	43
<b>Scheme 3.1.6</b> Synthetic approach for the synthesis of <b>Fmoc-Ala-Ile-BDP</b> and <b>Fmoc-Ile-Ile-BDP</b> . ....	44
<b>Scheme 3.1.7</b> Synthetic approach for the synthesis of <b>Fmoc-Lys(palmitoyl)-TPP</b> . ....	48
<b>Scheme 3.2.1</b> Schematic illustration of supramolecular nanoparticles constructed by self-assembly of PNA-photosensitizer conjugates for photodynamic therapy. ....	52
<b>Scheme 3.3.1</b> Possible oxidative and reductive quenching pathways for photosensitized H <sub>2</sub> production by <b>GdH(TPyP)<sub>2</sub></b> and <b>Gd(TPP)acac</b> . ....	75
<b>Scheme 3.4.1</b> The experimental procedure that we followed to synthesize <b>PNA-BDP</b> . ....	79
<b>Scheme 3.4.2</b> The experimental procedure that we followed to synthesize <b>PNA-TPP</b> . ....	80
<b>Scheme 3.4.3</b> The experimental procedure that we followed to synthesize <b>Py<sub>3</sub>P-FF</b> . ....	81
<b>Scheme 3.4.4</b> The experimental procedure that we followed to synthesize <b>ZnPy<sub>3</sub>P-FF</b> . ....	82
<b>Scheme 3.4.5</b> The experimental procedure that we followed to synthesize <b>SnPy<sub>3</sub>P-FF</b> . ....	83
<b>Scheme 3.4.6</b> The experimental procedure for the synthesis of <b>Boc-Ala-Ile-BDP</b> . ....	84
<b>Scheme 3.4.7</b> The experimental procedure for the synthesis of <b>Boc-Ile-Ile-BDP</b> . ....	85
<b>Scheme 3.4.8</b> The experimental procedure for the synthesis of <b>Fmoc-Ala-Ile-BDP</b> . ....	86
<b>Scheme 3.4.9</b> The experimental procedure for the synthesis of <b>Fmoc-Ile-Ile-BDP</b> . ....	87
<b>Scheme 3.4.10</b> The experimental procedure for <b>Fmoc-Lys(palmitoyl)-TPP</b> synthesis. ....	88
<b>Scheme 3.4.11</b> The experimental procedure for the synthesis of <b>FmocFF-FeTPP</b> . ....	88
<b>Scheme 4.1</b> Structures of <b>NiP-Ru</b> dyad, nickel tetra-toulylporphyrin, <b>NiP</b> , and ruthenium complex, <b>Ru-bpy</b> controls. ....	95
<b>Scheme 4.2</b> a) Energy diagram of the <b>NiP-Ru</b> dyad derived photo-induced electron transfer process resulting in water oxidation. b) Schematic diagram of the visible light-driven water oxidation by the <b>NiP-Ru</b> dyad modified TiO <sub>2</sub> /FTO photoanode. ....	95
<b>Scheme 4.3</b> Synthetic procedure followed for the preparation of <b>NiP-Ru</b> and <b>NiP-Ru-COOH</b> dyads. ....	96
<b>Scheme 4.4</b> Synthetic route to <b>HO<sub>2</sub>C-ZnP-TEMPO</b> and <b>hyd-ZnP-TEMPO</b> dyads. ....	111
<b>Scheme 4.5</b> Synthetic route to reference compound <b>hyd-ZnP</b> . ....	112
<b>Scheme 4.6</b> Synthetic route for the preparation of <b>PO(OH)<sub>2</sub>-ZnP-TEMPO</b> dyad. ....	113
<b>Scheme 4.7</b> Synthetic route to prepare <b>ZnPy<sub>3</sub>P-TEMPO</b> . ....	114
<b>Scheme 4.3.1</b> The experimental procedure for the synthesis of <b>TPP-bpy</b> . ....	138
<b>Scheme 4.3.2</b> The experimental procedure for the synthesis of <b>Ru(bpy)(COOMe)<sub>2</sub></b> . ....	139
<b>Scheme 4.3.3</b> The experimental procedure for the synthesis of <b>H<sub>2</sub>P-Ru</b> . ....	139
<b>Scheme 4.3.4</b> The experimental procedure for the synthesis of <b>NiP-Ru</b> . ....	140
<b>Scheme 4.3.5</b> The experimental procedure for the synthesis of <b>Ru-bpy</b> . ....	141
<b>Scheme 4.3.6</b> The experimental procedure for the synthesis of <b>NiP-Ru-COOH</b> . ....	141
<b>Scheme 4.3.7</b> Experimental procedure for the synthesis of <b>HO<sub>2</sub>C-ZnP-TEMPO</b> . ....	142
<b>Scheme 4.3.8</b> Experimental procedure for the synthesis of <b>hyd-ZnP-TEMPO</b> . ....	143
<b>Scheme 4.3.9</b> Experimental procedure for the synthesis of <b>hyd-ZnP</b> . ....	144

<b>Scheme 4.3.10</b> The experimental procedure for the synthesis of <b>PO(OEt)<sub>2</sub>PhCHO</b> . .....	145
<b>Scheme 4.3.11</b> The experimental procedure for <b>PO(OEt)<sub>2</sub>DMP-COOH</b> . .....	146
<b>Scheme 4.3.12</b> Synthetic procedure for <b>PO(OEt)<sub>2</sub>ZnP-COOH</b> . .....	147
<b>Scheme 4.3.13</b> The experimental procedure for the synthesis of <b>PO(OEt)<sub>2</sub>ZnP-TEMPO</b> . .....	147
<b>Scheme 4.3.14</b> The experimental procedure for the synthesis of <b>H<sub>2</sub>O<sub>3</sub>P-ZnP-TEMPO</b> . .....	148
<b>Scheme 4.3.15</b> The experimental procedure for the synthesis of <b>ZnPy<sub>3</sub>P-COOH</b> . .....	149
<b>Scheme 4.3.16</b> The experimental procedure for the synthesis of <b>ZnPy<sub>3</sub>P-TEMPO</b> . .....	149

## Table of Tables in the main text

<b>Table 3.1</b> H <sub>2</sub> production rate (nH <sub>2</sub> ), turnover number (TON) and turnover frequency data of the photocatalytic systems after 48 hours of irradiation. ....	75
<b>Table 4.1</b> Key electrochemical data recorded in benzonitrile containing 0.1 M (TBA)ClO <sub>4</sub> as the supporting electrolyte. The values are presented in V vs. Ag/AgCl. ....	99
<b>Table 4.2</b> Key electrochemical and spectroscopic data for the porphyrins discussed in this part. Oxidation potentials of the compounds recorded on meso-ITO and Gibbs free energy of the electron injection ( $\Delta G_{inj}$ ) in TiO <sub>2</sub> and hole shift reaction ( $\Delta G_{hs}$ ). ....	115
<b>Table 4.3</b> Oxidation potentials of the compounds recorded in DCM solution. The supporting electrolyte was TBAPF <sub>6</sub> (0.1 M), the working electrode was glassy carbon, the reference electrode was Ag/AgCl, scan speed 100 mV/sec, ferrocene was used as internal standard and in the above conditions exhibited a peak at 0.46 V vs. SCE. ....	118
<b>Table 4.4</b> Metrics of the different dyes in DSSCs under calibrated AM1.5 (100 mW/cm <sup>2</sup> ) sunlight simulator. ....	121
<b>Table 4.5</b> Photocurrent densities, TONs, TOFs and FEs measured at different electrolytes with <b>hyd-ZnP-TEMPO</b> or <b>hyd-ZnP + ac-TEMPO</b> on 1 cm <sup>2</sup> nanocrystalline TiO <sub>2</sub> films for <i>para</i> -methoxybenzyl alcohol oxidation. ....	127
<b>Table 4.6</b> Photocurrent densities recorded at 500 sec during the catalysis experiments with <b>hyd-ZnP-TEMPO</b> using three different benzyl alcohol substrates (50 mM). ....	134

## Abbreviations

Abbreviation	Meaning
Ala	Alanine
BChl	Bacteriochlorophylls
BDP	Boron-Dipyrromethene
Boc	tert-Butyloxycarbonyl
BPY	2,2'-bipyridine
CB	Conduction Band
Chl	Chlorophylls
CLSM	Confocal Laser Scanning Microscopy
COSY	Correlation Spectroscopy
CV	Cyclic Voltammetry
DCC	<i>N,N'</i> -dicyclohexylcarbodiimide
DCM	Dichloromethane
DDQ	2,3-Dichloro-5,6-dicyano- <i>p</i> -benzoquinone
DFT	Density-functional theory
DIPEA	<i>N,N</i> -Diisopropylethylamine
DLS	Dynamic light scattering
DMEM	Dulbecco's Modified Eagle Medium
DMF	Dimethylformamide
DMSO	Dimethyl sulfoxide

DNA	Deoxyribonucleic acid
DPV	Differential pulse voltammetry
DSPEC	Dye Sensitized Photoelectrochemical Cell
DSSCs	Dye Sensitized Solar Cells
EA	Electron acceptor
EDS	Energy dispersive spectroscopy
EPR	Enhanced permeation and retention
ESA	Excited-state absorption
EtOH	Ethanol
FE	Faradaic efficiency
FF	Diphenylalanine
Fmoc	9-Fluorenylmethoxycarbonyl chloride
FTO	Fluorine Doped Tin Oxide
GC	Gas chromatography
GSB	Ground-state bleach
HATU	1-[Bis(dimethylamino)methylene]-1H-1,2,3-triazolo[4,5-b]pyridinium 3-oxide hexafluorophosphate
HEC	Hydrogen evolving catalyst
HFIP	1,1,1,3,3,3-hexafluoroisopropanol
HMBC	Heteronuclear Multiple Bond Correlation
HOBt	1-hydroxybenzotriazole hydrate
HSQC	Heteronuclear single quantum coherence
IC	Internal conversions
IC50	Half maximal inhibitory concentration
Ile	Isoleucine
IPCE	Incident Photon-to-electron Conversion Efficiency
ISC	Intersystem crossing
ITO	Indium tin oxide
Jsc	Short circuit current
LED	Light-emitting diode
LSV	linear sweep voltammetry
Lys	Lysine
MALDI-TOF	Matrix-assisted laser desorption/ionization-Time of Flight
MCF-7	Michigan Cancer Foundation-7
MeCN	Acetonitrile
Me-Imd	N-methyl-imidazole
MeOH	methanol
MRI	Magnetic resonance imaging
MS	Mass spectroscopy
MTT	3-(4,5-dimethylthiazol-2-yl)-2,5-diphenyltetrazolium bromide
MV	Methyl Viologen
NHE	Normal Hydrogen Electrode
NMR	Nuclear magnetic resonance
NPs	Nanoparticles
PCE	Power conversion efficiency
PDT	Photodynamic therapy
PEC	Photoelectrochemical
PhCN	Benzonitrile
PNA	Peptide nucleic acid

POMs	Polyoxometalates
PS	Photosensitizer
PV	Photovoltaic
SCE	Saturated calomel electrode
SE	Stimulated emission
SEA	Sacrificial Electron Acceptor
SED	Sacrificial Electron Donor
SEM	Scanning electron microscopy
TA	Transient absorbance
TBA	Tetrabutylammonium
TCD	Thermal conductivity detector
TEM	Transmission electron microscopy
TEMPO	2,2,6,6-tetramethyl-1-piperidine N-oxyl
TEOA	Triethanolamine
TFA	Trifluoroacetic acid
THF	Tetrahydrofuran
TOF	Turnover Frequency
TON	Turnover Number
TPP	5, 10, 15, 20-tetraphenyl-porphyrin
TW	Terawatt
UV-Vis	Ultraviolet–visible
VB	Valence Band
Voc	open circuit voltage
VR	vibrational relaxation
WOC	water oxidation catalyst
$\Delta$ OD	$\Delta$ (Optical Density)

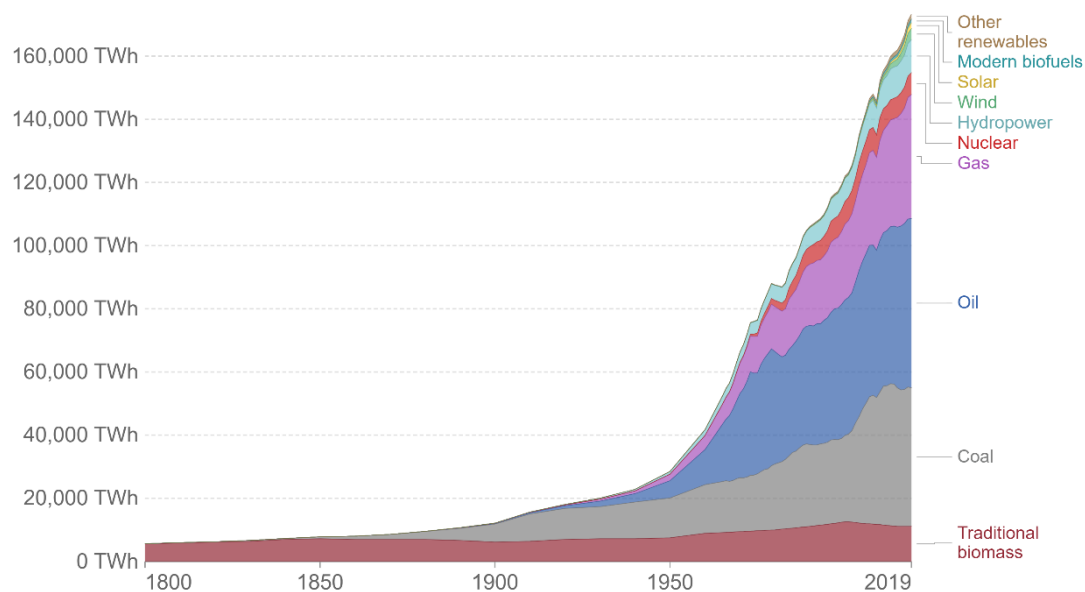
## Chapter 1: General Introduction

### 1.1 Energy problem

Over the last few centuries the availability of energy has improved the everyday-life of people. Plenty of new energy sources have been unlocked, initially the fossil fuels, the nuclear power and nowadays the renewable technologies.<sup>1</sup> At the same time, the quantity of energy we can produce and consume is constantly increasing. **Figure 1.1** presents the distribution of energy consumption based on the resource, revealing that the global energy demand is constantly growing. Energy and environmental issues are emerging today, as a result of the rapid technological development accompanied by the over-exploitation of fossil fuels, whose reserves are limited.<sup>2</sup> The combustion of natural gas, oil and coal is directly related to the global warming and the climate change due to the overproduction of green-house gases such as carbon dioxide (CO<sub>2</sub>).<sup>3</sup>

#### Global primary energy consumption by source

Primary energy is calculated based on the 'substitution method' which takes account of the inefficiencies in fossil fuel production by converting non-fossil energy into the energy inputs required if they had the same conversion losses as fossil fuels.



Source: Vaclav Smil (2017) & BP Statistical Review of World Energy

OurWorldInData.org/energy • CC BY

**Figure 1.1** Global energy consumption by source.

<sup>1</sup> Hannah Ritchie and Max Roser (2020) - "Energy". Published online at OurWorldInData.org. Retrieved from: 'https://ourworldindata.org/energy'

<sup>2</sup> J. Murray and D. King, *Nature*, 2012, **481**, 433.

<sup>3</sup> Hammarstrom, L.; Hammes-Schiffer, S., Artificial photosynthesis and solar fuels. *Accounts of chemical research* **2009**, *42* (12), 1859-60.

The above issues constitute a general energy problem, which can be solved by replacing fossil fuels with alternative, inexhaustible and environmental benign energy sources. The development of environmentally sustainable energy systems, based on renewable energy sources, is of vital importance in order to drastically reduce the use of fossil fuels and hopefully replace them completely in the future.

Among plenty renewable energy sources, solar energy is undoubtedly a great candidate, since it is the most abundant (**Figure 1.2**), clean, CO<sub>2</sub>-emission-free and inexhaustible.<sup>4,5</sup> Remarkably, the annual global energy consumption is less than the energy provided by the sun in only one day.<sup>6</sup> Therefore, if by achieving to efficiently capture and utilize only a small portion of solar energy, both the energy and the environmental problems will be solved. Notably, by simply covering 0.16% of earth's land with light harvesting systems that convert sunlight to electricity with only 10% efficiency, approximately 20 TW of energy would be provided, which is more than enough for the world energy demands.<sup>7</sup>

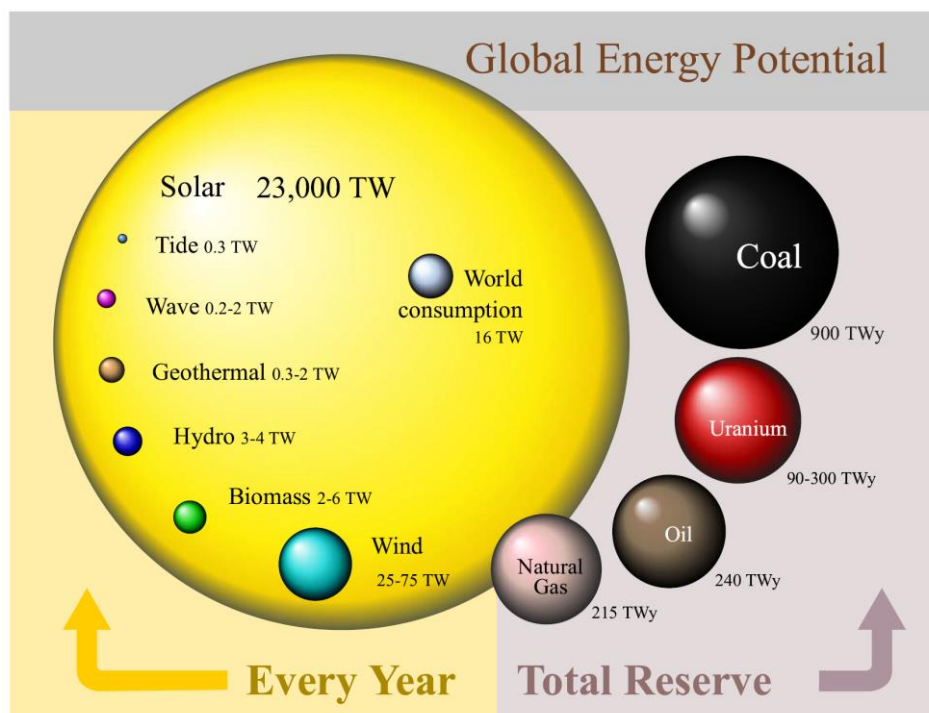


**Figure 1.2** Global energy potential illustrated by offer per year regarding the renewable energy sources and total reserves for the fossil fuels.

<sup>4</sup> M. Hosenuzzaman, N. A. Rahim, J. Selvaraj, M. Hasanuzzaman, A. B. M. A. Malek and A. Nahar, *Renew. Sust. Energ. Rev.*, 2015, **41**, 284-297.

<sup>5</sup> N. S. Lewis and D. G. Nocera, *PNAS*, 2006, **103**, 15729.

<sup>6</sup> J. K. B. Bishop and W. B. Rossow, *J. Geophys. Res. Oceans*, 1991, **96**, 16839-16858.

<sup>7</sup> R. F. Service, *Science*, 2005, **309**, 548-551.



Solar energy has enormous potential in preserving the future energy supplies.<sup>8</sup> To that end, sunlight should be initially captured and then converted into useful forms of energy. Unfortunately, there is not any current technology able to convert solar energy into heat, electricity or fuel more competitively than using fossil fuels. However, nature overcomes this challenge in a very efficient way.

For millions of years nature converts solar energy into chemical energy through the process of photosynthesis.<sup>9</sup> In natural photosynthesis the initial process is the absorption of sunlight by a supramolecular assembly based on chlorophylls.<sup>10</sup> The solar energy is utilized to split water ( $\text{H}_2\text{O}$ ) and convert the atmospheric  $\text{CO}_2$  into carbohydrates ( $[\text{CH}_2\text{O}]_n$ ) and the cycle of carbon continues as depicted in **Figure 1.3**.

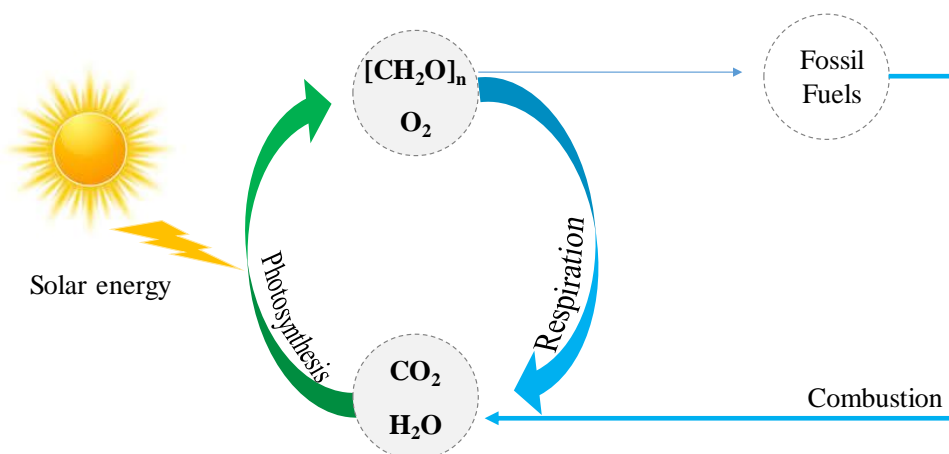


**Figure 1.3** Natural photosynthesis in the carbon cycle.

Inspired by photosynthesis, plenty of scientists are developing artificial photosynthetic systems in order to harvest and store solar energy. Understanding the fundamental principles of the natural photosynthesis process will assist the scientific community to the fabrication of devices that perform either direct solar energy conversion into electricity or storage into valuable fuels. The first approach concerns the development of photovoltaic (PV) devices and is considered quite promising.<sup>11</sup> The second approach is associated with the production of solar fuels, namely hydrogen ( $\text{H}_2$ ) and  $\text{CO}_2$  reduction products in photocatalytic or photoelectrocatalytic schemes by

<sup>8</sup> C.-D. Yue and G.-R. Huang, *Energy Policy*, 2011, **39**, 7988-8002.

<sup>9</sup> J. Barber, *Chem. Soc. Rev.*, 2009, **38**, 185-196.

<sup>10</sup> J. Otsuki, *J. Mater. Chem. A*, 2018, **6**, 6710-6753.

<sup>11</sup> R. E. Blankenship, D. M. Tiede, J. Barber, G. W. Brudvig, G. Fleming, M. Ghirardi, M. R. Gunner, W. Junge, D. M. Kramer, A. Melis, T. A. Moore, C. C. Moser, D. G. Nocera, A. J. Nozik, D. R. Ort, W. W. Parson, R. C. Prince and R. T. Sayre, *Science*, 2011, **332**, 805.

mimicking the natural photosynthetic processes.<sup>10,12,13</sup> Noteworthy, the above systems should be based on abundant, non-toxic and inexpensive materials in order to be environmentally friendly and economically affordable.

## 1.2 Porphyrinoids and their Properties

Porphyrinoid derivatives play a vital role in natural systems, especially in the process of photosynthesis,<sup>14</sup> attracting plenty of scientific interest during the last decades. All porphyrin derivatives are chromophores, getting their name from the Greek word “*porphura*” (“*πορφύρα*”) which means violet/purple color. They are considered the “pigments of life”<sup>15</sup> due to their importance in numerous biological processes. Metallated porphyrinoids are the active species in various natural systems, namely they are found in photosynthesis (chlorophyll a),<sup>16</sup> in electron transfer processes in cytochrome c (heme c),<sup>17</sup> in oxygen transfer and storage processes (hemoglobin and myoglobin),<sup>18</sup> in methanogenic archaea (Cofactor F430) and in processes related to brain and nervous system (vitamin B12)<sup>19</sup> (**Figure 1.4**).

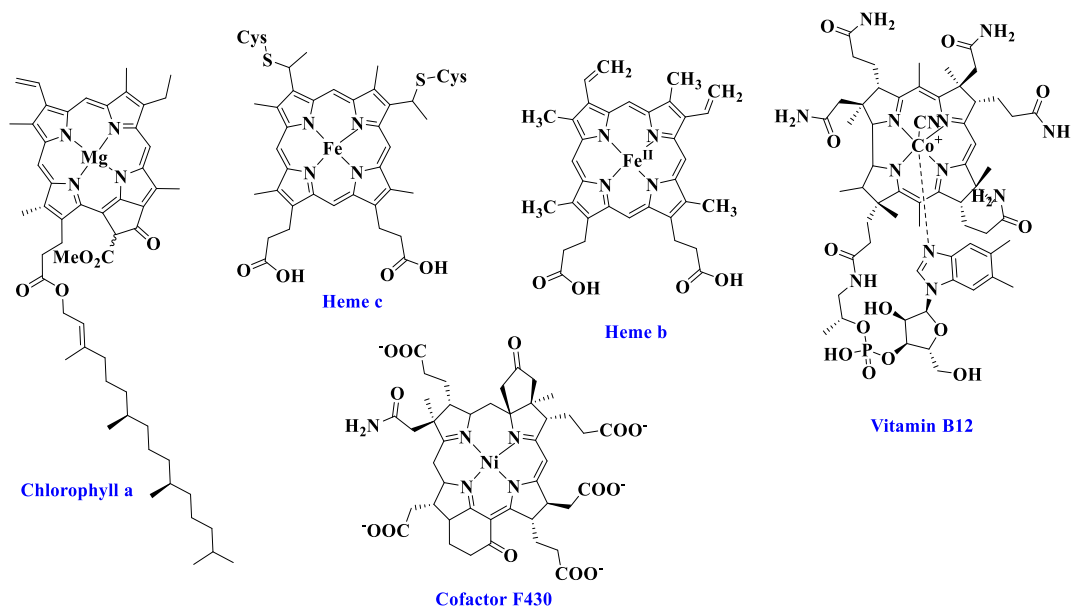


**Figure 1.4** Structures of chlorophyll a, heme c, heme b, vitamin B12, cofactor F430.

<sup>12</sup> S. Bensaïd, G. Centi, E. Garrone, S. Perathoner and G. Saracco, *ChemSusChem*, 2012, **5**, 500-521.

<sup>13</sup> K. J. Young, L. A. Martini, R. L. Milot, R. C. Snoeberger, III, V. S. Batista, C. A. Schmuttenmaer, R. H. Crabtree and G. W. Brudvig, *Coord. Chem. Rev.*, 2012, **256**, 2503-2520.

<sup>14</sup> Guilard, R.; Kadish, K.M.; Smith, K., *The Porphyrin Handbook*, Academic Press, **2012**.

<sup>15</sup> Alan R. Battersby, *Nat. Prod. Rep.*, 2000, **17**, 507-526

<sup>16</sup> A. R. Battersby, *Natural Product Reports*, 2000, **17**, 507-526.

<sup>17</sup> W. S. Caughey, G. A. Smythe, D. H. O’Keeffe, J. E. Maskasky and M. I. Smith, *Journal of Biological Chemistry*, 1975, **250**, 7602-7622.

<sup>18</sup> M. Nagai, N. Mizusawa, T. Kitagawa and S. Nagatomo, *Biophysical Reviews*, 2018, **10**, 271-284.

<sup>19</sup> J. M. Scott and A. M. Molloy, *Annals of Nutrition and Metabolism*, 2012, **61**, 239-245.

Nature utilizes porphyrin molecules due to their interesting properties. The following paragraphs summarize the photophysical properties of porphyrin chromophores.

Porphyrins are aromatic heterocyclic compounds with a macrocycle consisting of 20 carbons, 4 nitrogens and 22  $\pi$ -electrons (**Figure 1.5**).<sup>20</sup> More specifically, they have four pyrrole rings, that are linked together with methine bridges, while only 18  $\pi$ -electrons are delocalized according to the Hückel's rule of aromaticity ( $4n+2$  delocalized  $\pi$ -electrons, where  $n = 4$ ). The structure of the porphyrin macrocycle is planar due to the extended  $\pi$ -conjugated system.

Porphyrins have deep color, owing to their highly conjugated  $\pi$ -electron system and they display a characteristic UV-visible spectrum. Their electronic absorption spectrum of a typical porphyrin comprises of a strong band around 400 nm (called Soret or B band) which is attributed to second excited state transition ( $S_0$ - $S_2$ ) along with weak transitions towards the first excited state ( $S_0$ - $S_1$ ) in the 550-650 nm region (called Q bands).<sup>21,22</sup>

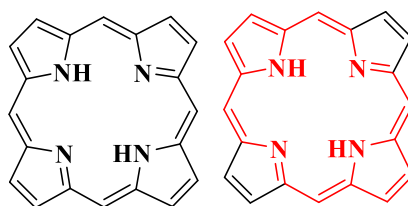


**Figure 1.5** Chemical structure of porphyrin macrocycles along with the number of  $\pi$ -electrons implied in aromaticity (depicted in red).

The spectroscopic features of the porphyrins vary depending on the porphyrin peripheral substitution as well as the metal complexation inside the core of the macrocycle. The peripheral substituents of the porphyrin usually affect slightly the intensity and location (red or blue shift) of the absorption bands, while the insertion of a metal ion into the macrocycle changes significantly the absorption features. For example, in the case of any free base porphyrin (non-metallated), the UV-Vis spectrum depicts four Q bands (I, II, III and IV) while for the corresponding zinc metallated porphyrin only two Q bands are observed. This is mainly attributed to the change of the porphyrin symmetry to  $D_{4h}$  instead of  $D_{2h}$ . Other metal insertions might yield to 3 Q

---

<sup>20</sup> Küster, W.Z.Z., *Physiol. Chem.* **1913**, 82, 463-483.

<sup>21</sup> M. Gouterman, *J. Mol. Spectrosc.*, 1961, **6**, 138-163.

<sup>22</sup> M. Gouterman, G. H. Wagnière and L. C. Snyder, *J. Mol. Spectrosc.*, 1963, **11**, 108-127.

bands or only one Q band. Representative UV-Vis spectra of a free base, a tin-metallated and a zinc-metallated porphyrin are illustrated in **Figure 1.6**.

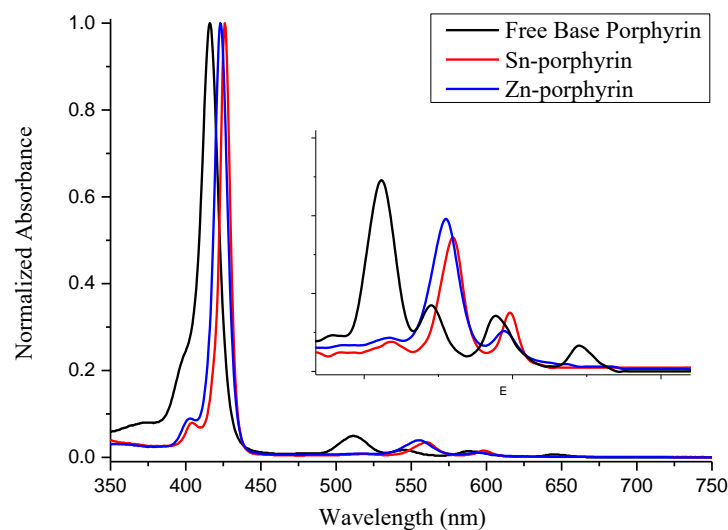


**Figure 1.6** Absorption spectra of a free base **TPP** (black line), a zinc-metallated **ZnTPP** (blue line) and a tin-metallated **SnTPP** (red line) porphyrin in DCM.

A simplified Perrin-Jablonski diagram is presented in **Figure 1.7** and provides a better understanding of all the possible procedures that take place upon photon excitation.<sup>23</sup> Initially, the PS is in the ground state ( $S_0$ ) and upon light excitation, the porphyrin molecule absorbs one photon leading to the population of any singlet excited state  $S_x$  ( $x=1, 2, 3\dots$ ). After the excitation the  $PS^*$  will return to the ground state via the lowest ( $S_1$ ) excited state, so all the electrons that are located to higher excited states will decay back to  $S_1$  through internal conversions (IC) and vibrational relaxation (VR) mechanisms. The  $S_1$  excited state can decay through three different processes: a) radiative decay ( $S_1 \rightarrow S_0$ , fluorescence emission), b) non-radiative decay back to  $S_0$  and c) intersystem crossing (ISC) to the lowest energy triplet state  $T_1$ . Finally, this newly formed  $T_1$  state can return to the ground state by non-radiative or radiative (phosphorescence) decay.

Porphyrins typically display two fluorescence emission bands in the range of 550 to 800 nm, which are attributed to the  $S_1 \rightarrow S_0$  decay process. Generally, the fluorescence spectra of porphyrins vary regarding their shape, location and intensity of the bands, depending on the substituents of the macrocycle, the presence of a metal ion inside the

<sup>23</sup> A. Jablonski, *Nature*, 1933, **131**, 839-840.

core and more importantly the nature of this metal ion.<sup>24</sup> Representative emission spectra of a free base and a zinc metallated porphyrin are illustrated in **Figure 1.8**.

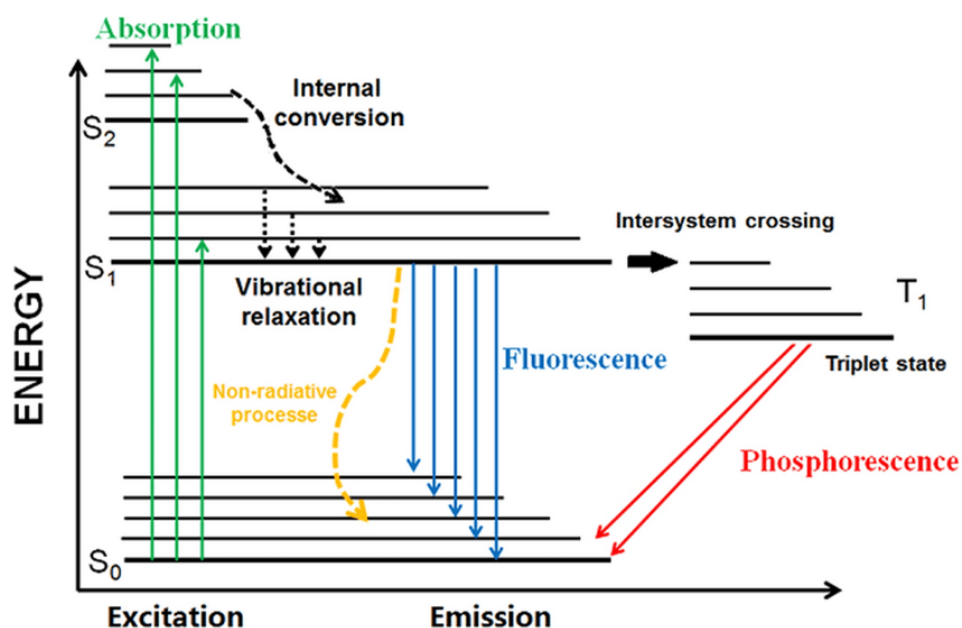


**Figure 1.7:** A simplified Perrin-Jablonski diagram for porphyrin molecules.

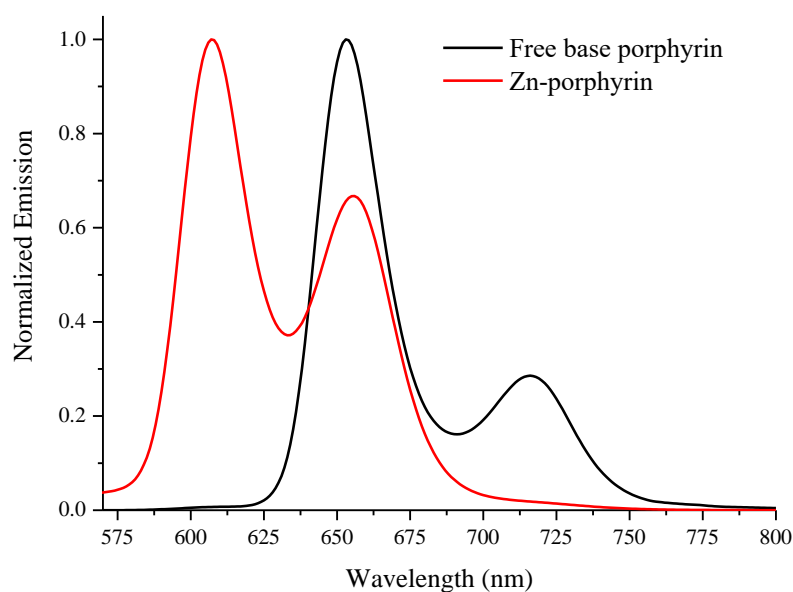


**Figure 1.8:** Characteristic emission spectra of a free base **TPP** (black line) and a zinc metallated porphyrin **ZnTPP** (red line) in DCM after excitation at 420 nm.

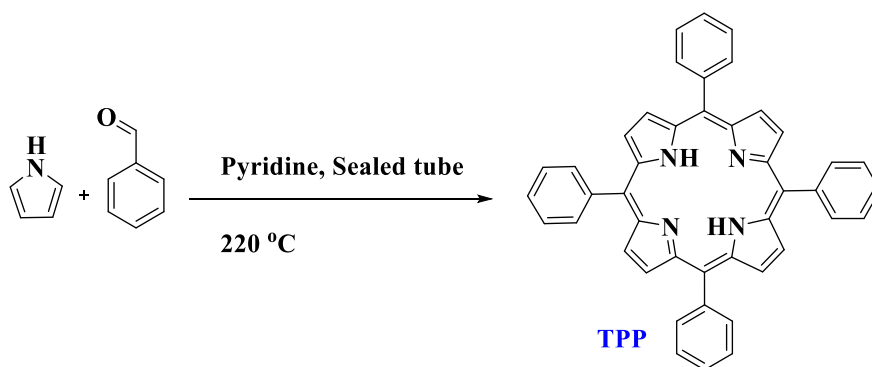
After summarizing the basic photophysical properties of this class of compounds, which nature has the wisdom to use in plenty of biological procedures; it is worth describing the synthetic approaches for the successful preparation of porphyrins.

<sup>24</sup> P. G. Seybold and M. Gouterman, *J. Mol. Spectrosc.*, 1969, **31**, 1-13.

Although plenty of porphyrins can be obtained directly from nature, in order to obtain specific functionalization on the macrocycle, it is necessary to synthesize the porphyrin from scratch. The first synthetically prepared porphyrin was reported by Rothmund in 1935,<sup>25</sup> and since then plenty of chemical strategies for the synthesis of such macrocyclic compounds have been used. The main building block for porphyrin synthesis is pyrrole and there are various synthetic protocols to synthesize different *meso*- and  $\beta$ -substituted porphyrins. The most important methodologies for the preparation of such porphyrin derivatives are presented below. Each one of them has both advantages and limitations and can be applied depending on the structure of the desired product.

### *Rothmund's method*

As already mentioned, Rothmund achieved the first synthesis of a porphyrin, specifically the 5,10,15,20-tetraphenylporphyrin (TPP).<sup>26</sup> This porphyrin was prepared by using pyrrole and benzaldehyde in presence of pyridine (in a sealed tube at 220 °C), affording TPP in almost 10% yield (**Scheme 1.1**).



**Scheme 1.1** Synthesis of 5,10,15,20-tetraphenylporphyrin (TPP) by Rothmund.

### *The Alder-Longo method*

The above method was limited by the stability of the aldehydes in the necessary high temperature. Adler, Longo and coworkers reported acid-catalyzed condensation reaction to obtain symmetrical tetraarylporphyrins in 1964.<sup>27</sup> In this reaction the acid initially activates the benzaldehyde by protonating the carbonyl group and then condensation with pyrrole yields a porphyrinogen intermediate (**Scheme 1.2**). Different organic acids have been applied as solvents while the most common one is the propionic

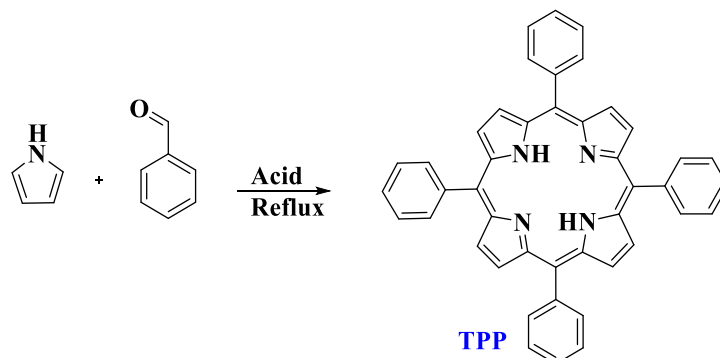
---

<sup>25</sup> P. Rothmund, *J. Am. Chem. Soc.*, 1936, **58**, 625-627.

<sup>26</sup> Rothmund, P.; Menotti, A.R., *J. Am. Chem. Soc.*, **1941**, 63, 267-270.

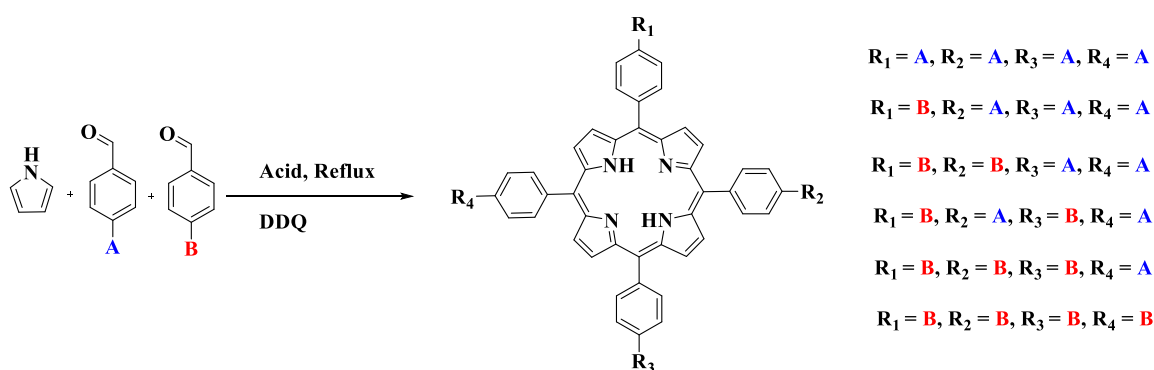
<sup>27</sup> Adler, A.D.; Longo, F.R.; Shergalis, W., *J. Am. Chem. Soc.* **1964**, 86, 3145-3149.

acid. This experimental protocol improved significantly the yield of the porphyrin synthesis, since tetraarylporphyrins can be prepared in pretty good yields. In addition, by changing the aldehyde, various symmetrical porphyrins can be synthesized with this method.



**Scheme 1.2** Synthesis of 5,10,15,20-tetraphenylporphyrin by Adler, Longo and coworkers.<sup>27</sup>

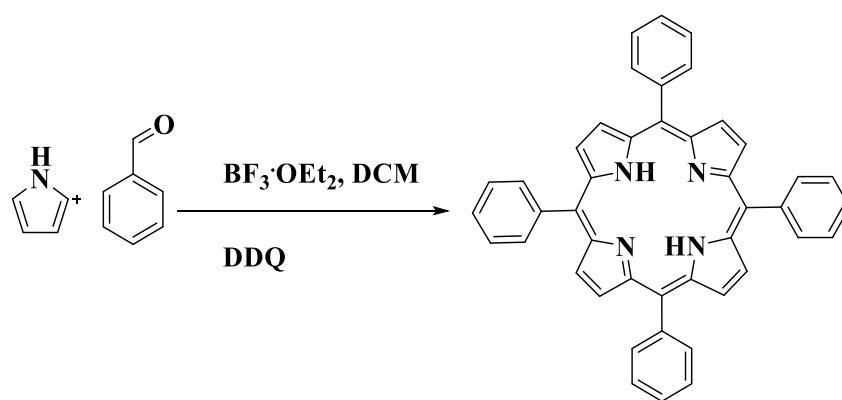
Unsymmetrical porphyrin compounds can be prepared following the Alder-Longo method as well. As presented in **Scheme 1.3** this is achieved through mixed condensation reactions of aldehydes in the presence of pyrrole. By using two different aldehydes, a statistical mixture of 6 products is obtained as illustrated in the figure below. In this case, the desired porphyrin is separated from the other produced porphyrin derivatives via purification by column chromatography. Noteworthy if more than 2 aldehydes are used, for example 3 different aldehydes, the reaction will yield to 21 different porphyrin analogues and the separation will be almost impossible.



**Scheme 1.3** Synthesis of unsymmetrical porphyrins via mixed condensation reaction of two different aldehydes and pyrrole.

*Lindsey's method*

Further improvement of the reaction conditions was provided by Lindsey and his collaborators, who developed a synthetic protocol for the preparation of tetraphenylporphyrin at room temperature (**Scheme 1.4**).<sup>28</sup> More specifically, in this preparation method benzaldehyde, pyrrole, a Lewis acid as the catalyst and an organic solvent were used to produce TPP. As catalysts, trifluoroacetic acid, (TFA) or boron trifluoride diethyl etherate ( $\text{BF}_3 \cdot \text{OEt}_2$ ) can be used while common solvents are chloroform, and dichloromethane. In this reaction, the thermodynamically favored porphyrinogen is obtained and gets oxidized into the desired porphyrin by addition of an oxidant, such as 2,3-dichloro-5,6-dicyano-*p*-benzoquinone (DDQ) or tetrachloro-1,4-benzoquinone (*p*-chloranil).



**Scheme 1.4** Lindsey's method for the preparation of TPP.

### *Dipyromethanes*

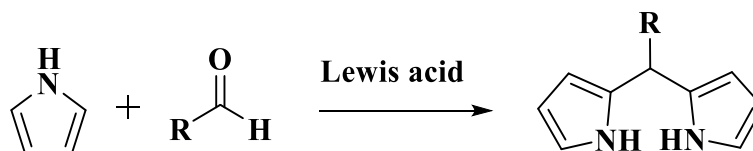
The previous approach is based on the condensation reaction between four pyrrole units and analogous equivalents of aldehydes. An alternative pathway for the preparation of porphyrin macrocycles is via condensation reaction with dipyromethane instead of pyrrole. Di(1*H*-pyrrol-2-yl)methane (dipyromethane) is a precursor in porphyrin synthesis prepared via a condensation reaction of two equivalents of unsubstituted pyrroles with any aryl benzaldehyde (**Scheme 1.5**). Lindsey and coworkers reported the synthesis of dipyromethanes by using a mild Lewis acid (i.e.  $\text{InCl}_3$ ,  $\text{MgBr}_2$ , etc.) that catalyzes the reaction.<sup>29,30</sup>

<sup>28</sup> Lindsey, J.S.; Schreiman, I.C.; Hsu, H.C.; Kearney, P.C.; Marguerettaz, A.M., *J. Org. Chem.* **1987**, *52*, 827-836.

<sup>29</sup> Littler, B.J.; Ciringh, Y.; Lindsey, J.S., *J. Org. Chem.*, **1999**, *64*, 2864-2872.

<sup>30</sup> Rao, P.D.; Dhanalekshmi, S.; Littler, B.J.; Lindsey, J.S., *J. Org. Chem.*, **2000**, *65*, 7323-7344.





**Scheme 1.5** Lindsey's method for the preparation of dipyrromethanes.

Dipyrromethanes are significant precursors for the synthesis of *trans*-substituted *meso*-porphyrins.<sup>31</sup> Additionally, they render plausible the preparation of porphyrins with 3 or even 4 peripheral substituents, which were almost impossible to purify from direct condensation between pyrrole and aldehydes. The following figure shows the different unsymmetrical porphyrins<sup>32,33,34</sup> that can be obtained only via this approach (**Figure 1.9**).

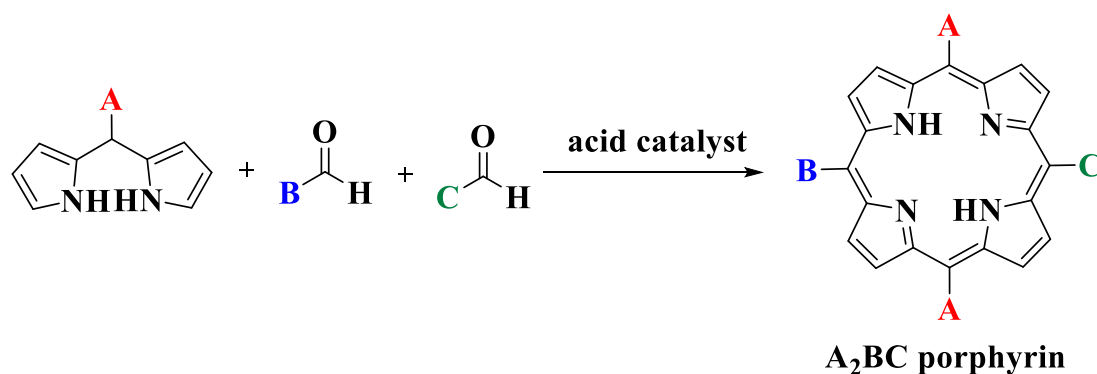


**Figure 1.9** Synthesis of the A<sub>2</sub>BC porphyrins.

#### *Boron Dipyrromethenes (BDP)*

The BORon DIPYrrromethenes (or 4,4-difluoro-4-bora-3a,4a-diaza-s-indacene) are chromophores which have a structural resemblance with the “half” of the porphyrinic macrocycle and are another important class of fluorescent organic dyes, with a highly conjugated system (**Figure 1.10**).<sup>35</sup>

<sup>31</sup> Arsenault, G.P.; Bullock, E.; MacDonald, S.F., *J. Am. Chem. Soc.*, **1960**, *82*, 4384-4389.

<sup>32</sup> T. Tanaka and A. Osuka, *Chem. Rev.*, 2017, **117**, 2584-2640.

<sup>33</sup> K. M. Smith, *New J. Chem.*, 2016, **40**, 5644-5649.

<sup>34</sup> G. de la Torre, G. Bottari, M. Sekita, A. Hausmann, D. M. Guldi and T. Torres, *Chem. Soc. Rev.*, 2013, **42**, 8049-8105.

<sup>35</sup> R. P., Haugland, J. Gregory, M. T. Z. Spence, I. D. Johnson, *Handbook of Fluorescent Probes and Research Products*; Molecular Probes, 2002.

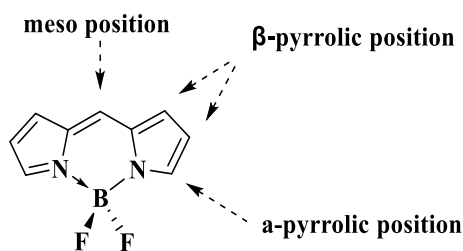


**Figure 1.10:** General structure of BDP derivatives.

These chromophores generally display relatively sharp absorption in the visible range and are extremely fluorescent with very high fluorescence quantum yields (sometimes close to 100%).<sup>36</sup> **Figure 1.11** shows representative absorption and emission spectra of a BDP dye. Another characteristic of BDP molecules is that they are moderately stable derivatives, due to the presence of the first row elements (boron, fluorine and nitrogen) and their delocalized  $\pi$ -system. Based on these properties, BDPs have been widely utilized in a vast number of applications, such as laser dyes,<sup>37,38</sup> solar energy conversion,<sup>39</sup> luminescent labelling agents,<sup>40</sup> artificial photosynthesis,<sup>41</sup> and photodynamic therapy.<sup>42</sup>

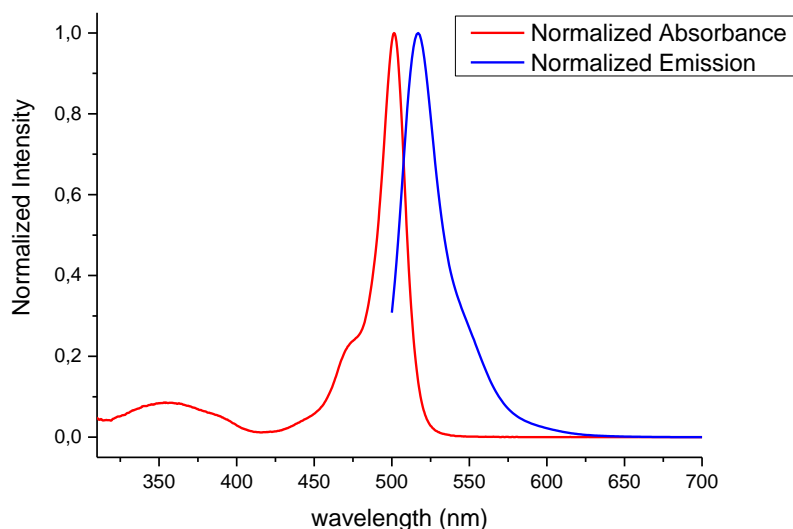


**Figure 1.11:** Normalized absorption and emission spectra of BDP-NH<sub>2</sub> in DCM.

<sup>36</sup> A. Loudet and K. Burgess, *Chem. Rev.*, 2007, **107**, 4891-4932.

<sup>37</sup> S. C. Guggenheimer, J. H. Boyer, K. Thangaraj, M. Shah, M.-L. Soong and T. G. Pavlopoulos, *Appl. Opt.*, 1993, **32**, 3942-3943.

<sup>38</sup> T. L. Arbeloa, F. L. Arbeloa, I. L. Arbeloa, I. García-Moreno, A. Costela, R. Sastre and F. Amat-Guerri, *Chem. Phys. Lett.*, 1999, **299**, 315-321.

<sup>39</sup> S. P. Singh and T. Gayathri, *Eur. J. Org. Chem.*, 2014, **2014**, 4689-4707.

<sup>40</sup> M.-c. Yee, S. C. Fas, M. M. Stohlmeyer, T. J. Wandless and K. A. Cimprich, *J. Biol. Chem.*, 2005, **280**, 29053-29059.

<sup>41</sup> M. E. El-Khouly, S. Fukuzumi and F. D'Souza, *ChemPhysChem*, 2014, **15**, 30-47.

<sup>42</sup> H. Abrahamse and Michael R. Hamblin, *Biochem. J.*, 2016, **473**, 347.

From a synthetic perspective, there are various synthetic protocols for the preparation of such chromophores. The two main strategies that are being commonly employed are based on the well-known porphyrin chemistry and are illustrated in the following figure.<sup>43</sup> Both approaches involve the use of pyrrole which reacts with the electrophilic carbonyl group of another molecule (Figure 1.12).<sup>44</sup>

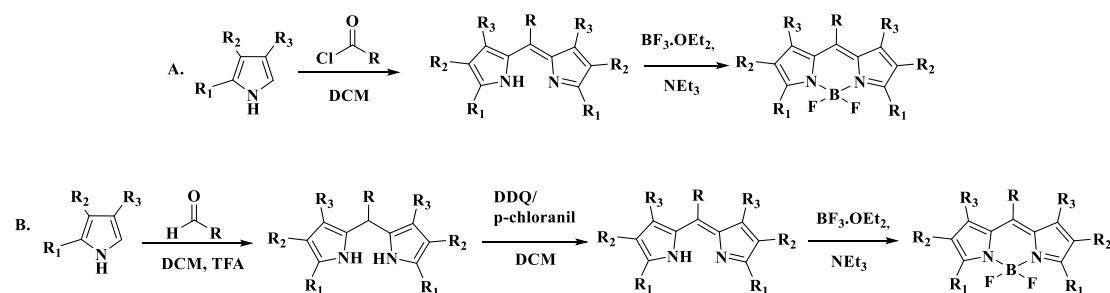


**Figure 1.12:** The two synthetic pathways (A and B) for the preparation of BDP dyes.

In route A, a pyrrole moiety is condensed with an acyl chloride in the presence of an acid catalyst, leading to the formation of an unstable intermediate, which cannot be isolated (**Figure 1.12A**). Subsequently, excess of boron trifluoride etherate ( $\text{BF}_3 \cdot \text{OEt}_2$ ) and a base ( $\text{NEt}_3$ ) are introduced to the reaction mixture, producing the desired BDP molecule. Alternatively, in route B an acid catalyzed condensation between an aldehyde and pyrrole is performed, yielding the corresponding dipyrromethane as intermediate. Afterwards the dipyrromethane is oxidized by the addition of DDQ or p-chloranil in the solution. Finally, excess of both  $\text{BF}_3 \cdot \text{OEt}_2$  and  $\text{NEt}_3$  are added and the desired product is formed.

### 1.3 Self-assembly of chromophores

In natural photosynthesis, organisms improve their light harvesting ability through highly organized assemblies of chromophores (chlorophylls, Chls and bacteriochlorophylls, BChls), by supramolecular pigment–protein and pigment–pigment interactions.<sup>45</sup> A characteristic example is provided by the green photosynthetic bacteria which form unique supramolecular structures. Their photosynthetic antenna complexes, called chlorosomes, are ellipsoidal particles which

<sup>43</sup> T. E. Wood and A. Thompson, *Chem. Rev.*, 2007, **107**, 1831-1861.

<sup>44</sup> N. Boens, V. Leen and W. Dehaen, *Chem. Soc. Rev.*, 2012, **41**, 1130-1172.

<sup>45</sup> M. R. Wasielewski, *Acc. Chem. Res.* **2009**, 42, 12, 1910–1921.

contain bacteriochlorophyll-c, -d, and -e molecules and form self-aggregates only through pigment–pigment interaction.<sup>46</sup> These BChls self-aggregates are surrounded by a lipid monolayer.

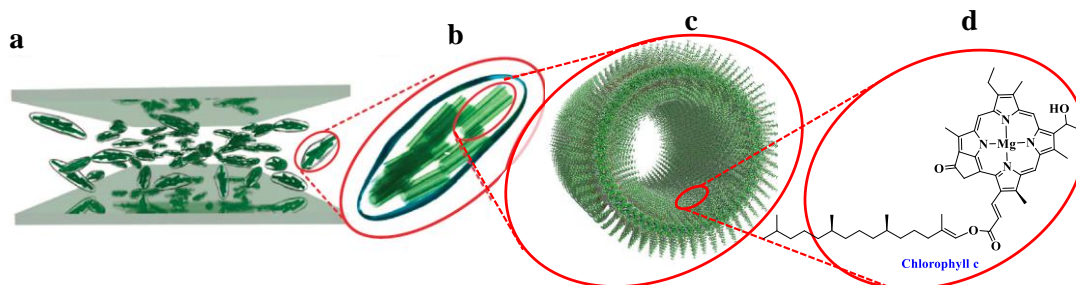


**Figure 1.13:** The self-assembly of bacteriochlorophylls in green sulfur bacteria: a) photosynthetic antenna assembly of chlorosomes, b) chlorosome, c) tubular assemblies of bacteriochlorophylls and d) molecular structure of bacteriochlorophyll-c.

Green sulfur bacteria have been found in depths of up to 145 m in the Black Sea, with low light availability. They achieve to collect enough solar energy for the photosynthesis process due to the self-assembly of their chlorophyll chromophores.

Inspired by these natural systems, scientists have applied a lot of efforts for the development of artificial photosynthetic systems for practical solar fuels production, able to collect solar energy, separate charges and transfer them to catalytic sites where multielectron redox processes will occur. While significant progress has been achieved towards this direction, researchers have not yet developed efficient self-assembling artificial photosynthetic systems.<sup>45</sup> Therefore, the fabrication of highly ordered nanostructures of chromophores via self-assembly is an active area of research, with diverse applications in materials science.<sup>47</sup>

Self-assembly is a well-established bottom-up approach for the construction of materials with improved properties. In the laboratory, scientists are synthesizing chemical analogs of chlorophylls, namely porphyrin, and try to produce self-assembled architectures of these chromophores in order to gain enhanced properties in the resulting material.<sup>48</sup> Supramolecular chromophore self-assemblies aim to improve light-

<sup>46</sup> Y. Saga, S. Akai, T. Miyatake, and H. Tamiaki, *Bioconjugate Chem.* **2006**, 17, 4, 988–994.

<sup>47</sup> Whitesides, G.; Mathias, J.; Seto, C. *Science* 1991, 254, 1312–1319

<sup>48</sup> C. M. Drain, A. Varotto and I. Radivojevic, *Chem. Rev.*, 2009, **109**, 1630-1658.

harvesting, energy and electron transfer properties, which are essential for visible-light-driven photocatalytic applications, such as H<sub>2</sub> production and CO<sub>2</sub> reduction.<sup>49</sup>

Porphyrin molecules are ideal self-assembly building blocks, since they possess symmetric molecular structures, planar geometry, chemical and thermal stability, are easily modified and can utilize plenty of supramolecular interactions such as hydrogen bonding,  $\pi$ - $\pi$  stacking, axial coordination and noncovalent interactions.<sup>49</sup> There are various protocols to induce self-assembly to chromophores, including reprecipitation or “good” and “bad” solvent method, ionic self-assembly, peptide-assisted self-assembly, acid-base neutralization assisted surfactant self-assembly, microemulsion-assisted self-assembly and other methods (**Figure 1.14**).<sup>50</sup>

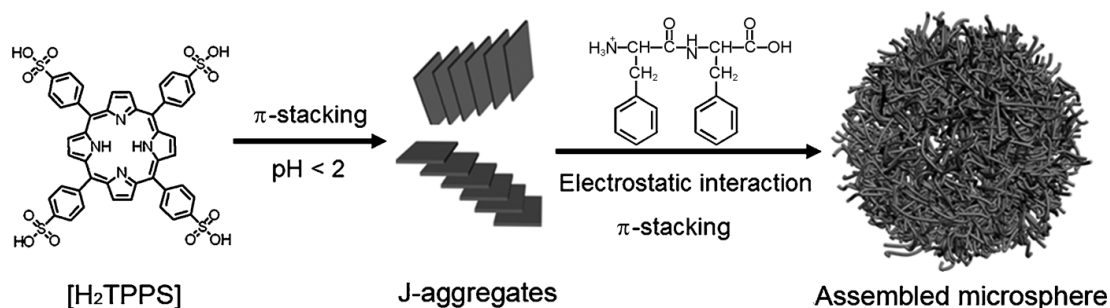


**Figure 1.14:** Example of porphyrin self-assembly based on ionic electrostatic interactions.

**Figure 1.15** illustrates the “good-bad” solvent self-assembly protocol. Initially the molecules are dissolved in a “good” solvent (effective at dissolving the solute) and then a “bad” solvent is introduced (the molecule has poor solubility in the latter one). The molecules begin to self-assemble and after an appropriate amount of incubation time (typically 24 hours), a sample is observed via scanning electron microscopy to study any supramolecular assemblies that might have been formed (**Figure 1.15**).

Although the self-assembly of porphyrins is known from the 80’s, self-assembled nanostructures of porphyrins had not been employed in photocatalytic H<sub>2</sub> evolution until recently.<sup>51</sup> Afterwards, several reports followed, with symmetrical and unsymmetrical porphyrins forming distinctive architectures via their self-assembly and subsequently applied in light-driven H<sub>2</sub> production.

<sup>49</sup> Y. Zhong, S. Liu, J. Wang, W. Zhang, T. Tian, J. Sun and F. Bai, *APL Mater.*, 2020, **8**.

<sup>50</sup> C. Zhang, P. Chen, H. Dong, Y. Zhen, M. Liu and W. Hu, *Adv. Mater.*, 2015, **27**, 5379-5387.

<sup>51</sup> H. Wang, Y. Song, Z. Wang, et al., *Chem. Mater.*, 2008, **20**, 7434-7439.

In peptide-assisted self-assembly, the most extensively studied small peptide, famous for its self-assembling properties, is diphenylalanine (Phe-Phe, FF).<sup>52,53</sup> Our group has extensively investigated chromophores such as BDPs,<sup>54</sup> porphyrins,<sup>55,56</sup> corroles,<sup>57</sup> and polyoxometalates (POMs)<sup>58</sup> covalently linked with Phe-Phe and the resulting conjugates retained the characteristic of self-assembly. In this concept, Nikolaou et al. recently synthesized FmocFF-ZnTPP (scheme 3.1.3) and examined its well-defined nanostructures as photocatalysts in H<sub>2</sub> production.<sup>59</sup> By following the “good-bad” solvent method spherical and fibrillar self-assembling architectures were obtained from the same porphyrin molecule and presented much different catalytic activity towards H<sub>2</sub> evolution.

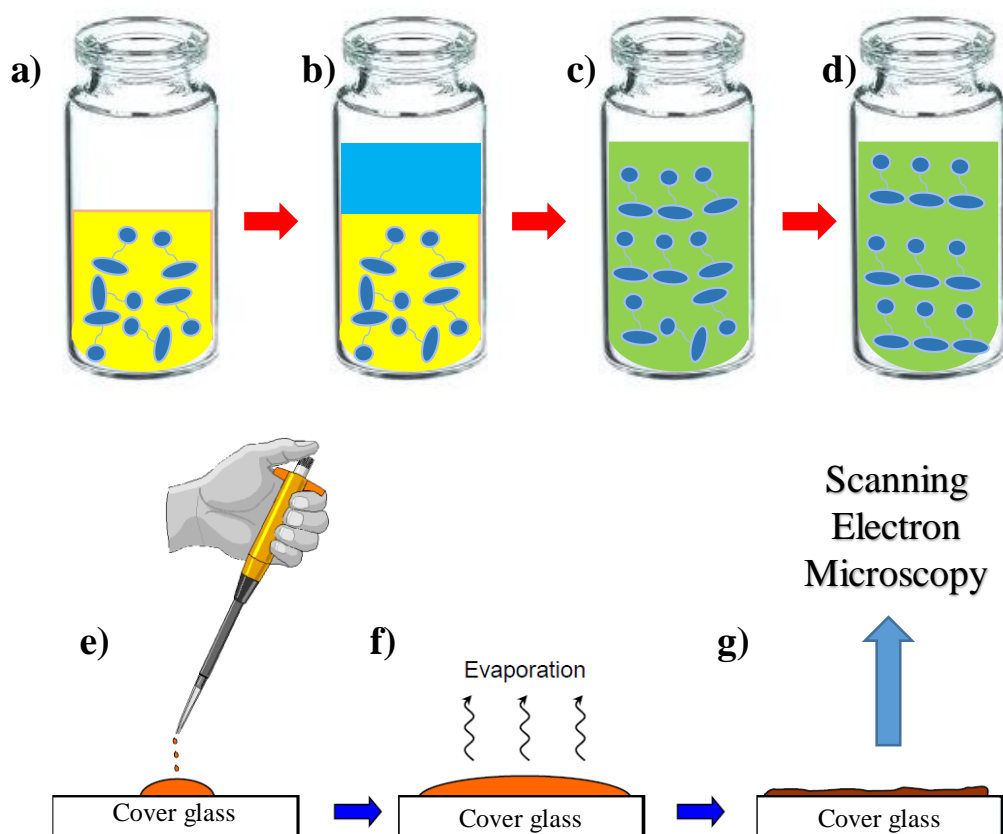


**Figure 1.15:** Schematic illustration the “good-bad” solvent self-assembly protocol.

<sup>52</sup> M. Reches and E. Gazit, *Science*, 2003, **300**, 625-627.

<sup>53</sup> N. Kol, L. Adler-Abramovich, D. Barlam, R. Z. Shneck, E. Gazit, *Nano Lett.*, 2005, **5**, 1343-1346.

<sup>54</sup> K. Karikis, A. Butkiewicz, F. Foliás, G. Charalambidis, C. Kokotidou, A. Charisiadis, V. Nikolaou, E. Nikoloudakis, J. Frelek, A. Mitraki and A. G. Coutsolelos, *Nanoscale*, 2018, **10**, 1735-1741.

<sup>55</sup> G. Charalambidis, E. Kasotakis, et al., *Chem-Eur J.*, 2011, **17**, 7213-7219.

<sup>56</sup> G. Charalambidis, E. Georgilis, M. K. Panda, et al., *Nat Commun*, 2016, **7**, 1-11.

<sup>57</sup> K. Karikis, E. Georgilis, G. Charalambidis, et al., *Chem-Eur J.*, 2016, **22**, 11245-11252.

<sup>58</sup> E. Nikoloudakis, K. Karikis, M. Laurans, C. Kokotidou, et al., *Dalton Trans.*, 2018, **47**, 6304-6313.

<sup>59</sup> V. Nikolaou, G. Charalambidis and A. G. Coutsolelos, *Chem. Commun.*, 2021, **57**, 4055-4058.

### **1.4 Water splitting: H<sub>2</sub> production and water oxidation**

As already discussed, the need to change into renewable, clean, and environmentally benign energy sources is unquestionably urgent. Also, the ideal candidate among the renewable sources is the sun, since it is abundant, clean, CO<sub>2</sub>-emission-free and inexhaustible. The next question that needs to be answered is which is the best solar fuel. The zero-emission energy carrier, H<sub>2</sub> is an ideal alternative to carbon-based fuels, since the only product from its combustion with oxygen is water.<sup>60</sup> Hydrogen is considered the fuel of the future, especially when it is generated from water via light driven catalytic reactions. Photocatalytic water splitting is an attractive reaction, which can contribute to an ultimate green sustainable future of our planet, solving energy and environmental issues. Hydrogen production via water splitting with TiO<sub>2</sub> as the photo-catalyst was first reported in 1972.<sup>61</sup> Till then a lot of scientific efforts have been made towards the development of efficient solar driven water splitting systems.<sup>62</sup>

There are two fundamental approaches to achieve light driven water splitting. The first one is a photoelectrochemical device (PEC) (**Figure 1.16**), where a photoanode is able to oxidize water to O<sub>2</sub> and H<sup>+</sup>, utilizing the photo-generated holes due to light irradiation.<sup>63</sup> Subsequently the photo-generated electrons are transferred through an external circuit to the cathode, where H<sub>2</sub> is produced by the reduction of H<sup>+</sup>. This reaction will occur only when all energetic requirements are met, in order to overcome the reaction's overpotential and possible energy losses. This overpotential could be gained from other renewable energy sources. Additionally, the use of molecular catalyst-photosensitizer dyads anchored on semiconductors is also a very promising approach to construct photoanode and photocathode to perform water oxidation and hydrogen production respectively, since no applied bias and no sacrificial agents are needed. The latter is a tandem dye-sensitized photoelectrochemical cell (DSPEC) to perform water splitting (**Figure 1.16b**).

---

<sup>60</sup> Xie Quanhua et al., *Catal Commun*, **2012**; 27 : 21–5.

<sup>61</sup> A. Fujishima, K. Honda *Nature*, 238 (**1972**), pp. 37-38

<sup>62</sup> H. Ahmad, S. K. Kamarudin, L. J. Minggu and M. Kassim, *Renewable and Sustainable Energy Reviews*, 2015, **43**, 599-610.

<sup>63</sup> C.-H. Liao, C.-W. Huang and J. C. S. Wu, *Catalysts*, 2012, **2**, 490-516.

The second approach is a photocatalytic reactor where no external circuit is necessary and the reactions of water oxidation and water reduction are conducted using molecular photocatalysts. In this case, the molecular photocatalysts, uses the energy from sunlight to drive the redox reactions of water splitting into  $H_2$  and  $O_2$ , while the two reactions are conducted in separate places, separated via a membrane (for example nafion), which allows the proton and electron exchange. The operating principle of the photocatalytic systems for water splitting are shown in **Figure 1.17**.<sup>63</sup>

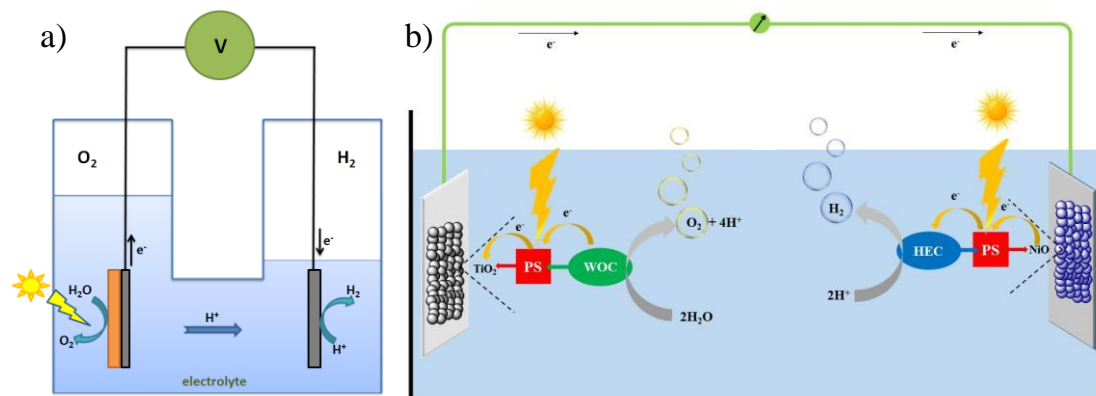


**Figure 1.16** a) Schematic illustration photoelectrochemical water splitting cell,<sup>63</sup> b) tandem dye-sensitized photoelectrochemical cell for water splitting consisting of catalyst-photosensitizer dyads.

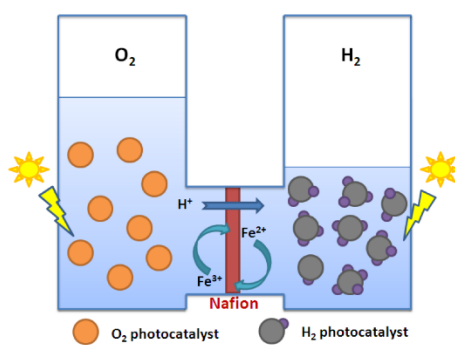


**Figure 1.17** Schematic illustration of photochemical water splitting cell.<sup>63</sup>

Although the ultimate target is to achieve both water reduction and oxidation reactions simultaneously, there are not many reports that have accomplished it. An appropriate strategy to facilitate this challenging purpose, is to isolate the half-reactions and study them separately by focusing either on hydrogen production or on water oxidation systems. In order to achieve this, it is necessary to provide the charges required on the opposite side with sacrificial agents for the regeneration of the catalytic scheme. In the case of hydrogen evolution, a sacrificial electron donor is used while for



water oxidation an acceptor. **Figure 1.18** illustrates a simplified mechanism for both half reactions of water splitting including their necessary components.

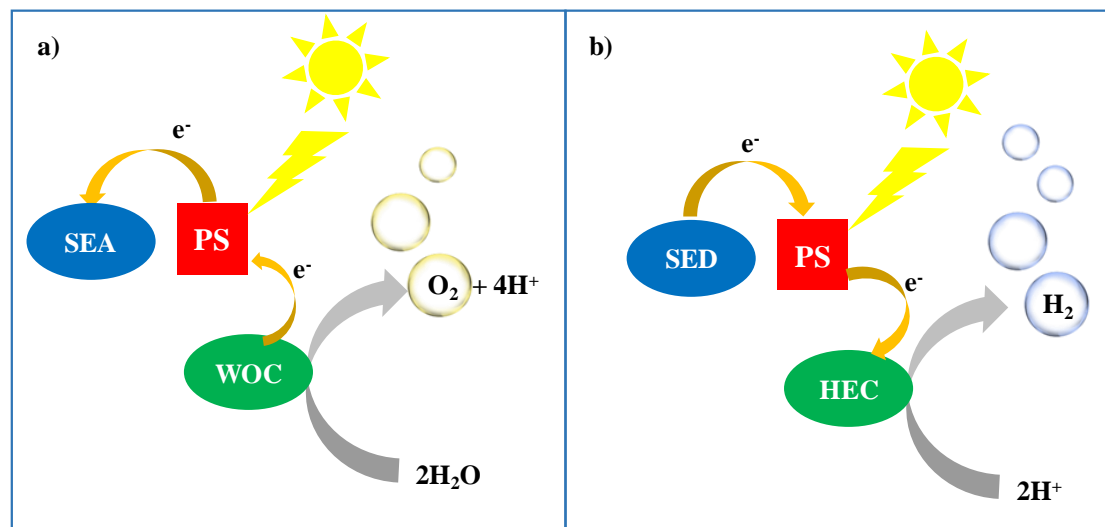


**Figure 1.18** Simplified scheme for photocatalytic water oxidation (a) and photocatalytic hydrogen evolution (b).<sup>64</sup>

In the photochemical hydrogen production system three components are essential: (i) a photosensitizer (PS) able to absorb visible light generating excited species  $PS^*$  with useful redox properties (ii) a catalyst, able to collect several electrons facilitating the water reduction into  $H_2$ , and (iii) a sacrificial electron donor (SED) that can regenerate the photosensitizer. The differences in the case of the photocatalytic water oxidation systems are that the catalyst is able to gain enough oxidizing strength to perform the desired reaction and the sacrificial agent is an acceptor of electrons which again regenerates the photosensitizer.

All the above components can be in the same or in different phases yielding homogenous or heterogeneous catalytic schemes. Each system has both benefits and drawbacks. In homogeneous photocatalysis, the molecular structure of the components is usually well-defined, and this enables the determination of the corresponding catalytic mechanism. The chemical versatility of the molecular catalysts provides control of the physical, optical, and electronic properties by chemical modifications, and allows the identification of the structural characteristics that impact catalytic activity easier. However, homogeneous catalysis suffers from high costs, difficult recovery and separation from the reaction process, and low stability. Although

<sup>64</sup> WOC = water oxidation catalyst, PS = photosensitizer, SEA = sacrificial electron acceptor, HEC = hydrogen evolving catalyst, SED = sacrificial electron donor.

heterogeneous systems have the advantage of efficient recovery, recyclability and stability, other factors such as low light-harvesting capacity and low reactivity limit the overall efficiency. On the other hand, a hybrid system with immobilized photosensitizer and/or catalyst on solid semiconductors, is a potential way to combine the advantages of both approaches.

Inspired by natural photosynthesis, plenty of artificial photocatalytic schemes based on porphyrinoids have been investigated. The unique properties of porphyrinoids enable their utilization both as chromophores and as catalysts. To improve the activity of these schemes it is important to understand in depth the catalytic mechanism of the photocatalytic processes and identify the key factors determining the activity and selectivity. Another challenging endeavor concerns the improvement of stability of the catalytic systems and eliminate the presence of sacrificial agents. The dye sensitization on semiconductors opened the way for the development of molecular-based DSPECs and tandem cell devices based on porphyrins. These systems are one step closer to a real-world application, since there is no need for sacrificial agents and they offer more stable catalysts and photosensitizers.

There are several approaches to design a photoelectrochemical cell and among them dye-sensitized PEC is particularly interesting, since it avoids low bandgap semiconductors, which are usually unstable in contact with an aqueous electrolytes.<sup>65</sup> However, there is a drawback regarding the performances of water splitting DSPECs which is usually modest, probably because the dye must feed the catalyst with several redox equivalents before catalysis occurs.<sup>66,67,68,69</sup>

### **1.5 Alcohol oxidation**

Based on the above limitation of water splitting DSPECs, it would be quite beneficial to choose an oxidation reaction which involves only two oxidizing equivalents, instead of four, improving the challenging multiple charge accumulation

---

<sup>65</sup> Bae, D.; Seger, B.; Vesborg, P. C. K.; Hansen, O.; Chorkendorff, I. *Chem. Soc. Rev.* **2017**, *46* (7), 1933.

<sup>66</sup> Song, W.; Vannucci, A. K.; Farnum, B. H.; Lapidés, A. M.; Brennaman, M. K.; Kalanyan, B.; Alibabaei, L.; Concepcion, J. J.; Losego, M. D.; Parsons, G. N. et al. *J. Am. Chem. Soc.* **2014**, *136* (27), 9773.

<sup>67</sup> Xu, P.; McCool, N. S.; Mallouk, T. E. *Nano Today* **2017**, *14*, 42.

<sup>68</sup> Bozal-Ginesta, C.; Mesa, C. A.; Eisenschmidt, A.; Francàs, L.; Shankar, R. B.; Antón-García, D.; Warnan, J.; Willkomm, J.; Reynal, A.; Reisner, E. et al. *Chem. Sci.* **2021**, *12* (3), 946.

<sup>69</sup> Bold, S.; Massin, J.; Giannoudis, E.; Koepf, M.; Artero, V.; Dietzek, B.; Chavarot-Kerlidou, M. *ACS Catal.* **2021**, *11* (6), 3662.

step. An attractive alternative reaction is the alcohol oxidation into aldehyde. On this field, the inspiring work of Meyer and co-workers<sup>70</sup> was followed by few other studies,<sup>71,72,73</sup> but alcohol oxidation in DSPEC still remains an unexplored research field today, particularly if one compares it with water oxidation.<sup>74,75</sup>

There are plenty of advantages concerning the utilization of light driven alcohol oxidation since it could represent an attractive, cheaper, safer and more environmentally benign oxidation protocol than the usual chemical approaches that employ stoichiometric amounts of toxic oxidants.<sup>76</sup> Moreover, plenty of alcohols are present in biomass which remains an unexploited supply of raw materials for the chemical industry.<sup>77</sup> A simplified scheme of a DSPEC for alcohol oxidation is presented in **Figure 1.19**

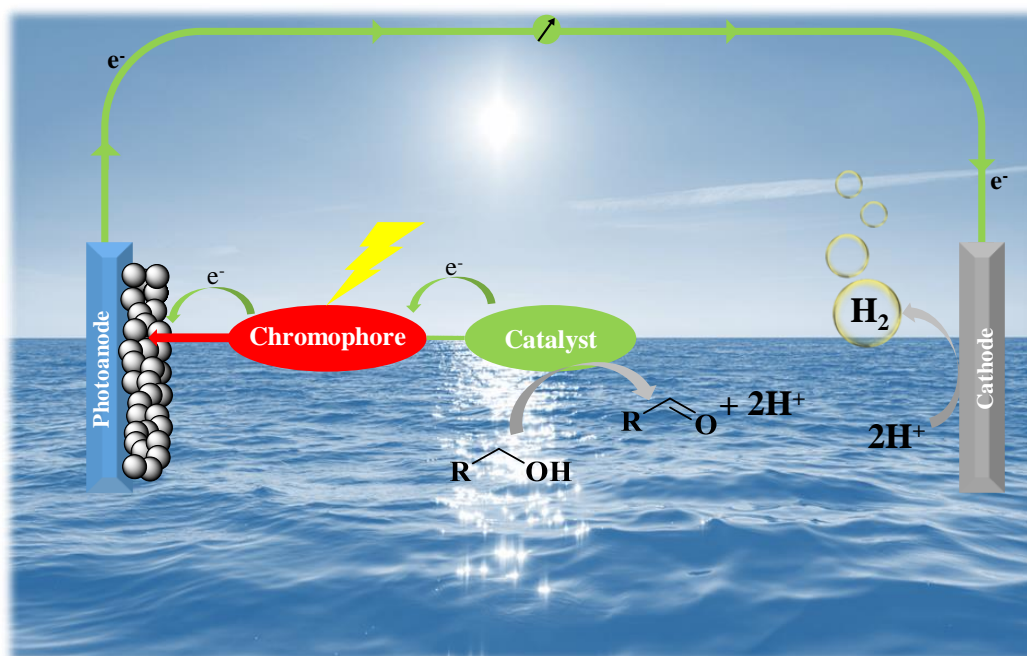


**Figure 1.19** Simplified scheme for photocatalytic alcohol oxidation in a DSPEC device.

<sup>70</sup> Treadway, J. A.; Moss, J. A.; Meyer, T. J. *Inorg. Chem.* **1999**, 38 (20), 4386.

<sup>71</sup> Jiang, J.; Sherman, B. D.; Zhao, Y.; He, R.; Ghiviriga, I.; Alibabaei, L.; Meyer, T. J.; Leem, G.; Schanze, K. S. *ACS Appl. Mater. Interfaces* **2017**, 9 (23), 19529.

<sup>72</sup> Song, W.; Vannucci, A. K.; Farnum, B. H.; Lapidus, A. M.; Brennaman, M. K.; Kalanyan, B.; Alibabaei, L.; Concepcion, J. J.; Losego, M. D.; et al. *J. Am. Chem. Soc.* **2014**, 136 (27), 9773.

<sup>73</sup> Badgurjar, D.; Shan, B.; Nayak, A.; Wu, L.; Chitta, R.; Meyer, T. J. *ACS Appl. Mater. Interfaces* **2020**, 12 (6), 7768.

<sup>74</sup> Ashford, D. L.; Gish, M. K.; Vannucci, A. K.; Brennaman, M. K.; Templeton, J. L.; Papanikolas, J. M.; Meyer, T. J. *Chem. Rev. (Washington, DC, United States)* **2015**, 115 (23), 13006.

<sup>75</sup> Brennaman, M. K.; Dillon, R. J.; Alibabaei, L.; Gish, M. K.; Dares, C. J.; Ashford, D. L.; House, R. L.; Meyer, G. J.; Papanikolas, J. M.; Meyer, T. J. *J. Am. Chem. Soc.* **2016**, 138 (40), 13085.

<sup>76</sup> *Organic Syntheses by Oxidation with Metal Compounds*; Springer: Boston, MA, 1986.

<sup>77</sup> Granone, L. I.; Sieland, F.; Zheng, N.; Dillert, R.; Bahnemann, D. W. *Green Chem.* **2018**, 20 (6), 1169.

## Chapter 2: Thesis Aims and Structure

### Thesis Aims

The present PhD dissertation is inspired by the diverse and versatile role that porphyrin moieties have in plenty of natural systems. The unique properties of porphyrin analogues have opened the way for their utilization in a wide number of applications. As discussed in the introduction of the present thesis, their light harvesting ability renders these molecules promising candidates for solar energy utilization systems. For this reason and in analogy with the title of this dissertation, the main scope of this work was the development of new porphyrin hybrid molecules (where the porphyrin macrocycle is covalently connected with appropriate moieties) and their incorporation as photosensitizers or catalysts in light harvesting applications (**Figure 2.1**).

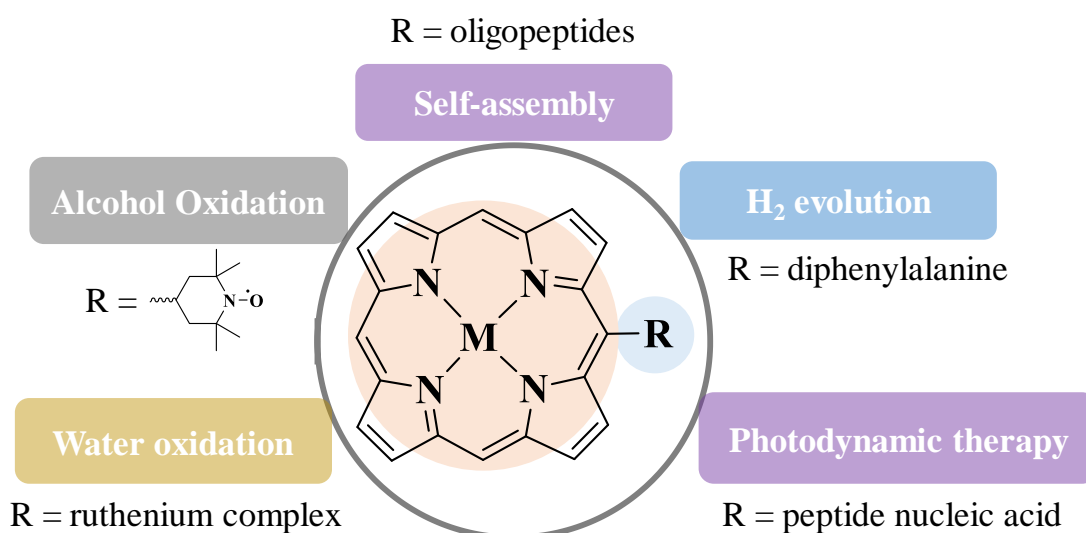


**Figure 2.1** Graphic illustration of bio-inspired solar energy utilization schemes investigated in the present thesis.

The well-organized assemblies that nature exploits in the process of photosynthesis inspired us to design molecular hybrids capable of self-assembling into well-organized nanostructures. Our target is to construct materials with enhanced properties in the self-assembly state. In order to achieve this, we select a molecular self-assembly inducer, that is known for its ability to self-assemble, and we covalently connect it with a porphyrinoid chromophore. The resulting hybrid molecule will possess both light harvesting and self-assembling properties. To this end, we utilize as self-assembly

inducer aromatic and aliphatic dipeptides as well as peptide nucleic acids (PNAs), bearing various protecting moieties, and linked them with porphyrin and boron-dipyrromethene chromophores (**Figure 2.2**).

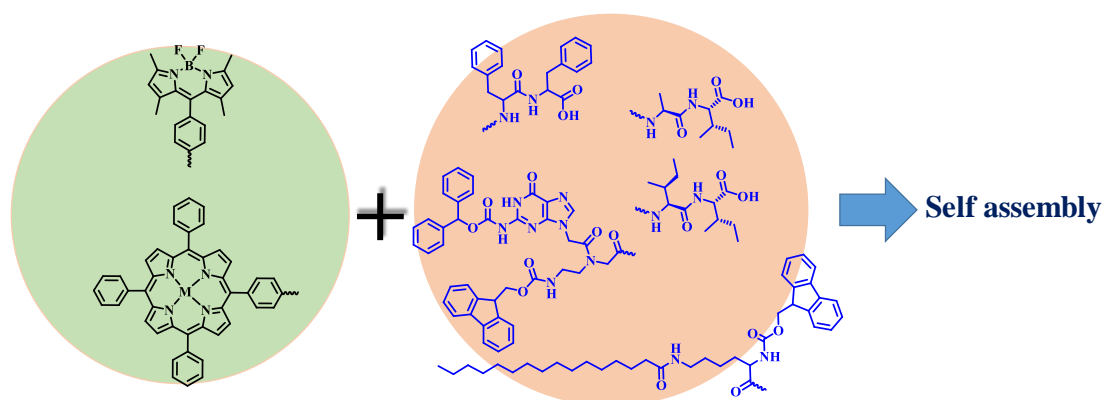


**Figure 2.2** Chromophore-peptide based hybrid compounds investigated in this thesis.

After establishing an efficient way to prepare self-assembled chromophores, we aim to employ them in light harvesting applications. In detail, through photocatalytic  $H_2$  production utilizing self-assembled nanostructures, we target to store solar energy into the chemical bond of hydrogen. This approach is mimicking the natural photosynthesis process, where solar energy is stored into the chemical bonds of glucose. Moreover, supramolecular nanostructures with appropriate size, were investigated in photodynamic therapy and presented promising results.

In the process of photosynthesis, the formation of glucose is accompanied by the production of  $O_2$ . Motivated from this oxidative transformation, we investigate herein the development of artificial photosynthetic systems, where porphyrins connected with appropriate units are employed in dye-sensitized photo-electrochemical (DSPEC) water devices. The important advantage of these systems is the absence of sacrificial agents and the recovery of the system is fairly easier than in homogeneous catalysis.

An alternative oxidative transformation, the selective oxidation of organic molecules, such as alcohols, is certainly a promising approach to obtain valuable carbonyl compounds. This approach requires lower potential demand compared to water oxidation, since only two holes are shifted instead of four. Therefore, one of our aims is to develop alcohol oxidation DSPEC devices producing valuable materials at both electrodes. Figure 2.3 illustrates the chromophore-catalyst dyad systems designed for water and alcohol oxidation photoanodes.

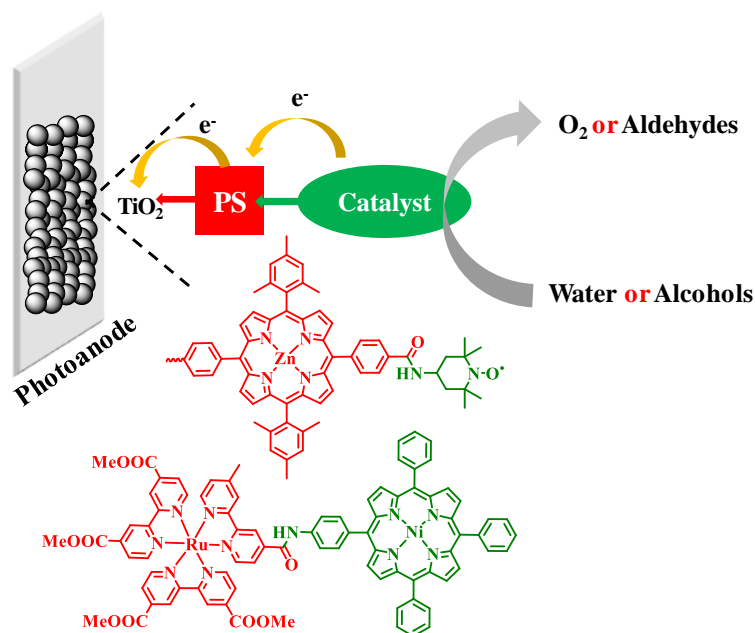


**Figure 2.3** Chromophore-catalyst dyads for water and alcohol oxidation.

### Thesis Structure

The present dissertation is comprised of 6 chapters. Initially a general introduction is presented in chapter 1, regarding the theoretical background supporting the concept of this thesis in combination with relevant literature. Since the successful synthesis of the investigated hybrid compounds was achieved following various synthetic approaches, chapter 1 describes also the main general synthetic procedures for the preparation of the porphyrin derivatives. There are two main chapters, which follow, and they are divided based on the target application. Each chapter consist of two or three sections discussing different individual applications, while the last section contains all the corresponding experimental details. The outline of these two main chapters with respect to their application is the following:

#### Chapter 3: Self-assembly of chromophores and their applications

In this chapter, we synthesized and investigated hybrid chromophore conjugates connected with peptide-based molecules. The main purpose for this coupling was the investigation of the self-assembling properties of the hybrid compounds since we expected that the self-assembly ability of the peptide-based molecule is conveyed to the resulting conjugate. The second purpose was the utilization of these materials in light harvesting applications and more specifically in photodynamic therapy and photocatalytic H<sub>2</sub> production.

*Self-assembly of chromophores for photodynamic therapy*

In this paragraph two hybrid materials were designed and synthesized by conjugating peptide nucleic acids (PNAs) to porphyrin or boron-dipyrromethene, generating PNA-TPP and PNA-BDP assemblies, respectively. Due to the combination of the supramolecular characteristics of PNAs and the porphyrinoid photosensitizers, the two hybrid conjugates readily self-assemble in aqueous solutions and produce well-defined nanoparticles with uniform particle sizes. The resulting two kinds of nanoparticles show good stability in biological solutions and upon dilution. Additionally, the nanoparticles can efficiently interact with cancer cells and the internalized nanoparticles are mainly distributed in the cytoplasm without conveying cytotoxicity in the dark, enabling them to be applied as photodynamic nanodrugs for selective killing of cells (**Figure 2.4**). Indeed, these self-assembled nanoparticles were proven to be efficient nanoagents for photodynamic therapy (PDT) in vitro. Overall, the self-assembly of PNA-chromophore conjugates is a promising approach for constructing supramolecular therapeutic nanoagents based on bioinspired biomaterials.



**Figure 2.4** Schematic illustration of supramolecular nanoparticles constructed by self-assembly of PNA-photosensitizer conjugates for photodynamic therapy.

*Self-assembly of chromophores for photocatalytic hydrogen production*

In this section, the diphenylalanine dipeptide was covalently attached to a tripyridyl porphyrin macrocycle and conveyed self-assembling properties to the resulting hybrid. This hybrid was metallated with non-noble metals, Zn and Sn, and investigated towards photocatalytic hydrogen evolution. The amorphous solid of the Sn derivative, was able to produce hydrogen photocatalytically in the presence of a known cobaloxime catalyst and TEOA as sacrificial electron donor. When the self-assembling nanostructures of the Sn metallated hybrid were employed in the photocatalytic system, enhanced hydrogen production was observed (**Figure 2.5**). Fluorescence and transient absorption



experiments were performed in order to shed light to the electron transfer processes that take place during the photocatalysis.

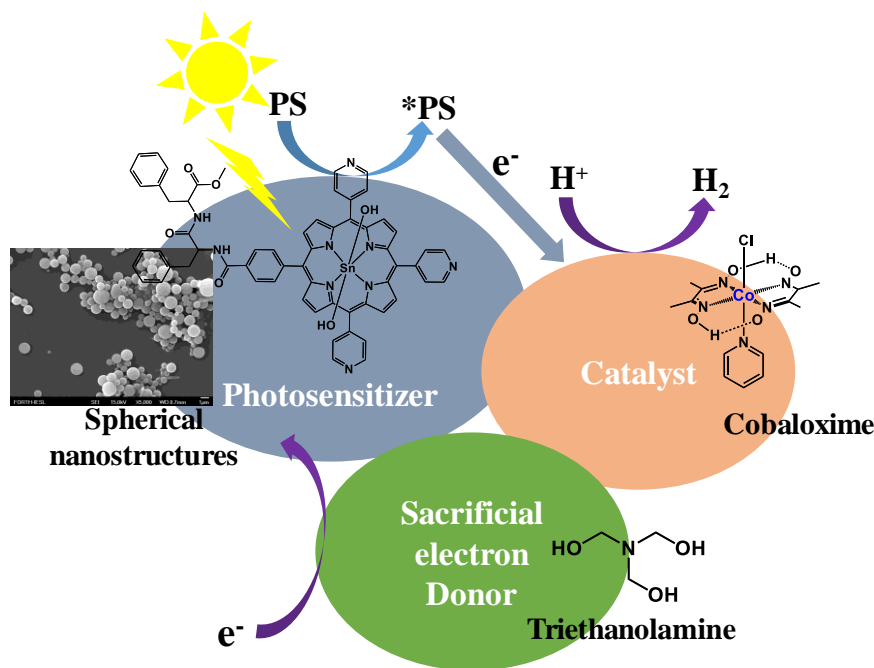


**Figure 2.5** Schematic illustration of the photocatalytic system for hydrogen production utilizing the supramolecular nanostructures of porphyrin-diphenylalanine hybrids.

#### *Chapter 4: Photocatalytic oxidation transformations*

In this section several chromophore-catalyst dyads have been synthesized, characterized and investigated in photocatalytic oxidation reactions, namely water and alcohol oxidation.

##### *Photocatalytic water oxidation*

This section describes the visible-light-induced oxidation of water to dioxygen, catalyzed by a newly synthesized **NiP-Ru** dyad consisting of a ruthenium tris(bipyridyl),  $[\text{Ru}(\text{bpy})_3]^{2+}$  as photosensitizer, and a nickel porphyrin, as water oxidation catalyst (**Figure 2.6**). Photocatalytic experiments in organic solutions were performed showing that the covalently connected dyad exhibited enhanced performance compared to the individual species. The efficient oxygen evolution was proven both by photocatalytic electron pooling experiments involving methyl viologen ( $\text{MV}^{2+}$ ) as electron acceptor, followed by UV-Vis spectral detection of the  $\text{MV}^{+}$ , and by photocatalytic experiments quantifying the evolved oxygen via an optical oxygen



sensor. Additionally, a dye sensitized photoelectrochemical cell (DSPEC) was fabricated using the **NiP-Ru** dyad (with carboxy anchoring groups onto the bipyridine) adsorbed on  $\text{TiO}_2$  photoanode and demonstrated its ability to perform water oxidation in aqueous media at neutral pH (**Figure 2.6**). This work demonstrates the significance of nickel porphyrins as a cheaper alternative to traditional Ru based water oxidation catalysts.

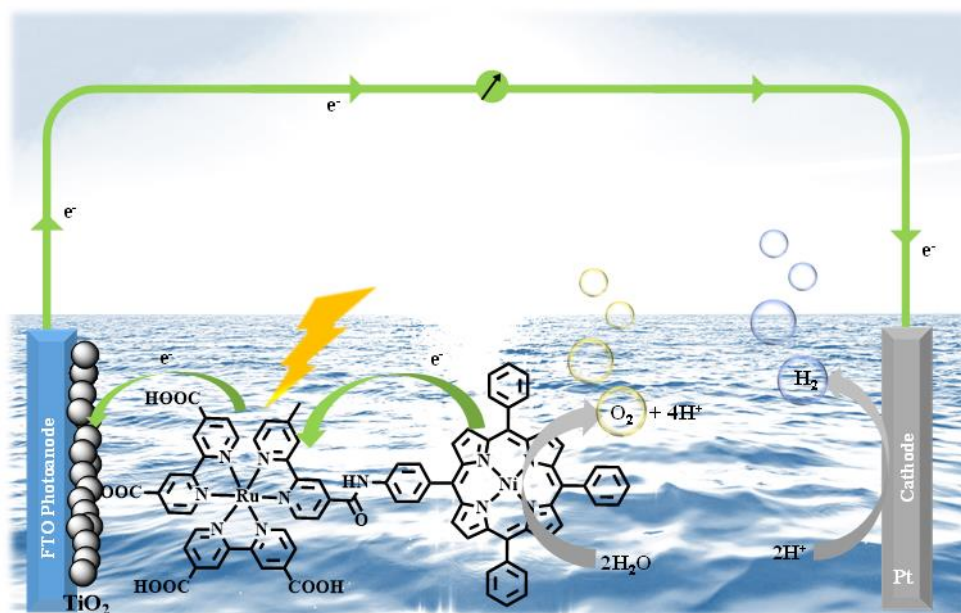


**Figure 2.6** Schematic illustration of the **NiP-Ru** DSPEC system for water oxidation.

#### *Photocatalytic alcohol oxidation*

In correlation with the previous section, we explored a new catalytic reaction, other than water oxidation, at the photoanode of a photoelectrochemical cell in order to provide the electrons needed for the production of useful fuels. For this purpose, we synthesized dyad compounds using a zinc porphyrin (ZnP) sensitizer connected to a TEMPO organo-catalyst and fabricated  $\text{TiO}_2$  based dye-sensitized photoelectrochemical (DSPEC) systems in order to perform light driven oxidation of methoxybenzyl alcohol into the corresponding aldehyde (**Figure 2.7**). Several ZnP-TEMPO dyads, bearing different anchoring groups on the ZnP, were prepared. Initially the photovoltaic performances in DSSCs were examined in order to optimize the dyeing conditions and compare the relative efficiencies of the compounds. The dyads substituted with TEMPO outperformed the reference zinc porphyrins lacking the TEMPO moiety. The photocatalytic activity of the chemisorbed on  $\text{TiO}_2$  dyads towards alcohol oxidation was investigated both in aqueous buffer and in organic (acetonitrile)

electrolyte. The stability of the anchor is very important in acetonitrile electrolyte, where the dyad is partially soluble, since only the dyad functionalized with hydroxamic acid was compatible under these organic solvent conditions. This study opens the way to the development of more efficient and more stable DSPECs for alcohol oxidation that could compete those applied to water oxidation by generating more valuable products.

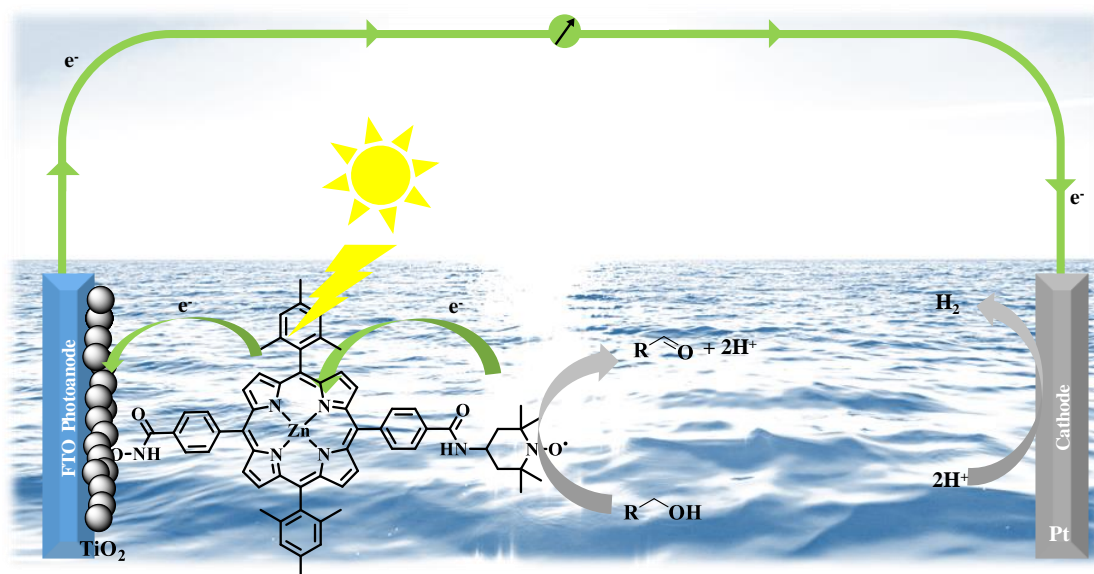


**Figure 2.7** Schematic illustration of the **ZnP-TEMPO** DSPEC system for alcohol oxidation.

In the end, the summary accompanied by some concluding remarks of this PhD dissertation are presented in chapter 5. The last chapter (chapter 6) contains all the supporting information regarding each project including photophysical measurements, NMR spectra (<sup>1</sup>H and <sup>13</sup>C), mass spectra, electrochemical characterization, etc.

### **Chapter 3: Self-assembly of chromophores and their applications**

Molecular self-assembly is a well-established bottom up approach towards the creation of nano- and micro- materials with enhanced properties.<sup>78</sup> Inspired by natural well organized assemblies, supramolecular chemists are investigating the molecular self-assembly of small building blocks to construct such materials. During the last decades, a large amount of molecular building blocks has been tested in order to form supramolecular architectures.<sup>79</sup> Apart from the selection of the building blocks, various other parameters such as the solvent, the temperature and the concentration play significant role in the formation of well-defined self-assemblies.<sup>80</sup> However, predicting and controlling the shape or size of the self-assembled nanostructures, remains a challenging task.<sup>81</sup> Since the building blocks involved in this bottom-up approach are molecules, which are not extended structures, their assembly must derive from their inherent properties.<sup>82</sup> In the formation of supramolecular structures, the selection of the building blocks is crucial, however another important challenge is to understand and dictate the cumulative non-covalent interactions that will participate throughout the formation of supramolecular structures. Such interactions are electrostatic and Van der Waals interactions including hydrogen bonds,  $\pi$ - $\pi$  stacking, hydrophobic forces etc.<sup>83</sup>

Diphenylalanine (FF) is a versatile building block with the ability to self-assemble, forming various nanostructures.<sup>84</sup> FF has been studied with a wide variety of complexes (covalently or non-covalently connected) and the tendency of such systems to form multifunctional nanostructures has been explored.<sup>85,86</sup> Covalent attachment of the FF dipeptide to porphyrins (**Figure 3.1.1**),<sup>87,88</sup> corroles,<sup>89</sup> boron-dipyrromethenes,<sup>90</sup>

---

<sup>78</sup> H. Zhang, L. Y. Guo, J. M. Jiao, X. Xin, D. Sun and S. L. Yuan, *ACS Sustain. Chem. Eng.*, **2017**, *5*, 1358-1367.

<sup>79</sup> Y. Y. Mai and A. Eisenberg, *Chem. Soc. Rev.*, **2012**, *41*, 5969-5985.

<sup>80</sup> W. L. Noorduin, A. Grinthal, L. Mahadevan and J. Aizenberg, *Science*, **2013**, *340*, 832-837.

<sup>81</sup> G. Izzet, and A. Proust et al., *J. Am. Chem. Soc.*, **2016**, *138*, 5093-5099.

<sup>82</sup> E. Bash, *Introduction to Nanoscale Science and Technology*, **2015**, vol. 1.

<sup>83</sup> X. H. Yan, P. L. Zhu and J. B. Li, *Chem. Soc. Rev.*, **2010**, *39*, 1877-1890.

<sup>84</sup> Gazzit and coworkers, *Science* **2003**, *300*, 625.

<sup>85</sup> K. Liu, R. Xing, Q. Zou, G. Ma, H. Mohwald and X. Yan, *Angew. Chem. int. Ed.*, **2016**, *55*, 3036-3039.

<sup>86</sup> Q. Zou et al., *Angew. Chem. int. Ed.*, **2014**, *53*, 2366-2370.

<sup>87</sup> G. Charalambidis et al., *Chem. Eur. J.*, **2011**, *17*, 7213-7219.

<sup>88</sup> G. Charalambidis et al., *Nat. Commun.*, **2016**, *7*, 12657.

<sup>89</sup> K. Karikis et al., *Chem. Eur. J.*, **2016**, *22*, 11245-11252.

<sup>90</sup> K. Karikis, A. Butkiewicz, F. Folias, G. Charalambidis, C. Kokotidou, A. Charisiadis, V. Nikolaou, E. Nikoloudakis, J. Frelek, A. Mitraki and A. G. Coutsolelos, *Nanoscale*, **2018**, *10*, 1735-1741.

ferrocene,<sup>91</sup> folic acid,<sup>92</sup> PEG polymers<sup>93</sup> and DNA<sup>94</sup> has been proven a successful methodology towards the formation of well-ordered aggregates with light harvesting properties.

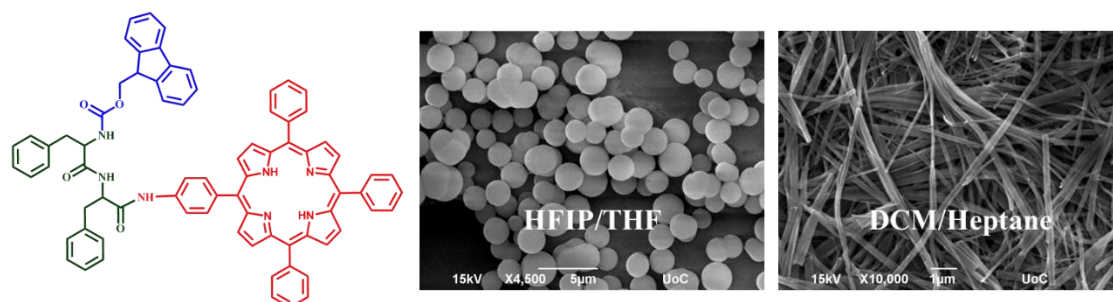


**Figure 3.1.1** Fmoc-FF-TPP self-assembles into spheres or fibers depending on the solvent system.<sup>87,88</sup>

These nanomaterials have unique properties and have found application in photodynamic therapy (PDT)<sup>95</sup> (**Figure 3.1.2**), drug delivery,<sup>96</sup> and catalysis.<sup>97</sup>

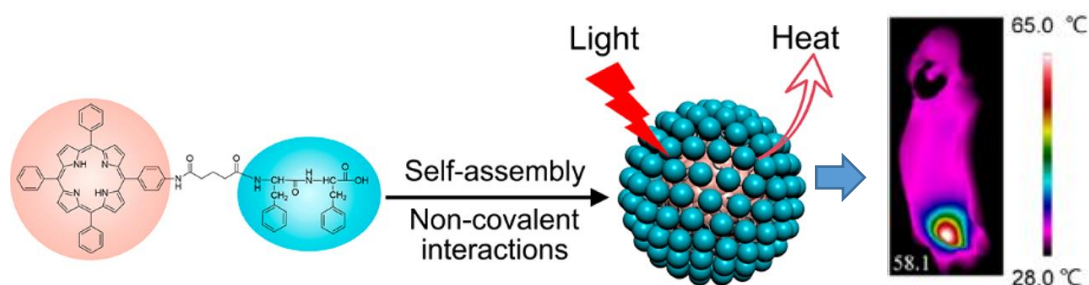


**Figure 3.1.2** TPP-G-FF self-assembles into nanodots with high light-to-heat conversion efficiency, providing a remote-controlled way to destroy carcinomatous cells.<sup>19</sup>

It is not only diphenylalanine (FF) that has the ability to self-assemble into supramolecular nanostructures, since there are also other simpler aliphatic peptides such as Isoleucine<sup>98</sup> and Alanine<sup>99</sup> that have similar properties. Therefore, dipeptides

<sup>91</sup> J. Wang, D. Li, M. Yang and Y. Zhang, *Anal. Methods*, **2014**, 6, 7161-7165.

<sup>92</sup> G. Emtiazi, T. Zohrabi, L. Y. Lee, N. Habibi and A. Zarrabi, *J. Drug Deliv. Sci. Technol.*, **2017**, 41, 90-98.

<sup>93</sup> C. Diaferia, E. Gianolio, A. Accardo and G. Morelli, *J. Pept. Sci.*, **2017**, 23, 122-130.

<sup>94</sup> N. Gour, D. Kedracki, I. Safir, K. X. Ngo and C. Vebert-Nardin, *Chem. Commun.*, **2012**, 48, 5440-5442.

<sup>95</sup> Q. Zou, M. Abbas, L. Zhao, S. Li, G. Shen and X. Yan, *J. Am. Chem. Soc.*, **2017**, 139, 1921-1927.

<sup>96</sup> *Angew. Chem. Int. Ed.* **2018**, 57, 17235–17239.

<sup>97</sup> K. Tao, B. Xue, S. Frere, I. Slutsky, Y. Cao, W. Wang and E. Gazit, *Chem. Mater.*, **2017**, 29, 4454-4460.

<sup>98</sup> Subbalakshmi C et al., *Biopolymers*. **2017**;108:e23033.

<sup>99</sup> Jichao Sun et al., *RSC Adv.*, **2015**, 5, 102182-102190

Isoleucine-Isoleucine (Ile-Ile or II) and Isoleucine-Alanine (Ile-Ala or IA) (**Figure 3.1.3**) are promising candidates for inducing self-assembly to chromophores.

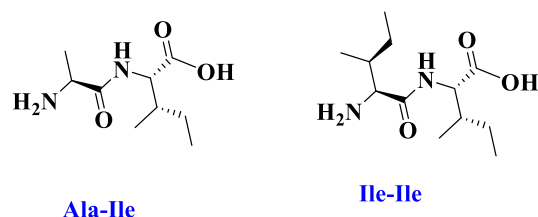


**Figure 3.1.3** Chemical structures of Isoleucine-Isoleucine and Alanine-Isoleucine.

Peptide scaffolds are attractive composites for molecular self-assembly due to their chemical and physical characteristics and constitute one of the main branches of bio-nanotechnology. DNA self-assemblies include a unique characteristic, the specific Watson–Crick base pairing through complementary hydrogen bonding interactions. Therefore, the combination of peptides and nucleic acids in synthetic peptide nucleic acids (PNAs) is a novel strategy to design self-organized materials.<sup>100</sup> An example is presented in **Figure 3.1.4**, where a PNA comprising of guanine DNA base and glycine peptide bearing two aromatic protecting groups was able to self-assemble into nanospheres which exhibited properties of photonic crystals.

PNAs were firstly synthesized in early 1990s<sup>101</sup> and due to their structural characteristics, which include DNA bases and a peptide backbone, may be regarded either as DNA or peptide mimics.<sup>102</sup> Recently, Gazit and coworkers explored the propensity of PNAs to self-assemble into more complex supramolecular structures.<sup>103</sup>

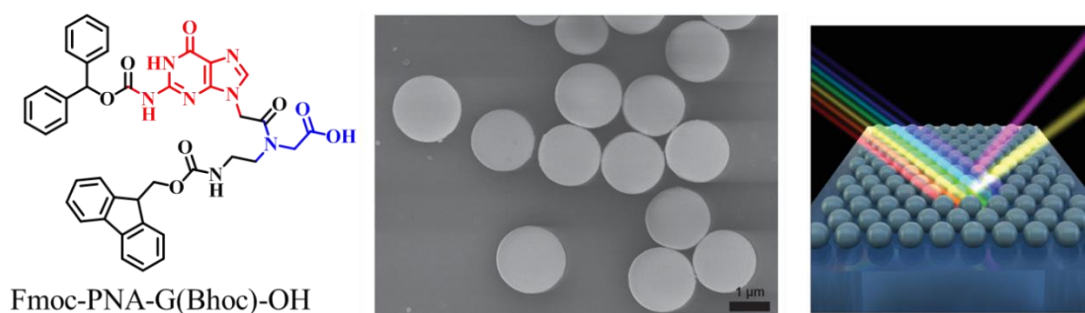


**Figure 3.1.4** PNA self-assembled nanospheres have properties of photonic crystals.<sup>100</sup>

Incorporation of biological scaffolds, such as DNA and peptides, has been proven a useful technique in order to create ordered structures with a wide range of

<sup>100</sup> O. Berger and E. Gazit et al., *Nat. Nanotechnol.*, **2015**, 10, 353–60.

<sup>101</sup> P. E. Nielsen, M. Egholm, R. H. Berg, O. Buchardt, *Science* **1991**, 254, 1497–1500.

<sup>102</sup> X.-L. Zhao, B.-C. Chen, J.-C. Han, L. Wei, X.-B. Pan, *Sci. Rep.* **2015**, 5, 17640.

<sup>103</sup> O. Berger and E. Gazit, *Biopolymers*, **2017**, 108, e22930.

chromophores, i.e. porphyrins, corroles, ferrocene and BODIPY. The covalent attachment with chromophores makes the resulting hybrids possible candidates for biological applications such as drug delivery,<sup>104</sup> photothermal therapy (PTT) and photodynamic therapy (PDT).<sup>105</sup> PNAs, which combine stacking interactions, hydrogen bonding and Watson–Crick base pairing, could serve as an excellent scaffold in order to create uniform supramolecular assemblies based on porphyrins and BODIPYs.

### **3.1 Synthesis and self-assembling studies**

Inspired from the above examples, we designed several hybrid molecules comprising of a porphyrin or BDP chromophore and a peptide-based molecule. We describe their synthesis and their self-assembling properties in the following section. In detail, we examined whether the self-assembly ability of the peptide-based molecule is conveyed to the resulting dyad.

- PNA-chromophore conjugates:

The synthetic procedure,<sup>106</sup> that was followed for the preparation of the PNA-chromophore conjugates (**Scheme 3.1.1**), begins with a straightforward reaction of **TPP-NH<sub>2</sub>**<sup>107</sup> or **BDP-NH<sub>2</sub>**<sup>108</sup> with commercially available Fmoc-PNA-G-(Bhoc)-OH. The **PNA-TPP** and **PNA-BDP** hybrids were obtained in high yields through amide coupling using DCC/HOBt coupling reagents, under low-temperature conditions (8 °C). Noteworthy, for the coupling of BDP-NH<sub>2</sub> with PNA, room temperature was necessary for the reaction to reach completion. The detailed experimental procedure is presented in section 3.4 while the corresponding <sup>1</sup>H and <sup>13</sup>C NMR spectra (**Figures 6.3.1 - 6.3.10**) which verified the successful synthesis are presented in chapter 6.

---

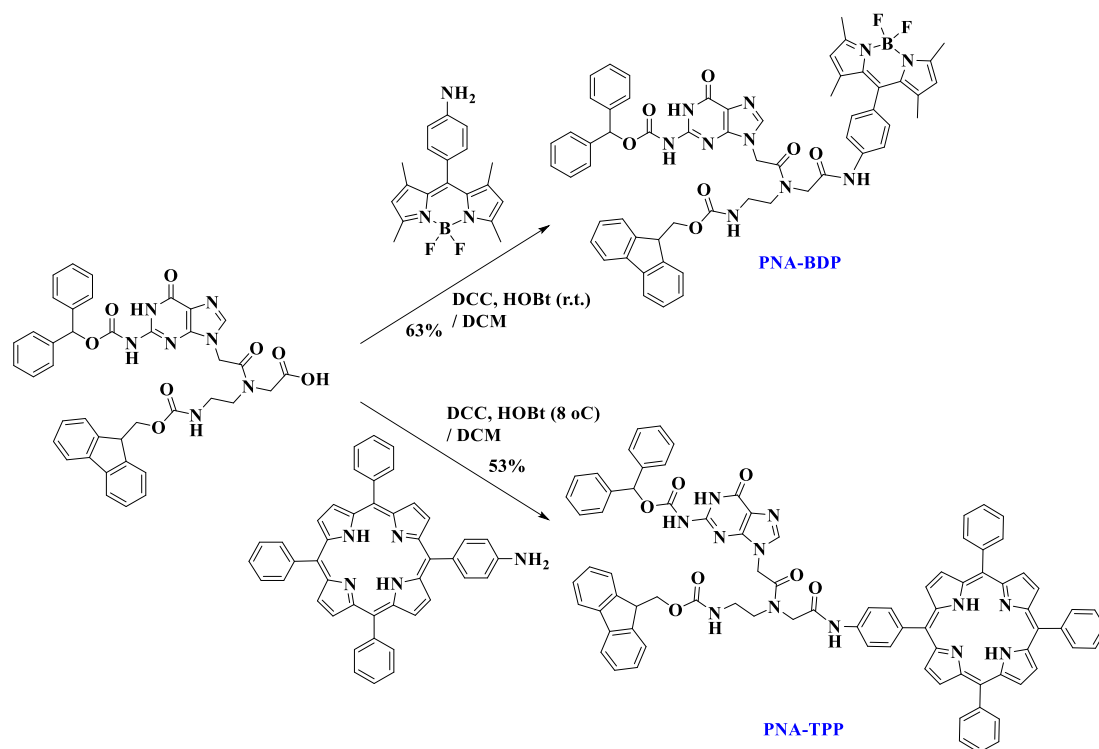
<sup>104</sup> *Angew. Chem. Int. Ed.* **2018**, *57*, 17235–17239.

<sup>105</sup> *J. Am. Chem. Soc.* **2017**, *139*, 1921–1927.

<sup>106</sup> Nikoloudakis E. et al. *Nanoscale*, **2019**, *11*, 3557–3566

<sup>107</sup> K. Ladomenou, T. Lazarides, M. K. Panda, G. Charalambidis, D. Daphnomili, A. G. Coutsolelos *Inorg. Chem.* **2012**, *51*, 20, 10548–10556.

<sup>108</sup> Imahori, H. et al. *J. Am. Chem. Soc.* **123**, 100–110 (2001).



**Scheme 3.1.1** Synthesis of **PNA-TPP** and **PNA-BDP**.

In the PNA-BDP or PNA-TPP conjugates, PNA was introduced as the core self-assembling motif while BDP and TPP chromophore moieties were introduced in order to provide  $\pi$ - $\pi$  stacking and hydrophobic interactions as well as light absorbing ability. The PNA-BDP nanoparticles (PNA-BDP NPs) and PNA-TPP nanoparticles (PNA-TPP NPs) were prepared readily via the self-assembly of PNA-BDP and PNA-TPP in aqueous media.<sup>109</sup> For the preparation of the PNA-BDP NPs and PNA-TPP NPs initially the hybrids were dissolved in DMSO ( $1 \text{ mg}\cdot\text{mL}^{-1}$ ). The PNA-chromophore NPs were prepared by mixing  $100 \text{ }\mu\text{L}$  of the DMSO solution with  $900 \text{ }\mu\text{L}$  pure water followed by adjusting the pH to 7 by aqueous NaOH. The resulting PNA-chromophore NPs were aged for 24 h and then washed by water before further use.

Transmission electron microscopy (TEM) images revealed that the PNA-BDP nanoparticles were uniform nanospheres as depicted in **Figure 3.1.5a**. The spherical morphology of the PNA-BDP nanoparticles was also confirmed by scanning electron microscopy (SEM) images (**Figure 3.1.5b**). Dynamic light scattering (DLS) measurements showed that the hydrodynamic diameter of the PNA-BDP NPs is about  $102 \pm 34 \text{ nm}$  (**Figure 3.1.5c**), which was comparable to the results derived from SEM

<sup>109</sup> Chang R., Nikoloudakis E. et al. *ACS Appl. Bio Mater.* **2020**, 3, 1, 2–9



and TEM images. Similarly, the PNA-TPP NPs were also characterized by TEM and SEM. The TEM results showed that the PNA-TPP NPs are solid nanospheres (**Figure 3.1.5d**) while SEM images revealed that the nanospheres were highly uniform (**Figure 3.1.5e**). A size distribution profile with the average value of about  $89 \pm 35$  nm (**Figure 3.1.5f**) was given by DLS results. These two kinds of nanoparticles with uniform morphology and sizes are suitable for cell uptake<sup>110,111</sup> and can find application in photodynamic therapy as explained in the section 3.2. The SEM, TEM and DLS experiments were conducted by Rui Chang in the laboratory of Dr. Xuehai Yan (*State Key Laboratory of Biochemical Engineering, Institute of Process Engineering, Chinese Academy of Sciences, Beijing 100190, China*).

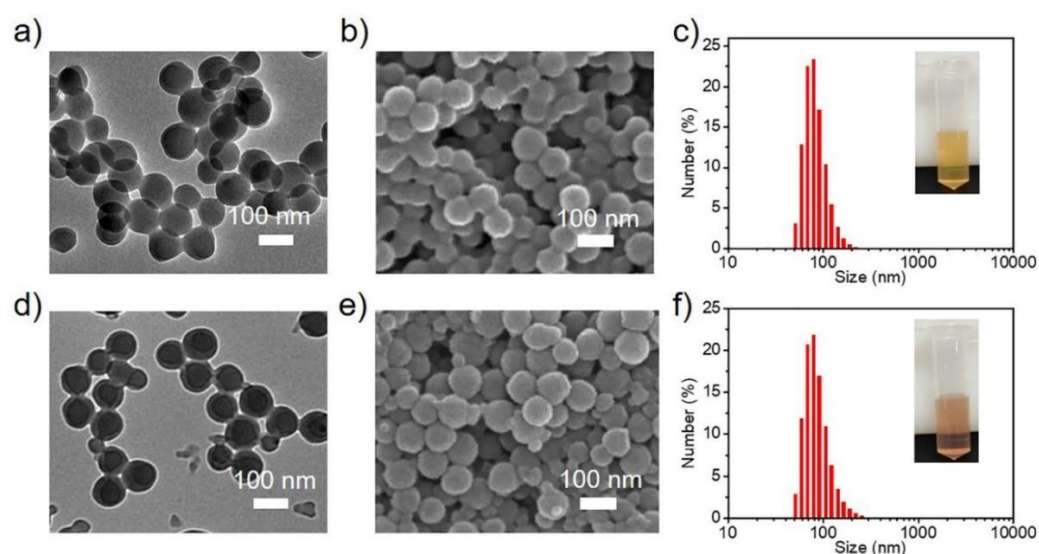


**Figure 3.1.5** The structures and size distribution of the PNA-BDP NPs and PNA-TPP NPs. (a) TEM image and (b) SEM image of the PNA-BDP NPs. (c) DLS profile of the PNA-BDP NPs with a picture of the sample shown in the inset. (d) TEM image and (e) SEM image of the PNA-TPP NPs. (f) DLS profile of the PNA-TPP NPs with a picture of the sample shown in the inset.

- Porphyrin-Diphenylalanine conjugates:

As we already mentioned the most extensively studied small peptide, famous for its self-assembling properties, is diphenylalanine (FF). Our group has extensively investigated chromophores such as BDPs,<sup>90</sup> porphyrins,<sup>87</sup> corroles<sup>89</sup> and polyoxometalates<sup>139</sup> covalently linked with FF and the resulting conjugates retained the

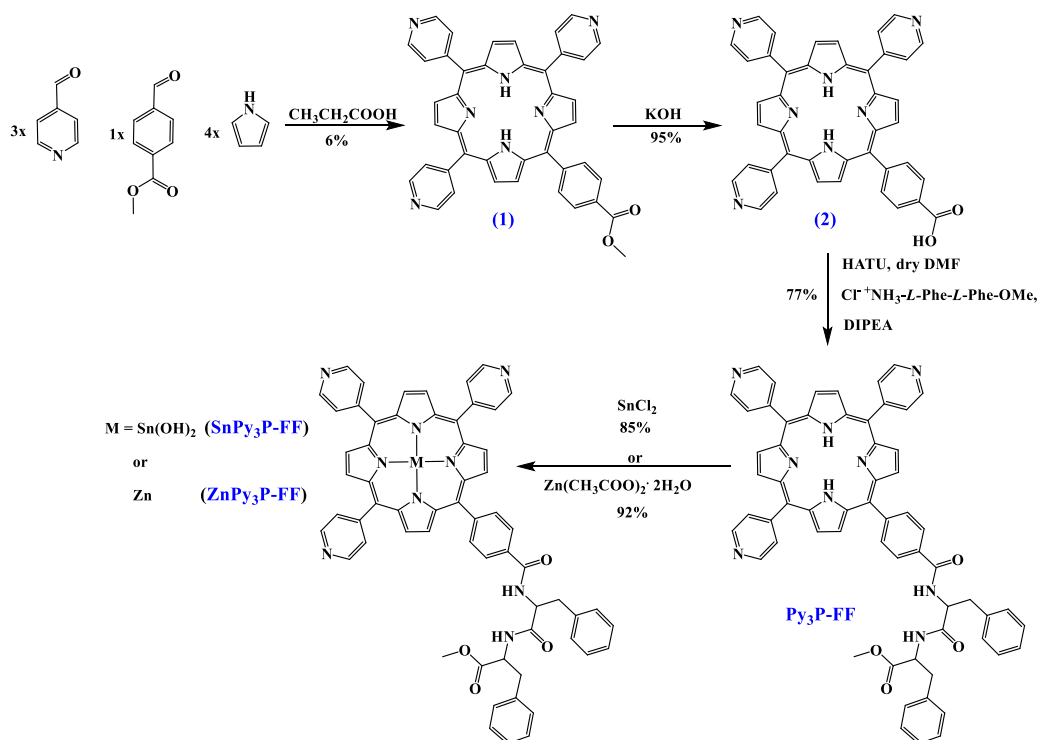
<sup>110</sup> Li, Y.; Li, N.; Pan, W.; Yu, Z.; Yang, L.; Tang, B., *ACS Appl. Mater. Interfaces* **2017**, 9, 2123-2129.

<sup>111</sup> Lu, F.; Wu, S.; Hung, Y.; Mou, C., *Small* **2009**, 5, 1408-1413.



characteristic of self-assembly. In this concept, we synthesized porphyrin – diphenylalanine conjugates having different peripheral substitution, namely pyridyl and phenyl. Additionally, the effect of the metal inside the porphyrin macrocycle was investigated as a parameter that might alter the self-assembling mode. We will initially describe the synthesis and self-assembly studies of the pyridyl derivatives and then continue with the phenyl ones.

The synthetic procedure<sup>112</sup> for the preparation of **Py<sub>3</sub>P-FF**, **SnPy<sub>3</sub>P-FF** and **ZnPy<sub>3</sub>P-FF** is illustrated in **Scheme 3.1.2**. Initially, a cyclisation reaction using pyridine-4-carboxaldehyde, 4-formyl benzoate and pyrrole in propionic acid resulted in the formation of methyl ester derivative **1**. Then, deprotection under basic conditions of porphyrin **1** led to the production of acid porphyrin **2**. Subsequently, an amide coupling with the carboxy protected dipeptide of diphenylalanine was achieved using HATU as coupling reagent yielding porphyrin **Py<sub>3</sub>P-FF**. Notably, no product formation was observed when the classic coupling reagents DCC/HOBt were employed, in contrary to similar coupling reactions of triphenyl porphyrins. The last step was the metalation of the free base porphyrin **Py<sub>3</sub>P-FF** with Sn and Zn to yield **SnPy<sub>3</sub>P-FF** and **ZnPy<sub>3</sub>P-FF** respectively.



**Scheme 3.1.2** Synthesis of **Py<sub>3</sub>P-FF**, **SnPy<sub>3</sub>P-FF** and **ZnPy<sub>3</sub>P-FF**.

<sup>112</sup> Nikoloudakis E. et al. *ACS Sustainable Chem. Eng.* **2021**, 9, 23, 7781–7791

The detailed experimental procedure is given in section 3.4 while the corresponding  $^1\text{H}$  and  $^{13}\text{C}$  NMR spectra (Figures 6.3.11 - 6.3.18) which verified the successful synthesis are presented in chapter 6. Additionally, cyclic and square wave voltammetry measurements were performed to investigate the electrochemical properties of the synthesized hybrids (Figures 6.3.19 - 6.3.20, Table 6.3.1).

#### *Scanning Electron Microscopy studies*

The ability of the synthesized porphyrin conjugates to self-assemble into distinctive architectures was investigated with scanning electron microscopy. Initially, the hybrid compounds were dissolved in a chaotropic “good” solvent, namely 1,1,1,3,3,3-hexafluoroisopropanol (HFIP), dichloromethane (DCM) or tetrahydrofuran (THF) and subsequently a “bad” solvent, namely methanol (MeOH) or heptane, was introduced in order to induce the self-assembly process. The major parameters investigated were the metal in the macrocycle of the porphyrin and the solvent mixture. To the best of our knowledge, this is the first report so far that examines the effect of the metal inside the porphyrin macrocycle in the self-assembling ability of the porphyrin.

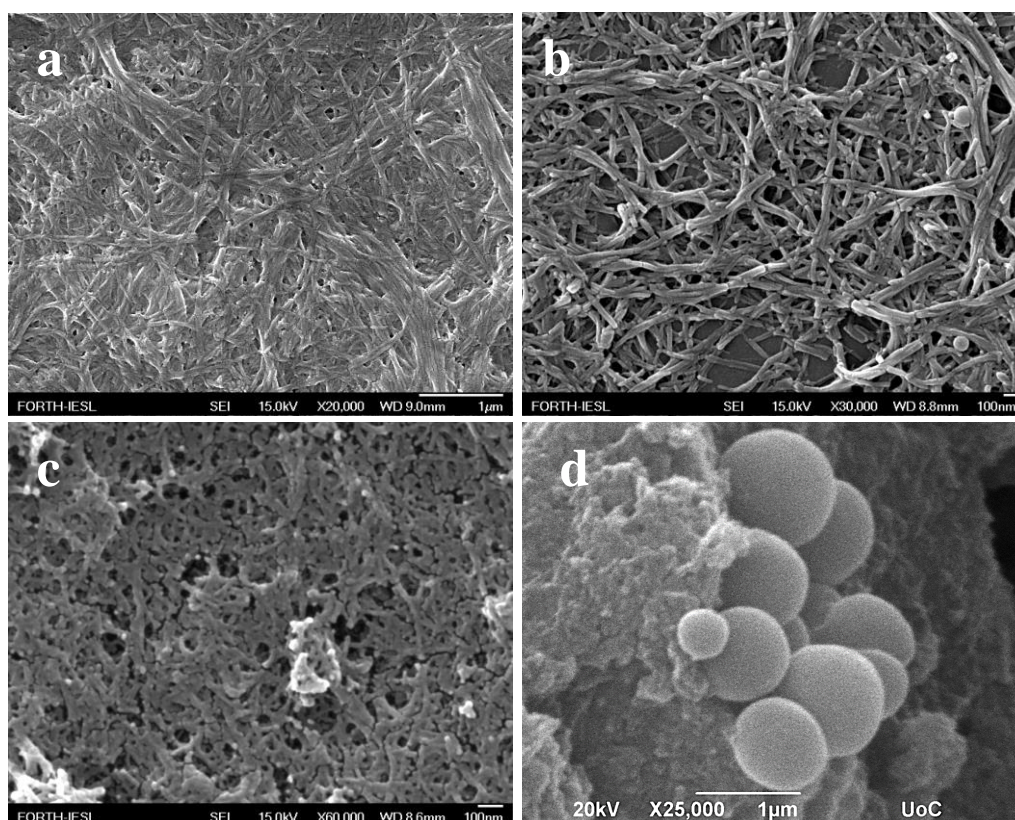


**Figure 3.1.6** Self-assembly behavior of Py<sub>3</sub>P-FF in (a) DCM-MeOH 2:8, (b) HFIP-MeOH 2:8, (c) DCM-Heptane 2:8, (d) THF-MeOH 2:8.

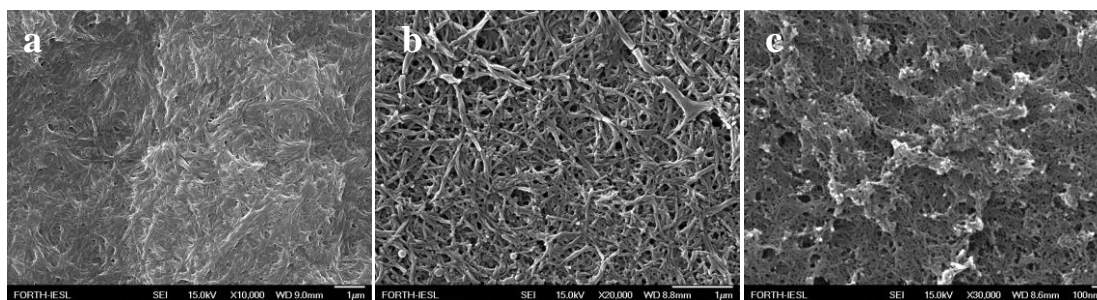


**Figure 3.1.7** Self-assembly behavior of **Py<sub>3</sub>P-FF** in (a) DCM-MeOH 2:8, (b) HFIP-MeOH 2:8, (c) DCM-Heptane 2:8.

As depicted in **Figures 3.1.6** and **3.1.7**, the hybrid chromophore **Py<sub>3</sub>P-FF** was able to self-assemble into fibrillar nanostructures in DCM-MeOH 2:8 and HFIP-MeOH 2:8 solvent mixtures, while when THF was used as “good” solvent spherical assemblies were obtained. The less polar system DCM-Heptane 2:8 gave rise to a thinner fibrillar network compared to the first ones. The introduction of a metal into the porphyrin macrocycle was not expected to affect significantly the morphology of the resulted nanostructures.<sup>113</sup> Interestingly, the tin metallated derivative exhibited much different self-assembling behavior (**Figures 3.1.8** and **3.1.9**). **SnPy<sub>3</sub>P-FF** assembled into spherical nanostructures in DCM-MeOH 2:8 and HFIP-MeOH 2:8 solvent systems, while the use of THF as a “good” solvent resulted in amorphous aggregation. When the less polar DCM-Heptane 2:8 system was used in the tin derivative, agglomerated spheres were obtained (**Figure 3.1.8c**).

The evaporation of the “good” solvent only did not result into defined self-assembled structures, but to a sponge-like network, as is depicted in **Figure 3.1.9f**, proving the necessity of the two different solvents for the induction of the self-assembling process. The use of zinc into the porphyrin core under the same self-assembling conditions did not show any well-defined nanostructures (**Figure 3.1.10**). This could be attributed to the interaction between the peripheral pyridyl groups of one porphyrin moiety and the Zn metal of another moiety towards the formation of an irregular network. Only in the mixture THF-MeOH 2:8, relatively well-defined nanospheres were observed for the **ZnPy<sub>3</sub>P-FF** hybrid (**Figure 3.1.10d**).

<sup>113</sup> Charalambidis, G.; Georgilis, E.; Panda, M. K.; Anson, C. E.; Powell, A. K.; Doyle, S.; Moss, D.; Jochum, T.; Horton, P. N.; Coles, S. J. et al. *Nat. Commun.* **2016**, 7, 1.

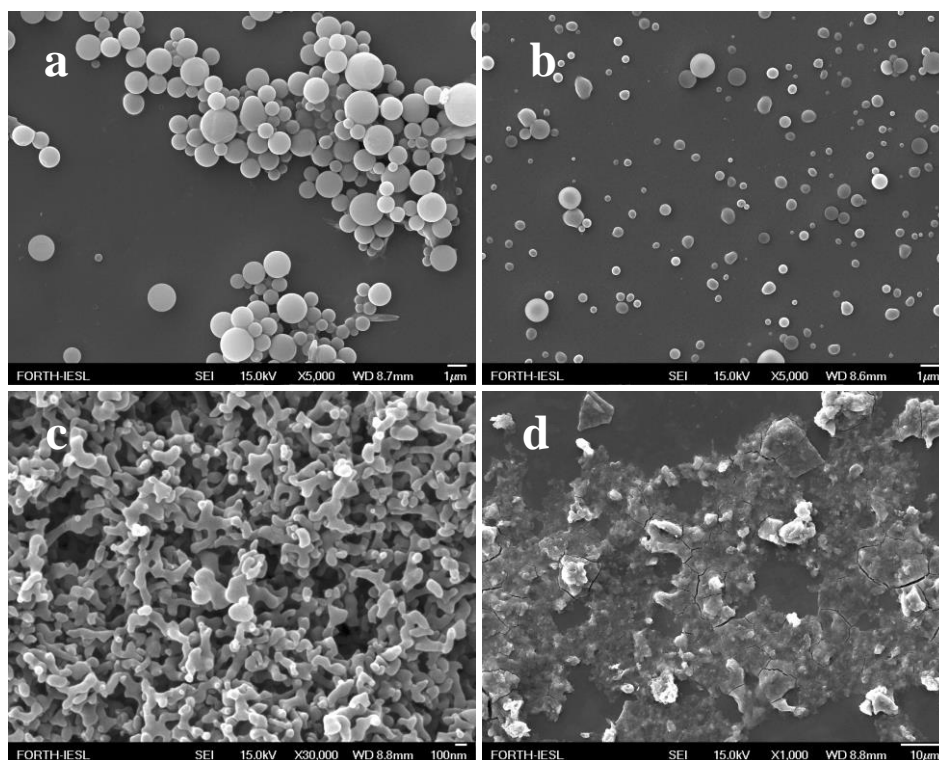


**Figure 3.1.8** Self-assembly behavior of **SnPy<sub>3</sub>P-FF** in (a) DCM-MeOH 2:8, (b) HFIP-MeOH 2:8, (c) DCM-Heptane 2:8, (d) THF-MeOH 2:8.

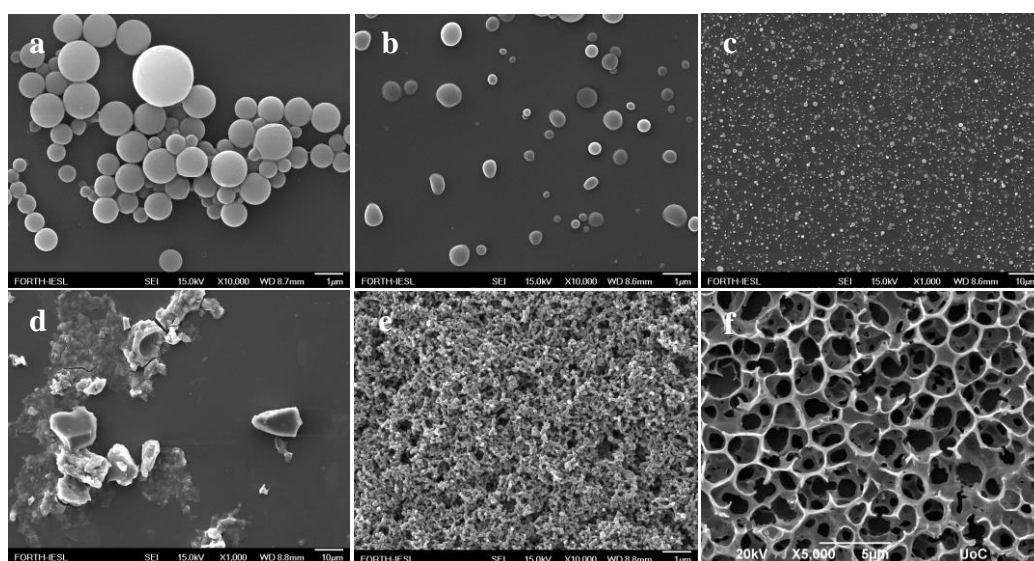


**Figure 3.1.9** Self-assembly behavior of **SnPy<sub>3</sub>P-FF** in (a) DCM-MeOH 2:8, (b,c) HFIP-MeOH 2:8, (d) THF-MeOH 2:8, (e) DCM-Heptane 2:8, (f) DCM solution.

The above results provide real evidence that the metal in the porphyrin ring plays a major role in the self-assembly behavior of the hybrid molecules, since it leads to different distinctive supramolecular architectures, namely fibrils, nanospheres or irregular aggregation. SEM/EDS analysis on the self-assembled structures confirmed



that the observed nanostructures correspond to the **SnPy<sub>3</sub>P-FF** and **ZnPy<sub>3</sub>P-FF** hybrids (Figures 6.3.21 - 6.3.22).

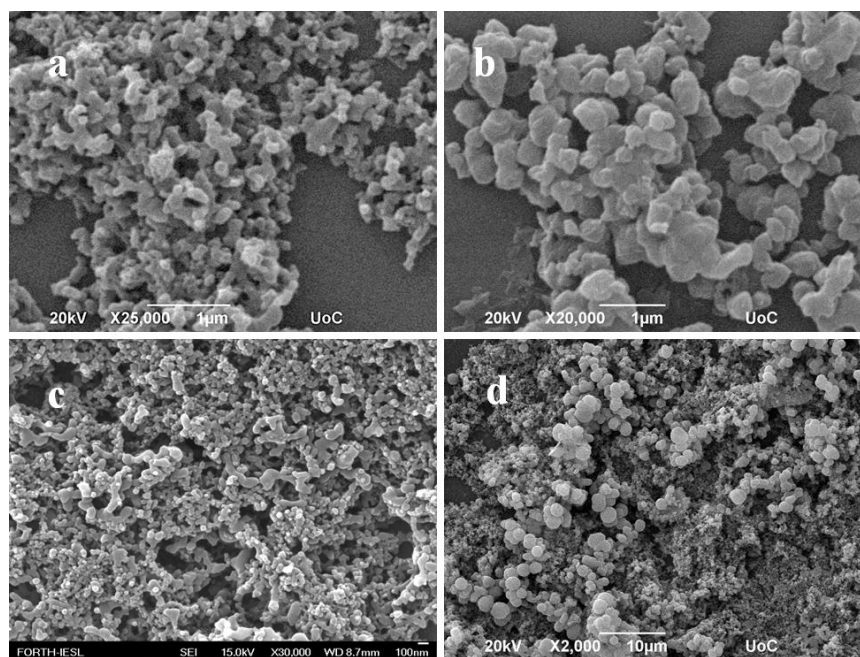


**Figure 3.1.10** Self-assembly behavior of **ZnPy<sub>3</sub>P-FF** in (a) DCM-MeOH 2:8, (b) HFIP-MeOH 2:8, (c) DCM-Heptane 2:8, (d) THF-MeOH 2:8.

#### *Absorption and Fluorescence spectroscopy studies*

The synthesized porphyrin-diphenylalanine derivatives investigated also via UV-Vis absorption spectroscopy in DCM solution (Figures 6.3.23 - 6.3.25) and in solid state after the formation of the nanostructures (Figure 3.1.11). All derivatives exhibited typical porphyrin absorbance and emission features in solution. Namely, the free base has a Soret band at 416 nm and four Q bands in the region 500 – 700 nm while the metallated **SnPy<sub>3</sub>P-FF** and **ZnPy<sub>3</sub>P-FF** porphyrins display two characteristic Q bands, as illustrated in Figures 6.3.23 - 6.3.25.

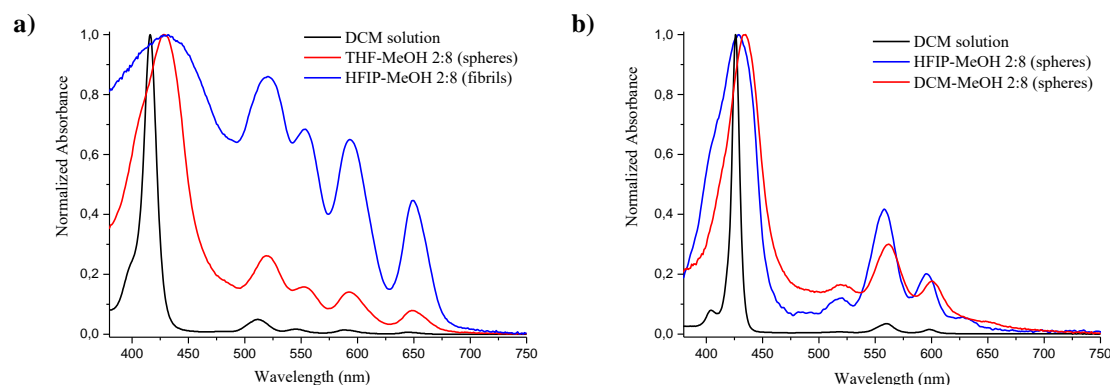


**Figure 3.1.11** Normalized absorption spectra of **Py<sub>3</sub>P-FF** (a) and **SnPy<sub>3</sub>P-FF** (b) in solution (black line) and in self-assembled states.

In the self-assembled state, with only one exception, all hybrids exhibited broadening and red shift of all absorption bands, in relation to the corresponding absorption maxima in solution. For example, the Soret band of **Py<sub>3</sub>P-FF** in the fibrillary state is 16 nm red-shifted compared to the monomers in solution. Noteworthy, the changes in the absorption spectra allow the determination of the structure of the molecular aggregates: a red shift indicates formation of *J*-aggregates that correspond to edge-to-edge arrangement of molecules, whereas blue-shift suggests formation of *H*-aggregates (face-to-face arrangement). Therefore, the previous observation indicates that *J*-aggregates (side-by-side) of the porphyrin moieties were formed in the assemblies (**Figure 3.1.11** and **3.1.13**). Analogous observations were made in fluorescence studies where the observed red shift provide further support the formation of *J*-aggregates (**Figure 3.1.12** and **3.1.13**). An interesting exception was the case of **SnPy<sub>3</sub>P-FF** in HFIP-MeOH 2:8 (spheres) where the Q bands are slightly blue-shifted (2 nm) and the Soret band has a shoulder on the left side. This observation indicates that in that system the self-assembled spheres consist of oblique aggregates.

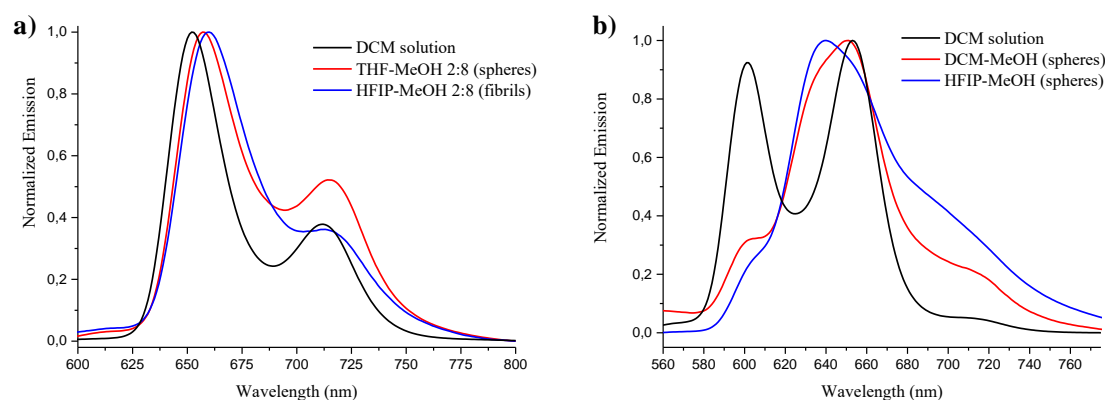


**Figure 3.1.12** Normalized emission spectra of (a) **Py<sub>3</sub>P-FF** (excitation at 525 nm) and (b) **SnPy<sub>3</sub>P-FF** in solution and in self-assembled states (excitation at 560 nm).

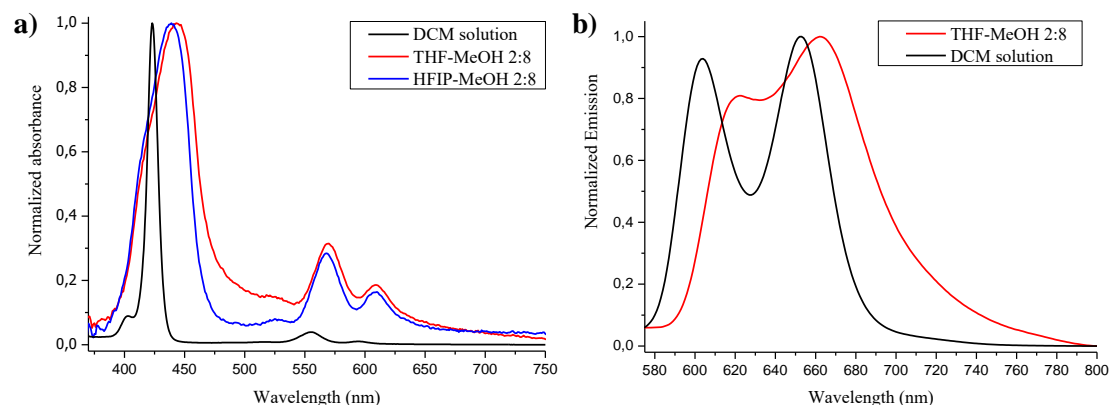
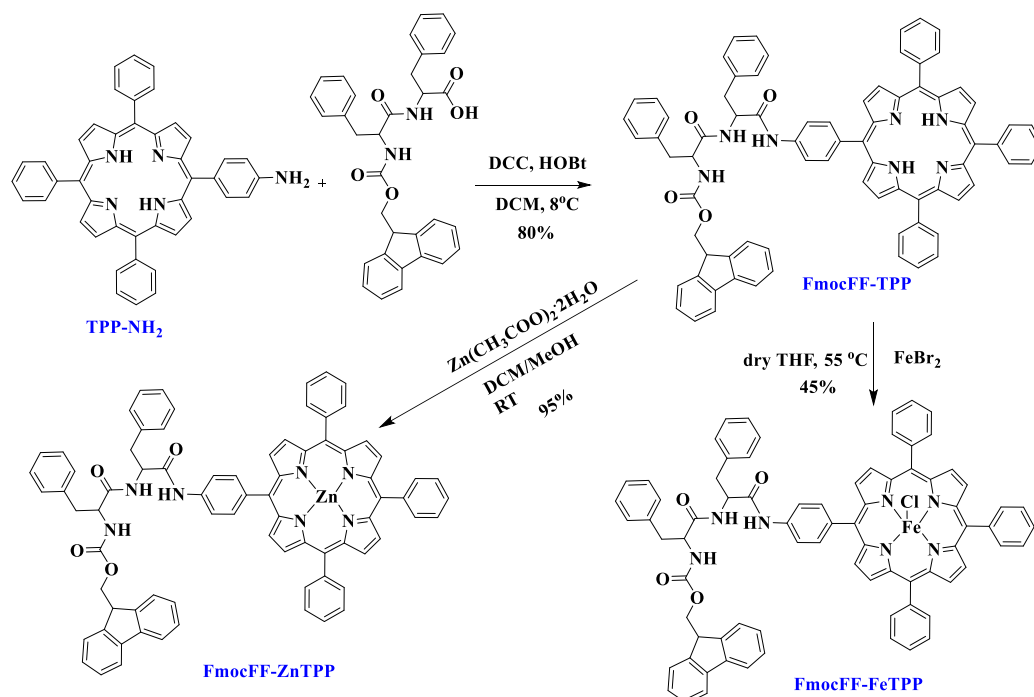


**Figure 3.1.13** Normalized absorption (a) and emission (b) spectra of **ZnPy<sub>3</sub>P-FF** in solution (black line) and in self-assembled states (excitation at 550 nm).

*Fmoc protected diphenylalanine-porphyrin hybrids*

Continuing the utilization of diphenylalanine as the self-assembling inducer to porphyrin chromophores, we synthesized two additional porphyrin-dipeptide derivatives **FmocFF-ZnTPP**<sup>114</sup> and **FmocFF-FeTPP**, and investigated their self-assembling properties. Besides the Fmoc- protecting group, the second variation of these derivatives is the peripheral substitution of the porphyrin which is phenyl and not pyridyl compared to the previous studies. We aim to investigate the influence of the different peripheral substitution as well as the different metal core in the self-assembling mode.



**Scheme 3.1.3** Synthesis of **FmocFF-ZnTPP**, **FmocFF-FeTPP**.

The synthetic procedure that was followed for the preparation of the metallated diphenylalanine-chromophore conjugates is outlined in **Scheme 3.1.3**. Straightforward reaction of **TPP-NH<sub>2</sub>**<sup>115</sup> with commercially available **Fmoc-Phe-Phe-OH** afforded the free base hybrid **FmocFF-TPP**<sup>116</sup> in high yield, by amide formation using DCC/HOBT coupling reagents, under low-temperature conditions (8 °C). Subsequently, a simple metalation reaction with Zn(CH<sub>3</sub>COO)<sub>2</sub> in DCM-MeOH afforded **FmocFF-ZnTPP**<sup>117</sup> almost quantitatively. Moreover, another metalation reaction of the free base **FmocFF-**

<sup>114</sup> Nikolaou, V.; Charalambidis, G.; Coutsolelos, A. G. *Chem. Commun.* **2021**, 57 (33), 4055.

<sup>115</sup> K. Ladomenou, et al. *Inorg. Chem.* **2012**, 51, 20, 10548–10556.

<sup>116</sup> Charalambidis G., et al. (2011), *Chem. Eur. J.*, 17: 7213-7219.

<sup>117</sup> Charalambidis, G., Georgilis, E., Panda, M. *et al. Nat Commun* 7, 12657 (2016).

**TPP** with  $\text{FeBr}_2$  was conducted in dry THF at 55 °C under inert atmosphere to yield the iron metallated derivative.

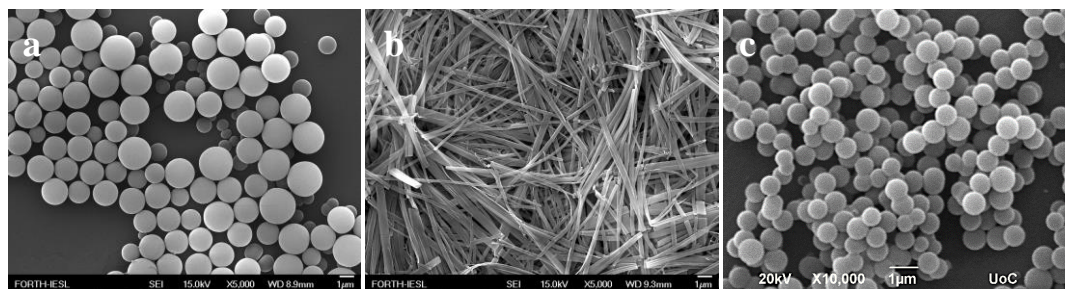


**Figure 3.1.14** Self-assembly behavior of **FmocFF-ZnTPP** in (a) THF-MeOH 2:8, (b) DCM-Heptane 1:1 and (c) **FmocFF-FeTPP** in DCM-Heptane 1:1.

In order to investigate of the self-assembly features of the phenyl substituted hybrids, the “good-bad” solvent methodology was applied followed by Scanning Electron Microscopy observation. As illustrated in **Figure 3.1.14**, **FmocFF-ZnTPP** can self-assemble into spheres or fibrils by utilizing different solvent mixtures. Nanosphere formation occurs when **FmocFF-ZnTPP** is dissolved in tetrahydrofuran (THF) and then mixed with a polar solvent, namely methanol. However, when dichloromethane/heptane solvent mixture was employed, the formation of micrometre long fibrils instead of nanospheres was observed, (**Figure 3.1.14b**). Noteworthy, just by altering the solvent mixture, the same compound can form self-assemblies in two distinctive nanostructures. Moving to the second metallated derivative, **FmocFF-FeTPP** we were able to obtain only spherical nanostructures as depicted in **Figure 3.1.14c**.

From the above, it is apparent that the utilization of mixed solvents is critical for the preparation of self-assemblies of different shapes. By comparing the phenyl and the pyridyl porphyrin conjugates, one can conclude that both approaches can result into both fibers and spherical architectures. Regarding the spherical nanostructures, the most uniform and well defined were obtained from the **FmocFF-ZnTPP** derivative in THF-MeOH 2:8 solvent mixture. Finally, it was found that the metal ion inside the porphyrin core can affect the self-assembly mode since different morphologies were observed just by varying the metal from Zn to Sn in the **MPy<sub>3</sub>P-FF** cases, or from Zn to Fe in the **FmocFF-MTPP** cases.

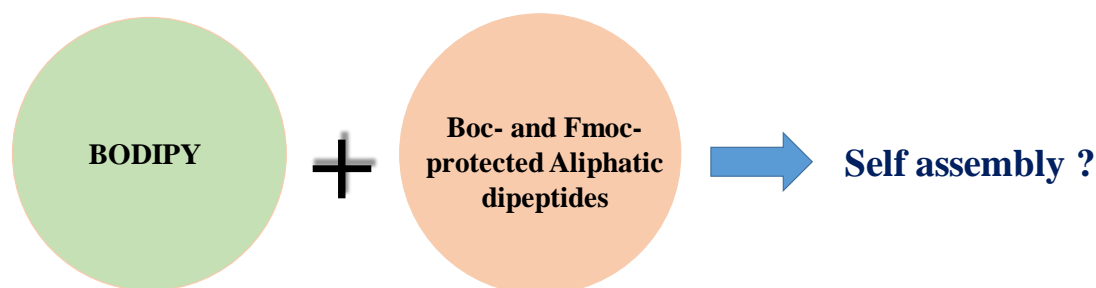
At this point it is important to state that the above synthesis and self-assembly investigation targeted to the utilization of the **MPy<sub>3</sub>P-FF** and **FmocFF-ZnTPP**



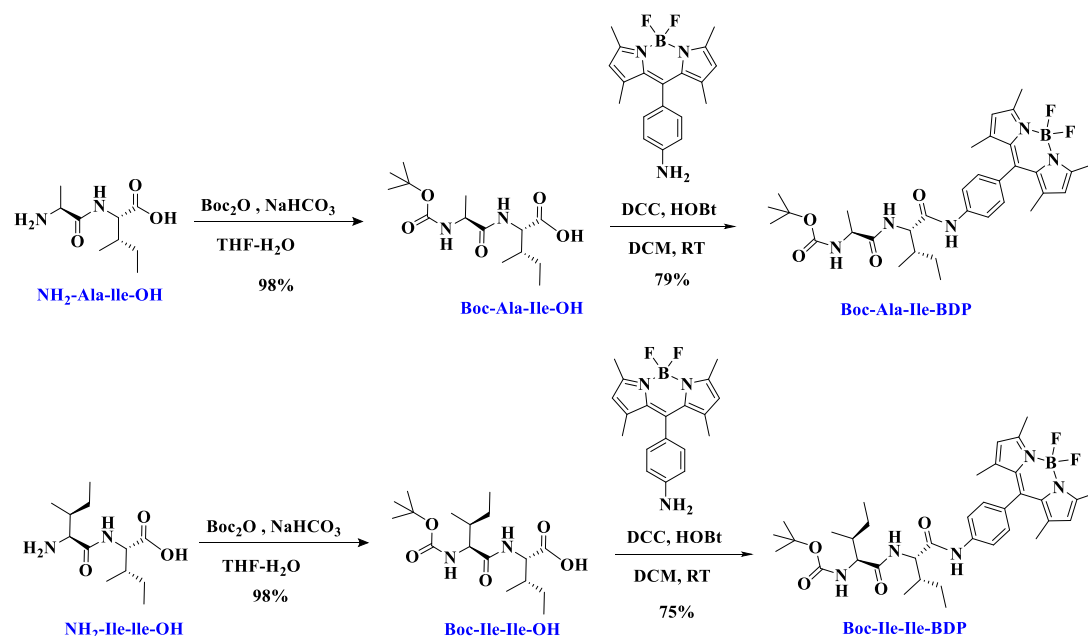
nanostructures in photocatalytic H<sub>2</sub> production (see section 3.3 and report<sup>118</sup> for more details). Moreover, the **FmocFF-FeTPP** assemblies were tested for photocatalytic CO<sub>2</sub> reduction, without however improving the overall performance compared to the control experiments.

- BDP-aliphatic peptide conjugates:

This paragraph describes the synthesis and self-assembly investigation of the Boc- and the Fmoc-protected dipeptides covalently coupled with boron-dipyrromethene chromophores (**Scheme 3.1.4**). These studies were conducted in order to complete the investigation I started during my master thesis, when I synthesized the analogous hybrids with porphyrin chromophores.<sup>119</sup>



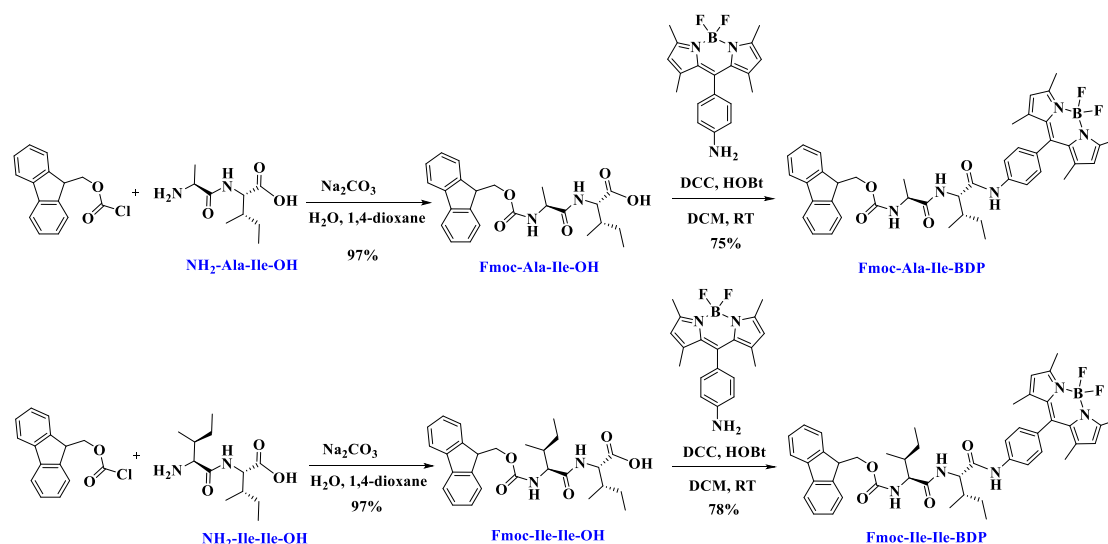
**Scheme 3.1.4** Concept for the study of the dipeptide-BDP hybrids.



**Scheme 3.1.5** Synthetic approach for the synthesis of **Boc-Ala-Ile-BDP** and **Boc-Ile-Ile-BDP**.

<sup>118</sup> Nikolaou, V.; Charalambidis, G.; Coutsolelos, A. G. *Chem. Commun.* **2021**, 57 (33), 4055.

<sup>119</sup> Nikoloudakis E. et al. *Chem. Commun.*, **2019**, 55, 14103-14106.



**Scheme 3.1.6** Synthetic approach for the synthesis of **Fmoc-Ala-Ile-BDP** and **Fmoc-Ile-Ile-BDP**.

The synthetic approach for the preparation of **Boc-Ala-Ile-BDP** and **Boc-Ile-Ile-BDP** (**Scheme 3.1.5**) begins with the N-protection of the commercially available dipeptides (Ile-Ile-OH and Ala-Ile-OH) with  $\text{Boc}_2\text{O}$  in the presence of  $\text{NaHCO}_3$ , followed by the covalent connection with  $\text{BDP-NH}_2$ , using DCC/HOBt amide coupling reagents. In order to successfully prepare the Fmoc protected hybrids, the initial approach was to build the dipeptides onto the BDP moiety. So, we started from the commercially available Fmoc-Ile-OH peptide and successfully connected it with  $\text{BDP-NH}_2$  using DCC/HOBt amide coupling reagents. However, the de-protection of the Fmoc group which followed was unsuccessful since the compound was destroyed and therefore we changed our synthetic approach (**Scheme 3.1.6**). It was necessary to protect the dipeptides Ala-Ile-OH and Ile-Ile-OH with Fmoc chloride and subsequently to proceed with an amide coupling reaction between Fmoc-Ala-Ile-OH or Fmoc-Ile-Ile-OH with  $\text{BDP-NH}_2$ . All the final and intermediate compounds were fully characterized with  $^1\text{H}$  and  $^{13}\text{C}$  NMR spectroscopies (**Figures 6.3.26 - 6.3.35**).

The self-assembling behavior of the synthesized hybrids **Boc-Ala-Ile-BDP** and **Boc-Ile-Ile-BDP** was studied in the same solvent systems as the corresponding porphyrin hybrids I studied during my master thesis. Interestingly, no self-assembling ability was observed in HFIP-EtOH and HFIP-MeOH mixtures (**Figure 3.1.15**) for the Boc-protected conjugates. This can be attributed to the partial solubility of BDP molecules in ethanol and methanol. Since BDP-dipeptide hybrids are quite soluble in EtOH and MeOH, there is not an actual “bad” solvent to induce self-assembly in these

two systems. On the other hand, when water was used as a “bad” solvent, well defined spherical nanostructures with uniform sized were formed (**Figure 3.1.16**).

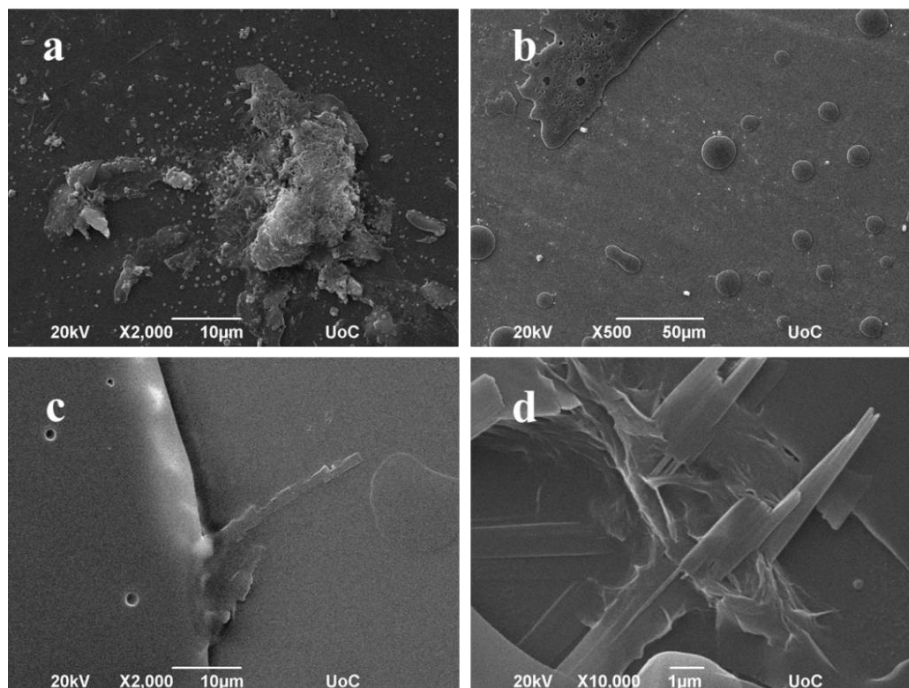


**Figure 3.1.15** SEM images of a) **Boc-Ile-Ile-BDP** in HFIP-EtOH 2:8, b) **Boc-Ile-Ile-BDP** in HFIP-MeOH 2:8, c) **Boc-Ala-Ile-BDP** in HFIP-EtOH 2:8, d) **Boc-Ala-Ile-BDP** in HFIP-MeOH 2:8.

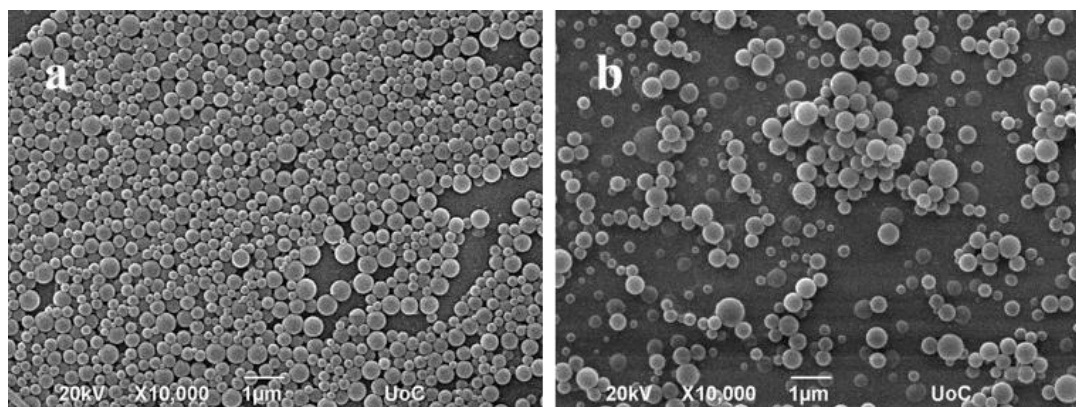


**Figure 3.1.16** Self-assembly behavior of (a) **Boc-Ala-Ile-BDP** in HFIP-H<sub>2</sub>O 2:8, (b) **Boc-Ile-Ile-BDP** in HFIP-H<sub>2</sub>O 2:8.

The insertion of bulkier protecting group, namely Fmoc, changed the solubility and the self-assembling pattern of the synthesized conjugates. In detail, the **Fmoc-Ile-Ile-BDP** displayed spherical nanostructures (~ 1µm diameter) both in HFIP-EtOH and HFIP-MeOH mixtures, while the use of water as a “bad” solvent did not result into

distinctive architectures. On the other hand, **Fmoc-Ala-Ile-BDP** displayed spherical assemblies in the HFIP-water system as depicted in **Figure 3.1.17d**.

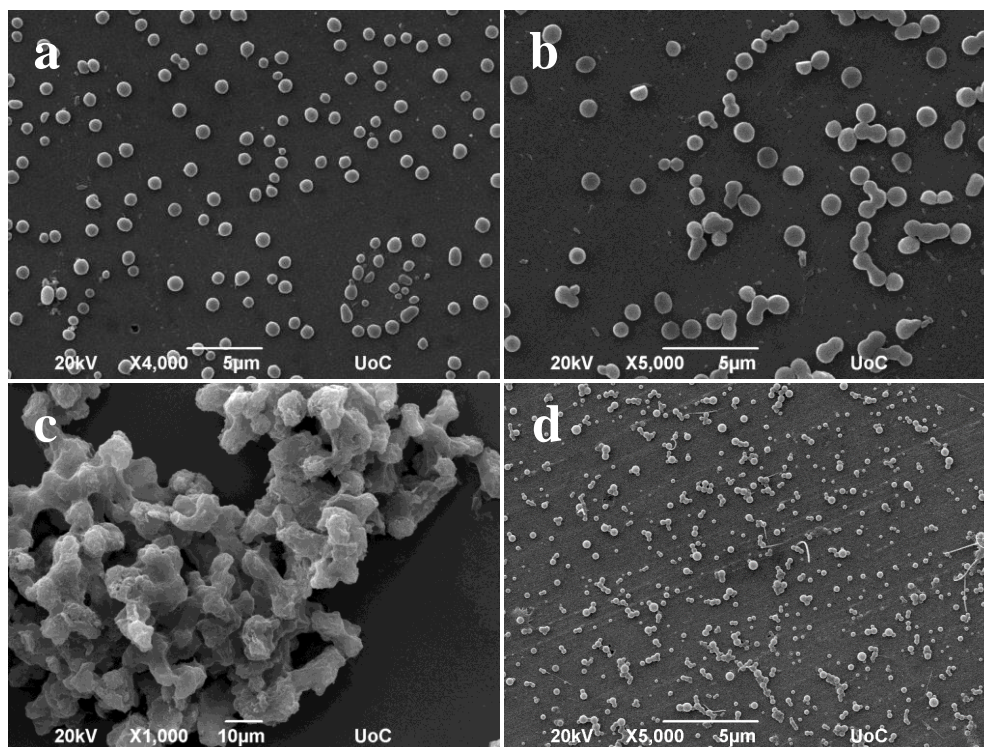


**Figure 3.1.17** Self-assembly behavior of (a) **Fmoc-Ile-Ile-BDP** in HFIP-MeOH 2:8, (b) **Fmoc-Ile-Ile-BDP** in HFIP-EtOH 2:8, (c) **Fmoc-Ile-Ile-BDP** in HFIP-H<sub>2</sub>O 2:8, (d) **Fmoc-Ala-Ile-BDP** in HFIP-H<sub>2</sub>O 2:8.

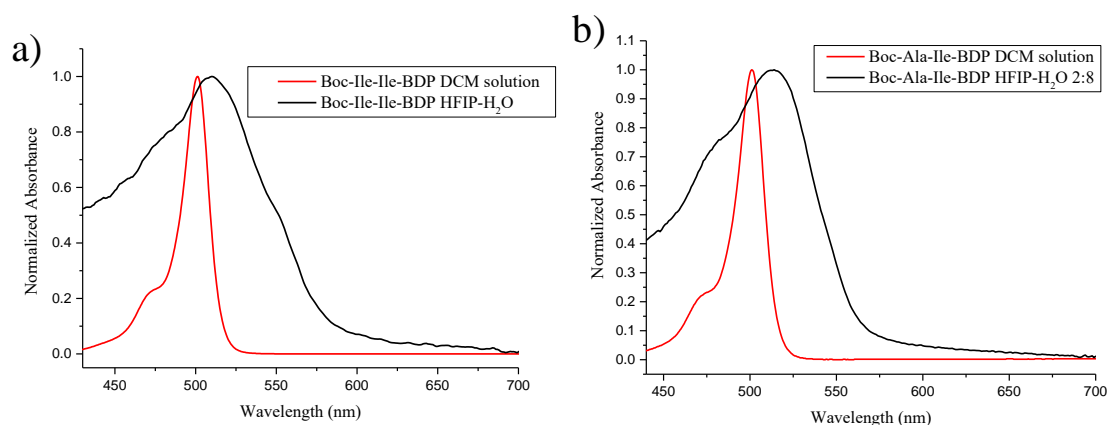


**Figure 3.1.18** Normalized absorbance spectra of **Boc-Ile-Ile-BDP** (a) and **Boc-Ala-Ile-BDP** (b) in solution (red line) and in self-assembled state.

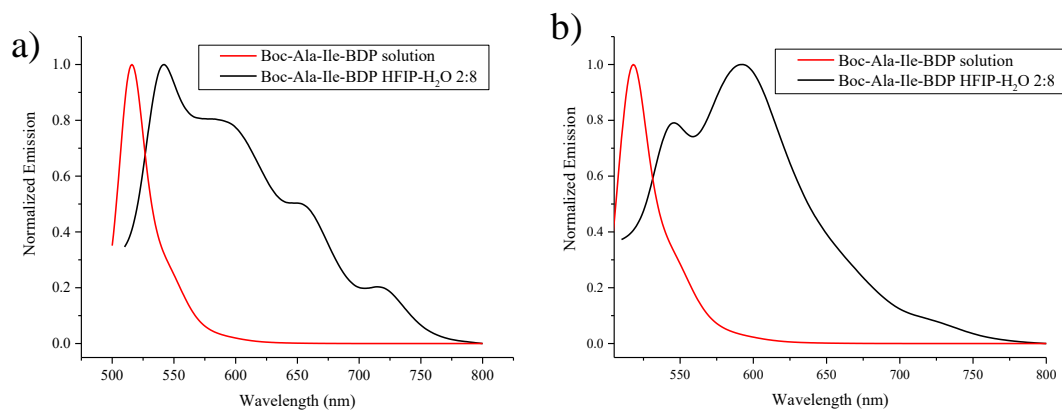


**Figure 3.1.19** Normalized emission spectra of **Boc-Ile-Ile-BDP** (a) and **Boc-Ala-Ile-BDP** (b) in solution (red line) and in self-assembled state (excitation at 490 nm).

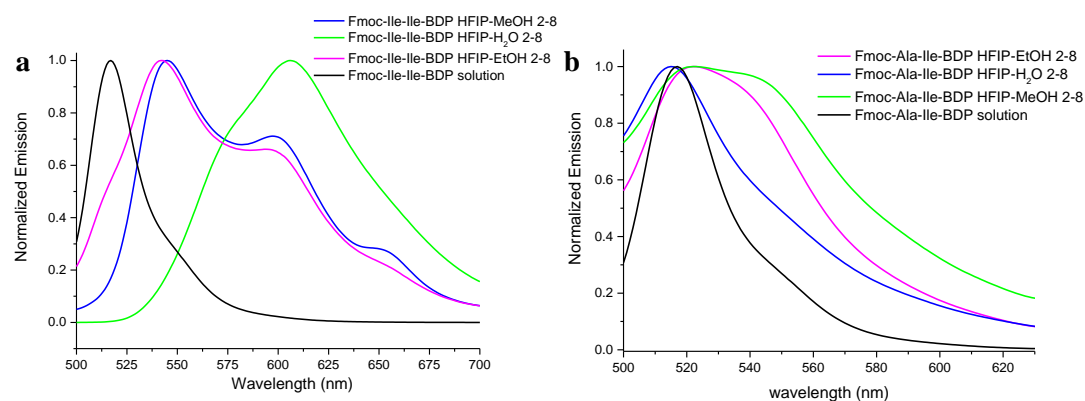
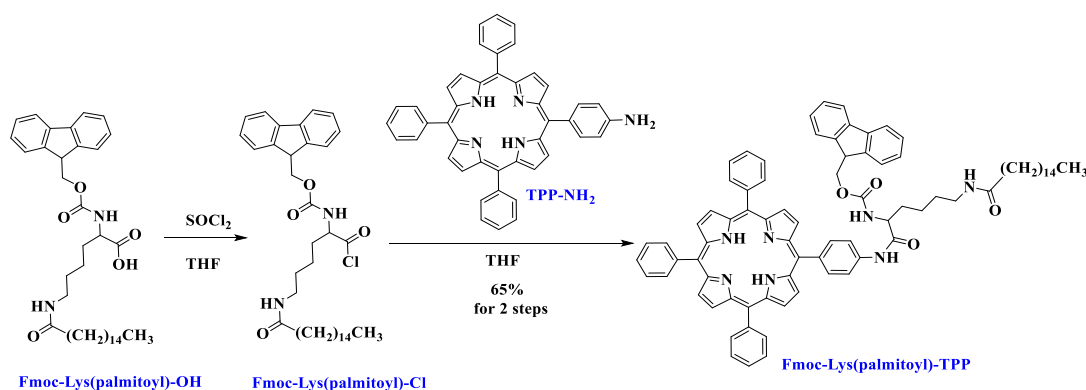


**Figure 3.1.20** Normalized emission spectra of **Fmoc-Ile-Ile-BDP** (a) and **Fmoc-Ala-Ile-BDP** (b) in solution (black line) and in self-assembled states (excitation at 510 nm).

The synthesized BDP hybrids were studied with UV-Vis absorption and emission spectroscopy in DCM solution (**Figure 6.3.36**) and in self-assembled states. The broadening and red shift of the chromophore characteristic band was observed in all cases in relation to the respective band of the compounds in solution (DCM). This observation indicates the formation of *J*-aggregates (side-by-side) of the BDP moiety in the assemblies (**Figure 3.1.18**). Equivalent observations were made during the fluorescence studies, where the observed red shift provides further support for the formation of *J*-aggregates (**Figures 3.1.19 – 3.1.20**). We have to point out that the highest red shift was observed in the case of **Fmoc-Ile-Ile-BDP** in HFIP-H<sub>2</sub>O, where the peak of BDP chromophore was ~100 nm shifted.

- Fmoc-Lys(palmitoyl)-TPP conjugate:

This paragraph describes the synthesis and self-assembly investigation of the **Fmoc-Lys(palmitoyl)-TPP** conjugate. This hybrid was the first attempt to covalently connect a big aliphatic chain with a porphyrin chromophore to achieve self-assembling properties. Notably the Fmoc-Lys(palmitoyl)- part bears a protecting group (Fmoc-), which is also a gelator moiety, an amino acid namely lysine and a fatty acid namely palmitic acid. The synthesis of **Fmoc-Lys(palmitoyl)-TPP** was inspired by the properties of Fmoc-Lys(palmitoyl)-OH, which found to form a robust fibrillar network in different conditions. Notably, it was found to form hydrogels under specific solvent conditions.



**Scheme 3.1.7** Synthetic approach for the synthesis of **Fmoc-Lys(palmitoyl)-TPP**.

The synthetic procedure that was followed for the preparation of the **Fmoc-Lys(palmitoyl)-TPP** hybrid is illustrated in **Scheme 3.1.7**. Initially, the commercially available Fmoc-Lys(palmitoyl)-OH was converted into the corresponding acyl chloride using SOCl<sub>2</sub> in pyridine. After complete evaporation of the solvents under vacuum TPP-NH<sub>2</sub><sup>120</sup> was inserted in THF affording the desired hybrid in high yield. The detailed experimental procedure is given in section 3.4, while the corresponding <sup>1</sup>H and <sup>13</sup>C NMR spectra (**Figures 6.3.37 - 6.3.41**) which verified the successful synthesis are given in the appendix (chapter 6). Noteworthy, we initially tried common coupling reagents, namely DCC/HOBt and HATU, but no product was formed.

<sup>120</sup>K. Ladomenou, T. Lazarides, M. K. Panda, G. Charalambidis, D. Daphnomili, A. G. Coutsolelos *Inorg. Chem.* **2012**, 51, 20, 10548–10556.



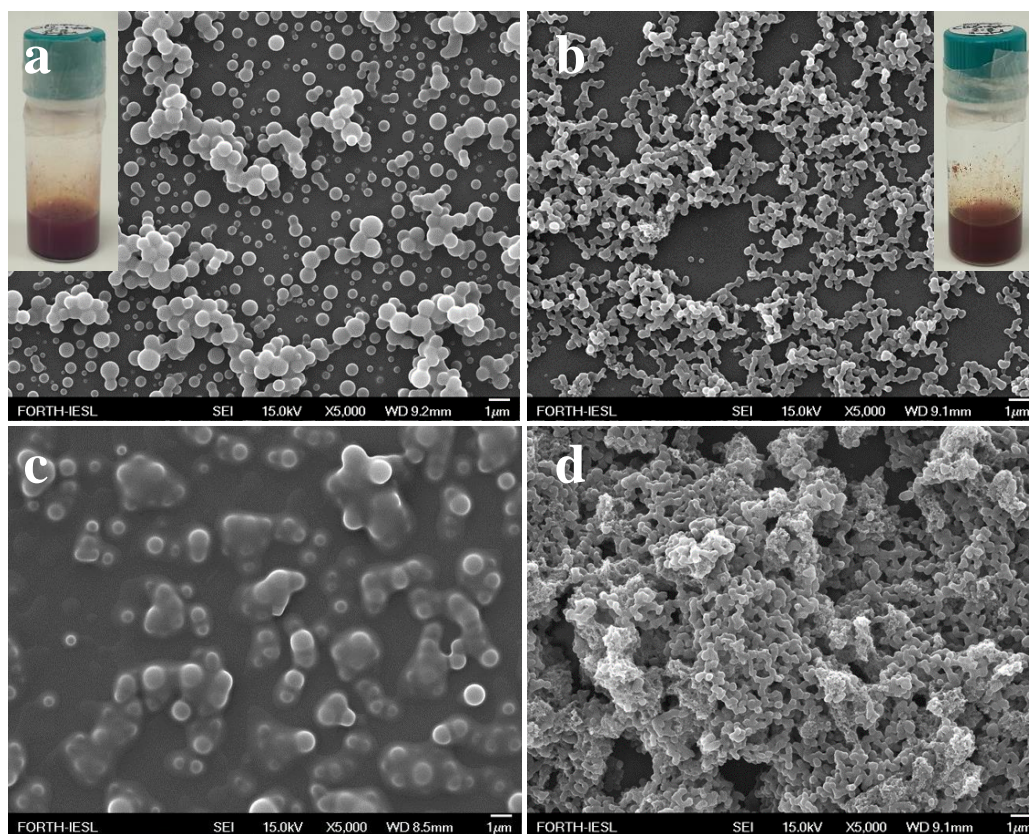


**Figure 3.1.21** Self-assembly behavior of **Fmoc-Lys(palmitoyl)-TPP** in (a) DCM-MeOH 2:8, (b) DCM-Heptane 2:8, (c) THF-MeOH 2:8, (d) THF-Heptane 2:8.

The self-assembling behavior of the synthesized hybrid was studied once again following the “good-bad” self-assembling protocol. As depicted in **Figure 3.1.21** the **Fmoc-Lys(palmitoyl)-TPP** conjugate self-assembles mainly into spherical nanostructures and not fibers as expected. Also, despite numerous attempts the formation of hydrogel was not achieved. The use of THF as a “good” solvent did not assist the formation of well-defined nanostructures. The nano-spheres obtained from the DCM-Heptane system might serve as candidates for potential application in PDT or photocatalysis since they have appropriate size and light harvesting ability. The self-assembling studies of **Fmoc-Lys(palmitoyl)-TPP** conjugate were conducted by Marita Vasila in the laboratory of prof. Anna Mitraiki (*Department of Materials Science and Technology and Institute of Electronic Structure and Laser (I.E.S.L.) Foundation for Research and Technology-Hellas (FO.R.T.H.), University of Crete, Vassilika Vouton, Heraklion 70013, Crete, Greece*)

### 3.2 Photodynamic therapy systems

Photodynamic therapy (PDT) is a therapeutic method for treating cancer with the characteristics of minimum invasiveness, simple operation, and low side effects.<sup>121,122,123</sup> In PDT, chromophore photosensitizers (PSs) are often applied despite their drawbacks such as low solubility, limited tumor accumulation as well as poor stability in the body.<sup>124,125</sup> However, it is known that plenty well-organized nano-assemblies exhibit the enhanced permeation and retention (EPR) effect, where molecules of certain sizes tend to accumulate in tumor tissue much more than they do in normal tissues. This approach led the way for chromophore delivery carriers with various morphologies and structures to be explored for delivering photosensitizer drugs to lesion sites.<sup>126,127,128</sup> Although a variety of building blocks and self-assembled systems have been investigated, controlling and optimizing the self-assembled nanostructures along with their properties towards better PDT treatments remain challenging.<sup>129</sup> At present, many researchers focus their studies on the design of novel nanomaterials with the features of controllable structures, versatile functions as well as good biocompatibility and biodegradation.<sup>130,131,132</sup> For this reason, selecting the appropriate building blocks with the above mentioned requirements is very important for the developing of photosensitizer delivery systems for application in PDT. Noteworthy, the aforementioned argument is true for other applications such as photocatalysis as it is going to be discussed in the next section.

---

<sup>121</sup> Brown, S. B.; Brown, E. A.; Walker, I. *Lancet Oncol.* **2004**, *5*, 497-508.

<sup>122</sup> Castano, A. P.; Mroz, P.; Hamblin, M. R., *Nat. Rev. Cancer* **2006**, *6*, 535-545.

<sup>123</sup> Li, X.; Bai, H.; Yang, Y.; Yoon, J.; Wang, S.; Zhang, X., *Adv. Mater.* **2019**, *31*, 1805092.

<sup>124</sup> Liu, K.; Xing, R.; Zou, Q.; Ma, G.; Mohwald, H.; Yan, X., *Angew. Chem. Int. Ed.* **2016**, *55*, 3036-3039.

<sup>125</sup> Zhao, L.; Liu, Y.; Chang, R.; Xing, R.; Yan, X., *Adv. Funct. Mater.* **2019**, *29*, 1806877.

<sup>126</sup> Bechet, D.; Couleaud, P.; Frochot, C.; Viriot, M. L.; Guillemin, F.; Barberi-Heyob, M., *Trends Biotechnol.* **2008**, *26*, 612-621.

<sup>127</sup> Chatterjee, D. K.; Fong, L. S.; Zhang, Y., *Adv. Drug Delivery Rev.* **2008**, *60*, 1627-1637.

<sup>128</sup> Chen, H.; Zhang, W.; Zhu, G.; Xie, J.; Chen, X., *Nat. Rev. Mater.* **2017**, *2*, 17024.

<sup>129</sup> Li, S.; Zou, Q.; Li, Y.; Yuan, C.; Xing, R.; Yan, X., *J. Am. Chem. Soc.* **2018**, *140*, 10794-10802.

<sup>130</sup> Wang, S.; Lin, J.; Wang, Z.; Zhou, Z.; Bai, R.; Lu, N.; Liu, Y.; Fu, X.; Jacobson, O.; Fan, W.; Qu, J.; Chen, S.; Wang, T.; Huang, P.; Chen, X., *Adv. Mater.* **2017**, *29*, 1701013.

<sup>131</sup> Jang, W. D.; Nishiyama, N.; Zhang, G. D.; Harada, A.; Jiang, D. L.; Kawauchi, S.; Morimoto, Y.; Kikuchi, M.; Koyama, H.; Aida, T.; Kataoka, K., *Angew. Chem. Int. Ed.* **2005**, *44*, 419-423.

<sup>132</sup> Wang, B.; Wang, M.; Mikhailovsky, A.; Wang, S.; Bazan, G. C., *Angew. Chem. Int. Ed.* **2017**, *56*, 5031-5034.



We already explained that peptide-chromophore conjugates not only maintain the self-assembling properties,<sup>133,134,135</sup> but also possess the function of the light harvesting ability of photosensitizers. Thus, nanomaterials constructed by self-assembly of the conjugates can be applied for phototherapy and catalysis.<sup>136,137,138</sup>

During my master thesis I investigated two PNA-photosensitizer conjugates (PNA-BDP and PNA-TPP) for their self-assembly behavior and their potential as catalysts.<sup>139</sup> The resulting supramolecular assemblies have the merits of well-defined structures, appropriate sizes, and also the characteristic light absorbing abilities of BDP and TPP. Since appropriate sizes and light absorbing abilities are important for constructing phototherapeutic nanomaterials, it worths to further investigate the assemblies of the PNA-photosensitizer conjugates as candidates in antitumor phototherapy.

Although the correlation of PDT with natural photosynthesis is not so obvious, we should mention here that in both processes the light energy is converted into chemical energy. In natural photosynthesis solar energy is stored in the chemical bonds of glucose while during the PDT treatment, the PS excited by light reacts with ground state oxygen  $^3\text{O}_2$ , generating singlet oxygen  $^1\text{O}_2$ , namely the major cytotoxic agent to kill the surrounding tissues and cells.

In the project described in this section (3.2), we investigated the self-assembly of PNA-BDP and PNA-TPP and the application of their assemblies for PDT (**Scheme 3.2.1**). Both PNA-BDP and PNA-TPP form nanospheres with well-defined dimensions and uniform size distributions through their self-assembly in aqueous solutions. These nanospheres exhibit good stability under various treatments, such as the dilution and the addition of cell culture media. Noteworthy, the nanospheres can be efficiently

---

<sup>133</sup> Charalambidis, G.; Georgilis, E.; Panda, M. K.; Anson, C. E.; Powell, A. K.; Doyle, S.; Moss, D.; Jochum, T.; Horton, P. N.; Coles, S. J.; Linares, M.; Beljonne, D.; Naubron, J.; Conradt, J.; Kalt, H.; Mitraki, A.; Coutsolelos, A. G.; Balaban, T. S., *Nat. Commun.* **2016**, *7*, 12657.

<sup>134</sup> Charalambidis, G.; Kasotakis, E.; Lazarides, T.; Mitraki, A.; Coutsolelos, A. G., *Chem. Eur. J.* **2011**, *17*, 7213-7219.

<sup>135</sup> Karikis, K.; Butkiewicz, A.; Folias, F.; Charalambidis, G.; Kokotidou, C.; Charisiadis, A.; Nikolaou, V.; Nikoloudakis, E.; Frelek, J.; Mitraki, A.; Coutsolelos, A. G., *Nanoscale* **2018**, *10*, 1735-1741.

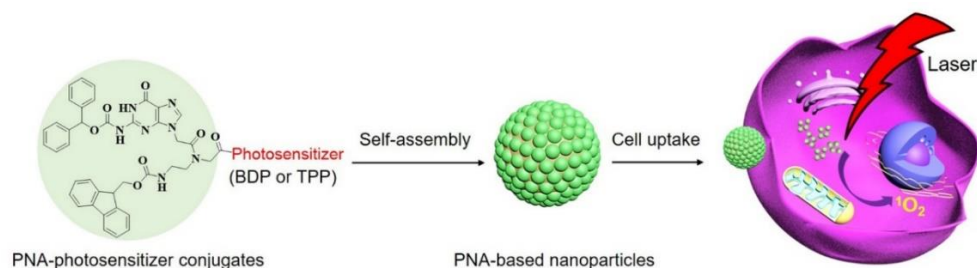
<sup>136</sup> Han, K.; Zhang, J.; Zhang, W.; Wang, S.; Xu, L.; Zhang, C.; Zhang, X.; Han, H., *ACS Nano* **2017**, *11*, 3178-3188.

<sup>137</sup> Li, S. Y.; Cheng, H.; Qiu, W. X.; Liu, L. H.; Chen, S.; Hu, Y.; Xie, B. R.; Li, B.; Zhang, X. Z., *ACS Appl. Mater. Interfaces* **2015**, *7*, 28319-28329.

<sup>138</sup> Zhang, D.; Qi, G. B.; Zhao, Y. X.; Qiao, S. L.; Yang, C.; Wang, H., *Adv. Mater.* **2015**, *27*, 6125-6130.

<sup>139</sup> Nikoloudakis, E.; Karikis, K.; Han, J.; Kokotidou, C.; Charisiadis, A.; Folias, F.; Douvas, A. M.; Mitraki, A.; Charalambidis, G.; Yan, X.; Coutsolelos, A. G., *Nanoscale* **2019**, *11*, 3557-3566.

internalized by cells without conveying significant cytotoxicity in the dark. Afterwards, the cells can be efficiently killed through the combination of incubation with the nanospheres and light irradiation. This versatile approach targets to demonstrate that the self-assembled nanospheres of PNA-BDP and PNA-TPP are efficient nanodrugs for *in vitro* PDT.



**Scheme 3.2.1** Schematic illustration of supramolecular nanoparticles constructed by self-assembly of PNA-photosensitizer conjugates for photodynamic therapy.

#### *Absorption, Emission and DLS studies*

After the self-assembly studies analyzed in section 3.1, the PNA-BDP and PNA-TPP nanoparticles were investigated with UV-Vis absorption spectroscopy, by using solutions of PNA-BDP and PNA-TPP in DMSO as control groups. As compared to the spectrum of PNA-BDP in solution, the absorption band of the PNA-BDP assemblies showed a slight broadening, indicating aggregation of PNA-BDP in the PNA-BDP nanoparticles (**Figure 3.2.1a**). Similar aggregation was observed after comparing the spectra of PNA-TPP nanoparticles and the PNA-TPP solution (**Figure 3.2.1b**). Both the S- and Q-bands of porphyrin in the PNA-TPP self-assemblies show significant broadening and red shifts as compared to that of molecular PNA-TPP, indicating that PNA-TPP forms *J*-aggregates during self-assembly.<sup>140,141</sup> The aggregation also suggests the existence of  $\pi$ - $\pi$  and hydrophobic interactions in the PNA-BDP and PNA-TPP nanostructures.<sup>142,143</sup> Since the stability of the nanodrugs is important for their biomedical applications, the two assemblies were investigated for their anti-dilution and physiological stability. A solution of the PNA-BDP NPs in water was diluted to

<sup>140</sup> Choi, S.; Bouffard, J.; Kim, Y., *Chem. Sci.* **2014**, *5*, 751-755.

<sup>141</sup> Wang, Y.; Liu, T.; Bu, L.; Li, J.; Yang, C.; Li, X.; Tao, Y.; Yang, W., *J. Phys. Chem. C* **2012**, *116*, 15576-15583.

<sup>142</sup> Elemans, J. A. A. W.; van Hameren, R.; Nolte, R. J. M.; Rowan, A. E., *Adv. Mater.* **2006**, *18*, 1251-1266.

<sup>143</sup> Nam, Y. S.; Shin, T.; Park, H.; Magyar, A. P.; Choi, K.; Fantner, G.; Nelson, K. A.; Belcher, A. M., *J. Am. Chem. Soc.* **2010**, *132*, 1462-1463.

various concentrations and the size variation of the resulting samples was monitored by DLS (**Figure 3.2.1c**). The samples in DMEM were incubated at 37 °C for 24 h before the DLS characterization. The results revealed that the average size showed no significant change, demonstrating that the PNA-BDP NPs were stable even at low concentrations. The PNA-TPP NPs also displayed good stability under the same treatment (**Figure 3.2.1d**).

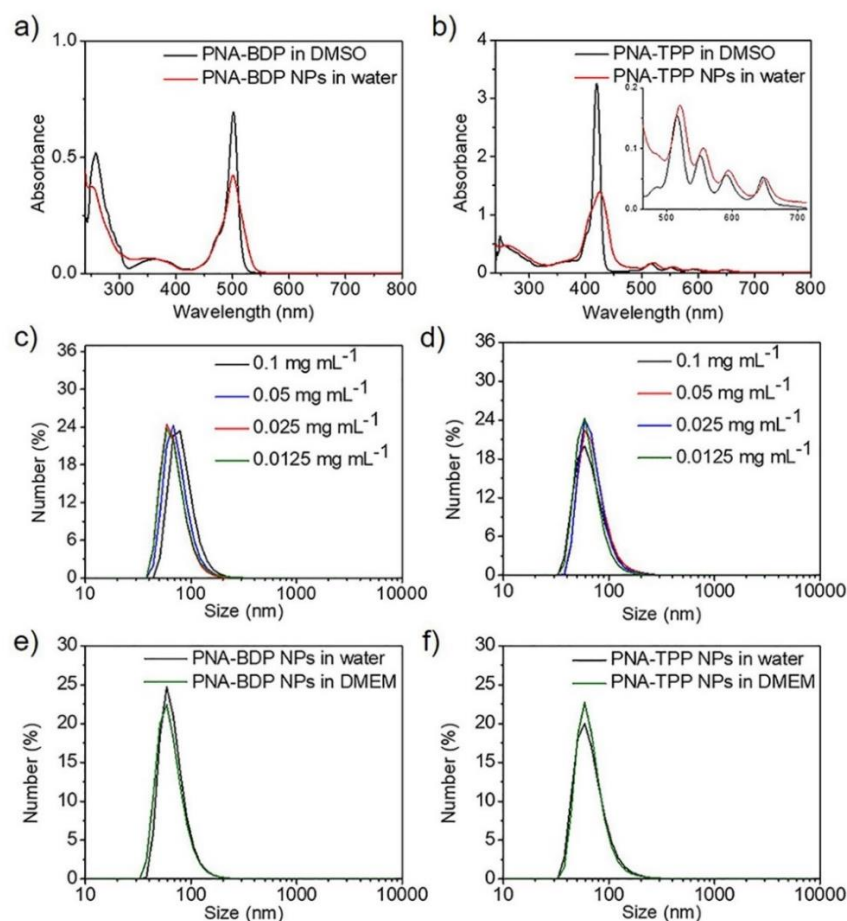


**Figure 3.2.1** UV/Vis absorption spectra of (a) the PNA-BDP NPs and molecular PNA-BDP and (b) PNA-TPP NPs and molecular PNA-TPP. DLS size profiles of (c) the PNA-BDP and (d) PNA-TPP NPs under diluted concentrations.<sup>144</sup> DLS size profiles of (e) the PNA-BDP NPs and (f) PNA-TPP NPs dispersed in water and in DMEM showing that the samples are highly stable in the presence of DMEM.

The stability of the PNA-BDP and PNA-TPP nanostructures was also studied in cell culture media. The DLS profiles revealed that the incubation of the PNA-BDP NPs or PNA-TPP NPs in DMEM for 24 hours did not change their size distributions (**Figure 3.2.1e** and **Figure 3.2.1f**). The high stability in water and cell culture media suggests

<sup>144</sup> All samples were prepared by diluting the 0.1 mg mL<sup>-1</sup> sample with the addition of water.

that the PNA-BDP NPs and PNA-TPP NPs are stable enough for *in vitro* biomedical applications.

The PNA-BDP and PNA-TPP nanostructures were further characterized by fluorescence spectroscopy. The fluorescence intensity of the PNA-BDP NPs in water was weakened as compared to that of molecular PNA-BDP in DMSO, representative of the fluorescence quenching caused by self-aggregation (**Figure 3.2.2a**).<sup>54</sup> Similarly, fluorescence of the PNA-TPP NPs in water was largely quenched as compared to that of molecular PNA-TPP in DMSO solution (**Figure 3.2.2b**).

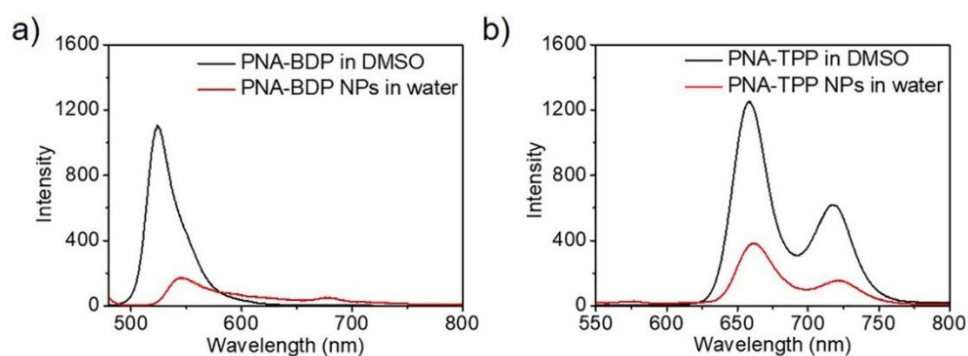


**Figure 3.2.2** Emission spectra of (a) PNA-BDP NPs versus molecular PNA-BDP in DMSO solution (excitation at 510 nm) and (b) PNA-TPP NPs versus molecular PNA-TPP in DMSO solution (excitation at 515 nm).

Based on their fluorescence characteristics, the PNA-BDP NPs and PNA-TPP NPs it was possible to investigate them in experiments *in-vitro*. MCF-7 cells (breast cancer cell) incubated with the PNA-BDP NPs or PNA-TPP NPs were imaged by Confocal Laser Scanning Microscopy (CLSM). Green fluorescence was clearly observed on cells incubated with the PNA-BDP NPs, suggesting that the cells can uptake the PNA-BDP nanoparticles efficiently (**Figure 3.2.3**). The cells incubated with the PNA-TPP NPs showed significant red fluorescence and the fluorescence intensity increased during prolonged incubation (**Figure 3.2.4a**). The cells incubated with the PNA-TPP NPs for 24 h were further stained with two dyes for staining the cell membrane (Alexa 488) and the nucleus (Hoechst 33342). It was clear that the red fluorescence from the PNA-TPP NPs did not overlap with those from the Alexa 488 and Hoechst 33342, indicating that

the PNA-TPP nanoparticles were located only in the cytoplasm (**Figure 3.2.4b**). Such intracellular location is believed to be beneficial to improved PDT efficiency.<sup>145,146,147</sup>

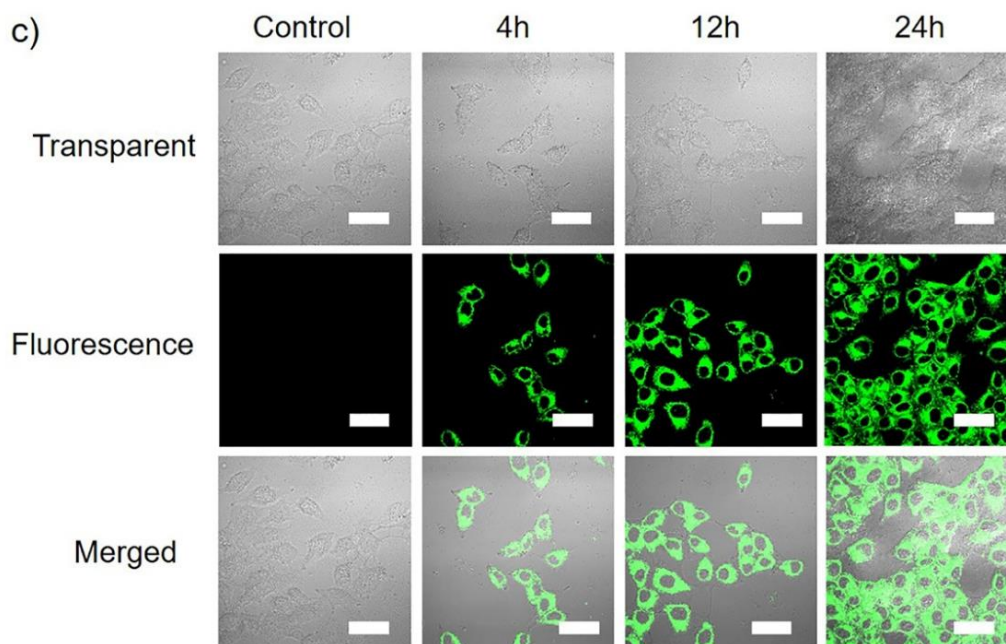


**Figure 3.2.3** CLSM images showing in vitro fluorescence of the PNA-BDP NPs. The cells were incubated with the PNA-BDP NPs and imaged by CLSM at various time points. Scale bars represent 30  $\mu\text{m}$ .

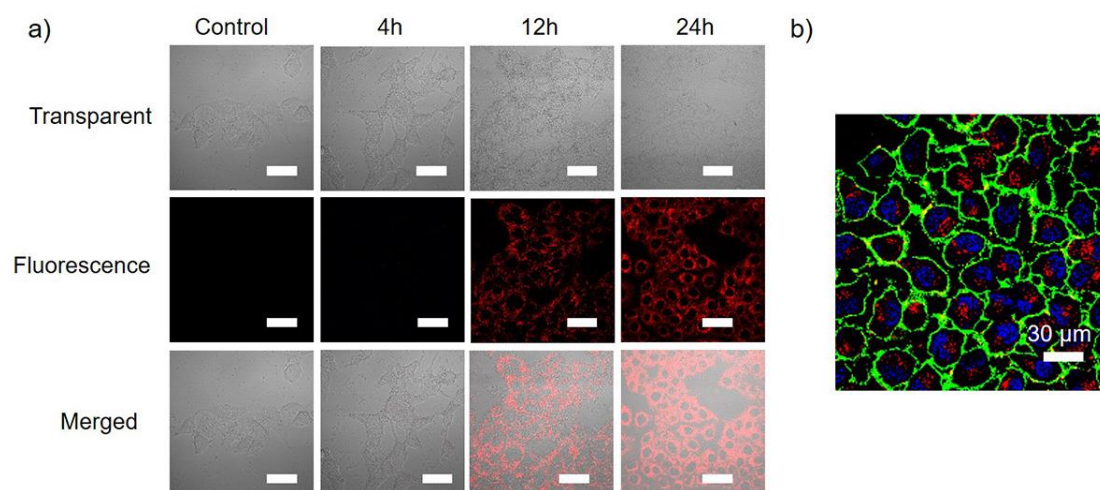


**Figure 3.2.4** (a) CLSM images of MCF-7 cells that have been incubated with the PNA-TPP NPs for various time periods. Scale bars denote 30  $\mu\text{m}$ . (b) CLSM image of MCF-

<sup>145</sup> Fan, H.; Yan, G.; Zhao, Z.; Hu, X.; Zhang, W.; Liu, H.; Fu, X.; Fu, T.; Zhang, X. B.; Tan, W. *Angew. Chem. Int. Ed.* **2016**, *55*, 5477-5482.

<sup>146</sup> Jing, C.; Wang, R.; Ou, H.; Li, A.; An, Y.; Guo, S.; Shi, L., *Chem. Commun.* **2018**, *54*, 3985-3988.

<sup>147</sup> Lupu, M.; Maillard, P.; Mispelter, J.; Poyer, F.; Thomas, C. D., *Photochem. Photobiol. Sci.* **2018**, *17*, 1599-1611.

7 cells incubated with the PNA-TPP NPs for 24 h followed by the staining with both Hoechst 33342 and Alexa 488.<sup>148</sup>

### *In vitro Photodynamic Therapy studies*

After the above encouraging results, the PNA-BDP NPs and PNA-TPP NPs were evaluated for in vitro PDT. The PDT effect of the PNA-BDP NPs was first investigated by CLSM. MCF-7 cancer cells that have been incubated with the PNA-BDP NPs for 24 h were selectively scanned continuously under 488 nm excitation (4 mW) for 10 min. Staining the cells by using propidium iodide as a stain to evaluate cell viability showed that the cells in the selected area were efficiently killed while the cells outside the selected area were still alive (**Figure 3.2.5a**), thus, confirming that the combination of the PNA-BDP NPs and light can induce efficient cytotoxicity. Cell viability test based on an MTT method (colorimetric technique) revealed that the PNA-BDP NPs themselves cannot induce cytotoxicity at the evaluated concentrations (**Figure 3.2.5b**). In contrast, the cell viability was significantly inhibited under irradiation (400-900 nm white light, 0.28 W cm<sup>-2</sup>, 3 min) with an IC<sub>50</sub> value (half maximal inhibitory concentration) of 60 µg mL<sup>-1</sup>. For the PNA-TPP nanoparticles, selective inhibition of cells in the selected area was also demonstrated by CLSM images (**Figure 3.2.5c**). In addition, no discernible cytotoxicity was observed when the cells were incubated with the PNA-TPP NPs in dark (**Figure 3.2.5d**). Under irradiation (635 nm, 0.3 W cm<sup>-2</sup>, 1 min), the IC<sub>50</sub> value was 30 µg mL<sup>-1</sup>. These results demonstrate that both the PNA-BDP NPs and PNA-TPP NPs are efficient nanoagents for in vitro PDT.

The study presented in section 3.2 has identified an alternative option for construction of PDT nanodrugs by combining photosensitizers with peptide nucleic acids. It was demonstrated that nanoparticles with well-defined nanostructures and uniform sizes can be readily produced through the self-assembly of PNA-BDP and PNA-TPP hybrid molecules. The resulting nanoparticles were stable in biological solutions and can be efficiently internalized by cells. Confocal Laser Scanning Microscopy (CLSM) results showed that the nanoparticles can induce selective cytotoxicity with the assistance of light irradiation. In contrast, the nanoparticles have negligible cytotoxicity in the dark. Therefore, these self-assembled nanoparticles are proven to be efficient nanoagents for

---

<sup>148</sup> Green fluorescence from Alexa 488 is indicative of membranes, blue fluorescence from Hoechst 33342 is indicative of nuclei, and red fluorescence is indicative of the location of the PNA-TPP NPs.



photodynamic therapy (PDT) *in vitro*. The peptide nucleic acid motifs can be further modified to meet specific requirements for tumor diagnosis and therapy, such as linking tumor-targeting groups or introducing tumor-responsive sequences. Therefore, the self-assembly of PNA-chromophore conjugates is promising approach for constructing supramolecular therapeutic nanoagents based on bioinspired biomaterials.

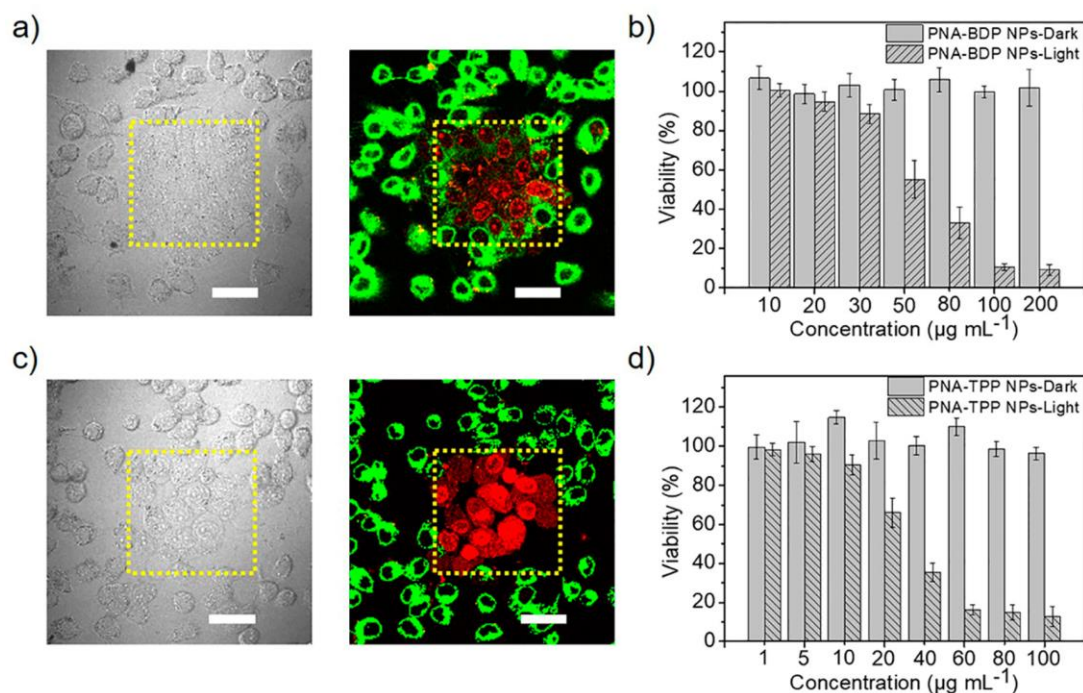


**Figure 3.2.5** (a) Bright field (left) and CLSM (right) images showing selective PDT effect of the PNA-BDP NPs on MCF-7 cells.<sup>149</sup> (b) Viability of MCF-7 cells incubated with the PNA-BDP NPs and treated with or without light irradiation. (c) Bright field (left) and CLSM (right) images showing selective PDT effect of the PNA-TPP NPs on MCF-7 cells.<sup>150</sup> (d) Viability of MCF-7 cells incubated with the PNA-TPP NPs and treated with or without light irradiation.<sup>151</sup>

The above photodynamic therapy experiments were conducted by Rui Chang in the laboratory of Dr. Xuehai Yan (*State Key Laboratory of Biochemical Engineering, Institute of Process Engineering, Chinese Academy of Sciences, Beijing 100190, China*).

<sup>149</sup> The cells were incubated with the PNA-BDP NPs for 24 h and cells in the yellow square were scanned continuously under 488 nm excitation for 10 min. Then, the cells were stained by propidium iodide (PI) and imaged. The red signal from PI indicates dead cells. Scale bars denote 50  $\mu\text{m}$ .

<sup>150</sup> The cells were incubated with the PNA-TPP NPs for 24 h and cells in the yellow square were scanned continuously under 633 nm excitation for 10 min. Then, the cells were stained by PI and imaged. Scale bars denote 50  $\mu\text{m}$ .

<sup>151</sup> Error bars represent standard deviation ( $n = 5$ ).

### 3.3 Photocatalytic H<sub>2</sub> production systems

- Self-assembled porphyrin dipeptide conjugates towards hydrogen production

As explained in the introduction, plenty of natural processes are achieved through the utilization of self-assembling molecules that adopt a specific configuration in order to accomplish their biological function. An important and inspiring natural process, which utilizes the self-assembly of chromophores, is the process of photosynthesis, which efficiently stores solar energy into chemical bonds.<sup>152,153</sup> Motivated by natural photosynthesis, plenty of scientific reports deal with the direct conversion of sunlight into H<sub>2</sub> through photocatalytic or photoelectrocatalytic systems.<sup>154,155,156</sup> In these systems the protons are converted into H<sub>2</sub>, which is one of the most desirable solar fuel due to its high energy capacity and environmental benignity.<sup>157,158,159</sup> H<sub>2</sub> produces only water through its reaction with oxygen, in contrast to hydrocarbons whose combustion emits the green-house gas CO<sub>2</sub>.<sup>160</sup> Moreover, it can be applied in any existing natural gas system and its chemical energy can be efficiently transformed into electricity by utilizing fuel cells.<sup>161,162,163</sup>

Interestingly, although natural photosynthesis is achieved through the well-organized self-assembly of chlorophylls, in the literature there are not many reports that investigate H<sub>2</sub> production via the self-assembly of chromophores.<sup>164,165,166</sup> This is a promising approach to enhance photocatalytic hydrogen evolution activity, since the self-assembled chromophores have illustrated superior light harvesting ability owing to their improved absorption features and their increased photostability.

<sup>152</sup> Magnuson, A.; Mamedov, F.; Messinger, J. *Joule* **2020**, *4* (6), 1157.

<sup>153</sup> Dasgupta, C. N.; Jose Gilbert, J.; Lindblad, P.; Heidorn, T.; Borgvang, S. A.; Skjanes, K.; Das, D. *Int. J. Hydrog. Energy* **2010**, *35* (19), 10218.

<sup>154</sup> Liu, Y.; Huang, D.; Cheng, M.; Liu, Z.; Lai, C.; Zhang, C.; Zhou, C.; Xiong, W.; Qin, L.; Shao, B. et al. *Coord. Chem. Rev.* **2020**, *409*, 213220.

<sup>155</sup> Hisatomi, T.; Domen, K. *Nat. Catal.* **2019**, *2* (5), 387.

<sup>156</sup> Christoforidis, K. C.; Fornasiero, P. *ChemCatChem* **2017**, *9* (9), 1523.

<sup>157</sup> Dolui, D.; Ghorai, S.; Dutta, A. *Coord. Chem. Rev.* **2020**, *416*, 213335.

<sup>158</sup> Li, Y.-H.; Li, J.-Y.; Xu, Y.-J. *EnergyChem* **2021**, *3* (100047), 1.

<sup>159</sup> Yuan, L.; Han, C.; Yang, M.-Q.; Xu, Y.-J. *Int. Rev. Phys. Chem.* **2016**, *35* (1), 1.

<sup>160</sup> Suen, N. T.; Hung, S. F.; Quan, Q.; Zhang, N.; Chen, H. M. *Chem. Soc. Rev.* **2017**, *46* (2), 337.

<sup>161</sup> Saraswat, S. K.; Rodene, D. D.; Gupta, R. B. *Renew. Sust. Energ. Rev.* **2018**, *89*, 228.

<sup>162</sup> Willkomm, J.; Orchard, K. L.; Reynal, A.; Pastor, E.; Durrant, J. R.; Reisner, E. *Chem. Soc. Rev.* **2016**, *45* (1), 9.

<sup>163</sup> Swierk, J. R.; Mallouk, T. E. *Chem. Soc. Rev.* **2013**, *42* (6), 2357.

<sup>164</sup> Zhang, N.; Wang, L.; Wang, H.; Cao, R.; Wang, J.; Bai, F.; Fan, H. *Nano Lett.* **2018**, *18* (1), 560.

<sup>165</sup> Liu, Y.; Wang, L.; Feng, H.; Ren, X.; Ji, J.; Bai, F.; Fan, H. *Nano Lett.* **2019**, *19* (4), 2614.

<sup>166</sup> Bodedla, G. B.; Huang, J.; Wong, W.-Y.; Zhu, X. *ACS Appl. Nano Mater.* **2020**, *3* (7), 7040.



Motivated from the above concept, we synthesized the free base **Py<sub>3</sub>P-FF** porphyrin conjugate as described in section 3.1 along with the metallated **ZnPy<sub>3</sub>P-FF** and **SnPy<sub>3</sub>P-FF** derivatives. After determining their self-assembling ability, we applied them as photosensitizers in photocatalytic hydrogen production utilizing a known cobaloxime complex, which is also noble metal-free, as a molecular catalyst. The pyridyl groups were selected since previous reports from our group showed that pyridyl substituted porphyrin derivatives exhibited superior photocatalytic activity.<sup>167,168</sup> The two different non-noble metals which were introduced inside the porphyrin core were expected to alter the electrochemical characteristics of the photosensitizer. The self-assembled supramolecular chromophore architectures were employed in the photocatalytic system in order to improve the activity of the photosensitizer, mimicking the self-assembled chlorophylls in photosynthesis.

### *Photocatalytic H<sub>2</sub> evolution studies*

Photo-induced hydrogen (H<sub>2</sub>) production experiments were conducted in order to evaluate the catalytic activity of the synthesized porphyrin derivatives as photosensitizers (PS). The photocatalytic experiments were performed in 3 mL solvent mixture of 1:1 CH<sub>3</sub>CN:H<sub>2</sub>O containing 5% (v/v) triethanolamine (TEOA) as sacrificial electron donor (SED) at pH=7. The molecular catalyst that was utilized in this study was the cobaloxime complex [Co(dmgh)<sub>2</sub>(Cl)(Py)], which is known for its activity as hydrogen evolution catalyst.<sup>169</sup> The **ZnPy<sub>3</sub>P-FF** and **Py<sub>3</sub>P-FF** hybrids did not exhibit any photocatalytic efficiency while the **SnPy<sub>3</sub>P-FF** was able to act as a photosensitizer towards hydrogen production (TON = 217 vs PS). Afterwards, we employed the self-assembled nanostructures of **SnPy<sub>3</sub>P-FF** in the photocatalytic system and investigated their influence. As it is depicted in **Figure 3.3.1**, the spherical nanostructures of **SnPy<sub>3</sub>P-FF**, which were obtained from the DCM-MeOH solvent mixture, exhibit a maximum TON of 305 (vs PS) after 120 hours of irradiation. This catalytic efficiency was improved compared to the TON obtained from the amorphous solid, showing that the self-assembly of **SnPy<sub>3</sub>P-FF** into nanospheres is essential towards enhancing the photocatalytic efficiency. Furthermore, the nanospheres obtained from the HFIP-

---

<sup>167</sup> Giannoudis, E.; Benazzi, E.; Karlsson, J.; Copley, G.; Panagiotakis, S.; Landrou, G.; Angaridis, P.; Nikolaou, V.; Matthaiaki, C.; Charalambidis, G. et al. *Inorg. Chem.* **2020**, *59* (3), 1611.

<sup>168</sup> Landrou, G.; Ladomenou, K.; Coutsolelos, A. G. *J. Porphyr. Phthalocyanines* **2016**, *20*, 534.

<sup>169</sup> Lazarides, T.; Delor, M.; Sazanovich, I. V.; McCormick, T. M.; Georgakaki, I.; Charalambidis, G.; Weinstein, J. A.; Coutsolelos, A. G. *Chem. Commun.* **2014**, *50* (5), 521.

MeOH solvent mixture exhibited less hydrogen production compared to the ones from DCM-MeOH. This might be attributed to fact that the later nanospheres were more well defined and had bigger diameter (**Figures 3.1.4** and **3.3.1**). The present photocatalytic system exhibits similar and, in some cases, improved efficiency, compared to analogous homogenous photocatalytic systems, which utilize cobaloxime catalysts and porphyrin photosensitizers.<sup>170,171</sup>

In order to examine why H<sub>2</sub> production stops after 120 h of irradiation, we added extra **SnPy<sub>3</sub>P-FF** in the photocatalytic experiment after it reached plateau and we observed the regeneration of the photocatalytic system. However, when additional amount of the cobaloxime catalyst was inserted, no regeneration was observed. This verifies that the activity of the system stops due to the decomposition of the photosensitizer.

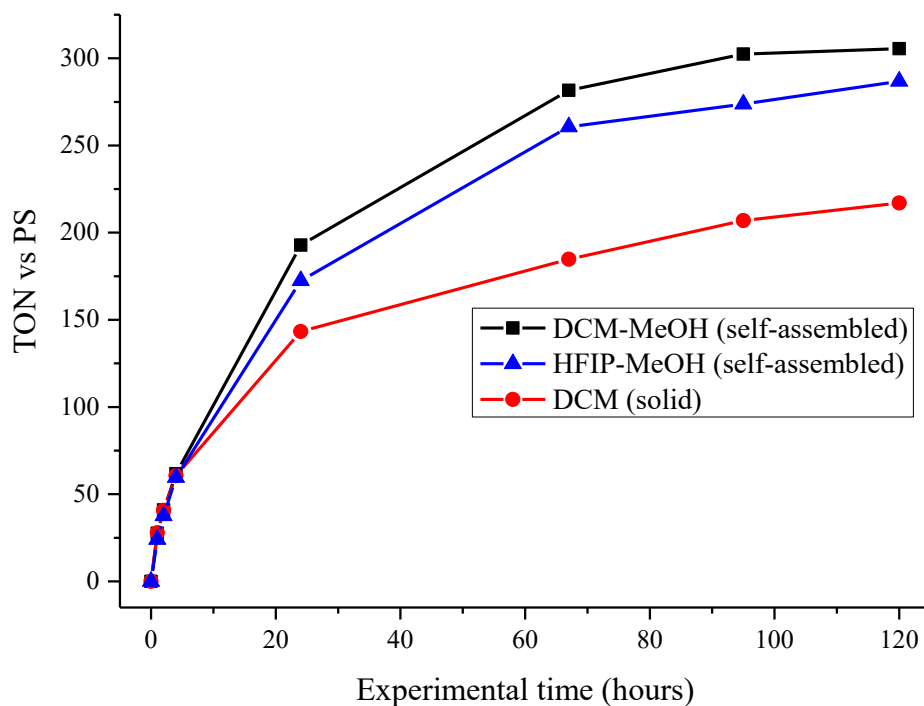


**Figure 3.3.1** Photocatalytic hydrogen production plots of **SnPy<sub>3</sub>P-FF** in self-assembled states and in solid state. The photocatalytic experiments were conducted in a 1:1 CH<sub>3</sub>CN:H<sub>2</sub>O solvent mixture containing 5% (v/v) TEOA at pH=7. The concentrations of the porphyrin PS was  $8 \times 10^{-5}$  M and [Co(dmgh)<sub>2</sub>(Cl)(Py)] catalyst was  $9.8 \times 10^{-4}$  M.

<sup>170</sup> Giannoudis, E.; Benazzi, E.; Karlsson, J.; Copley, G.; Panagiotakis, S.; Landrou, G.; Angaridis, P.; Nikolaou, V.; Matthaiki, C.; Charalambidis, G. et al. *Inorg. Chem.* **2020**, *59* (3), 1611.

<sup>171</sup> Lazarides, T.; Delor, M.; Sazanovich, I. V.; McCormick, T. M.; Georgakaki, I.; Charalambidis, G.; Weinstein, J. A.; Coutsolelos, A. G. *Chem. Commun.* **2014**, *50* (5), 521.

*Photophysical studies*

In order to shed light on the electron transfer processes that take place during the photocatalysis, transient absorption experiments were conducted using only the **SnPy<sub>3</sub>P-FF** derivative since it was the only photocatalytically active. The transient absorbance (TA) spectra at various temporal delays with respect to the pump beam are presented in **Figure 3.3.2**. As expected, the spectrum at negative delay time (-4 ps) is flat. For positive time delays, the excitation of an aqueous solution of **SnPy<sub>3</sub>P-FF** ( $4 \times 10^{-5}$  M) resulted in negative  $\Delta A$  in the  $\lambda < 430$  nm region (attributed to the Soret band depletion) and in positive  $\Delta A$  in the range 430-700 nm, excluding a negative feature at 540-560 nm (due to depletion corresponding to the strongest of the Q bands).

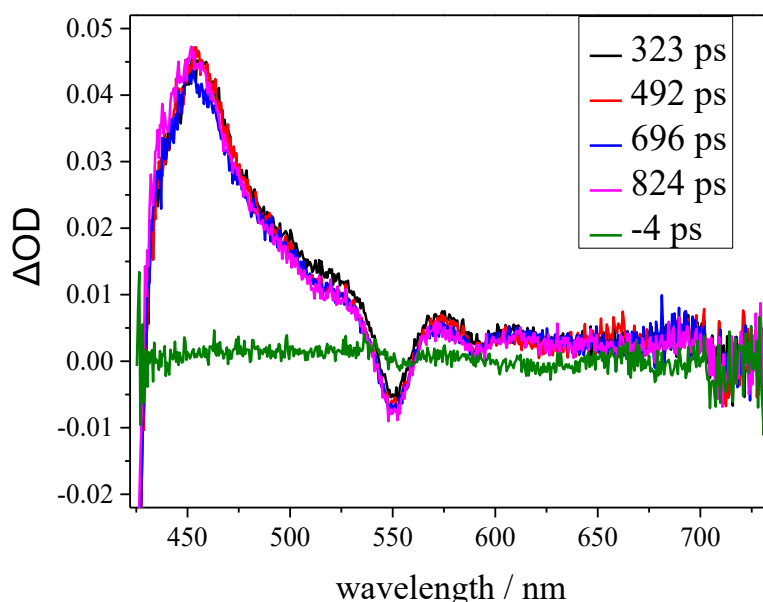


**Figure 3.3.2** TA spectra of **SnPy<sub>3</sub>P-FF** in water at different delay times ( $t_D$ : -4 ps (green line), 323 ps (black line), 492 ps (red), 696 ps (blue line), 824 ps (magenta line).

The major photophysical processes, which occur after excitation of the porphyrin, are indicated in the energy diagram shown in **Figure 3.3.3**. The pumping laser beam at 395 nm results in the excitation of the porphyrin Soret band, namely from  $S_0$  level to higher vibrational levels of  $S_2$ . This is demonstrated through the strong bleaching signal at wavelength  $\lambda < 428$  nm (**Figure 3.3.2**). Similar behavior is observed in two more spectral characteristics, namely the minima at 552 nm and 592 nm, which correspond to the Q bands of the porphyrin. Subsequently, the excited porphyrin, **SnPy<sub>3</sub>P-FF\***, in the  $S_2$  state, undergoes ultrafast vibrational relaxation (VR), followed by internal conversion (IC) to  $S_1$  that occurs within the first few picoseconds following

excitation.<sup>172,173</sup> Intersystem crossing (ISC) is also a possible process for the depopulation of the  $S_2$  to the triplet manifold and is ultrafast ( $\sim 2$  ps) according to the literature.<sup>174</sup> A small fraction of molecules in the  $S_2$  state might follow fluorescence emission in order to return to the ground state.<sup>175,176</sup> Noteworthy, the steady state fluorescence emission measurements at 590 nm and 640 nm of isoabsorption solutions of **SnPy<sub>3</sub>P-FF** in water ( $A_{426\text{nm}} = A_{560\text{nm}} = 0.11$ ), clearly demonstrate that the fluorescence yield from  $S_1$  after excitation in the Soret band is significantly reduced compared to the emission after excitation in the Q-band region (**Figure 3.3.4**).

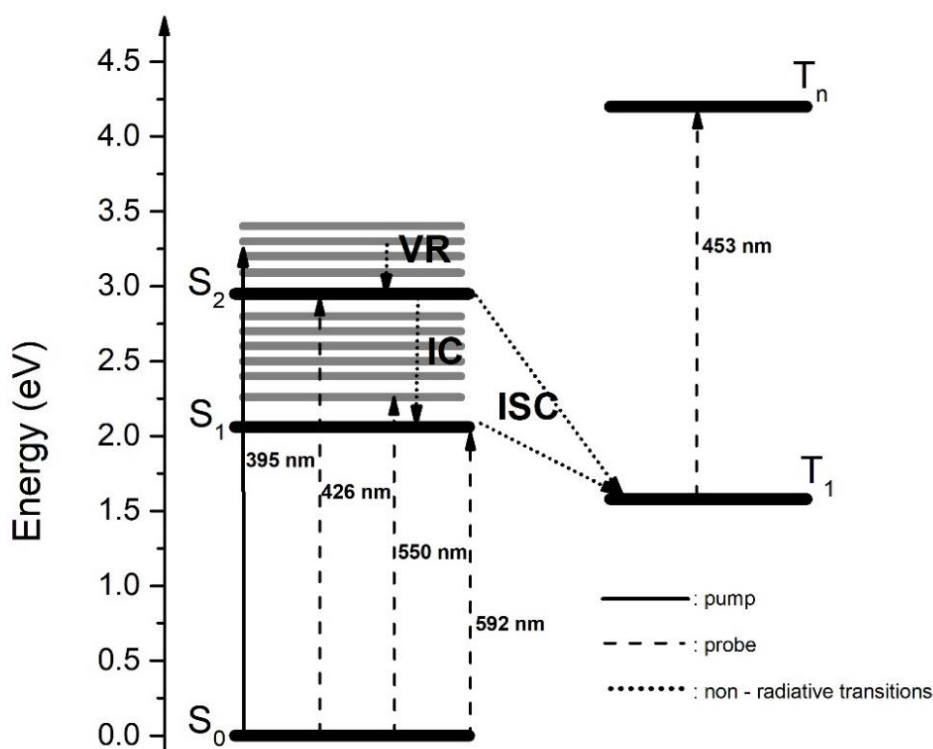


**Figure 3.3.3** Energy diagram depicting the fundamental photophysical processes of porphyrins following excitation in the Soret band ( $\lambda_{\text{exc}} = 395$  nm). Energy values of singlet and triplet states are based on experimental and computational studies.<sup>177,178</sup>

<sup>172</sup> Białkowski, B.; Stepanenko, Y.; Nejbauer, M.; Radzewicz, C.; Waluk, J. *J. Photochem. Photobiol. A* **2012**, *234*, 100.

<sup>173</sup> Yu, H.-Z.; Baskin, J. S.; Zewail, A. H. *J. Phys. Chem. A* **2002**, *106* (42), 9845.

<sup>174</sup> Liu, X.; Yeow, E. K.; Velate, S.; Steer, R. P. *Phys. Chem. Chem. Phys.* **2006**, *8* (11), 1298.

<sup>175</sup> Karolczak, J.; Kowalska, D.; Lukaszewicz, A.; Maciejewski, A.; Steer, R. P. *J. Phys. Chem. A* **2004**, *108* (21), 4570.

<sup>176</sup> Velate, S.; Liu, X.; Steer, R. P. *Chem. Phys. Lett.* **2006**, *427* (4-6), 295.

<sup>177</sup> Giannoudis, E.; Benazzi, E.; Karlsson, J.; Copley, G.; Panagiotakis, S.; Landrou, G.; Angaridis, P.; Nikolaou, V.; Matthaiaki, C.; Charalambidis, G. et al. *Inorg. Chem.* **2020**, *59* (3), 1611.

<sup>178</sup> Agnihotri, N.; Steer, R. P. *J. Porphyr. Phthalocyanines* **2014**, *18* (06), 475.

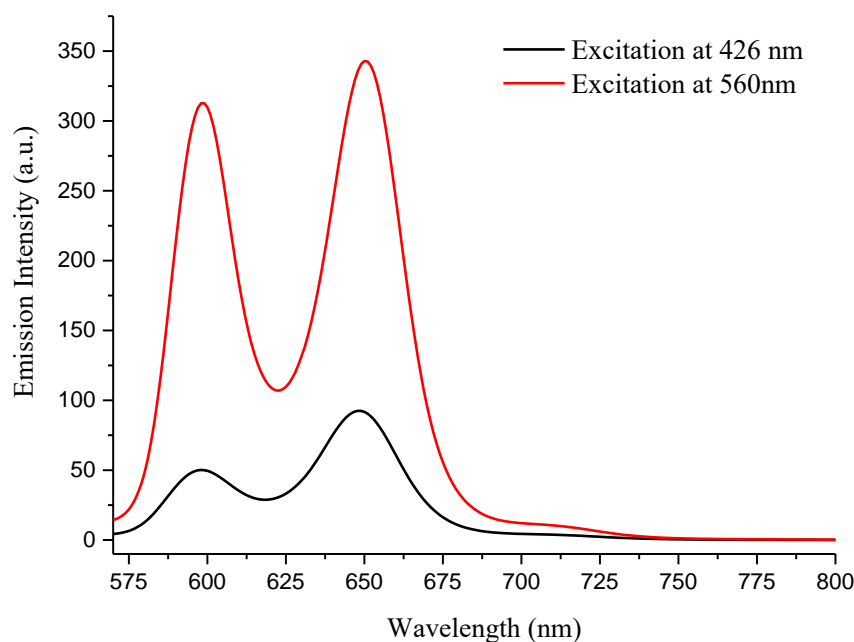


**Figure 3.3.4** Emission spectra of **SnPy<sub>3</sub>P-FF** in CH<sub>3</sub>CN-H<sub>2</sub>O 1:1 after excitation at Soret (426 nm) and the first Q band (550 nm), where  $A_{426\text{nm}} = A_{550\text{nm}} = 0.11$ .

This is strong evidence of other processes, besides the  $S_2 \rightarrow S_1$  IC channel, which efficiently depopulate the  $S_2$  state, including ISC. Relaxation of the  $S_1$  takes place via fluorescence emission and intersystem crossing with the latter expected to dominate given the heavy-atom induced enhancement of the ISC rate brought about by the presence of Sn.

Looking into the spectral data (**Figure 3.3.2**), one can observe the positive  $\Delta\text{OD}$  broad band with a maximum at 453 nm, which appears to be quite similar to spectral bands of with various porphyrins and assigned to transitions involving triplet states:  $T_1 \rightarrow T_n$ <sup>179,180,181,182</sup> without, however, excluding transition bands originating from  $S_1$ .<sup>183,184</sup> The kinetics recorded at 453 nm is depicted in **Figure 3.3.5** over a time window close to 1000 ps. The positive  $\Delta\text{OD}$  signal develops rapidly ( $< 1$  ps), within the response limits of our spectrometer, and this provides a strong evidence for an

<sup>179</sup> Giannoudis, E.; Benazzi, E.; Karlsson, J.; Copley, G.; Panagiotakis, S.; Landrou, G.; Angaridis, P.; Nikolaou, V.; Matthaiaki, C.; Charalambidis, G. et al. *Inorg. Chem.* **2020**, *59* (3), 1611.

<sup>180</sup> Gouterman, M. Spectra of porphyrins. *J. Mol. Spectrosc.* **1961**, *6*, 138.

<sup>181</sup> Peuntinger, K.; Lazarides, T.; Dafnomili, D.; Charalambidis, G.; Landrou, G.; Kahnt, A.; Sabatini, R. P.; McCamant, D. W.; Gryko, D. T.; Coutsolelos, A. G. et al. *J. Phys. Chem. C* **2013**, *117* (4), 1647.

<sup>182</sup> Linschitz, H.; Pekkarinen, L. *J. Am. Chem. Soc.* **1960**, *82* (10), 2411.

<sup>183</sup> Barbosa Neto, N. M.; Correa, D. S.; De Boni, L.; Parra, G. G.; Misoguti, L.; Mendonça, C. R.; Borissevitch, I. E.; Zilio, S. C.; Gonçalves, P. J. *Chem. Phys. Lett.* **2013**, *587*, 118.

<sup>184</sup> Kumar, P. H.; Venkatesh, Y.; Siva, D.; Ramakrishna, B.; Bangal, P. R. *J. Phys. Chem. A* **2015**, *119* (8), 1267.

efficient population of the triplet states through a channel involving  $S_2$ . The transient absorbance feature at 453 nm continues on a time window much longer than 1 ns and for this reason an accurate estimation of its kinetics is not possible, yet the apparently long time kinetics indicates that a triplet state is present.

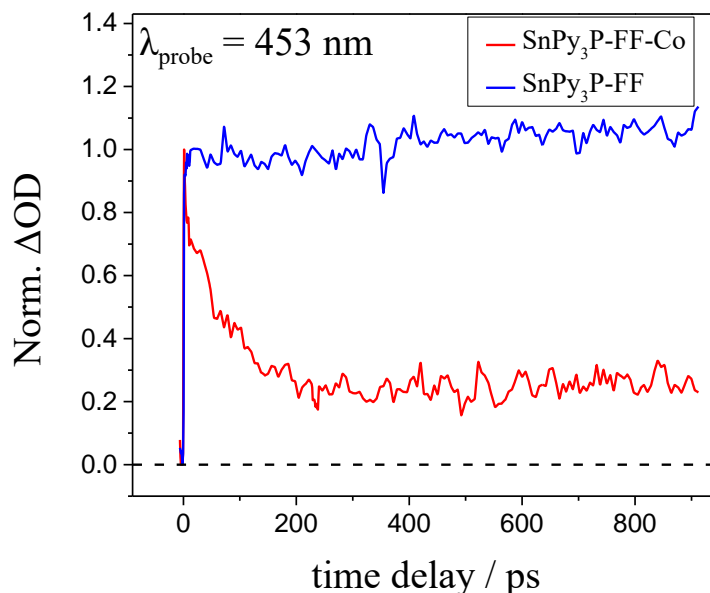


**Figure 3.3.5** Normalized kinetic curves of **SnPy<sub>3</sub>P-FF** sample (blue line,  $4 \times 10^{-5}$  M) and **SnPy<sub>3</sub>P-FF**–[Co(dmgh)<sub>2</sub>(Cl)(Py)] catalyst (**SnPy<sub>3</sub>P-FF-Co**) sample (red line), probing at 450 nm.

Interestingly, the presence of molar excess of [Co(III)(dmgh)<sub>2</sub>(py)Cl],  $5 \times 10^{-4}$  M, in the solution, drastically changes the porphyrin dynamics as shown in **Figure 3.3.5** (red line). For both cases (**SnPy<sub>3</sub>P-FF** and **SnPy<sub>3</sub>P-FF-Co**), the signal attains a rapid increase at time zero, indicating an ultrafast build-up population. Generally, the transient spectra profiles of **SnPy<sub>3</sub>P-FF-Co** are similar to those of **SnPy<sub>3</sub>P-FF**. However, the decay profiles of the transient absorbance at 453 nm are completely different between **SnPy<sub>3</sub>P-FF** and **SnPy<sub>3</sub>P-FF-Co**. The  $\Delta OD$  in the case of **SnPy<sub>3</sub>P-FF-Co** decays fast, within the first 200 ps after excitation, reaching nearly a plateau, which is down to 30% of the initial  $\Delta OD$  value. To quantify the decay kinetics, the data were fitted with a double-exponential function (**equation 3.1**) to account for the two distinctly different rate process.

$$y(t) = A_1 \exp\left(-\frac{t}{t_1}\right) - A_2 \exp\left(-\frac{t}{t_2}\right) + C \quad (\text{equation 3.1})$$

The fast component was found to have a characteristic decay time of  $t_1 = 80$  ps while the second exponential has a characteristic growth time  $t_2 > 1$  ns (roughly estimated). The fast decay component illustrates an efficient depopulation of the porphyrin triplet state and this is attributed to a strong electronic interaction of the cobaloxime with the porphyrin. Potentially, the **SnPy<sub>3</sub>P-FF-Co** mixture, following formation of the porphyrin triplet, undergoes an electron transfer, with an electron being transferred from the porphyrin to the cobaloxime catalyst, producing a charge separated state (CSS) (**Figure 3.3.6**).<sup>185,186,187</sup>

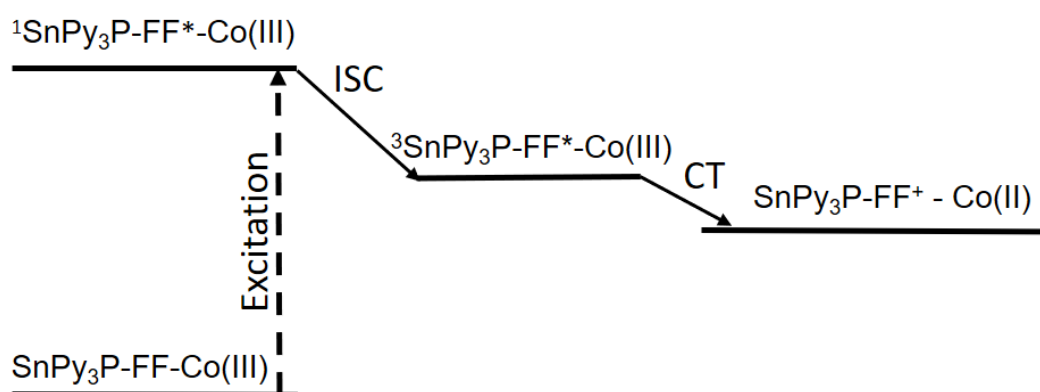


**Figure 3.3.6** Energy diagram indicating main photophysical processes occurring following excitation of **SnPy<sub>3</sub>P-FF-Co** at 395 nm.

This fact is in agreement with the assumption that the porphyrin triplet participates in the hydrogen production pathway demonstrated with **SnPy<sub>3</sub>P-FF-Co**. Noteworthy, there were no obvious  $\Delta$ OD signals observed across the spectral window explored (422 - 735 nm) that would indicate production of a charge transfer product. However, it is noted that diffusion phenomena (for example the catalyst diffusing towards the excited porphyrin) are not contributing to the observed electron transfer dynamics because they are much slower in the time-scale of the pump-probe measurements. As a consequence, the electron transfer is most probably intramolecular rather than bimolecular. The remaining slow transient absorbance signal of **SnPy<sub>3</sub>P-FF-Co** (**Figure 3.3.5**) has

<sup>185</sup> Giannoudis, E.; Benazzi, E.; Karlsson, J.; Copley, G.; Panagiotakis, S.; Landrou, G.; Angaridis, P.; Nikolaou, V.; Matthaiki, C.; Charalambidis, G. et al. *Inorg. Chem.* **2020**, *59* (3), 1611.

<sup>186</sup> Peuntinger, K.; Lazarides, T.; Dafnomili, D.; Charalambidis, G.; Landrou, G.; Kahnt, A.; Sabatini, R. P.; McCamant, D. W.; Gryko, D. T.; Coutsolelos, A. G. et al. *J. Phys. Chem. C* **2013**, *117* (4), 1647.

<sup>187</sup> Lazarides, T.; Delor, M.; Sazanovich, I. V.; McCormick, T. M.; Georgakaki, I.; Charalambidis, G.; Weinstein, J. A.; Coutsolelos, A. G. *Chem. Commun.* **2014**, *50* (5), 521.

almost an identical kinetic profile with that observed with **SnPy<sub>3</sub>P-FF**. Most probably, this mainly represents an amount of porphyrin which cobaloxime has not been linked to. The above transient experiments were conducted by Maria Pigiaki in the laboratory of Dr. Panagiotis A. Loukakos (*Foundation for Research and Technology (FORTH), Institute of Electronic Structure and Laser (IESL), 70013 Heraklion, Greece*).

In order to identify the nature of this intramolecular interaction between the **SnPy<sub>3</sub>P-FF** and the cobaloxime catalyst, NMR spectroscopy studies were performed. As it is illustrated in **Figure 3.3.7**, after the addition of 10 equivalents of [Co(dmgH)<sub>2</sub>(Cl)(Py)] to a solution of **SnPy<sub>3</sub>P-FF** in CD<sub>3</sub>CN, all the *ortho*-pyridyl protons exhibit a considerable upfield shift. This observation proves that **SnPy<sub>3</sub>P-FF** can coordinate with three cobaloxime moieties as it has been observed in the literature.<sup>188</sup> Hence, we show a structural proposition of the complex between the self-assembled Sn-porphyrin and the cobaloxime catalyst at **Figure 3.3.8**.

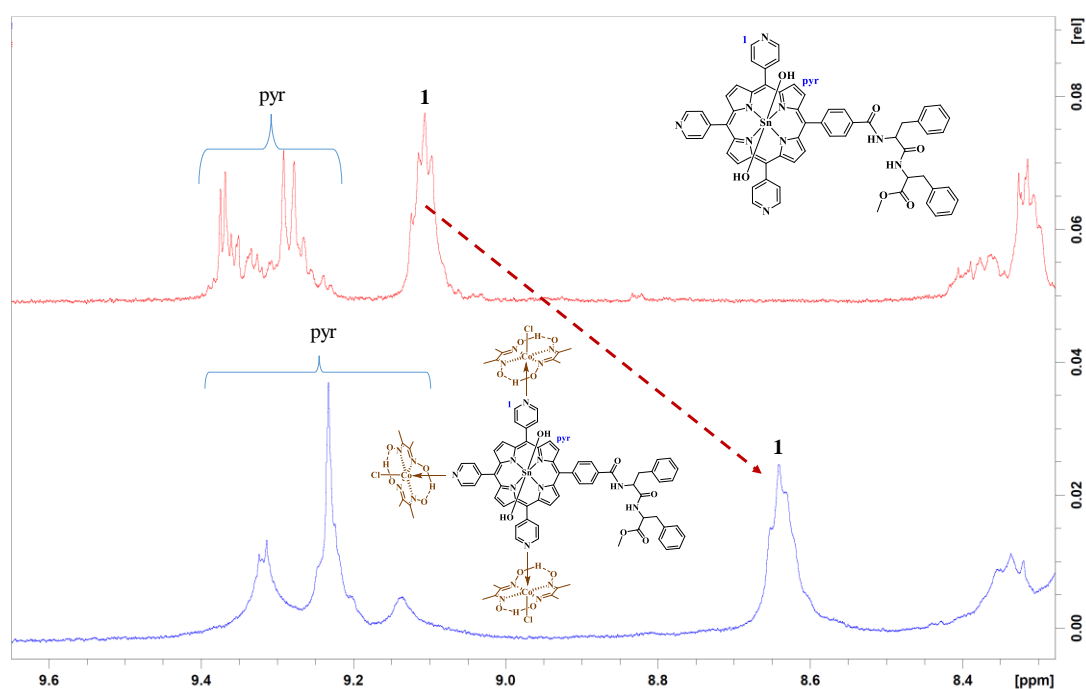


**Figure 3.3.7** <sup>1</sup>H NMR in CD<sub>3</sub>CN of **SnPy<sub>3</sub>P-FF** before (red line) and after the addition of 10 equivalents of [Co(dmg)<sub>2</sub>ClPy] cobaloxime.

<sup>188</sup> Peuntinger, K.; Lazarides, T.; Dafnomili, D.; Charalambidis, G.; Landrou, G.; Kahnt, A.; Sabatini, R. P.; McCamant, D. W.; Gryko, D. T.; Coutsolelos, A. G. et al. . *J. Phys. Chem. C* **2013**, *117* (4), 1647.



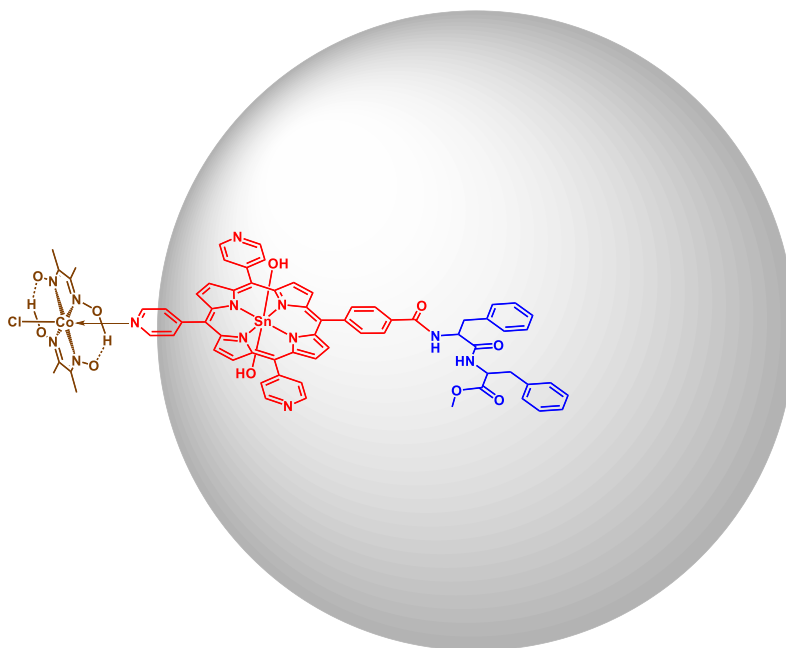


**Figure 3.3.8** Structural proposition of the ‘complex’ between the self-assembled tin-porphyrin with cobaloxime.

Fluorescence spectroscopy experiments were performed in order to identify the mechanism of our photocatalytic system. As illustrated in **Figure 3.3.9** addition of excess of  $[\text{Co}(\text{dmgH})_2(\text{Cl})(\text{Py})]$  into a solution of **SnPy<sub>3</sub>P-FF** in  $\text{CH}_3\text{CN}-\text{H}_2\text{O}$  (1:1) results in quenching of the porphyrin-based fluorescence by 67%, while adding excess of the sacrificial electron donor (TEOA) caused only 8% quenching. This observation indicates that hydrogen production in our system is initiated via oxidative quenching of the photosensitizer.<sup>189,190</sup>

In the project described in this section, a porphyrin-peptide hybrid molecule was synthesized via the covalent attachment of the diphenylalanine peptide with a tripyridyl porphyrin, endowing the resulting derivative with self-assembling properties. This hybrid was metallated with non-noble metals, Zn and Sn, and investigated in various self-assembling conditions using the “good-bad” solvent self-assembling protocol. We demonstrated that the metal in the porphyrin core plays a major role in the self-assembly behavior of the hybrid molecules since it leads to different supramolecular architectures namely fibrils, nanospheres or irregular aggregation. The nanostructures were applied

<sup>189</sup> Han, Z.; Shen, L.; Brennessel, W. W.; Holland, P. L.; Eisenberg, R. *J. Am. Chem. Soc.* **2013**, *135* (39), 14659.

<sup>190</sup> Natali, M.; Deponti, E.; Vilona, D.; Sartorel, A.; Bonchio, M.; Scandola, F. A. *Eur. J. Inorg. Chem.* **2015**, *2015* (21), 3467.

towards photocatalytic hydrogen evolution using a known cobaloxime complex as molecular catalyst and TEOA as sacrificial electron donor. Although the Zn and free base derivatives did not exhibit any photocatalytic efficiency, **SnPy<sub>3</sub>P-FF** was able to act as a photosensitizer and produced hydrogen. Noteworthy, the efficiency of the self-assembled chromophore was superior compared to the amorphous chromophore molecules. Photophysical studies suggest that there is an electron transfer process from the triplet excited state of the porphyrin to the cobaloxime catalyst and the photocatalytic H<sub>2</sub> evolution follows mainly the oxidative quenching pathway. The photocatalytic system proposed herein is an artificial mimic of photosynthesis, where self-assembling chromophores are utilized to improve the storage of solar energy into chemical bonds (H<sub>2</sub>), like self-assembling chlorophylls in nature are used to store the solar energy into the bonds of glucose.

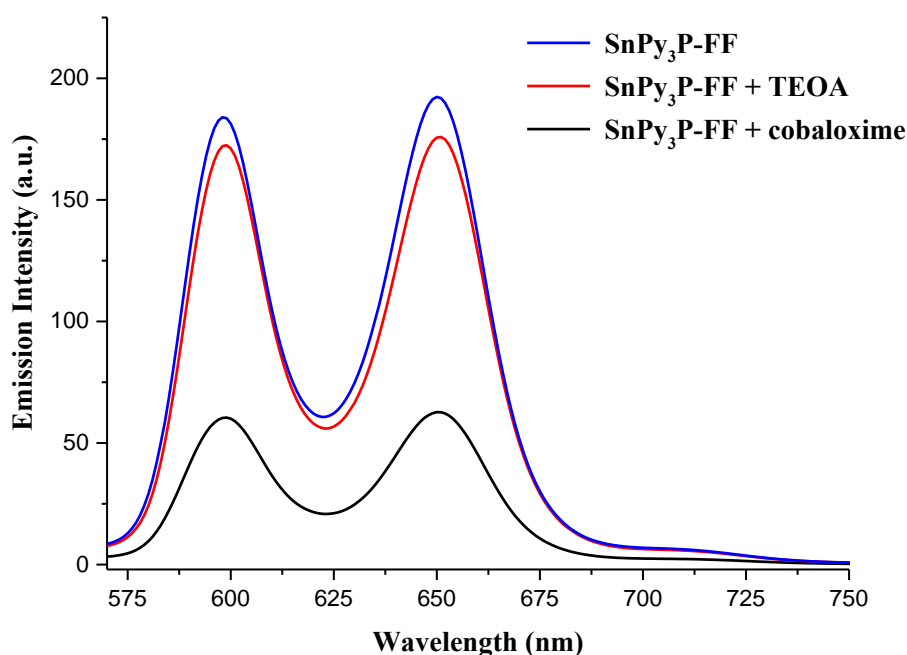


**Figure 3.3.9** Emission spectra of **SnPy<sub>3</sub>P-FF** in CH<sub>3</sub>CN-H<sub>2</sub>O 1:1 ( $8 \times 10^{-6}$  M) after excitation the first Q band (550 nm) where  $A_{550\text{nm}} = 0.09$  (blue line), after adding only TEOA (red line, 0.5% v/v), after adding only the cobaloxime catalyst (black line,  $9.8 \times 10^{-5}$  M).

- Gadolinium porphyrinate double-deckers towards hydrogen production

In the work presented in this section, we examined a series of gadolinium porphyrin double deckers towards photocatalytic hydrogen evolution. Porphyrin sandwich-type double deckers have encouraging features like near-infrared emission and singlet oxygen production for photodynamic therapy (PDT),<sup>191,192</sup> rotatable properties for molecular rotors<sup>193</sup> and they provide a stable chelate for the carriage of paramagnetic metals which can be utilized as MRI agents.<sup>194,195</sup> Moreover, porphyrin double deckers represent a good model for the special pair found in the photosynthetic membranes of plants and photosynthetic bacteria, because the distance between the two macrocycles is short and the face-to-face dimer behaves as a single entity.<sup>196</sup> Interestingly, although porphyrins have been extensively investigated as photosensitizers for hydrogen production,<sup>197</sup> to the best of our knowledge, there was no report that examines H<sub>2</sub> production from double decker porphyrins till our studies<sup>198</sup>. Moreover, there are only a few reports studying the self-assembly behaviour of porphyrin double decker derivatives.<sup>199,200,201</sup>

The complexes utilized in this work were varied both on the *meso*- and on the *beta*-positions of the porphyrin macrocycle. For comparison reasons we also studied the corresponding monoporphyrinate gadolinium complexes as shown in **Figure 3.3.10**. For the photocatalytic measurements a platinum salt was utilized as a source for Pt nanoparticles co-catalyst, under visible light excitation of the porphyrin chromophores. This was the first report that investigates double decker porphyrins for H<sub>2</sub> production. Moreover, we investigated the self-assembling properties of these complexes and the

---

<sup>191</sup> Zhang, J. X.; Chan, W. L.; Xie, C.; Zhou, Y.; Chau, H. F.; Maity, P.; Harrison, G. T.; Amassian, A.; Mohammed, O. F.; Tanner, P. A. et al. *Light Sci. Appl.* **2019**, *8*, 46.

<sup>192</sup> Wang, J.; Wang, Z.; Zhong, Y.; Zou, Y.; Wang, C.; Wu, H.; Lee, A.; Yang, W.; Wang, X.; Liu, Y. et al. *Biomaterials* **2020**, *229*, 119576

<sup>193</sup> Otsuki, J.; Komatsu, Y.; Kobayashi, D.; Asakawa, M.; Miyake, K. *J. Am. Chem. Soc.* **2010**, *132* (20), 6870

<sup>194</sup> Jin, M.; Zhang, Y.; Gao, G.; Xi, Q.; Tong, J.; Zhao, Y.; Wu, C.; Zhou, H.; Yang, Q.; Yang, W. et al. *Appl. Organomet. Chem.* **2019**, DOI:10.1002/aoc.4953 10.1002/aoc.4953.

<sup>195</sup> Zang, L.; Zhao, H.; Hua, J.; Qin, F.; Zheng, Y.; Zhang, Z.; Cao, W. *Dyes Pigm.* **2017**, *142*, 465.

<sup>196</sup> Langlois, A.; Camus, J. M.; Karsenti, P. L.; Guillard, R.; Harvey, P. D. *Inorg. Chem.* **2017**, *56* (5), 2506.

<sup>197</sup> Ladomenou, K.; Natali, M.; Iengo, E.; Charalampidis, G.; Scandola, F.; Coutsolelos, A. G. *Coord. Chem. Rev.* **2015**, *304-305*, 38.

<sup>198</sup> Nikoloudakis et al. *Polyhedron* **2021** *208* 115421.

<sup>199</sup> Lu, J.; Zhou, L.; Meng, Q.; Sui, H.; Li, Y.; Tai, X. *Dyes Pigm.* **2015**, *113*, 138.

<sup>200</sup> Abd El-Mageed, A. I. A.; Ogawa, T. *RSC Adv.* **2019**, *9* (48), 28135.

<sup>201</sup> Wu, X.; Lv, W.; Wang, Q.; Wang, H.; Zhang, X.; Jiang, J. *Dalton Trans.* **2011**, *40* (1), 107.

possible relation to the photocatalytic performance. The present work is a case study to investigate parameters that remained until now unstudied, in the field of visible light driven H<sub>2</sub> production using porphyrin chromophores and Pt nanoparticles.

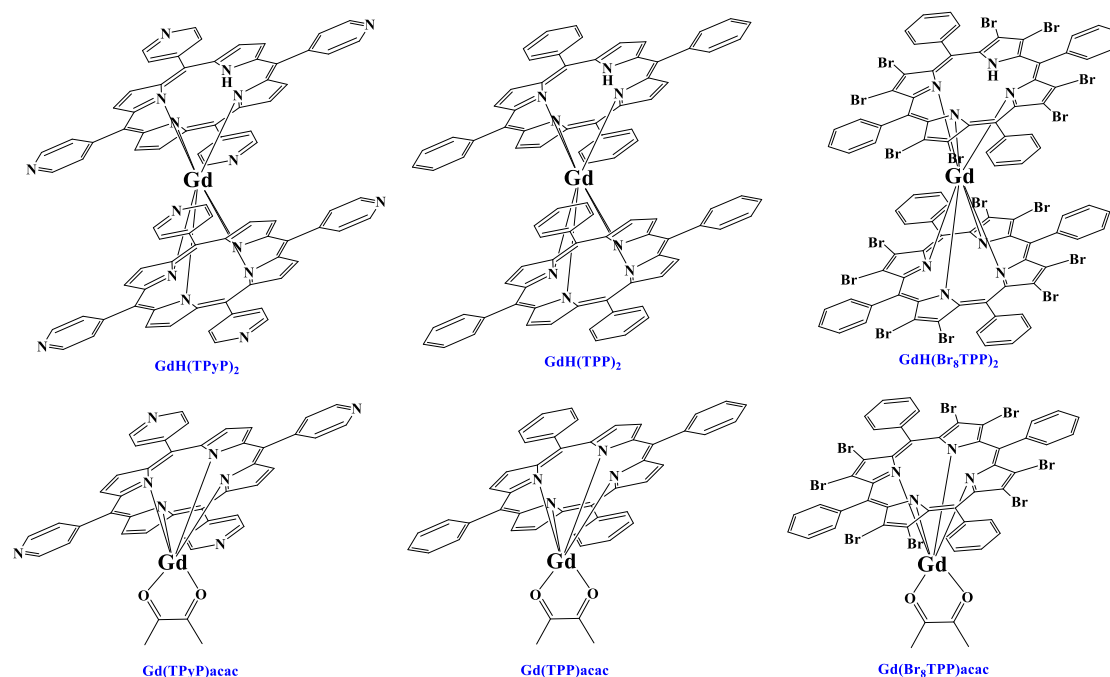


**Figure 3.3.10** Structures of the gadolinium porphyrin double deckers and monomers that were studied in this work.

The synthesis of the porphyrin derivatives studied in this work (**Figure 3.3.10**) has been previously reported from our group.<sup>202,203,204,205,206,207,208,209</sup>

The structures of the six compounds were investigated by powder X-ray diffraction analysis using solid samples and the obtained diffraction patterns are depicted in **Figure 3.3.11**. Unfortunately, indexing and space group determination were not possible for

<sup>202</sup> Spyroulias, G. A.; Sioubara, M. P.; Coutsolelos, A. G. *Polyhedron* **1995**, *14* (23-24), 3563.

<sup>203</sup> Agondanou, J. H.; Spyroulias, G. A.; Purans, J.; Tsikalas, G.; Souleau, C.; Coutsolelos, A. G.; Benazeth, S. *Inorg. Chem.* **2001**, *40* (24), 6088.

<sup>204</sup> Spyroulias, G. A.; Despotopoulos, A.; Raptopoulou, C. P.; Terzis, A.; Coutsolelos, A. G. *Chem. Commun.* **1997**, DOI:10.1039/a608013h 10.1039/a608013h(8), 783.

<sup>205</sup> Agondanou, J. H.; Nicolis, I.; Curis, E.; Purans, J.; Spyroulias, G. A.; Coutsolelos, A. G.; Benazeth, S. *Inorg. Chem.* **2007**, *46* (17), 6871.

<sup>206</sup> Spyroulias, G. A.; Raptopoulou, C. P.; de Montauzon, D.; Mari, A.; Poilblanc, R.; Terzis, A.; Coutsolelos, A. G. *Inorg. Chem.* **1999**, *38* (8), 1683.

<sup>207</sup> Spyroulias, G. A.; Despotopoulos, A. P.; Raptopoulou, C. P.; Terzis, A.; de Montauzon, D.; Poilblanc, R.; Coutsolelos, A. G. *Inorg. Chem.* **2002**, *41* (10), 2648.

<sup>208</sup> Babailov, Sergey P.; Coutsolelos, Athanassios G.; Dikiy, A.; Spyroulias, Georgios A. *Eur. J. Inorg. Chem.* **2001**, *2001* (1), 303.

<sup>209</sup> Spyroulias, G. A.; Coutsolelos, A. G. *Inorg. Chem.* **1996**, *35* (5), 1382.

any of the studied samples, due to the low resolution of the experimental data, as a result of their low crystallinity. Moreover, a comparative analysis as the above one could not be performed, due to the low availability of X-ray diffraction data for rare earth porphyrinato compounds in the literature.

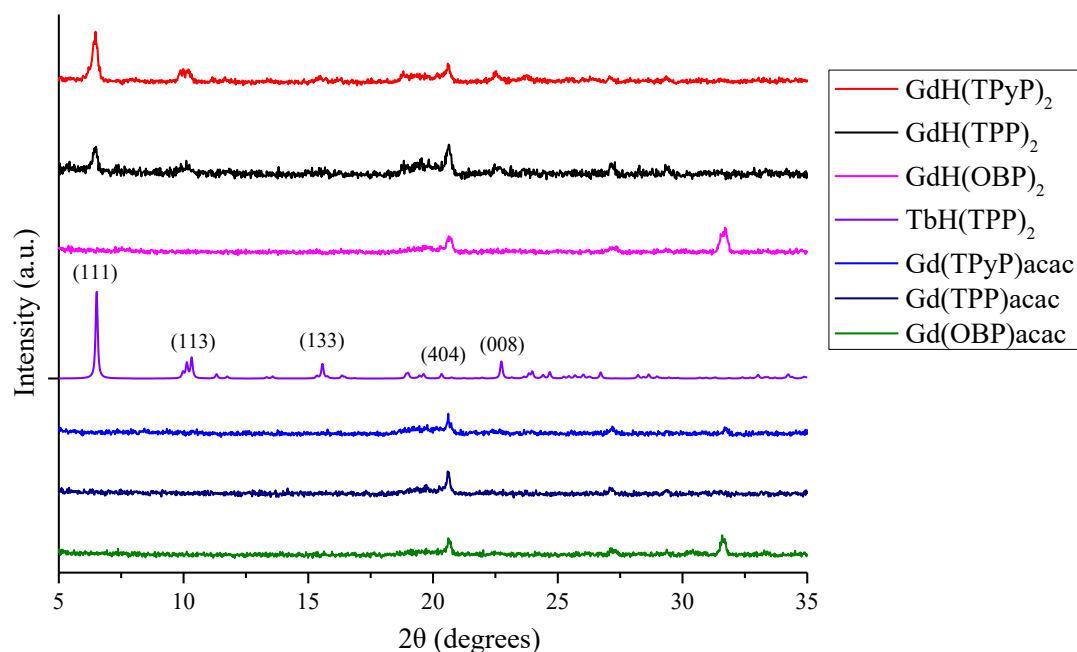


**Figure 3.3.11** Powder XRD patterns of all studied compounds. The data for  $\text{TbH(TPP)}_2$  were obtained from the literature.<sup>210</sup>

All compounds were additionally characterized via IR-spectroscopy (**Figure 3.3.12**). For the  $\text{Gd(TPyP)acac}$  and the  $\text{GdH(TPyP)}_2$  complexes, we observed the characteristic strong band at  $1593\text{ cm}^{-1}$ , due to the C=N stretching vibration of the pyridyl substituents. Moreover, the peaks at  $1406$ ,  $1330$ ,  $1200$ ,  $1068$ ,  $984$ ,  $792$  and  $663\text{ cm}^{-1}$  are also attributed to the TPyP porphyrin ligand. The characteristic peak at  $534\text{ cm}^{-1}$  is assigned to the acetylacetonate ligand and is present only in the spectrum of  $\text{Gd(TPyP)acac}$  (**Figure 3.3.13**). In the IR spectra of  $\text{Gd(TPP)acac}$  and  $\text{GdH(TPP)}_2$ , we detected the absorption bands at  $1593$  and  $1471\text{ cm}^{-1}$  which correspond to the stretching vibration of C=C and C-C of the benzene ring. The peak at  $964\text{ cm}^{-1}$  is associated to the skeleton of the porphyrin ring, while the band at  $796\text{ cm}^{-1}$  is assigned to the out-plane bending vibration of pyrrole C-H. Finally, the bands at  $698$  and  $721\text{ cm}^{-1}$  derive from the bending vibration modes of the C-H on the benzene ring. One

<sup>210</sup> K.-i. Yamashita, N. Sakata, T. Ogawa, *Inorg. Chem.*, 55 (2016) 8935-8942.

characteristic difference between these two spectra is the peak at  $985\text{ cm}^{-1}$ , which was attributed to the acetylacetonate ligand of **Gd(TPP)acac** (Figure 3.3.13). In the case of **Gd(OBP)acac** and **GdH(OBP)<sub>2</sub>**, we observed porphyrin based signals at 1439, 1257 and  $1009\text{ cm}^{-1}$ , while acetylacetonate based peaks at 1587, 1380 and  $916\text{ cm}^{-1}$  appeared only in the spectrum of **Gd(OBP)acac** (Figure 3.3.14).

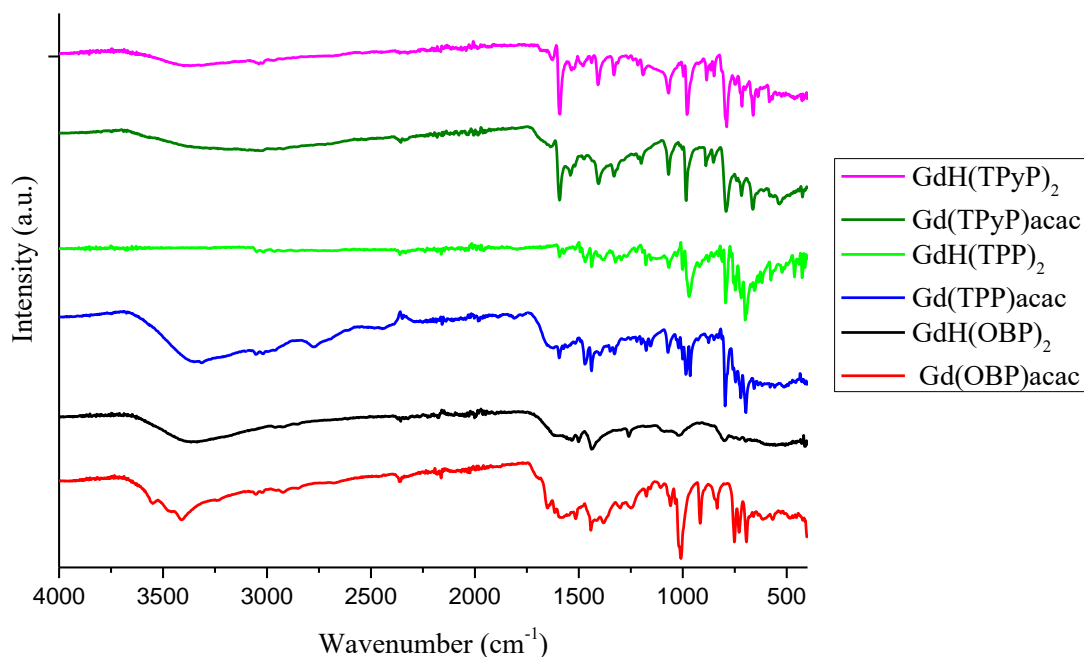


Figure 3.3.12 FT-IR spectra of all studied compounds.

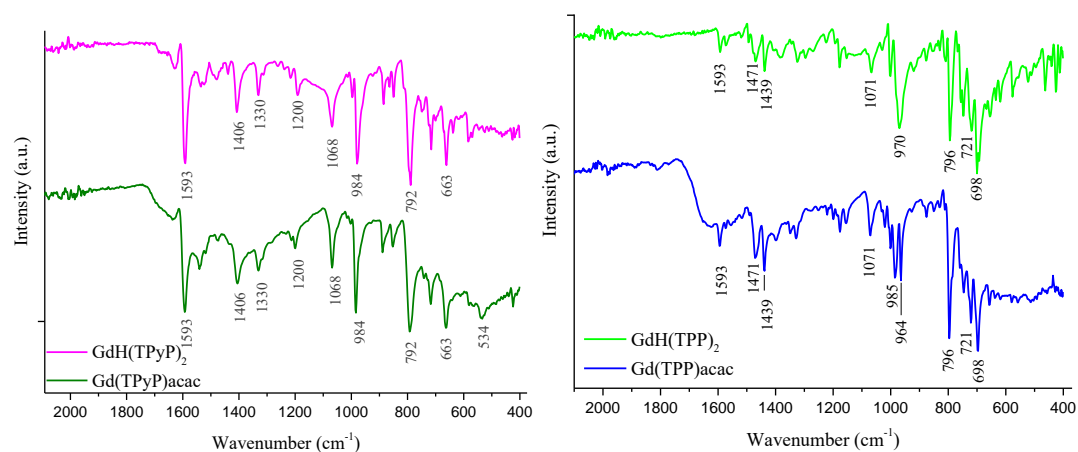
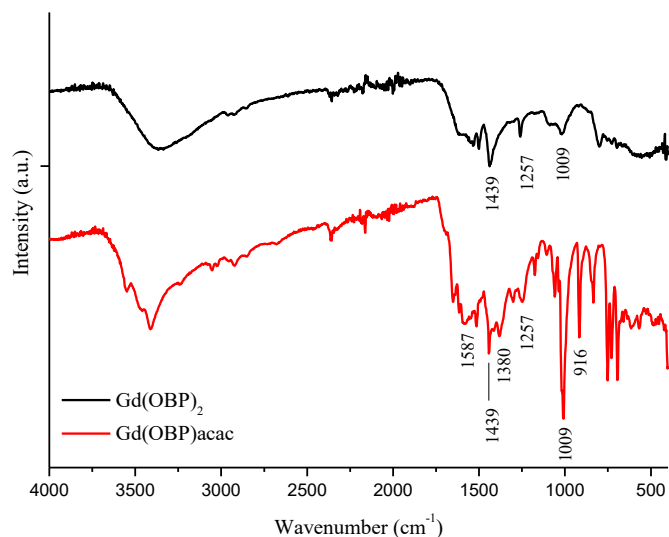


Figure 3.3.13 FT-IR spectra of **GdH(TPyP)<sub>2</sub>**, **Gd(TPyP)acac**, **GdH(TPP)<sub>2</sub>** and **Gd(TPP)acac**.



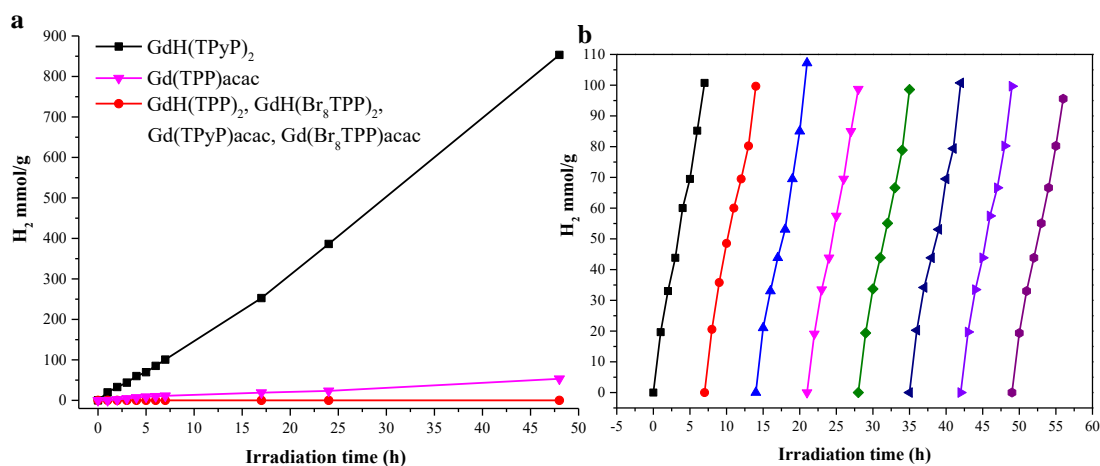
**Figure 3.3.14** FT-IR spectra of **GdH(OBP)<sub>2</sub>** and **Gd(OBP)acac**.

Photo-induced hydrogen ( $H_2$ ) production experiments were conducted in order to evaluate the catalytic activity of the gadolinium double decker porphyrins and the corresponding monoporphyrinate complexes.  $Na_2PtCl_6 \cdot 6H_2O$  was used as catalyst source in order to form Pt nanoparticles under visible excitation of the porphyrin chromophores. Ascorbic acid 1M was utilized as a sacrificial electron donor to provide the necessary electrons for the reductive process while no organic solvents were present in the aqueous medium. Noteworthy, all porphyrin chromophores were not soluble in water, even the pyridyl derivatives since they were not methylated. However, this did not prevent the formation of Pt nanoparticles onto the porphyrin aggregates.

The **GdH(TPP)<sub>2</sub>**, **GdH(Br<sub>8</sub>TPP)<sub>2</sub>**, and **Gd(Br<sub>8</sub>TPP)acac** derivatives did not exhibit any photocatalytic efficiency while the **Gd(TPP)acac** displayed negligible performance. On the other hand, the **GdH(TPyP)<sub>2</sub>** double decker demonstrated high photocatalytic activity towards hydrogen evolution reaching a maximum of 853 mmol/g after 48 hours of visible light irradiation (**Figure 3.3.15a**), which is translated to 166 TON over the Pt co-catalyst. The **Gd(TPyP)acac** derivative, which had the same peripheral substitution with **GdH(TPyP)<sub>2</sub>** was totally inactive towards hydrogen production, verifying that the presence of the double decker is essential for photocatalytic activity towards  $H_2$  production.

It is known that organic photocatalysts are limited by their photostability because they may be decomposed due to photobleaching or solvolysis. Notably, the rate of hydrogen production in our system maintained linear for at least 48 hours revealing the

high stability of the system. We also performed reusability experiments in order to investigate in more detail the stability and robustness of the **GdH(TPyP)<sub>2</sub>** photocatalyst. As shown in **Figure 3.3.15b**, after up to eight recycling cycles (56 h) under visible light irradiation the hydrogen production rate remains stable with no obvious decay. The hydrogen evolution rate in the first 7 h is  $13.8 \text{ mmol}\cdot\text{h}^{-1}\cdot\text{g}^{-1}$  (**Table 3.1**). These results point out that **GdH(TPyP)<sub>2</sub>** is fairly stable with very good recycling ability for photocatalytic hydrogen production. Moreover, the performance of this system is competitive with analogous work in the recent literature.<sup>211</sup> The photosensitized H<sub>2</sub> production in our system could possibly occur via either oxidative or reductive quenching of excited gadolinium porphyrin, as diagrammed in **Scheme 3.3.1**.<sup>212</sup> However, according to the literature in similar photocatalytic systems the most probable operating mechanism is the reductive quenching pathway.<sup>213</sup>



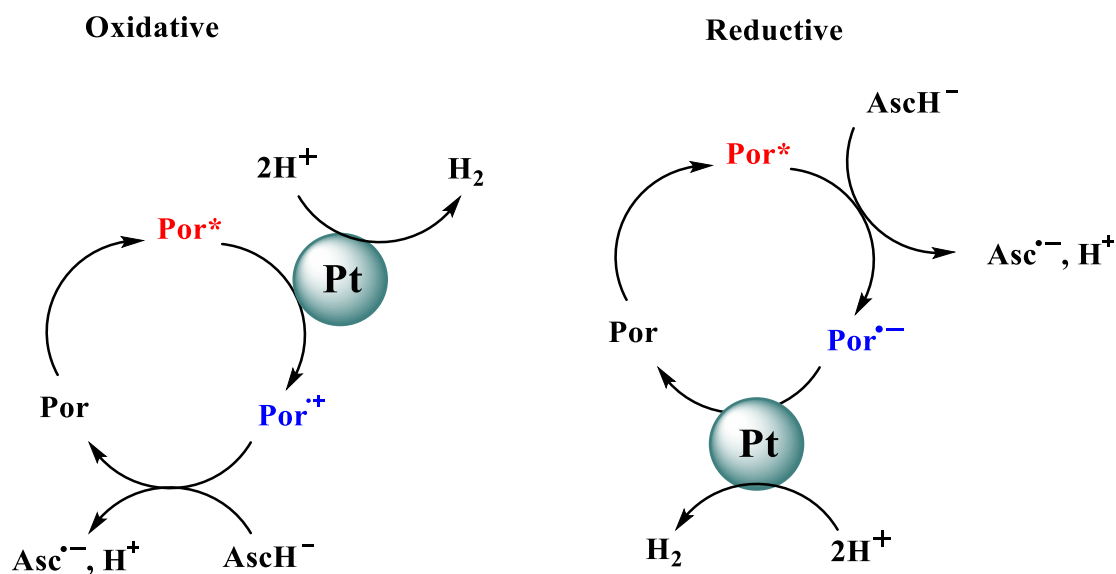
**Figure 3.3.15** (a) Photocatalytic hydrogen production plots of the gadolinium porphyrin complexes studied herein. The photocatalytic experiments were conducted in a water with ascorbic acid 1 M at pH=4. Each experiment contained 2.5 mg of the porphyrin photosensitizer and 5% w/w of Na<sub>2</sub>PtCl<sub>6</sub>·6H<sub>2</sub>O as co-catalyst, (b) Cycling runs for the photocatalyzed hydrogen evolution of **GdH(TPyP)<sub>2</sub>**.

<sup>211</sup> Zhang, N.; Wang, L.; Wang, H.; Cao, R.; Wang, J.; Bai, F.; Fan, H. *Nano Lett.* **2018**, *18* (1), 560.

<sup>212</sup> Clark, E. R.; Kurtz, D. M. *Inorg. Chem.* **2017**, *56* (8), 4584.

<sup>213</sup> Kotani, H.; Miyazaki, T.; Aoki, E.; Sakai, H.; Hasobe, T.; Kojima, T. *ACS Appl. Energy Mater.* **2020**, *3* (4), 3193.





**Scheme 3.3.1** Possible oxidative and reductive quenching pathways for photosensitized H<sub>2</sub> production by **GdH(TPyP)<sub>2</sub>** and **Gd(TPP)acac**.

**Table 3.1** H<sub>2</sub> production rate (nH<sub>2</sub>), turnover number (TON) and turnover frequency data of the photocatalytic systems after 48 hours of irradiation.

Compound	n H <sub>2</sub> (mmol g <sup>-1</sup> )	H <sub>2</sub> rate (mmol g <sup>-1</sup> h <sup>-1</sup> )	TON <sub>Pt</sub>	TON <sub>porph</sub>
Gd(TPP)acac	53	2.3	10	1
GdH(TPyP) <sub>2</sub>	853	13.8	166	21

Photophysical investigation of **GdH(TPyP)<sub>2</sub>** via UV-Vis absorption experiments showed that in solid state (drop-casted from water) the spectrum of the porphyrin is broadened and red shifted, in relation to the corresponding bands in THF. This observation demonstrates that in water which is the medium of the photocatalysis, the formation of *J*-aggregates (side-by-side) takes place in the porphyrin assemblies.

In order to shed more light to the aggregation of the **GdH(TPyP)<sub>2</sub>** porphyrin derivative, scanning electron microscopy (SEM) images were obtained. SEM images of **GdH(TPyP)<sub>2</sub>** drop-casted from water showed flake shaped microstructures (**Figure 3.3.16a, 6.3.42**) and EDS experiment verified the presence of Gd on these flakes (**Figure 6.3.43**). This indicates that **GdH(TPyP)<sub>2</sub>** self-assembled into flakes in water and Pt NPs were photodeposited during the catalysis onto these flakes. In an attempt to elucidate why **GdH(TPyP)<sub>2</sub>** exhibited enhanced photocatalytic activity, while the rest

of the gadolinium porphyrins studied herein did not, we obtained the SEM images of all the other derivatives through drop-casting from water. As depicted in **Figure 3.3.16**, each porphyrin displayed different aggregation behavior. Noteworthy, **Gd(TPP)acac** self-assembled into flower-like flakes, while in the case of **GdH(TPP)<sub>2</sub>** octahedral prisms were observed. The rest three gadolinium porphyrins, namely **Gd(TPyP)acac**, **Gd(Br<sub>8</sub>TPP)acac** and **GdH(Br<sub>8</sub>TPP)<sub>2</sub>** didn't self-assemble into any distinctive architecture.

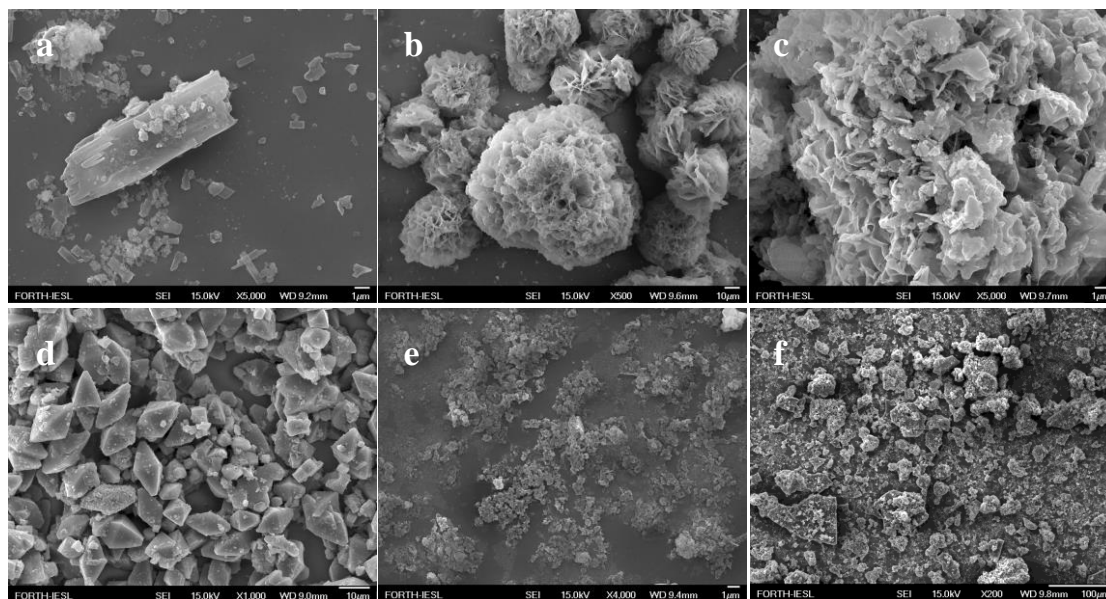


**Figure 3.3.16** SEM images of (a) **GdH(TPyP)<sub>2</sub>**, (b) **Gd(TPP)acac**, (c) **Gd(TPyP)acac**, (d) **GdH(TPP)<sub>2</sub>**, (e) **Gd(Br<sub>8</sub>TPP)acac** and (f) **GdH(Br<sub>8</sub>TPP)<sub>2</sub>**.

Subsequently, we wanted to change the self-assembling mode of the porphyrins in order to check whether this affects the photocatalytic hydrogen production. For this purpose, we utilized once again the “good-bad solvent” self-assembling protocol. Initially, the sandwich porphyrin compounds were dissolved in a chaotropic “good” solvent, namely DCM and afterwards a “bad” solvent, namely MeOH or heptane, was introduced in order to induce the self-assembly process. The ability of the gadolinium porphyrins to self-assemble into distinctive architectures was investigated with scanning electron microscopy.

Following this approach, we were able to make the flakes of **GdH(TPyP)<sub>2</sub>** disappear using DCM-MeOH 1:1 solvent mixture (**Figure 3.3.17a**) or improve their morphology in DCM-Heptane 1:1 mixture (**Figure 3.3.17b**). Regarding the **Gd(TPP)acac** derivative we observed uniform nanospheres in DCM-MeOH 1:1

(**Figure 3.3.17c**), while the use of heptane as a “bad” solvent altered completely the morphology of the assemblies (**Figure 3.3.17d**). Another interesting self-assembling mode was obtained from **GdH(TPP)<sub>2</sub>**, which self-assembled into octahedral prisms in all solvent systems that were examined (**Figure 3.3.18**). However, in DCM-MeOH 1:1 the prisms were well-formed and had more smooth surfaces while in DCM-Heptane 1:1 their surface was rough (**Figure 3.3.17b**).

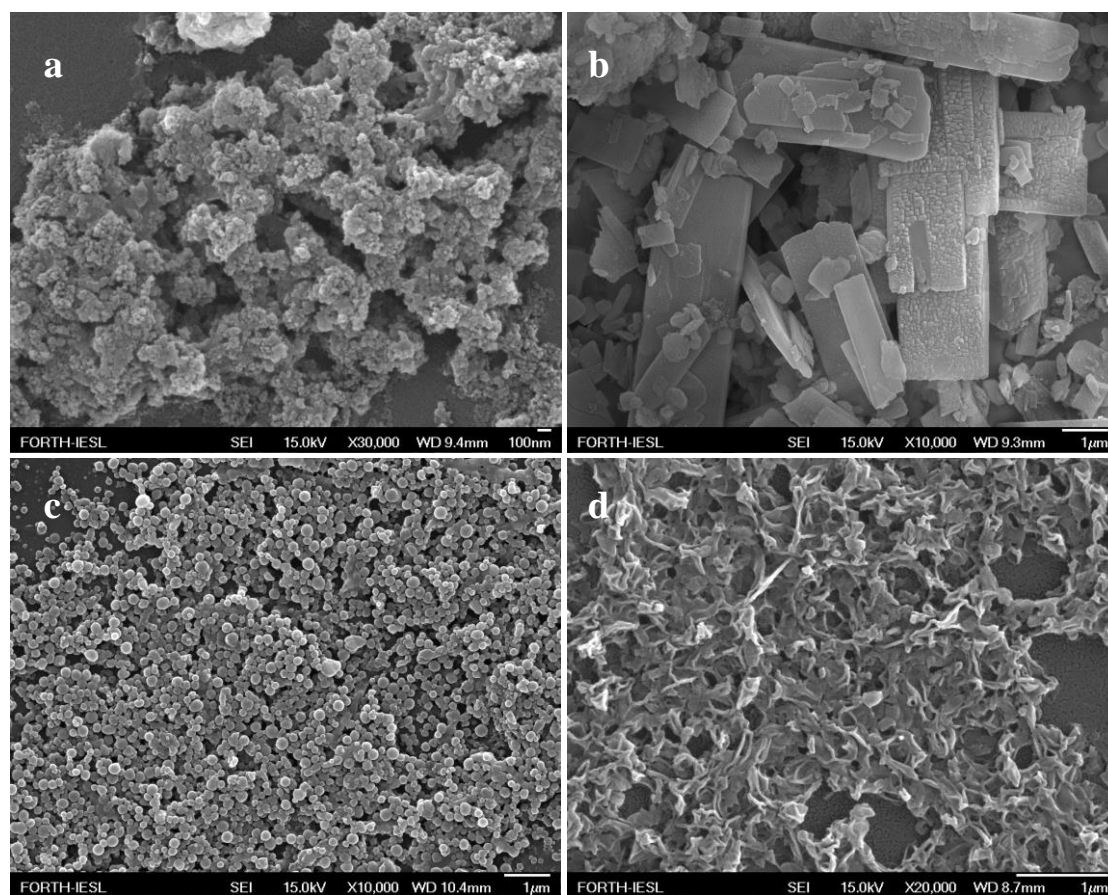


**Figure 3.3.17** SEM images of (a) **GdH(TPyP)<sub>2</sub>** in DCM-MeOH 1:1, (b) **GdH(TPyP)<sub>2</sub>** in DCM-Heptane 1:1, (c) **Gd(TPP)acac** in DCM-MeOH 1:1 and (d) **Gd(TPP)acac** in DCM-Heptane 1:1.

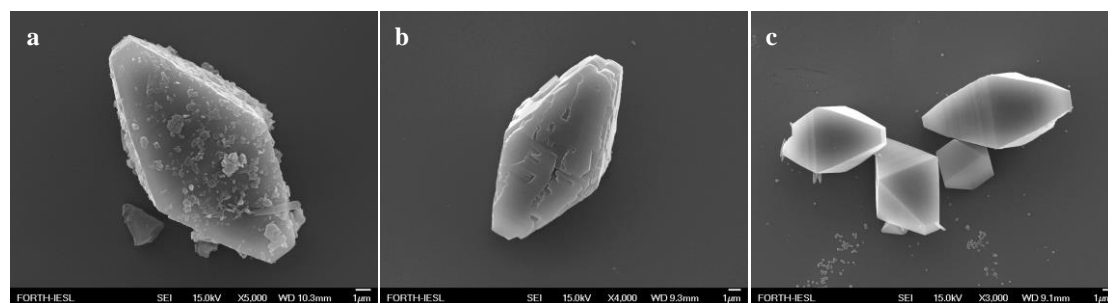


**Figure 3.3.18** SEM images of **GdH(TPP)<sub>2</sub>** (a) in water, (b) in DCM-Heptane 1:1 and (c) in DCM-MeOH 1:1.

When we employed the irregular aggregates of **GdH(TPyP)<sub>2</sub>** (**Figure 3.3.17a**) and the improved flake-shaped self-assemblies (**Figure 3.3.17b**) in the photocatalytic system we didn't observe any difference in the H<sub>2</sub> evolution unlike similar reports.<sup>214</sup> Likewise, the photocatalytic activity of **Gd(TPP)acac** didn't vary when the nanospheres (**Figure 3.3.17c**) nor the assemblies of **Figure 3.3.17d** were employed. These results prove that the substitution on the periphery of the gadolinium porphyrins is the key towards the photocatalytic performance and highlight the importance of the double decker substitution.

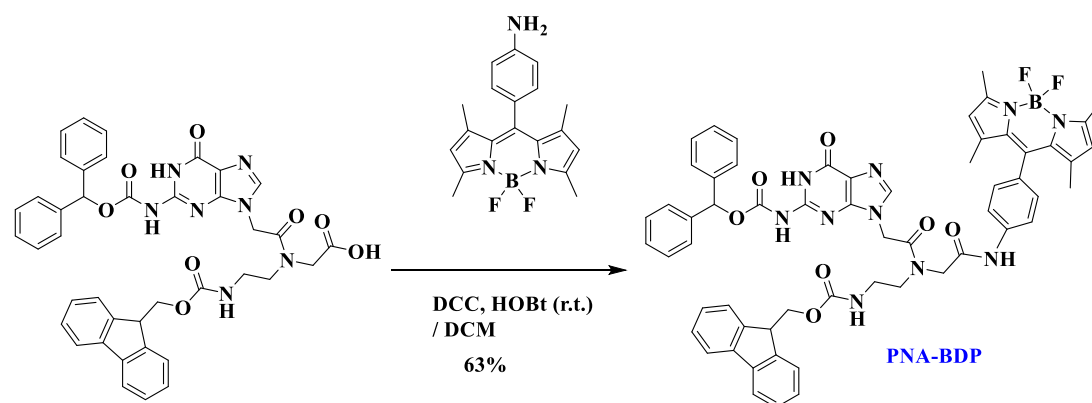
In the work presented in this section, we examined several gadolinium porphyrin double deckers and the corresponding monoporphyrinates towards photocatalytic hydrogen evolution. For the photocatalytic experiments, we employed Pt nanoparticles as catalyst and ascorbic acid as SED, while the reaction medium was pure water. The presence of the double decker was proved essential towards the photocatalytic activity, since **GdH(TPyP)<sub>2</sub>** displayed the higher performance, which reached 166 TON after 48 hours of irradiation and maintained a hydrogen production rate of 13.8 mmol·h<sup>-1</sup>·g<sup>-1</sup>. This system exhibited high stability over 48 hours, where it kept linear productivity. SEM experiments revealed the self-assembly of **GdH(TPyP)<sub>2</sub>** into flake shaped microstructures in water and absorption spectroscopy studies showed the presence of *J*-aggregates in these assemblies. Finally, we utilized the “good-bad solvent” self-assembling protocol to change the self-assembling mode of the porphyrins and we were able to obtain flakes, nanospheres or octahedral prisms. However, the morphology of the assemblies did not affect the photocatalytic hydrogen production in these systems. This result demonstrates that the peripheral substitution of the gadolinium porphyrins is the key towards the photocatalytic performance.

---

<sup>214</sup> Nikolaou, V.; Charalambidis, G.; Coutsolelos, A. G. *Chem. Commun.* **2021**, 57 (33), 4055.

### 3.4 Experimental Section

The subsequent paragraph describes the synthetic experimental procedures that were followed for the preparation of the compounds investigated in chapter 3. Noteworthy, the identity and purity of the synthesized molecules were verified by  $^1\text{H}$ - and  $^{13}\text{C}$ -NMR as well as COSY, HMBC and HSQC 2D-NMR spectroscopy experiments, while MALDI-TOF mass spectrometry was also crucial for the identification of the intermediate as well as the final product. Additionally, the detailed experimental conditions of the photocatalytic  $\text{H}_2$  production experiments are presented.



**Scheme 3.4.1** The experimental procedure that we followed to synthesize **PNA-BDP**.

- Synthesis of PNA-BDP:

Fmoc-PNA-G-(Bhoc)-OH (105 mg, 0.14 mmol, 1.2 equiv) was dissolved in 5 mL dichloromethane and the solution was cooled in an ice bath to 0 °C. *N,N'*-dicyclohexylcarbodiimide (DCC, 30 mg, 0.15 mmol, 1.2 equiv) and 1-hydroxybenzotriazole hydrate (HOBT, 20 mg, 0.15 mmol, 1.2 equiv) were added and stirred for extra 30 min at 0 °C. Subsequently BDP-NH<sub>2</sub><sup>215</sup> (40 mg, 0.12 mmol, 1 equiv) (**Figure 6.3.44**) was added and the resulting mixture was stirred at room temperature for 48 h. After addition of CH<sub>2</sub>Cl<sub>2</sub> to the reaction mixture, extraction with H<sub>2</sub>O followed and the organic layer was dried over Na<sub>2</sub>SO<sub>4</sub>, filtered and concentrated. The title compound was isolated by column chromatography (silica gel, polarity gradually changed from CH<sub>2</sub>Cl<sub>2</sub> to CH<sub>2</sub>Cl<sub>2</sub>/MeOH, 100:7 v/v) as an orange solid (80 mg, 63 %).

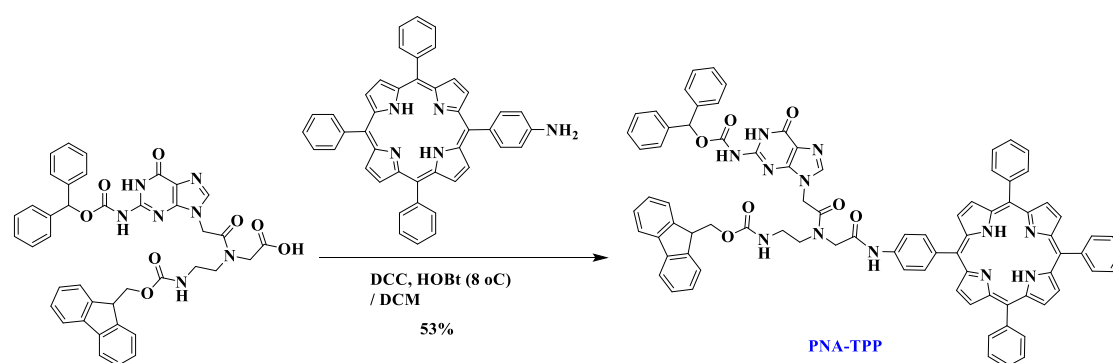
$^1\text{H}$  NMR (DMSO-*d*<sub>6</sub>, 500 MHz):  $\delta$  11.72 & 11.65 (1H), 11.24 & 11.22 (1H), 10.58 & 10.34 & 10.13 (1H), 7.96 (d, *J*=8.45 Hz, 1H), 7.87 (m, 2H), 7.85 & 7.83 (1H), 7.77 (d,

<sup>215</sup> Imahori, H. *et al.*. *J. Am. Chem. Soc.* **123**, 100–110 (2001).

$J=8.60$  Hz, 1H), 7.69 (m, 2H), 7.51 (m, 1H), 7.45 (m, 4H), 7.37 (m, 8H), 7.29 (m, 4H), 6.86 (bs, 1H), 6.20 & 6.17 & 6.16 (2H), 5.15 (s, 1H), 5.04 (s, 1H), 4.46 (s, 1H), 4.38 (d,  $J=6.75$  Hz, 1H), 4.29 (d,  $J=6.95$ , 1H), 4.23 (t,  $J=6.58$  Hz, 1H), 4.18 (bs, 1H), 3.59 (m, 1H), 3.40 (m, 2H), 3.17 (m, 1H), 2.45 (s, 3H), 2.44 (s, 3H), 1.40 (m, 6H) ppm.

$^{13}\text{C NMR}$ :  $\delta$  167.5, 167.4, 167.2, 166.6, 156.4, 156.2, 155.1, 154.8, 153.7, 149.6, 149.4, 147.0, 143.9, 142.7, 141.9, 140.8, 140.5, 140.0, 139.7, 139.5, 130.9, 128.6, 128.4, 128.0, 127.6, 127.0, 126.5, 125.1, 124.5, 121.3, 120.1, 119.6, 119.4, 119.1, 78.1, 65.5, 54.9, 50.9, 50.0, 47.6, 47.1, 46.7, 44.2, 44.0, 37.9, 14.2 ppm.

*UV-Vis* (DCM):  $\lambda_{\text{max}}$  nm ( $\epsilon/\text{mM}^{-1}\text{cm}^{-1}$ ) = 257 nm (50), 502 nm (78.5).



**Scheme 3.4.2** The experimental procedure that we followed to synthesize **PNA-TPP**.

- **Synthesis of PNA-TPP:**

Fmoc-PNA-G-(Bhoc)-OH (70.5 mg, 0.095 mmol, 1.2 equiv) was dissolved in 5 mL dichloromethane and the solution was cooled in an ice bath to 0 °C. *N,N'*-dicyclohexylcarbodiimide (DCC, 20 mg, 0.095 mmol, 1.2 equiv) and 1-hydroxybenzotriazole hydrate (HOBt, 13 mg, 0.095 mmol, 1.2 equiv) were added and stirred for extra 30 min at 0 °C. Subsequently TPP-NH<sub>2</sub><sup>216</sup> (50 mg, 0.08 mmol, 1 equiv) (**Figure 6.3.45**) was added and the resulting mixture was stirred at 8 °C for 48 h. After addition of CH<sub>2</sub>Cl<sub>2</sub> to the reaction mixture, extraction with H<sub>2</sub>O followed, and the organic layer was dried over Na<sub>2</sub>SO<sub>4</sub>, filtered and concentrated. The title compound was isolated by column chromatography (silica gel, polarity gradually changed from CH<sub>2</sub>Cl<sub>2</sub> to CH<sub>2</sub>Cl<sub>2</sub>/MeOH, 100:2 v/v) as an orange solid (80 mg, 63%).

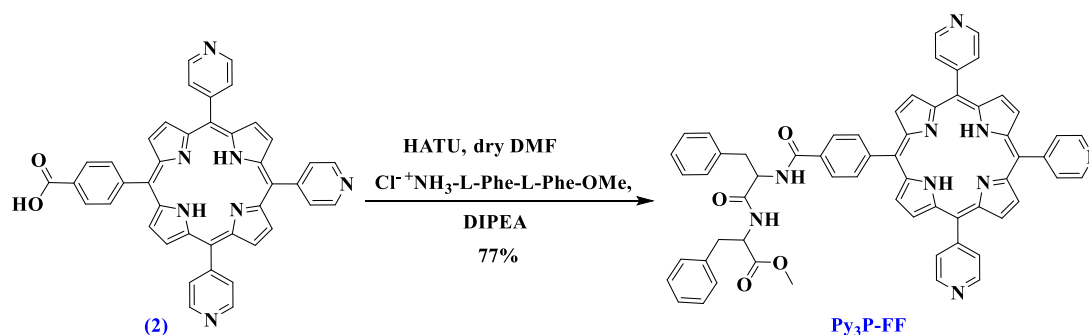
<sup>216</sup> K. Ladomenou, T. Lazarides, M. K. Panda, G. Charalambidis, D. Daphnomili, A. G. Coutsolelos *Inorg. Chem.* **2012**, 51, 20, 10548–10556.

$^1\text{H NMR}$  ( $\text{DMSO-}d_6$ , 500 MHz):  $\delta$  11.79 & 11.72 (1H), 11.28 (s, 1H), 10.87 & 10.60 (1H), 8.85 (m, 8H), 8.26 (m, 6H), 8.15 (m, 3H), 8.05 (d,  $J = 8.40$  Hz, 1H), 7.97 & 7.93 (1H), 7.87 (d,  $J=6.60$  Hz, 2H), 7.84 (m, 9H), 7.70 (m, 2H), 7.62 (t,  $J=5.70$  Hz, 1H), 7.43 (m, 4H), 7.38 (m, 2H), 7.32 (m, 6H), 7.24 (m, 2H), 6.86 & 6.85 (1H), 5.23 (s, 1H), 5.17 (s, 1H), 4.62 (bs, 1H), 4.41 (d,  $J=6.75$  Hz, 1H), 4.34 (d,  $J=7.55$  Hz, 1H), 4.32 (s, 1H), 4.24 (m, 1H), 3.69 (m, 1H), 3.51 (m, 2H), 3.27 (m, 1H), -2.91 (bs, 2H) ppm.

$^{13}\text{C NMR}$ :  $\delta$  167.6, 167.5, 167.4, 166.7, 156.49, 156.29, 155.0, 153.8, 149.6, 149.5, 147.2, 143.9, 141.2, 140.8, 140.6, 140.03, 139.96, 138.9, 138.7, 136.4, 136.0, 134.8, 134.3, 131.4, 128.6, 128.1, 128.0, 127.7, 127.0, 126.5, 125.1, 120.2, 120.0, 119.1, 117.8, 17.5, 78.1, 65.6, 51.19, 51.15, 47.7, 47.5, 46.8, 44.4, 44.1, 38.1 ppm.

$\text{UV-Vis}$  ( $\text{DCM}$ ):  $\lambda_{\text{max}}$  ( $\epsilon/\text{mM}^{-1}\text{cm}^{-1}$ ) = 257 nm (48), 418.5 nm (446), 515 nm (17.2), 550 nm (8.0), 590 nm (5.1), 646 nm (4.0).

- **Synthesis of  $\text{Py}_3\text{P-FF}$**



**Scheme 3.4.3** The experimental procedure that we followed to synthesize  $\text{Py}_3\text{P-FF}$ .

4-(10,15,20-tri(pyridin-4-yl)porphyrin-5-yl)benzoic acid<sup>217</sup> (69 mg, 0.104 mmol, 1.0 equiv) was dissolved in dry DMF (10 mL) in a schlenk tube and the solution was cooled in an ice bath to 0 °C. Then 200  $\mu\text{L}$  of DIPEA were added followed by the coupling reagent 1-[Bis(dimethylamino)methylene]-1H-1,2,3-triazolo[4,5-b]pyridinium 3-oxide hexafluorophosphate (HATU, 160 mg, 0.417 mmol, 4 equiv). The reaction mixture was stirred for 2 hours at 0 °C. Subsequently  $[\text{Cl}^-][^+\text{NH}_3\text{-PhePhe-OMe}]$  (56 mg, 0.166 mmol, 1.6 equiv) (**Figure 6.3.46**) was added and the resulting mixture was stirred at room temperature for 24 h. After the completion of the reaction DMF was evaporated under vacuum. The residue was dissolved in DCM and washed with  $\text{H}_2\text{O}$  twice. The organic

<sup>217</sup> Sirish, M.; Chertkov, V. A.; Schneider, H.-J. *Chem. – Eur. J.* **2002**,8, 1181–1188.

layers were dried over  $\text{Na}_2\text{SO}_4$ , filtered and the solvent was removed to dryness. The title compound was isolated by column chromatography (silica gel, polarity gradually changed from DCM/EtOH 3% to DCM/EtOH, 8% v/v) followed by a precipitation from DCM with pentane as a purple solid (78 mg, 77%).

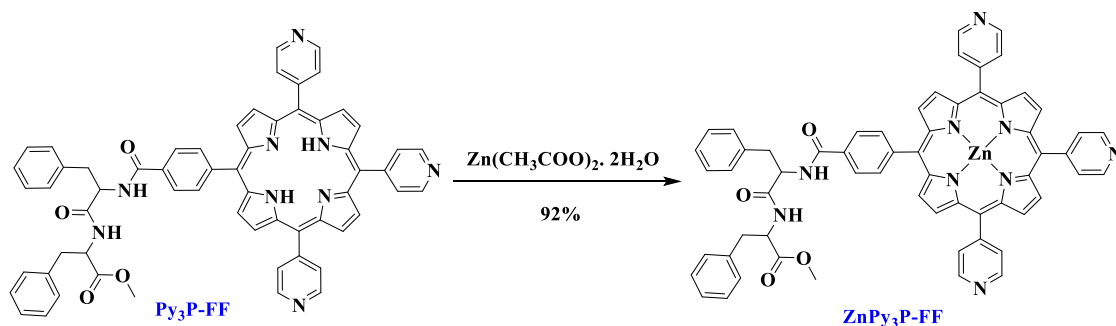
$^1\text{H NMR}$  (500 MHz,  $\text{CDCl}_3$ ):  $\delta$  = 9.07 (bs, 6H), 8.86 (bs, 8H), 8.28 (d,  $J$  = 8.0 Hz, 2H), 8.18 (d,  $J$  = 4.1 Hz, 6H), 8.12 (d,  $J$  = 8.1 Hz, 2H), 7.38 (m, 8H), 7.24 (m, 2H), 7.13 (d,  $J$  = 7.4 Hz, 1H), 7.08 (d,  $J$  = 7.7 Hz, 2H), 6.33 (d,  $J$  = 7.5 Hz, 1H), 5.01 (m, 1H), 4.86 (m, 1H), 3.76 (s, 3H), 3.38 (m, 1H), 3.27 (m, 1H), 3.19 (m, 1H), 3.06 (m, 1H), -2.89 (s, 2H) ppm.

$^{13}\text{C NMR}$  (125 MHz,  $\text{CDCl}_3$ ):  $\delta$  = 171.4, 170.6, 167.1, 150.4, 148.2, 145.3, 136.6, 135.7, 134.8, 133.7, 131.3, 129.7, 129.6, 129.4, 129.0, 128.8, 128.5, 127.4, 125.8, 120.3, 117.7, 117.5, 55.0, 53.7, 52.6, 38.6, 38.1 ppm.

*HRMS*-(MALDI-TOF):  $m/z$  calc. for  $\text{C}_{61}\text{H}_{47}\text{N}_9\text{O}_4$   $[\text{M}]^+$ : 969.3751, found 969.3759.

*UV-Vis*: (DCM)  $\lambda_{\text{max}}$ , nm ( $\epsilon$ ,  $\text{mM}^{-1}\text{cm}^{-1}$ ) 416.0 (382.5), 511.0 (19.5), 545.0 (7.0), 588.5 (6.0), 645.0 (3.0).

- **Synthesis of ZnPy<sub>3</sub>P-FF**



**Scheme 3.4.4** The experimental procedure that we followed to synthesize **ZnPy<sub>3</sub>P-FF**.

In a 50 mL flask, 25 mg of **Py<sub>3</sub>P-FF** (0.026 mmol, 1 equiv) were dissolved in 14 mL DMF/CH<sub>3</sub>COOH 1:1. Subsequently, Zn(CH<sub>3</sub>COO)<sub>2</sub>·2H<sub>2</sub>O (86 mg, 0.39 mmol, 15 equiv) was added and the reaction mixture was refluxed at 150 °C overnight. After the completion of the reaction, the mixture was cooled to room temperature, the product was precipitated through the addition of cold water and filtered. The title compound was isolated by column chromatography (silica gel, DCM/EtOH, 7% v/v) as a purple solid (25 mg, 92%).



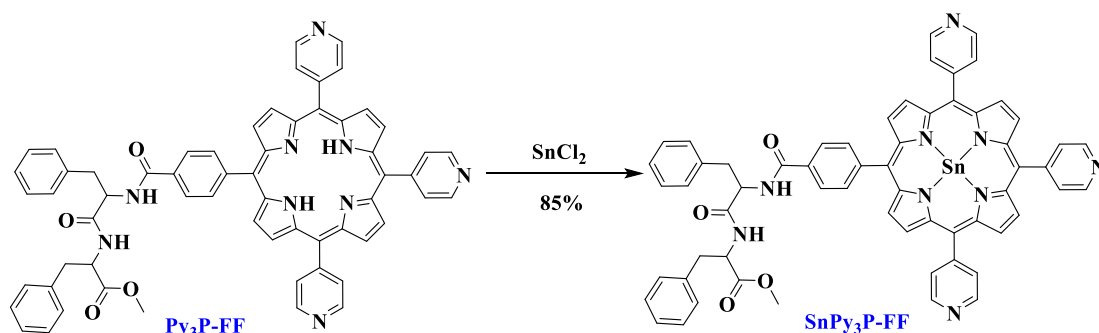
$^1\text{H NMR}$  (500 MHz,  $\text{CDCl}_3$ ):  $\delta$  = 9.00 (m, 6H), 8.92 (d,  $J$  = 8.5 Hz, 1H), 8.82 (m, 8H), 8.65 (d,  $J$  = 7.5 Hz, 1H), 8.23 (m, 10H), 7.48 (d,  $J$  = 7.5 Hz, 2H), 7.35 (m, 6H), 7.25 (m, 2H), 4.95 (m, 1H), 4.62 (m, 1H), 3.66 (s, 3H), 3.13 (m, 4H) ppm.

$^{13}\text{C NMR}$  (125 MHz,  $\text{DMSO}-d_6$ ):  $\delta$  = 171.9, 171.7, 166.3, 150.3, 148.7, 149.3, 148.6, 148.5, 147.9, 145.4, 138.5, 137.1, 134.0, 133.1, 132.2, 131.9, 131.8, 131.7, 129.3, 129.2, 128.3, 128.2, 126.6, 126.3, 125.8, 120.4, 117.9, 117.7, 54.7, 53.8, 51.9, 37.0, 36.7 ppm.

$\text{HRMS-(MALDI-TOF)}$ :  $m/z$  calc. for  $\text{C}_{61}\text{H}_{45}\text{N}_9\text{O}_4\text{Zn}$   $[\text{M}]^+$ : 1031.2886, found 1031.2892.

$\text{UV-Vis}$ : (DCM)  $\lambda_{\text{max}}$ , nm ( $\epsilon$ ,  $\text{mM}^{-1}\text{cm}^{-1}$ ) 403.0 (36.0), 423.0 (394.0), 555.0 (16.5), 594.5 (5.0).

• Synthesis of  $\text{SnPy}_3\text{P-FF}$



**Scheme 3.4.5** The experimental procedure that we followed to synthesize  $\text{SnPy}_3\text{P-FF}$ .

$\text{Py}_3\text{P-FF}$  (24 mg, 0.025 mmol, 1 equiv) was dissolved in 10 mL  $\text{CHCl}_3$ . Subsequently, a solution of  $\text{SnCl}_2 \cdot 2\text{H}_2\text{O}$  (54 mg, 0.25 mmol, 10 equiv) in 10 mL EtOH was added and the reaction mixture was refluxed at 70 °C for 4 hours. After the completion of the reaction, the mixture was cooled to room temperature, 0.5 mL of  $\text{Et}_3\text{N}$  were added and the solvents were evaporated under vacuum. The title compound was isolated by column chromatography (basic alumina, DCM/EtOH, 5% v/v) as a purple solid (23 mg, 85%).

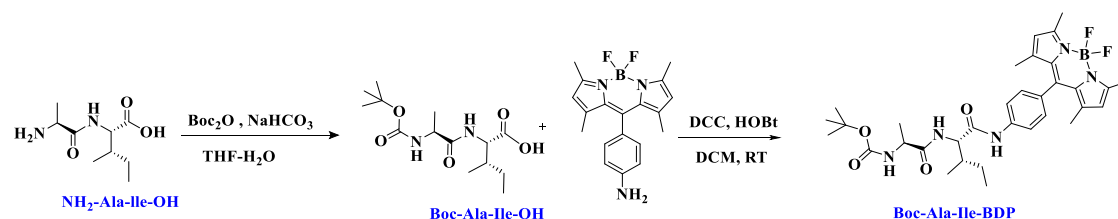
$^1\text{H NMR}$  (500 MHz,  $\text{CDCl}_3$ ):  $\delta$  = 9.23 (m, 8H), 9.14 (m, 6H), 8.40 (m, 2H), 8.28 (m, 6H), 8.18 (d,  $J$  = 8.0 Hz, 2H), 7.40 (m, 8H), 7.14 (d,  $J$  = 7.5 Hz, 1H), 7.08 (d,  $J$  = 6.5 Hz, 2H), 6.26 (d,  $J$  = 7.5 Hz, 1H), 5.01 (m, 1H), 4.86 (m, 1H), 3.77 (s, 3H), 3.37 (m, 1H), 3.27 (m, 1H), 3.19 (m, 1H), 3.06 (m, 1H) ppm.

$^{13}\text{C NMR}$  (125 MHz,  $\text{CDCl}_3$ ):  $\delta = 171.4, 170.5, 166.9, 150.0, 148.7, 148.4, 146.3, 146.0, 145.8, 143.7, 136.5, 135.7, 135.2, 133.0, 129.7, 129.6, 129.4, 129.0, 128.9, 127.4, 126.2, 121.2, 118.8, 55.0, 53.7, 52.6, 38.6, 38.1$  ppm.

$\text{HRMS-(MALDI-TOF)}$ :  $m/z$  calc. for  $\text{C}_{61}\text{H}_{46}\text{N}_9\text{O}_5\text{Sn}$   $[\text{M-OH}]^+$ : 1104.2644, found 1104.2649.

$\text{UV-Vis}$ : (DCM)  $\lambda_{\text{max}}$ , nm ( $\epsilon$ ,  $\text{mM}^{-1}\text{cm}^{-1}$ ) 404.0 (29.0), 426.0 (365.0), 560.0 (13.0), 598.5 (6.0).

- **Synthesis of Boc-Ala-Ile-BDP**



**Scheme 3.4.6** The experimental procedure for the synthesis of **Boc-Ala-Ile-BDP**.

Boc-Ala-Ile-OH (22 mg, 0.073 mmol, 1.2 equiv) was dissolved in DCM (4 mL) and the solution was cooled in an ice bath to 0 °C. *N,N'*-dicyclohexylcarbodiimide (DCC, 15 mg, 0.073 mmol, 1.2 equiv) and 1-hydroxybenzotriazole hydrate (HOBt, 10 mg, 0.073 mmol, 1.2 equiv) were added and stirred for extra 30 min at 0 °C. Subsequently **BDP-NH<sub>2</sub>** (21 mg, 0.061 mmol, 1 equiv) was added and the resulting mixture was stirred at r.t for 24 h. After the completion of the reaction the organic layer was washed with H<sub>2</sub>O, dried over Na<sub>2</sub>SO<sub>4</sub>, filtered and the solvent removed to dryness. The title compound was isolated by column chromatography (silica gel, CH<sub>2</sub>Cl<sub>2</sub>/EtOH, 0.8% v/v) as an orange solid (30 mg, 79%).

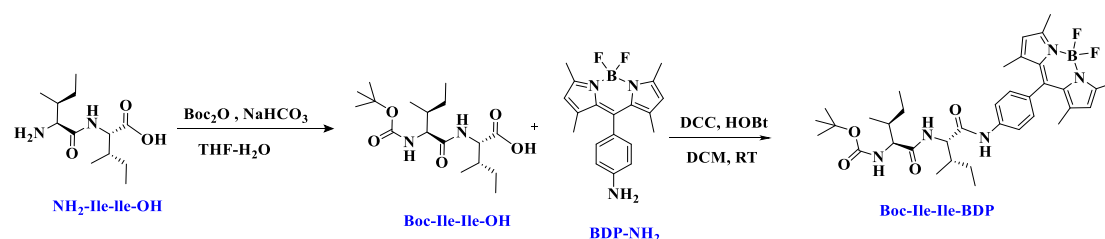
$^1\text{H NMR}$ : ( $\text{CDCl}_3$ , 500 MHz):  $\delta$  8.72 (s, 1H), 7.82 (d,  $J = 7.9$  Hz 2H), 7.20 (d,  $J = 8.0$  Hz, 2H), 6.75 (d,  $J = 8.4$  Hz, 1H), 5.97 (s, 2H), 4.98 (bs, 1H), 4.49 (bs, 1H), 4.17 (bs, 1H), 2.54 (s, 6H), 2.30 (bs, 1H), 1.54 (m, 1H), 1.44 (s, 3H), 1.43 (s, 9H), 1.41 (s, 6H), 1.15 (m, 1H), 1.01 (d,  $J = 6.8$  Hz 3H), 0.96 (t,  $J = 7.3$ , 3H) ppm.

$^{13}\text{C NMR}$  ( $\text{CDCl}_3$ , 75 MHz):  $\delta$  173.0, 169.6, 156.4, 155.5, 143.3, 141.6, 138.9, 131.7, 130.6, 128.6, 121.7, 121.3, 120.5, 81.5, 58.6, 51.7, 36.0, 28.3, 24.5, 17.7, 16.2, 14.8, 14.7, 11.8 ppm.

$\text{MS-(MALDI-TOF)}$ :  $m/z$  calculated for  $\text{C}_{33}\text{H}_{44}\text{BF}_2\text{N}_5\text{O}_4$   $[\text{M}]^+$ : 623.34; found: 623.35.

$\text{UV-Vis}$ : (DCM):  $\lambda$  ( $\epsilon$ ,  $\text{mM}^{-1}\text{cm}^{-1}$ ) = 501 (47.2) nm.

- **Synthesis of Boc-Ile-Ile-BDP**



**Scheme 3.4.7** The experimental procedure for the synthesis of **Boc-Ile-Ile-BDP**.

Boc-Ile-Ile-OH (25 mg, 0.072 mmol, 1.2 equiv) was dissolved in DCM (4 mL) and the solution was cooled in an ice bath to 0 °C. DCC (14.8 mg, 0.072 mmol, 1.2 equiv) and HOBT (9.7 mg, 0.072 mmol, 1.2 equiv) were added and stirred for extra 30 min at 0 °C. Subsequently **BDP-NH<sub>2</sub>** (20 mg, 0.06 mmol, 1 equiv) was added and the resulting mixture was stirred at 8 °C for 48 h. After the completion of the reaction the organic layer was washed with H<sub>2</sub>O, dried over Na<sub>2</sub>SO<sub>4</sub>, filtered and the solvent removed to dryness. The title compound was isolated by column chromatography (silica gel, polarity gradually changed from CH<sub>2</sub>Cl<sub>2</sub> to CH<sub>2</sub>Cl<sub>2</sub>/EtOH, 1 % v/v) as a purple solid (30 mg, 75%).

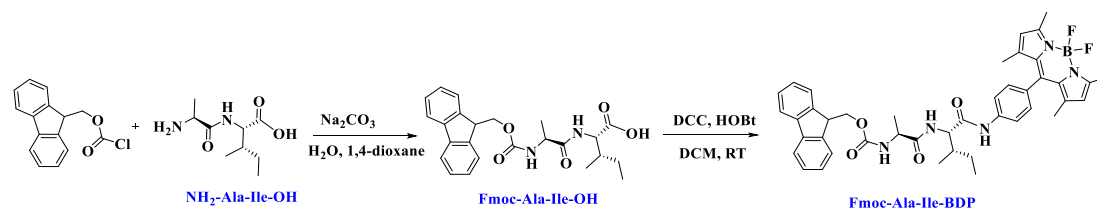
<sup>1</sup>H NMR (CDCl<sub>3</sub>, 500 MHz): δ 8.75 (s, 1H), 7.83 (d, *J* = 7.4 Hz 2H), 7.20 (d, *J* = 8.5 Hz, 2H), 6.57 (d, *J* = 7.4 Hz, 1H), 5.97 (s, 2H), 4.96 (bs, 1H), 4.50 (bs, 1H), 4.03 (bs, 1H), 2.54 (s, 6H), 2.34 (bs, 1H), 2.00 (bs, 1H), 1.53 (m, 2H), 1.42 (m, 15H), 1.17 (m, 2H), 1.01 (t, *J* = 7.6 Hz, 6H), 0.95 (m, 6H), ppm.

<sup>13</sup>C NMR (CDCl<sub>3</sub>, 75 MHz): δ 171.7, 169.6, 156.8, 155.5, 143.3, 141.6, 138.9, 131.7, 130.5, 128.6, 121.3, 120.5, 81.4, 60.8, 58.8, 36.5, 35.6, 28.3, 25.0, 24.5, 16.5, 16.1, 14.8, 14.7, 11.8 ppm.

HRMS-(MALDI-TOF): *m/z* calculated for C<sub>36</sub>H<sub>50</sub>BF<sub>2</sub>N<sub>5</sub>O<sub>4</sub> [M]<sup>+</sup>: 665.3924; found: 665.3945.

UV-Vis: (DCM): λ (ε, mM<sup>-1</sup>cm<sup>-1</sup>) = 501 (50.2) nm.

- **Synthesis of Fmoc-Ile-Ile-BDP**

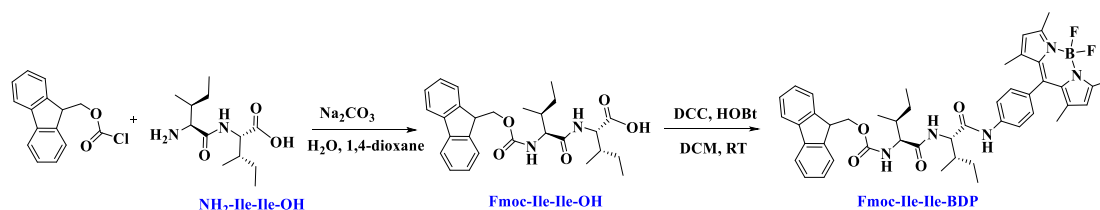


**Scheme 3.4.8** The experimental procedure for the synthesis of **Fmoc-Ala-Ile-BDP**.

The commercially available dipeptide NH<sub>2</sub>-Ile-Ile-OH (40 mg, 0.16 mmol) was dissolved in water (2.5 mL), 42.5 mg of Na<sub>2</sub>CO<sub>3</sub> (0.40 mmol) were added and the solution was cooled in an ice bath to 0 °C. Fmoc-chloride (50 mg, 0.192 mmol) was dissolved in 2.5 mL of 1,4-dioxane and was inserted dropwise into the reaction. The mixture was left stirring at 0 °C for another 2 hours and then left overnight at room temperature. Evaporation of the solvent under vacuum followed. We added 4 extra mL of H<sub>2</sub>O and adjusted the pH at pH=2 using HCl(aq) 1M. Several extractions with Ethyl-Acetate (4 extraction of 3 mL each) were conducted and the organic phase was dried over Na<sub>2</sub>SO<sub>4</sub> and condensed under vacuum. Fmoc-Ile-Ile-OH was obtained and used without any further purification to the next step. Fmoc-Ile-Ile-OH (58mg, 0.124mmol, 1.2 equiv), *N,N'*-dicyclohexylcarbodiimide (DCC, 26 mg, 0.124 mmol, 1.2 equiv) and 1-hydroxybenzotriazole hydrate (HOBT, 17 mg, 0.124 mmol, 1.2 equiv) were dissolved in 8 mL DCM at at 0 °C and stirred for 30 min. Subsequently **BDP-NH<sub>2</sub>** (35 mg, 0.103 mmol, 1 equiv) was added and the resulting mixture was stirred at r.t for 24 h. After the completion of the reaction the organic layer was washed with H<sub>2</sub>O, dried over Na<sub>2</sub>SO<sub>4</sub> and the solvent removed to dryness. **Fmoc-Ala-Ile-BDP** was isolated by column chromatography (silica gel, CH<sub>2</sub>Cl<sub>2</sub>/EtOH, 1% v/v) as an orange solid (60 mg, 75%).

<sup>1</sup>H NMR: (CDCl<sub>3</sub>, 500 MHz): δ 8.50 (s, 1H), 7.75 (m, 4H), 7.54 (m, 2H), 7.38 (t, *J* = 7.4 Hz, 2H), 7.27 (m, 2H), 7.16 (d, *J* = 8.35 Hz, 2H), 6.73 (d, *J* = 6.30 Hz, 1H), 5.95 (s, 2H), 5.39 (d, *J* = 6.13 Hz, 1H), 4.47 (m, 3H), 4.19 (t, *J* = 6.45 Hz, 1H), 4.12 (bs, 1H), 2.55 (s, 6H), 2.14 (bs, 1H), 1.93 (bs, 1H), 1.50 (bs, 2H), 1.37 (s, 6H), 1.19 (bs, 1H), 1.08 (m, 1H), 1.01 (d, *J* = 6.80 Hz, 3H), 0.93 (m, 9H) ppm. <sup>13</sup>C NMR (CDCl<sub>3</sub>, 75 MHz): δ 171.9, 169.6, 157.1, 155.6, 143.6, 143.2, 141.5, 138.7, 131.7, 130.9, 129.9, 128.8, 128.0, 127.2, 125.0, 124.8, 121.3, 120.2, 67.3, 60.6, 59.0, 47.3, 37.1, 36.0, 25.0, 24.8, 16.0, 15.8, 14.8 ppm. MS-(MALDI-TOF): m/z calculated for C<sub>46</sub>H<sub>52</sub>BF<sub>2</sub>N<sub>5</sub>O<sub>4</sub> [M]<sup>+</sup>: 787.41; found: 787.42. UV-Vis: (DCM): λ (ε, mM<sup>-1</sup>cm<sup>-1</sup>) = 501 (45.5) nm.

- **Synthesis of Fmoc-Ala-Ile-BDP**



**Scheme 3.4.9** The experimental procedure for the synthesis of **Fmoc-Ile-Ile-BDP**.

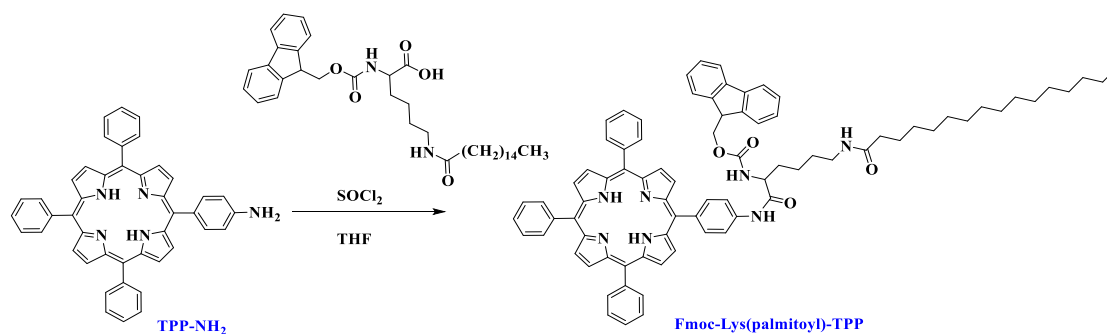
The commercially available dipeptide NH<sub>2</sub>-Ala-Ile-OH (30 mg, 0.15 mmol) was dissolved in water (3 mL), 40 mg of Na<sub>2</sub>CO<sub>3</sub> (0.37 mmol) were added and the solution was cooled in an ice bath to 0 °C. Fmoc-chloride (46 mg, 0.191782 mmol) was dissolved in 3 mL of 1,4-dioxane and was inserted dropwise into the reaction. The mixture was left stirring at 0 °C for another 2 hours and then left overnight at room temperature. Evaporation of the organic solvent under vacuum followed. We added 7 extra mL of water and adjusted the pH at pH=2 using HCl(aq) 1M. Several extractions with Ethyl-Acetate (5 extraction of 3 mL each) were conducted and the organic phase was dried over Na<sub>2</sub>SO<sub>4</sub> and condensed under vacuum. Fmoc-Ala-Ile-OH was obtained and used without any further purification to the next step. Fmoc-Ala-Ile-OH (52 mg, 0.124 mmol, 1.2 equiv), *N,N'*-dicyclohexylcarbodiimide (DCC, 26 mg, 0.124 mmol, 1.2 equiv) and 1-hydroxybenzotriazole hydrate (HOBT, 17 mg, 0.124 mmol, 1.2 equiv) were dissolved in 8 mL DCM at at 0 °C and stirred for 30 min. Subsequently **BDP-NH<sub>2</sub>** (35 mg, 0.103 mmol, 1 equiv) was added and the resulting mixture was stirred at r.t for 24 h. After the completion of the reaction the organic layer was washed with H<sub>2</sub>O, dried over Na<sub>2</sub>SO<sub>4</sub>, filtered and the solvent removed to dryness. The title compound was isolated by column chromatography (silica gel, CH<sub>2</sub>Cl<sub>2</sub>/EtOH, 1% v/v) as an orange solid (60 mg, 78%).

<sup>1</sup>H NMR: (CDCl<sub>3</sub>, 500 MHz): δ 8.42 (s, 1H), 7.78 (m, 4H), 7.54 (m, 2H), 7.38 (m, 2H), 7.30 (m, 2H), 7.20 (d, *J* = 8.20, 2H), 6.60 (d, *J* = 8.61 Hz, 1H), 5.96 (s, 2H), 5.21 (d, *J* = 4.77 Hz, 1H), 4.47 (m, 3H), 4.19 (m, 2H), 2.55 (s, 6H), 2.17 (bs, 1H), 1.42 (s, 6H), 1.27 (bs, 3H), 1.08 (m, 1H), 1.01 (m, 3H), 0.93 (m, 3H) ppm.

MS-(MALDI-TOF): m/z calculated for C<sub>43</sub>H<sub>46</sub>BF<sub>2</sub>N<sub>5</sub>O<sub>4</sub> [M]<sup>+</sup>: 745.36; found: 745.38.

UV-Vis: (DCM): λ (ε, mM<sup>-1</sup>cm<sup>-1</sup>) = 501 (48) nm.

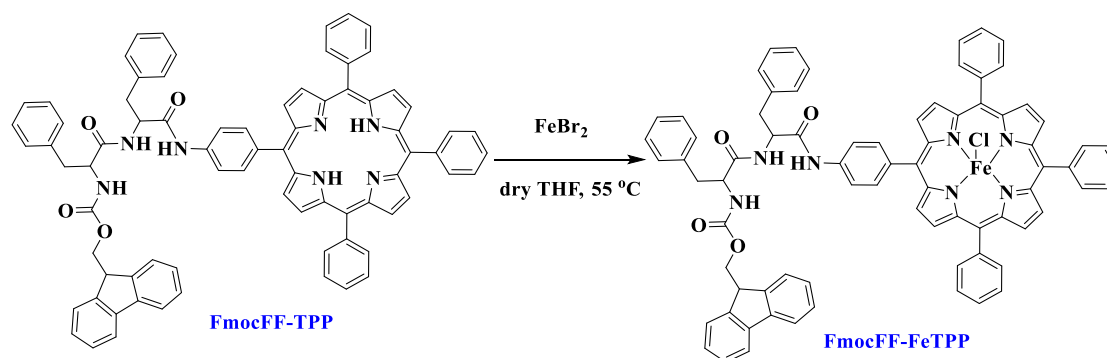
- **Synthesis of Fmoc-Lys(palmitoyl)-TPP**



**Scheme 3.4.10** The experimental procedure for **Fmoc-Lys(palmitoyl)-TPP** synthesis.

Fmoc-Lys(palmitoyl)-OH (29 mg, 0.048 mmol) was dissolved in 3 mL dry THF and 5.5  $\mu$ L of pyridine (0.068 mmol) were added along with 4  $\mu$ L of SOCl<sub>2</sub> (0.056 mmol). The reaction was left stirring at room temperature for 30 minutes to form the desired acyl-chloride intermediate. After evaporation of the solvents under reduced pressure the solid residue was dissolved in 4 mL of dry THF and TPP-NH<sub>2</sub> (25 mg, 0.04 mmol) was added along with 156  $\mu$ L of DIPEA. The reaction was left stirring for 4 days at room temperature. The title compound was isolated by column chromatography (silica gel, CH<sub>2</sub>Cl<sub>2</sub>/MeOH, 1% v/v) as a purple solid (32 mg, 65%).

- **Synthesis of FmocFF-FeTPP**



**Scheme 3.4.11** The experimental procedure for the synthesis of **FmocFF-FeTPP**.

Excess of FeBr<sub>2</sub> (115 mg, 0.534 mmol) transferred under inert atmosphere in a schlenk flask together with 47 mg of FmocFF-TPP<sup>218</sup> (0.041 mmol). 5 mL of dry THF are degassed with N<sub>2</sub> flow and sonication for 15 minutes and then added into the reaction mixture. The mixture is stirred at 55 °C overnight and the completion of the reaction is monitored via UV-Vis. After evaporation of the solvent, the solid residue is dissolved

<sup>218</sup> Charalambidis G., et al. (2011), *Chem. Eur. J.*, 17: 7213-7219.

in DCM and washed 3 times with 4N HCl (15 mL) and then 2 times with water (15 mL). The organic phase is evaporated to dryness. The title compound was isolated by column chromatography (silica gel, CH<sub>2</sub>Cl<sub>2</sub>/MeOH, 1% v/v) as an orange solid (22.7 mg, 45%).

*UV-Vis:* (DCM):  $\lambda$  ( $\epsilon$ , mM<sup>-1</sup>cm<sup>-1</sup>) = 374 (66.7), 417 (109), 499 (14.6), 509 (11.0), 574 (4.7), 691 (3.8) nm. (**Figure 6.3.47**)

#### *Preparation of self-assembled microstructures*

For the preparation of the samples, the corresponding compounds were dissolved in a chaotropic “good” solvent and subsequently a “bad” solvent was introduced. The final concentration was 1 mM in all cases. After 24 hours of incubation, 10  $\mu$ L of each sample were placed on a 12 mm cover glass and left to dry overnight.

#### *Photocatalytic H<sub>2</sub> evolution using MPy<sub>3</sub>P-FF hybrids*

For the photocatalytic hydrogen evolution experiments, each sample was prepared in a 11 mL glass vial that capped with a silicone septum. In this vial the self-assembled nanostructures of the porphyrin hybrid were formed by using the appropriate solvent mixture. The solvents were left to dry in open air similarly to the SEM studies procedure. A fresh aqueous buffer solution of TEOA (10 vol%) pH=7 was prepared using con. HCl to adjust the pH. Subsequently, 3 mL of a 1:1 v/v mixture of acetonitrile and the buffer solution were added to the vial with the self-assemblies, the amount of [Co(dmgH)<sub>2</sub>(Cl)(Py)] catalyst was inserted and then the mixture was degassed for 5 min using nitrogen. Finally, the vials were closed with a silicon septum and placed in the experimental setup, where they were irradiated with a white LED lamp ring of 40 W under continuous stirring. The H<sub>2</sub> production was determined via gas chromatography (GC) using a Shimadzu GC 2010 plus chromatograph with a TCD detector and a molecular sieve 5 E column (30 m–0.53 mm). For the regeneration experiments, we used the amorphous solid of **SnPy<sub>3</sub>P-FF**. We followed the same procedure for photocatalytic hydrogen evolution and after 120h of irradiation the H<sub>2</sub> production stopped. We opened the glass vials and in one of them we added 0.27 mg of **SnPy<sub>3</sub>P-FF** and degassed the mixture for 5 min using N<sub>2</sub>. In the second vial 1.19 mg of the [Co(dmgH)<sub>2</sub>(Cl)(Py)] catalyst was added and after closing the vials with new silicon septums we placed them back in the white LED lamp ring setup.

### *Photocatalytic H<sub>2</sub> production using gadolinium porphyrin complexes*

For the photocatalytic hydrogen evolution experiments, each sample was prepared in a 11 mL glass vial that capped with a silicone septum. A fresh aqueous buffer solution of ascorbic acid (1M) pH = 4 was prepared using NaOH<sub>(aq)</sub> to adjust the pH. The porphyrin derivative (2.5 mg) was dispersed in 5 mL the buffer solution, 5% w/w of Na<sub>2</sub>PtCl<sub>6</sub>·6H<sub>2</sub>O from a stock solution were added and then the mixture was degassed for 5 min using nitrogen. Finally, the vials were closed with a silicon septum and placed in the experimental setup, where they were irradiated with a white LED lamp ring of 40 W under continuous stirring. The H<sub>2</sub> production was determined via gas chromatography (GC) using a Shimadzu GC 2010 plus chromatograph with a TCD detector and a molecular sieve 5 E column (30 m–0.53 mm).



## Chapter 4: Light driven Oxidation transformations

The process of photosynthesis involves both reductive reactions resulting into the synthesis of glucose and oxidative reactions resulting into the formation of molecular O<sub>2</sub>. In direct correlation with photosynthesis, the process of water splitting involves both water oxidation and water reduction half-reactions (**Figure 4.1**). This chapter focuses on the oxidation transformations that ought to be investigated in order to develop efficient artificial photosynthetic systems.

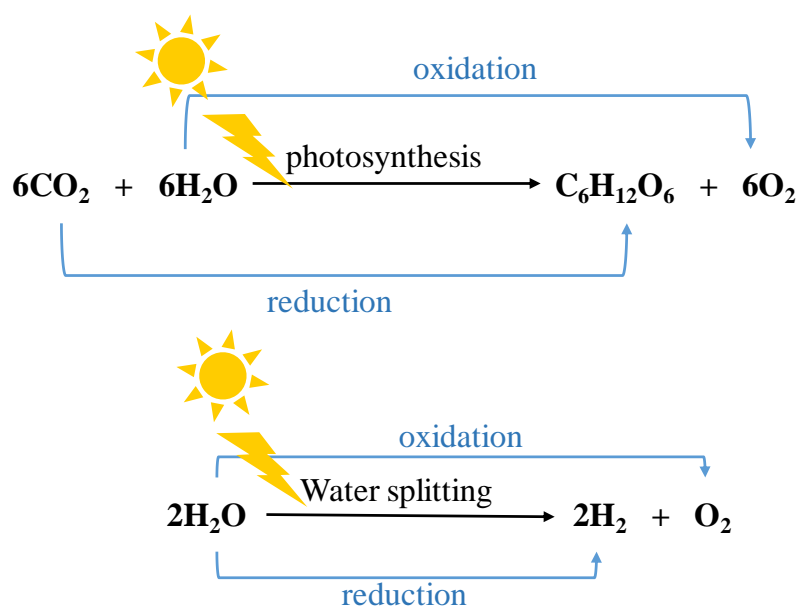


**Figure 4.1** Oxidation and reduction reactions in photosynthesis and water splitting.

### 4.1 Photocatalytic Water Oxidation

This chapter deals with the photocatalytic water splitting into H<sub>2</sub> and O<sub>2</sub>, which has attracted significant scientific interest for solar energy conversion applications during the last two decades.<sup>219</sup> Although plenty of material-based catalysts have been applied as water oxidation catalysts (WOCs), molecular catalysts have recently gained greater attention.<sup>220</sup> Their versatile properties allow the rational design of chemical structures to optimize catalytic activity. While plenty of molecular catalysts based on noble metals such as Ru or Ir have been employed as WOCs and exhibited high

<sup>219</sup> Lewis, N. S.; Nocera, D. G. *Proc. Natl. Acad. Sci. U.S.A.* **2006**, *103* (43), 15729

<sup>220</sup> S. Ye, C. Ding, M. Liu, A. Wang, Q. Huang, C. Li, *Adv. Mater.* **2019**, *31*, 1902069.

performances,<sup>221,222,223,224</sup> there is a need to switch to low-cost and earth-abundant first-row transition metals.<sup>225,226</sup> Porphyrins have been extensively investigated for water oxidation due to their high chemical stability during catalysis, which is an important advantage among other molecular catalysts.<sup>227,228</sup> Moreover, porphyrins can accommodate any first-row transition metal, which can serve as catalytic center for water oxidation.<sup>229</sup>

Noteworthy, the examples of electrocatalytic water oxidation systems, which utilize porphyrinoids as catalysts are numerous<sup>230,231,232,233,234</sup> compared to the photocatalytic systems, where no external bias is applied.<sup>235,236</sup> Recently, Bonnet and co-workers prepared a series of water-soluble nickel porphyrin photocatalysts for water oxidation using  $[\text{Ru}(\text{bpy})_3]^{2+}$  as photosensitizer (PS) and  $[\text{S}_2\text{O}_8]^{2-}$  as sacrificial electron acceptor (**Figure 4.2**).<sup>237</sup>

To the best of our knowledge, there is no report on covalently linked  $\text{Ni}^{2+}$  porphyrin – ruthenium complex dyad that has been investigated towards photocatalytic water oxidation. Furthermore, in most of the reported photocatalytic systems utilizing porphyrins and ruthenium complexes for this application, the porphyrin was playing the role of PS and not that of a water oxidation catalyst.<sup>238</sup>

---

<sup>221</sup> Tong, L.; Thummel, R. P. *Chemical Science* **2016**, 7 (11), 6591.

<sup>222</sup> Kaveevivitchai, N.; Chitta, R.; Zong, R.; El Ojaimi, M.; Thummel, R. P. *J. Am. Chem. Soc.* **2012**, 134 (26), 10721.

<sup>223</sup> Joya, K. S.; Subbaiyan, N. K.; D'Souza, F.; de Groot, H. J. M. Surface-Immobilized Single-Site Iridium Complexes for Electrocatalytic Water Splitting. *Angew. Chem. Int. Ed.* **2012**, 51 (38), 9601.

<sup>224</sup> Schley, N. D.; Blakemore, J. D.; Subbaiyan, N. K.; Incarvito, C. D.; D'Souza, F.; Crabtree, R. H.; Brudvig, G. W. *J. Am. Chem. Soc.* **2011**, 133 (27), 10473.

<sup>225</sup> Parent, A. R.; Sakai, K. *ChemSusChem* **2014**, 7 (8), 2070.

<sup>226</sup> Wang, D.; Bruner, C. O. *Inorganic Chemistry* **2017**, 56 (22), 13638.

<sup>227</sup> Wang, D.; Groves, J. T. *Proc. Natl. Acad. Sci. U.S.A.* **2013**, 110 (39), 15579.

<sup>228</sup> Limburg, B.; Bouwman, E.; Bonnet, S. *Coord. Chem. Rev.* **2012**, 256 (15), 1451.

<sup>229</sup> Nakazono, T.; Parent, A. R.; Sakai, K. *Chem. Commun.* **2013**, 49 (56), 6325.

<sup>230</sup> Dogutan, D. K.; McGuire, R.; Nocera, D. G. *J. Am. Chem. Soc.* **2011**, 133 (24), 9178.

<sup>231</sup> Li, X.; Zhang, X.-P.; Guo, M.; Fukuzumi, S.; et al. *J. Am. Chem. Soc.* **2021**, 143 (36), 14613.

<sup>232</sup> Han, A.; Jia, H.; et al. *Phys. Chem. Chem. Phys.* **2014**, 16 (23), 11224.

<sup>233</sup> Daniel, Q.; Ambre, R. B.; et al. *ACS Catal.* **2017**, 7 (2), 1143.

<sup>234</sup> Han, Y.; Wu, Y.; Lai, W.; Cao, R. *Inorganic Chemistry* **2015**, 54 (11), 5604.

<sup>235</sup> Nakazono, T.; Parent, A. R.; Sakai, K. *Chem. Eur. J.* **2015**, 21 (18), 6723.

<sup>236</sup> Nam, Y. S.; Magyar, A. P.; Lee, et al. *Nat. Nanotechnol.* **2010**, 5 (5), 340.

<sup>237</sup> Liu, C.; Bos, D.; Hartog, B.; Meij, D.; Ramakrishnan, A.; Bonnet, S. *Angew. Chem. Int. Ed.* **2021**, 60 (24), 13463.

<sup>238</sup> Yamamoto, M.; Wang, L.; Li, F.; Fukushima, T.; Tanaka, K.; Sun, L.; Imahori, H. *Chem. Sci.* **2016**, 7 (2), 1430.

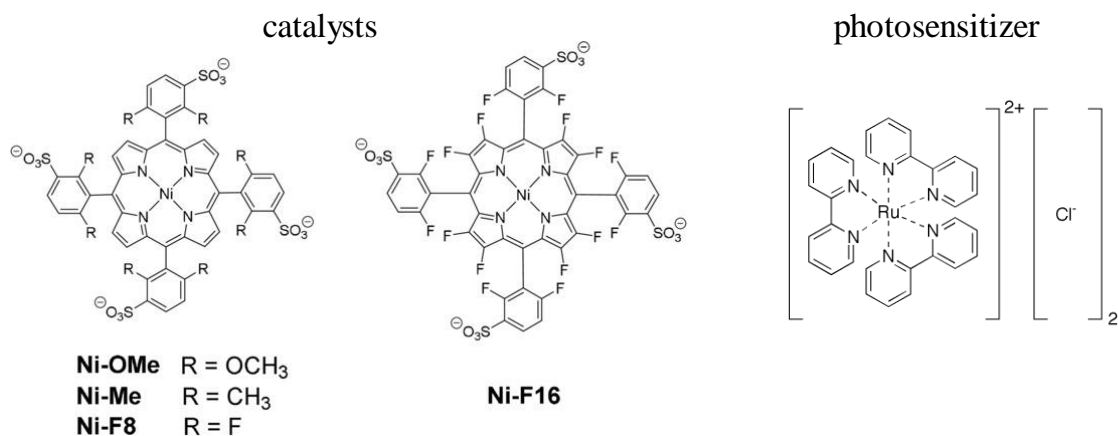


**Figure 4.2** Chemical structures of water-soluble nickel porphyrin photocatalysts for water oxidation and [Ru(bpy)<sub>3</sub>]<sup>2+</sup> photosensitizer.<sup>237</sup>

One common drawback of photocatalytic systems is the need for a sacrificial agent, which is unavoidable for the completion of the catalytic cycle.<sup>239,240</sup> One very promising approach to overcome this issue is the development of photoelectrochemical cells (PECs), where the catalyst and the PS are adsorbed onto an inorganic semiconductor electrode.<sup>241</sup> In these devices, the adsorbed PS harvests solar energy and injects an electron into the conduction band of the semiconductor. Subsequently, the generated radical cation PS<sup>+</sup> is reduced from the WOC to regenerate the photosensitizer, while repeating cycles of this process results in a highly oxidized catalytic moiety, able to convert water molecules into protons and molecular oxygen.

A relative work from the literature was reported by Meyer T. and co-workers, who developed a DSPEC using a ruthenium catalyst connected with a ruthenium photosensitizer anchored on SnO<sub>2</sub>/TiO<sub>2</sub> nanoparticle oxide films (**Figure 4.3**).<sup>242</sup> Their system was able to perform water oxidation at pH = 7 with an applied bias of 0.4 V versus SCE.

<sup>239</sup> Nikoloudakis, E.; Pati, P. B.; Charalambidis, G.; Budkina, D. S.; Diring, S.; Planchat, A.; Jacquemin, D.; Vauthey, E.; Coutsolelos, A. G.; Odobel, F. *ACS Catal.* **2021**, *11* (19), 12075.

<sup>240</sup> Materna, K. L.; Jiang, J.; Regan, K. P.; Schmuttenmaer, C. A.; Crabtree, R. H.; Brudvig, G. W. *ChemSusChem* **2017**, *10* (22), 4526.

<sup>241</sup> Decavoli, C.; Boldrini, C. L.; Trifiletti, V.; Luong, S.; Fenwick, O.; Manfredi, N.; Abbotto, A. *RSC Adv.* **2021**, *11* (10), 5311.

<sup>242</sup> B. D. Sherman, D. L. Ashford, A. M. Lapidés, M. V. Sheridan, K. R. Wee, and T. J. Meyer, *J. Phys. Chem. Lett.* **2015**, *6*, 3213–3217.

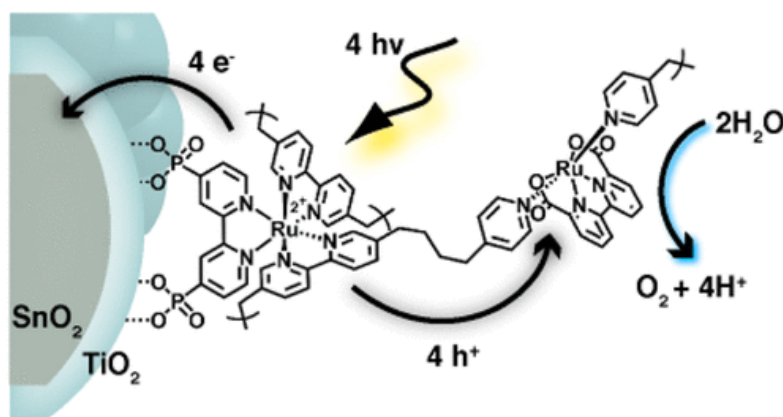
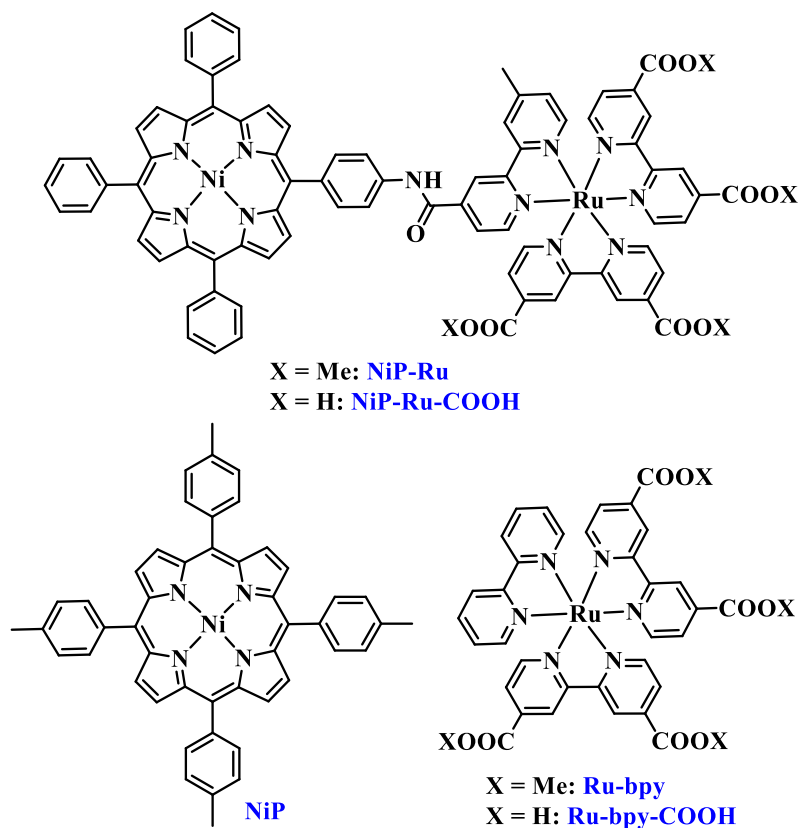


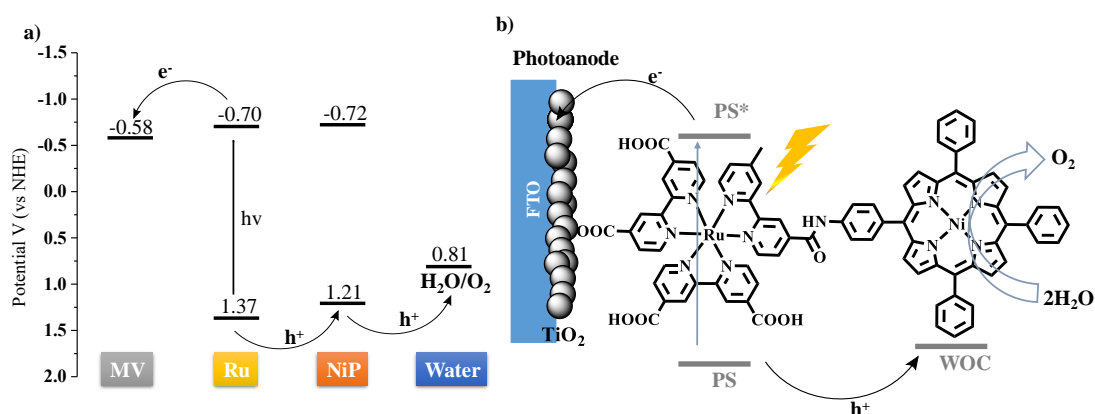
**Figure 4.3** DSPEC for water oxidation utilizing ruthenium-based catalyst and photosensitizer.<sup>242</sup>

Herein we synthesized a catalyst-photosensitizer dyad **NiP-Ru (Scheme 4.1)**, comprised of nickel porphyrin and ruthenium tris-bipyridine complex covalently linked via an amide bond, and investigated their ability to produce oxygen via water oxidation under visible light irradiation. The dyad was found active in organic solvent and demonstrated higher photocatalytic performance compared to the non-covalent two-component system. A simplified photocatalytic mechanism for the oxidation of water of this system can be derived from the energy diagram of **Scheme 4.2a**. Initially the ruthenium complex acts as photosensitizer absorbing a photon and transferring an electron to the methyl viologen which has the role of electron acceptor (EA). The hole from the oxidized  $PS^+$  is transferred to the nickel porphyrin catalytic moiety and repetitions of the same sequence afford higher oxidation states of the catalyst. The latter is able to oxidize water producing molecular  $O_2$  and protons. The photocatalytic performance of the dyad in solution was investigated both in water and organic solvents and was compared to the non-covalent two-component system. The homogeneous experiments, conducted in organic solvent, facilitate the potential coupling of this system with photocatalytic  $CO_2$  reduction in a future tandem photocatalytic device. Furthermore, for the first time a dye-sensitized photoelectrochemical cell (DSPEC) utilizing  $Ni^{2+}$  porphyrin moiety as WOC and ruthenium complex as PS is fabricated and applied in water oxidation in aqueous media. **Scheme 4.2b** illustrates the possible electron transfer processes on the photoanode of the DSPEC device. After the photoexcitation of the Ru complex moiety an electron is injected to the conduction band of the  $TiO_2$  and travels through the external circuit to the Pt cathode. The holes are

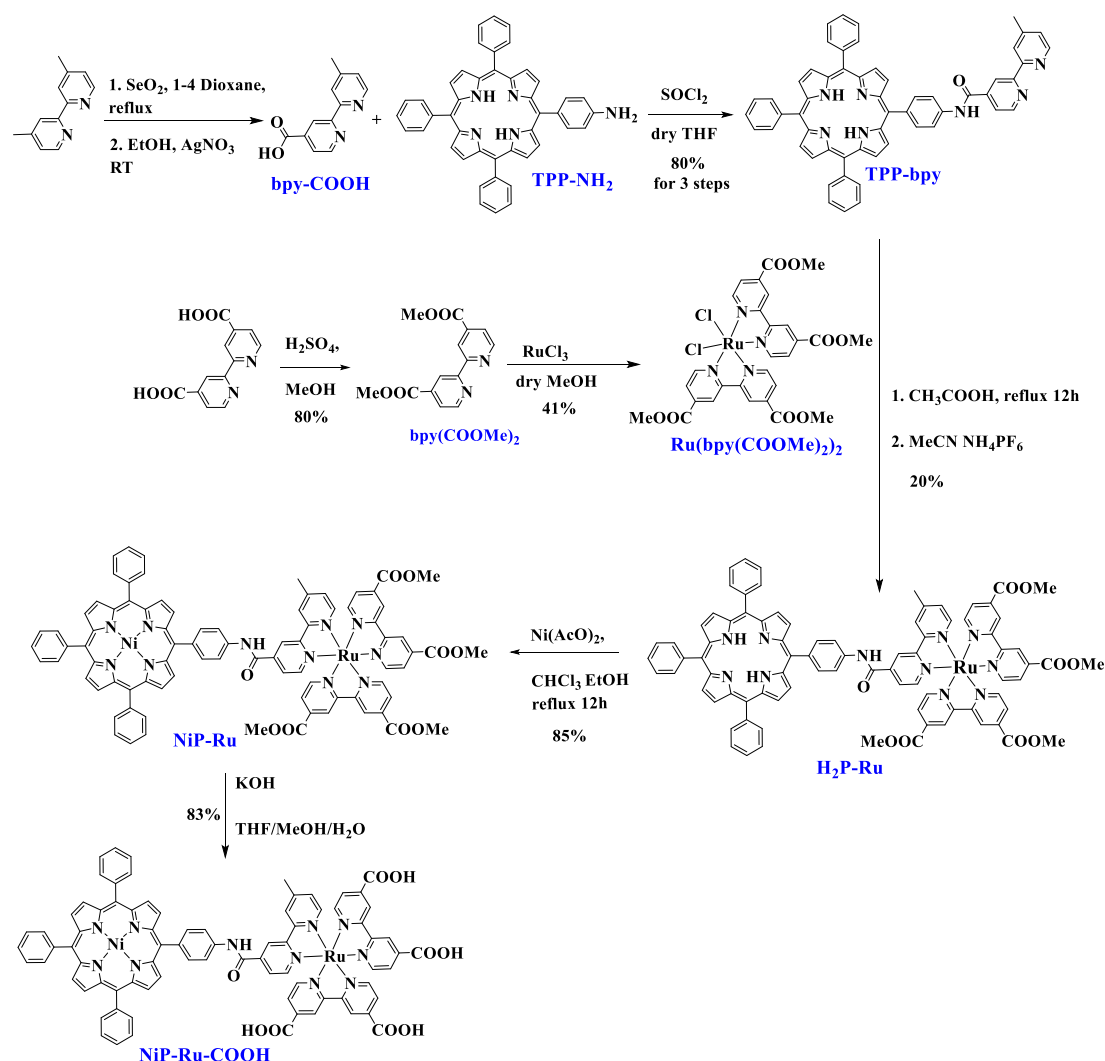
moved from the ruthenium to the nickel porphyrin catalytic moiety, which gains the appropriate oxidation state to perform water oxidation.



**Scheme 4.1** Structures of **NiP-Ru** dyad, nickel tetra-tolouylporphyrin, **NiP**, and ruthenium complex, **Ru-bpy** controls.



**Scheme 4.2** a) Energy diagram of the **NiP-Ru** dyad derived photo-induced electron transfer process resulting in water oxidation. b) Schematic diagram of the visible light-driven water oxidation by the **NiP-Ru** dyad modified TiO<sub>2</sub>/FTO photoanode.

Synthesis

**Scheme 4.3** Synthetic procedure followed for the preparation of **NiP-Ru** and **NiP-Ru-COOH** dyads.

The synthetic approach for the successful preparation of **NiP-Ru** dyad, is illustrated in **Scheme 4.3**, and the experimental details are provided in section 4.3. The bis-bipyridine intermediates, **bpy-COOH**<sup>243</sup> and **bpy(COOMe)<sub>2</sub>**<sup>244</sup>, were synthesized according to already published procedures starting from commercially available 4,4'-dimethyl-2,2'-bipyridine and [2,2'-bipyridine]-4,4'-dicarboxylic acid, respectively. The next step, was the amide coupling between TPP-NH<sub>2</sub> and **bpy-COOH** using  $\text{SOCl}_2$  as coupling reagent. The intermediate ruthenium complex, that is **Ru(bpy(COOMe)<sub>2</sub>)<sub>2</sub>**,

<sup>243</sup> McCafferty, D. G.; Bishop, B. M.; Wall, C. G.; Hughes, S. G.; Mecklenberg, S. L.; Meyer, T. J.; Erickson, B. W. *Tetrahedron* **1995**, *51* (4), 1093.

<sup>244</sup> Barbante, G. J.; Hogan, C. F.; Wilson, D. J. D.; Lewcenko, N. A.; Pfeffer, F. M.; Barnett, N. W.; Francis, P. S. *Analyst* **2011**, *136* (7), 1329.

was obtained by refluxing RuCl<sub>3</sub> and bpy(COOMe)<sub>2</sub> in dry MeOH. Subsequently, via a complexation reaction between TPP-bpy and Ru(bpy(COOMe)<sub>2</sub>)<sub>2</sub> the successful formation of H<sub>2</sub>P-Ru dyad was achieved.<sup>245</sup> The next step was the insertion of Ni(II) into the porphyrin core affording the **NiP-Ru** dyad. The hydrolyzed dyad derivative **NiP-Ru-COOH**, bearing four carboxylic anchoring groups was obtained via basic hydrolysis. Note that, the reference, nickel tetra-toluene porphyrin **NiP** and the ruthenium tris(bipyridyl) **Ru-bpy** and **Ru-bpy-COOH** were synthesized according to literature procedures.<sup>246,247</sup> The successful formation of all final and intermediate compounds was verified through <sup>1</sup>H and <sup>13</sup>C NMR spectroscopies (**Figure 6.4.1-6.4.14**) and MALDI-TOF mass spectrometry.

### Photophysical characterization.

The photophysical properties of all porphyrin and ruthenium complexes were studied by UV-Vis absorption and emission spectroscopies (**Figure 6.4.15**). **NiP** and **NiP-Ru** dyad exhibited typical porphyrin absorbance features using N,N-dimethylformamide (DMF) as solvent. **NiP** displayed the characteristic Soret band at 416 nm and one Q band at 527 nm with a shoulder peak around 560 nm. **Ru-bpy** has a broad spectrum, with peak maxima centered at around 464 nm, which is attributed to MLCT transition.<sup>248</sup>

As depicted in **Figure 4.4**, the absorption spectrum of **NiP-Ru** is a superposition of the absorption features of **NiP** and **Ru-bpy**. Nickel porphyrins are not emissive, and hence only the ruthenium-based emission in the region 570-800 nm with peak maxima at 658 nm is observed. As illustrated in **Figure 4.5**, an almost quantitative quenching of the ruthenium-based emission (~98%) in the dyad was detected, a phenomenon correlated with the covalent attachment of nickel porphyrin. This observation provides important evidence for the interaction between the Ru complex and Ni porphyrin moieties in the excited state.

---

<sup>245</sup> Charisiadis, A.; Glymenaki, E.; Planchat, A.; Margiola, S.; Nikoloudakis, E.; Nikolaou, V.; Charalambidis, G.; Coutsolelos, A. G.; Odobel, F. *Dyes and Pigments* **2021**, *185*, 108908.

<sup>246</sup> Buchler, J. W.; Herget, G. XLV. *Zeitschrift für Naturforschung B* **1987**, *42* (8), 1003.

<sup>247</sup> Kent, C. A.; Mehl, B. P.; Ma, L.; Papanikolas, J. M.; Meyer, T. J.; Lin, W. *J. Am. Chem. Soc.* **2010**, *132* (37), 12767.

<sup>248</sup> Hager, G. D.; Crosby, G. A. *J. Am. Chem. Soc.* **1975**, *97* (24), 7031.

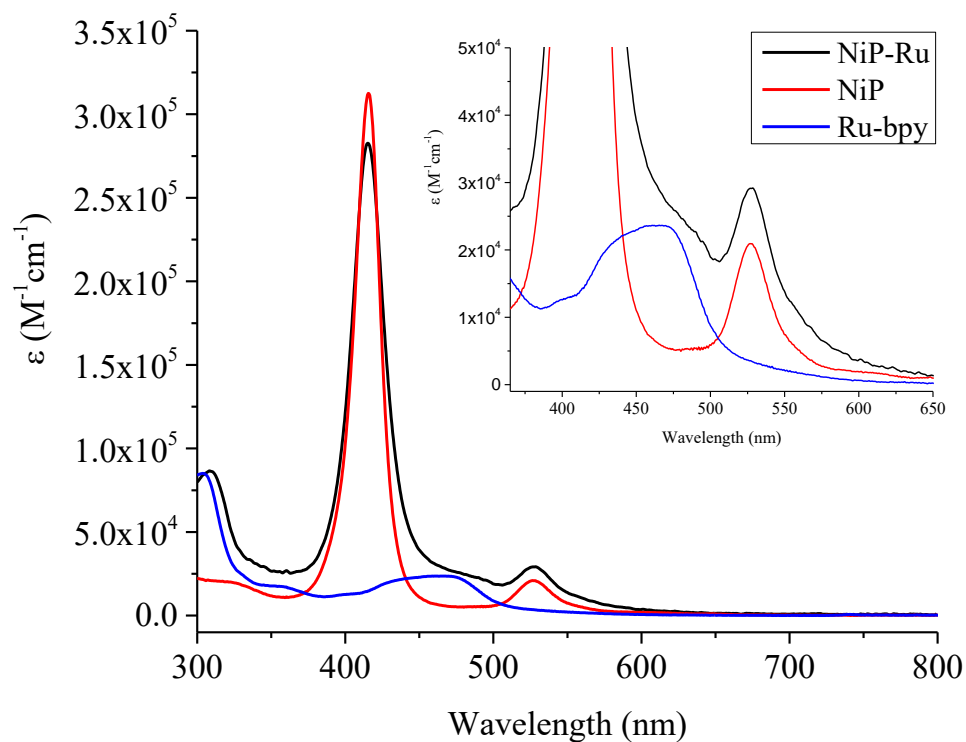


**Figure 4.4** Absorption spectrum of **NiP-Ru** dyad, **NiP** and **Ru-bpy** in DMF.

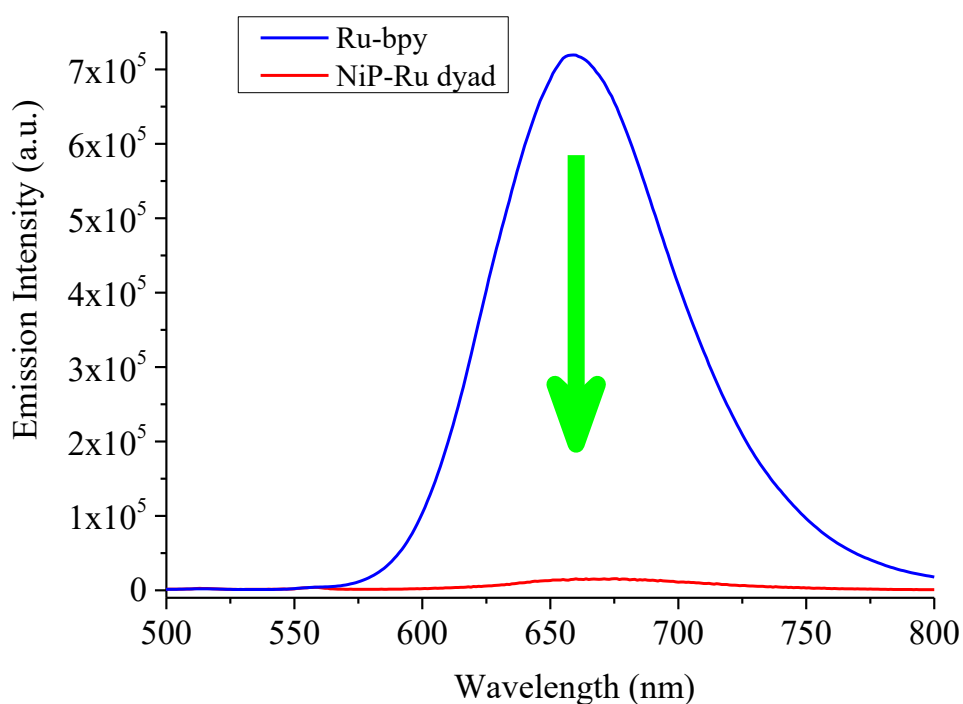


**Figure 4.5** Emission intensity of **Ru-bpy** (blue line) and **NiP-Ru** dyad (red line) after excitation at 480 nm, recorded in DMF solutions with a concentration of 0.01 mM of individual compounds (the solutions were not degassed).



The electrochemical properties of **NiP**, **Ru-bpy**, and **NiP-Ru** were evaluated using cyclic (CV) and differential pulse voltammetry (DPV) in benzonitrile containing 0.1 M tetrabutylammonium perchlorate ((TBA)ClO<sub>4</sub>) as the supporting electrolyte (**Table 4.1**). The **NiP** revealed two oxidations at 1.01 and 1.27 V and two reductions at -0.92 and -1.25 V vs. Ag/AgCl. On the other hand, two oxidations at 1.14 and 1.55 V and two reductions at -0.80 and -1.02 V were observed for **Ru-bpy**. Both the first oxidation and the first reduction were not well defined on the cyclic voltammetric time scale, therefore the peak potentials were obtained from DPVs. The **NiP-Ru** dyad exhibited oxidations at 1.01 and 1.30 V, and three reduction peaks at -0.80 and -1.24. Based on the redox potentials of **NiP** and **Ru-bpy** reference compounds, it was possible to assign the corresponding peaks in the dyad. More specifically, in **NiP-Ru** the first reduction at -0.80 V and the first oxidation at 1.01 V were attributed to the Ru and the porphyrin part, respectively. In detail, the role of **NiP** as electron donor due to its facile oxidation, and the role of **Ru-bpy** as electron acceptor due to its facile reduction was possible to access. Free-energy calculations using the redox data of the **NiP-Ru** dyad, and excited state energy of **Ru-bpy** according to Rehm-Weller approach,<sup>249</sup> resulted in a  $\Delta G_{CS}$  value of -0.30 eV for the reductive electron transfer yielding **NiP**<sup>+</sup> - **Ru**<sup>+</sup> charge separated state of the dyad. The  $E_{00} = 2.105$  eV of **Ru-bpy** was determined from the intersection of the normalized absorption and emission spectra (**Figure 6.4.15**) and is in accordance with the literature.<sup>250</sup> Further, to assist in spectral characterization of the electron transfer products, spectroelectrochemical studies of **NiP** and **Ru-bpy** were performed, as shown in **Figure 4.6**. The one-electron oxidized product of **NiP** was characterized by a new peak at 620 nm.

**Table 4.1** Key electrochemical data recorded in benzonitrile containing 0.1 M (TBA)ClO<sub>4</sub> as the supporting electrolyte. The values are presented in V vs. Ag/AgCl.

Dye	$E_{00}^a$ (eV)	$E_{red}^2$ (V)	$E_{red}^1$ (V)	$E_{ox}^1$ (V)	$E_{ox}^2$ (V)	$\Delta G_{CS}^b$ (eV)
NiP	-	-1.25	-0.92	1.01	1.27	-
Ru-bpy	2.105	-1.02	-0.80	1.30	1.55	-
NiP-Ru	-	-1.24	-0.80	1.01	1.30	-0.30

<sup>a</sup>determined with the wavelength ( $\lambda_{inter}$ ) at the intersection of the normalized absorption and emission spectra with the equation  $E_{00} = 1240/\lambda_{inter}$  and was in accordance with the literature values.

<sup>249</sup> Rehm, D.; Weller, A. *Israel Journal of Chemistry* **1970**, 8 (2), 259.

<sup>250</sup> Borgström, M.; Johansson, O.; Lomoth, R.; Baudin, H. B.; Wallin, S.; Sun, L.; Åkermark, B.; Hammarström, L. *Inorg. Chem.* **2003**, 42 (17), 5173.

<sup>b</sup>calculated according to the equation:  $\Delta G_{CS} = E_{Ox}(NiP) - E_{00} - E_{red}(Ru-bpy)$

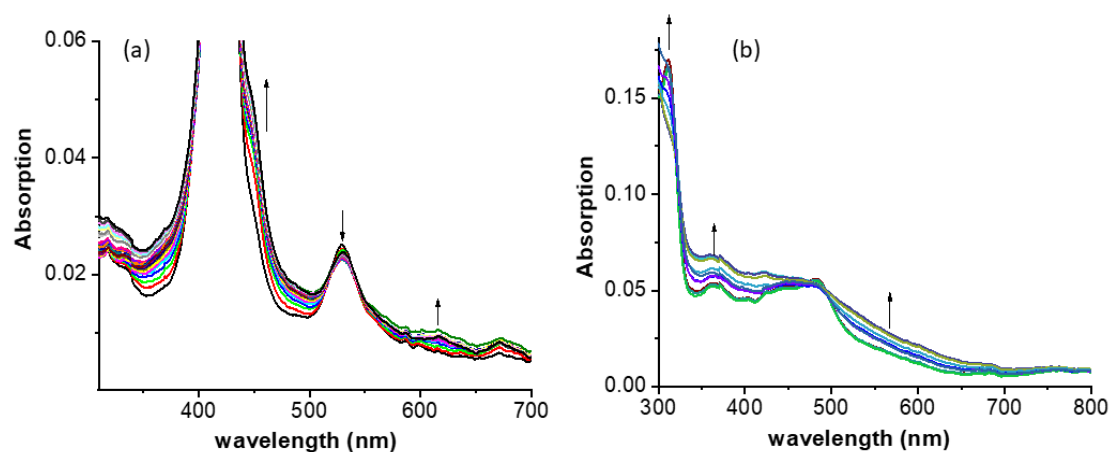


**Figure 4.6** Spectral changes observed during (a) first oxidation of **NiP** and (b) first reduction of **Ru-bpy** in benzonitrile containing 0.2 M (TBA)ClO<sub>4</sub>.

In order to establish the excited state electron transfer in the **NiP-Ru** dyad, femtosecond transient absorption (fs-TA) spectral studies were performed. **Figure 4.7a** shows the fs-TA spectra at the indicated delay times of **Ru-bpy** in benzonitrile. In agreement with the literature report,<sup>251</sup> in the visible region, the instantaneously formed excited state involving metal-to-ligand charge transfer revealed an excited state absorption peak at 590 nm (see spectrum at 0.92 ps) and a negative signal at 658 nm. The peak maxima of the negative signal matched that of the emission of **Ru-bpy** (see inverted emission spectrum shown in green dash line) suggesting that it is due to stimulated emission (SE). With time this peak experienced a 6 nm blue-shift, while the decay of the ESA peak was accompanied by a new broad signal in the 715 nm, which might be attributed to long-lived triplet state.

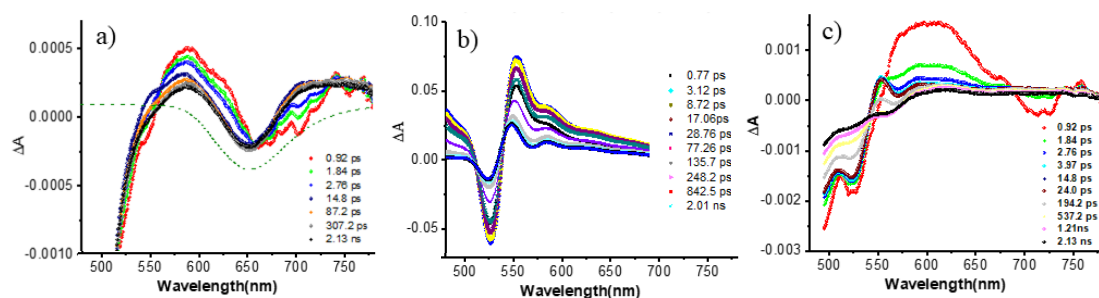


**Figure 4.7** Femtosecond TA spectra at the indicated delay times of (a) **Ru-bpy** ( $\lambda_{ex} = 464$  nm), (b) **NiP** ( $\lambda_{ex} = 424$  nm) and (c) **NiP-Ru** dyad ( $\lambda_{ex} = 464$  nm) in benzonitrile.

<sup>251</sup> Wallin, S.; Davidsson, J.; Modin, J.; Hammarström, L. *J. Phys. Chem. A* **2005**, *109* (21), 4697.

Although non-emissive, the fs-TA spectra of **NiP** was also recorded at the Soret band excitation to capture transient spectral details, as shown in **Figure 4.7b**. ESA peaks at 553 and 584 nm, and a ground state bleach at 525 nm was observed. As expected, no signal corresponding to SE was observed. Decay of the ESA and recovery of GSB peak did not result in any new peaks corresponding to  $^3\text{NiP}^*$  within the monitoring time window of 3 ns.

The fs-TA spectra of **NiP-Ru** dyad was much different from that of **Ru-bpy** monomer, as shown in **Figure 4.7c**. Spectrum recorded at the earlier delay time (0.92 ps) revealed a broad ESA peak covering the 550-660 nm region with a maxima around 615 nm, expected for the **NiP<sup>+</sup>-Ru<sup>+</sup>** charge separated state from the earlier discussed spectroelectrochemical studies. Decay of this signal was fast, which resulted in a much less intense, new peak at 620 nm. In addition, a ESA peak at 553 nm and a GSB peak at 525 nm were observed. The time constants for these signals were close to that of **NiP** suggesting this is due to simultaneous excitation of a small fraction of **NiP** fo the dyad. From decay kinetics, a lifetime of 25 ps the **NiP<sup>+</sup> - Ru<sup>+</sup>** charge separated state (fast decay component) was possible to arrive. These results unequivocally proved charge separation in the **NiP-Ru** dyad. The above transient experiments were conducted by Ajyal Alsaleh in the laboratory of Dr. Fransis D'Souza (*Department of Chemistry University of North Texas 1155 Union Circle, #305070, Denton, TX 76203-5017, USA*).

In order to prove electron/hole migration from the initial **NiP<sup>+</sup>-Ru<sup>+</sup>** charge separated state, photocatalytic electron pooling experiments using methyl viologen ( $\text{MV}^{2+}$ ) as terminal electron acceptor and water as electron donor were performed, as described previously **Scheme 4.2a**. For this purpose, the UV-Vis spectra of a mixture of **NiP-Ru** dyad,  $\text{MV}^{2+}$ , in DMF containing trace amounts of water, before and after irradiation was monitored, as shown in **Figure 4.8**. The characteristic peak of  $\text{MV}^{+}$  appeared at 608 nm accompanied by absorption bands in the region 370 nm – 410 nm, which were also attributed to the accumulation of  $\text{MV}^{+}$ .<sup>252</sup> This result suggests that in the **NiP<sup>+</sup>-Ru<sup>+</sup>** charge separated product the electron from **Ru<sup>+</sup>** is effectively shifting to  $\text{MV}^{2+}$ . The absorption changes of  $\text{MV}^{+}$  at 608 nm was plotted versus the irradiation time for **NiP-Ru** photocatalyst and a 1:1 mixture of **NiP** and **Ru-bpy** (**Figure 4.9**) with same amounts of  $\text{MV}^{2+}$  and  $\text{H}_2\text{O}$ . Both systems were photocatalytically active and

---

<sup>252</sup> Barrejón, M.; et al. *Chemical Science* **2018**, 9 (43), 8221.

showed that the activity reached a plateau after about one hour of irradiation, and that the performance of the **NiP-Ru** dyad system was much superior to the non-covalent system. The latter result can be attributed to the regeneration of the **NiP-Ru** photocatalyst, release of water oxidation product, namely  $O_2$  and  $H^+$ , along with the accumulation of reduced methyl viologen,  $MV^+$ .

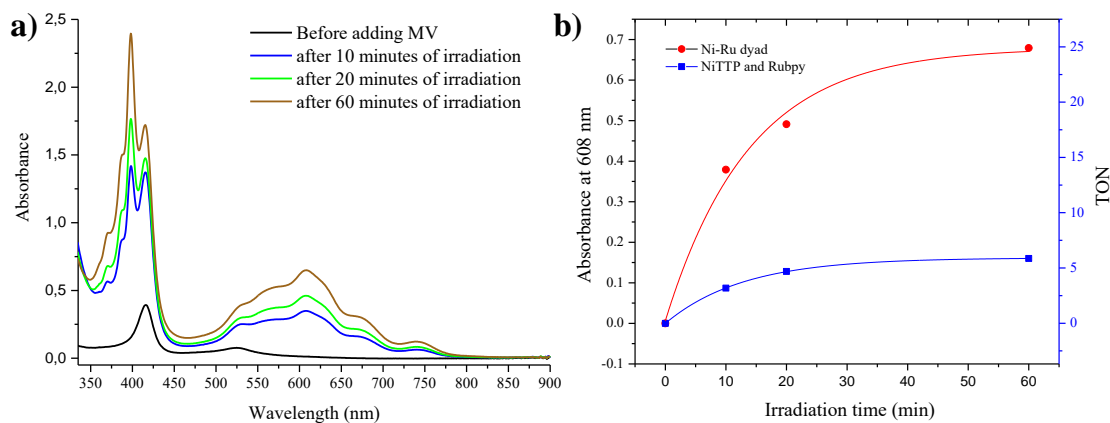


**Figure 4.8** a) UV-Vis spectral changes observed during electron pooling experiment. **NiP-Ru** dyad containing methyl viologen in DMF as a function of irradiation time is shown. A 450 W Xe lamp with a 400 nm filter was used, b) changes of the absorption maxima at 608 nm, attributed to  $MV^+$ , versus the irradiation time for covalently linked **NiP-Ru** dyad and 1:1 mixture of **NiP** and **Ru-bpy** revealing much improved photocatalytic effect by the dyad.

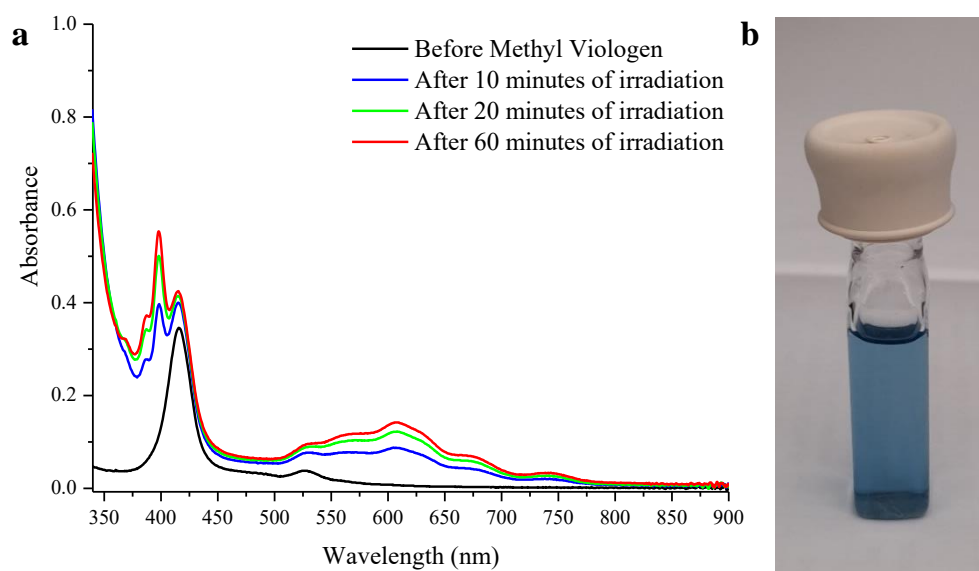


**Figure 4.9** a) UV-Vis spectra of **NiP** and **Rubpy** photocatalytic system in DMF before and after irradiation with Xenon lamp (in the presence of Methyl Viologen), b) photograph of the UV-Vis cell where the blue color of  $MV^+$  is easily seen.

Next, photocatalytic irradiation experiments for O<sub>2</sub> evolution were performed in DMF using methyl viologen as sacrificial electron acceptor and oxygen was detected via an optical oxygen sensor.<sup>253</sup> In agreement with the electron pooling experiments, the **NiP-Ru** dyad exhibited significantly higher O<sub>2</sub> evolution compared to the non-covalent system comprised of **NiP** and **Rubpy** as PS (**Figure 4.10**). The overall activity of **NiP-Ru** dyad reached a turn over number of 18 after one hour of continuous irradiation. The later system was additionally used to examine the impact of the PS concentration. After increasing PS concentration by a factor 10, no impact on the photocatalytic activity was observed. Control experiments with no catalyst, or no sacrificial agent or no water failed to reveal any photocatalytic O<sub>2</sub> production. Varying the concentration of the **NiP-Ru** dyad (**Figure 4.11**) showed a first order dependence of the oxygen evolution rate on the dyad concentration. Since the previous experiment showed no dependence on the PS concentration, the later result suggests that the rate-determining step of the water oxidation reaction involves one nickel center.

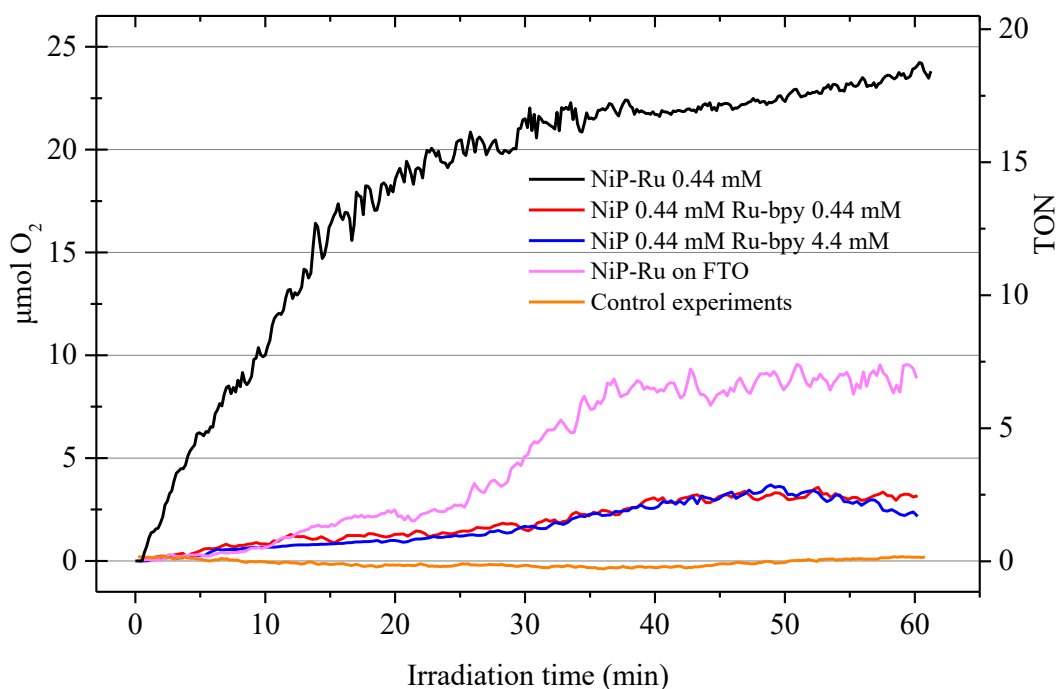


**Figure 4.10** O<sub>2</sub> evolution during photocatalytic H<sub>2</sub>O oxidation after irradiation with a 450 W Xenon lamp (cut-off filter  $\lambda > 400$  nm). All solutions besides the **NiP-Ru** on TiO<sub>2</sub>/FTO (magenta line) contained 50 mM of MV in DMF and 4% H<sub>2</sub>O.

<sup>253</sup> Pintado, S.; Goberna-Ferrón, S.; Escudero-Adán, E. C.; Galán-Mascarós, J. R. *J. Am. Chem. Soc.* **2013**, *135* (36), 13270.

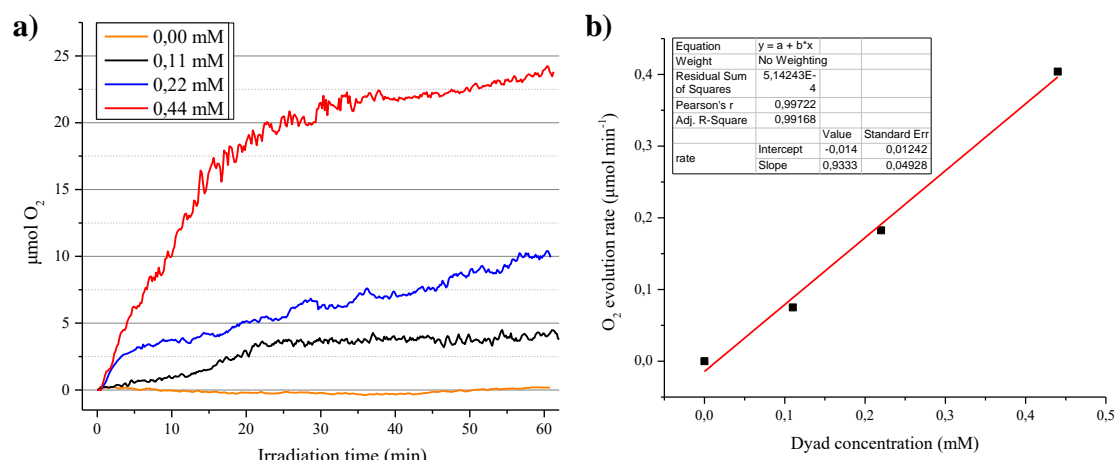


**Figure 4.11** a) Photocatalytic O<sub>2</sub> evolution plots versus irradiation time using **NiP-Ru** dyad under different concentrations, (b) O<sub>2</sub> evolution rate as a function of the dyad concentration. Conditions: 50 mM of MV in DMF and 4% H<sub>2</sub>O.

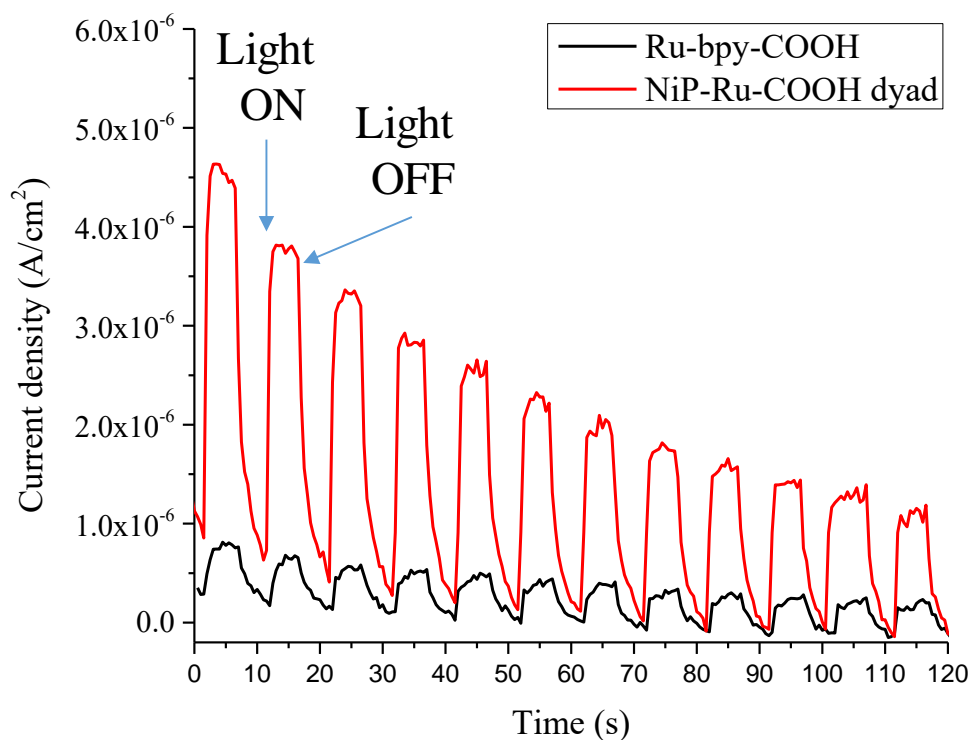


**Figure 4.12** Photoelectrochemical performance illustrated by light on and off experiments from TiO<sub>2</sub> (1 cm<sup>2</sup>) on FTO sensitized with **NiP-Ru** dyad, and **Ru-bpy** reference after applying 0 V versus Ag/AgCl reference electrode in phosphate buffer of pH = 7.

In an effort to examine the ability of the dyad to operate in aqueous media, since water is the greenest solvent and the oxygen source in our photocatalytic system, we

deposited the hydrolyzed dyad **NiP-Ru-COOH** on FTO glass and conducted the photocatalysis in an aqueous solution of  $\text{Na}_2\text{S}_2\text{O}_8$  as electron acceptor. The last attempt was proved successful (magenta line in **Figure 4.10**) and motivated us to move towards a photoelectrocatalytic (PEC) aqueous system with no need for sacrificial agents.

In detail, we conducted photoelectrochemical (PEC) studies in an aqueous phosphate buffer solution ( $\text{pH} = 7$ ) in the absence of sacrificial electron acceptor. For these experiments, a 450 W Xenon lamp equipped with a 400 nm cut-off filter was also used as a light source. The photoelectrochemical performance of the hydrolyzed dyad was studied by using a standard three-electrode PEC system. The **NiP-Ru-COOH/TiO<sub>2</sub>/FTO** was utilized as photoanode, while Pt mesh and Ag/AgCl were used as counter and reference electrodes, respectively. The photoelectrochemical responses were recorded at an applied bias potential of 0.0 V (**Figure 4.12**). The light switching experiments displayed that the photocurrent produced by the **NiP-Ru/TiO<sub>2</sub>/FTO** electrode was much higher than that compared to the reference anode, where no **NiP** catalyst moiety was present. The above result demonstrates a proof of concept, where the PEC device fabricated from a **NiP-Ru** dyad is able to perform light induced water oxidation in neutral aqueous media. Noteworthy, to the best of our knowledge, this is the first PEC device utilizing nickel porphyrin WOC and ruthenium PS.

The work presented in this section analyzed the successful utilization of a nickel(II) porphyrin- ruthenium tris(bipyridine), **NiP-Ru** dyad in photocatalytic water oxidation under visible light irradiation.  $\text{Ni}^{2+}$  porphyrin moiety was utilized as WOC, while the  $\text{Ru}^{2+}$  complex had the role of the light-harvesting sensitizer. Initial photocatalytic experiments in organic solutions showed that the covalently connected dyad displayed improved performance compared to the non-covalent two-component system. This was verified both in an electron pooling experiment followed by UV-Vis spectral detection of electron transfer products as well as direct detection of generated dioxygen using an optical oxygen sensor. The overall activity of **NiP-Ru** dyad reached a TON of 18 after one hour of irradiation. It may be mentioned here that the employment of organic solvent could serve a dual role of placing water oxidation and  $\text{CO}_2$  reduction catalysts in a same cell for  $\text{CO}_2$  conversion. Finally, for the first time, a photoelectrochemical cell was fabricated using the **NiP-Ru** dyad anchored on  $\text{TiO}_2$  as a photoanode and was shown to perform water oxidation at neutral pH conditions.

## 4.2 Photocatalytic Alcohol Oxidation

In correlation with the previous section which described a photocatalytic system for water oxidation, we move one step forward in the following section and present similar systems for alcohol oxidation. The motivation for this research is the storage of solar energy as chemical fuels towards a sustainable society, which will provide the answer to many problems caused by the combustion of fossil fuels.<sup>254,255,256</sup> A promising approach for achieving this significant goal is the development of photoelectrochemical cells (PEC), which do not require any toxic and expensive sacrificial agents.<sup>257,258,259</sup> These systems contain a photocathode, where a reduction reaction occurs (usually H<sup>+</sup> reduction to H<sub>2</sub>) by the electrons generated at the photoanode, due to the oxidation of water or the oxidation of an organic substrate, such as alcohol.

Water oxidation is a challenging transformation because four electrons are necessary to perform the reaction ( $2\text{H}_2\text{O} \rightarrow 4\text{H}^+ + 4\text{e}^- + \text{O}_2$ ). Furthermore, the required oxidation potential (1.23 V vs. NHE, at pH = 0) renders the reaction energetically demanding, and it is usually accomplished by noble metal based catalysts.<sup>260,261</sup> Due to all the above mentioned aspects water oxidation is often considered as the limiting factor that decreases the overall efficiency of photoelectrochemical cells. The reaction product, namely molecular oxygen (O<sub>2</sub>), has a limited economic value although it is environmentally useful for aerobic organisms.

Plenty alternative reactions which can produce more valuable products have attracted a lot of scientific attention.<sup>262,263,264</sup> Instead of water oxidation, the selective oxidation of organic molecules, such as alcohols, is certainly a promising approach to obtain valuable carbonyl compounds. Various substrates such as protons, carbon dioxide or nitrogen can be reduced at the cathode, constructing a tandem system which

---

<sup>254</sup> Balzani, V.; Credi, A.; Venturi, M. *ChemSusChem* **2008**, *1* (1-2), 26.

<sup>255</sup> Dau, H.; Fujita, E.; Sun, L. *ChemSusChem* **2017**, *10* (22), 4228.

<sup>256</sup> Barber, J.; Tran, P. D. *J. R. Soc. Interface* **2013**, *10* (81), 20120984.

<sup>257</sup> Kirner, J. T.; Finke, R. G. *J. Mater. Chem. A* **2017**, *5* (37), 19560.

<sup>258</sup> Pinaud, B. A.; Benck, J. D.; Seitz, L. C.; Forman, A. J.; Chen, Z.; Deutsch, T. G.; James, B. D.; Baum, K. N.; Baum, G. N.; Ardo, S. et al. *Energy Environ. Sci.* **2013**, *6* (7), 1983.

<sup>259</sup> Yang, X.; Wang, D. *ACS Appl. Energy Mater.* **2018**, *1* (12), 6657.

<sup>260</sup> Liang, X.; Cao, X.; Sun, W.; Ding, Y. *ChemCatChem* **2019**, *11* (24), 6190.

<sup>261</sup> Zhang, B.; Sun, L. *Chem. Soc. Rev.* **2019**, *48* (7), 2216.

<sup>262</sup> Lhermitte, C. R.; Sivula, K. *ACS Catal.* **2019**, *9* (3), 2007.

<sup>263</sup> Kampouri, S.; Stylianou, K. C. *ACS Catal.* **2019**, *9* (5), 4247.

<sup>264</sup> Xu, Y.; Zhang, B. *ChemElectroChem* **2019**, *6* (13), 3214.



is one step closer to a real-world application.<sup>265,266,267</sup> An additional advantage of alcohol oxidation, besides producing more valuable materials at both electrodes, derives from the lower potential demand of this reaction compared to water oxidation (-0.143 V vs. NHE for benzyl alcohol oxidation *versus* 1.23 V vs. NHE for water oxidation),<sup>268</sup> and only two holes are shifted instead of four.

In the literature, alcohol oxidation in DSPEC systems is explored by utilizing Ru<sup>2+</sup> polypyridine complexes as catalysts<sup>269,270,271,272</sup> and organic sensitizers.<sup>273,274,275,276</sup> A representative example reported by T. Meyer and coworkers is depicted in **Figure 4.13**. The researchers utilized a BDP chromophore moiety co-grafted on a SnO<sub>2</sub>/TiO<sub>2</sub> photoanode while a ruthenium catalyst was able to oxidize benzyl alcohol into benzaldehyde. The advantages of moving to noble metal-free catalysts in such systems are numerous. One of the most promising candidates is 2,2,6,6-tetramethyl-1-piperidine N-oxyl (TEMPO), which is very efficient, inexpensive and green catalyst for alcohol oxidation,<sup>277</sup> that is even applied to chemical industry.<sup>278,279</sup>

---

<sup>265</sup> Reid, Lacey M.; Li, T.; Cao, Y.; Berlinguette, C. P. *Sustainable Energy Fuels* **2018**, 2 (9), 1905.

<sup>266</sup> Mei, B.; Mul, G.; Seger, B. *Adv. Sustainable Syst.* **2017**, 1 (1-2), 1600035.

<sup>267</sup> Cha, H. G.; Choi, K.-S. *Nature Chem.* **2015**, 7, 328.

<sup>268</sup> Wang, F.; Stahl, S. S. *Acc. Chem. Res.* **2020**, 53 (3), 561.

<sup>269</sup> Treadway, J. A.; Moss, J. A.; Meyer, T. J. *Inorg. Chem.* **1999**, 38 (20), 4386.

<sup>270</sup> Song, W.; Vannucci, A. K.; Farnum, B. H.; Lapidus, A. M.; Brennaman, M. K.; Kalanyan, B.; Alibabaei, L.; Concepcion, J. J.; Losego, M. D.; et al. *J. Am. Chem. Soc.* **2014**, 136 (27), 9773.

<sup>271</sup> Ashford, D. L.; Gish, M. K.; Vannucci, A. K.; Brennaman, M. K.; Templeton, J. L.; Papanikolas, J. M.; Meyer, T. J. *Chem. Rev. (Washington, DC, United States)* **2015**, 115 (23), 13006.

<sup>272</sup> Brennaman, M. K.; Dillon, R. J.; Alibabaei, L.; Gish, M. K.; Dares, C. J.; Ashford, D. L.; House, R. L.; Meyer, G. J.; Papanikolas, J. M.; Meyer, T. J. *J. Am. Chem. Soc.* **2016**, 138 (40), 13085.

<sup>273</sup> Jiang, J.; Sherman, B. D.; Zhao, Y.; He, R.; Ghiviriga, I.; Alibabaei, L.; Meyer, T. J.; Leem, G.; Schanze, K. S. *ACS Appl. Mater. Interfaces* **2017**, 9 (23), 19529.

<sup>274</sup> Badgurjar, D.; Shan, B.; Nayak, A.; Wu, L.; Chitta, R.; Meyer, T. J. *ACS Appl. Mater. Interfaces* **2020**, 12 (6), 7768.

<sup>275</sup> Pho, T. V.; Sheridan, M. V.; Morseth, Z. A.; Sherman, B. D.; Meyer, T. J.; Papanikolas, J. M.; Schanze, K. S.; Reynolds, J. R. *ACS Appl. Mater. Interfaces* **2016**, 8 (14), 9125.

<sup>276</sup> Charisiadis, A.; Glymenaki, E.; Planchat, A.; Margiola, S.; Lavergne-Bril, A.-C.; Nikoloudakis, E.; Nikolaou, V.; Charalambidis, G.; Coutsolelos, A. G.; Odobel, F. *Dyes Pigments* **2021**, 185, 108908.

<sup>277</sup> Nutting, J. E.; Rafiee, M.; Stahl, S. *Chem. Rev.* **2018**, 118 (9), 483.

<sup>278</sup> Ciriminna, R.; Pagliaro, M. *Org. Process Res. Dev.* **2010**, 14 (1), 245.

<sup>279</sup> Caron, S.; Dugger, R. W.; Ruggeri, S. G.; Ragan, J. A.; Ripin, B. *Chem. Rev.* **2006**, 106 (7), 2943.

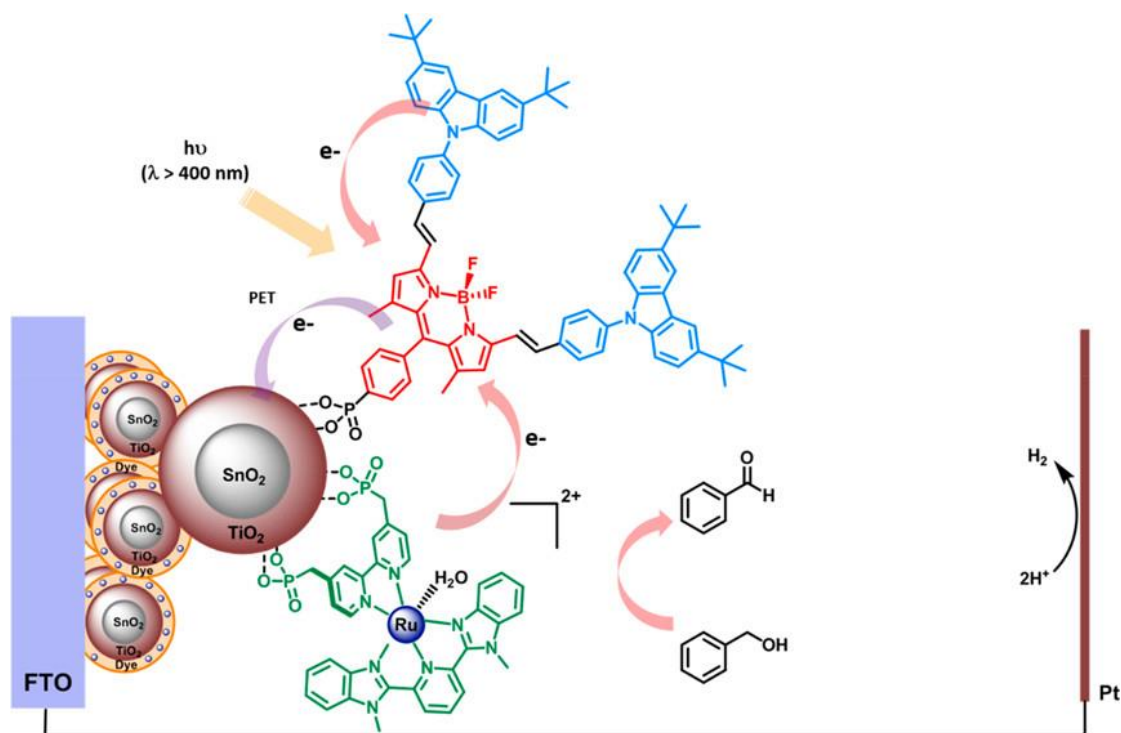


**Figure 4.13** DSPEC system for alcohol oxidation reported by Meyer and co-workers.<sup>274</sup>

Homogeneous photocatalytic systems for alcohol oxidation utilizing TEMPO derivatives as catalysts has been investigated in the presence of a dye and a sacrificial electron acceptor.<sup>280,281,282,283,284</sup> In addition, alcohol oxidation with TEMPO was also demonstrated with a visible light harvesting semiconductor such as BiVO<sub>4</sub> or WO<sub>3</sub> as photoanode.<sup>285,286,287,288</sup> Moreover, TEMPO catalytic moieties have been successfully employed as redox mediators in dye sensitized solar cells (DSSCs), showing that the hole can be efficiently transferred from an oxidized photosensitizer to the nitroxide radical even with a weak driving force.<sup>289,290,291,292</sup> Light driven oxidation of alcohols to aldehydes catalyzed by TEMPO derivatives has also been reported in combination with dyes upon oxidative quenching by a sacrificial electron acceptor both in

<sup>280</sup> Zhang, M.; Chen, C.; Ma, W.; Zhao, J. *Angewandte Chemie* **2008**, *47* (50), 9730.

<sup>281</sup> Nagasawa, T.; Allakhverdiev, I.; Kimura, Y.; Nagata, T. *Photochem. Photobiol. Sci.* **2009**, *8* (2), 174.

<sup>282</sup> Jeena, V.; Robinson, R. S. *Dalton Trans.* **2012**, *41* (11), 3134.

<sup>283</sup> Jeena, V.; Robinson, R. S. *Chem. Commun.* **2012**, *48* (2), 299.

<sup>284</sup> Liu, D.; Zhou, H.; Gu, X.; Shen, X.; Li, P. *Chin. J. Chem.* **2014**, *32* (2), 117.

<sup>285</sup> Li, T.; Kasahara, T.; He, J.; Dettelbach, K. E.; et al. *Nature Commun.* **2017**, *8* (1), 390.

<sup>286</sup> Bai, L.; Li, F.; Wang, Y.; Li, H.; Jiang, X.; Sun, L. *Chem. Commun.* **2016**, *52* (62), 9711.

<sup>287</sup> Chadderton, D. J.; Wu, L.-P.; McGraw, Z. A.; et al. *ChemElectroChem* **2019**, *6* (13), 3387.

<sup>288</sup> Cha, H. G.; Choi, K.-S. *Nature Chem.* **2015**, *7*, 328.

<sup>289</sup> Yang, W.; Vlachopoulos, N.; Hao, Y.; et al. *Phys. Chem. Chem. Phys.* **2015**, *17* (24), 15868.

<sup>290</sup> Zhang, Z.; Chen, P.; Grätzel, M. et al. *Adv. Funct. Mater.* **2008**, *18* (2), 341.

<sup>291</sup> Murakami, T.; Kato, F.; Oyaizu, K.; Nishide, H. *J. Photopolymer Sci. Technology* **2010**, *23* (3), 353.

<sup>292</sup> Kato, F.; Kikuchi, A.; Okuyama, T.; Oyaizu, K.; Nishide, H. *Angew. Chem.* **2012**, *51* (40), 10177.

homogenous systems and in hybrid systems involving TiO<sub>2</sub> or ZnO dye-sensitized nanoparticles.<sup>280,281,283,284</sup>

Inspired from the above, we explore in this section the development of a TiO<sub>2</sub> based DSPECs for alcohol oxidation utilizing (for the first time) a TEMPO catalyst covalently connected to a porphyrin photosensitizer (**Figure 4.14**). The initial target of this investigation was to prove the advantage of choosing a two hole-oxidation reaction. To that end, we evaluated its efficiency by comparing it to other reported DSPECs for water instead of alcohol oxidation. Secondly, we studied the fabrication of DSPEC systems using only abundant elements via replacing the typical Ru<sup>2+</sup> catalyst<sup>293</sup> by a TEMPO moiety and we evaluated its photocatalytic properties. In total, four photosensitizer-catalyst dyads, composed of a zinc porphyrin covalently linked to a TEMPO moiety, were prepared and their photocatalytic properties in DSPECs was investigated. Several anchoring groups, namely carboxylic acid, hydroxamic acid, phosphonic acid and pyridyl group, have been utilized. Overall, the hydroxamic acid was the optimal anchoring groups since it maintained a robust linkage to the TiO<sub>2</sub> surface during photocatalysis.<sup>294,295,296,297,298</sup>

Indeed, since oxidation catalysis occurs more favorably in neutral and even basic conditions,<sup>299,300</sup> it is crucial to functionalize the photosensitizer with a strong anchoring group avoiding the desorption of the dyad from the surface of the semiconductor. Zinc porphyrin chromophores have been already used in DSPEC systems for water oxidation,<sup>301,302,303</sup> and this selection is additionally supported from the suitable

---

<sup>293</sup> Ishizuka, T.; Kotani, H.; Kojima, T. *Dalton Trans.* **2016**, 45 (42), 16727.

<sup>294</sup> Veldkamp, B. S.; Han, W.-S.; Dyar, S. M.; et al. *Energy Environ. Sci.* **2013**, 6 (6), 1917.

<sup>295</sup> Koenigsmann, C.; Ripolles, T. S.; Brennan, B. J.; Negre, C. F. A.; Koepf, M.; Durrell, A. C.; Milot, R. L.; Torre, J. A.; Crabtree, R. H.; Batista, V. S. et al. *Phys. Chem. Chem. Phys.* **2014**, 16 (31), 16629.

<sup>296</sup> McNamara, W. R.; Snoeberger III, R. C.; Li, G.; Richter, C.; Allen, L. J.; Milot, R. L.; Schmuttenmaer, C. A.; Crabtree, R. H.; et al. *Energy Environ. Sci.* **2009**, 2 (11), 1173.

<sup>297</sup> Higashino, T.; Kurumisawa, Y.; Cai, N.; Fujimori, Y.; Tsuji, Y.; Nimura, S.; Packwood, D. M.; Park, J.; Imahori, H. *ChemSusChem* **2017**, 10 (17), 3347.

<sup>298</sup> Young, K. J.; Martini, L. A.; Milot, R. L.; Snoeberger, R. C.; Batista, V. S.; Schmuttenmaer, C. A.; Crabtree, R. H.; Brudvig, G. W. *Coord. Chem. Rev.* **2012**, 256 (21), 2503.

<sup>299</sup> Rafiee, M.; Miles, K. C.; Stahl, S. S. *J. Am. Chem. Soc.* **2015**, 137 (46), 14751.

<sup>300</sup> Hickey, D. P.; McCammant, M. S.; Giroud, F.; Sigman, M. S.; Minter, S. D. *J. Am. Chem. Soc.* **2014**, 136 (45), 15917.

<sup>301</sup> Yamamoto, M.; Wang, L.; Li, F.; Fukushima, T.; Tanaka, K.; Sun, L.; Imahori, H. *Chem. Sci.* **2016**, 7 (Copyright (C) 2021 American Chemical Society (ACS). All Rights Reserved.), 1430.

<sup>302</sup> Moore, G. F.; Blakemore, J. D.; Milot, R. L.; Hull, J. F.; Song, H.-e.; Cai, L.; Schmuttenmaer, C. A.; Crabtree, R. H.; Brudvig, G. W. *Energy Environ. Sci.* **2011**, 4 (7), 2389.

<sup>303</sup> Orbelli Biroli, A.; Tessore, F.; Di Carlo, G.; Pizzotti, M.; Benazzi, E.; Gentile, F.; Berardi, S.; Bignozzi, C. A.; Argazzi, R.; Natali, M. et al. *ACS Applied Mater. Interfaces* **2019**, 11 (36), 32895.

catalytic potential of TEMPO based on the electrochemical characterization (paragraph 4.1).

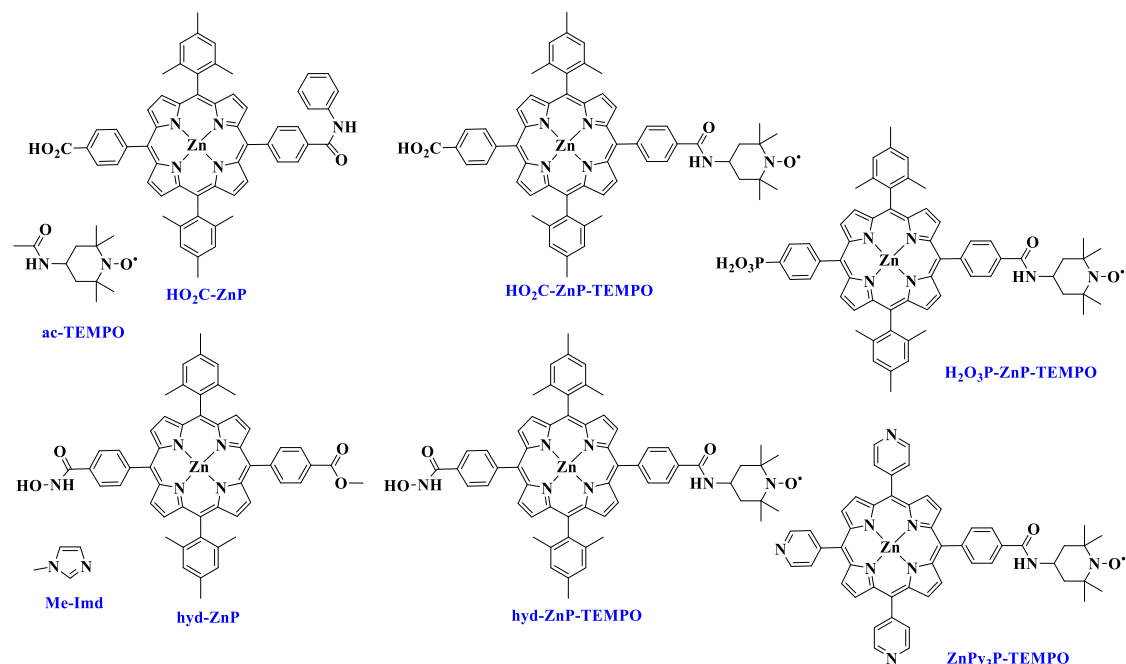


**Figure 4.14** Structures of the compounds used in this section.

The work presented in this section highlights that alcohol oxidation using photosensitizer-TEMPO dyads is a promising approach to replace water oxidation. ZnP-TEMPO dyads were active both in water and organic solvents, while through the covalent attachment of the catalyst to the dye high photocatalytic performances were obtained. Moreover, the covalent linkage provides an easier electron-recovery pathway for the catalyst and is unavoidable when the catalyst is insoluble in the electrolyte.

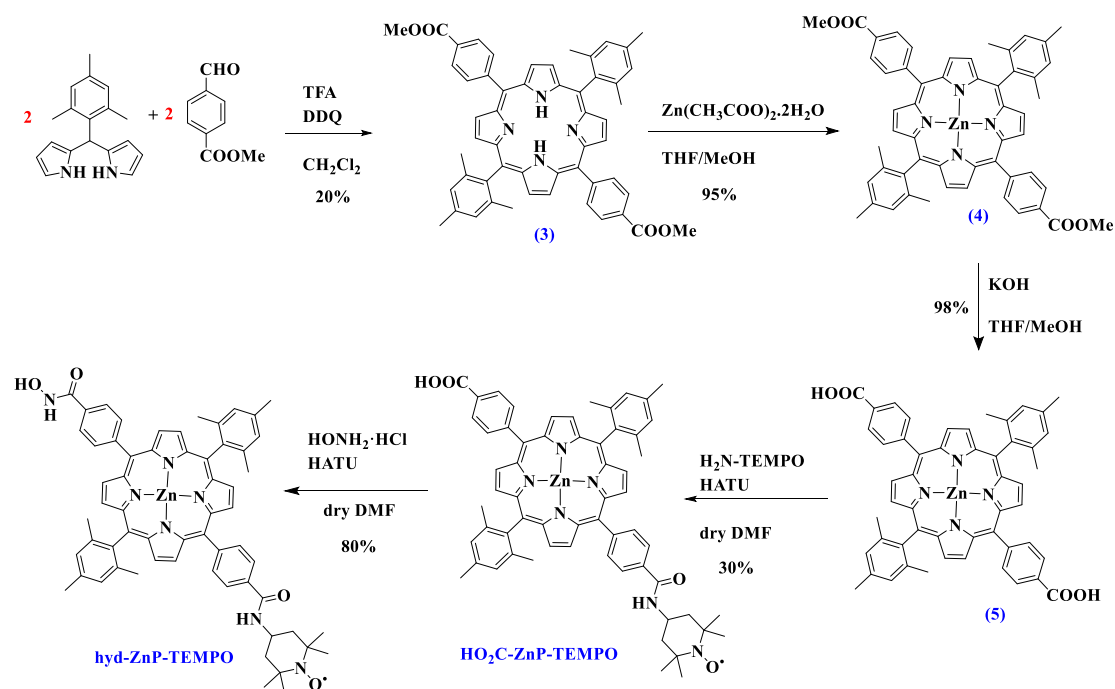
#### Zinc(II) Porphyrin – TEMPO Dyad for benzyl alcohol oxidation

This section describes the synthesis of ZnP-TEMPO dyads bearing 4 different anchoring groups, namely carboxylic acid, hydroxamic acid, phosphoric acid and pyridyl group. The synthetic approach for the preparation of **HO<sub>2</sub>C-ZnP-TEMPO** and **hyd-ZnP-TEMPO** porphyrin dyads is illustrated in **Scheme 4.4**.

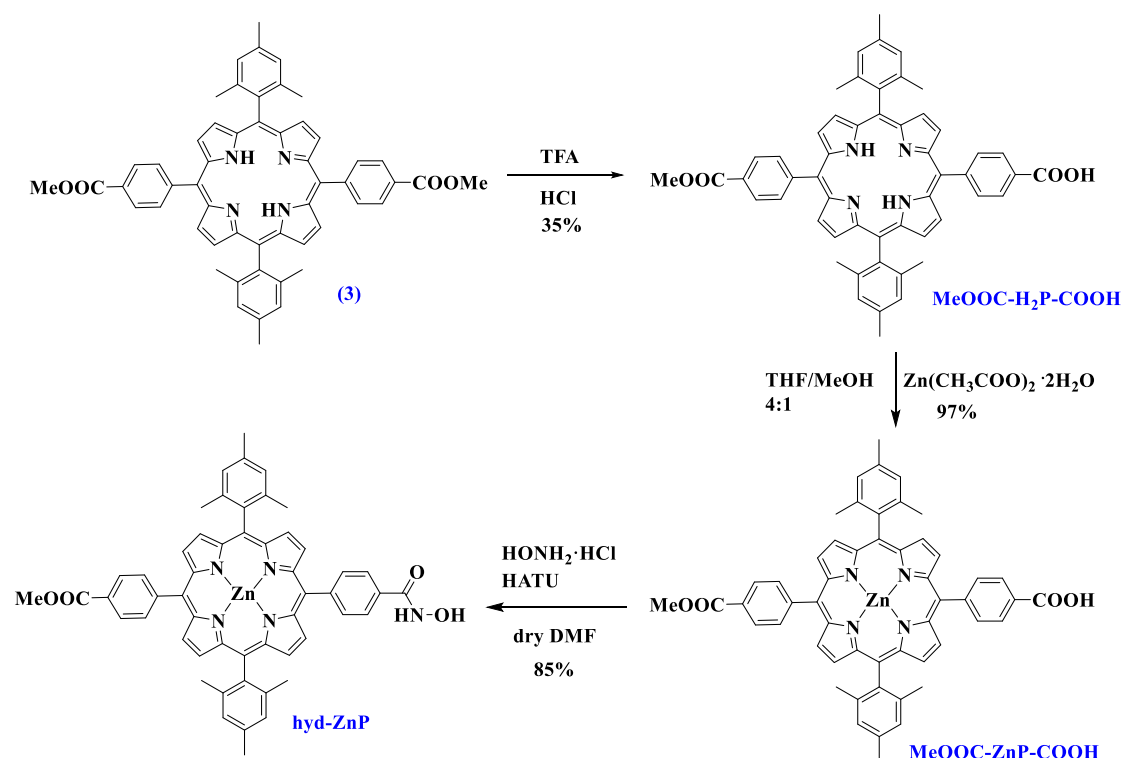
The preparation of **HO<sub>2</sub>C-ZnP-CO<sub>2</sub>H (5)** porphyrin was based on already published experimental procedures.<sup>304</sup> In detail, a condensation reaction of mesityl dipyrromethane and methyl 4-formylbenzoate yielded porphyrin derivative **3**, which was subsequently metallated to afford porphyrin **4**. Consequently, a basic hydrolysis of

<sup>304</sup> Kim, D.; Lee, S.; Gao, G.; Seok Kang, H.; Ko, J. *J. Organomet. Chem.* **2010**, 695 (1), 111

the ester groups resulted in the desired **HO<sub>2</sub>C-ZnP-CO<sub>2</sub>H (5)** intermediate. The later, was transformed to the **HO<sub>2</sub>C-ZnP-TEMPO** dyad through an amide coupling reaction with NH<sub>2</sub>-TEMPO using HATU as coupling reagent. In order to convert the carboxylic acid into a hydroxamic acid, hydroxylamine hydrochloride was utilized and the formation of **hyd-ZnP-TEMPO** dyad was achieved. The reference compound **hyd-ZnP** was prepared following similar reactions (**Scheme 4.5**). In detail, we performed partial hydrolysis of only one of the methyl-ester groups using acidic conditions followed by a simple metalation reaction with Zn(CH<sub>3</sub>COO)<sub>2</sub>. The obtained -COOH intermediate was converted into hydroxamic acid by using hydroxylamine hydrochloride.

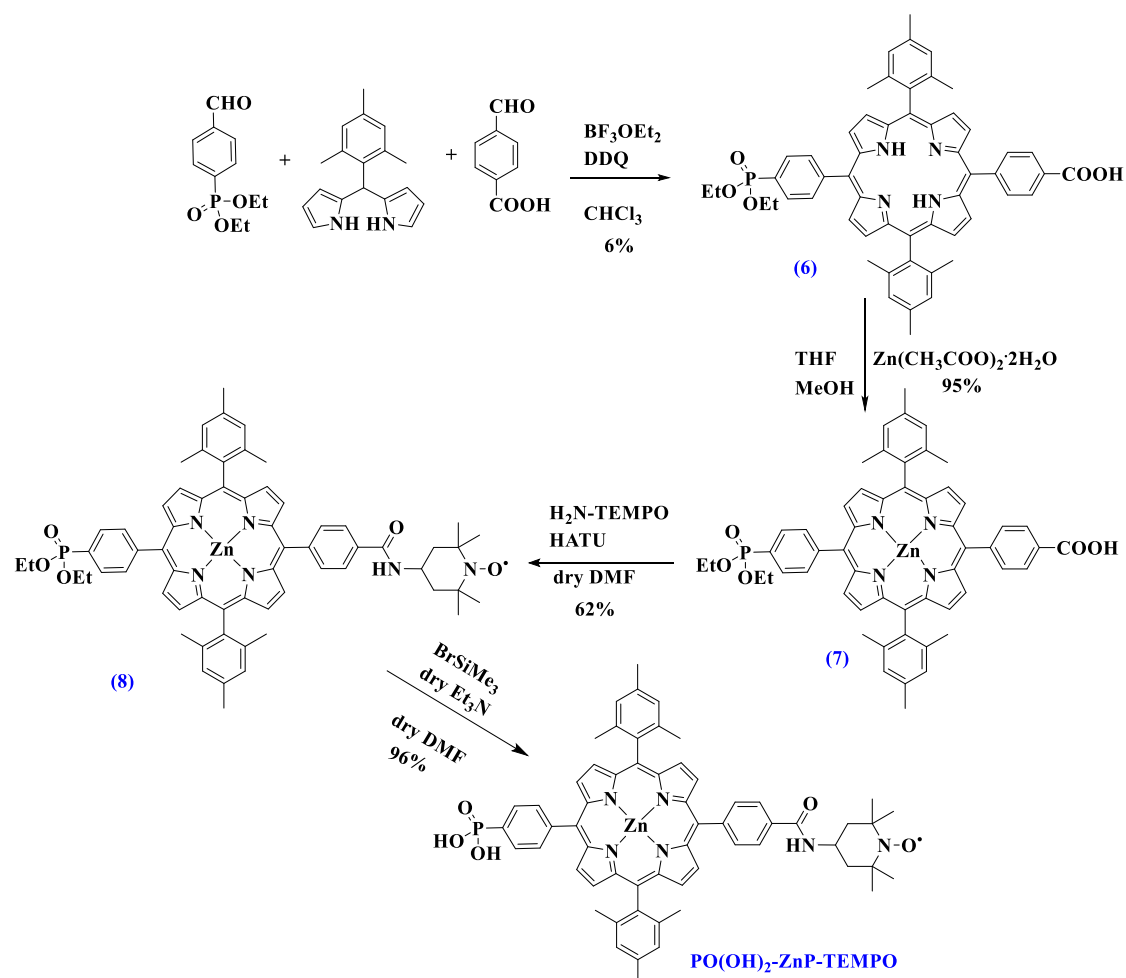


**Scheme 4.4** Synthetic route to **HO<sub>2</sub>C-ZnP-TEMPO** and **hyd-ZnP-TEMPO** dyads.



**Scheme 4.5** Synthetic route to reference compound **hyd-ZnP**.

We have additionally synthesized another porphyrin-TEMPO dyad, namely **PO(OH)<sub>2</sub>-ZnP-TEMPO** dyad which bears phosphoric acid as an alternative anchoring group. The experimental procedure is outlined in **Scheme 4.6**. We started with the synthesis of the diethyl (4-formylphenyl)phosphonate starting material and then performed a cyclisation reaction with mesityl dipyrromethane and 4-formylbenzoic acid to obtain porphyrin intermediate **6**. To afford derivative **7**, a metalation reaction with  $\text{Zn}(\text{CH}_3\text{COO})_2$  was followed by an amide coupling with  $\text{NH}_2$ -TEMPO using HATU as coupling reagent. Dyad **8** was hydrolyzed utilizing  $\text{BrSiMe}_3$  under inert and dry conditions. Although the final compound **PO(OH)<sub>2</sub>-ZnP-TEMPO** dyad was not soluble enough in any of the different solvents that we tried, we were able to verify the successful hydrolysis of porphyrin **8** from  $^1\text{H-NMR}$  spectra where the peaks corresponding to the ethyl groups of the phosphoric ester were completely disappeared (**Figure 4.15**).



**Scheme 4.6** Synthetic route for the preparation of  $\text{PO}(\text{OH})_2\text{-ZnP-TEMPO}$  dyad.

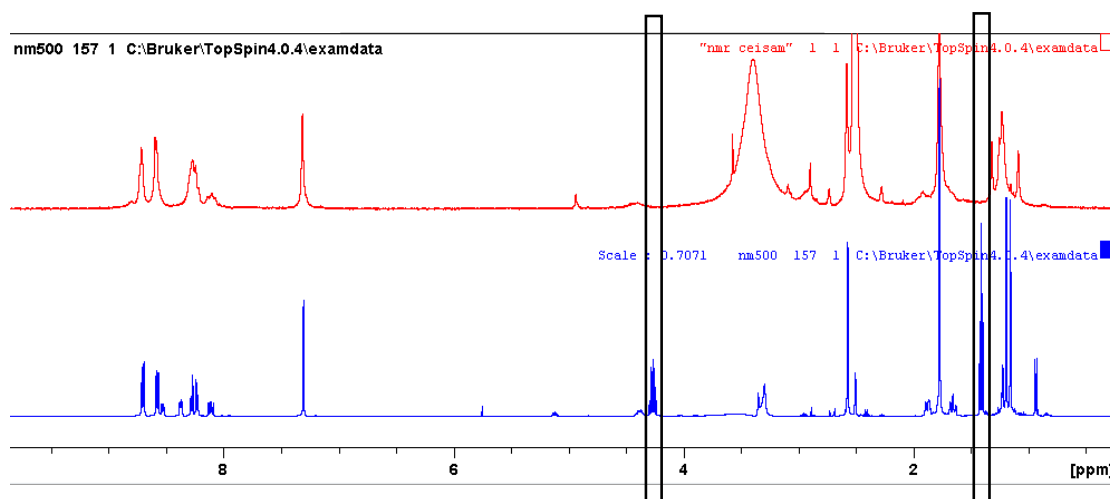
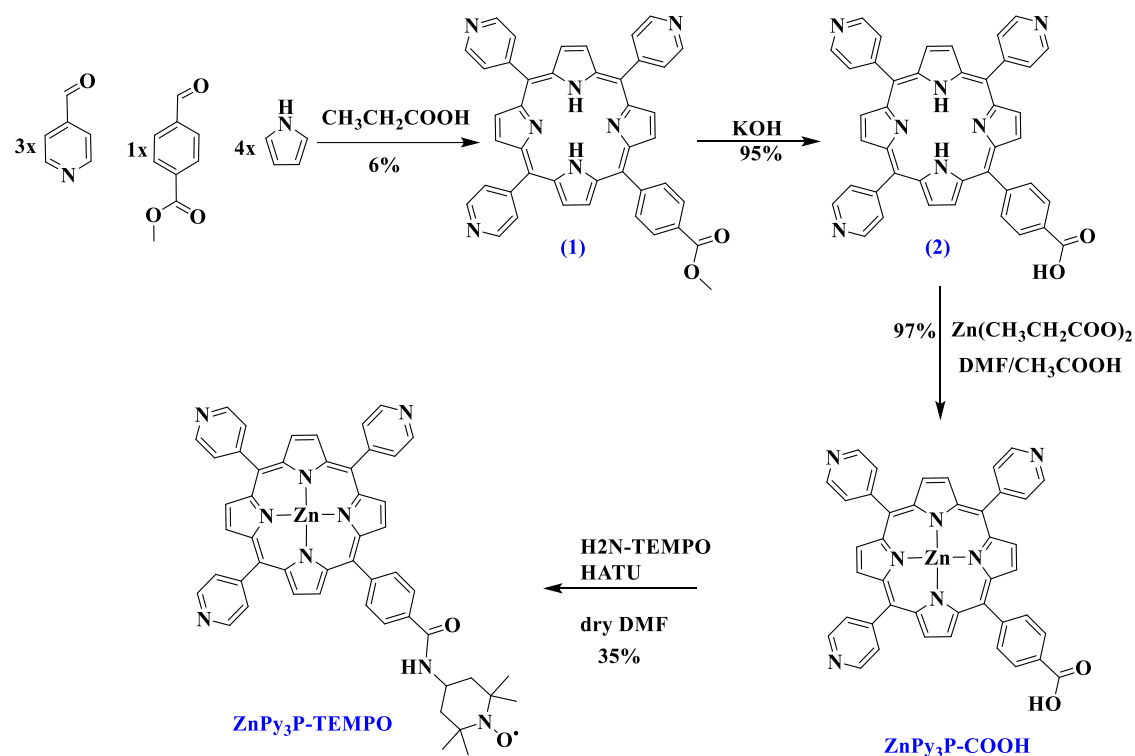


**Figure 4.15**  $^1\text{H-NMR}$  spectra which verify the hydrolysis of the phosphoric ester group for the synthesis of  $\text{PO}(\text{OH})_2\text{-ZnP-TEMPO}$  dyad.

$\text{ZnP}_3\text{P-TEMPO}$  dyad, which bears three pyridyl anchoring groups, was prepared according to the synthetic route illustrated in **Scheme 4.7**. The initial step is the

preparation of porphyrin **2** (section 3.1); subsequently we performed the metalation of the latter with  $\text{Zn}(\text{CH}_3\text{COO})_2\cdot 2\text{H}_2\text{O}$  in DMF/ $\text{CH}_3\text{COOH}$ . The final step was an amide coupling with  $\text{NH}_2\text{-TEMPO}$  using HATU, affording the desired dyad.



**Scheme 4.7** Synthetic route to prepare **ZnPy<sub>3</sub>P-TEMPO**.

The successful synthesis of all the above final and intermediate compounds was verified via  $^1\text{H}$  and  $^{13}\text{C}$  NMR spectroscopies and MALDI-TOF mass spectrometry (**Figure 6.4.17- 6.4.42**).

#### Photophysical investigation

The ground and excited state features of the synthesized compounds were investigated by means of steady-state absorption and fluorescence spectroscopy (**Figures 4.16, 6.4.43-6.4.45**). In addition, upon their adsorption onto thin  $\text{TiO}_2$  films, their absorption and emission properties were explored in solid state as well (**Figures 6.4.46**). The corresponding spectroscopic data are collected in **Table 4.2**. As illustrated in **Figure 4.16**, typical absorption features of Zn-metalated tetraphenyl-porphyrins are detected for **HO<sub>2</sub>C-ZnP-TEMPO**, namely a Soret band located at 426 nm and two Q bands peaking at 555 and 598 nm. In all cases, the presence of the TEMPO moiety did not impact the absorption properties of the ZnP-TEMPO dyads, since there is no electronic communication between ZnP and TEMPO due to the absence of a  $\pi$ -



conjugated pathway connecting the two moieties. Interestingly, both the reference zinc porphyrins, and ZnP-TEMPO dyads are emissive without exhibiting any significant quenching of the fluorescence in the dyads. Since the singlet excited of the porphyrin is not quenched by the TEMPO moiety, neither an electron transfer nor an intersystem crossing process occurs (**Figures 4.17**).

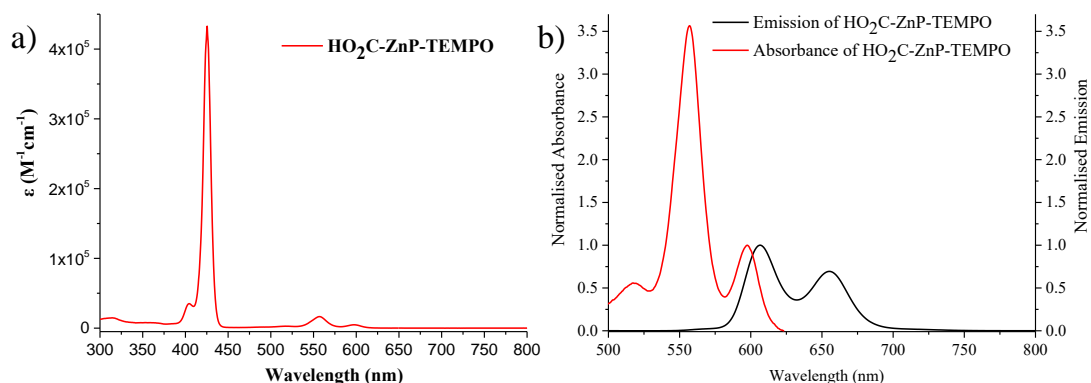


**Figure 4.16** UV-Vis absorption spectrum (a) and overlay of the absorption and emission spectra ( $\lambda_{\text{exc}} = 430$  nm) (b) of **HO<sub>2</sub>C-ZnP-TEMPO** in THF.

**Table 4.2** Key electrochemical and spectroscopic data for the porphyrins discussed in this part. Oxidation potentials of the compounds recorded on meso-ITO and Gibbs free energy of the electron injection ( $\Delta G_{\text{inj}}$ ) in TiO<sub>2</sub> and hole shift reaction ( $\Delta G_{\text{hs}}$ ).

Dye	$\lambda_{\text{abs}}/ \text{nm}$ ( $\epsilon/\text{M}^{-1}\text{cm}^{-1}$ )	$\lambda_{\text{em}}$ (nm)	$E_{00}^{\text{a}}$ (eV)	$E_{\text{Ox}}(\text{TEMPO})$ (V vs. SCE)	$E_{\text{Ox}}(\text{ZnP})$ (V vs. SCE)	$\Delta G_{\text{inj}}^{\text{b}}$ (eV)	$\Delta G_{\text{hs}}^{\text{c}}$ (eV)
<b>HO<sub>2</sub>C-ZnP</b>	426 (452.3), 555 (16.6), 598 (5.7)	607, 656	2.06	-	0.78	-0.58 (-0.41)	-
<b>HO<sub>2</sub>C-ZnP-TEMPO</b>	426 (432.8), 557 (16.8), 598 (4.8)	607, 655	2.06	0.73	0.79	-0.57 (-0.40)	-0.06
<b>hyd-ZnP</b>	426 (445.3), 556 (16.6), 598 (4.9)	607, 656	2.06	-	0.86	-0.50 (-0.34)	-
<b>hyd-ZnP-TEMPO</b>	426 (417.8), 557 (15.5), 597 (4.7)	606, 655	2.06	0.74	0.84	-0.52 (-0.35)	-0.1

<sup>a</sup>determined with the wavelength ( $\lambda_{\text{inter}}$ ) at the intersection of the normalized absorption and emission spectra with the equation  $E_{00} = 1240/\lambda_{\text{inter}}$ .

<sup>b</sup>calculated according to the equation:  $\Delta G_{\text{inj}} = E_{\text{Ox}}(\text{ZnP}) - E_{00} - E_{\text{CB}}(\text{TiO}_2)$ , with  $E_{\text{CB}}(\text{TiO}_2) = -0.7$  V vs. SCE in acetonitrile<sup>305</sup> and in parentheses in buffer at pH = 8 with  $E_{\text{CB}}(\text{TiO}_2) = -0.87$  V vs. SCE at pH = 8.<sup>306</sup>

<sup>c</sup>calculated according to the equation:  $\Delta G_{\text{hs}} = E_{\text{Ox}}(\text{TEMPO}) - E_{\text{Ox}}(\text{ZnP})$ .

<sup>305</sup> Hagfeldt, A.; Graetzel, M. *Chemical Reviews (Washington, DC, United States)* **1995**, 95 (1), 49.

<sup>306</sup> Kavan, L.; T etreault, N.; Moehl, T.; Gr atzel, M. *J. Phys. Chem. C* **2014**, 118 (30), 16408.

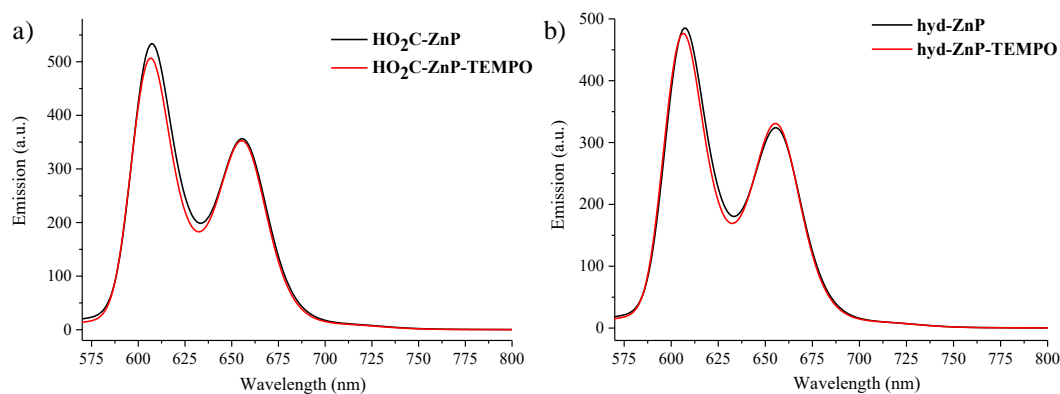


**Figure 4.17** Emission spectra recorded in THF from isoabsorbing solutions at the excitation wavelength with  $\lambda_{\text{exc}} = 556$  nm of (a) **HO<sub>2</sub>C-ZnP** and **HO<sub>2</sub>C-ZnP-TEMPO** and (b) of **hyd-ZnP** and **hyd-ZnP-TEMPO**.

#### Electrochemical properties

The redox potentials of the zinc porphyrin reference and the porphyrin-TEMPO dyads were investigated by means of cyclic voltammetry upon their chemisorption on mesoporous indium tin oxide (meso-ITO), in acetonitrile containing lithium perchlorate (0.1 M) as supporting electrolyte (**Figure 4.18**). The two oxidation processes are quite close and consequently not well separated in the cyclic voltammograms. However, it is clear that the oxidation of zinc porphyrin occurs at about 100 mV higher potential than that of TEMPO, leaving a modest (but non null) driving force for the hole shift reaction from the oxidized zinc porphyrin to the TEMPO unit ( $^+\text{ZnP-TEMPO} \rightarrow \text{ZnP-TEMPO}^+$ ). However, this small driving force does not exclude an electron transfer process from TEMPO to an oxidized sensitizer on TiO<sub>2</sub> as demonstrated by Yang et al.<sup>307</sup> On the other hand, the electron injection is thermodynamically favorable by at least -0.37 eV in borate buffer pH = 8 (**Table 4.2**). Upon the addition of methoxybenzyl alcohol in acetonitrile electrolyte, the cyclic voltammogram of the **HO<sub>2</sub>C-ZnP-TEMPO** on meso-ITO shows the appearance of an irreversible wave attributed to the catalytic oxidation of alcohol by TEMPO (onset potential at 0.74 V vs. SCE, **Figure 4.19**).

<sup>307</sup> Yang, W.; Vlachopoulos, et al., *G. Phys. Chem. Chem. Phys.* **2015**, *17* (24), 15868.

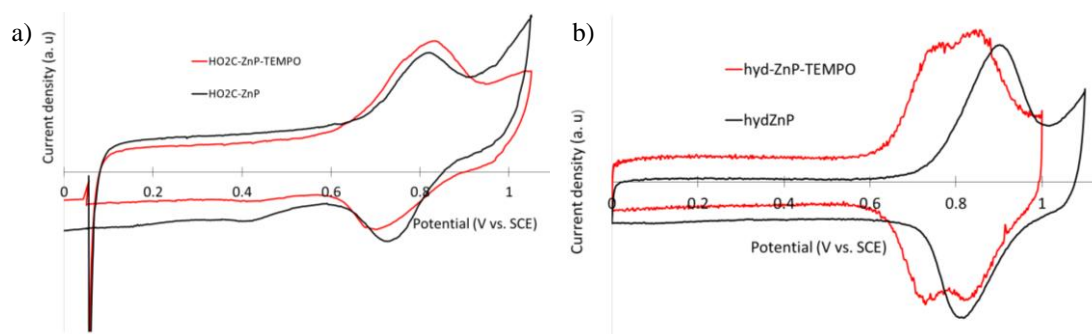


**Figure 4.18** Overlay of cyclic voltammograms of (a) **HO<sub>2</sub>C-ZnP** and **HO<sub>2</sub>C-ZnP-TEMPO** and (b) **hyd-ZnP** and **hyd-ZnP-TEMPO**, chemisorbed on meso-ITO and recorded in acetonitrile with LiClO<sub>4</sub> (0.1 M) as supporting electrolyte solutions.

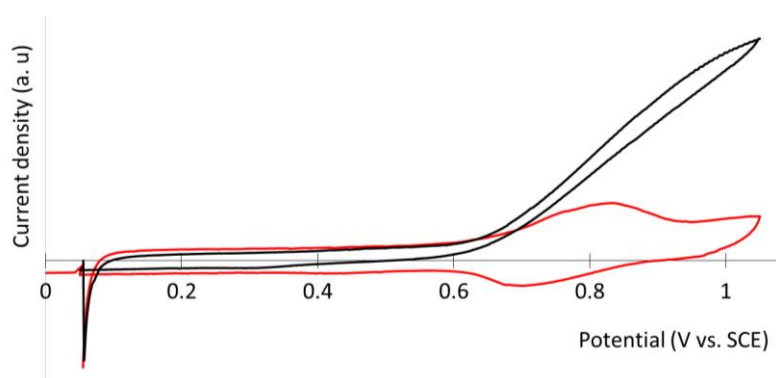


**Figure 4.19** Cyclic voltammograms of **HO<sub>2</sub>C-ZnP-TEMPO** chemisorbed on meso-ITO and recorded in acetonitrile with LiClO<sub>4</sub> (0.1 M) as supporting electrolyte solutions without (red trace) and with methoxybenzyl-alcohol (black trace). Scan rate 50 mV/s.

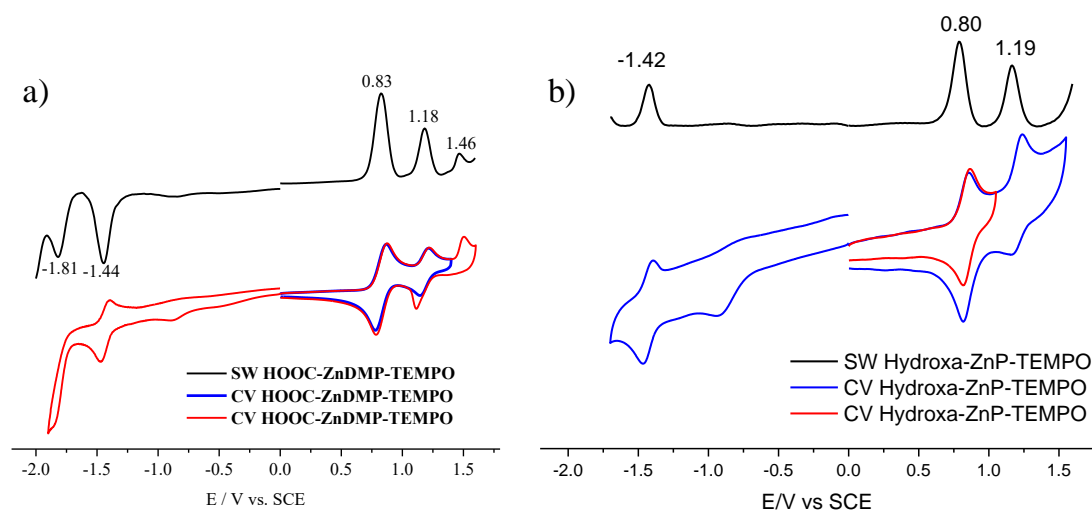


**Figure 4.20** Cyclic voltammograms and square wave spectra of **HO<sub>2</sub>C-ZnP-TEMPO** and **hyd-ZnP-TEMPO** in DCM solution.

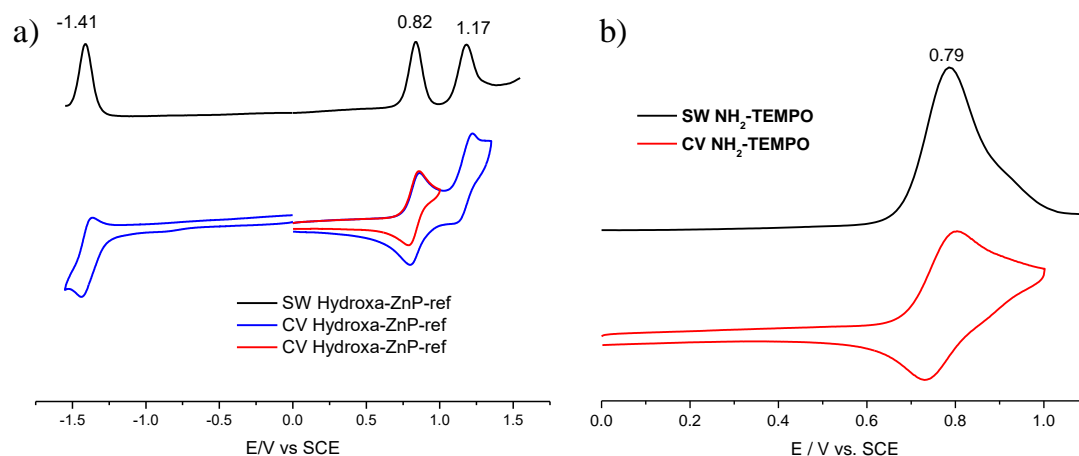


**Figure 4.21** Cyclic voltammograms and square wave spectra of **hyd-ZnP** and **NH<sub>2</sub>-TEMPO** in DCM solution.

Additionally, to the above electrochemical studies on the indium tin oxide surface, we also investigated the redox potentials of the zinc porphyrin reference and porphyrin-TEMPO dyads in solution. The two oxidation processes are not separated at all in the cyclic voltammograms in DCM (**Figures 4.20 - 4.21**), however we present the corresponding data for comparison reasons in **Table 4.3**.

**Table 4.3** Oxidation potentials of the compounds recorded in DCM solution. The supporting electrolyte was TBAPF<sub>6</sub> (0.1 M), the working electrode was glassy carbon, the reference electrode was Ag/AgCl, scan speed 100 mV/sec, ferrocene was used as internal standard and in the above conditions exhibited a peak at 0.46 V vs. SCE.

Compound	$E_{1/2}(\text{red}^2)$	$E_{1/2}(\text{red}^1)$	$E_{1/2}(\text{ox}^1)$	$E_{1/2}(\text{ox}^2)$
<b>Hydroxa-ZnP-TEMPO</b>		-1.42	0.80	1.19
<b>HO<sub>2</sub>C-ZnP-TEMPO</b>	-1.81	-1.44	0.83	1.18
<b>Hydroxa-ZnP-ref</b>		-1.41	0.82	1.17
<b>NH<sub>2</sub>-TEMPO</b>			0.79	

#### *Quantum chemical calculations and transient absorption photophysical study*

Further characterization with quantum chemical calculations and transient absorption spectroscopy was followed and focused on the most promising dyad system. We have performed DFT calculations on **hyd-ZnP-TEMPO**, which confirmed that the

unpaired electron is confined on the **TEMPO** and that the oxidation yields a change of density localized on that unit specifically. The saturated bridge prevents the delocalization between the two moieties (there is no  $\pi$ -conjugated system). The studies showed also that there is a small driving force for the hole shift, once **hyd-ZnP-TEMPO** is oxidized, which is consistent with the electrochemical experimental results.

Electronic transient absorption (TA) measurements were performed with the **hyd-ZnP-TEMPO** dyad and the reference **hyd-ZnP** dye onto TiO<sub>2</sub> films in the borate buffer pH 8. The fs-ps measurements were carried out upon 550 nm excitation of films (**Figure 4.22A**). After excitation, the TA spectra exhibit an intense excited-state absorption (ESA) band around 460 nm that can be attributed to the local S<sub>1</sub> state of ZnP. ESA is also observed above 590 nm and is modulated by the overlapping negative contributions from the ground-state bleach (GSB) at 600 nm as well as the stimulated emission (SE) around 610 and 660 nm. The 460 nm band loses about 80% of its intensity within 100 ps and the contribution of the SE at 670 nm decays as well. The changes in the TA spectra were consistent with the formation of the radical cation of the ZnP subunit upon charge injection into TiO<sub>2</sub>. Clear detection of ZnP cation was achieved with a second series of fs-ps TA measurements with low concentration of adsorbed dyes to allow for monitoring the Soret band region. **Figure 4.22B** shows that the decay of the S<sub>1</sub> band at 460 nm is accompanied by a partial recovery of the GSB in the Soret region as well as by the rise of a new band at 405-410 nm, which can be assigned to the radical cation of ZnP.

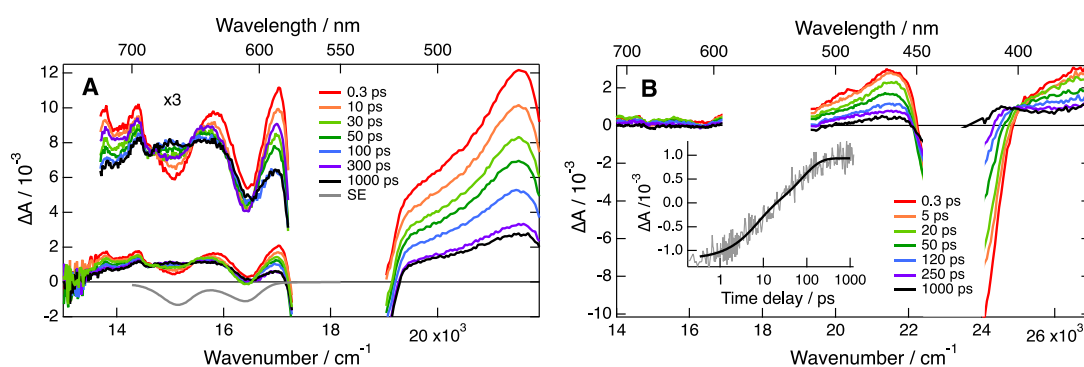


**Figure 4.22** Fs-ps transient absorption spectra recorded at various time delays after 550 nm excitation of TiO<sub>2</sub> films with high (A) and low (B) concentrations of adsorbed **hyd-ZnP-TEMPO**. The gray line in A represents the stimulated emission spectrum in acetonitrile. The inset in B shows the time evolution of the absorbance of the porphyrin cation band at 405 nm.

The slower cation dynamics were monitored using ns- $\mu$ s TA upon 532 nm excitation. As shown in **Figure 4.23**, both the GSB and the ZnP cation bands decay concurrently on multiple timescales with 2, 50 ns and 10  $\mu$ s time constants to a weak residual spectrum with  $>100 \mu$ s decay time. Because of the absence of spectroscopic signature of the TEMPO cation in the 370-1500 nm region, it is impossible to determine whether the decay of the ZnP cation and the recovery of the GSB are due to a hole shift from ZnP cation to TEMPO or to charge recombination with the semi-conductor. The same TA measurements, performed with the **hyd-ZnP** reference compound in TiO<sub>2</sub>, also show the formation of the ZnP cation. The decay of the ZnP cation band does not differ significantly from that measured with **hyd-ZnP-TEMPO**. However, this similarity does not exclude occurrence of hole shift to TEMPO, but could result from a slow hole shift that only partially competes with recombination.

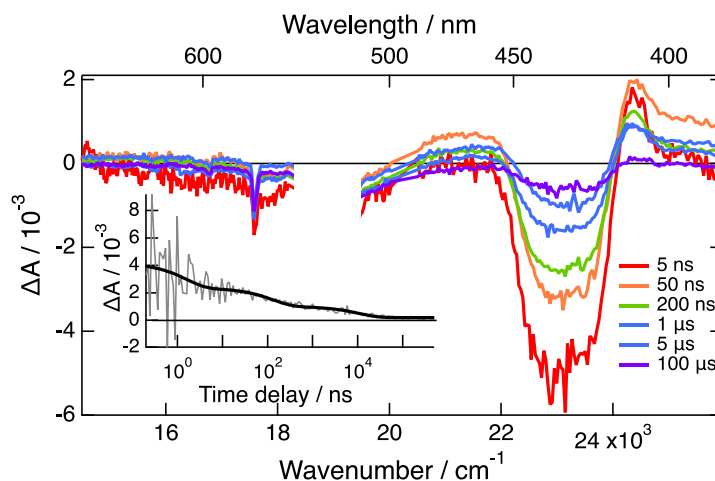


**Figure 4.23** ns-  $\mu$ s transient absorption spectra recorded at various time delays after 532 nm excitation of a TiO<sub>2</sub> film with a low concentration of adsorbed **hyd-ZnP-TEMPO**. The inset shows the time evolution of the absorbance of the porphyrin cation band at 410 nm.

#### Photovoltaic performances in dye sensitized solar cells

Before studying the photocatalytic activity of the synthesized dyads, their photovoltaic performances were assessed in DSSC (**Figure 4.24**). This examination enables to screen the best conditions for dyeing the TiO<sub>2</sub> films. Additionally, in order for a “dye-catalyst” dyad to be efficient in DSPECs, the evolution of enough photocurrent in DSSC is required, so the photovoltaic efficiency in DSSC will show initial insights into the potential of these systems for photocatalysis.



**Figure 4.24** Pictures of the fabricated DSSCs.

Initially, we tested different soaking times varying from 1 to 8 hours and concluded that 3 hours is the optimal amount of soaking time (toluene/ethanol (1/1) at the concentration of 0.2 mM). Then, these conditions were used to chemisorb the dyes on nanocrystalline TiO<sub>2</sub> electrodes that were used as photoanodes to fabricate DSSCs with iodide/triiodide redox couple in acetonitrile electrolyte. The characteristics of the solar cells, such as short circuit current density ( $J_{sc}$ ), open circuit voltage ( $V_{oc}$ ), fill factor (FF) and power conversion efficiency (PCE) are summarized in **Table 4.4**. Typical current/voltage curves and incident photon-to-current efficiency (IPCE) spectra are shown in **Figure 6.4.47** and **Figure 6.4.48** respectively.

**Table 4.4** Metrics of the different dyes in DSSCs under calibrated AM1.5 (100 mW/cm<sup>2</sup>) sunlight simulator.

	$J_{sc}$ (mA/cm <sup>2</sup> )	$V_{oc}$ (mV)	FF (%)	PCE (%)
<b>hyd-ZnP</b>	1.82 ± 0.08	573 ± 3	69 ± 1	0.72 ± 0.01
<b>hyd-ZnP-TEMPO</b>	3.45 ± 0.2	632 ± 5	72 ± 1	1.65 ± 0.05
<b>HO<sub>2</sub>C-ZnP</b>	1.77 ± 0.2	570 ± 2	69 ± 2	0.70 ± 0.02
<b>HO<sub>2</sub>C-ZnP-TEMPO</b>	4.3 ± 0.4	645 ± 10	72 ± 2	2.0 ± 0.2

We have to point out that the power conversion efficiencies (PCEs) of these porphyrin systems are indeed much lower than those of the best push-pull porphyrin sensitizers, which reach PCEs around 13-14%.<sup>308,309</sup> Compared with previously reported analogous simple tetra-aryl zinc porphyrins,<sup>310</sup> the dyes of this study display

<sup>308</sup> Ji, J.-M.; Zhou, H.; Eom, Y. K.; Kim, C. H.; Kim, K. *Adv. Energy Mater.* **2020**, *10* (15), 2000124.

<sup>309</sup> Mathew, S.; Yella, A.; Gao, P.; Humphry-Baker, R.; Curchod, B. F. E.; Ashari-Astani, N.; Tavernelli, I.; Rothlisberger, U.; Nazeeruddin, M. K.; Grätzel, M. *Nature Chem.* **2014**, *6* (3), 242.

<sup>310</sup> Kumar, R.; Sankar, M.; Sudhakar, V.; Krishnamoorthy, K. *New J. Chem.* **2016**, *40* (7), 5704.

lower PCEs mainly due to their lower  $J_{sc}$ , although one publication from Diau and co-workers<sup>311</sup> reports similar performances with our systems. There is a possibility that the electron withdrawing substituent (amide or ester) in *trans* position compared to the anchoring group changes the electron distribution in the excited state and renders the electron injection efficiency less favored.

Moreover, based on the results of the photovoltaic measurements, two significant conclusions can be drawn. First, the “ZnP-TEMPO” dyads outperforms the parent reference zinc porphyrins without the TEMPO moiety. When the TEMPO moiety is present higher  $J_{sc}$  and  $V_{oc}$  values are obtained, resulting in more than twice or even three times higher PCEs. The higher photovoltaic performances in DSSCs of the dyads can be attributed to a longer-lived charge separated state, which is the result from the hole shift from the zinc porphyrin radical cation that is formed after electron injection in  $TiO_2$ . Indeed, the longer distance between the  $TiO_2$  surface and the positive charge on TEMPO most certainly decreases the rate of charge recombination, which enhances the  $V_{oc}$  and the  $J_{sc}$ .<sup>312</sup> Although the driving force of the hole shift reaction is weak as discussed in paragraph 4.1 (about -0.1 eV), it appears sufficient for it to happen quite efficiently. Furthermore, the dyad with the hydroxamic acid illustrated higher photocurrent density compared to the one with carboxylic acid. Similar results were reported before and can be ascribed to faster electron injection in  $TiO_2$ , probably due to a larger electronic coupling.<sup>313,314</sup>

### Photocatalytic performances in DSPEC

The photocatalytic performances of the Zn-porphyrin-TEMPO dyads were explored using the *para*-methoxybenzyl alcohol as substrate, since it is a common reference compound used in many studies with TEMPO catalysts, however the systems can be compatible with other alcohols as well.<sup>315</sup> In addition, two different reaction media were explored, water and acetonitrile (MeCN). The latter solvent can also be

---

<sup>311</sup> Shrestha, M.; Si, L.; Chang, C.-W.; He, H.; Sykes, A.; Lin, C.-Y.; Diau, E. W.-G. *J. Phys. Chem. C* **2012**, *116* (19), 10451.

<sup>312</sup> Bonhôte, P.; Moser, J.-E.; Humphry-Baker, R.; Vlachopoulos, N.; Zakeeruddin, S. M.; Walder, L.; Grätzel, M. *J. Am. Chem. Soc.* **1999**, *121* (6), 1324.

<sup>313</sup> Higashino, T.; Kurumisawa, Y.; Cai, N.; Fujimori, Y.; Tsuji, Y.; Nimura, S.; Packwood, D. M.; Park, J.; Imahori, H. *ChemSusChem* **2017**, *10* (17), 3347.

<sup>314</sup> Koenigsmann, C.; Ripolles, T. S.; Brennan, B. J.; Negre, C. F. A.; Koepf, M.; Durrell, A. C.; Milot, R. L.; Torre, J. A.; Crabtree, R. H.; Batista, V. S. et al. *Phys. Chem. Chem. Phys.* **2014**, *16* (31), 16629.

<sup>315</sup> Nutting, J. E.; Rafiee, M.; Stahl, S. S. *Chem. Rev.* (**2018**, *118* (9), 4834.



appropriate for alcohols that are not water soluble. Additionally, acetonitrile is compatible with CO<sub>2</sub> reduction photocatalysis,<sup>316</sup> which might be a valuable reaction to perform at the cathode in future tandem photocatalytic devices. The photocatalytic properties were analyzed with the dye chemisorbed on nanocrystalline TiO<sub>2</sub> films (**Figure 4.25**), similar to those used in the DSSCs experiments discussed above. Then, the films were dipped in an electrolyte solution containing 50 mM of *para*-methoxybenzyl alcohol using a standard three-electrode photoelectrochemical cell under 1 sun illumination (about 100mW/cm<sup>2</sup> with 400 nm cutoff filter), with a platinum grid as the counter electrode and a saturated calomel electrode (SCE) as reference. The quantity of *para*-methoxybenzaldehyde produced in the electrolyte under light irradiation was determined by gas chromatography after its extraction with DCM.

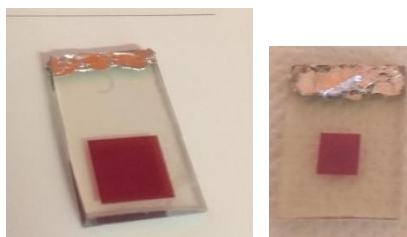


**Figure 4.25** Pictures of a **hyd-ZnP-TEMPO** chemisorbed on the nanocrystalline TiO<sub>2</sub> films.

### *Measurements in aqueous solutions*

There are three types of experiments described in this section:

- Long-term photolysis experiments, where the photocurrent density responses are monitored over a period of time, recorded at a constant potential of 0 V vs. SCE
- chopped light voltammetry measurements, where the photocurrent responses are recorded at a constant potential of 0 V vs. SCE; and the light was turned on and off over a short period of time to demonstrate the photoresponse of the electrode and
- chopped light linear sweep voltammetry measurements recorded under white light irradiation where the potential was varied from -0.5 V to 0.3 V vs. SCE with scan rate 5 mV/s; and the light was turned on and off over a short period of time

---

<sup>316</sup> Kumar, B.; Llorente, M.; Froehlich, J.; Dang, T.; Sathrum, A.; Kubiak, C. P. Photochemical and Photoelectrochemical Reduction of CO<sub>2</sub>. *Annu. Rev. Phys. Chem.* **2012**, *63* (1), 541.

In an effort to identify the most appropriate anchoring group for the Zn-porphyrin-TEMPO dyads, we investigated the photo-response of the dyads **hyd-ZnP-TEMPO**, **HOOC-ZnP-TEMPO**, **H<sub>2</sub>O<sub>3</sub>P-ZnP-TEMPO**, **Py<sub>3</sub>ZnP-TEMPO** along with the **hyd-ZnP** and **HOOC-ZnP** reference compounds. In order to compare their activity, we recorded the photocurrent density responses versus the irradiation time in long-term experiments (**Figure 4.26**) as well as chopped light photocatalysis experiments (**Figure 4.27**). As it is illustrated in **Figure 4.26**, the best performing dyad is the one that bears a hydroxamic acid group while the carboxylic acid exhibits similar performance in aqueous borate buffer solution. Regarding the phosphonic acid and the pyridyl peripheral substitution on the porphyrin photosensitizer, we observed reduced catalytic activity compared to the hydroxamic and carboxylic acid derivatives (**Figures 4.26 - 4.27**).

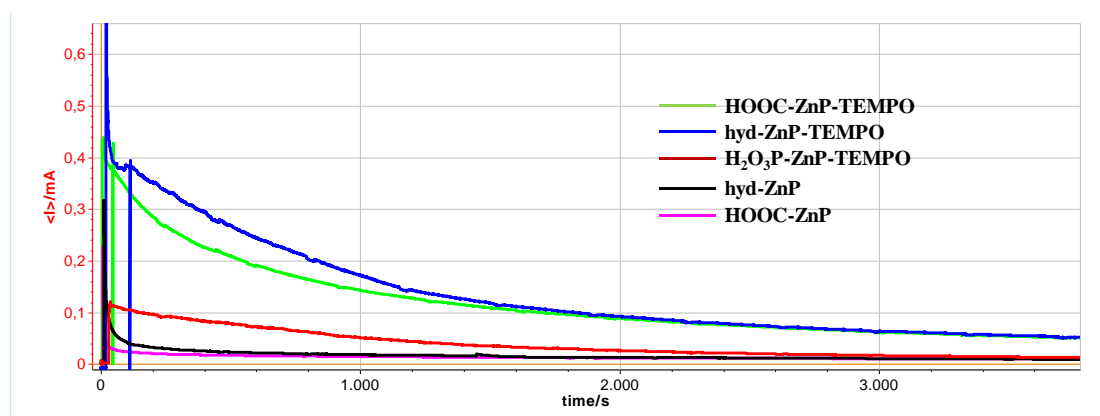


**Figure 4.26** Photocurrent density responses during long-term photolysis experiments with TiO<sub>2</sub> photoelectrodes coated with dyads **hyd-ZnP-TEMPO**, **HOOC-ZnP-TEMPO**, **H<sub>2</sub>O<sub>3</sub>P-ZnP-TEMPO** and **hyd-ZnP** and **HOOC-ZnP** reference compounds in 0.1 M borate buffer pH = 9 containing *para*-methoxybenzyl alcohol (50 mM) and [NaClO<sub>4</sub>] = 0.1 M. All experiments were recorded under white light with a 400 nm cutoff filter.

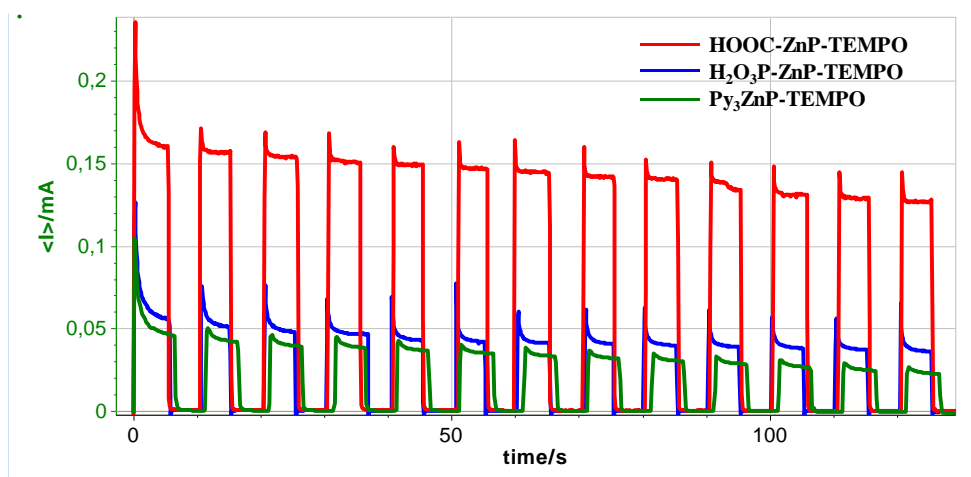


**Figure 4.27** Chopped light voltammetry measurements recorded at a constant potential of 0 V vs. SCE of  $\text{TiO}_2$  photoelectrodes coated with **HOOC-ZnP-TEMPO**, **H<sub>2</sub>O<sub>3</sub>P-ZnP-TEMPO** and **Py<sub>3</sub>ZnP-TEMPO** in 0.1 M borate buffer at pH = 9 containing [para-methoxybenzyl alcohol] = 50 mM, [NaClO<sub>4</sub>] = 0.1. All experiments were recorded under light with a 400 nm cutoff filter.

The above ranking of the photocatalytic activity was verified from analogous chopped light linear sweep voltammetry measurements (**Figure 4.28**).

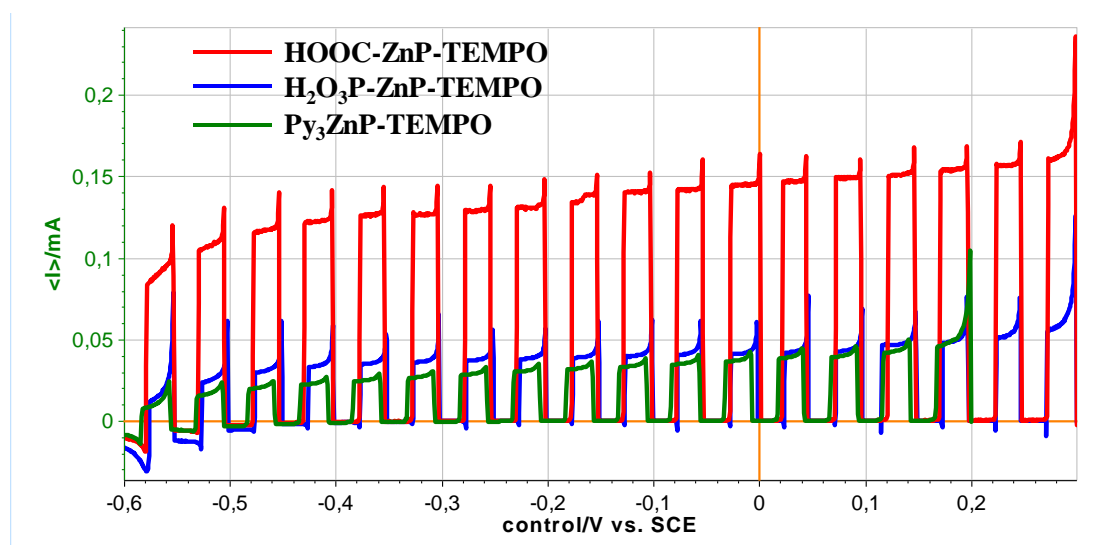


**Figure 4.28** Chopped light linear sweep voltammetry measurements recorded under white light irradiation (white light Zhaner lamp about  $350 \text{ W/m}^2$ ) of **HOOC-ZnP-TEMPO**, **H<sub>2</sub>O<sub>3</sub>P-ZnP-TEMPO** and **Py<sub>3</sub>ZnP-TEMPO** on  $\text{TiO}_2$  film with 0.1 M borate buffer at pH = 9 containing [para-methoxybenzyl alcohol] = 50 mM, [NaClO<sub>4</sub>] = 0.1 M. Scan starts from -0.5 V and ends at 0.3 V vs. SCE with scan rate 5 mV/s.

Subsequently, we proceeded with the optimization of the catalytic conditions testing different buffer electrolytes. Since alcohol oxidation catalyzed by TEMPO is pH dependent and usually works better in basic medium with an optimal pH situated around 10,<sup>315,317,318</sup> we initially tested carbonate and borate buffer solutions at pH = 10. As it is depicted in **Figure 4.29**, the borate buffer was proved more efficient than the carbonate (**Figures 6.4.49-6.4.50**) and therefore we performed our experiments in borate buffer.

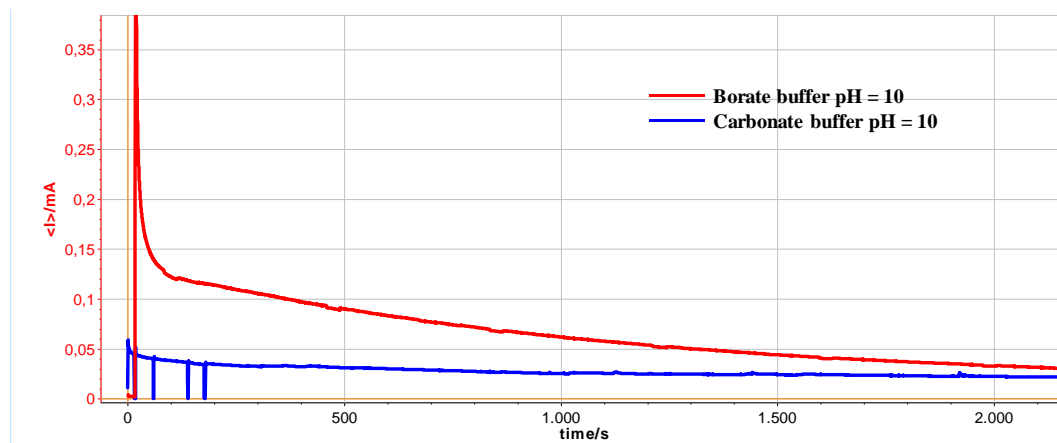


**Figure 4.29** Photocurrent density responses during long-term photolysis experiments with  $\text{TiO}_2$  photoelectrodes coated with the dyad **hyd-ZnP-TEMPO**, containing *para*-methoxybenzyl alcohol (50 mM) in 0.1 M borate buffer (red trace) and 0.1 M carbonate buffer both at pH = 10.

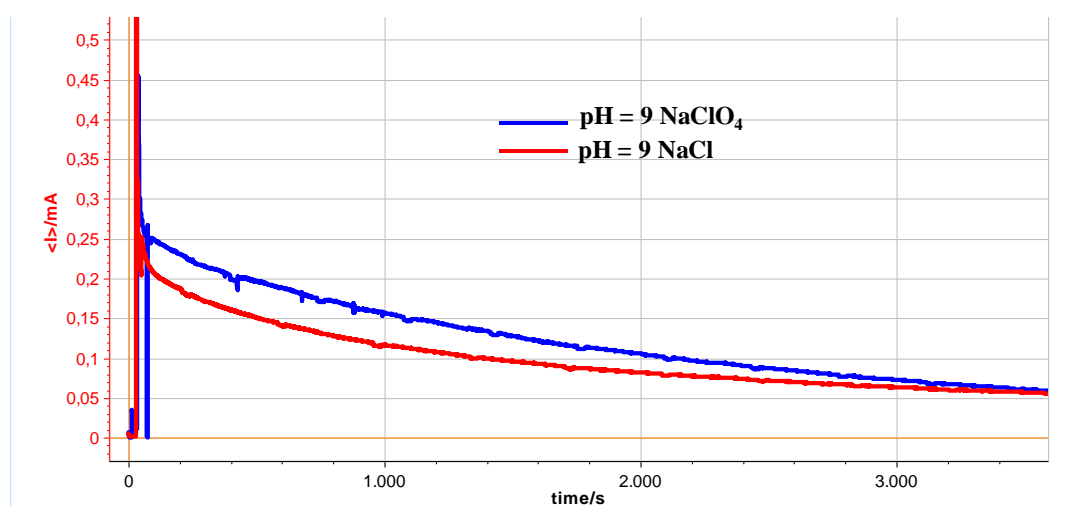


**Figure 4.30** Photocurrent density responses during long-term photolysis experiments with  $\text{TiO}_2$  photoelectrodes coated with the dyad **hyd-ZnP-TEMPO**, containing *para*-

<sup>317</sup> Rafiee, M.; Miles, K. C.; Stahl, S. S. *J. Am. Chem. Soc.* **2015**, *137* (46), 14751.

<sup>318</sup> Hickey, D. P.; McCamant, M. S.; Giroud, F.; Sigman, M. S.; Minter, S. D. *J. Am. Chem. Soc.* **2014**, *136* (45), 15917.

methoxybenzyl alcohol (50 mM) in 0.1 M borate buffer (red trace) and 0.1 M carbonate buffer both at pH = 10.

Different electrolytes in borate buffer were tested, namely NaCl and NaClO<sub>4</sub> as presented in **Figure 4.30**. NaClO<sub>4</sub> presented increased photocurrent response, so we conducted our further optimization using this electrolyte in borate buffer. We examined the impact of the pH, using borate buffer solutions between pH 7.5 and 10. The photocurrent responses under long-term irradiation of **hyd-ZnP-TEMPO** at different pHs is shown in **Figure 4.31** while the turnover number, turnover frequency (TOF) and faradic efficiency (FE) are gathered in **Table 4.5**.

**Table 4.5** Photocurrent densities, TONs, TOFs and FEs measured at different electrolytes with **hyd-ZnP-TEMPO** or **hyd-ZnP + ac-TEMPO** on 1 cm<sup>2</sup> nanocrystalline TiO<sub>2</sub> films for *para*-methoxybenzyl alcohol oxidation.

Catalyst	hyd-ZnP-TEMPO				hyd-ZnP + ac-TEMPO <sup>a</sup>	
	Borate pH = 7.5	Borate pH = 8	Borate pH = 9	Borate pH = 10	CH <sub>3</sub> CN + MeImd	CH <sub>3</sub> CN + MeImd
J at 500 sec (mA/cm <sup>2</sup> )	0.15±0.02	0.20±0.05	0.13±0.02	0.09±0.02	0.10±0.02	0.12±0.04
TON	16±2	26±4	15±3	9±2	13±2	10±2 <sup>b</sup> (0.15±0.03)
TOF (h <sup>-1</sup> )	28±3	47±7	28±5	15±4	24±4	18±3 <sup>b</sup> (0.27±0.05)
FE (%)	86±5	82±6	80±10	93±10	76±8	85±6

<sup>a</sup>Experiments with **hyd-ZnP** : [**ac-TEMPO**] = 1 mM; calculated from the quantity of **hyd-ZnP-TEMPO** loaded on the electrode;

<sup>b</sup>calculated from the quantity of **hyd-ZnP** loaded on the electrode and in parentheses from the number of mole of **ac-TEMPO** in solution.

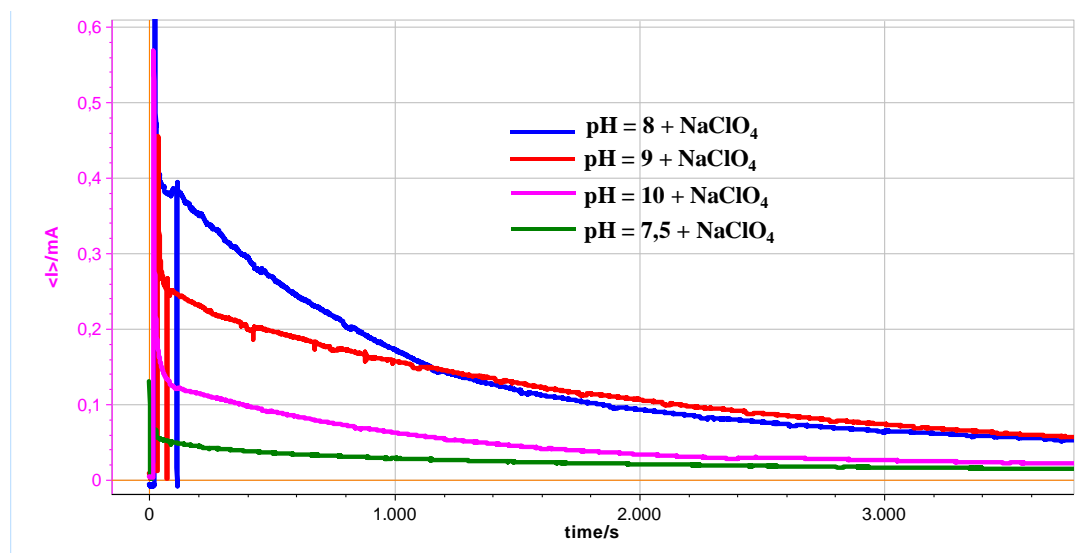


**Figure 4.31** Typical photocurrent density responses during long-term photolysis experiments with TiO<sub>2</sub> photoelectrodes coated with hyd-ZnP-TEMPO in 0.1 M borate buffer containing *para*-methoxybenzyl alcohol (50 mM) and [NaClO<sub>4</sub>] = 0.1 M at different pHs. All experiments were recorded in the same irradiation conditions: white light (about 100 mW/cm<sup>2</sup>) with a 400 nm cutoff filter.

Upon implementing all the optimized conditions, we carried on with chopped light linear sweep voltammetry (LSV) experiments using the **hyd-ZnP-TEMPO** and the **hyd-ZnP** reference molecule between 0.3 V until -0.5 V vs. SCE in borate buffer at pH = 8 with *para*-methoxybenzyl alcohol. As depicted in **Figure 4.32**, the current density produced by the dyad is much higher than by the zinc porphyrin lacking the TEMPO moiety, highlighting the crucial role of the organic catalyst. As expected, the photocurrent density decreased in negative potentials, however, it was clearly high enough until potential -0.3 V vs. SCE. This means that under light irradiation the photoanode can perform alcohol oxidation at much easier (at more negative potential) than in the dark (**Figure 4.19**). In these electrocatalytic conditions, *para*-methoxybenzyl alcohol oxidation occurs at an onset potential of 0.74 V vs. SCE, indicating that light irradiation provides a significant improvement of approximately 1 V. However, in comparison with the thermodynamic oxidation potential of benzyl alcohol (-0.51 V vs. SCE at pH = 8),<sup>319</sup> the applied potential is still more positive by about 0.5 V.

<sup>319</sup> Wang, Y.; Gonell, S.; et al. *ACS Appl. Energy Mater.* **2019**, 2 (1), 97.

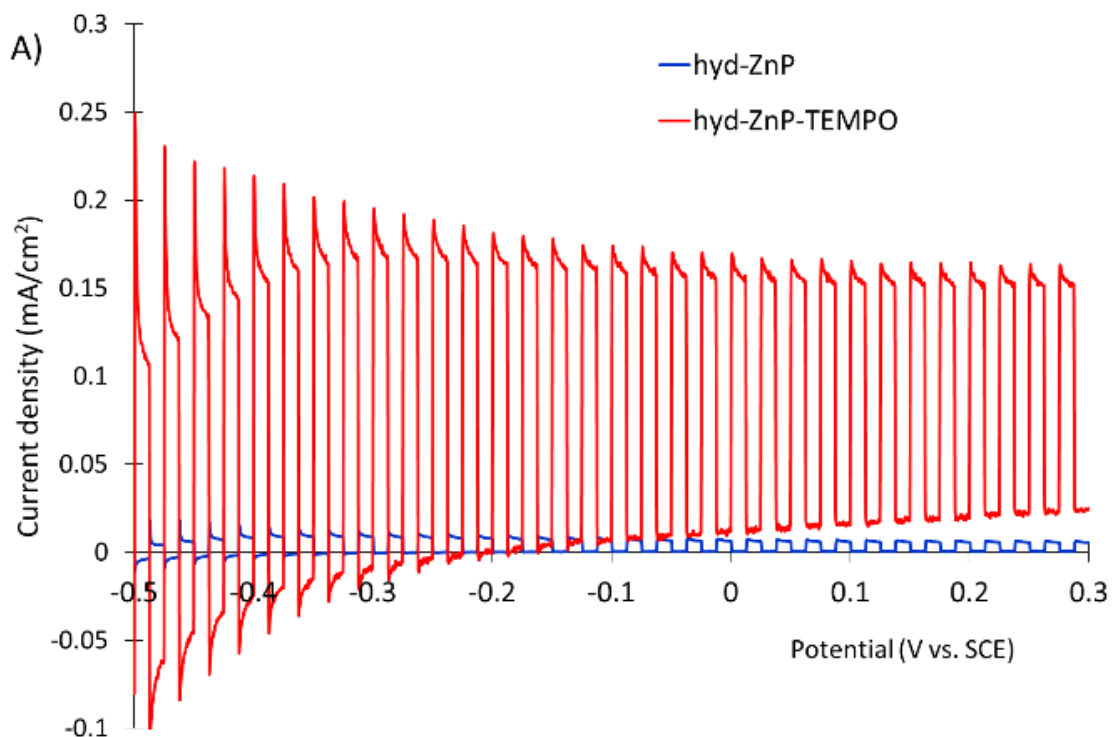


**Figure 4.32** Chopped light linear sweep voltammetry measurements recorded under white light irradiation (white light Zhaner lamp about  $350 \text{ W/m}^2$ ) of **hyd-ZnP-TEMPO** and **hyd-ZnP** on  $\text{TiO}_2$  film with 0.1 M borate buffer at  $\text{pH} = 8$  containing [*para*-methoxybenzyl alcohol] = 50 mM,  $[\text{NaClO}_4] = 0.1 \text{ M}$ . Scan starts from -0.5 V and ends at 0.3 V vs. SCE with scan rate 5 mV/s.

We conducted experiments at a constant potential of 0 V vs. SCE recording the chopped light photocurrent densities for **hyd-ZnP-TEMPO** in borate buffer at  $\text{pH} = 8$  in presence and in absence of alcohol (**Figure 4.33**). The photocurrent density is significantly lower in the absence of methoxybenzyl alcohol than in its presence, a result which proves indirectly the catalysis accomplished by the TEMPO moiety (**Figure 4.33**). Moreover, the voltamogram exhibits spikes of larger amplitudes without the alcohol in solution during the switch on and off light cycles. The cathodic spikes, observed when the light is turned off, might result from charge recombination between the injected electrons in  $\text{TiO}_2$  and the oxidized TEMPO, because it cannot be reset to its neutral state by reaction with the alcohol. The spikes that are observed directly after light irradiation most likely indicate that the photocurrent density is limited by mass transport of alcohol to the photocatalyst inside the pores of  $\text{TiO}_2$ .

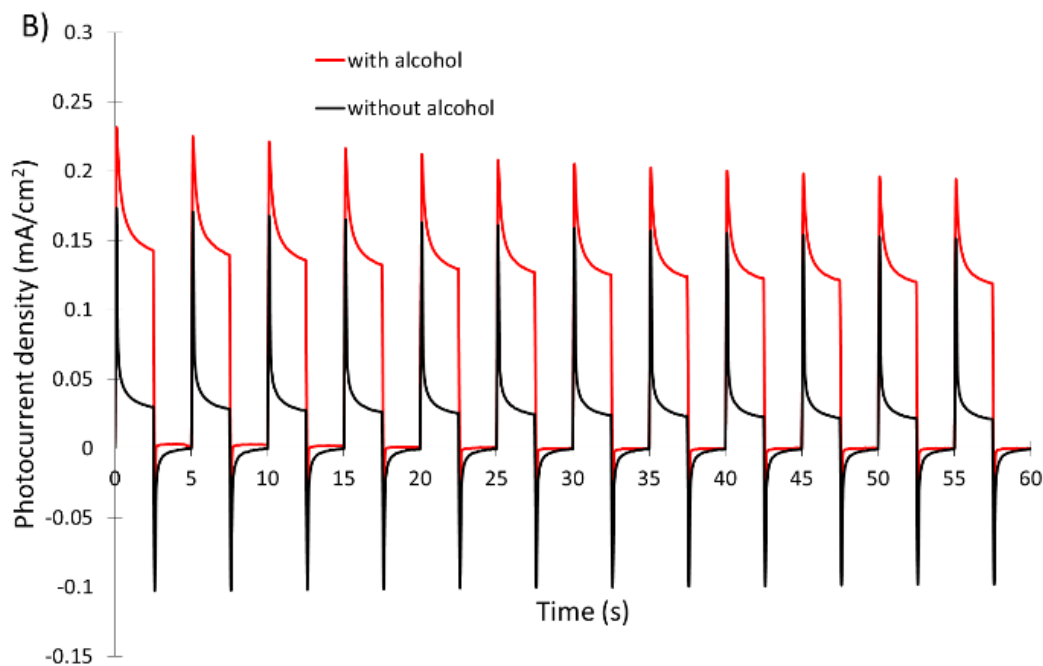


**Figure 4.33** Chopped light voltammetry measurements of **hyd-ZnP-TEMPO** recorded at a constant potential of 0 V vs. SCE with (red trace) and without (black trace) *para*-methoxybenzyl alcohol (10 mM) in the same conditions as above (**Figure 4.32**).

The previous photocatalytic investigation conducted at different pHs under light irradiation, provided several interesting conclusions. Firstly, the parent **hyd-ZnP** compound has no photocatalytic activity, since no significant quantity of *para*-methoxybenzaldehyde was found by GC analysis, even in the optimal conditions with borate buffer at pH = 8. Secondly, the dyad **hyd-ZnP-TEMPO** can indeed catalyze the light driven oxidation of *para*-methoxybenzyl alcohol with a quite high efficiency in aqueous electrolytes, since the FE is superior or equal to 80% and the DSPEC can reach a current density of about 200  $\mu\text{A}/\text{cm}^2$ . These values are relatively high not only in comparison with those previously reported for alcohol oxidation in DSPEC with ruthenium catalyst,<sup>320,321,322</sup> but also with those obtained for water oxidation in TiO<sub>2</sub> based DSPECs<sup>323,324</sup> and for H<sub>2</sub> evolution in NiO DSPECs.<sup>325</sup>

<sup>320</sup> Badgurjar, D.; Shan, B.; Nayak, A.; Wu, L.; Chitta, R.; Meyer, T. J. *ACS Appl. Mater. Interfaces* **2020**, *12* (6), 7768.

<sup>321</sup> Pho, T. V.; Sheridan, M. V.; Morseth, Z. A.; Sherman, B. D.; Meyer, T. J.; Papanikolas, J. M.; Schanze, K. S.; Reynolds, J. R. *ACS Appl. Mater. Interfaces* **2016**, *8* (14), 9125.

<sup>322</sup> Treadway, J. A.; Moss, J. A.; Meyer, T. J. *Inorg. Chem.* **1999**, *38* (20), 4386.

<sup>323</sup> Ashford, D. L.; Gish, M. K.; Vannucci, A. K.; et al. *Chem. Rev.* **2015**, *115* (23), 13006.

<sup>324</sup> Song, W.; Vannucci, A. K.; et al. *J. Am. Chem. Soc.* **2014**, *136* (27), 9773.

<sup>325</sup> Gibson, E. A. Dye-sensitized photocathodes for H<sub>2</sub> evolution. *Chem. Soc. Rev.* **2017**, *46* (20), 6194.



We have concluded that the photocatalytic efficiency depends on: i) the different pH (reaching a maximum activity at pH = 8), ii) the intrinsic catalytic nature of TEMPO, iii) the mass transport within TiO<sub>2</sub> pores, iv) the compound degradation (dye or catalyst), and v) the desorption from the TiO<sub>2</sub> electrode. Comparison of the absorption spectra of the TiO<sub>2</sub> photoelectrode recorded before and after 1 hour of photocatalysis at pH = 8, indicates that dye desorption is probably not the main cause of photocatalytic loss in these conditions since the spectra are quite similar (**Figure 6.4.51**). The photocatalysis decreases for pH above 8, while the electrocatalytic oxidation activity of TEMPO increases with pH, might be attributed to the diffusion of the alcohol inside the pores of TiO<sub>2</sub> or to TEMPO degradation.<sup>326</sup> Another, even more probable, reason for the decrease of the long-term stability of the present system is the degradation of the zinc porphyrin during the catalysis. Employing more photo- and/or electro-chemically stable dyes would likely enhance the stability of this type of DSPEC.

The Incident Photon-to-electron Conversion Efficiency (IPCE) spectrum of the dyad **hyd-ZnP-TEMPO** was recorded in the optimal conditions of borate buffer at pH = 8 (**Figure 4.34**). The maximum value reaches ~2.6% on the Soret band at 430 nm and the IPCE spectrum is fairly similar with the absorption bands of the zinc porphyrin of the dyad recorded in a thin TiO<sub>2</sub> film.

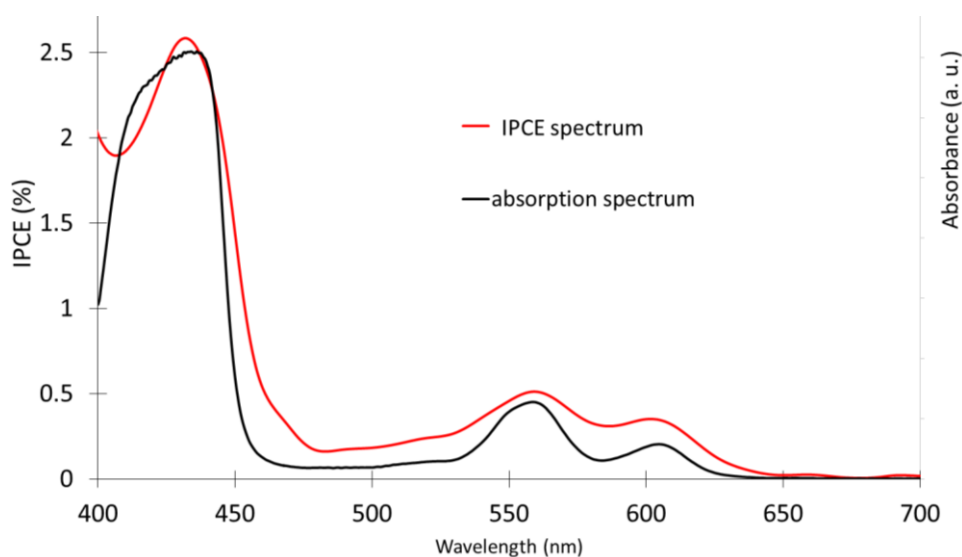


**Figure 4.34** IPCE spectrum of **hyd-ZnP-TEMPO** recorded at a constant potential of 0 V vs. SCE in borate buffer at pH = 8 and its and absorption spectrum recorded on thin (4  $\mu\text{m}$ ) monocrystalline TiO<sub>2</sub> film without scattering layer.

<sup>326</sup> Golubev, V. A.; Sen', V. D. *Russian J. Org. Chem.* **2011**, 47 (6), 869.

*Photocatalysis in organic media.*

Following our investigation in aqueous electrolytes, we proceeded with organic media, namely acetonitrile. TEMPO catalyzed electro-oxidation of alcohol is commonly reported in organic solvents in the presence of a base, which is necessary to neutralize the protons released by the formation of aldehyde. Acetonitrile was used as solvent due to its compatibility with proton reduction and with CO<sub>2</sub> reduction since CO<sub>2</sub> is much more soluble in acetonitrile than in water.<sup>327</sup> Two organic bases, 2,6-lutidine and N-methyl-imidazole (Me-Imd) usually used for this purpose, were investigated here.<sup>315</sup> The chopped light photocurrent densities of these two bases at different concentrations were recorded at a constant potential of 0 V vs. SCE with **hyd-ZnP-TEMPO** coated on TiO<sub>2</sub> (**Figure 4.35**). The experiments showed that the optimal concentrations of lutidine and N-methyl-imidazole were 10 mM and 100 mM, respectively, and that N-methyl-imidazole results in 3-times higher photocurrent densities than lutidine. This trend can be easily attributed to the higher basicity of N-methyl-imidazole and the possibility to bind axially the ZnP photosensitizer limiting the unfavorable aggregation.

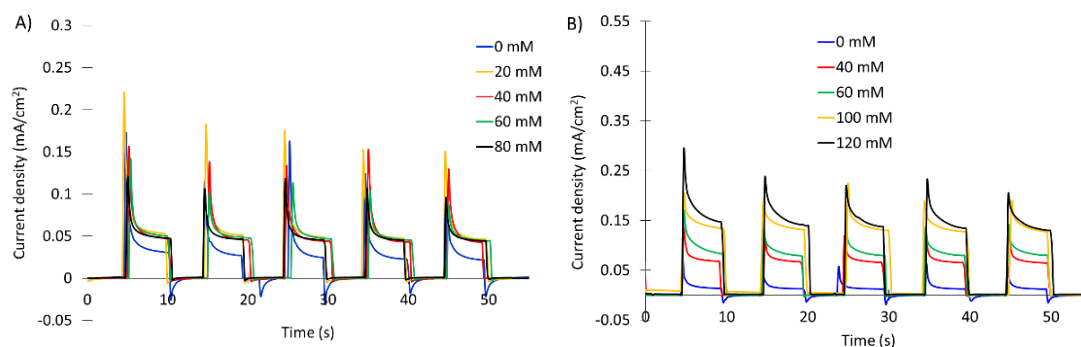


**Figure 4.35** Chopped light voltammetry measurements of **hyd-ZnP-TEMPO** recorded at a constant potential of 0 V vs. SCE in presence of different concentrations of (A) 2,6-lutidine and (B) N-methyl-imidazole in acetonitrile recorded under white light irradiation (1000 W/m<sup>2</sup>) with *para*-methoxybenzyl alcohol (10 mM) and [LiClO<sub>4</sub>] = 0.1 M.

We conducted long-term photocatalytic experiments using Me-Imd (100 mM) in acetonitrile to determine the photocatalytic efficiency of **hyd-ZnP-TEMPO** in these conditions (**Table 4.5** and **Figure 4.36**). Compared to borate buffer at pH = 8, the values

<sup>327</sup> Kumar, B.; Llorente, M.; Froehlich, J.; Dang, T.; Sathrum, A.; Kubiak, C. P. *Annu. Rev. Phys. Chem.* **2012**, *63* (1), 541.

of TON and TOF are reduced by about a factor of two. This is presumably due to faster desorption of the photocatalyst in acetonitrile, because the dyad is partial soluble in acetonitrile in contrast to borate buffer which it totally insoluble. Additional experiments in acetonitrile utilizing ZnP-TEMPO dyads are presented in the appendix in **Figures 6.4.52 – 6.4.56**.

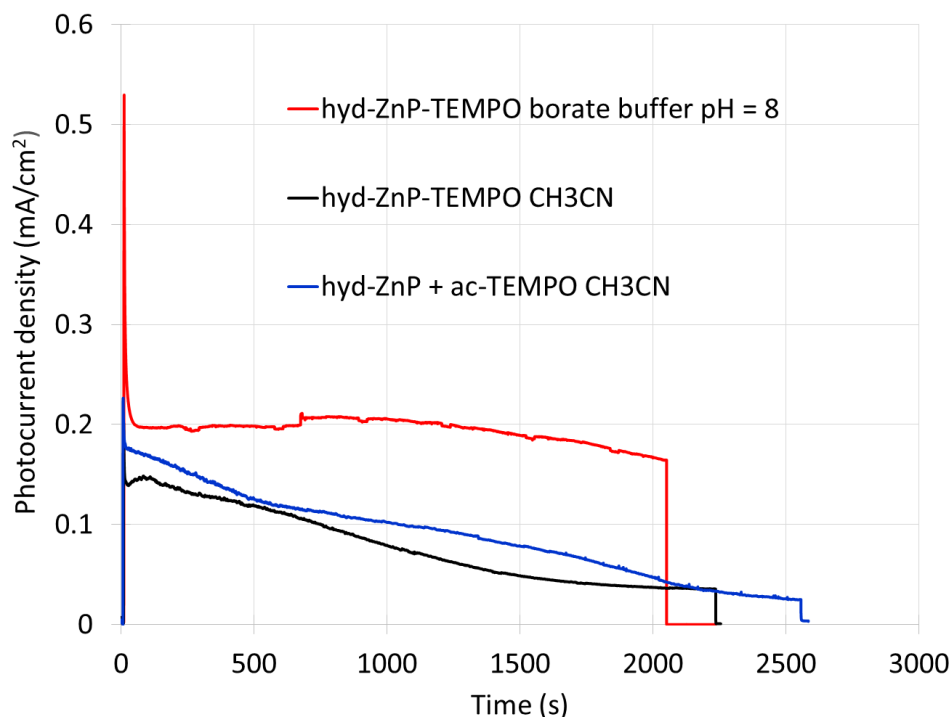


**Figure 4.36** Typical photocurrent density responses during long-term photolysis experiments with TiO<sub>2</sub> photoelectrodes recorded in either aqueous 0.1 M borate buffer at pH = 8 with [NaClO<sub>4</sub>] = 0.1 M or in acetonitrile electrolyte containing [Me-Imd] = 0.1 M and [LiClO<sub>4</sub>] = 0.1 M.<sup>328</sup>

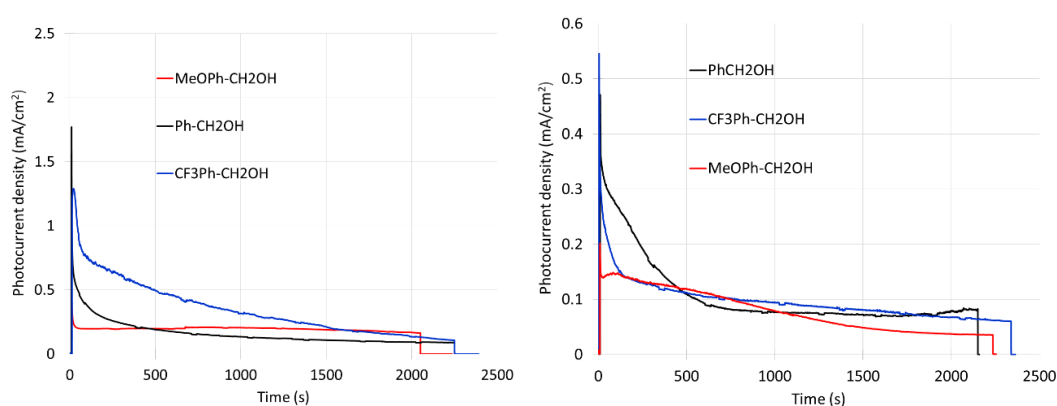
In all the above experiments, *para*-methoxybenzyl alcohol substrate was examined. Since the chosen catalyst **ac-TEMPO** is very active for many alcohol substrates,<sup>315,317,,329</sup> two additional benzyl alcohols: i) benzyl alcohol and ii) *para* trifluoromethyl benzyl alcohol (an electron deficient substrate) were also studied both in borate buffer (pH=8) and in acetonitrile electrolyte in presence of methyl imidazole. The average photocurrent densities are gathered in **Table 4.6** and the current *versus* time curves are shown in **Figure 4.37**.

<sup>328</sup> All experiments were recorded in presence of *para*-methoxybenzyl alcohol (50 mM) in the electrolyte and in the same irradiation conditions: white light (about 100 mW/cm<sup>2</sup>) with a 400 nm cutoff filter. The concentration of **ac-TEMPO** was 1 mM in acetonitrile electrolyte.

<sup>329</sup> Mercadante, M. A.; Kelly, C. B.; Bobbitt, J. M.; Tilley, L. J.; Leadbeater, N. E. *Nature Protocols* **2013**, 8 (4), 666.

**Table 4.6** Photocurrent densities recorded at 500 sec during the catalysis experiments with **hyd-ZnP-TEMPO** using three different benzyl alcohol substrates (50 mM).

	MeO-Ph-CH <sub>2</sub> OH	Ph-CH <sub>2</sub> OH	CF <sub>3</sub> -Ph-CH <sub>2</sub> OH
<b>Borate buffer pH =8</b>	0.20±0.05 mA/cm <sup>2</sup>	0.19±0.08 mA/cm <sup>2</sup>	0.50±0.05 mA/cm <sup>2</sup>
<b>CH<sub>3</sub>CN+ Me-Imd</b>	0.10±0.02 mA/cm <sup>2</sup>	0.10±0.01 mA/cm <sup>2</sup>	0.11±0.02 mA/cm <sup>2</sup>

**Figure 4.37** Typical photocurrent density responses of **hyd-ZnP-TEMPO** during long-term photolysis experiments in 0.1 M borate buffer at pH = 8 (left) or in acetonitrile in presence of 0.1 M of Me-Imd (right) with different benzyl alcohol substrates (50 mM). Irradiation conditions: white light (about 100 mW/cm<sup>2</sup>).

As illustrated in the above figure, benzyl alcohol gives approximately the same photocurrent density as *p*-methoxybenzyl alcohol in borate buffer, while *p*-trifluoromethyl alcohol produces much higher photocurrent density. We attributed this unexpected result to the higher hydrophobicity of *p*-trifluoromethyl alcohol, which probably improves its affinity to the TiO<sub>2</sub> photoanode coated with the chromophore-catalyst dyad. This is in agreement with the conducted experiments in acetonitrile, where all three substrates exhibited similar photocurrent densities (within experimental errors).

Overall, the above results demonstrate that our ZnP-TEMPO system is active towards benzyl alcohol substrates, in agreement with previous studies,<sup>315,317,330</sup>

<sup>330</sup> Mercadante, M. A.; Kelly, C. B.; Bobbitt, J. M.; Tilley, L. J.; Leadbeater, N. E. *Nature Protocols* **2013**, 8 (4), 666.

The last analyzed parameter was the impact of covalent linkage of TEMPO with ZnP photosensitizer on the photocatalysis. Usually in DSPECs, the catalyst is covalently connected to the photosensitizer or co-grafted with the latter on the surface of the semiconductor.<sup>271,272</sup> In some rare cases, it is solubilized in the electrolyte.<sup>331,332</sup> Although the latter approach involves less synthetic efforts, it requires a larger quantity of the catalyst and is less practical in terms of recycling since the catalyst must be separated from the product in the electrolyte.

Despite this limitation, we investigated the photocatalytic performance of **hyd-ZnP** together with **ac-TEMPO** in the electrolyte. We observed no change in the produced photocurrent density on TiO<sub>2</sub> sensitized with **hyd-ZnP**, when increasing concentrations of **ac-TEMPO** from 0 to 10 mM were used in borate buffer (pH = 8) with 10 mM of *para*-methoxybenzyl alcohol. This might be the result of the low solubility of **ac-TEMPO** in water, which limits the reaction with the oxidized porphyrin photosensitizer before charge recombination.

Consequently, we conducted the same experiment in the acetonitrile electrolyte containing **Me-Imd** by adding increasing quantities of **ac-TEMPO** (from 0 mM to 10 mM, **Figure 4.38**). Interestingly, the photocurrent density of the photoelectrode sensitized by **hyd-ZnP** increased upon addition of **ac-TEMPO**, and it reached a plateau at around 1 mM. By using this concentration, we performed long-term photocatalysis experiments to compare its performance with the covalently linked system (**hyd-ZnP-TEMPO**). Within experimental error, the performances of the two systems are pretty similar (**Table 4.5** and **Figure 4.36**). The TOF is significantly higher with the dyad **hyd-ZnP-TEMPO** than the intermolecular system **hyd-ZnP + ac-TEMPO** and this could be attributed to the proximity brought by covalent linkage which provides a faster hole shift to the catalyst. Noteworthy, the dyad system offers a much easier recovery of the photocatalyst (simple rinsing of the photoelectrode) and the quantity of the used catalyst is much lower (84 nmol *versus* 7000 nmol).

---

<sup>331</sup> Li, S.; Li, Z.-J.; Yu, H.; Sytu, M. R.; Wang, Y.; Beeri, D.; Zheng, W.; Sherman, B. D.; Yoo, C. G.; Leem, G. *ACS Energy Lett.* **2020**, *5* (3), 777.

<sup>332</sup> Brimblecombe, R.; Koo, A.; Dismukes, G. C.; Swiegers, G. F.; Spiccia, L.. *J. Am. Chem. Soc.* **2010**, *132* (9), 2892.

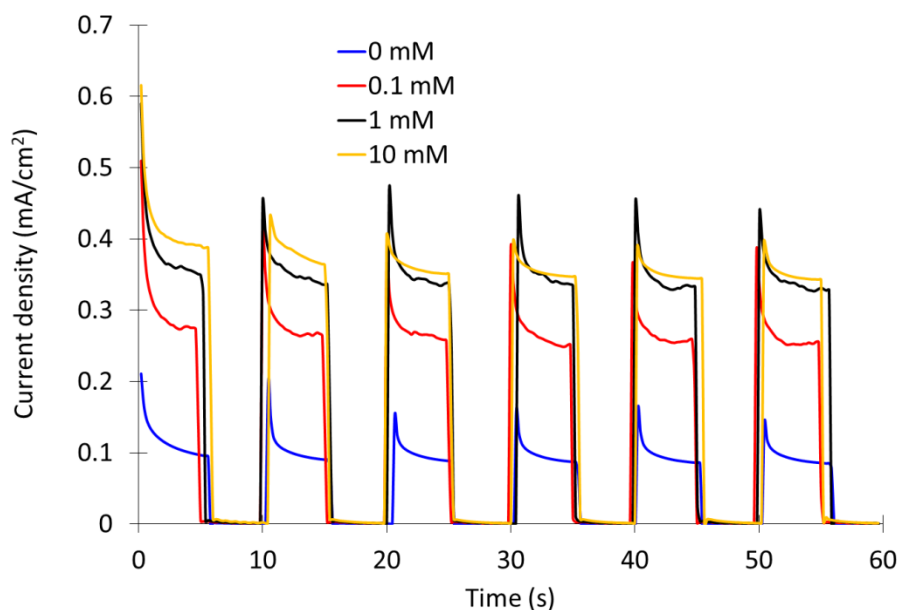


**Figure 4.38** Chopped light linear sweep voltammetry measurements recorded under white light irradiation (about  $1000 \text{ W/m}^2$ ) at a constant potential of 0 V vs. SCE with of **hyd-ZnP** on  $\text{TiO}_2$  film in acetonitrile containing [*para*-methoxybenzyl alcohol] = 50 mM, [ $\text{LiClO}_4$ ] = 0.1 M, [MeImd]=0.1 M with increasing concentration of **ac-TEMPO**.

The concluding remarks of this section can be summarized with the following. A new photocatalytic system comprised of a Zn-porphyrin photosensitizer covalently connected to a TEMPO organo-catalyst was prepared and investigated for solar driven benzyl alcohol oxidation in a  $\text{TiO}_2$ -based DSPEC. Several ZnP-TEMPO dyads, bearing different anchoring groups, were synthesized with the best performing being **hyd-ZnP-TEMPO**. The latter compound effectively catalyzed the methoxybenzyl alcohol oxidation upon light irradiation when it is coated on a  $\text{TiO}_2$ -based photoanode. The system was proven active both in aqueous and organic electrolytes. The optimal performance was observed in aqueous electrolyte at  $\text{pH} = 8$ , but it worked with comparable efficiency in acetonitrile in the presence of N-methyl-imidazole base. The major reason for the decrease of the catalytic activity in the organic electrolyte is the desorption of the photocatalyst from the  $\text{TiO}_2$  surface due to its partial solubility. On the other hand, the porphyrin degradation is probably the main cause for the reduction of catalytic efficiency in aqueous conditions.

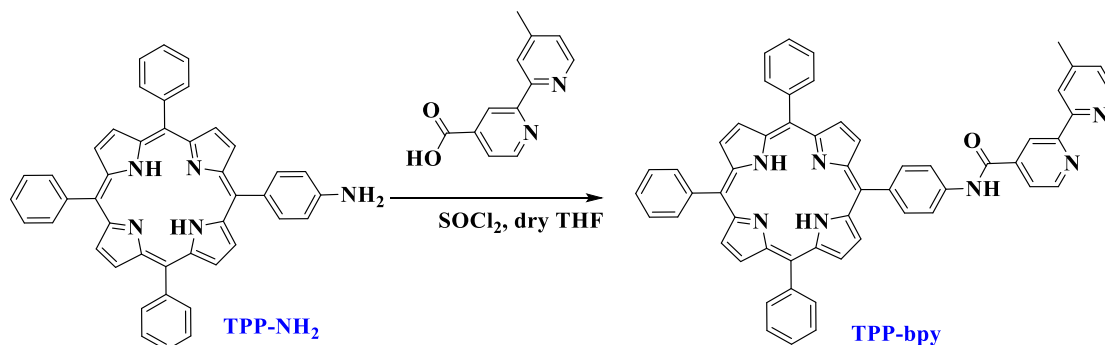
Regardless of its low driving force, the hole shift reaction from the zinc porphyrin radical cation occurs quite efficiently, as proved by the enhanced photovoltaic performances in DSSCs of the dyad **hyd-ZnP-TEMPO** relative to the reference **hyd-**

**ZnP** lacking the TEMPO moiety. The comparison of the intra-molecular dyad **hyd-ZnP-TEMPO** system with the intermolecular “**hyd-ZnP + ac-TEMPO**” system, was achieved in acetonitrile, and showed that both approaches result in similar performances. However, the recovery of the catalyst is much easier in the dyad case and the quantity of the catalyst involved is much lower. It was also observed that hydroxamic acid is a more stable anchoring group compared to the carboxylic acid, the phosphonic acid, and the pyridyl group. This enhanced stability has little impact in aqueous electrolyte where the dyad is poorly soluble, but it becomes crucial in acetonitrile electrolyte in which the solubility is sufficiently high, enabling quick desorption of the dyad within a few minutes.

The photocatalytic system presented herein exhibits very high performance compared to other reports for alcohol oxidation in DSPECs along with the reports for oxygen or hydrogen evolution in such photoelectrosynthetic systems. Alcohol photo-oxidation is an attractive reaction to pair with water or CO<sub>2</sub> reduction in order to develop tandem photoelectrosynthetic cells producing valuable compounds at both electrodes.

## 4.3 Experimental Section

- Synthesis of 5-[4-(4-methyl-2,2'-bipyridine-4'-carboxamidyl)phenyl]-10,15,20-triphenyl porphyrin: **TPP-bpy**



**Scheme 4.3.1** The experimental procedure for the synthesis of **TPP-bpy**.

A solution of 4-methyl-2,2'-bipyridine-4'-carboxylic acid, **bpy-COOH**<sup>333</sup> (153 mg, 0.715 mmol) in 15 mL thionyl chloride (SOCl<sub>2</sub>) was heated at reflux under an Ar atmosphere for 2 h. The excess thionyl chloride was removed *in vacuo* and the yellow residue was dried under vacuum. A solution of **TPP-NH<sub>2</sub>**<sup>334</sup> (150 g, 0.24 mmol) in dry THF (30 mL,) and dry triethylamine (330 μL) were added and the mixture was stirred at 50 °C under argon overnight. The solvents were removed *in vacuo* and the product was purified by column chromatography (silica gel, DCM:MeOH 97:3 v/v) to yield the title compound, **TPP-bpy** (157 mg, 0.19 mmol, 80%).

<sup>1</sup>H NMR (CDCl<sub>3</sub>, 500 MHz): δ (ppm) 8.90 (m, 10H), 8.68 (s, 1H), 8.62 (d, *J* = 4.8 Hz, 1H), 8.37 (bs, 1H), 8.26 (d, *J* = 8.3 Hz, 2H), 8.23 (d, *J* = 6.3 Hz, 6H), 8.13 (d, *J* = 8.3 Hz, 2H), 8.02 (dd, *J*<sub>1</sub> = 4.8 Hz, *J*<sub>2</sub> = 1.8 Hz, 1H), 7.76 (m, 9H), 7.24 (bs, 1H), 2.51 (s, 3H), -2.75 (s, 2H).

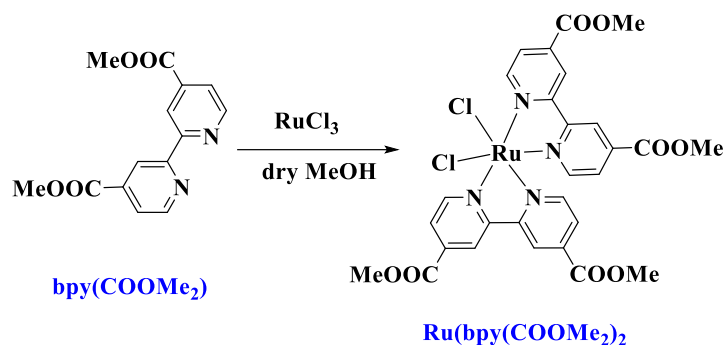
<sup>13</sup>C NMR (CDCl<sub>3</sub>, 125 MHz): δ (ppm) 164.3, 157.4, 155.2, 150.7, 149.2, 148.9, 143.2, 142.3, 139.1, 137.4, 135.4, 134.7, 131.2, 127.9, 126.8, 125.6, 122.5, 122.2, 120.4, 119.4, 118.8, 117.5, 21.4.

<sup>333</sup> D. G. McCafferty, B. M. Bishop, C. G. Wall, S. G. Hughes, S. L. Mecklenberg, T. J. Meyer and B. W. Erickson, *Tetrahedron*, 1995, **51**, 1093-1106.

<sup>334</sup> K. Ladomenou, T. Lazarides, M. K. Panda, G. Charalambidis, D. Daphnomili, A. G. Coutsolelos *Inorg. Chem.* **2012**, 51, 20, 10548–10556.



- Synthesis of **Ru(bpy(COOMe)<sub>2</sub>)<sub>2</sub>**

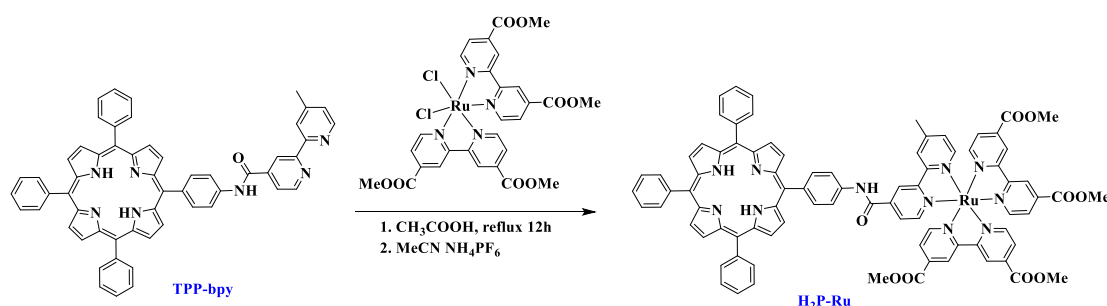


**Scheme 4.3.2** The experimental procedure for the synthesis of **Ru(bpy(COOMe)<sub>2</sub>)<sub>2</sub>**.

Dimethyl [2,2'-bipyridine]-4,4'-dicarboxylate **Bpy(COOMe)<sub>2</sub>** (50 mg, 0.184 mmol) was dissolved in 2 mL of dry MeOH and RuCl<sub>3</sub> (19 mg, 0.092 mmol) was added. The solution was refluxed in a schlenk tube under argon atmosphere overnight. After the completion of the reaction the solution was cooled to 0 °C, the crude product was precipitated and filtered. The title compound was purified by column chromatography (silica gel, DCM:MeOH 97:5 v/v) (27 mg, 41%).

<sup>1</sup>H NMR (CDCl<sub>3</sub>, 500 MHz): δ (ppm) 10.44 (d, *J* = 5.0 Hz, 2H), 8.84 (s, 2H), 8.68 (s, 2H), 8.17 (d, *J* = 5.0 Hz, 2H), 7.69 (d, *J* = 5.5 Hz, 2H), 7.49 (d, *J* = 5.5 Hz, 2H), 4.11 (s, 6H), 3.97 (s, 6H). <sup>13</sup>C NMR (CDCl<sub>3</sub>, 125 MHz): δ (ppm) 164.8, 164.2, 160.6, 158.1, 155.4, 152.8, 136.1, 134.9, 125.2, 124.6, 122.0, 121.8, 53.5, 53.4.

- Synthesis of **H<sub>2</sub>P-Ru**



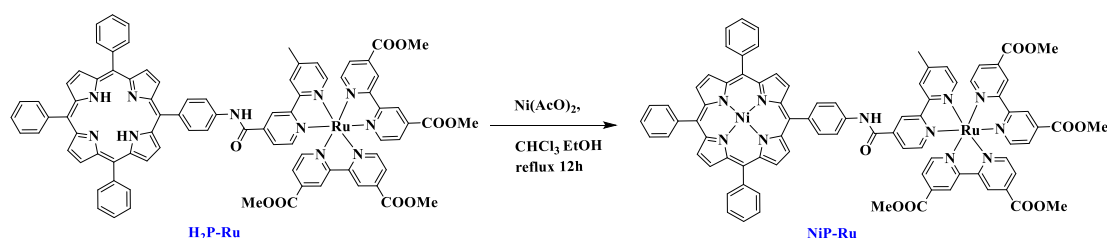
**Scheme 4.3.3** The experimental procedure for the synthesis of **H<sub>2</sub>P-Ru**.

In a two-neck round flask **TPP-bpy** (52.4 mg, 0.0636 mmol) was dissolved in 38 mL of CH<sub>3</sub>COOH. The solution was degassed with N<sub>2</sub> for 15 minutes, then **Ru(bpy(COOMe)<sub>2</sub>)<sub>2</sub>** (91 mg, 0.127 mmol) was added and the reaction mixture was refluxed at 118 °C overnight under N<sub>2</sub>. Subsequently the solvent was evaporated and

the solid residue was washed with Et<sub>2</sub>O. The title compound was purified by column chromatography (silica gel, polarity changed from DCM/MeOH 97/3 v/v to MeCN/H<sub>2</sub>O/KNO<sub>3</sub>(saturated in water) 30/2/1 v/v/v). Precipitation followed by dissolving the compound in minimum amount of MeCN, adding MeOH saturated with PF<sub>6</sub><sup>-</sup> and final adding water. After filtration **H<sub>2</sub>P-Ru** was obtained (19 mg, 20%).

<sup>1</sup>H NMR (CDCl<sub>3</sub>, 500 MHz): δ (ppm) 9.24 (bs, 1H), 8.89 (m, 13H), 8.20 (m, 12H), 7.97 (m, 8H), 7.74 (m, 11H), 7.33 (bs, 1H), 3.91 (m, 12H), 2.57 (bs, 3H), -2.79 (bs, 2H).  
UV-Vis (DMF): λ<sub>max</sub>, nm (ε, mM<sup>-1</sup>cm<sup>-1</sup>) 419.0 (308.6), 513.0 (23.1), 550.0 (14.1), 591.0 (10.7), 646.5 (6.2).

- Synthesis of **NiP-Ru**



**Scheme 4.3.4** The experimental procedure for the synthesis of **NiP-Ru**.

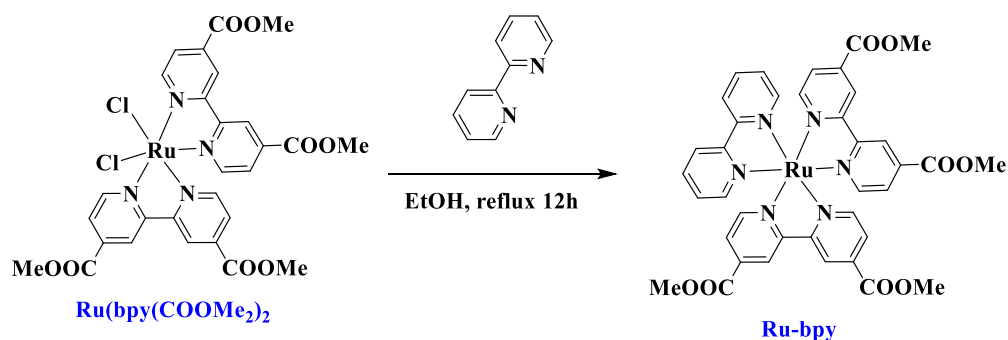
For the metalation reaction, **H<sub>2</sub>P-Ru** (50 mg, 0.034 mmol) was dissolved in 10 mL CHCl<sub>3</sub> and heated to 55 °C. Excess of Ni(CH<sub>3</sub>COO)<sub>2</sub>·4H<sub>2</sub>O salt (85 mg, 0.34 mmol) were dissolved in 10 mL EtOH, heated to 55 °C and then inserted to the porphyrin-ruthenium solution. Heating the two solutions before mixing was important so that **H<sub>2</sub>P-Ru** will remain soluble after the addition of ethanol. The reaction mixture was stirred for 24 hours at 58 °C. The organic solvents were evaporated and then the solid residue was washed with water in order to remove the excess of nickel salt. The title compound was purified by column chromatography (silica gel, MeCN/H<sub>2</sub>O/KNO<sub>3</sub>(saturated in water) 30/2/1 v/v/v). Precipitation followed by dissolving the compound in minimum amount of MeCN, adding MeOH saturated with PF<sub>6</sub><sup>-</sup> and final adding water. After filtration **NiP-Ru** was obtained (44 mg, 85%).

<sup>1</sup>H NMR (DMSO-d<sub>6</sub>, 500 MHz): δ (ppm) 11.18 (bs, 1H), 9.40 (bs, 4H), 9.04 (bs, 2H), 8.75 (bs, 8H), 8.05 (m, 18H), 7.80 (m, 12H), 7.46(m, 1H), 4.01 (bs, 12H), 2.61 (bs, 3H).

MS-(MALDI-TOF): m/z calc. for C<sub>84</sub>H<sub>61</sub>N<sub>11</sub>NiO<sub>9</sub>Ru [M]<sup>+</sup>: 1527.31, found 1527.35.

UV-Vis (DMF): λ<sub>max</sub>, nm (ε, mM<sup>-1</sup>cm<sup>-1</sup>) 308.0 (86.5), 415.0 (282.6), 527.0 (29.1).

- Synthesis of **Ru-bpy**



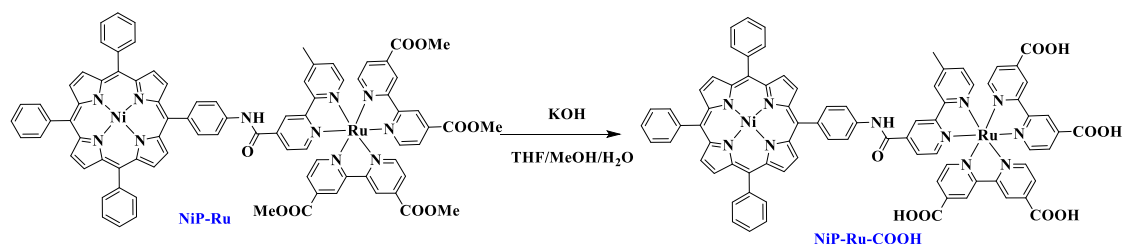
**Scheme 4.3.5** The experimental procedure for the synthesis of **Ru-bpy**.

**Ru(bpy(COOMe)<sub>2</sub>)<sub>2</sub>** (32 mg, 0.045 mmol) was dissolved in 10 mL EtOH and 2,2'-bipyridine (10.5 mg, 0.067 mmol) was added. The reaction mixture was refluxed at 90 °C overnight and then the solvents were removed under vacuum. Purification was conducted via column chromatography (silica gel, MeCN/H<sub>2</sub>O/KNO<sub>3</sub>(saturated in water) 30/2/1 v/v/v) to yield the title compound (20 mg, 55%).

<sup>1</sup>H NMR (CD<sub>3</sub>CN, 300 MHz): δ (ppm) 9.05 (s, 4H), 8.52 (d, *J* = 8.1 Hz, 2H), 8.10 (t, *J* = 7.5 Hz, 2H), 7.87 (m, 8H), 7.65 (d, *J* = 5.3 Hz, 2H), 7.41 (t, *J* = 6.3 Hz, 2H), 4.46 (m, 12H).

<sup>13</sup>C NMR (CDCl<sub>3</sub>, 75 MHz): δ (ppm) 164.3, 158.4, 158.3, 157.4, 154.0, 153.7, 152.7, 140.2, 139.6, 128.8, 127.6, 127.5, 125.5, 124.7, 63.7. UV-Vis (DMF): λ<sub>max</sub>, nm (ε, mM<sup>-1</sup>cm<sup>-1</sup>) 304.0 (85.1), 469.0 (23.6).

- Synthesis of **NiP-Ru-COOH**

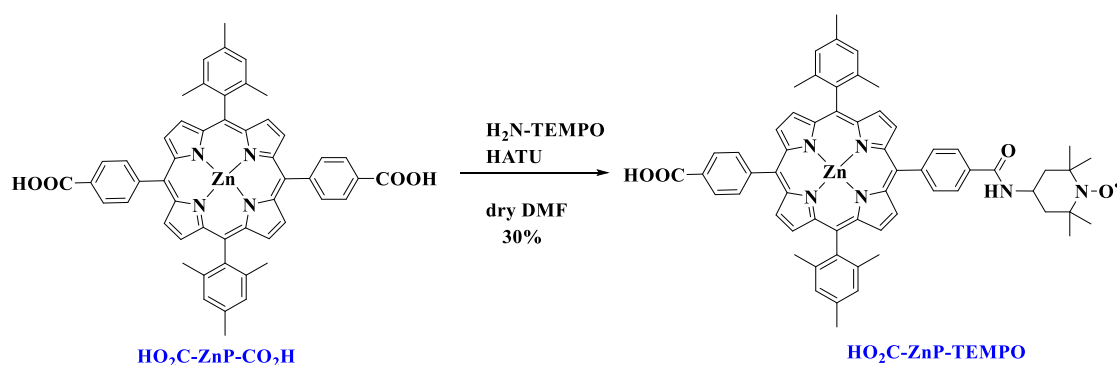


**Scheme 4.3.6** The experimental procedure for the synthesis of **NiP-Ru-COOH**.

**NiP-Ru** (56 mg, 0.036 mmol) was dissolved in 24 mL of a THF/MeOH mixture (2 : 1), followed by the addition of an aqueous solution (9 mL) of KOH (525 mg, 9.4 mmol) and the reaction was left under stirring at room temperature overnight. The organic solvents were evaporated under reduced pressure, and then a solution of 1 M HCl (aq)

was added dropwise for the acidification of the mixture till pH = 5, resulting to the precipitation of the desired product. Finally, after the dyad was filtered, washed with H<sub>2</sub>O and dried under vacuum 45 mg of NiP-Ru-COOH were isolated (yield: 83%). <sup>1</sup>H NMR and <sup>13</sup>C NMR spectra could not be recorded due to solubility reasons. *MS*-(MALDI-TOF): m/z calcd for C<sub>80</sub>H<sub>53</sub>N<sub>11</sub>NiO<sub>9</sub>Ru [M]<sup>+</sup>: 1471.24, found 1471.28. *UV-Vis* (DMF): λ<sub>max</sub>, nm (ε, mM<sup>-1</sup>cm<sup>-1</sup>) 309.0 (53.5), 416.0 (190.9), 526.5 (19.5).

- Synthesis of **HOOC-ZnP-TEMPO**



**Scheme 4.3.7** Experimental procedure for the synthesis of **HO<sub>2</sub>C-ZnP-TEMPO**.

**HOOC-ZnP-COOH** (50 mg, 0.059 mmol, 1.0 equiv) was dissolved in 10 mL of dry DMF and cooled at 0 °C. Then the HATU coupling reagent 1-[Bis(dimethylamino)methylene]-1H-1,2,3-triazolo[4,5-b]pyridinium 3-oxide hexafluorophosphate (22 mg, 0.059 mmol, 1.0 equiv) was added and the reaction mixture was stirred for 2 hours at 0 °C. Subsequently, NH<sub>2</sub>-TEMPO (25 mg, 0.146 mmol, 2.5 equiv) and 150 μL DIPEA were introduced in the reaction which was stirred for 48 hours at room temperature. After the completion of the reaction 0.5 mL of EtOH were added in order to counteract the remaining activated intermediate and left stirring overnight. The desired product was purified via silica gel column chromatography with CHCl<sub>3</sub>-EtOH (97-3) followed by precipitation in DCM/Pentane. The title compound was isolated as a purple solid (18 mg, 30%).

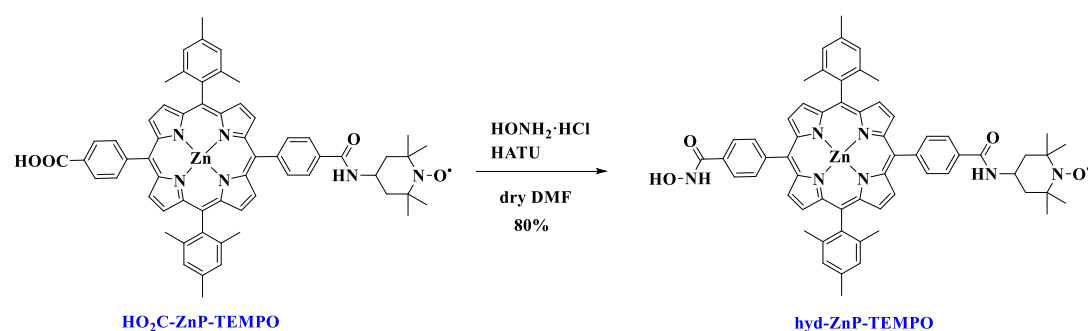
<sup>1</sup>H NMR (500 MHz, DMSO-d<sub>6</sub> + 5% hydrazine): δ = 8.74 (d, J = 4.6 Hz, 2H), 8.69 (d, J = 4.6 Hz, 2H), 8.55 (m, 5H), 8.25 (m, 6H), 8.12 (d, J = 8.1 Hz, 2H), 7.30 (s, 4H), 4.38 (m, 1H), 2.56 (s, 6H), 1.88 (m, 2H), 1.77 (s, 12H), 1.65 (m, 2H), 1.19 (s, 6H), 1.15 (s, 6H) ppm.

$^{13}\text{C}$  NMR (75 MHz,  $\text{DMSO-}d_6$  + 5% hydrazine):  $\delta$  = 170.7, 165.9, 149.3, 149.2, 149.1, 148.9, 145.7, 143.6, 139.2, 138.6, 138.3, 136.9, 134.1, 133.6, 132.2, 131.8, 130.2, 130.0, 127.6, 127.2, 125.5, 120.1, 118.6, 118.2, 58.2, 45.0, 41.1, 32.8, 21.6, 21.1, 19.9 ppm.

MALDI-TOF: calcd for  $\text{C}_{61}\text{H}_{58}\text{N}_6\text{O}_4\text{Zn}$   $[\text{M}+\text{H}]^+$  1002.3811, found 1002.3863.

UV-Vis in THF [ $\lambda_{\text{max}}/\text{nm}$  ( $\epsilon/\text{mM}^{-1} \text{cm}^{-1}$ ): 426 (432.8), 557 (16.8), 598 (4.8)

• Synthesis of **Hydroxa-ZnP-TEMPO**



**Scheme 4.3.8** Experimental procedure for the synthesis of **hyd-ZnP-TEMPO**.

**HOOC-ZnP-TEMPO** (20 mg, 0.020 mmol, 1.0 equiv) was dissolved in 5 mL dry DMF and HATU coupling reagent (15.2 mg, 0.040 mmol, 2.0 equiv) along with 15  $\mu\text{L}$  DIPEA (0.08 mmol, 4 equiv) were added in the solution. The mixture was stirred at room temperature for 30 minutes and then 10 equivalents of  $\text{HCl} \cdot \text{NH}_2\text{OH}$  (13.9 mg, 0.2 mmol) were introduced in the reaction which was left under stirring for additional 6 hours at room temperature. After the completion of the reaction 25 mL of water were added and the product was precipitated, filtrated and washed with water. The title compound was isolated as a purple solid (16.3 mg, 80%).

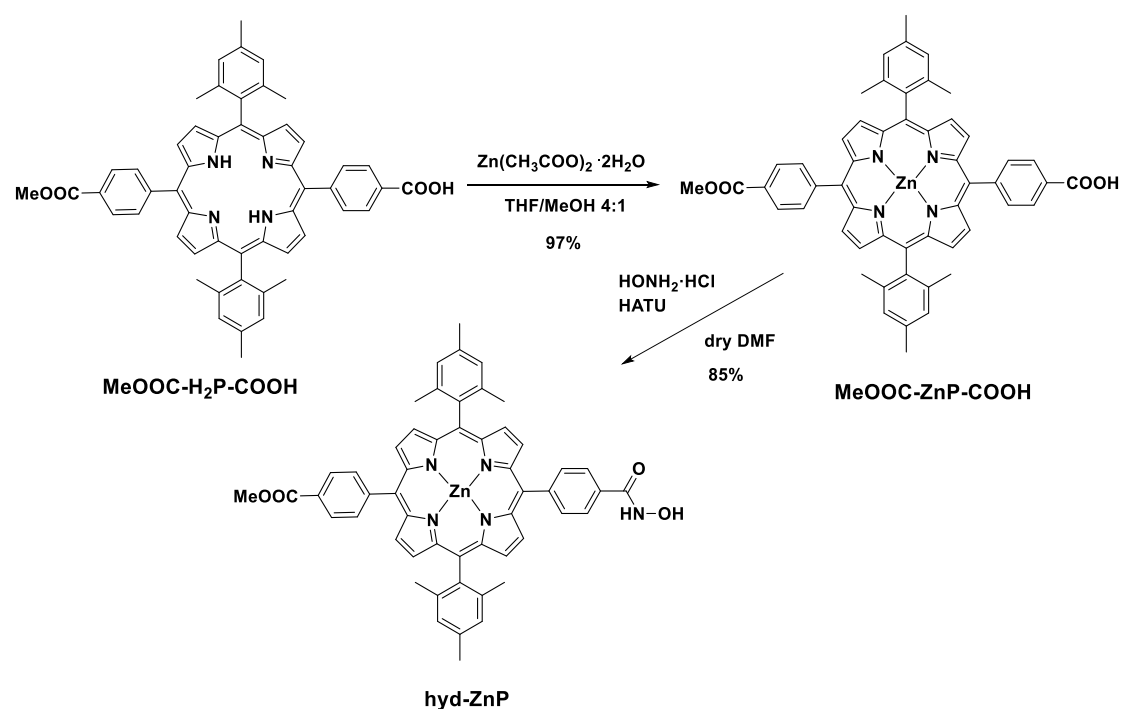
$^1\text{H}$  NMR (500 MHz,  $\text{DMSO-}d_6$  + 5% hydrazine):  $\delta$  = 8.71 (m, 4H), 8.55 (m, 5H), 8.25 (m, 6H), 8.15 (m, 2H), 7.30 (s, 4H), 4.37 (m, 1H), 2.56 (s, 6H), 1.88 (m, 2H), 1.76 (s, 12H), 1.65 (m, 2H), 1.19 (s, 12H) ppm.

$^{13}\text{C}$  NMR (125 MHz,  $\text{DMSO-}d_6$  + 5% hydrazine):  $\delta$  = 168.6, 165.9, 149.2, 149.1, 149.0, 146.0, 145.7, 139.2, 138.6, 136.9, 134.1, 133.7, 131.9, 130.2, 127.6, 125.5, 118.9, 118.3, 58.2, 45.0, 41.1, 32.8, 21.5, 21.1, 19.9 ppm.

MALDI-TOF: calcd for  $\text{C}_{61}\text{H}_{59}\text{N}_7\text{O}_4\text{Zn}$   $[\text{M}+\text{H}]^+$  1017.3920, found 1017.3982.

UV-Vis in THF [ $\lambda_{\text{max}}/\text{nm}$  ( $\epsilon/\text{mM}^{-1} \text{cm}^{-1}$ ): 426 (417.8), 557 (15.5), 597 (4.7).

- Synthesis of **hyd-ZnP**



**Scheme 4.3.9** Experimental procedure for the synthesis of **hyd-ZnP**.

To a solution of **MeOOC-H<sub>2</sub>P-COOH**<sup>335</sup> (16.5 mg, 0.021 mmol) in 7 mL of THF, a solution of  $(\text{CH}_3\text{COO})_2\text{Zn} \cdot 2\text{H}_2\text{O}$  (43.9 mg, 0.2 mmol) in 1.2 mL of MeOH was added. The reaction mixture was stirred at room temperature for 24 h. Then, half of the solvent mixture was distilled off under vacuum. After the addition of water the desired product was precipitated, filtered, washed with water and directly used in the next reaction without any other purification and characterization. **MeOOC-ZnP-COOH** (17.3 mg, 0.020 mmol, 1.0 equiv) was dissolved in 5 mL dry DMF and HATU coupling reagent (15.4 mg, 0.040 mmol, 2.0 equiv) along with 15  $\mu\text{L}$  DIPEA (0.081 mmol, 4 equiv) were added in the solution. The mixture was stirred at room temperature for 30 minutes and then 10 equivalents of  $\text{HCl} \cdot \text{NH}_2\text{OH}$  (14.1 mg, 0.202 mmol) were introduced in the reaction which was stirred overnight at room temperature. After the completion of the reaction 25 mL of water were added and the product was precipitated, filtrated and washed with water. The title compound was isolated as a purple solid (15.2 mg, 85%)

<sup>335</sup> Melomedov, J.; Wünsche von Leupoldt, A.; Meister, M.; Laquai, F.; Heinze, K. *Dalton Trans.* **2013**, 42 (26), 9727.

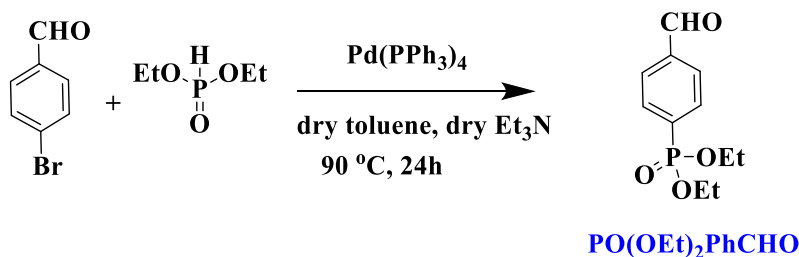
$^1\text{H NMR}$  (500 MHz,  $\text{CDCl}_3 + 2\% \text{MeOD}$ ):  $\delta = 8.65$  (m, 8H), 8.33 (d,  $J = 7.9$  Hz, 2H), 8.25 (m, 4H), 8.05 (d,  $J = 7.9$  Hz, 2H) 7.21 (s, 4H), 4.04 (s, 3H), 2.56 (s, 6H), 1.77 (s, 12H) ppm.

$^{13}\text{C NMR}$  (125 MHz,  $\text{CDCl}_3 + 2\% \text{MeOD}$ ):  $\delta = 167.9, 166.6, 150.0, 149.4, 148.5, 147.2, 139.4, 139.3, 137.4, 134.7, 134.6, 131.7, 130.8, 130.4, 128.9, 127.8, 127.6, 125.0, 124.7, 119.2, 118.5, 52.4, 21.6, 21.4$  ppm.

MALDI-TOF: calcd for  $\text{C}_{53}\text{H}_{44}\text{N}_5\text{O}_4\text{Zn}$   $[\text{M}+\text{H}]^+$  878.2685, found 878.2724.

UV-Vis in THF [ $\lambda_{\text{max}}/\text{nm}$  ( $\epsilon/\text{mM}^{-1} \text{cm}^{-1}$ ): 426 (445.3), 556 (16.6), 598 (4.9).

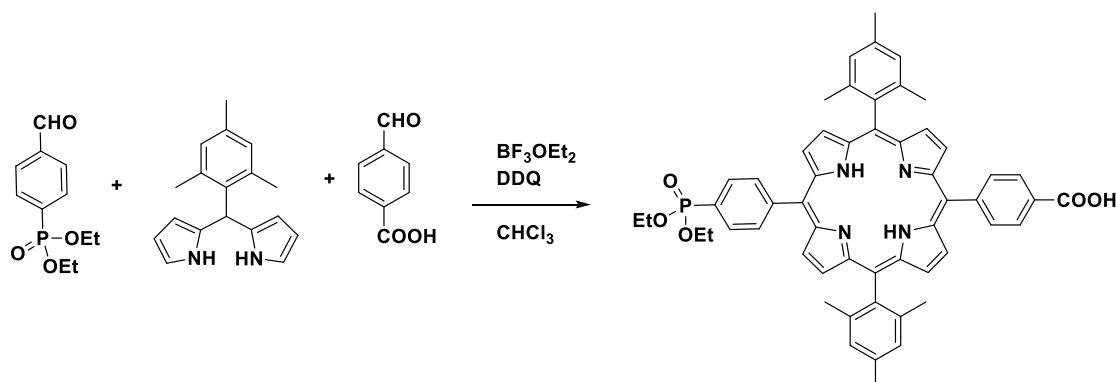
- Synthesis of diethyl-4-aldehydephenylphosphonate **PO(OEt)<sub>2</sub>PhCHO**



**Scheme 4.3.10** The experimental procedure for the synthesis of **PO(OEt)<sub>2</sub>PhCHO**.

4-bromobenzaldehyde (500 mg, 2.70mmol) was taken in a 100 mL two-necked bottom flask. To this solution, dry toluene (4mL), dry  $\text{Et}_3\text{N}$  (4 mL) and diethylphosphite (0.4 mL, 6 mmol) were added and purged with Ar gas for 2min. Finally,  $\text{Pd(PPh}_3)_4$  (155 mg, 0.135 mmol) was added and the reaction mixture heated to  $90^\circ\text{C}$  for 24h under Ar atmosphere. The reaction mixture was cooled to room temperature and the solvent evaporated to dryness under vacuum, re-dissolved in  $\text{CH}_3\text{Cl}$  (35 mL), washed with distilled water ( $3 \times 50$  mL), followed by brine solution (50 mL), and finally dried over with  $\text{Na}_2\text{SO}_4$ . The crude product was purified on a silica column chromatography using  $\text{CH}_3\text{Cl} - \text{EtOAc}$  (70:30, v/v) as the eluent. Yield: 300 mg (47%).

- Synthesis of **PO(OEt)<sub>2</sub>DMP-COOH**



**Scheme 4.3.11** The experimental procedure for **PO(OEt)<sub>2</sub>DMP-COOH**.

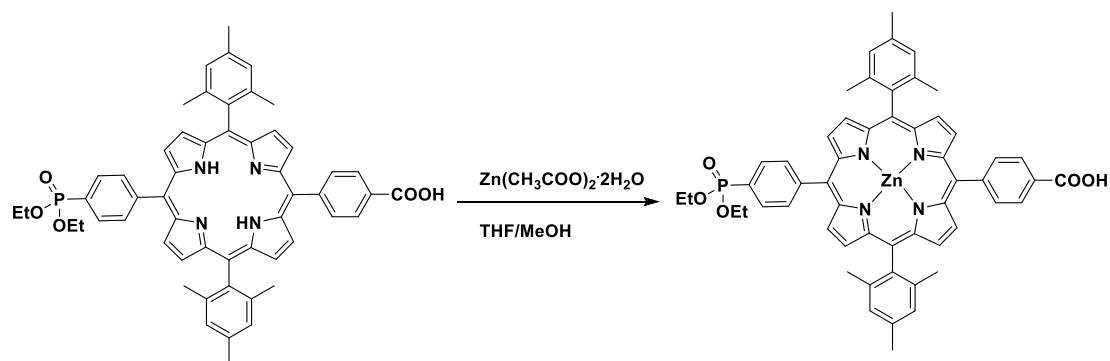
In a 500 mL two-necked bottom flask were dissolved in 250 mL of  $\text{CHCl}_3$  the following: diethyl-4-aldehydephenylphosphonate (138 mg, 0.57 mmol), mesityl-dipyrromethane (300 mg, 1.136 mmol) and 4-formylbenzoic acid (85 mg, 0.57 mmol). Noteworthy the stabilizer of chloroform solvent was traces of ethanol. The solution was degassed with  $\text{N}_2$  flow for 15 minutes and then  $\text{BF}_3\text{OEt}_2$  (75  $\mu\text{L}$ , 0.6 mmol) were added. The solution was stirred at room temperature under  $\text{N}_2$  atmosphere for 5 hours protected from light. After the completion of the reaction 2,3-Dichloro-5,6-dicyano-p-benzoquinone (DDQ) (204 mg, 0.9 mmol) were added and the reaction was left stirring for additional 20 hours. The majority of the solvent was evaporated and the crude mixture was passed through column chromatography (silica gel,  $\text{CHCl}_3$  – EtOH 95:5, v/v). The fractions containing the product were collected and evaporated to dryness. The solid residue was washed with methanol and filtrated (this is a necessary step to eliminate unreacted aldehydes). Finally, the title compound was purified by column chromatography (silica gel, DCM – MeOH, 98:2, v/v) (30mg, 6%).

$^1\text{H NMR}$  (500 MHz,  $\text{DMSO}-d_6$ ):  $\delta$  = 8.73 (m, 8H), 8.55 (d,  $J$  = 8.0 Hz, 2H), 8.36 (m, 4H), 8.22 (m, 2H), 7.30 (s, 4H), 4.40 (m, 4H), 2.64 (s, 6H), 1.85 (s, 12H), 1.53 (t,  $J$  = 7.1 Hz, 6H), -2.62 (bs, 2H) ppm.

$^{13}\text{C NMR}$  (125 MHz,  $\text{DMSO}-d_6$ ):  $\delta$  = 170.5, 147.7, 146.4, 139.5, 138.3, 138.1, 134.8, 134.7, 134.6, 130.6, 130.3, 130.2, 128.9, 128.7, 128.0, 127.1, 119.0, 118.2, 62.8, 62.7, 21.8, 21.6, 16.7 ppm.



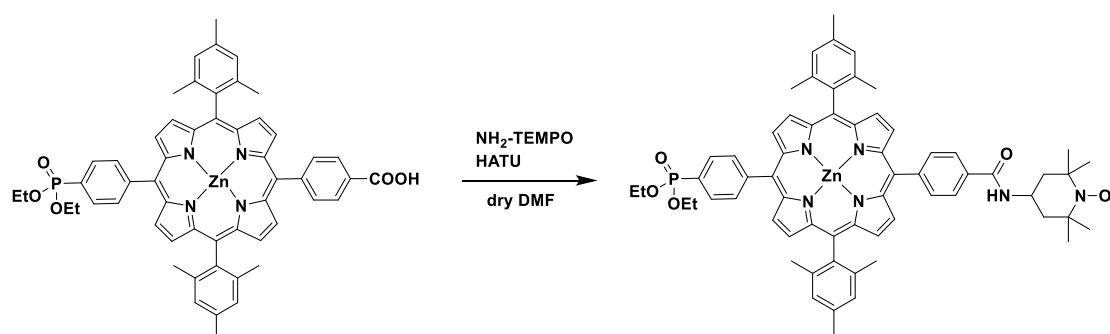
- Synthesis of **PO(OEt)<sub>2</sub>ZnP-COOH**



**Scheme 4.3.12** Synthetic procedure for **PO(OEt)<sub>2</sub>ZnP-COOH**.

In a solution of porphyrin **PO(OEt)<sub>2</sub>DMP-COOH** (30 mg, 0.034 mmol) in THF (12 mL) in a round bottom flask, a solution of  $\text{Zn}(\text{CH}_3\text{COO})_2 \cdot 2\text{H}_2\text{O}$  (75 mg, 0.34 mmol) in MeOH (2 mL) was added and the reaction mixture was stirred at room temperature overnight. The crude product was purified by silica column chromatography eluting with  $\text{CH}_2\text{Cl}_2 - \text{MeOH}$  (98:2, v/v). Yield: 30mg (95%).

- Synthesis of **PO(OEt)<sub>2</sub>ZnP-TEMPO**



**Scheme 4.3.13** The experimental procedure for the synthesis of **PO(OEt)<sub>2</sub>ZnP-TEMPO**.

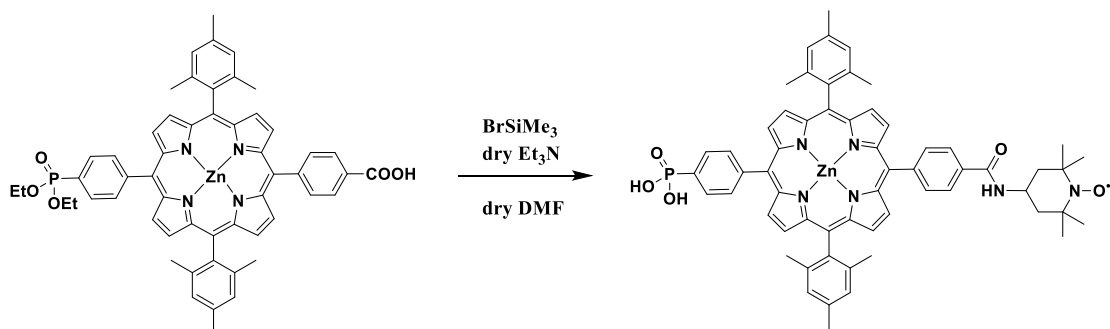
**PO(OEt)<sub>2</sub>ZnP-COOH** (35 mg, 0.037 mmol, 1.0 equiv) was dissolved in 4 mL of dry DMF and cooled at 0 °C. Then the HATU coupling reagent 1-[Bis(dimethylamino)methylene]-1H-1,2,3-triazolo[4,5-b]pyridinium 3-oxide hexafluorophosphate (28 mg, 0.074 mmol, 1.0 equiv) was added and the reaction mixture was stirred for 2 hours at 0 °C. Subsequently,  $\text{NH}_2\text{-TEMPO}$  (9.5 mg, 0.056 mmol, 1.5 equiv) and 10  $\mu\text{L}$  DIPEA were introduced in the reaction which was stirred for 72 hours at room temperature. After the completion of the reaction 0.5 mL of EtOH were added in order to counteract the remaining activated intermediate and left stirring

overnight. The desired product was purified via silica gel column chromatography with  $\text{CHCl}_3$ -MeOH (99-1) followed by precipitation in DCM/Pentane. The title compound was isolated as a purple solid (14 mg, 35%).

$^1\text{H NMR}$  (500 MHz,  $\text{DMSO}-d_6$ ):  $\delta$  = 8.70 (m, 4H), 8.56 (m, 4H), 8.52 (d,  $J$  = 8.0 Hz, 1H), 8.36 (m, 2H), 8.27 (d,  $J$  = 8.2 Hz, 2H), 8.22 (d,  $J$  = 8.2 Hz, 2H), 8.10 (m, 2H), 7.30 (s, 4H), 4.37 (m, 1H), 4.26 (m, 4H), 2.57 (s, 6H), 1.87 (m, 2H), 1.77 (s, 12H), 1.65 (m, 2H), 1.40 (t,  $J$  = 7.1 Hz, 6H), 1.19 (bs, 6H), 1.15 (bs, 6H) ppm.

$^{13}\text{C NMR}$  (125 MHz,  $\text{DMSO}-d_6$ ):  $\delta$  = 165.9, 149.3, 149.2, 149.0, 148.8, 147.2, 145.7, 139.1, 138.5, 136.9, 134.5, 134.0, 131.9, 131.8, 130.3, 130.2, 129.4, 127.6, 125.4, 119.0, 118.3, 118.2, 62.1, 58.1, 44.9, 32.8, 21.5, 21.1, 20.7, 19.8, 16.4 ppm.

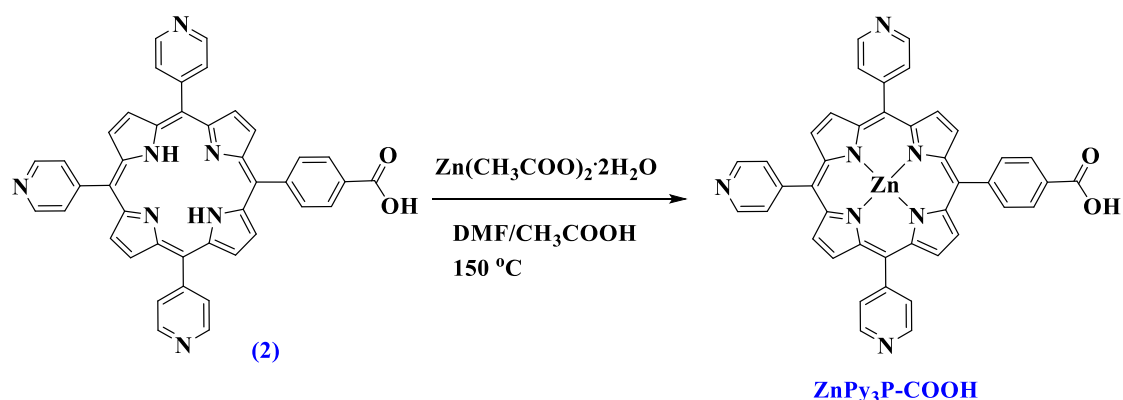
- Synthesis of  **$\text{H}_2\text{O}_3\text{P-ZnP-TEMPO}$**



**Scheme 4.3.14** The experimental procedure for the synthesis of  **$\text{H}_2\text{O}_3\text{P-ZnP-TEMPO}$** .

In a round-bottom flask,  **$\text{PO}(\text{OEt})_2\text{ZnP-TEMPO}$**  (20 mg, 0.0183 mmol), was dissolved in dry DMF (5 mL) and freshly distilled dry  $\text{Et}_3\text{N}$  (64  $\mu\text{L}$ ) was added.  $(\text{CH}_3)_3\text{SiBr}$  (48  $\mu\text{L}$ ), was also added and the reaction mixture was heated under Ar atmosphere at  $50^\circ\text{C}$  for 24h. After the completion of the reaction MeOH (10 drops) was added and the solvents were evaporated under vacuum. The solid residue was dispersed in water and it was filtered off and dried under vacuum. Yield: 14 mg (74%).

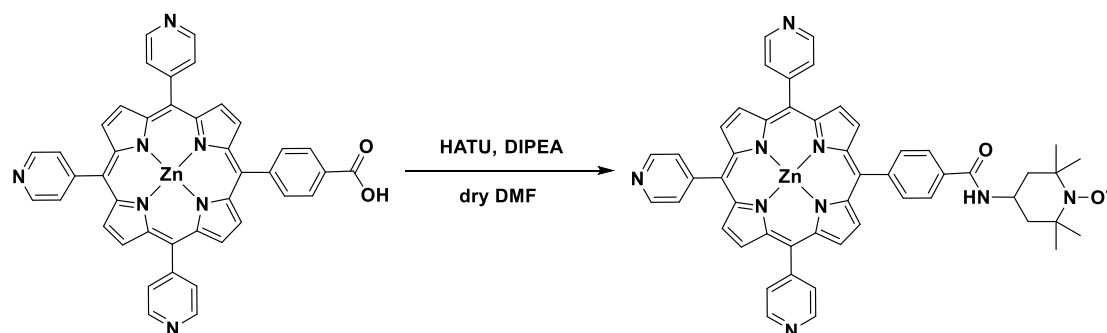
- Synthesis of **ZnPy<sub>3</sub>P-COOH**



**Scheme 4.3.15** The experimental procedure for the synthesis of **ZnPy<sub>3</sub>P-COOH**.

In a 50 mL flask, 25mg of **2** (0.029 mmol, 1 equiv) were dissolved in 16 mL DMF/CH<sub>3</sub>COOH 1:1. Subsequently, Zn(CH<sub>3</sub>COO)<sub>2</sub>·2H<sub>2</sub>O (95 mg, 0.43 mmol, 15 equiv) was added and the reaction mixture was refluxed at 150 °C overnight. After the completion of the reaction, the mixture was cooled to room temperature, the solvents were evaporated under vacuum and the product was washed with water and filtered. The title compound was used without further purification.

- Synthesis of **ZnPy<sub>3</sub>P-TEMPO**



**Scheme 4.3.16** The experimental procedure for the synthesis of **ZnPy<sub>3</sub>P-TEMPO**.

**ZnPy<sub>3</sub>P-COOH** (21 mg, 0.029 mmol, 1.0 equiv) was dissolved in dry DMF (5 mL) in a schlenk tube and the solution was cooled in an ice bath to 0 °C. Then 150 μL of DIPEA were added followed by the coupling reagent 1-[Bis(dimethylamino)methylene]-1H-1,2,3-triazolo[4,5-b]pyridinium 3-oxide hexafluorophosphate (HATU, 44 mg, 0.117 mmol, 4 equiv). The reaction mixture was stirred for 2 hours at 0 °C. Subsequently **NH<sub>2</sub>-TEMPO** (10 mg, 0.058 mmol, 1.6 equiv) was added and the resulting mixture was stirred at room temperature for 24 h. After the completion of the reaction DMF was

evaporated under vacuum. The title compound was isolated by column chromatography (silica gel, THF) as a purple solid (16 mg, 61%).

$^1\text{H NMR}$  (400 MHz, THF- $d_4$ ):  $\delta$  = 8.91 (m, 6H), 8.85 (m, 8H), 8.24 (bs, 4H), 8.13 (m, 6H), 7.75 (d,  $J$  = 7.7 Hz, 1H), 7.03 (bs, 1H), 4.52 (m, 1H), 2.00 (m, 1H), 1.63 (m, 2H), 1.29 (s, 6H), 1.22 (s, 6H).

### *Photocatalytic experiments using the NiP-Ru dyads*

In the photocatalytic experiments a 450 W Xenon lamp equipped with a 400nm cut-off filter was used. For the detection of O<sub>2</sub> during photocatalysis a NeoFox optical oxygen sensor<sup>[6]</sup> purchased from Ocean Optics was used. In detail the reaction solvent was DMF containing 4% of water while the final volume was 3 mL. In all examined cases the concentration of Methyl Viologen (sacrificial electron acceptor) was 50 mM. The turn-over-number was obtained from the following equation:

$$TON = \frac{\text{mol } O_2}{\text{mol catalyst}}$$

The photoelectrocatalytic experiments were performed using a VersaSTAT 4 Potentiostat and a three-electrode electrochemical cell with the NiP-Ru-COOH/TiO<sub>2</sub>/FTO working electrode, a platinum mesh as the counter electrode, and the Ag/AgCl (3 M NaCl aqueous solution) reference electrode. The photocurrent was measured at 0 V vs. Ag/AgCl without stirring. 450 W Xenon lamp equipped with a 400 nm cut-off filter was used. In order to prepare the NiP-Ru-COOH/TiO<sub>2</sub>/FTO working electrode we incubated the TiO<sub>2</sub>/FTO glass in a 0.5mM solution of NiP-Ru-COOH (CHCl<sub>3</sub>:EtOH 1:1) for 4 hours, washed it with ethanol and let it dry in the air.

### *Photocatalytic experiments using the ZnP-TEMPO dyads*

The photocatalytic experiments were carried out in a doubly jacketed Pyrex glass reactor with and an external cooling jacket maintained at room temperature with a constant flow of tap water. A 1 cm<sup>2</sup> sensitized TiO<sub>2</sub> film was used as working electrode and a saturated calomel electrode and Pt-mesh were used as reference and counter electrode, respectively. All experiments were carried out in 7 mL solution containing 50 mM of *para*-methoxybenzyl alcohol or benzyl alcohol or *para*-trifluoromethyl benzyl alcohol. Before every experiment, the solution was degassed by Ar for at least 15 min. A white LED PAR38 lamp (17 W, 5000 K) was used as a light source with 400

nm cutoff filter and the distance between the light source and photoelectrochemical cell was always 12 cm to maintain the light power to be about 1 sun. The power of the lamp is about 1000 W/m<sup>2</sup> as determined with a calibrated silicon cell. The reaction mixture was kept under gentle constant stirring (300 rpm) during the course of irradiation and the composition of the resulting electrolyte were analyzed by gas chromatography. For that goal, the compounds were extracted twice with dichloromethane (3 + 4 mL) and dried over MgSO<sub>4</sub> before being analyzed by gas chromatography (Agilent Technologies 7890B GC) system equipped with a thermal conductivity detector. Calibration curves for *para*-methoxy benzylalcohol and *para*-methoxy benzaldehyde were determined separately by injecting known volumes of them respectively. Generated product from long term photocatalysis was quantified through that calibration curve. From product quantification, TON was calculated as follow:

$$\text{TON} = n_{\text{product}} / n_{\text{catalyst, film}}$$

$$\text{TOF} = \text{TON} / \text{duration of the experiment}$$

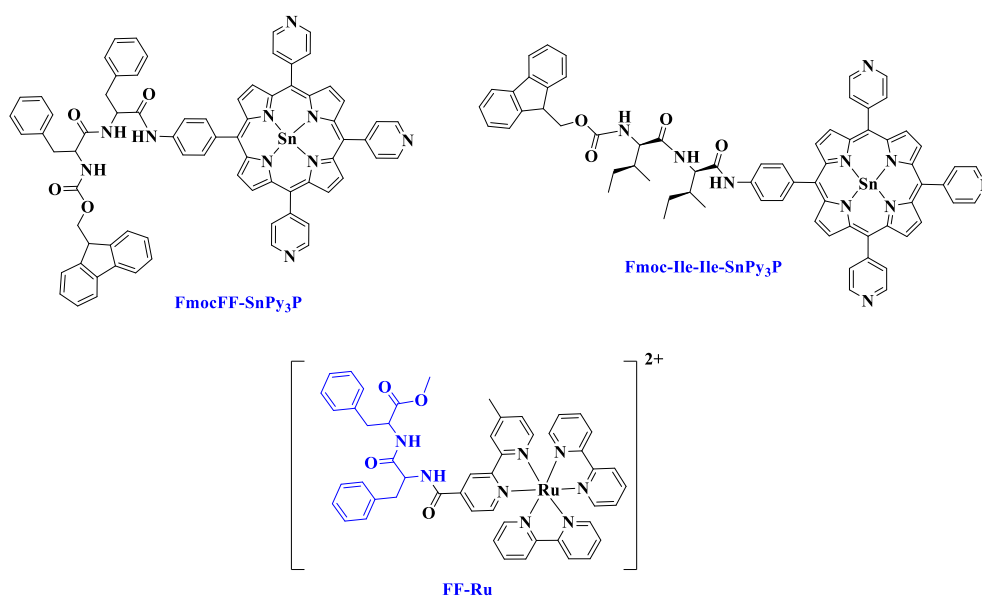
The Faradaic efficiency was calculated according to the integrated charge (Q) passed during photocatalysis and the amount of aldehyde produced with the equation:

$$\text{FE}(\%) = (96485 \times n(\text{aldehyde}) \times 2) / Q$$

## Chapter 5: Conclusions and Perspectives

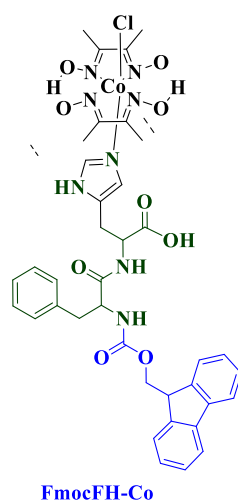
The present PhD dissertation provided insights regarding the utilization of porphyrin derivatives as photosensitizers and catalyst in light harvesting applications. The newly synthesized porphyrin hybrid conjugates have been studied for their self-assembling ability, as light-harvesters in photocatalytic hydrogen evolution schemes, as catalysts in water oxidation and as photosensitizers in alcohol oxidation systems. The obtained results from this thesis could be valuable in designing novel porphyrin moieties regarding those applications. In this chapter, some perspectives concerning the synthesis and the application of novel porphyrin hybrids will be suggested.

As it is already discussed in chapter 3, the strategy of connecting peptide-based moieties to porphyrin chromophores enhances the properties of the resulting hybrid molecule. Therefore, we propose the porphyrin conjugates illustrated in **Figure 5.1** as photosensitizers in light-driven hydrogen evolution. The intention is to create self-assembly hydrogels, which might further improve the photocatalytic activity of the system. We support this suggestion, since Fmoc-protecting group is a known gelator moiety and the Fmoc-FF and Fmoc-Ile-Ile- entities have already shown their ability to create hydrogels in mixed solvent systems. Additionally, an alternative chromophore that could be investigated for its ability to self-assemble is a ruthenium complex after its covalent attachment to diphenylalanine (**Figure 5.1**). This would be also a promising candidate for light harvesting applications.



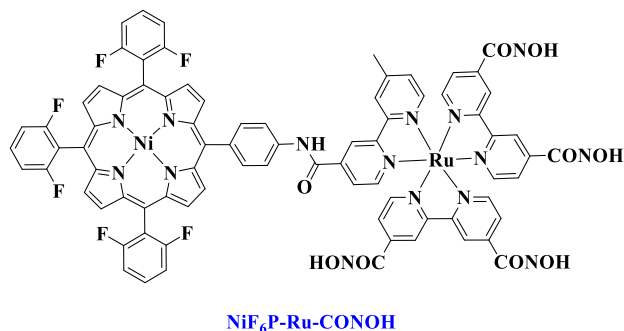
**Figure 5.1** Chemical structures of the proposed **Fmoc-FF-SnPy<sub>3</sub>P** and **Fmoc-Ile-Ile-SnPy<sub>3</sub>P** hybrids as photosensitizers for photocatalytic H<sub>2</sub> production.

Another approach that has not yet been investigated is the self-assembly of the hydrogen production catalyst. For this reason, we propose the following cobaloxime hybrid molecule, which will probably be an efficient H<sub>2</sub> evolution catalyst, since it is a cobaloxime and will possess self-assembling properties. The latter ability is expected to improve the overall efficiency of the system, especially if both the catalyst and the photosensitizer are in the self-assembly state.



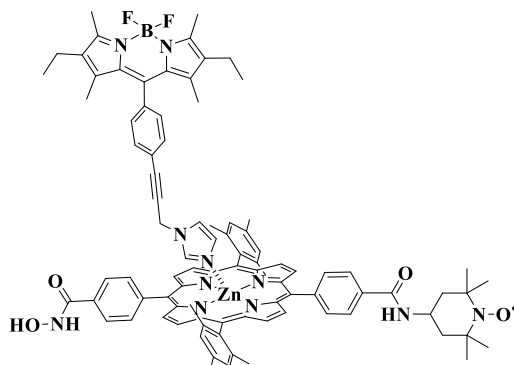
**Figure 5.2** Chemical structure of the proposed **Fmoc-FH-Co** hybrid as catalyst for photocatalytic H<sub>2</sub> production.

According to the results of chapter 4, where we showed the significance of nickel porphyrins as a cheaper alternative to water oxidation catalysis, we propose the following nickel porphyrin – ruthenium complex dyad as WOC (**Figure 5.3**). The modification on the periphery of the porphyrin macrocycle is expected to improve the electrochemical properties of the Ni<sup>2+</sup> catalytic center, while the hydroxamic group might enhance the connection to the semiconductor in order to create a robust DSPEC system for water oxidation.



**Figure 5.3** Chemical structure of the proposed **NiF<sub>6</sub>P-Ru-CONOH** dyad for photocatalytic water oxidation.

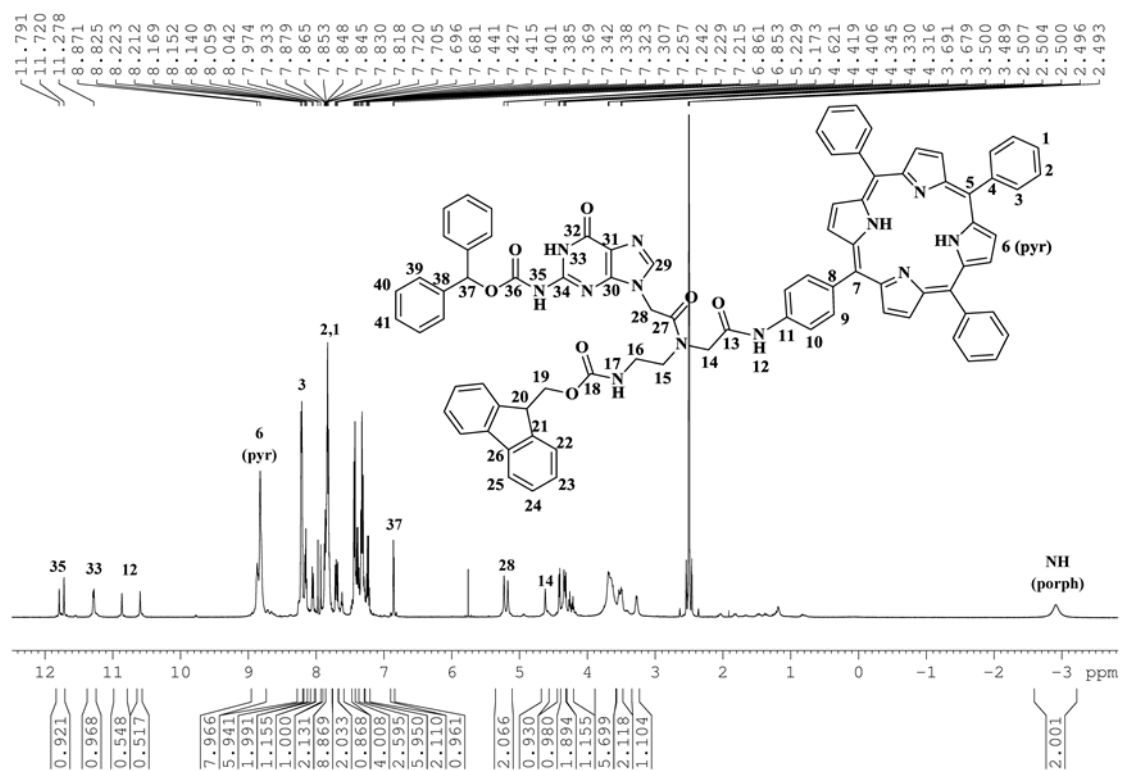
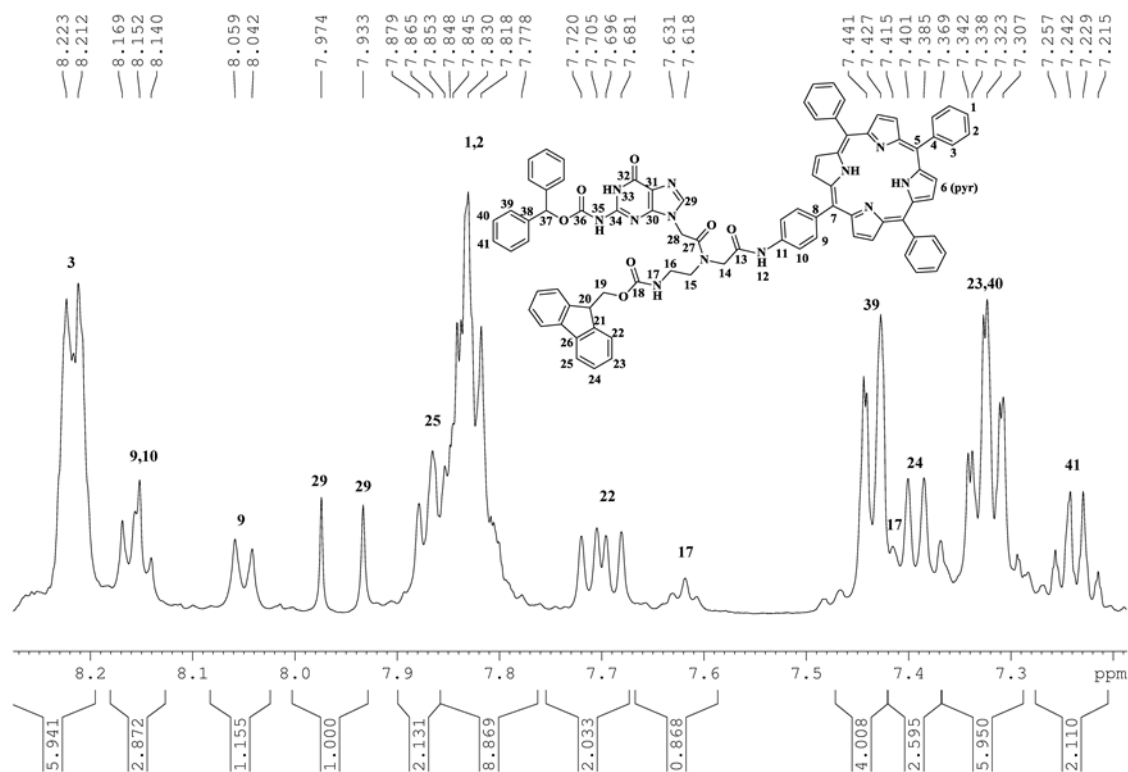
Finally, regarding the application of porphyrin derivatives in alcohol oxidation, we demonstrated in chapter 4 that porphyrin-TEMPO dyads can efficiently catalyze this reaction under light irradiation. In order to achieve even better catalytic performance, we suggest the synthesis of a BDP-porphyrin-TEMPO triad (**Figure 5.4**), which will utilize the antenna effect to achieve wider harvesting of the visible spectrum.



**Figure 5.4** Chemical structure of the proposed **hyd-ZnP-BDP(Im)-TEMPO** dyad for photocatalytic alcohol oxidation.



## Chapter 6: Appendix

Figure 6.3.1  $^1\text{H}$  NMR spectrum of PNA-TPP (500 MHz, DMSO).Figure 6.3.2  $^1\text{H}$  NMR spectrum of PNA-TPP (500 MHz, DMSO).

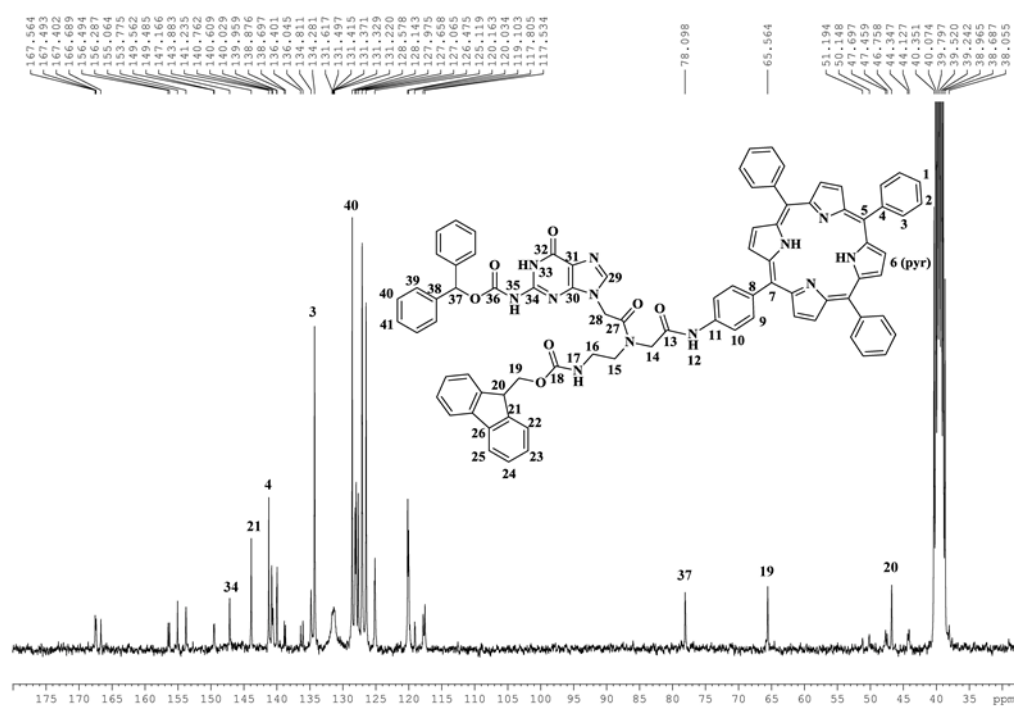


Figure 6.3.3  $^{13}\text{C}$  NMR spectrum of PNA-TPP (75 MHz, DMSO).

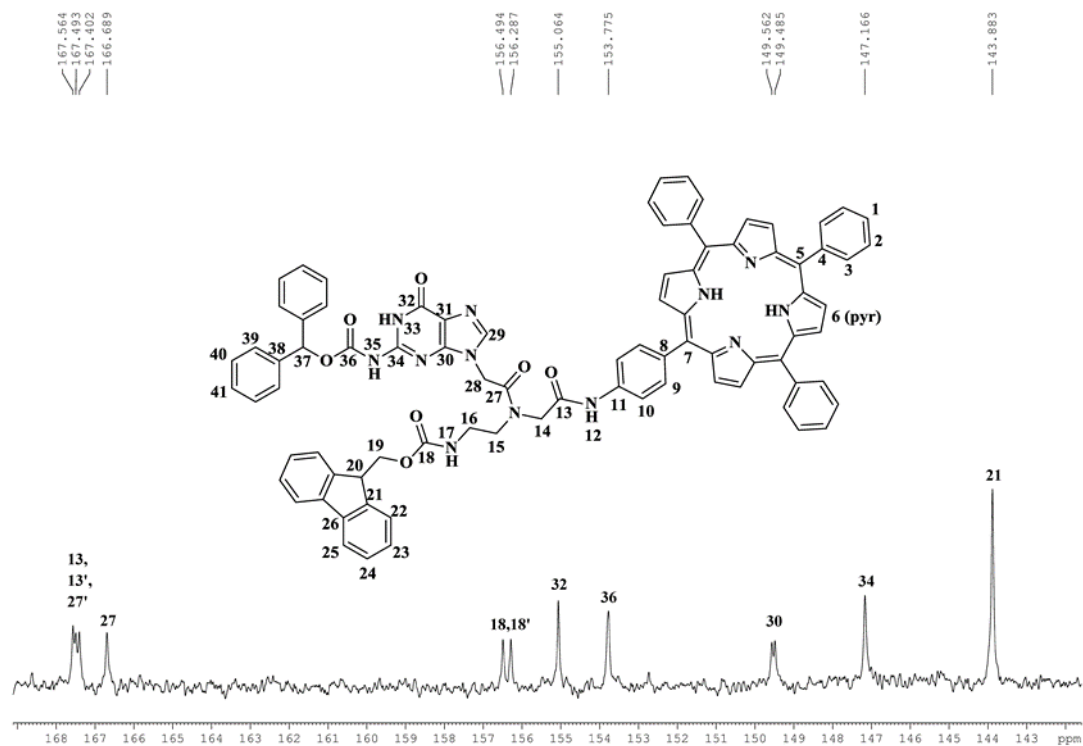


Figure 6.3.4  $^{13}\text{C}$  NMR spectrum of PNA-TPP (75 MHz, DMSO).

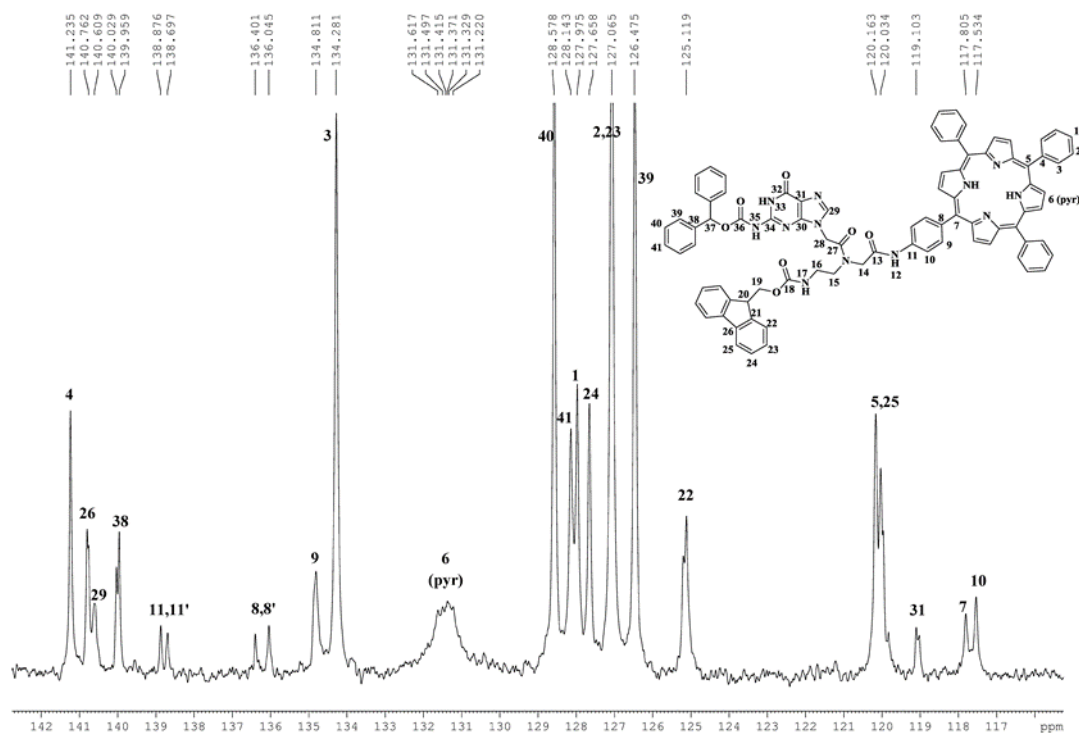


Figure 6.3.5 <sup>13</sup>C NMR spectrum of PNA-TPP (75 MHz, DMSO).

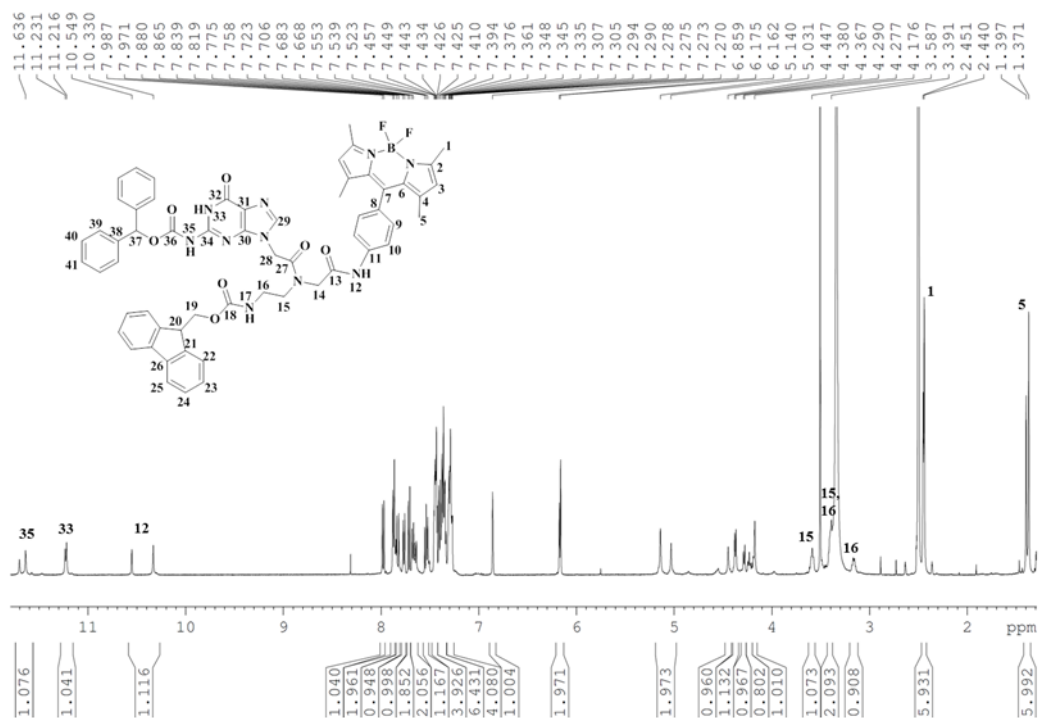
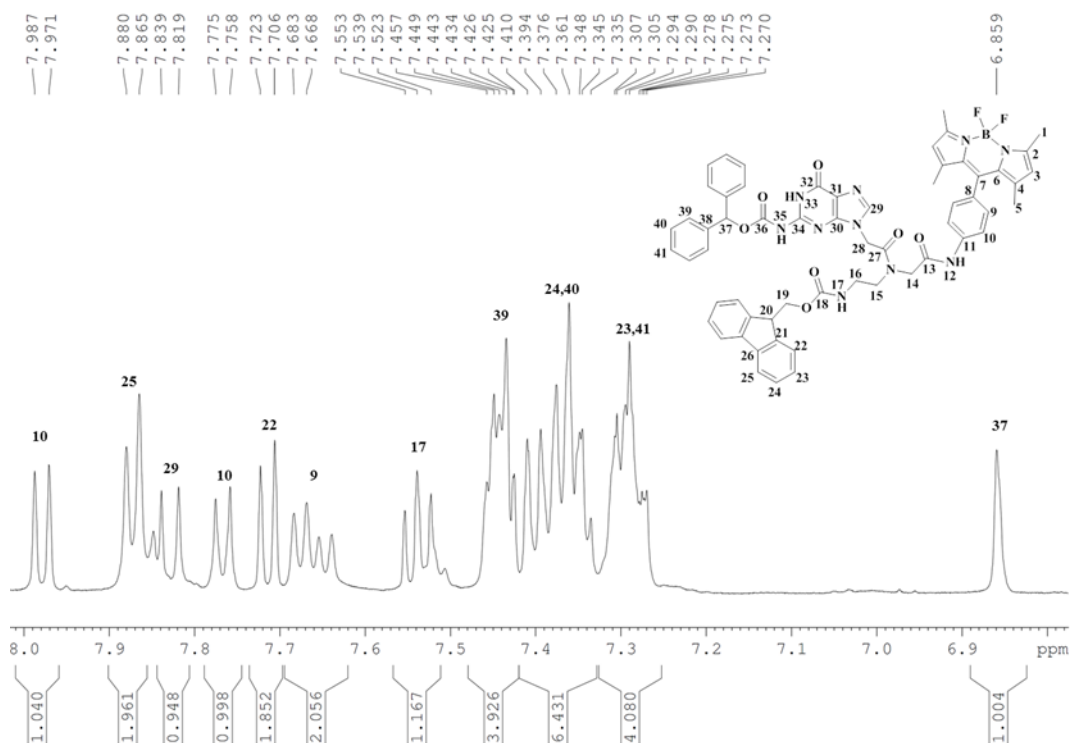
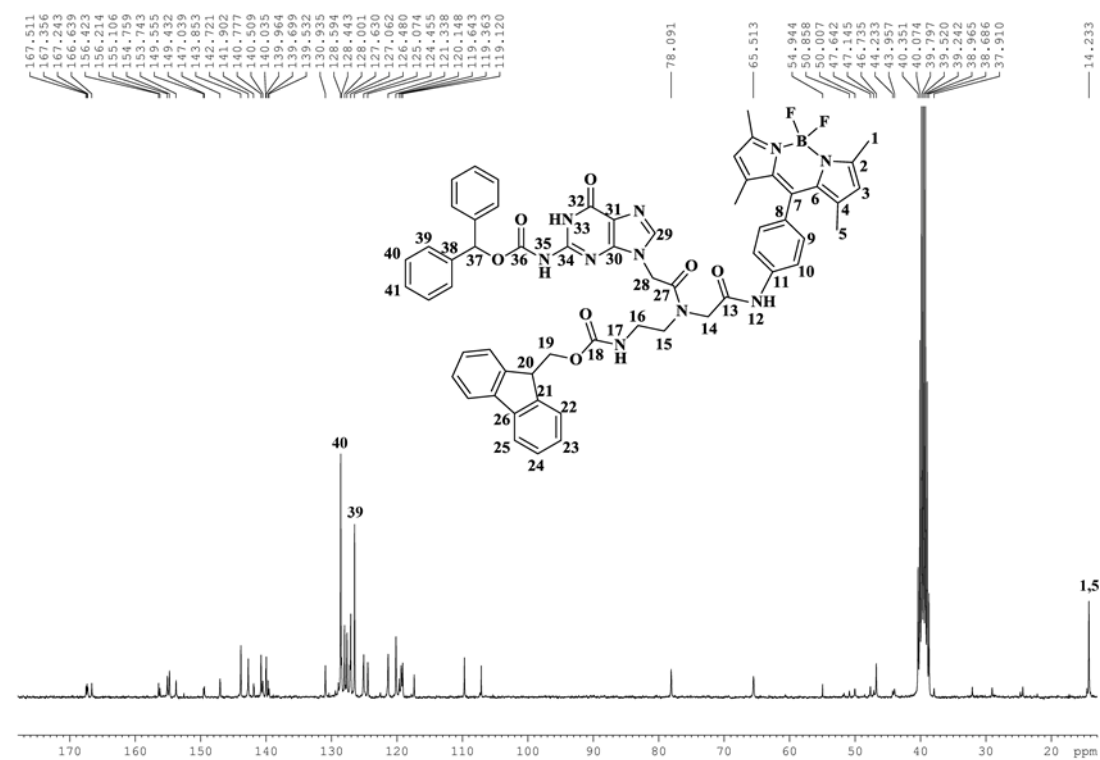


Figure 6.3.6 <sup>1</sup>H NMR spectrum of PNA-BDP (500 MHz, DMSO).



**Figure 6.3.7**  $^1\text{H}$  NMR spectrum of PNA-BDP (500 MHz, DMSO).



**Figure 6.3.8**  $^{13}\text{C}$  NMR spectrum of PNA-BDP (75 MHz, DMSO).

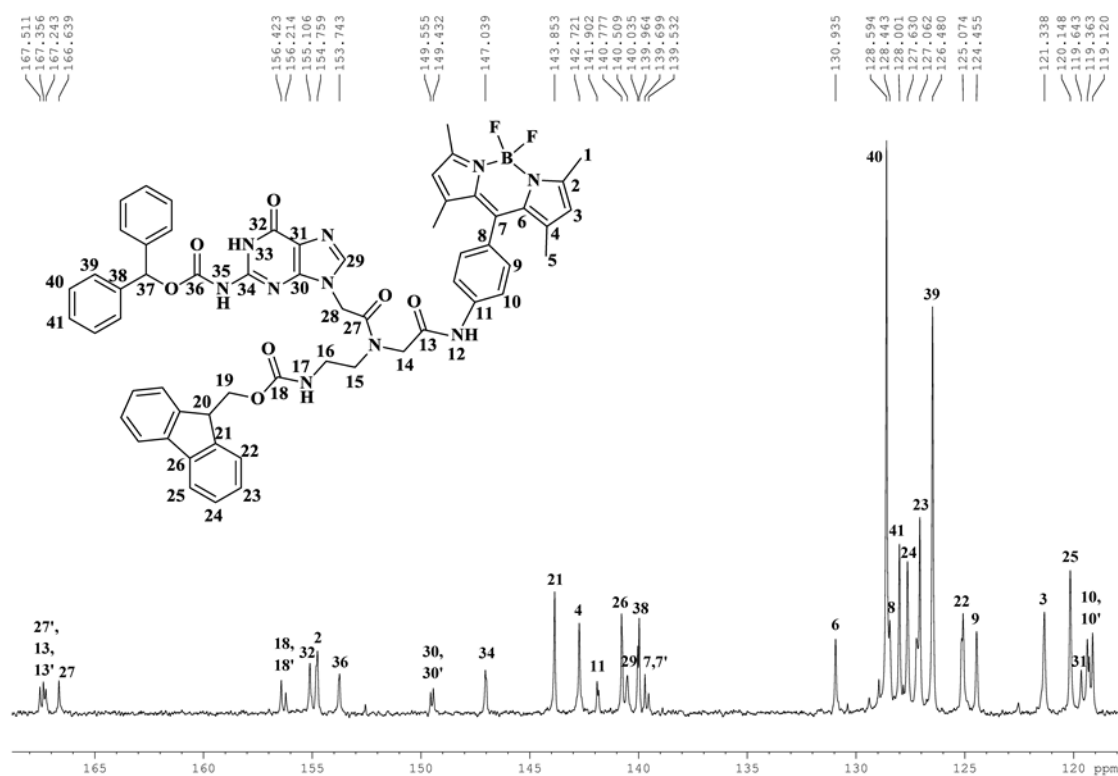


Figure 6.3.9  $^{13}\text{C}$  NMR spectrum of PNA-BDP (75 MHz, DMSO).

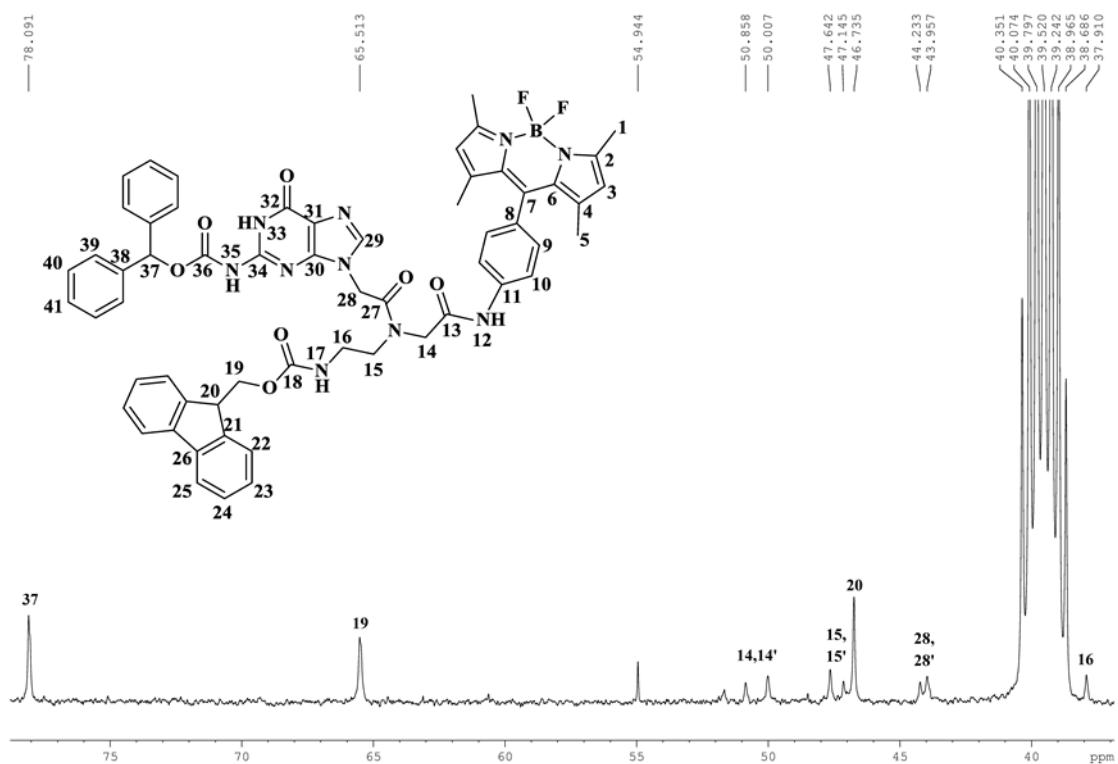
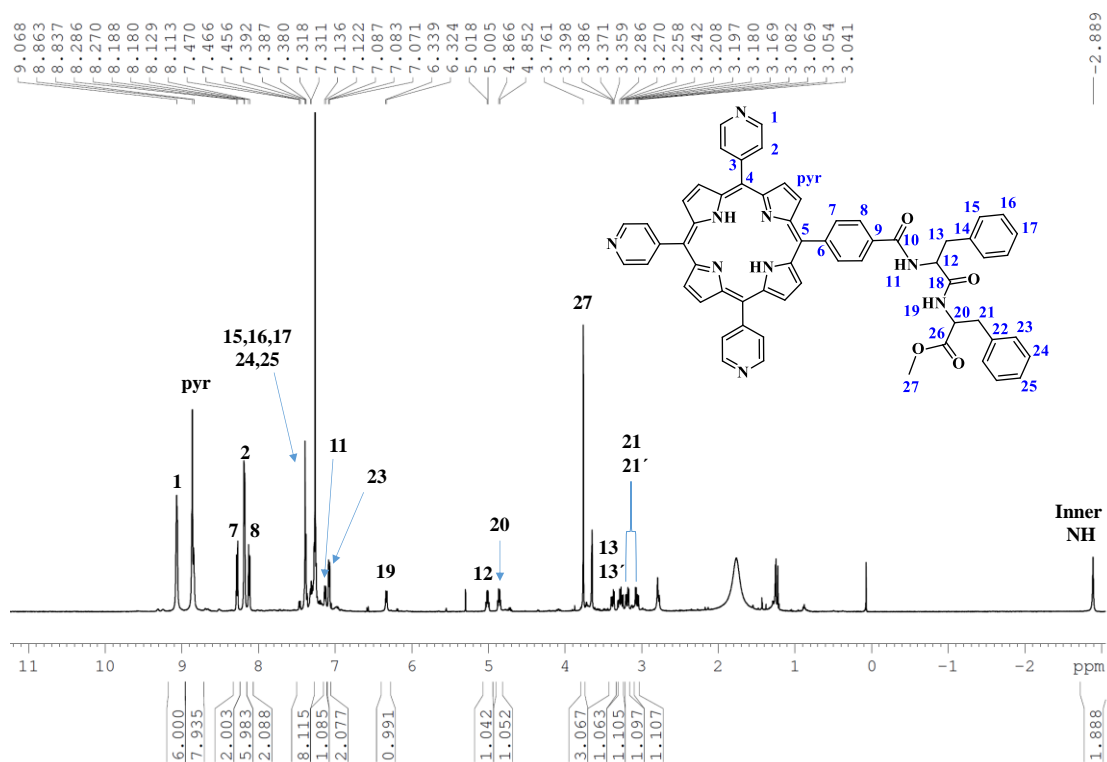
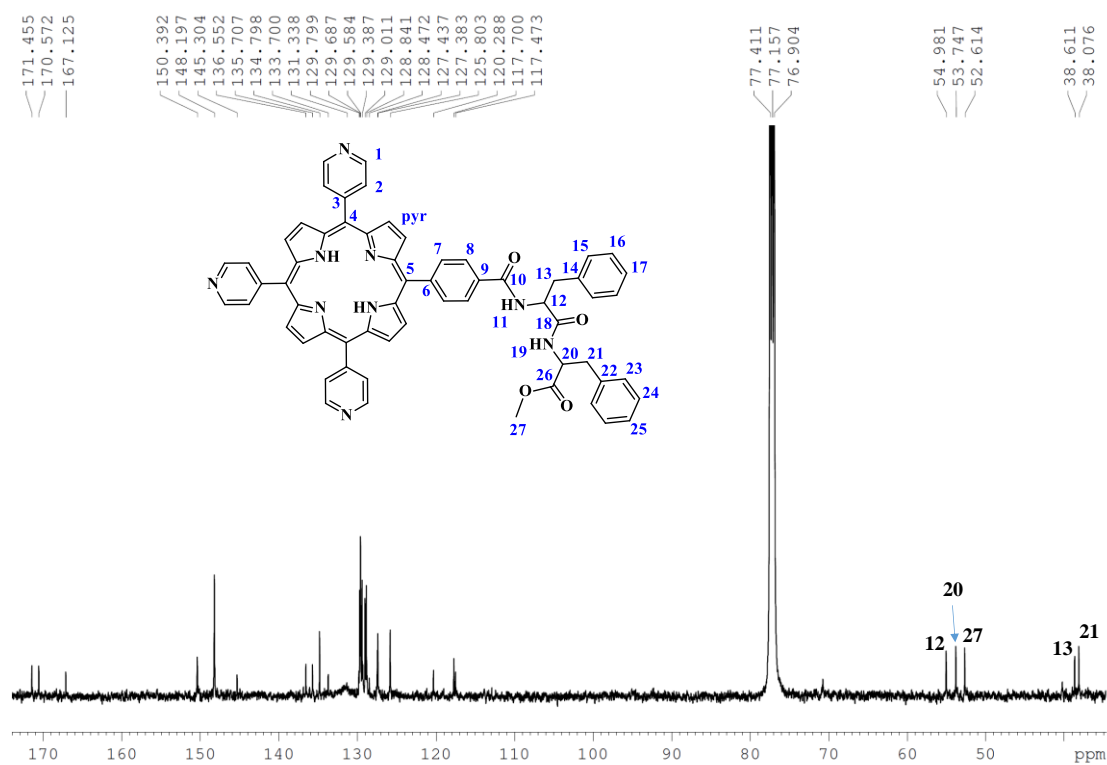


Figure 6.3.10  $^{13}\text{C}$  NMR spectrum of PNA-BDP (75 MHz, DMSO).



**Figure 6.3.11**  $^1\text{H}$  NMR spectrum of compound **Py<sub>3</sub>P-FF** in  $\text{CDCl}_3$ .



**Figure 6.3.12**  $^{13}\text{C}$  NMR spectrum of compound **Py<sub>3</sub>P-FF** in  $\text{CDCl}_3$ .

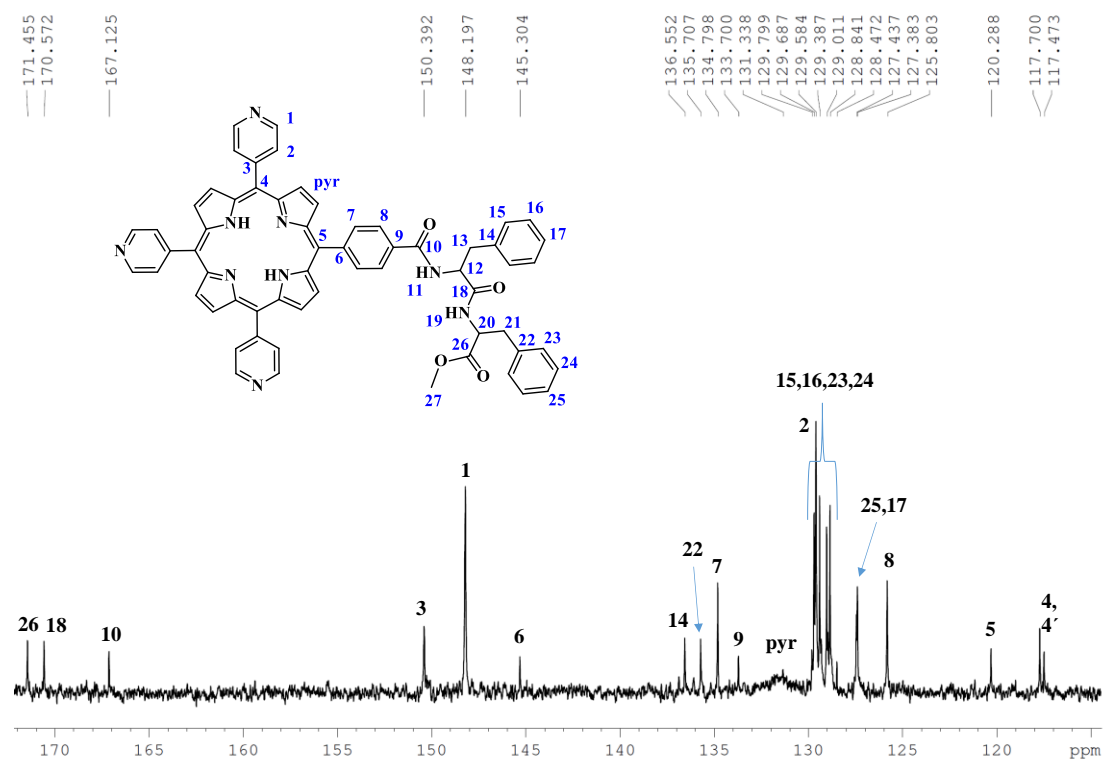


**Figure 6.3.13**  $^{13}\text{C}$  NMR spectrum of compound **Py<sub>3</sub>P-FF** in  $\text{CDCl}_3$ .

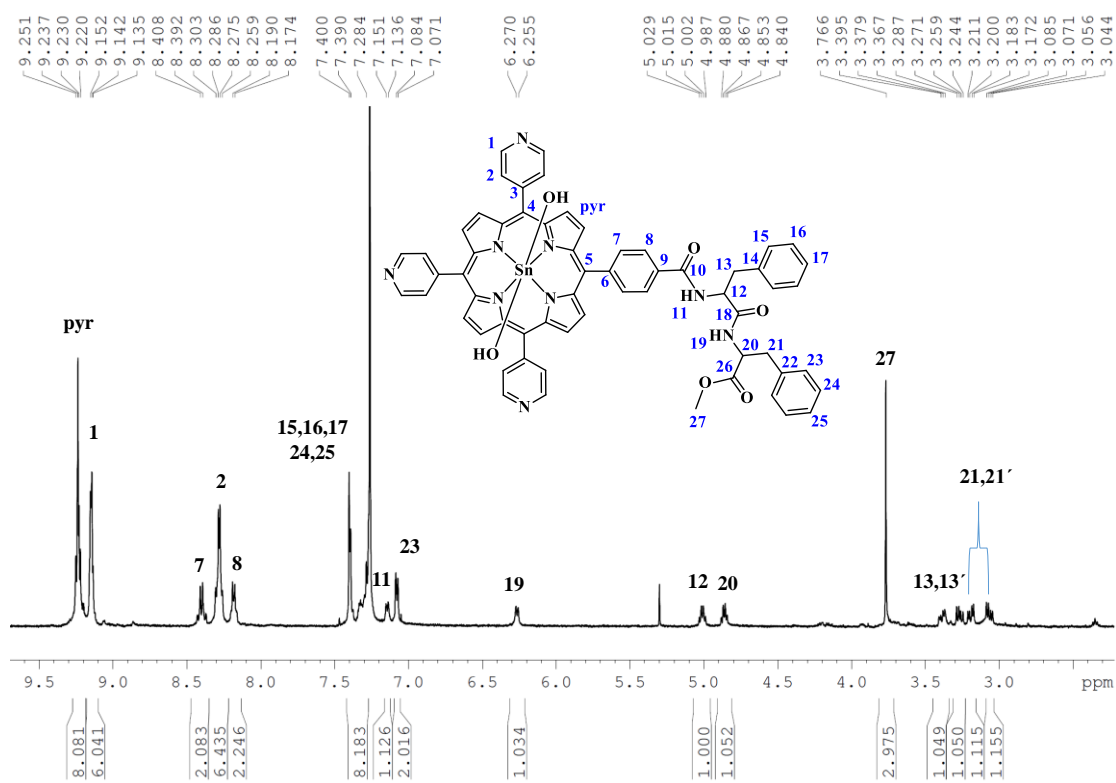


**Figure 6.3.14**  $^1\text{H}$  NMR spectrum of compound **SnPy<sub>3</sub>P-FF** in  $\text{CDCl}_3$ .

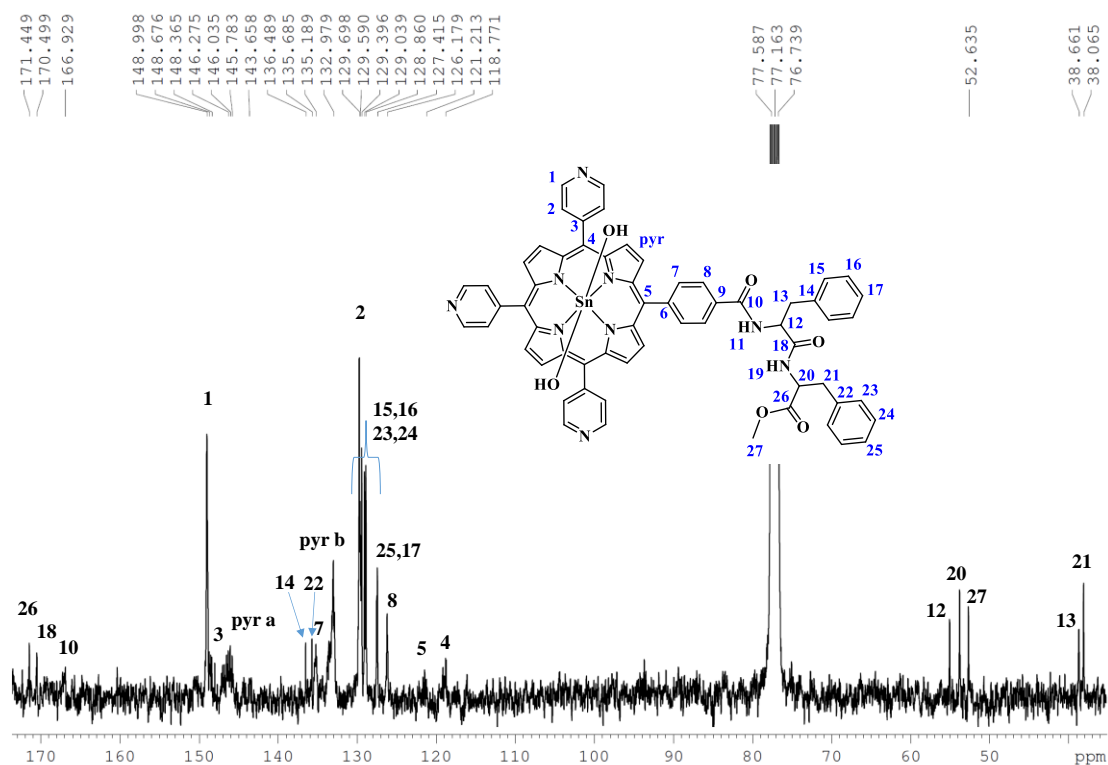


**Figure 6.3.15**  $^{13}\text{C}$  NMR spectrum of compound **SnPy<sub>3</sub>P-FF** in  $\text{CDCl}_3$ .

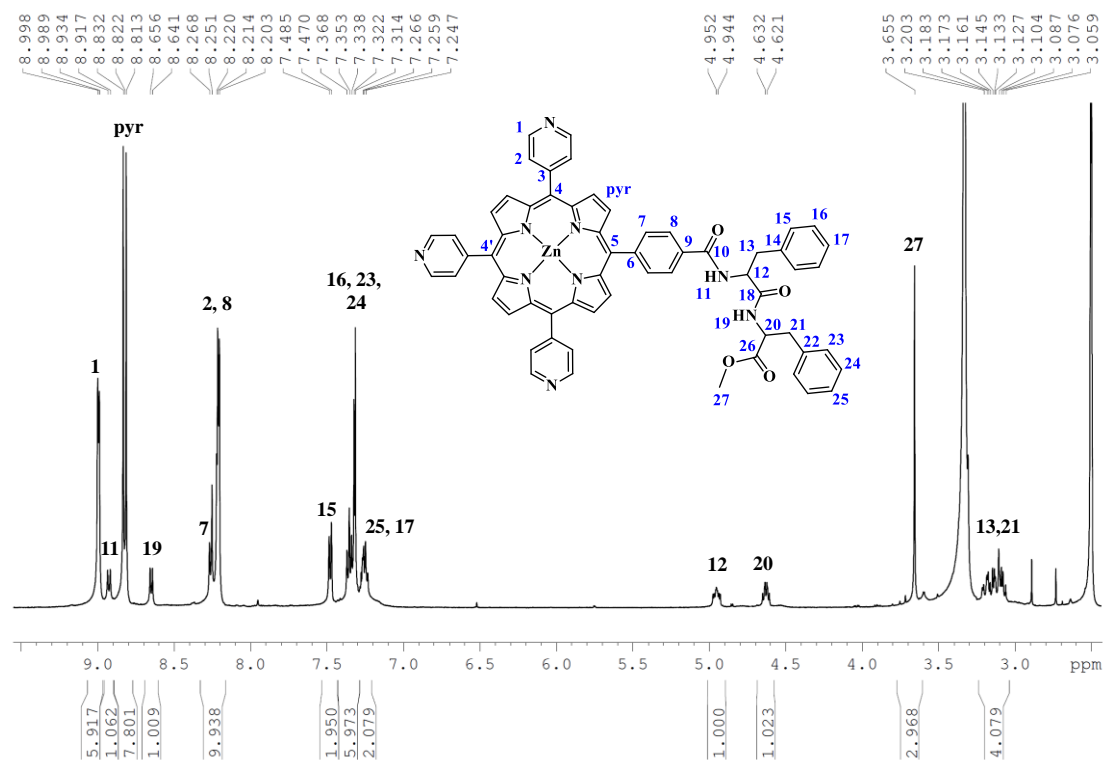


**Figure 6.3.16**  $^1\text{H}$  NMR spectrum of compound **ZnPy<sub>3</sub>P-FF** in  $\text{DMSO}$ .



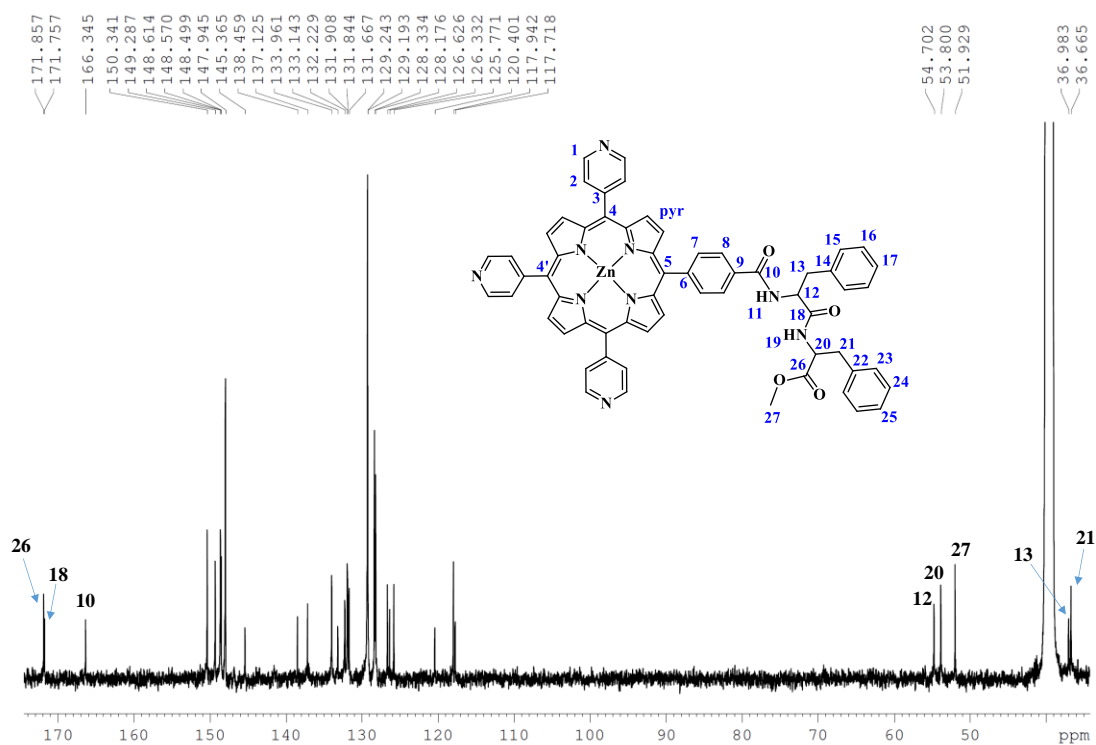


Figure 6.3.17  $^{13}\text{C}$  NMR spectrum of compound  $\text{ZnPy}_3\text{P-FF}$  in  $\text{DMSO}$ .

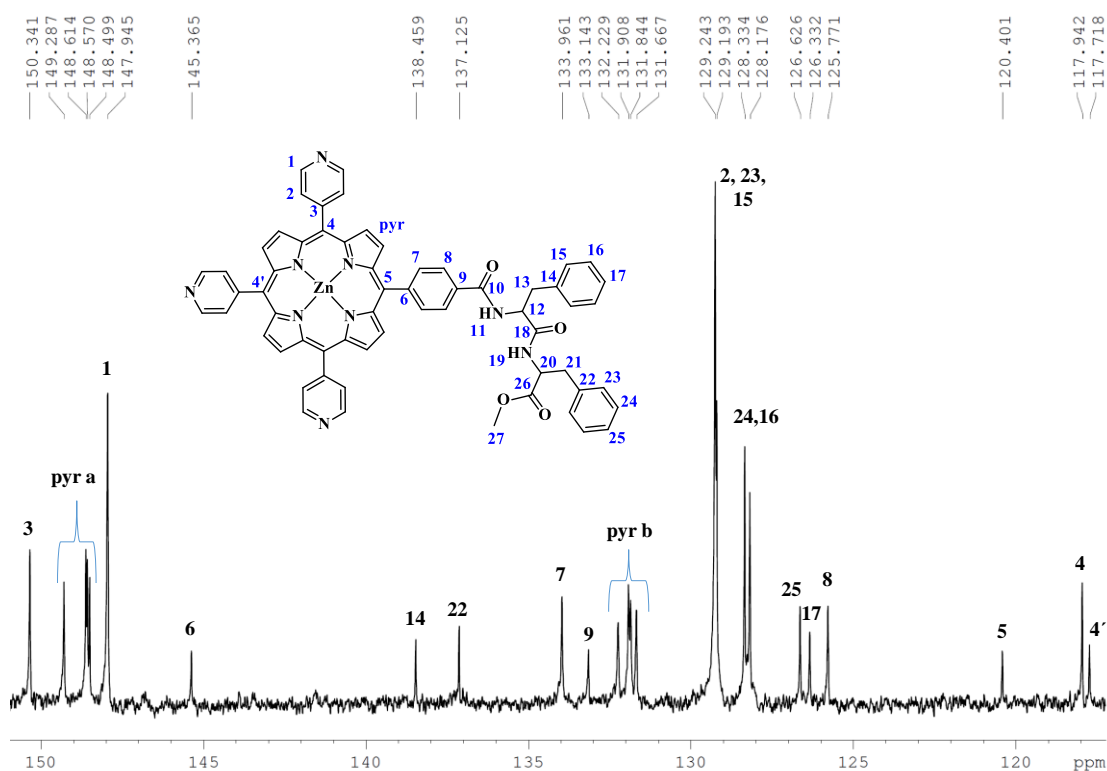
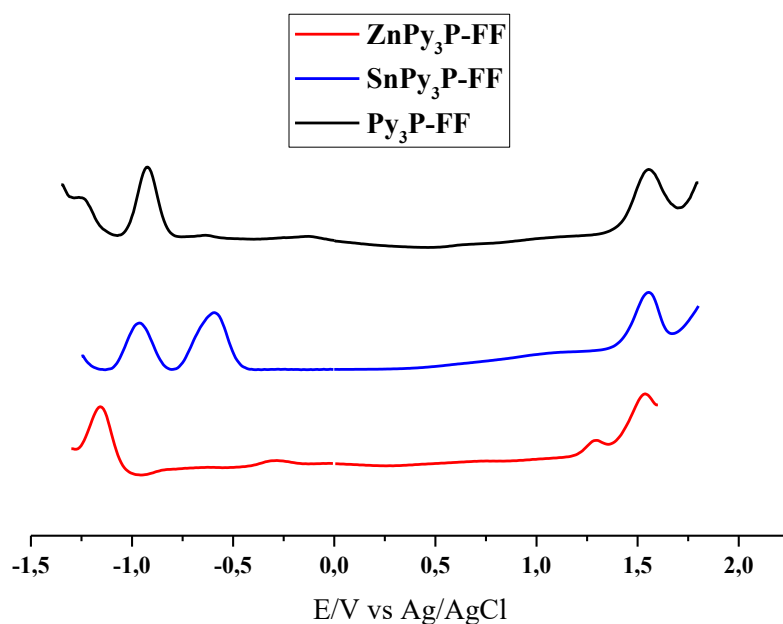


Figure 6.3.18  $^{13}\text{C}$  NMR spectrum of compound  $\text{ZnPy}_3\text{P-FF}$  in  $\text{DMSO}$ .



**Figure 6.3.19** Square wave (SW) voltammograms of **ZnPy<sub>3</sub>P-FF**, **SnPy<sub>3</sub>P-FF** and **Py<sub>3</sub>P-FF**.

The experimental conditions were the following:

The solvent was DCM, the supporting electrolyte was TBAPF<sub>6</sub> (0.1 M), the working electrode was glassy carbon, the reference electrode was Ag/AgCl, scan speed 100 mV/sec, ferrocene was used as internal standard and in the above conditions exhibited a peak at 0.62 V vs. Ag/AgCl. In the following table you find a summary of the electrochemical data:

**Table 6.3.1:** Redox potentials of ZnPy<sub>3</sub>P-FF, SnPy<sub>3</sub>P-FF and Py<sub>3</sub>P-FF (vs. Ag/AgCl) determined by square wave voltammetry at a Pt electrode

Compound	E <sub>1/2</sub> (red <sup>2</sup> )	E <sub>1/2</sub> (red <sup>1</sup> )	E <sub>1/2</sub> (ox <sup>1</sup> )	E <sub>1/2</sub> (ox <sup>2</sup> )
<b>ZnPy<sub>3</sub>P-FF</b>		-1.16	1.29	1.54
<b>SnPy<sub>3</sub>P-FF</b>	-0.96	-0.59	1.56	
<b>Py<sub>3</sub>P-FF</b>	-1.3	-0.93	1.55	

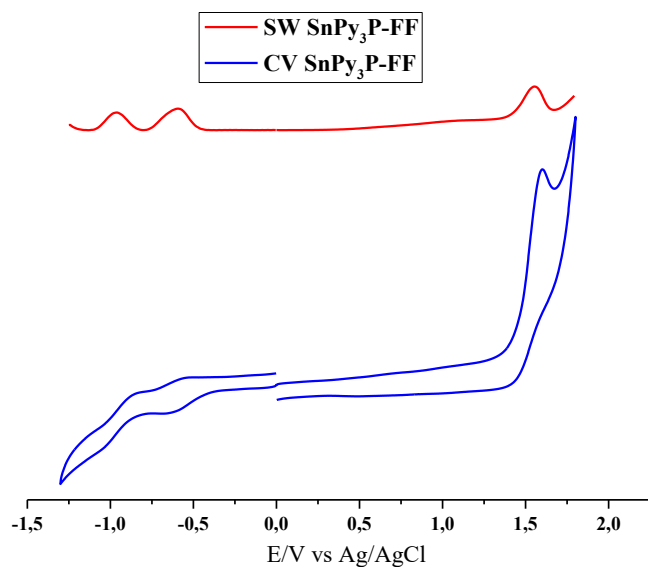


**Figure 6.3.20** Cyclic (CV) and square wave (SW) voltammograms of **SnPy<sub>3</sub>P-FF**.

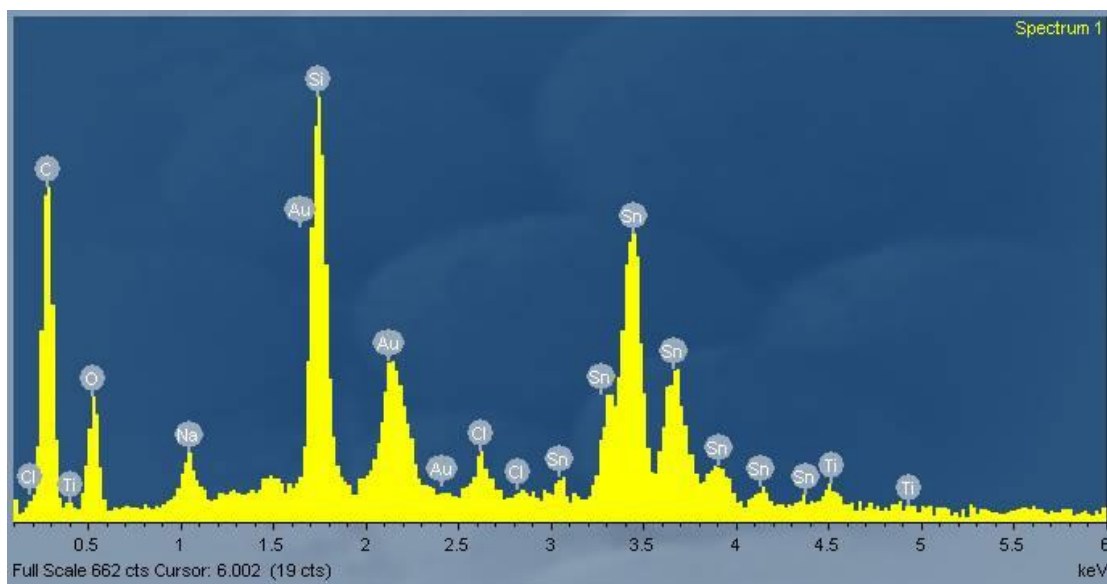


**Figure 6.3.21** EDS spectra analysis of compound **SnPy<sub>3</sub>P-FF**. Structure composition of **SnPy<sub>3</sub>P-FF** was verified by conducting SEM/EDS analysis on the nanospheres obtained from DCM-MeOH 2:8 mixture. The tin peak is indicative for defining our compound.

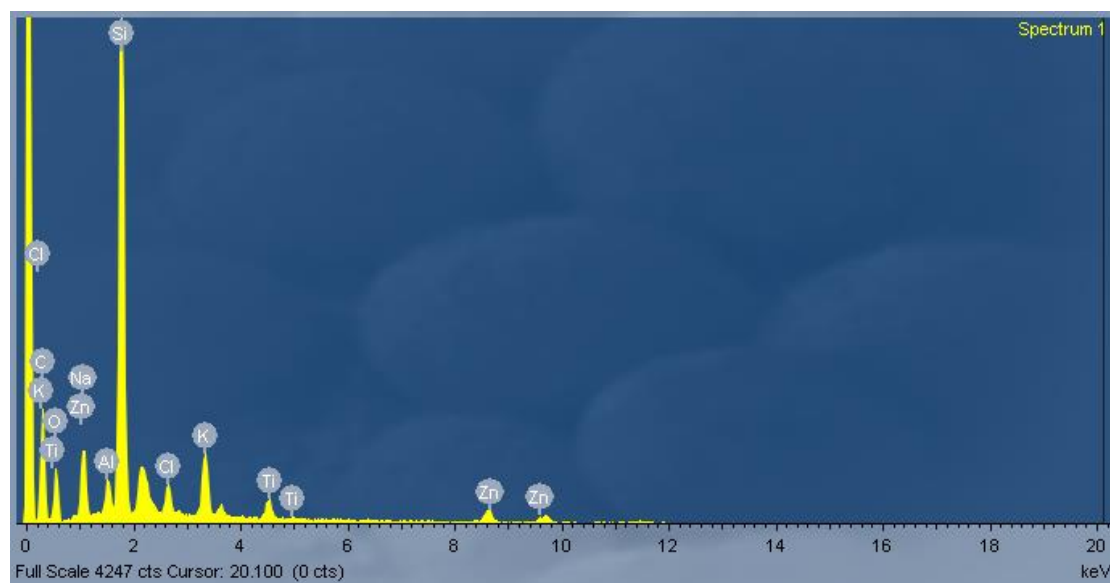


**Figure 6.3.22** EDS spectra analysis of compound **ZnPy<sub>3</sub>P-FF**. Structure composition of **ZnPy<sub>3</sub>P-FF** was verified by conducting SEM/EDS analysis on the assemblies obtained from DCM-MeOH 2:8 mixture. The zinc peak is indicative for defining our compound.

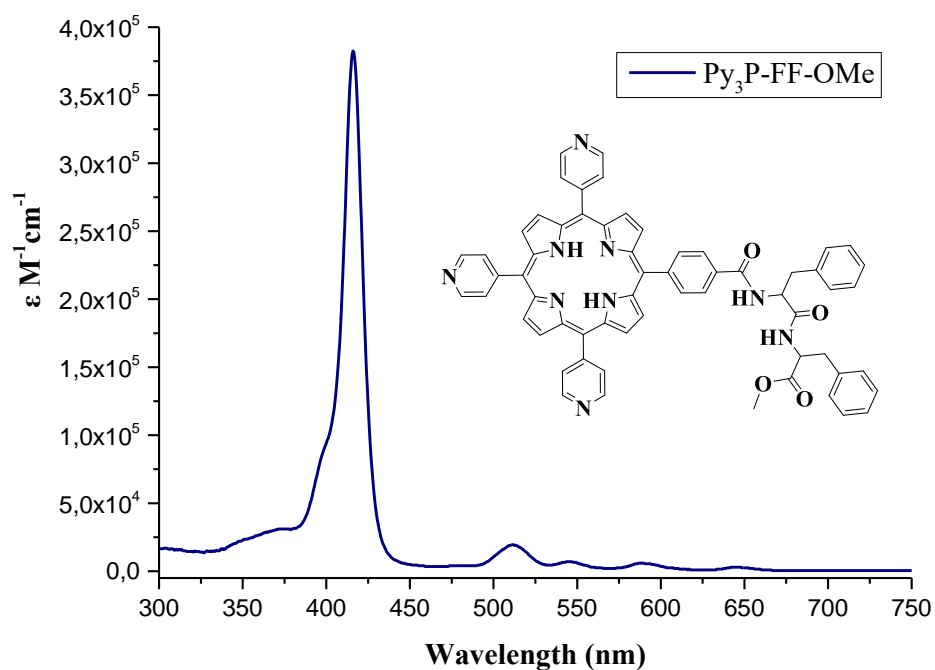


**Figure 6.3.23** UV-Vis spectrum of **Py<sub>3</sub>P-FF** in DCM solution.

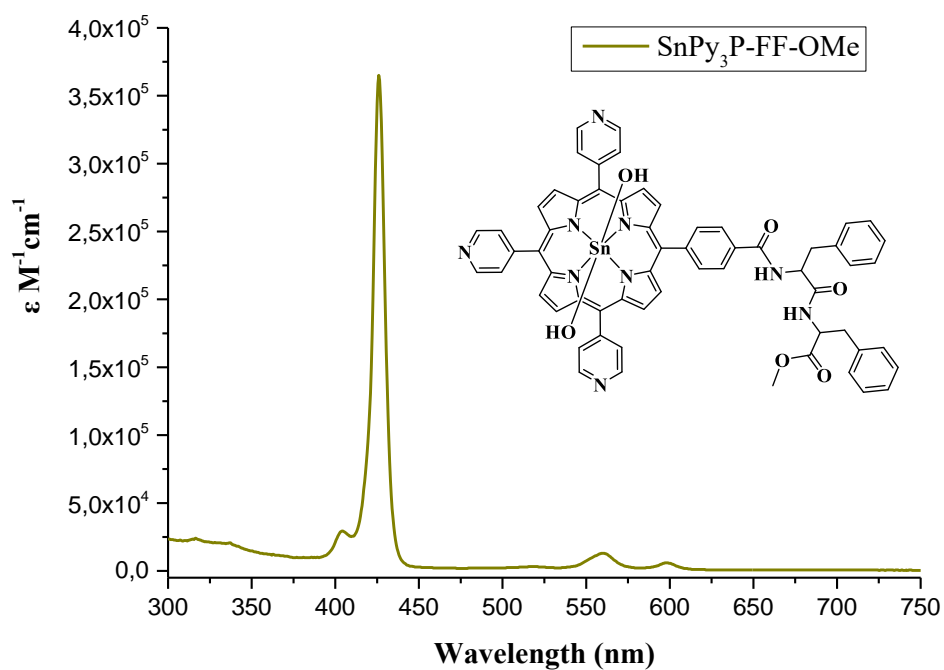


Figure 6.3.24 UV-Vis spectrum of SnPy<sub>3</sub>P-FF in DCM solution.

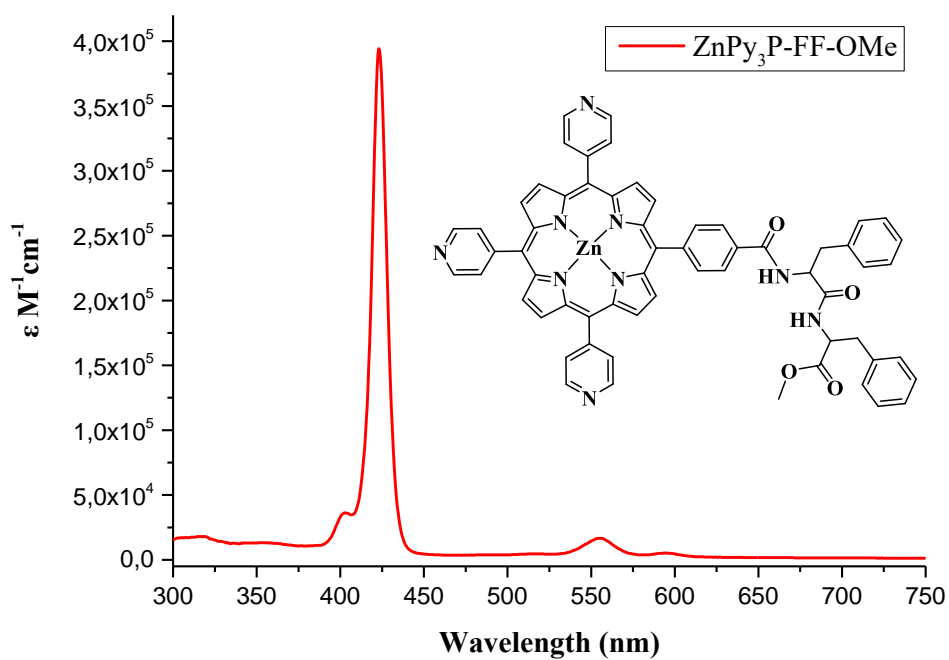
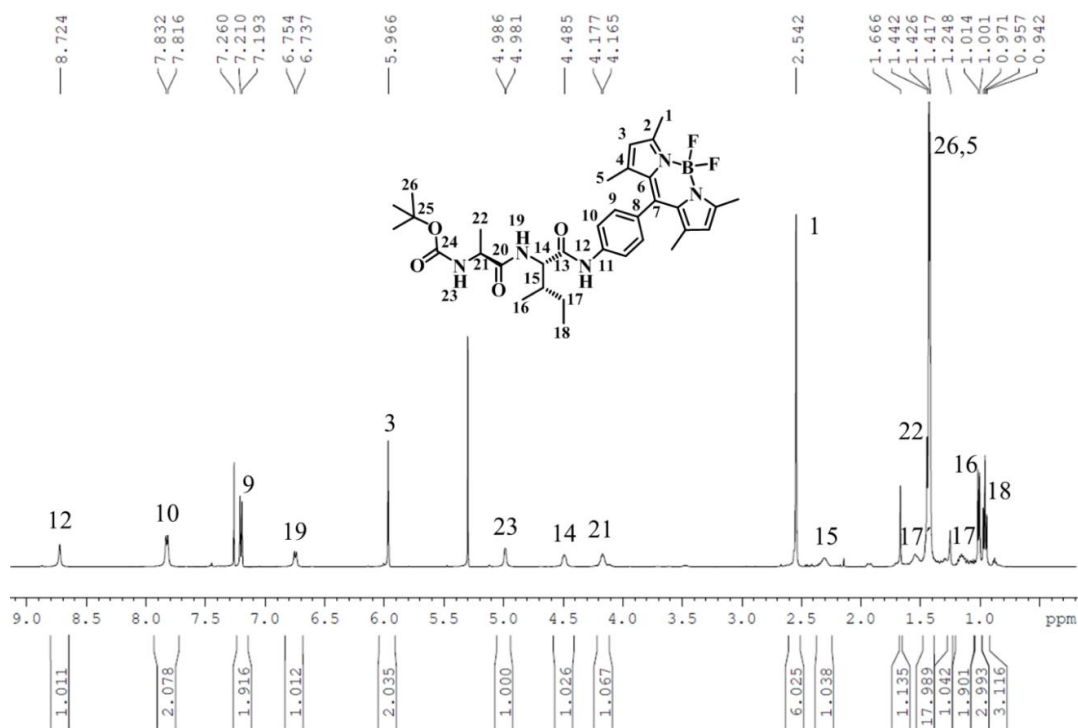
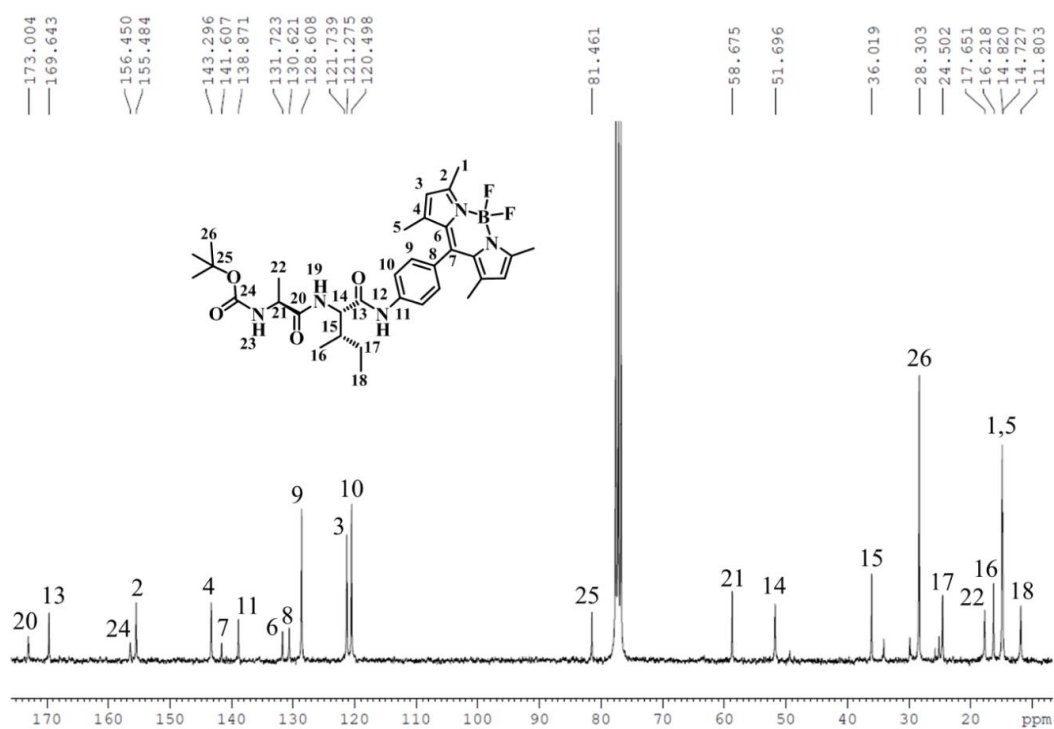


Figure 6.3.25 UV-Vis spectrum of ZnPy<sub>3</sub>P-FF in DCM solution.



**Figure 6.3.26** <sup>1</sup>H NMR spectrum of **Boc-Ala-Ile-BDP** (500 MHz, CDCl<sub>3</sub>).



**Figure 6.3.27** <sup>13</sup>C NMR spectrum of **Boc-Ala-Ile-BDP** (75 MHz, CDCl<sub>3</sub>).

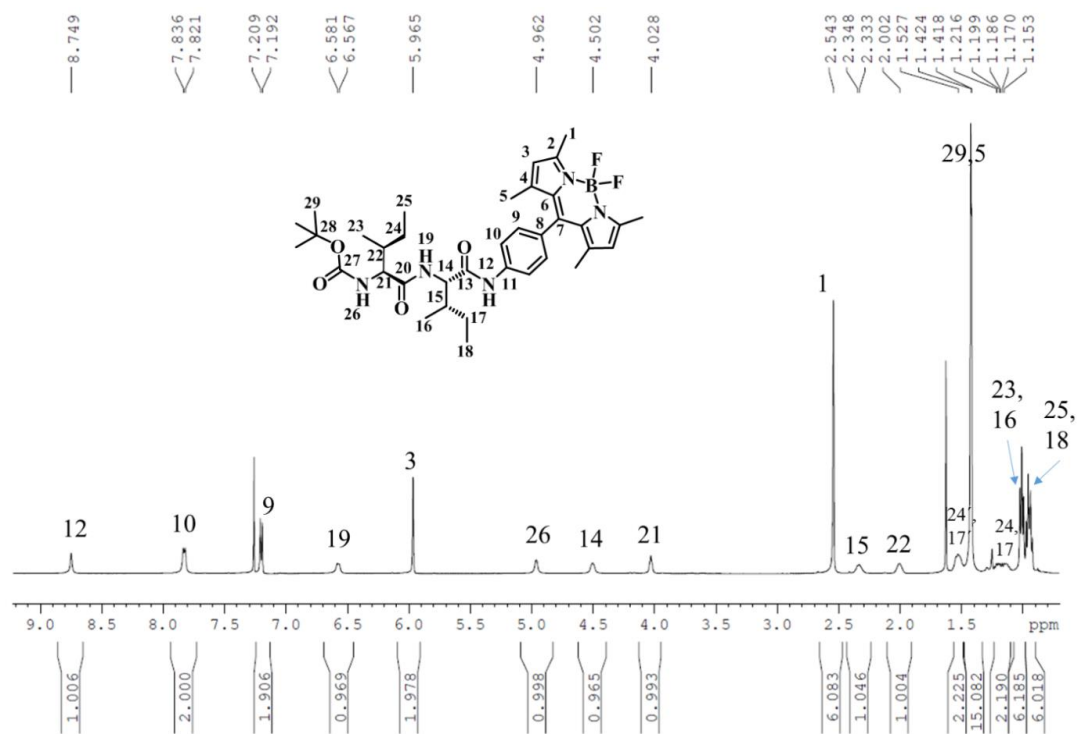


Figure 6.3.28  $^1\text{H}$  NMR spectrum of Boc-Ile-Ile-BDP (500 MHz,  $\text{CDCl}_3$ ).

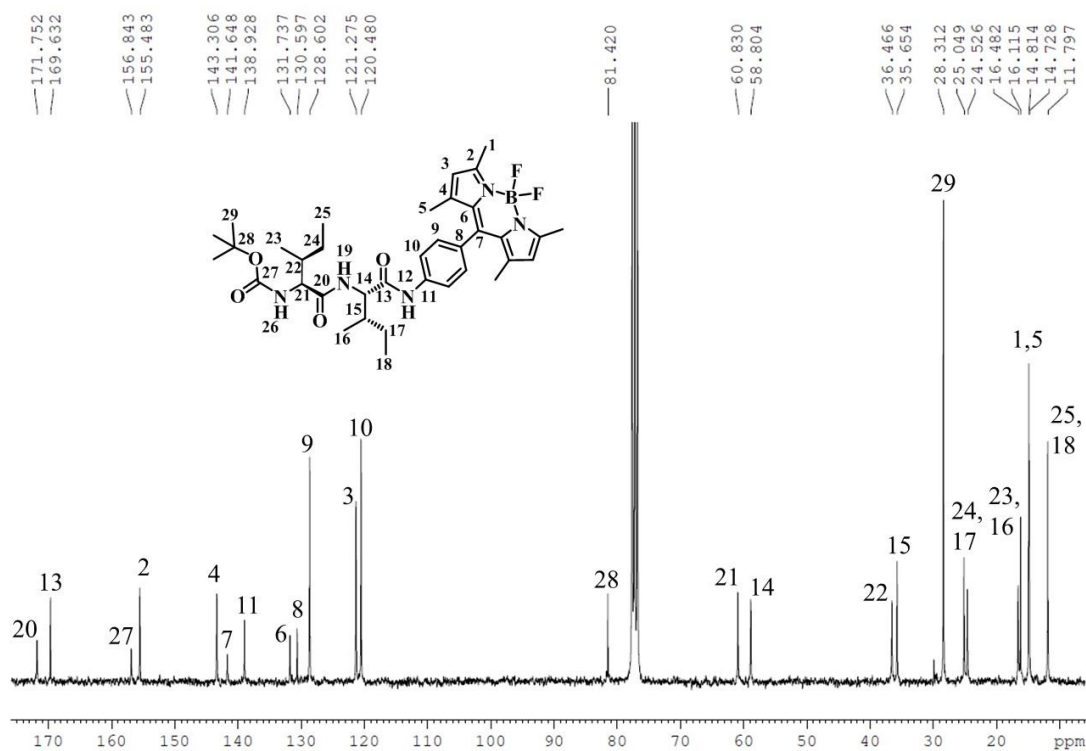


Figure 6.3.29  $^{13}\text{C}$  NMR spectrum of Boc-Ile-Ile-BDP (75 MHz,  $\text{CDCl}_3$ ).

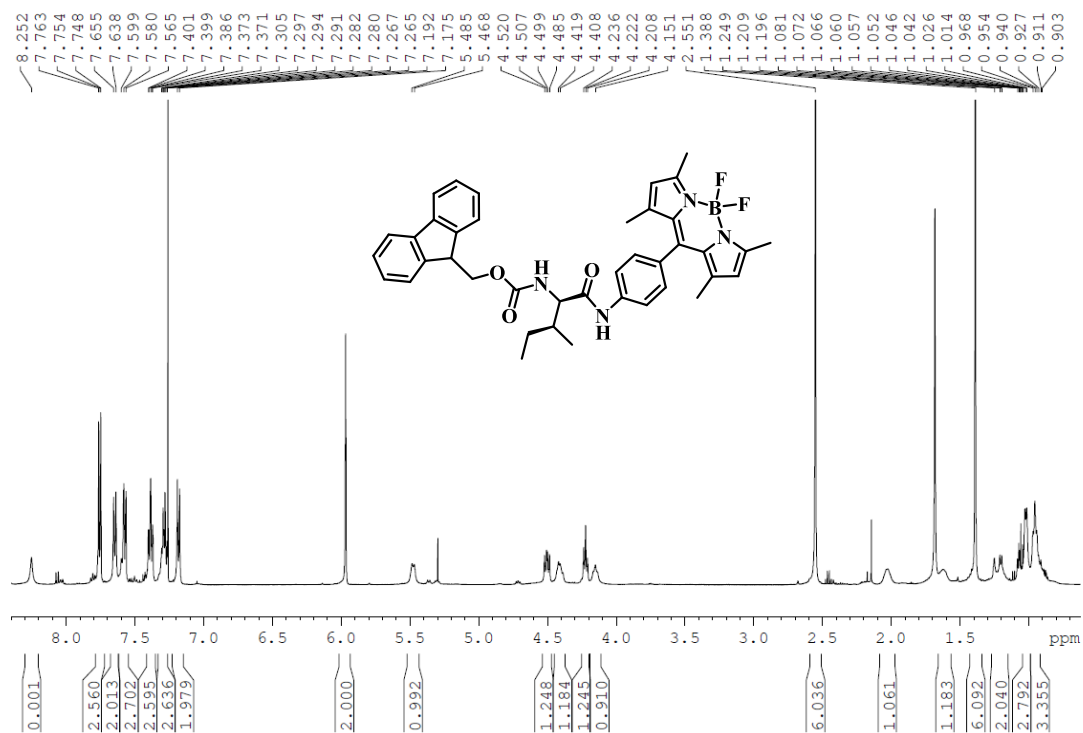


Figure 6.3.30  $^1\text{H}$  NMR spectrum of **Fmoc-Ile-BDP** (500 MHz,  $\text{CDCl}_3$ ).

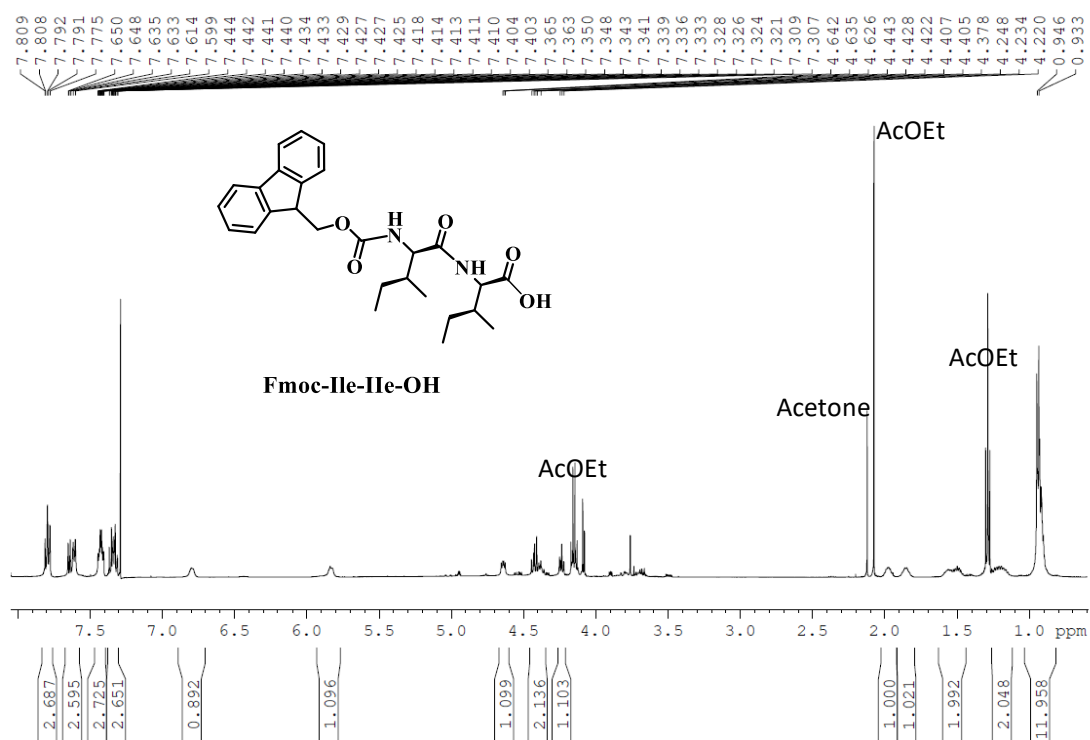


Figure 6.3.31  $^1\text{H}$  NMR spectrum of **Fmoc-Ile-Ile-OH** (500 MHz,  $\text{CDCl}_3$ ).



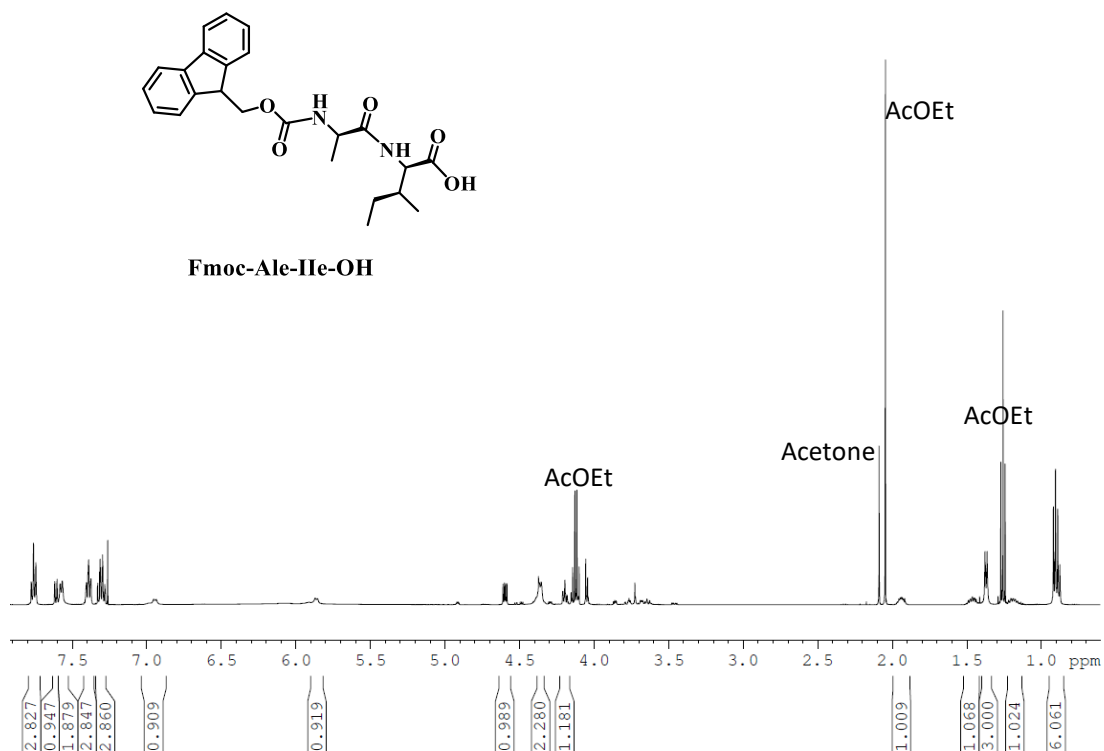


Figure 6.3.32  $^1\text{H}$  NMR spectrum of Fmoc-Ala-Ile-OH (500 MHz,  $\text{CDCl}_3$ ).

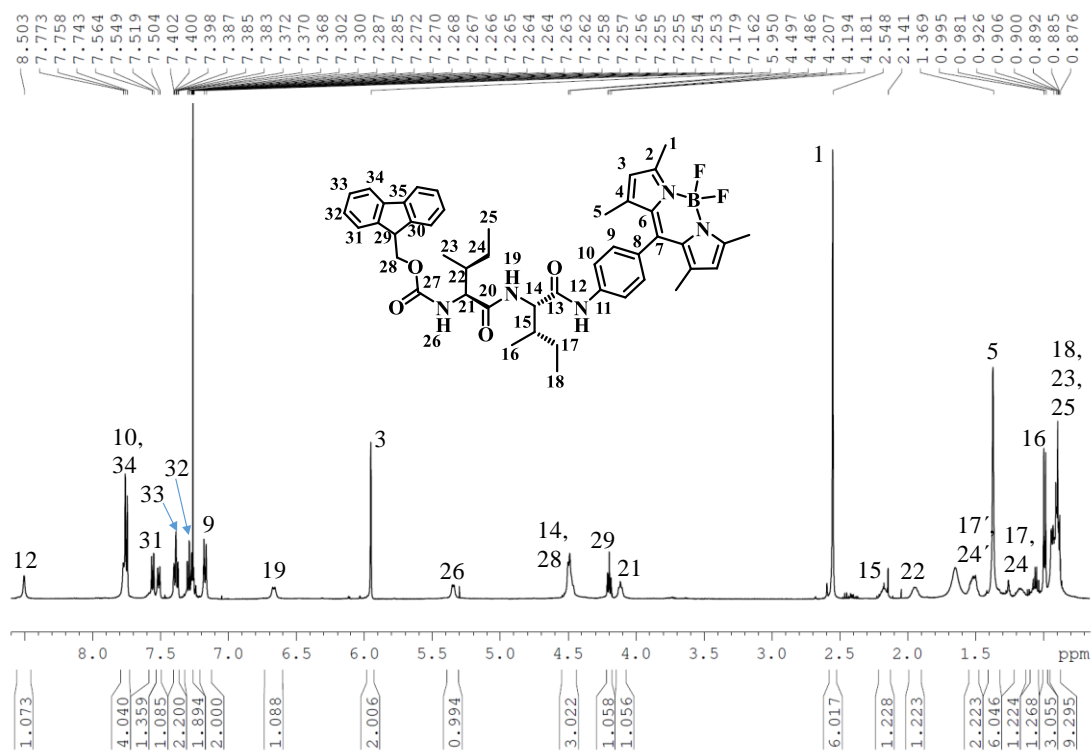


Figure 6.3.33  $^1\text{H}$  NMR spectrum of Fmoc-Ile-Ile-BDP (500 MHz,  $\text{CDCl}_3$ ).

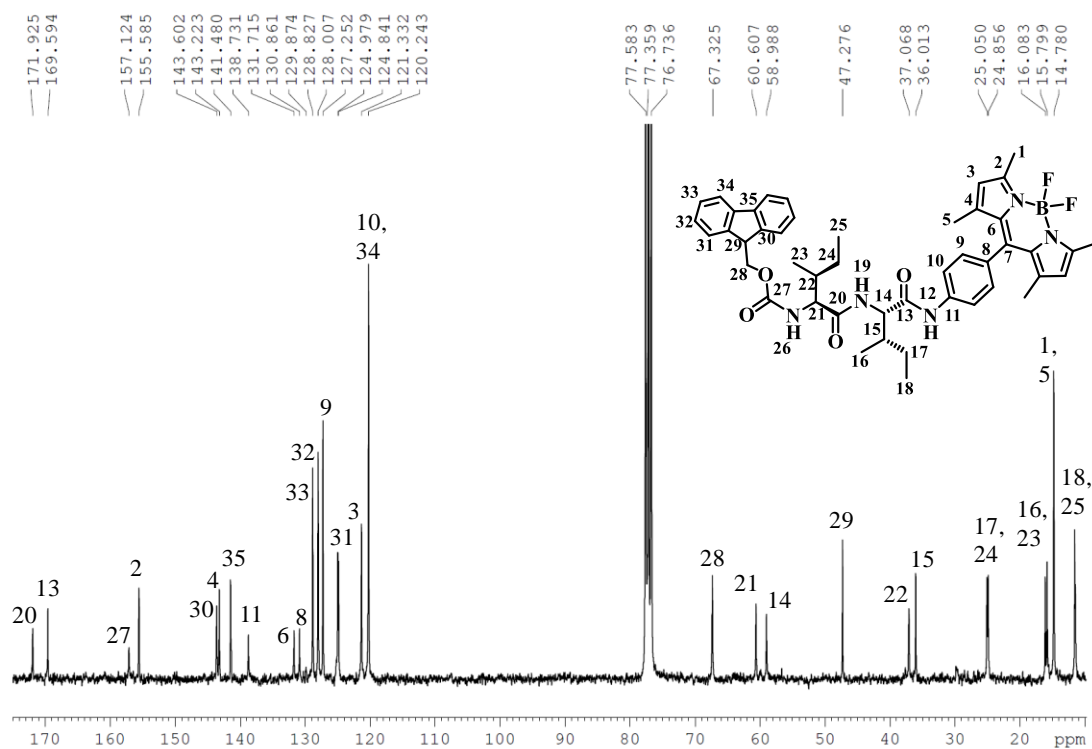


Figure 6.334  $^1\text{H}$  NMR spectrum of Fmoc-Ile-Ile-BDP (500 MHz,  $\text{CDCl}_3$ ).

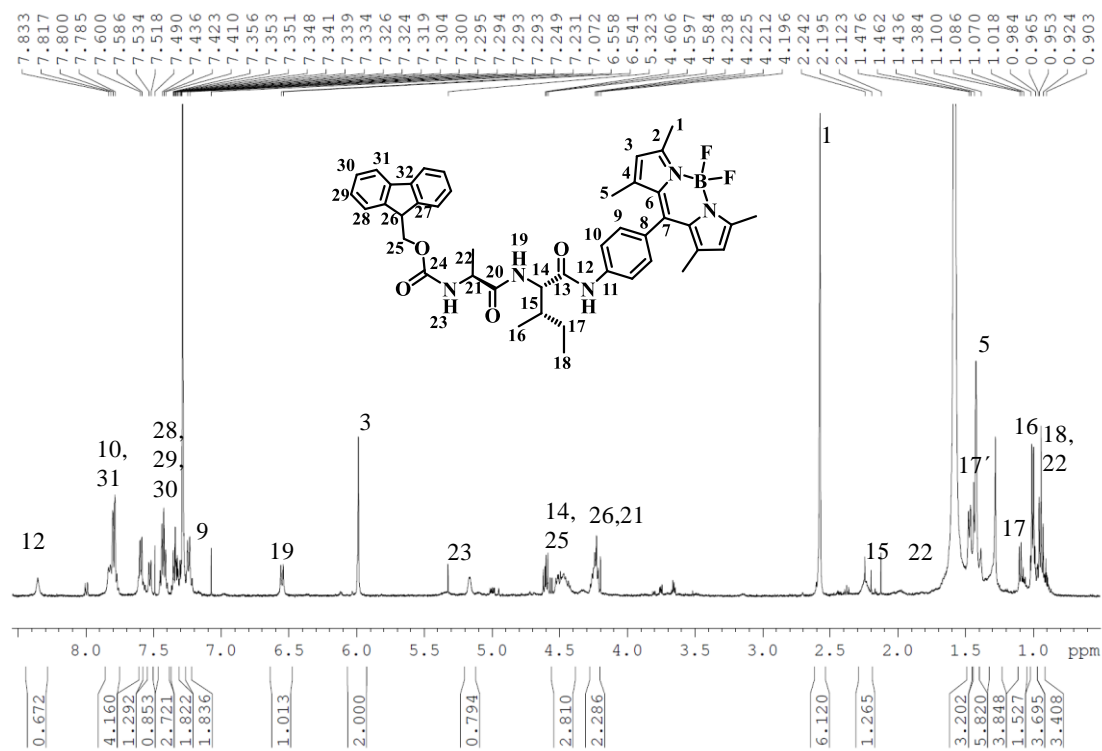
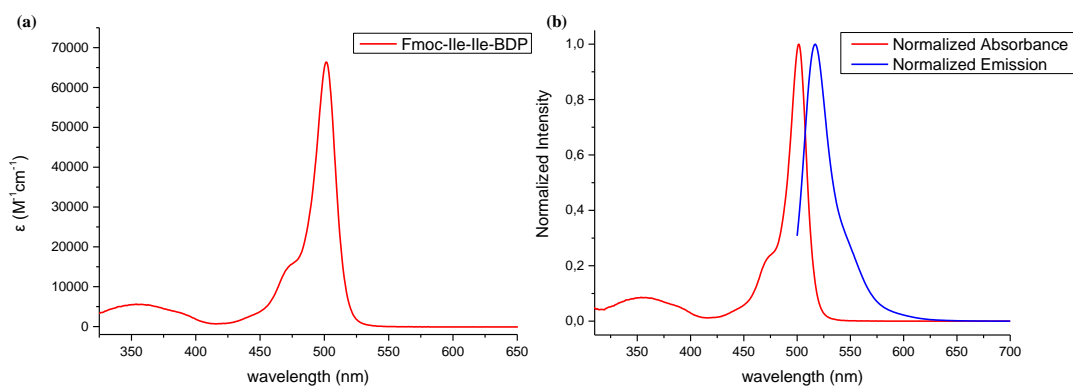
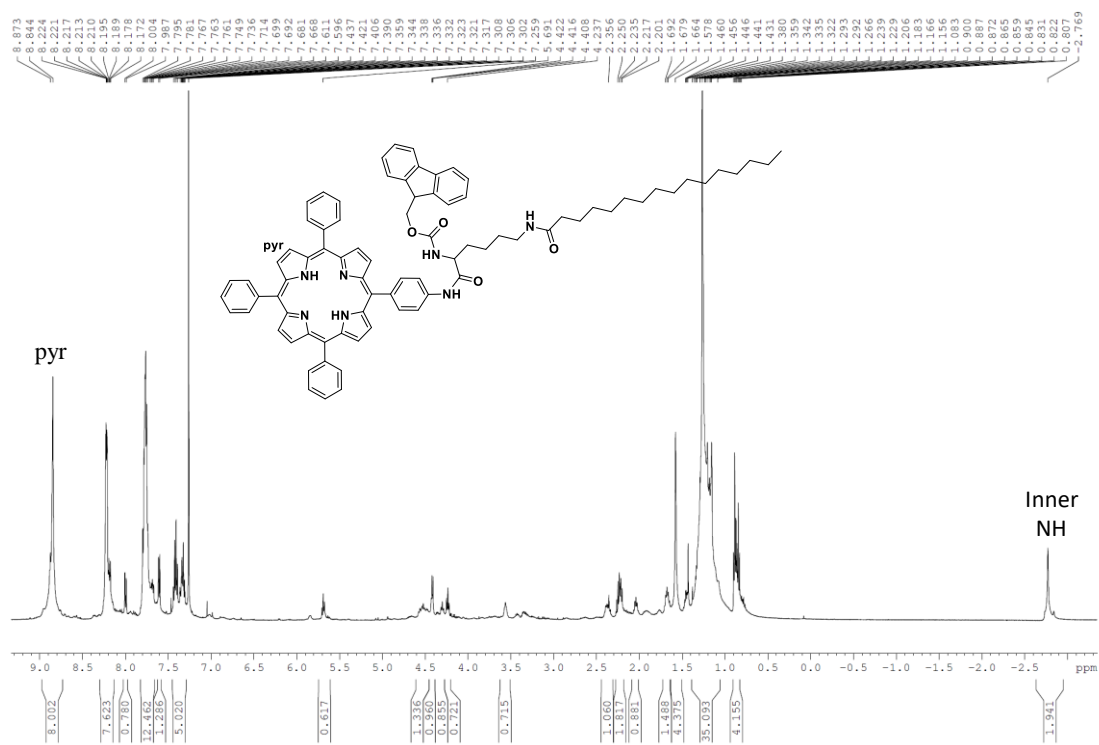


Figure 6.335  $^1\text{H}$  NMR spectrum of Fmoc-Ala-Ile-BDP (500 MHz,  $\text{CDCl}_3$ ).



**Figure 6.3.36** UV-Vis spectrum and normalized absorption and emission spectra (excitation at 490 nm) of **Fmoc-Ile-Ile-BDP** in DCM.



**Figure 6.3.37**  $^1H$  NMR spectrum of **Fmoc-Lys(palmitoyl)-TPP** (500 MHz,  $CDCl_3$ ).

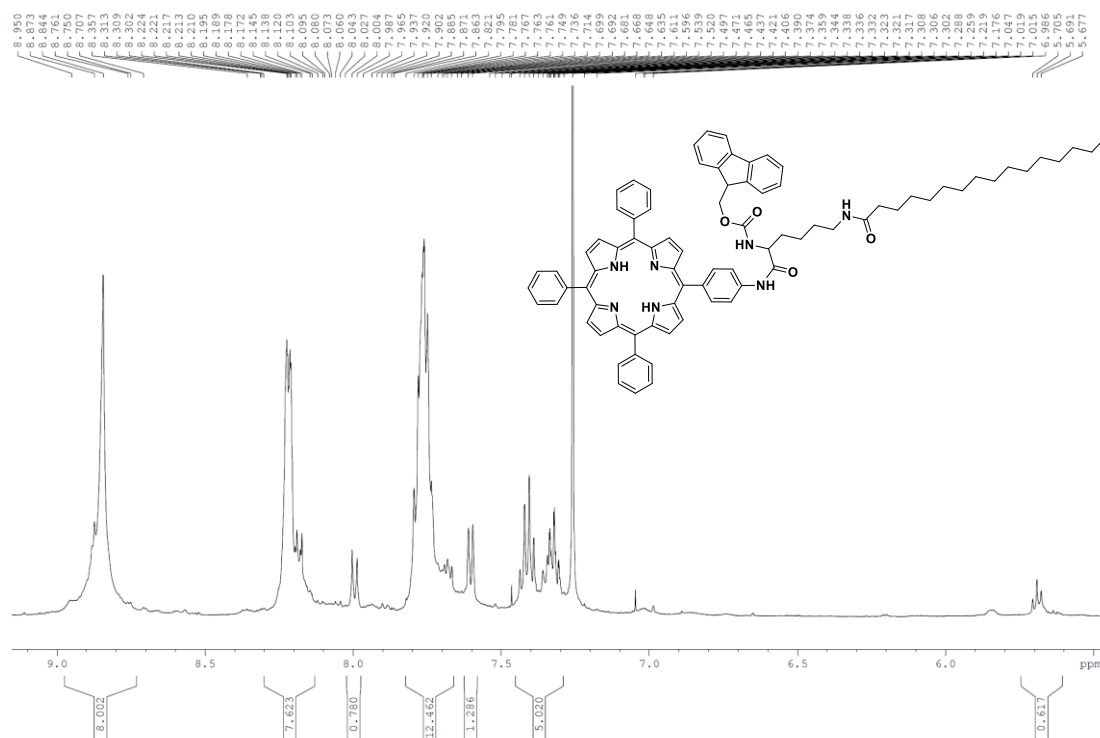


Figure 6.3.38  $^1\text{H}$  NMR spectrum of Fmoc-Lys(palmitoyl)-TPP (500 MHz,  $\text{CDCl}_3$ ).

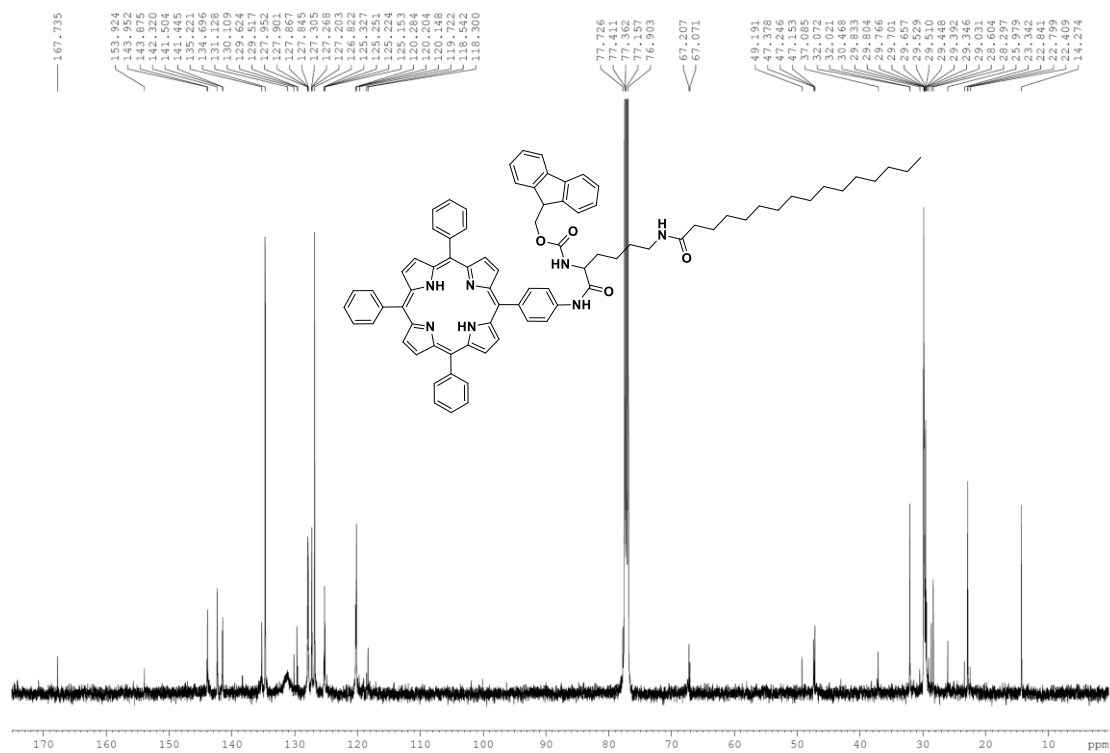


Figure 6.3.39  $^{13}\text{C}$  NMR spectrum of Fmoc-Lys(palmitoyl)-TPP (75 MHz,  $\text{CDCl}_3$ ).

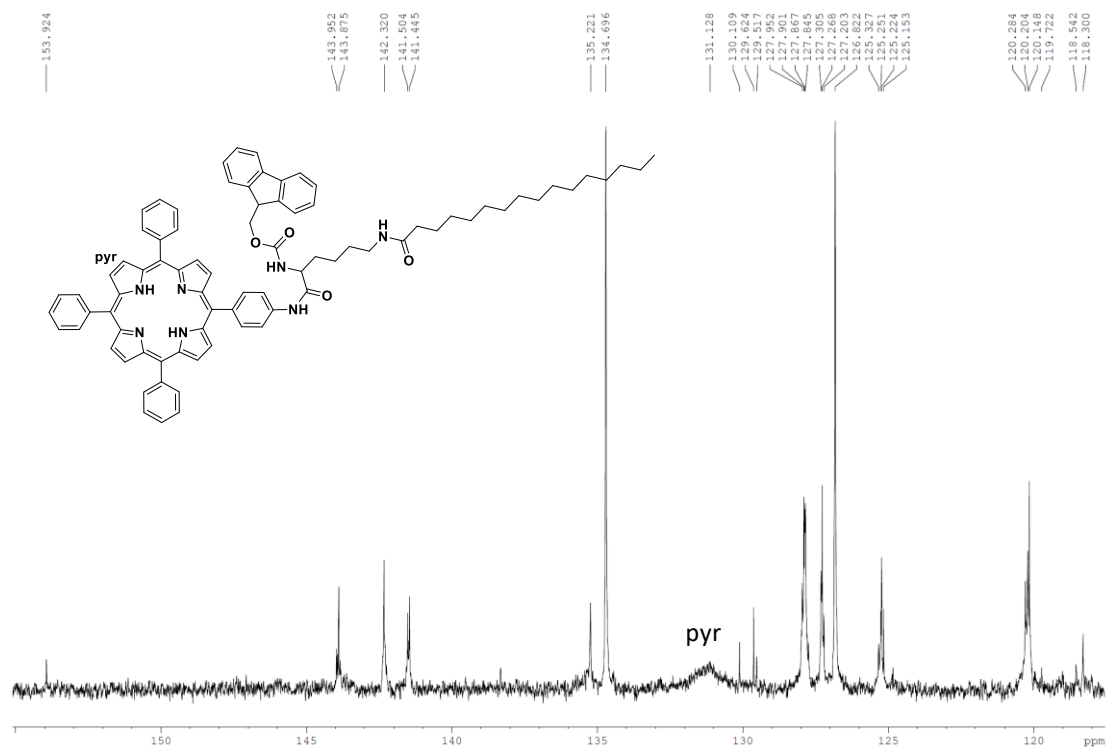


Figure 6.3.40  $^{13}\text{C}$  NMR spectrum of Fmoc-Lys(palmitoyl)-TPP (75 MHz,  $\text{CDCl}_3$ ).

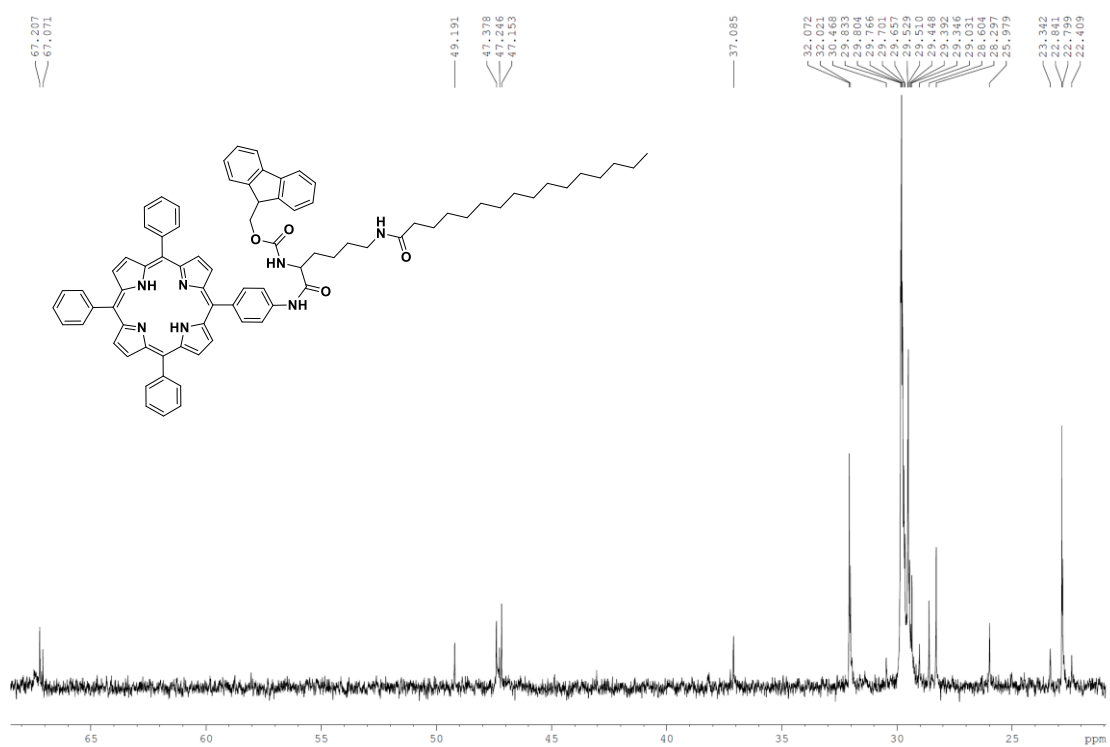
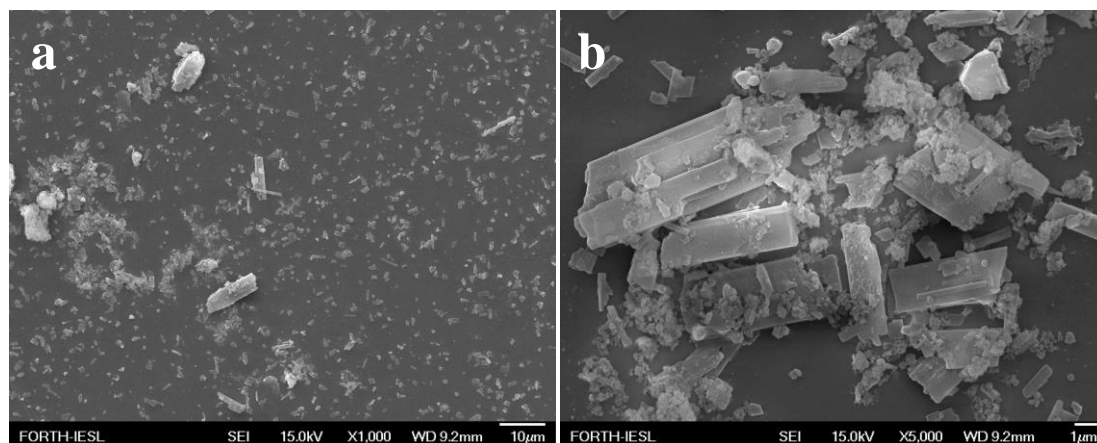
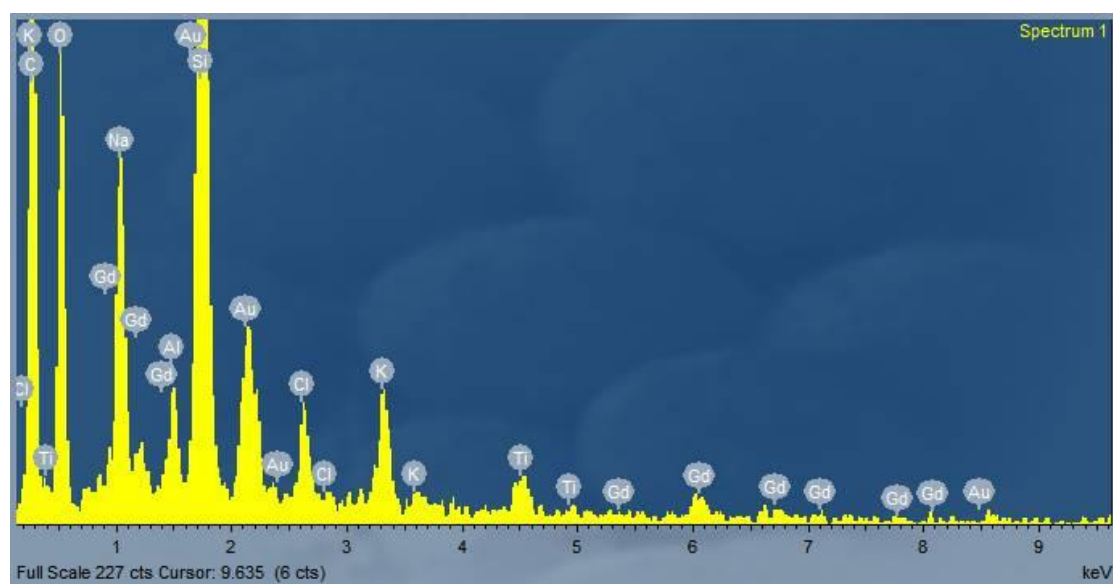


Figure 6.3.41  $^{13}\text{C}$  NMR spectrum of Fmoc-Lys(palmitoyl)-TPP (75 MHz,  $\text{CDCl}_3$ ).



**Figure 6.3.42** SEM images of  $\text{GdH}(\text{TPyP})_2$ , drop-casted from water.



**Figure 6.3.43** EDS spectrum of the flakes obtained from  $\text{GdH}(\text{TPyP})_2$ . Structure composition of  $\text{GdH}(\text{TPyP})_2$  was verified by conducting SEM/EDS analysis on the assemblies obtained in water. The gadolinium peaks are indicative for defining our compound.

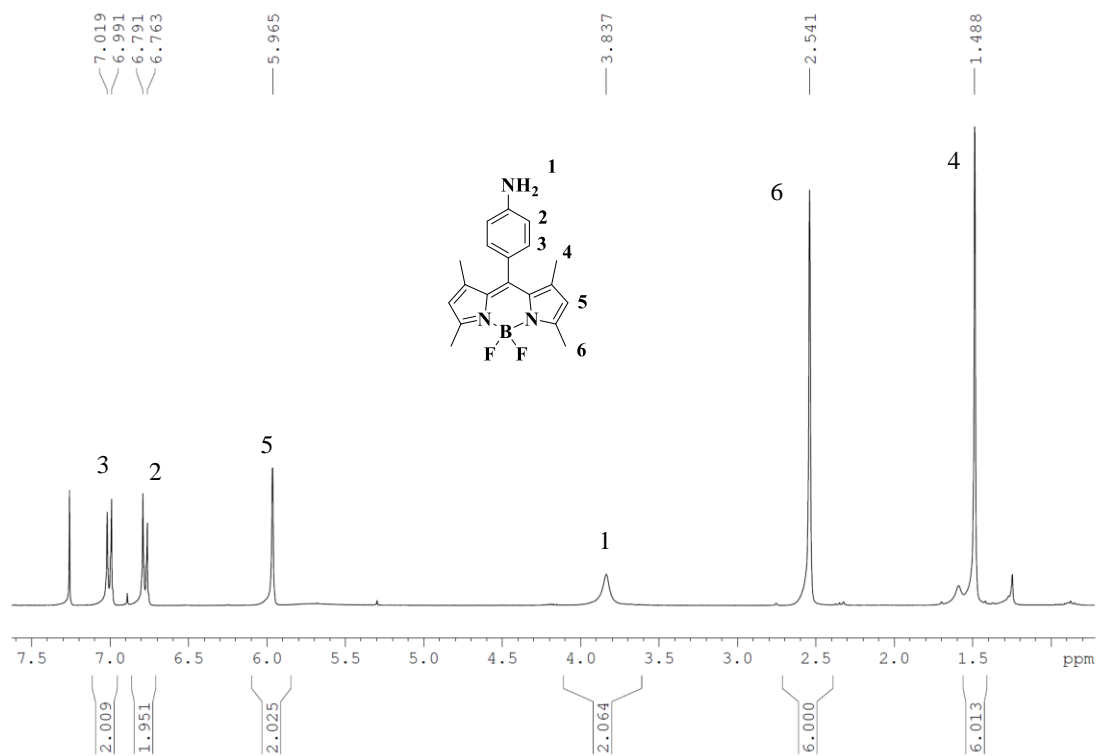


**Figure 6.344**  $^1\text{H}$  NMR spectrum of **BDP-NH<sub>2</sub>** (300 MHz,  $\text{CDCl}_3$ ).

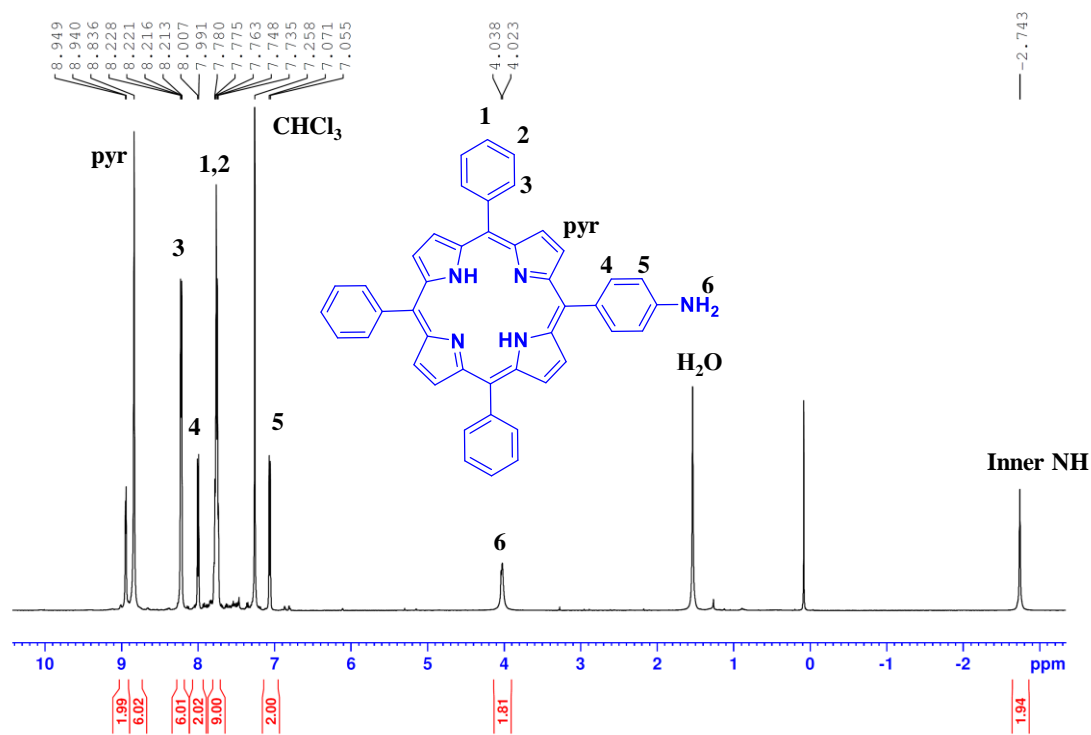


**Figure 6.345**  $^1\text{H}$  NMR spectrum of **TPP-NH<sub>2</sub>** (500 MHz,  $\text{CDCl}_3$ ).

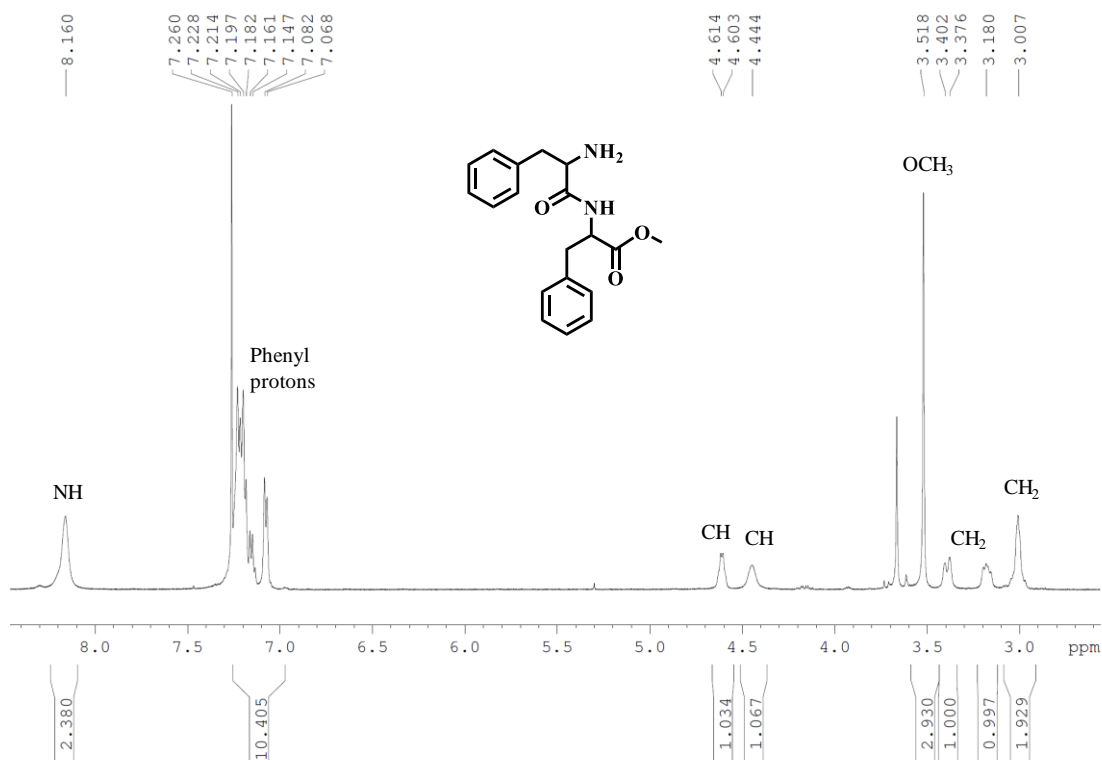


**Figure 6.3.46**  $^1\text{H}$  NMR spectrum of  $\text{NH}_2\text{-PhePhe-OMe}$  (500 MHz,  $\text{CDCl}_3$ ).

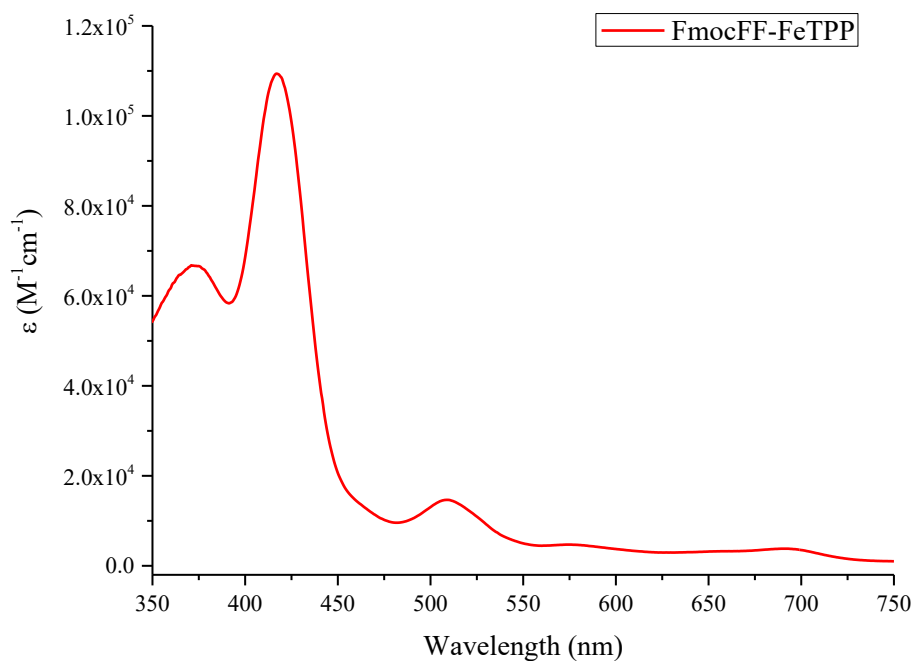


**Figure 6.3.47** UV-Vis spectrum of  $\text{FmocFF-FeTPP}$  in THF.



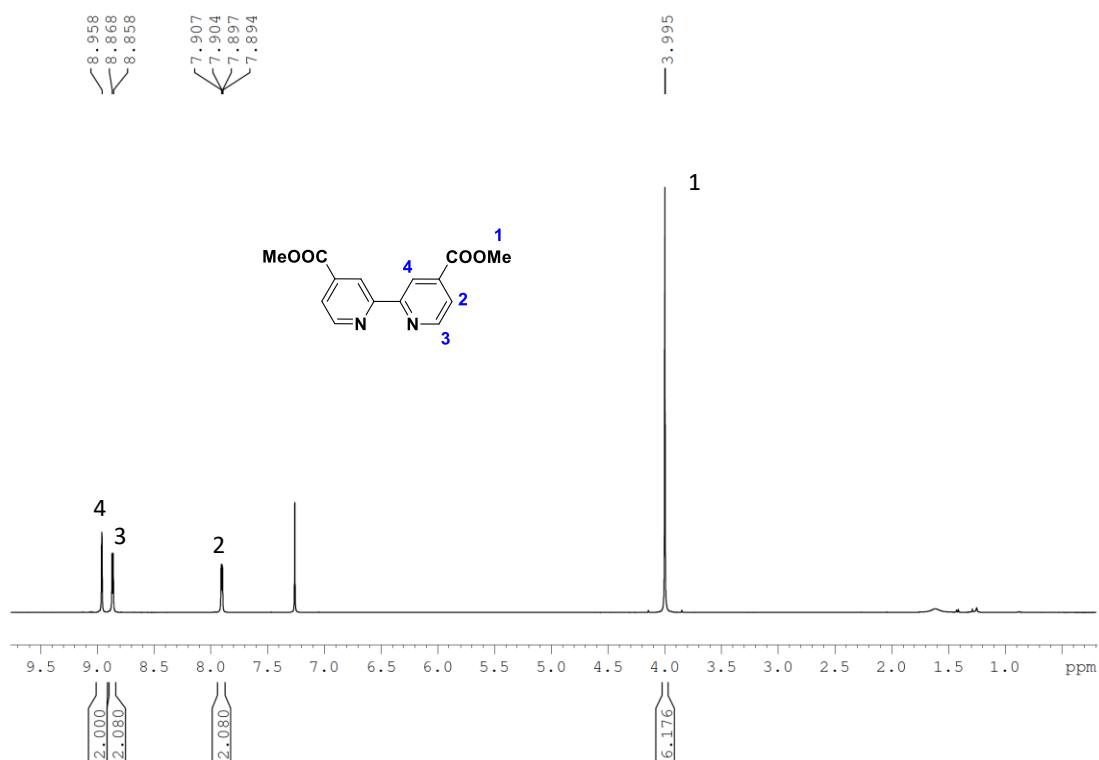


Figure 6.4.1  $^1\text{H}$  NMR spectrum of compound **bpy(COOMe)<sub>2</sub>** in  $\text{CDCl}_3$ .

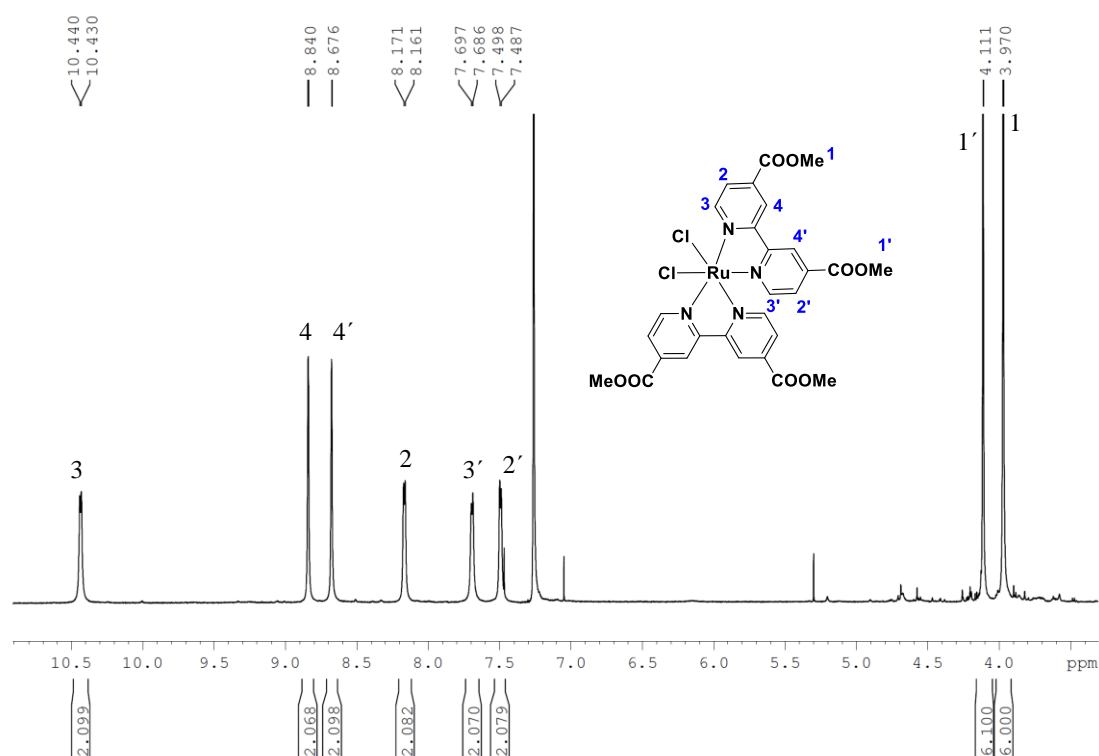
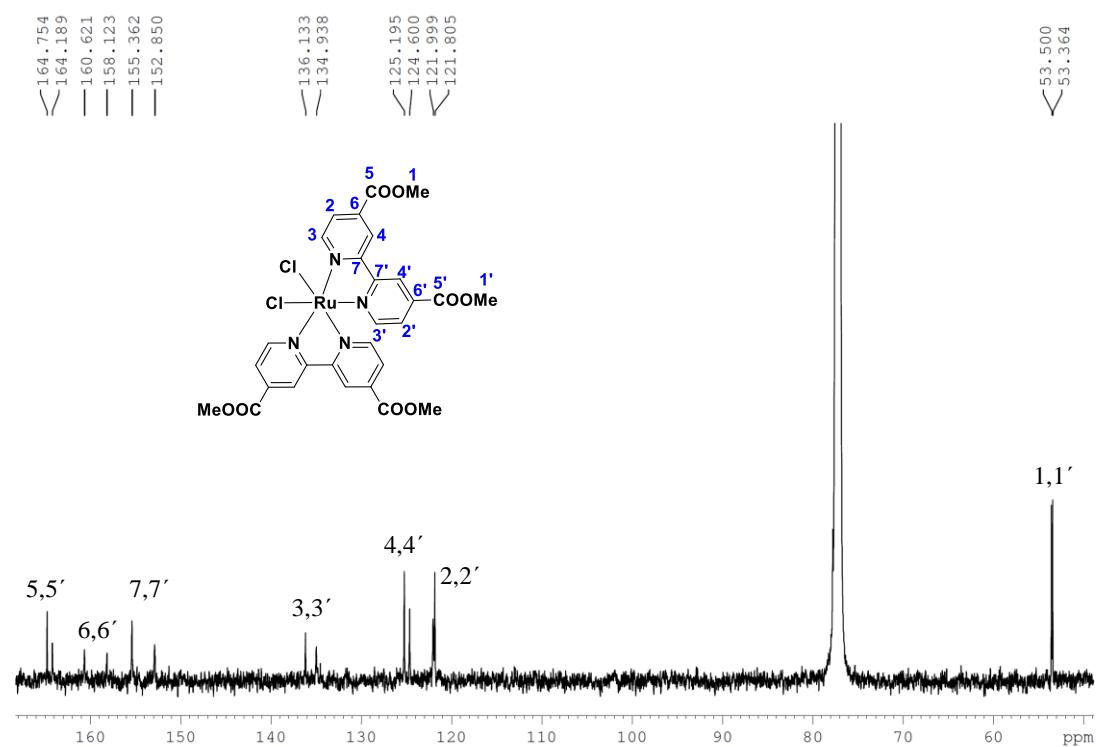
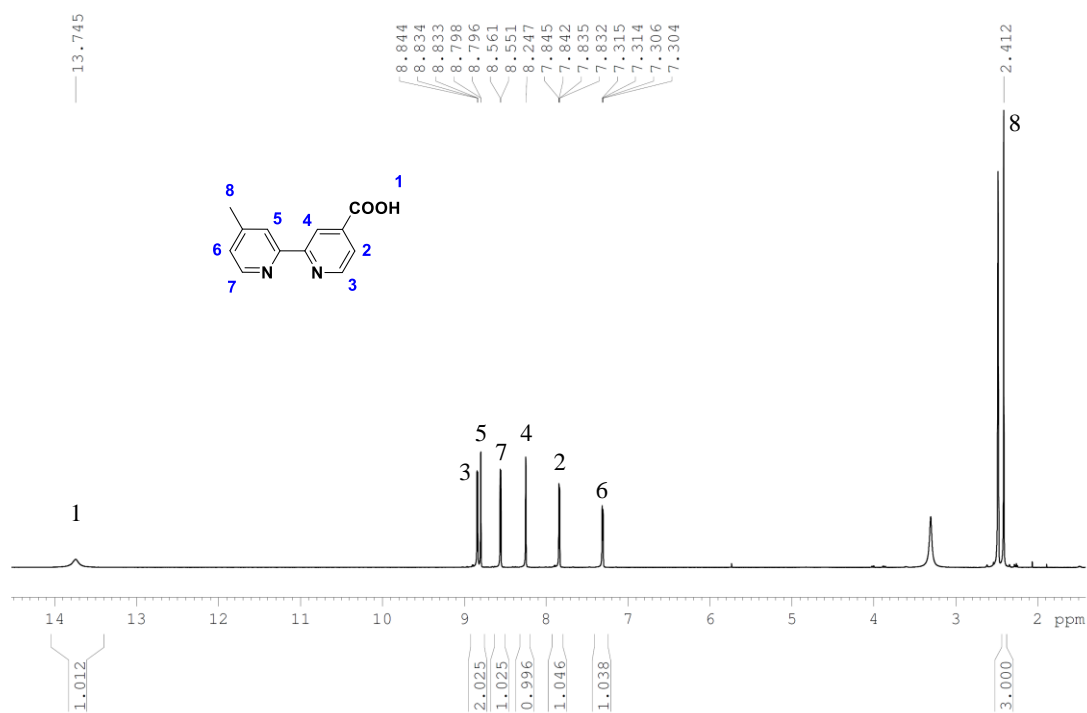


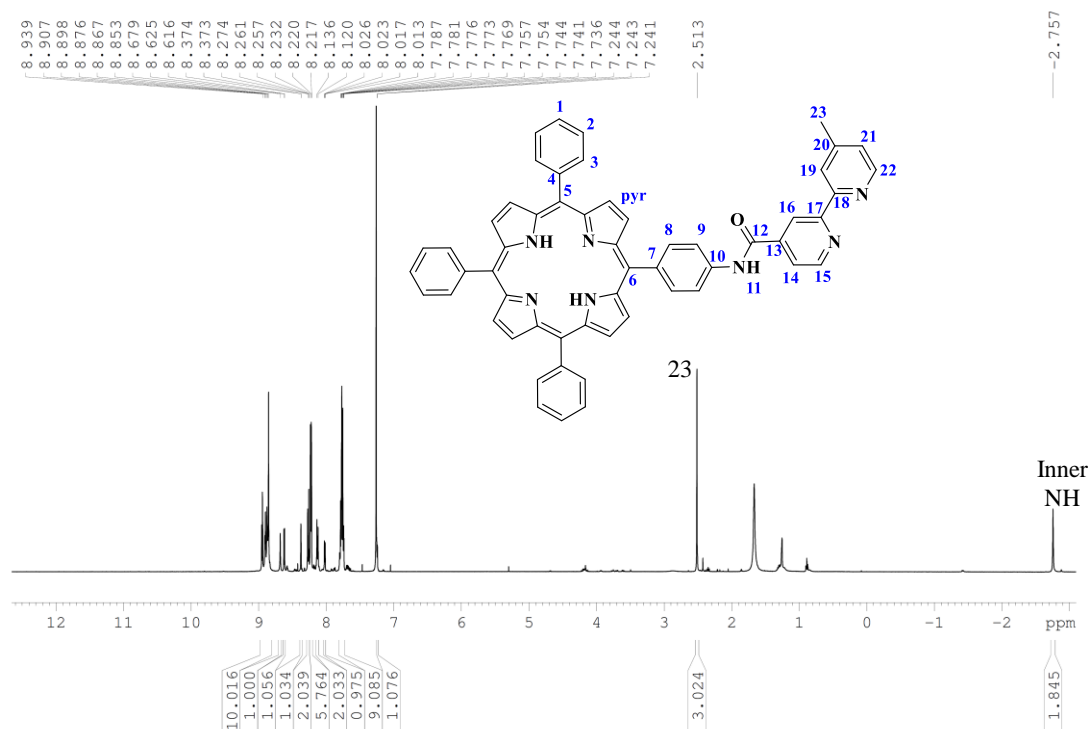
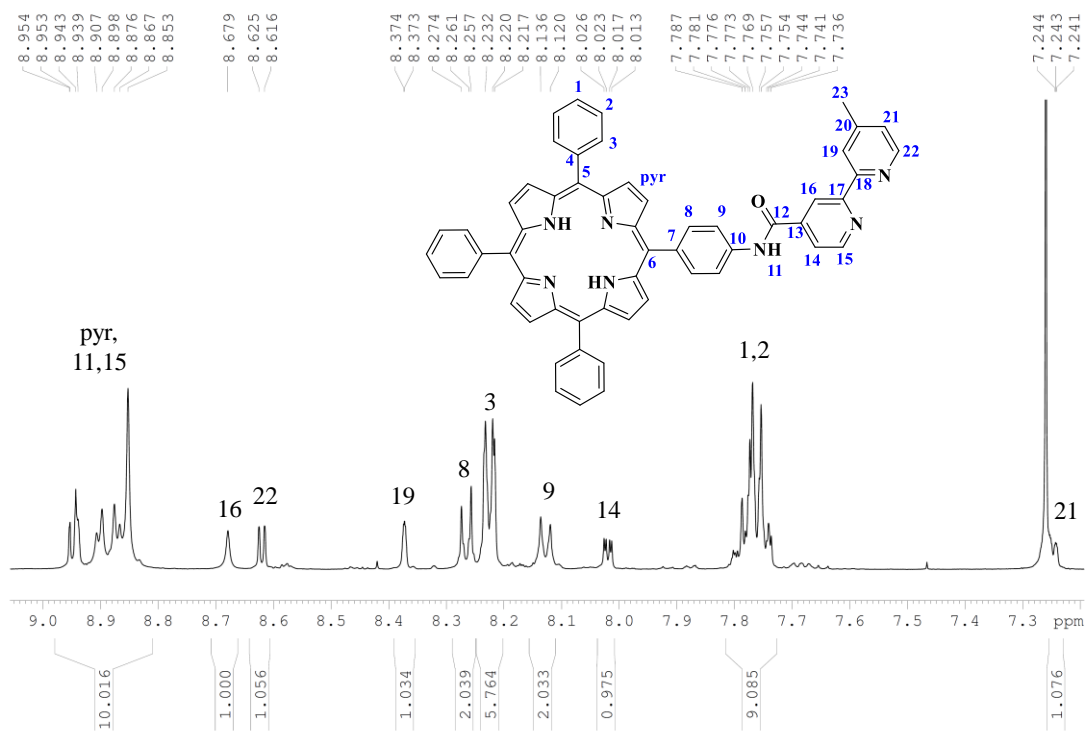
Figure 6.4.2  $^1\text{H}$  NMR spectrum of compound **Ru(bpy(COOMe)<sub>2</sub>)<sub>2</sub>** in  $\text{CDCl}_3$ .



**Figure 6.4.3** <sup>13</sup>C NMR spectrum of compound **Ru(bpy(COOMe)<sub>2</sub>)<sub>2</sub>** in CDCl<sub>3</sub>.



**Figure 6.4.4** <sup>1</sup>H NMR spectrum of compound **4'-methyl-[2,2'-bipyridine]-4-carboxylic acid**, **bpy-COOH** in DMSO-d<sub>6</sub>.

Figure 6.4.5  $^1\text{H}$  NMR spectrum of TPP-bpy in  $\text{CDCl}_3$ .Figure 6.4.6 Aromatic region of  $^1\text{H}$  NMR spectrum of TPP-bpy in  $\text{CDCl}_3$ .

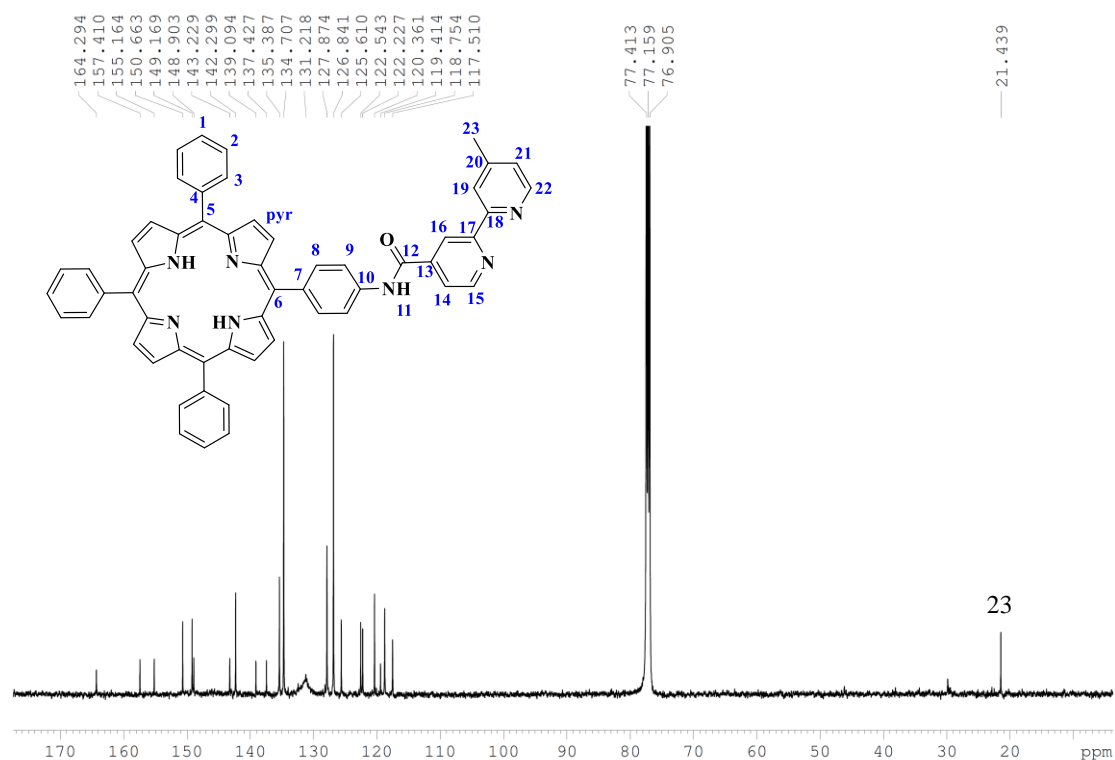


Figure 6.4.7  $^{13}\text{C}$  NMR spectrum of TPP-bpy in  $\text{CDCl}_3$ .

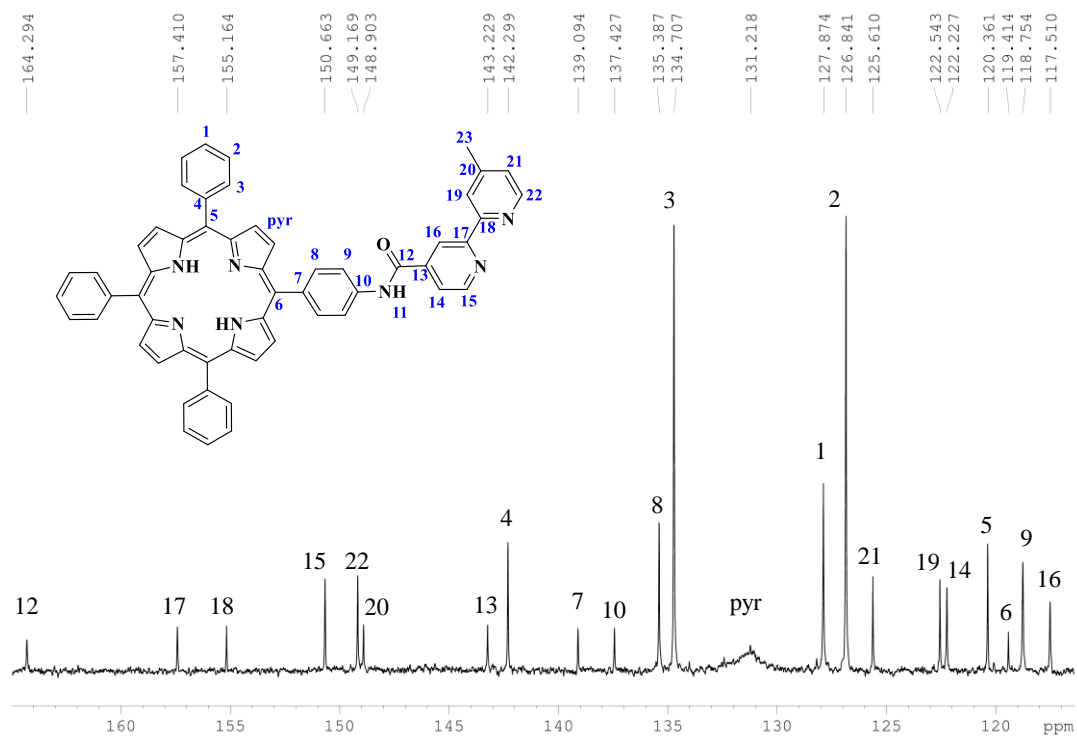
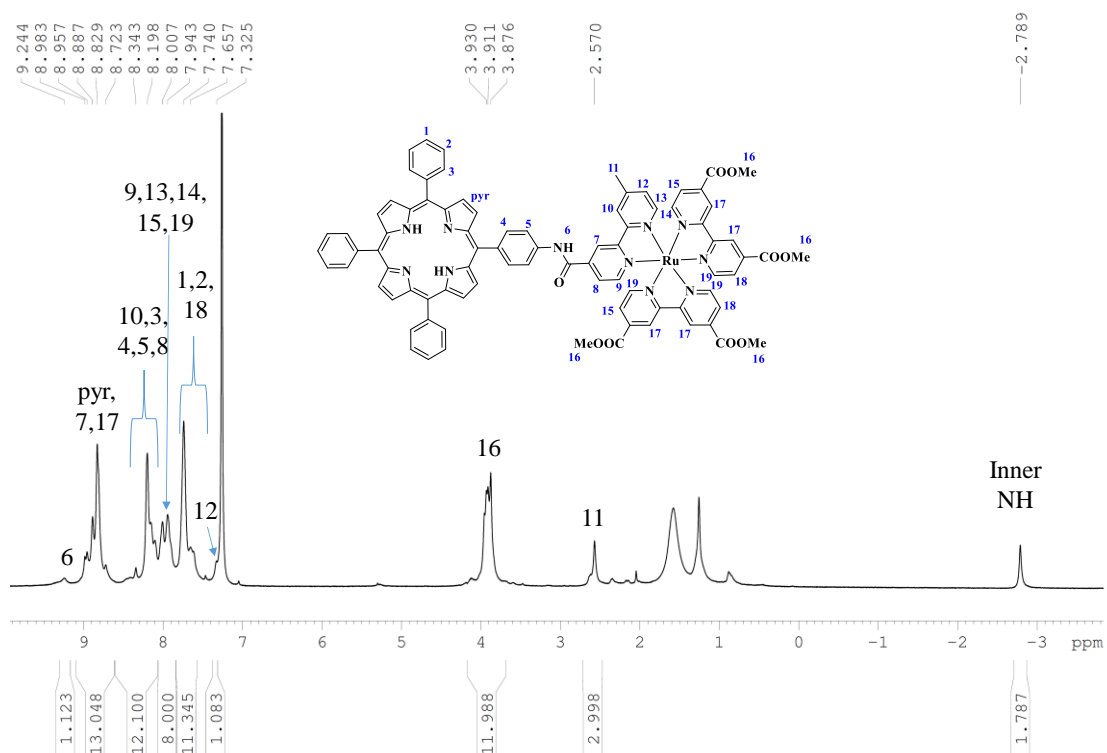
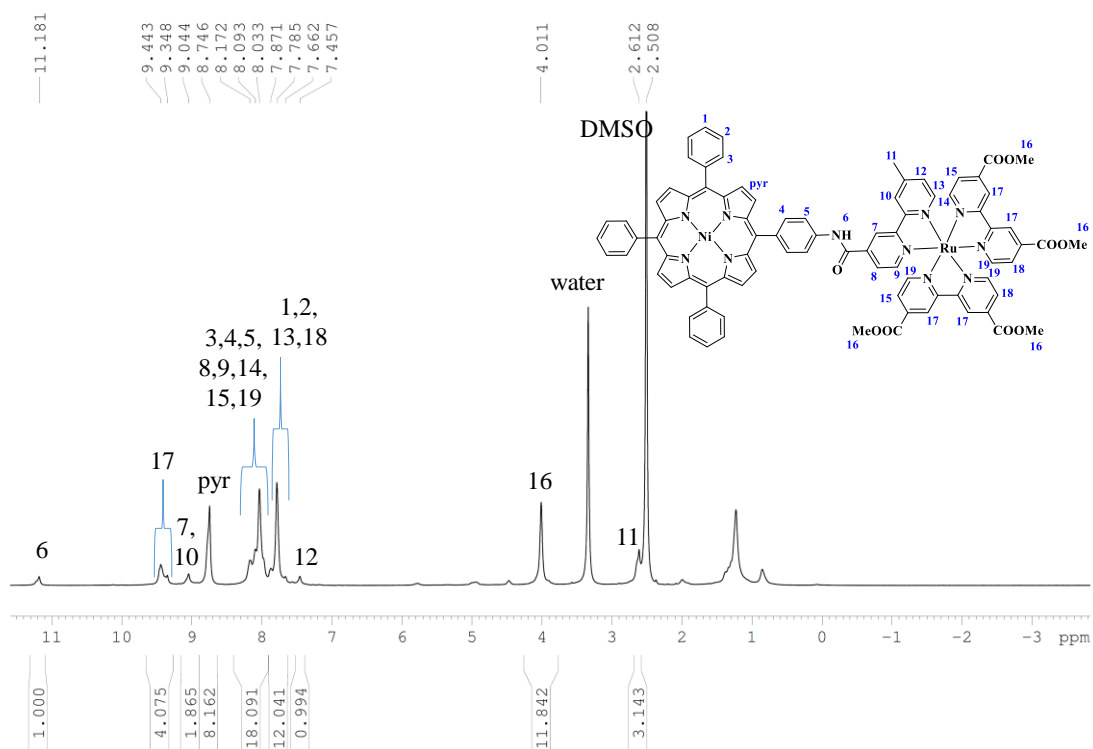


Figure 6.4.8 Aromatic region of  $^{13}\text{C}$  NMR spectrum of TPP-bpy in  $\text{CDCl}_3$ .



**Figure 6.4.9**  $^1\text{H}$  NMR spectrum of **H<sub>2</sub>P-Ru** in  $\text{CDCl}_3$ .



**Figure 6.4.10**  $^1\text{H}$  NMR spectrum of **NiP-Ru** in  $\text{DMSO-d}_6$ .

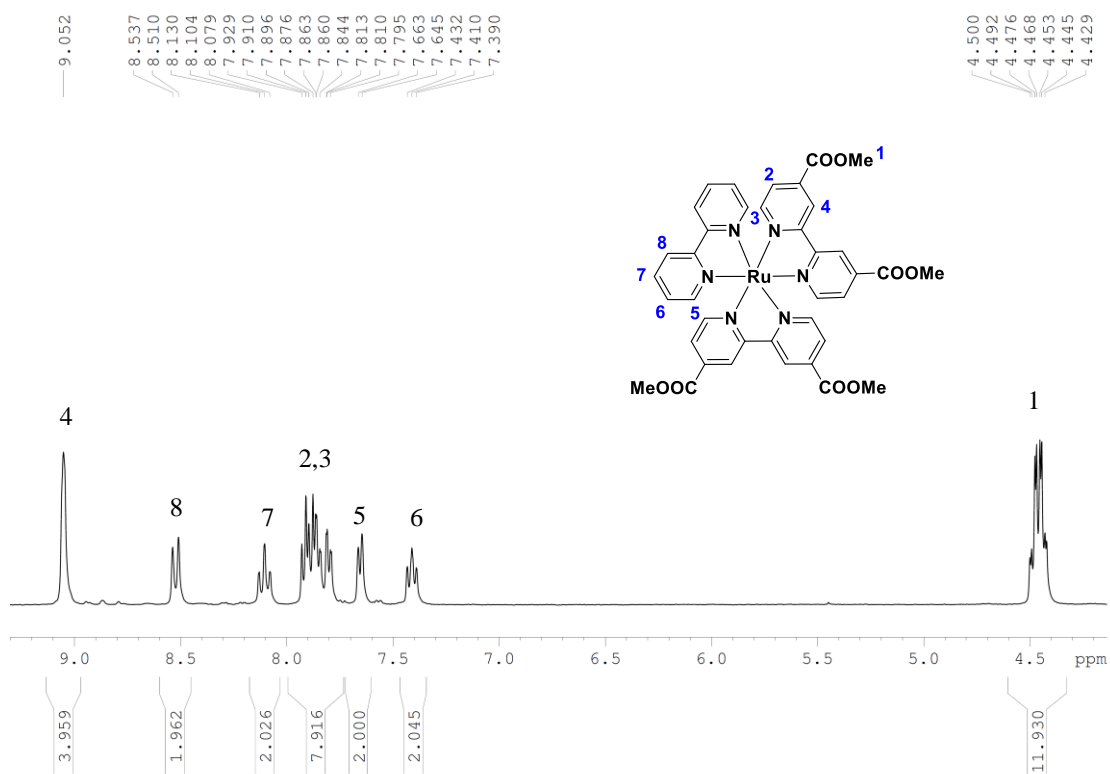


**Figure 6.4.11** <sup>1</sup>H NMR spectrum of Ru-bpy in CD<sub>3</sub>CN.

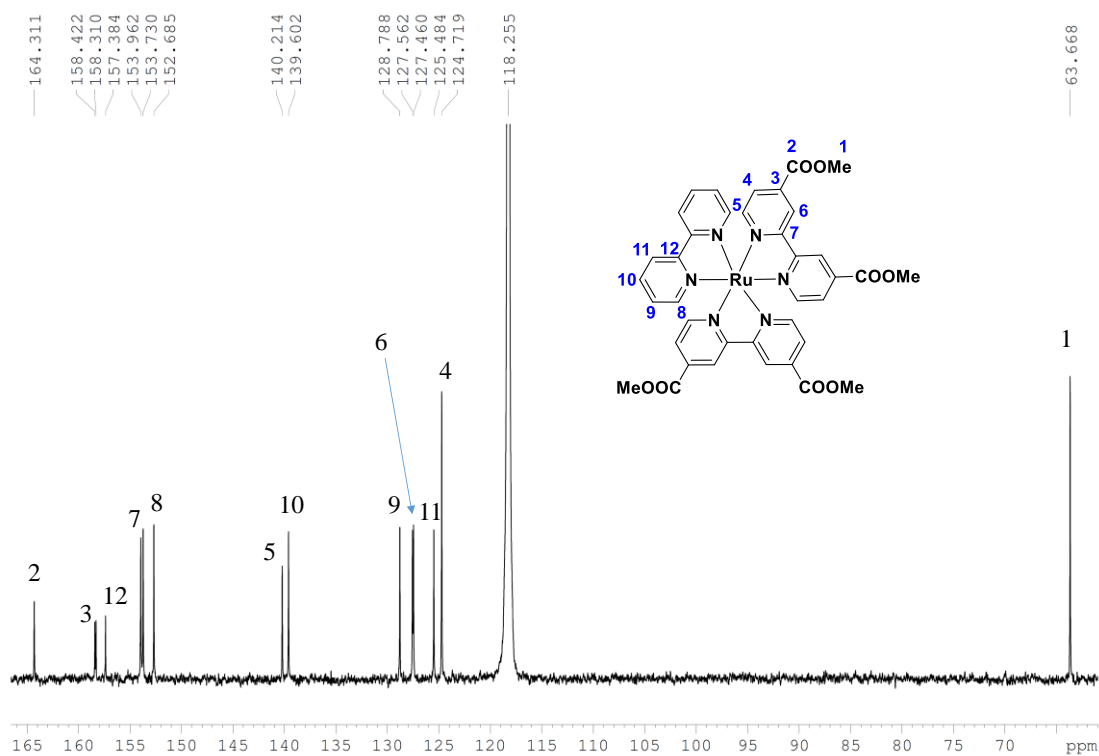


**Figure 6.4.12** <sup>13</sup>C NMR spectrum of Ru-bpy in CD<sub>3</sub>CN.

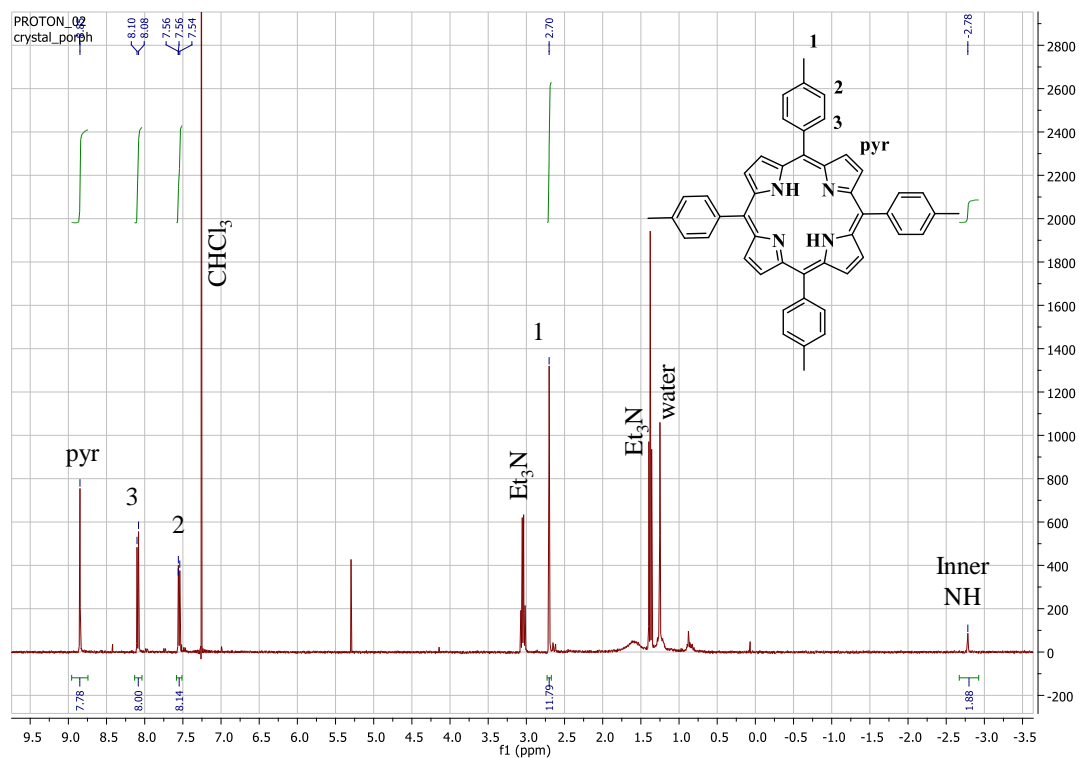


Figure 6.4.13  $^1\text{H}$  NMR spectrum of TTP in  $\text{CDCl}_3$  (300MHz).

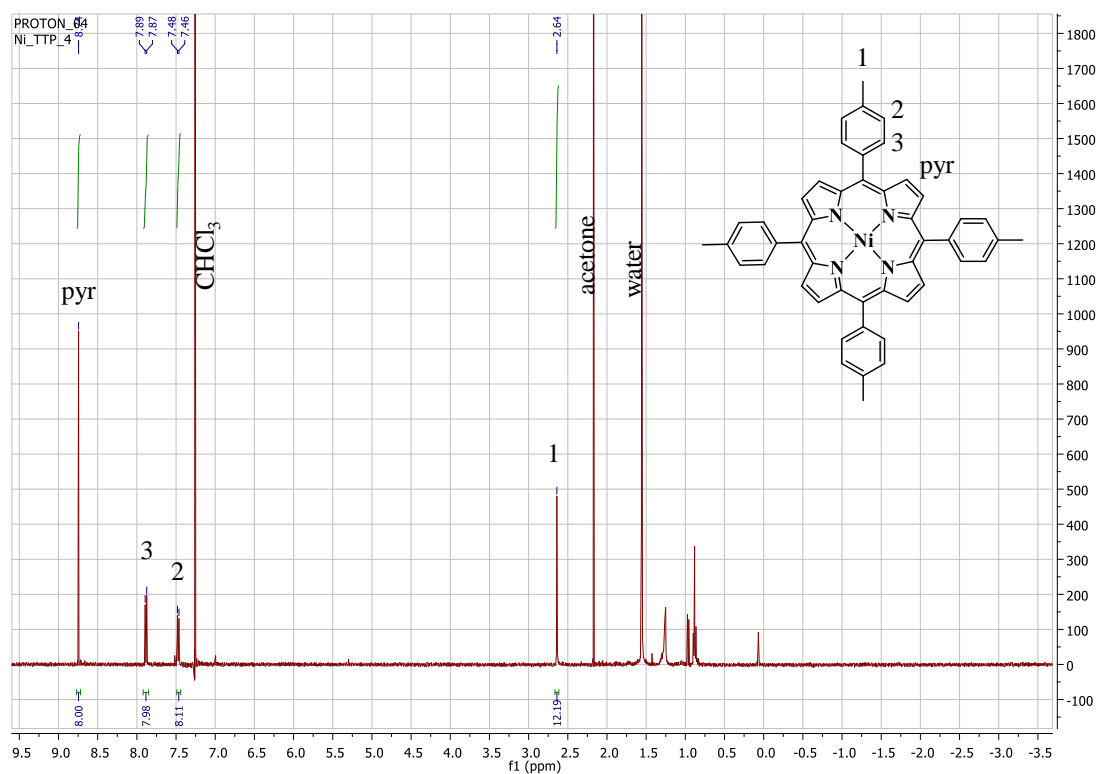
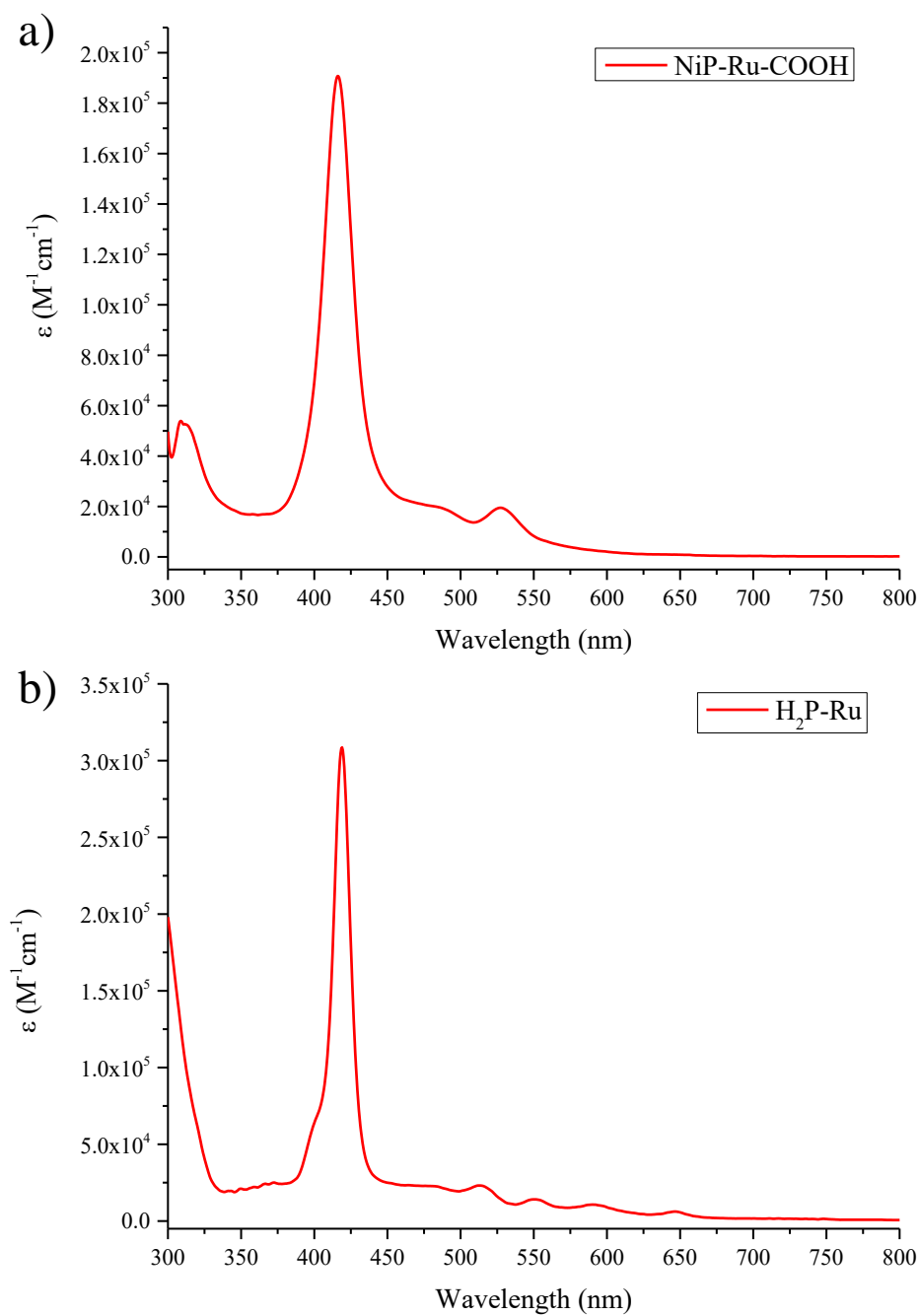
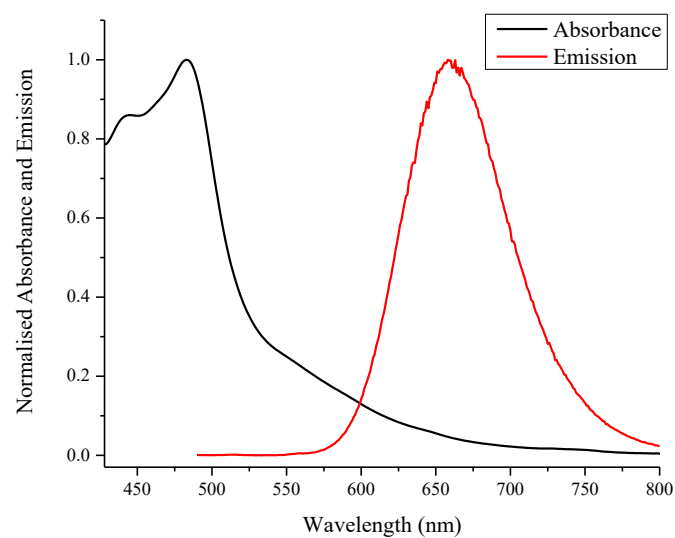


Figure 6.4.14  $^1\text{H}$  NMR spectrum of NiP in  $\text{CDCl}_3$  (300MHz).



**Figure 6.4.15** UV-Vis spectrum of a) **NiP-Ru-COOH** and b)  **$\text{H}_2\text{P-Ru}$**  in DMF.





**Figure 6.4.16** Normalized absorption and emission spectra of **Ru-bpy** in DMF (excitation at 480 nm).

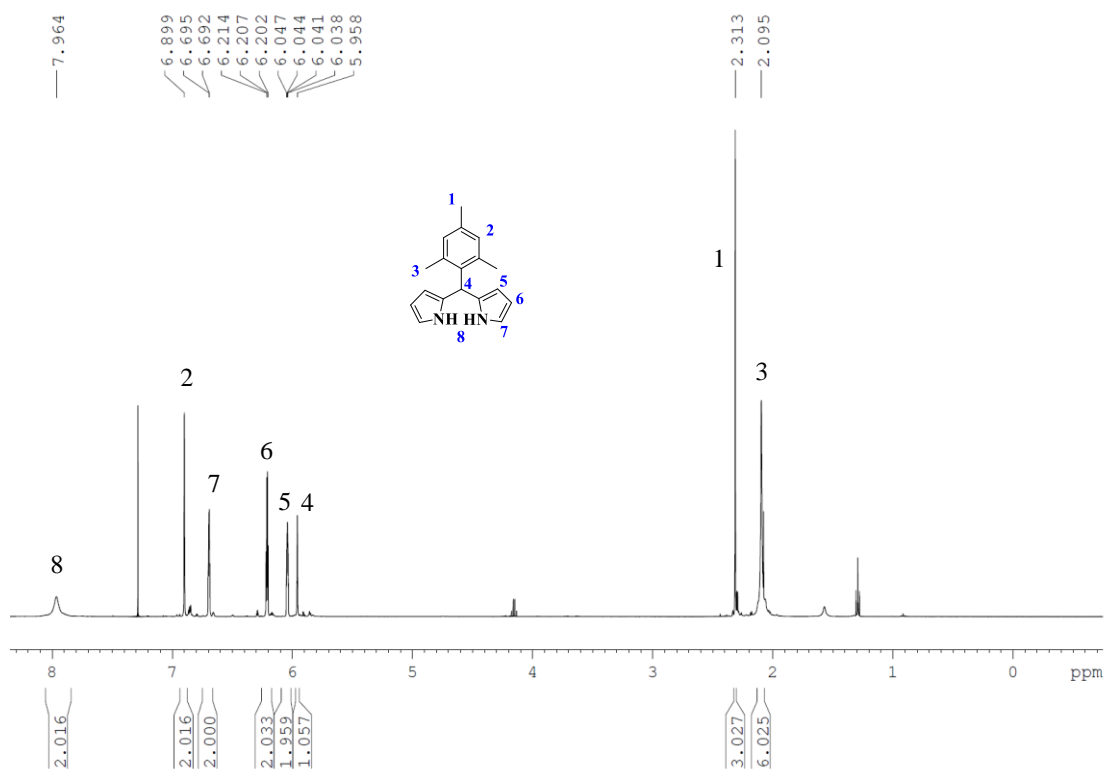


**Figure 6.4.17** <sup>1</sup>H NMR spectrum of mesityl-dipyrromethane (CDCl<sub>3</sub>, 500MHz).

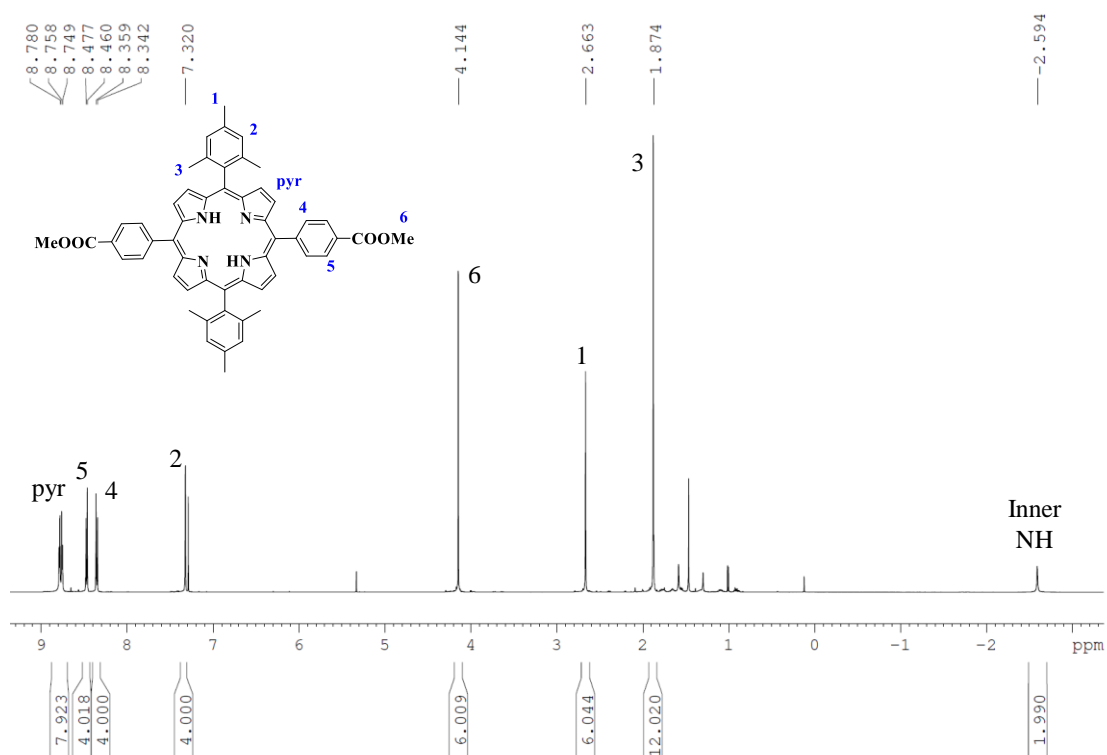


Figure 6.4.18 <sup>1</sup>H NMR spectrum of compound 3 (CDCl<sub>3</sub>, 500MHz).

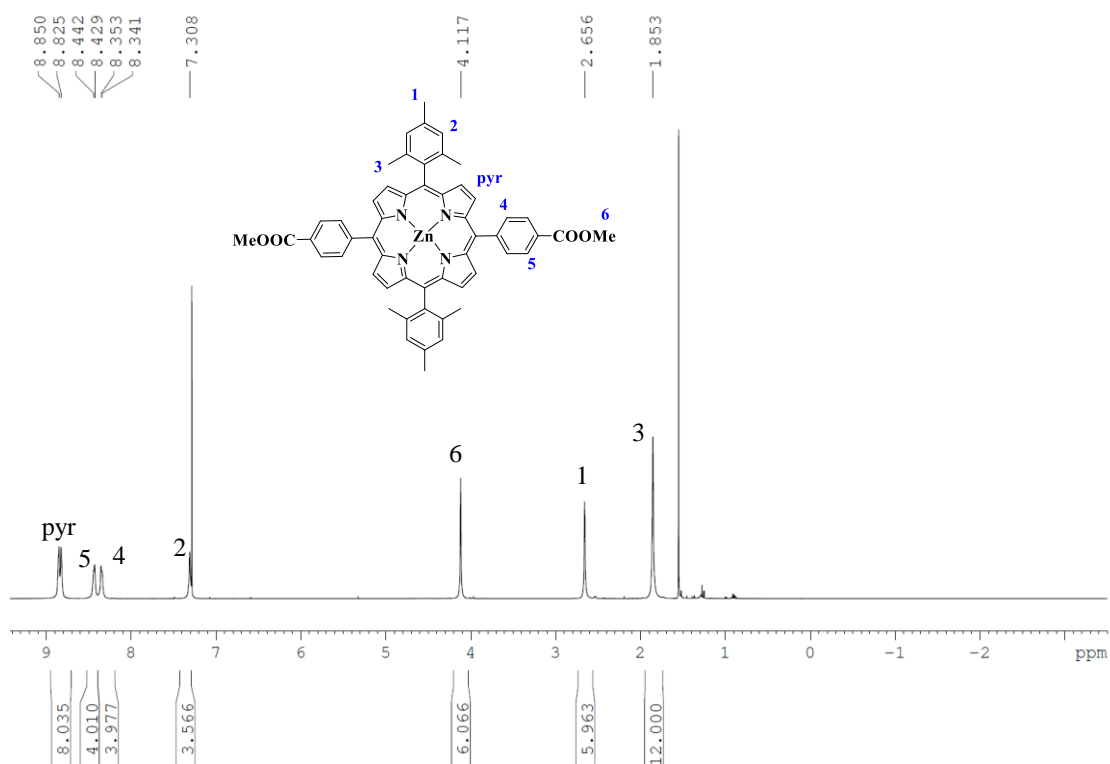
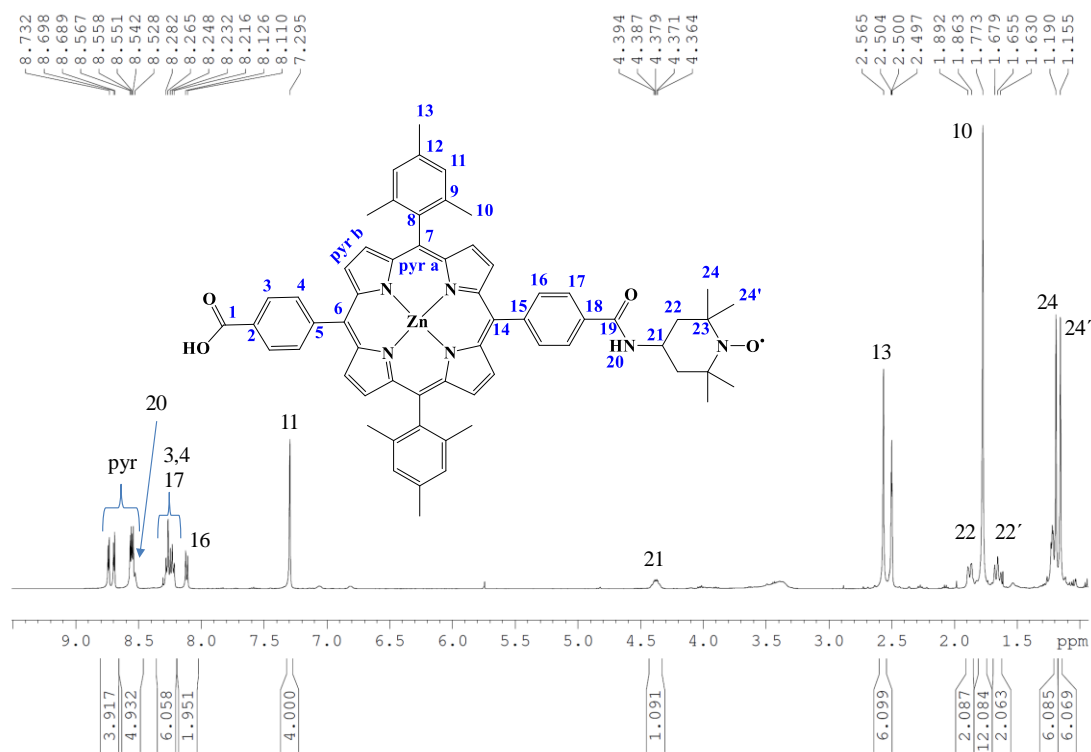
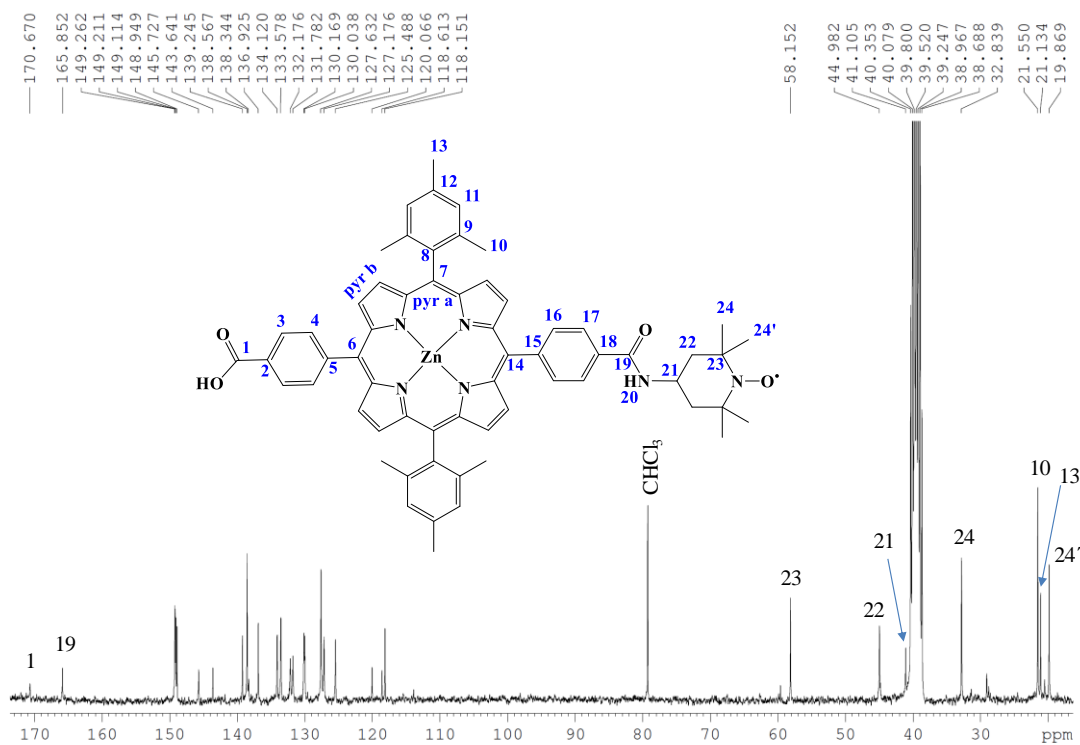


Figure 6.4.19 <sup>1</sup>H NMR spectrum of compound 4 (CDCl<sub>3</sub>, 500MHz).



**Figure 6.4.20**  $^1\text{H}$  NMR spectrum of compound **HOOC-ZnP-TEMPO** in  $\text{DMSO-d}_6 + 5\%$  hydrazine.



**Figure 6.4.21**  $^{13}\text{C}$  NMR spectrum of compound **HOOC-ZnP-TEMPO** in  $\text{DMSO-d}_6 + 5\%$  hydrazine.



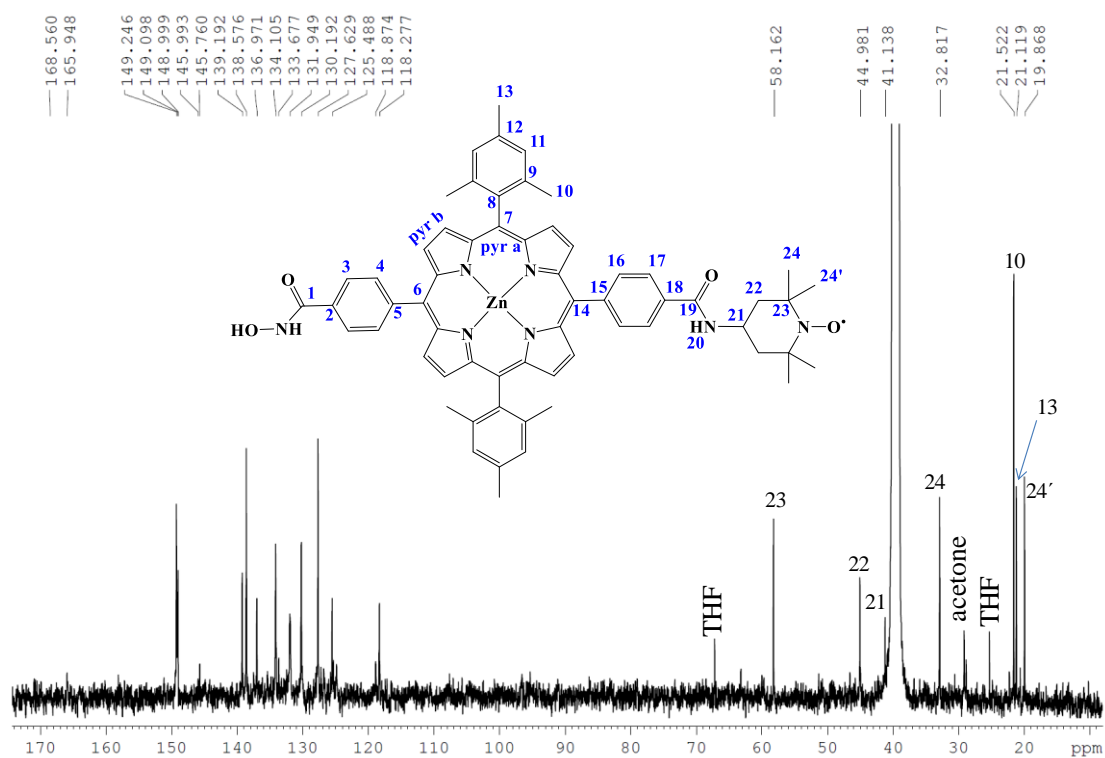


**Figure 6.4.24**  $^{13}\text{C}$  NMR spectrum of compound **hyd-ZnP-TEMPO** in  $\text{DMSO-d}_6$  + 5% hydrazine.

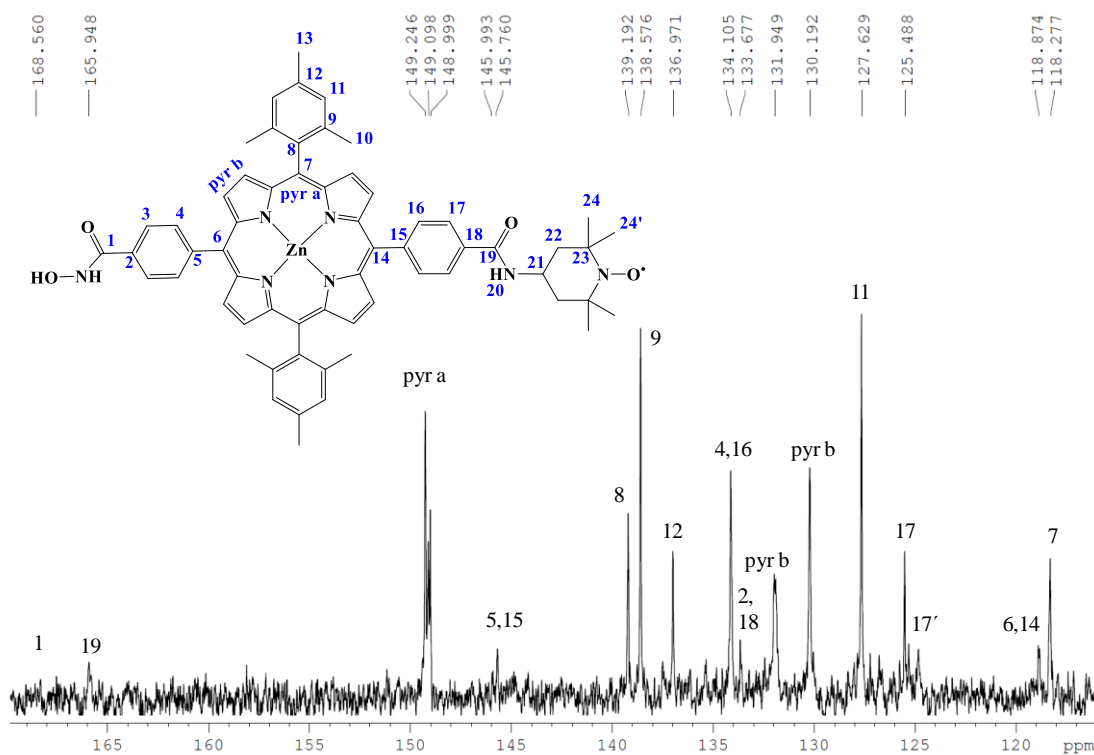


**Figure 6.4.25**  $^{13}\text{C}$  NMR spectrum of compound **hyd-ZnP-TEMPO** in  $\text{DMSO-d}_6$  + 5% hydrazine.

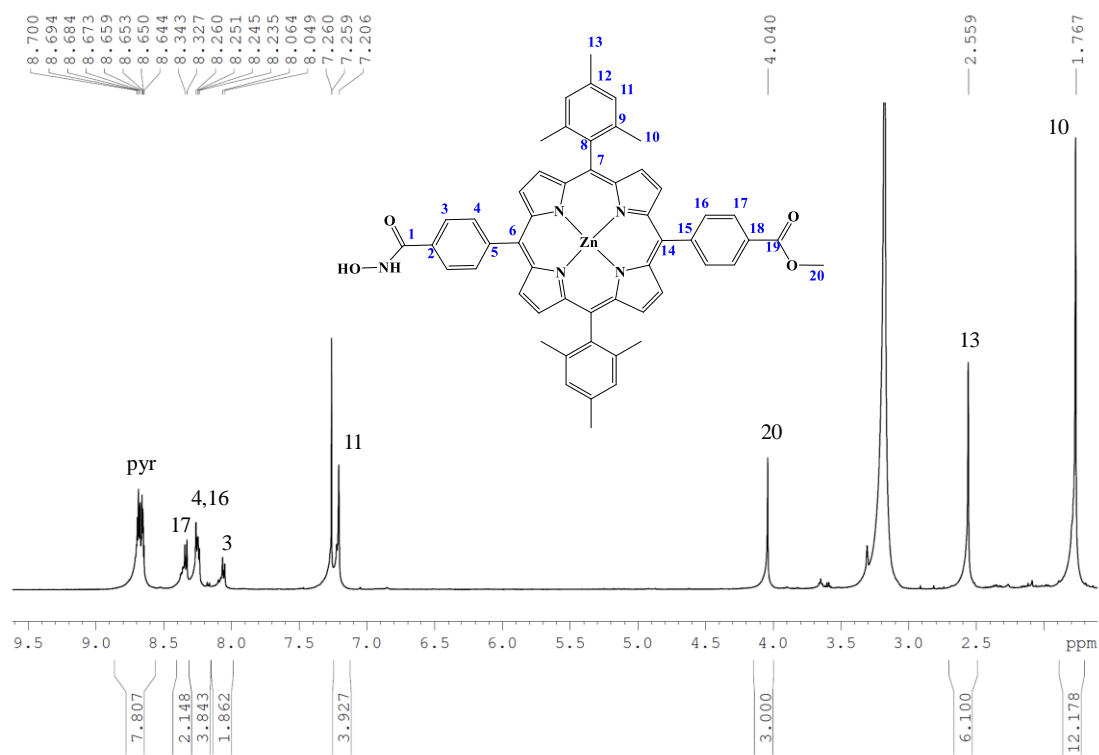


Figure 6.4.26 <sup>1</sup>H NMR spectrum of compound **hyd-ZnP** in CDCl<sub>3</sub> + 10 μL MeOD.

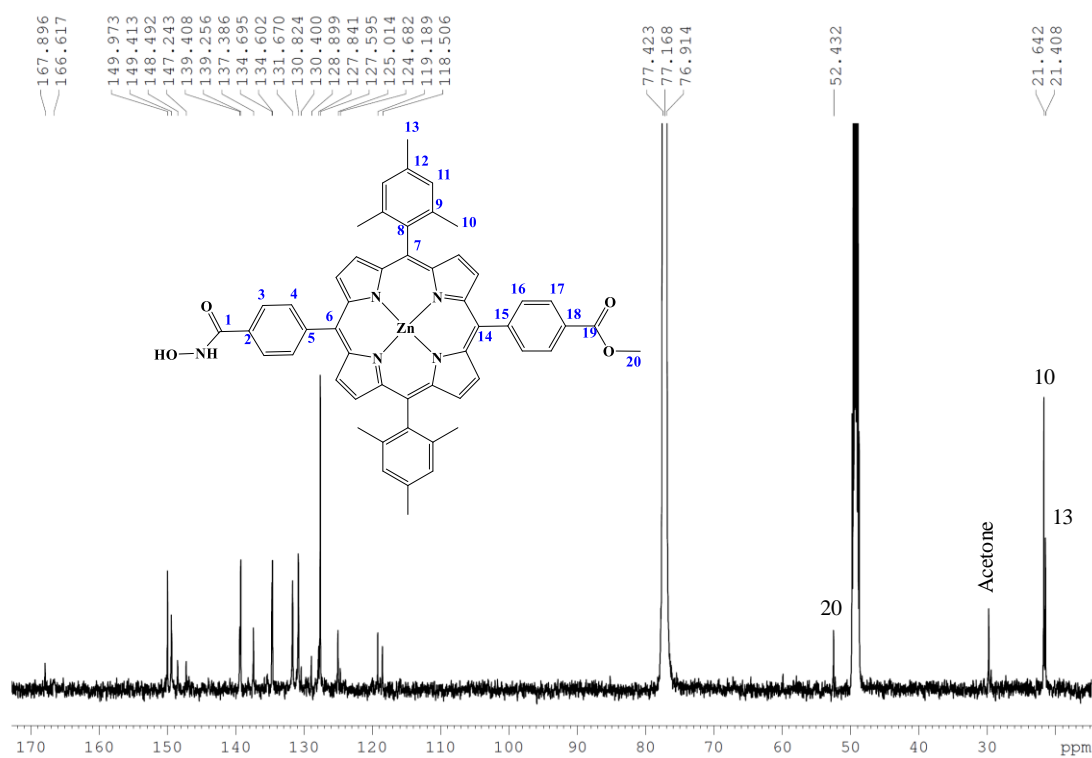
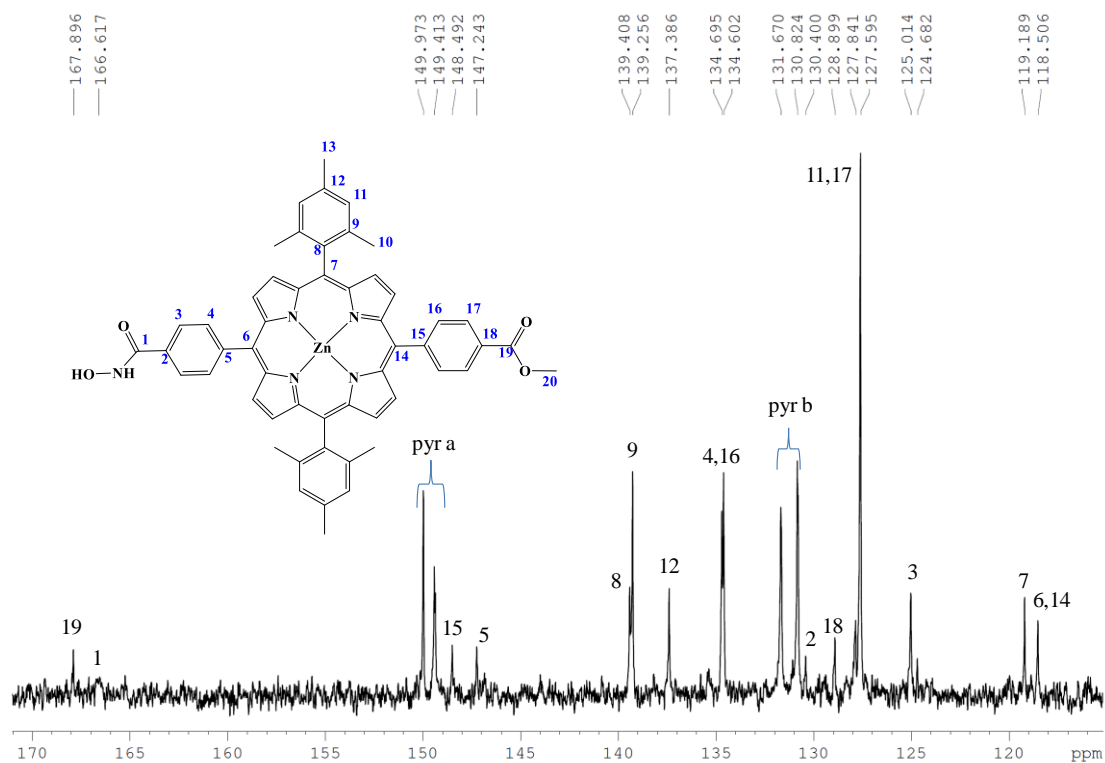
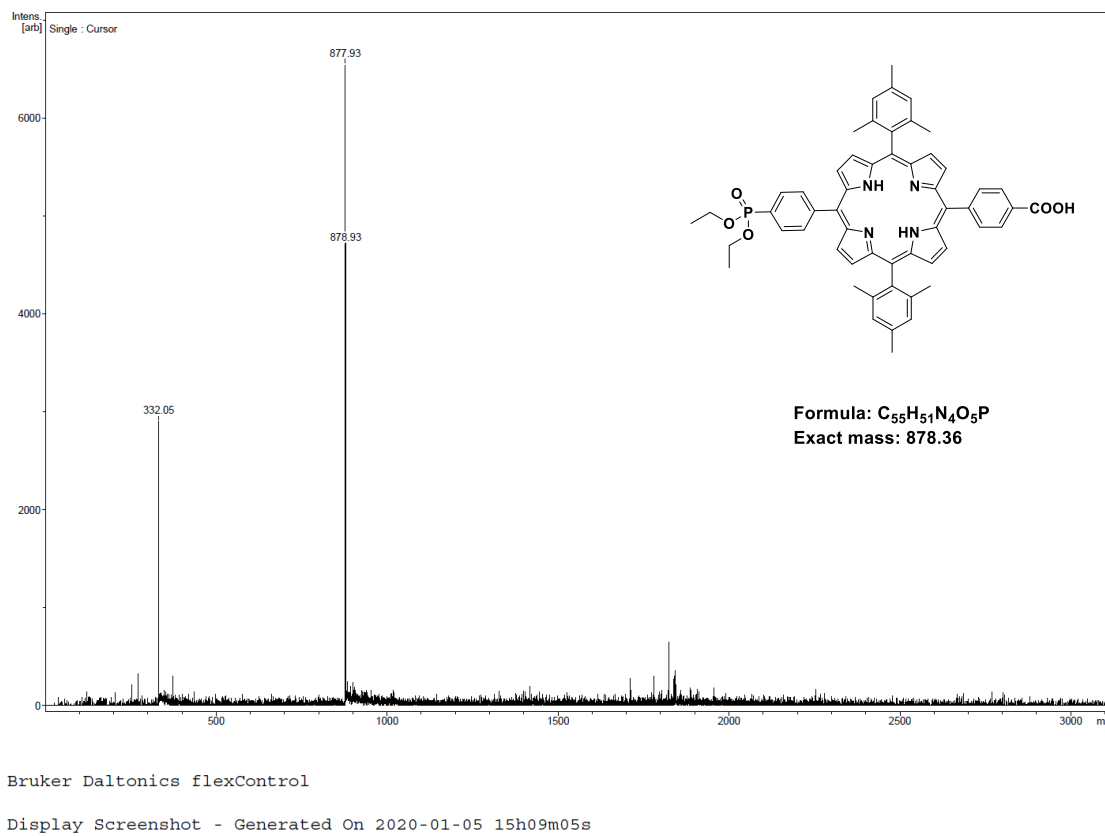


Figure 6.4.27 <sup>13</sup>C NMR spectrum of compound **hyd-ZnP** in CDCl<sub>3</sub> + 10 μL MeOD.



**Figure 6.4.28**  $^{13}\text{C}$  NMR spectrum of compound **hyd-ZnP** in  $\text{CDCl}_3 + 10 \mu\text{L MeOD}$ .



**Figure 6.4.29** MALDI-TOF mass spectrum of compound **PO(OEt)<sub>2</sub>-DMP-COOH**.

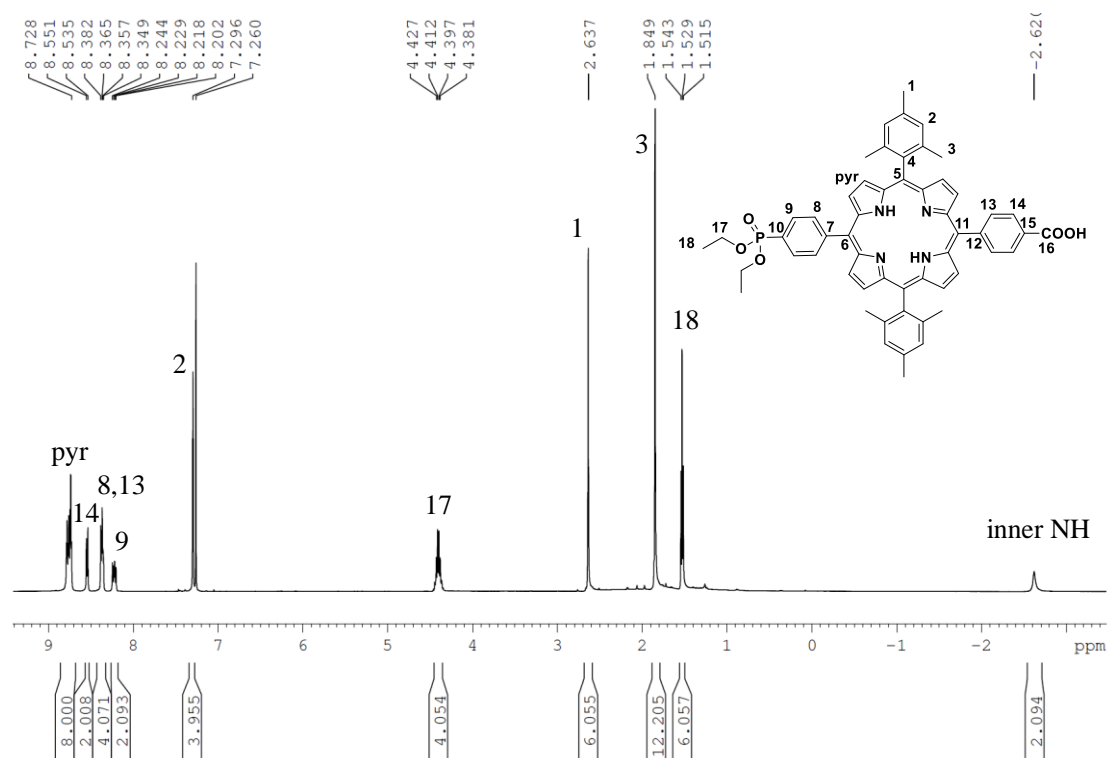


Figure 6.4.30 <sup>1</sup>H NMR spectrum of compound PO(OEt)<sub>2</sub>-DMP-COOH in CDCl<sub>3</sub>.

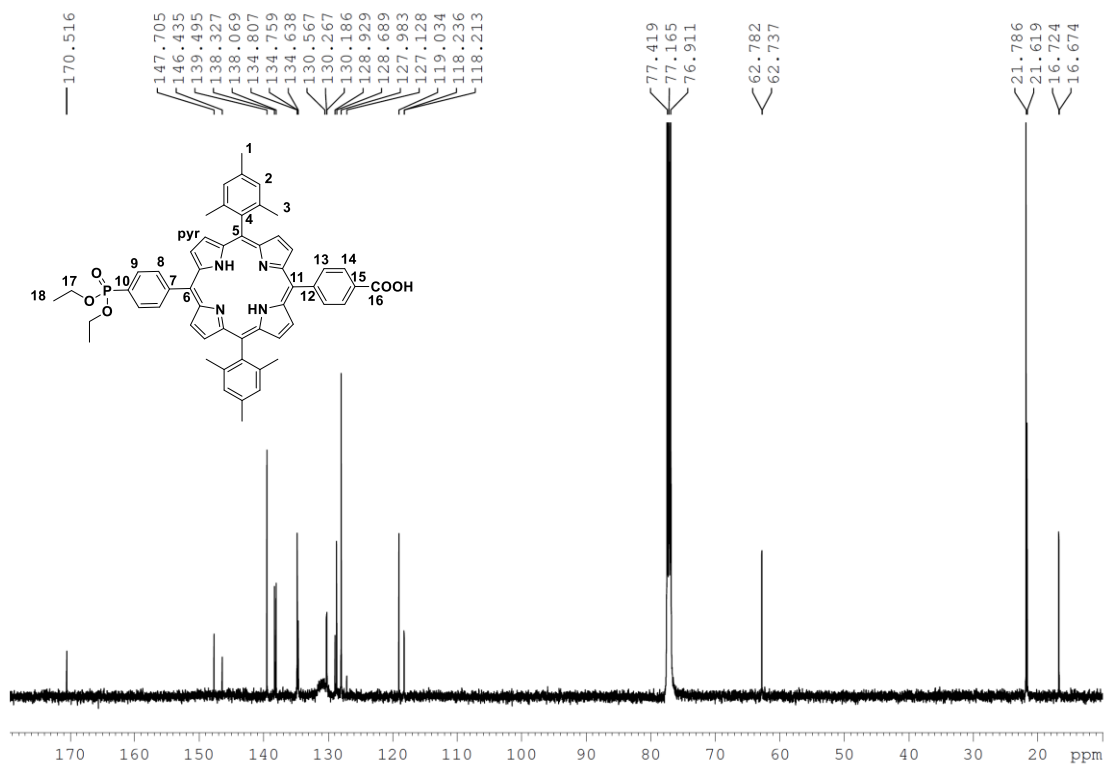
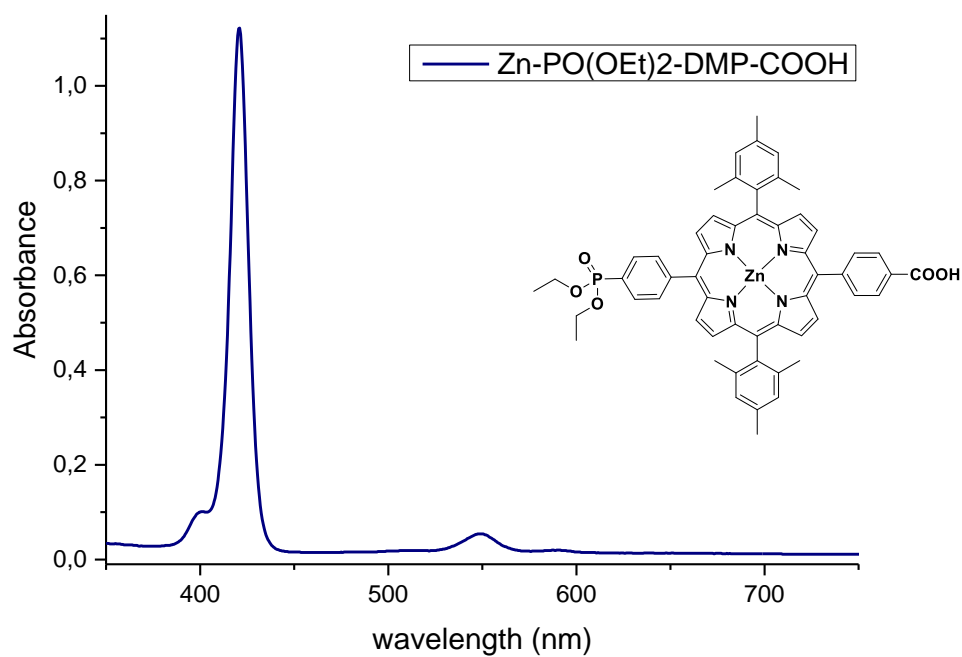
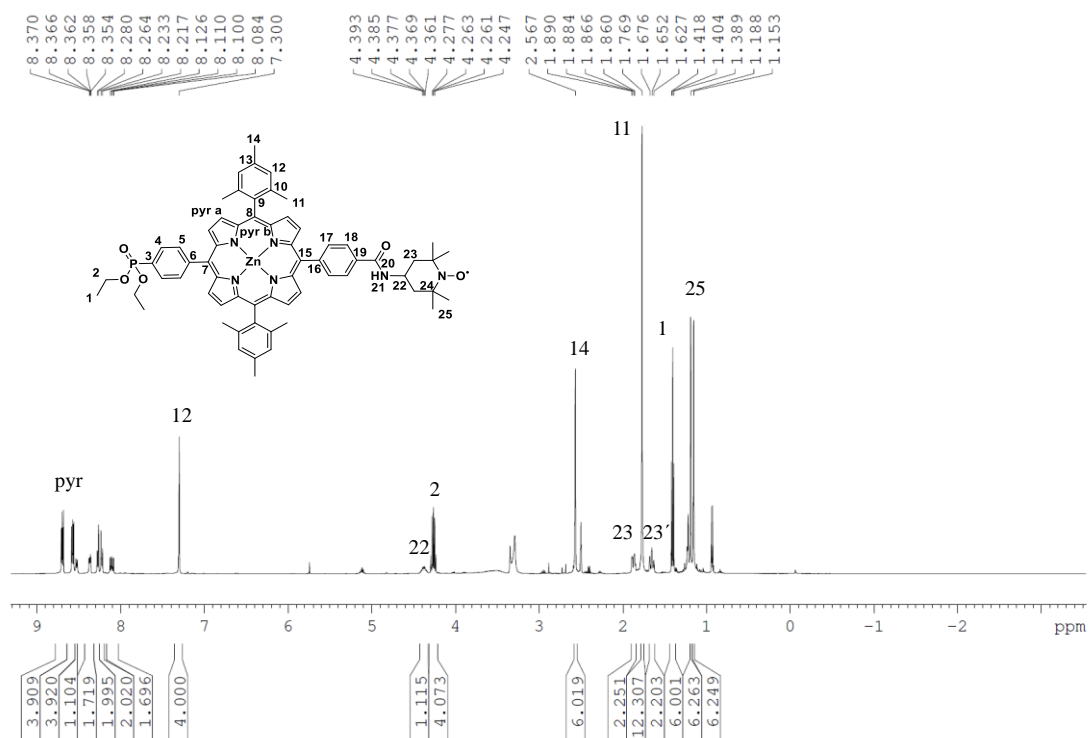


Figure 6.4.31 <sup>13</sup>C NMR spectrum of compound PO(OEt)<sub>2</sub>-DMP-COOH in CDCl<sub>3</sub>.





**Figure 6.4.32** UV-Vis spectrum of compound **PO(OEt)<sub>2</sub>-ZnP-COOH** in CDCl<sub>3</sub>.



**Figure 6.4.33** <sup>1</sup>H NMR spectrum of compound **PO(OEt)<sub>2</sub>-ZnP-TEMPO** in DMSO-d<sub>6</sub>.

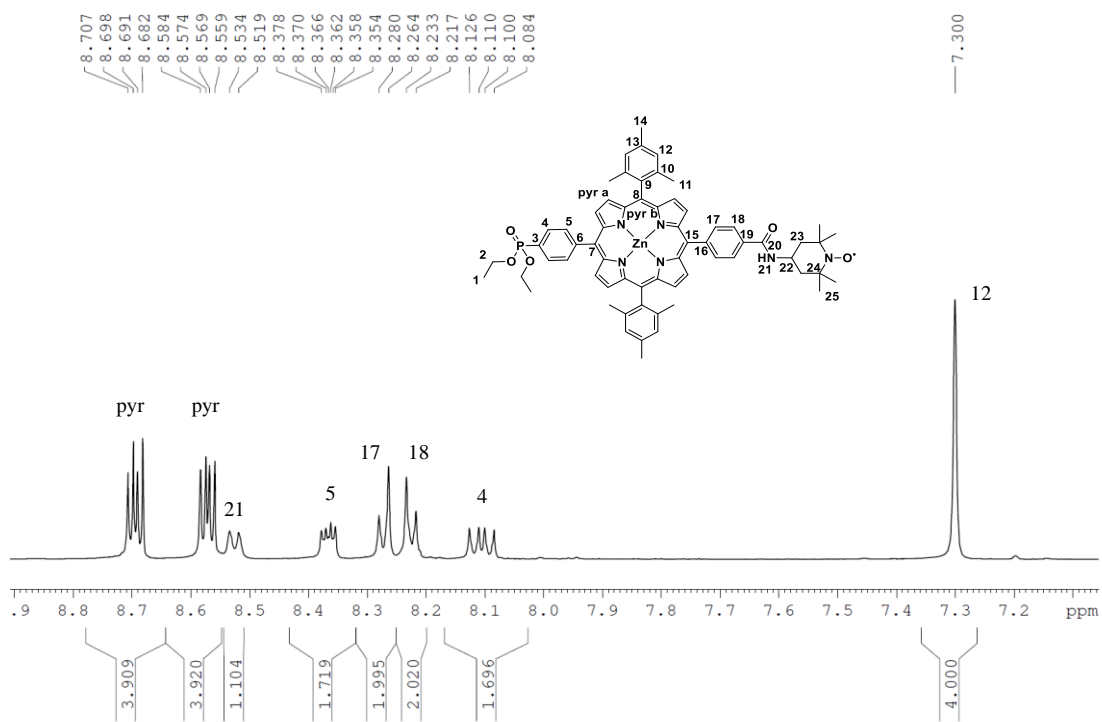


**Figure 6.4.34**  $^1\text{H}$  NMR spectrum of compound  $\text{PO}(\text{OEt})_2\text{-ZnP-TEMPO}$  in  $\text{DMSO-}d_6$ .

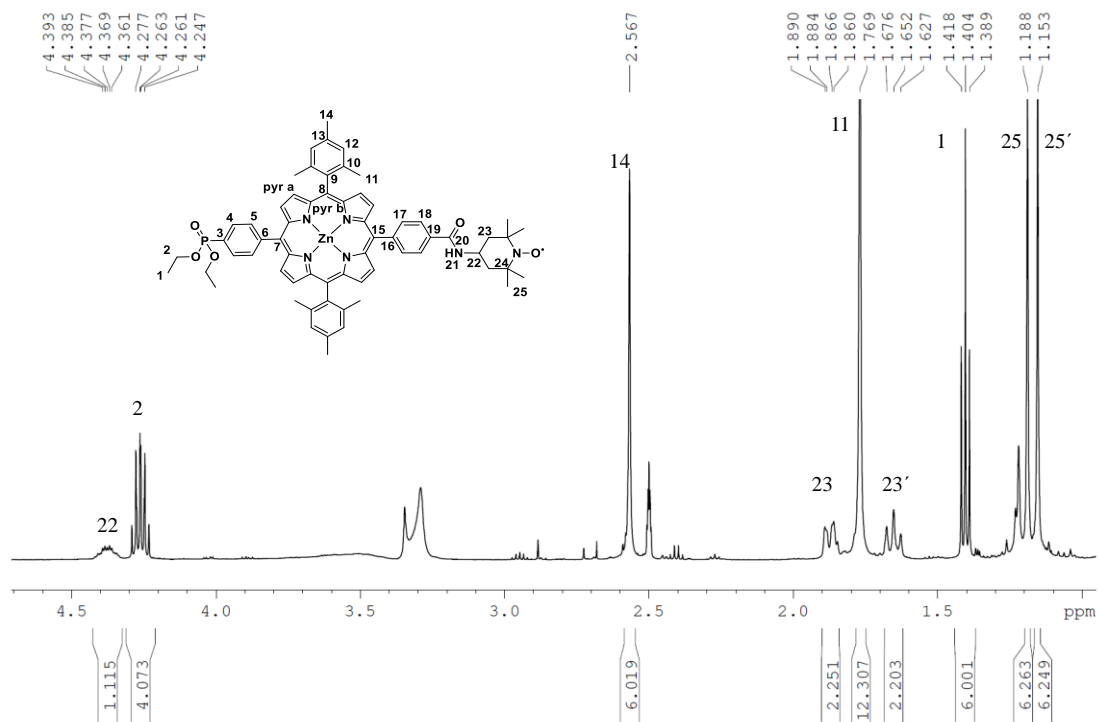


**Figure 6.4.35**  $^1\text{H}$  NMR spectrum of compound  $\text{PO}(\text{OEt})_2\text{-ZnP-TEMPO}$  in  $\text{DMSO-}d_6$ .

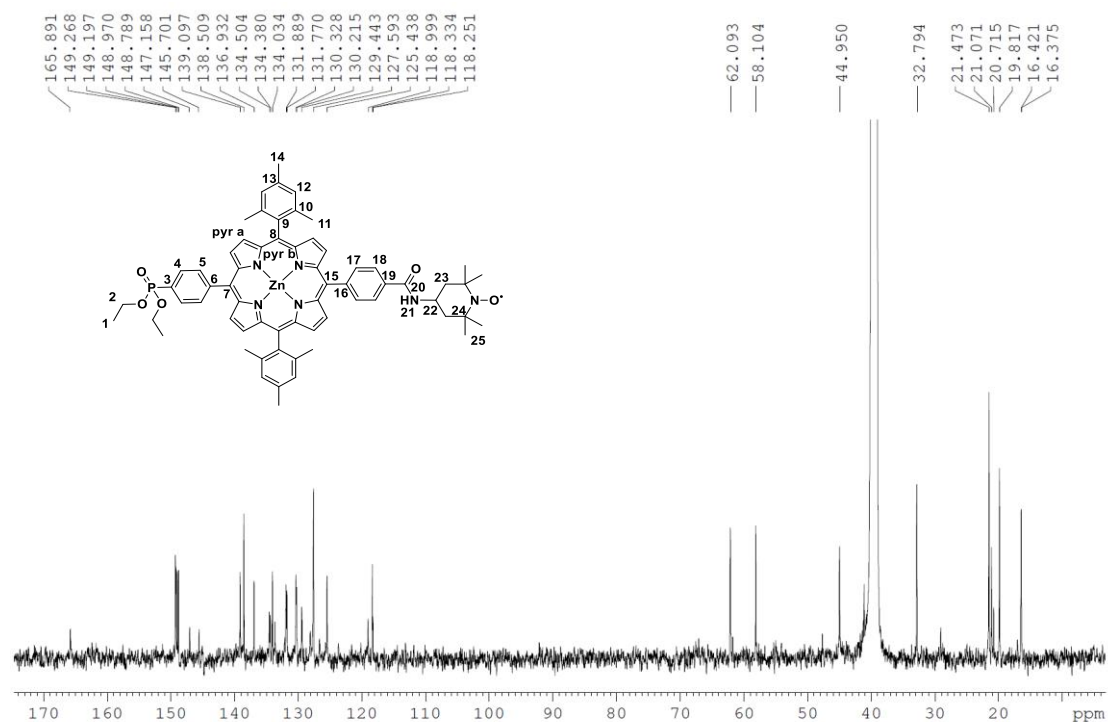


**Figure 6.4.36**  $^{13}\text{C}$  NMR spectrum of compound  $\text{PO}(\text{OEt})_2\text{-ZnP-TEMPO}$  in  $\text{DMSO-}d_6$ .

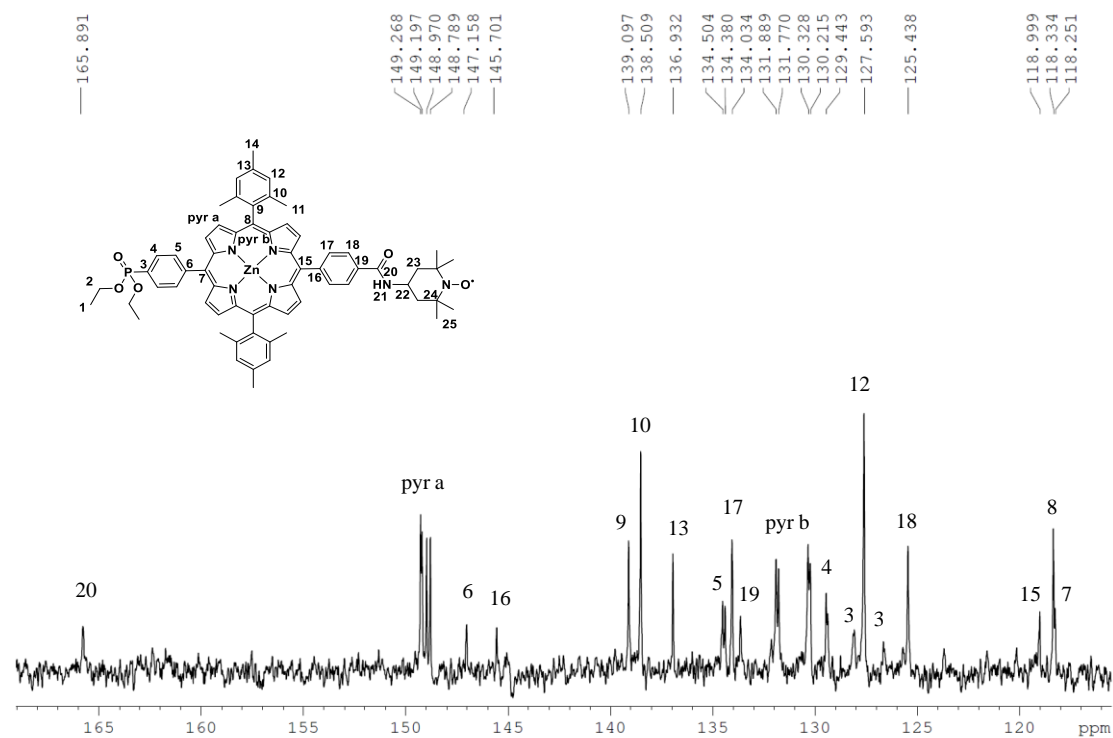


**Figure 6.4.37**  $^{13}\text{C}$  NMR spectrum of compound  $\text{PO}(\text{OEt})_2\text{-ZnP-TEMPO}$  in  $\text{DMSO-}d_6$ .

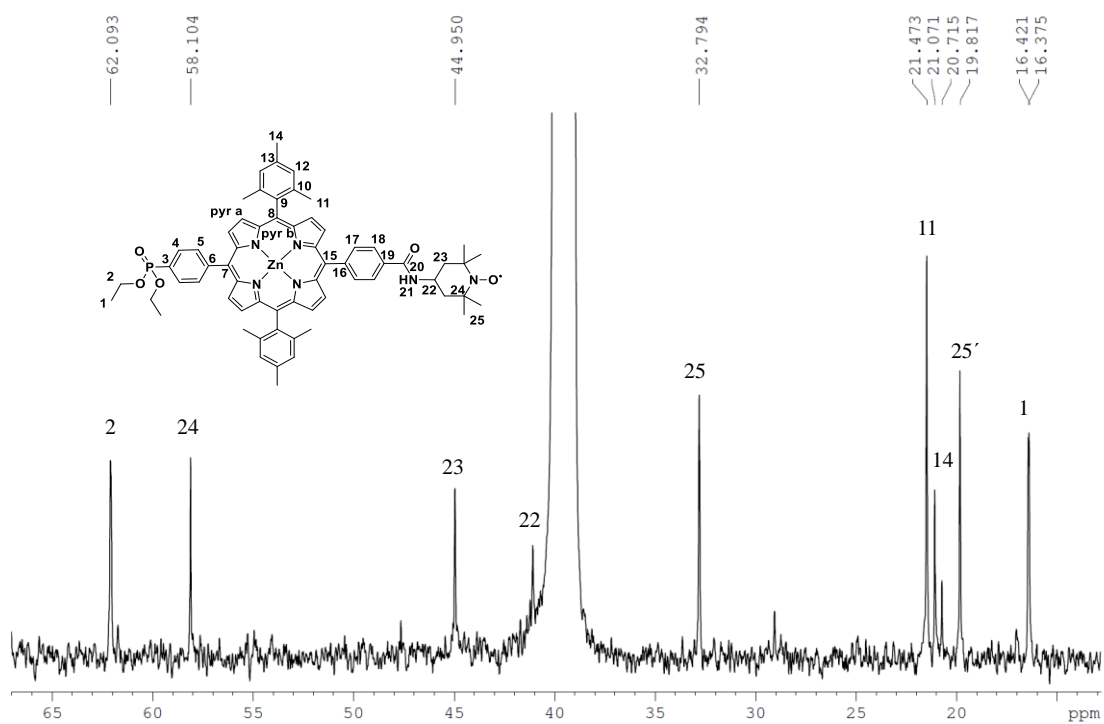


**Figure 6.4.38**  $^{13}\text{C}$  NMR spectrum of compound  $\text{PO}(\text{OEt})_2\text{-ZnP-TEMPO}$  in  $\text{DMSO-}d_6$ .

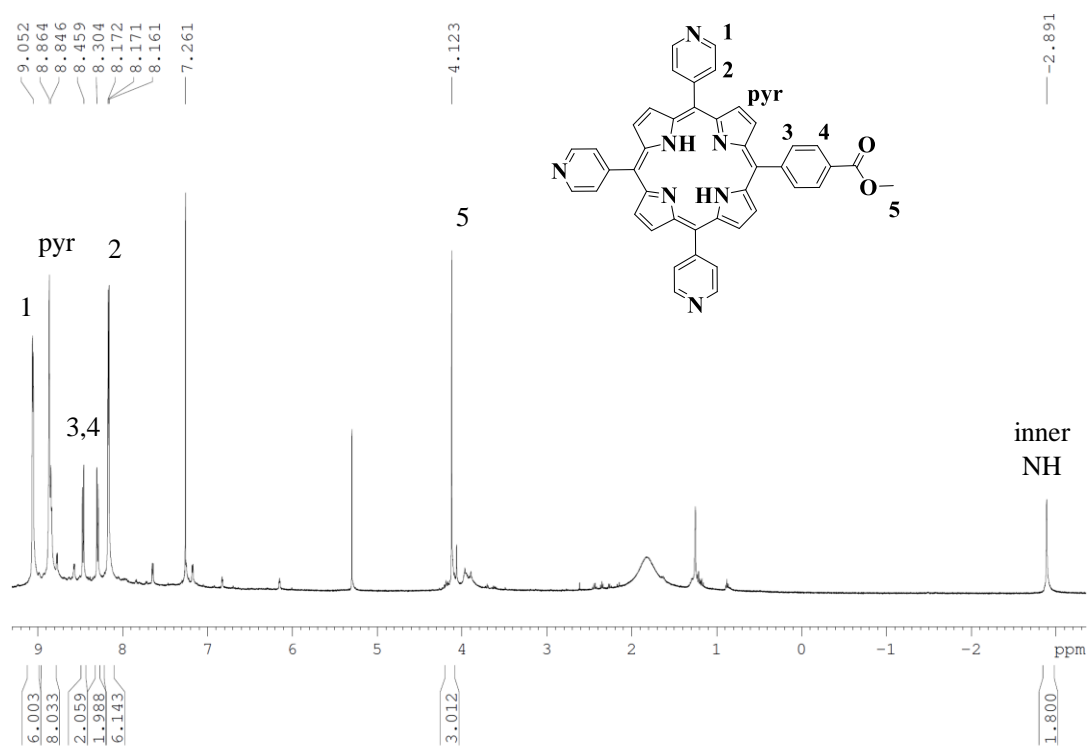


**Figure 6.4.39**  $^1\text{H}$  NMR spectrum of compound  $\text{Py}_3\text{P-COOMe}$  in  $\text{CDCl}_3$ .

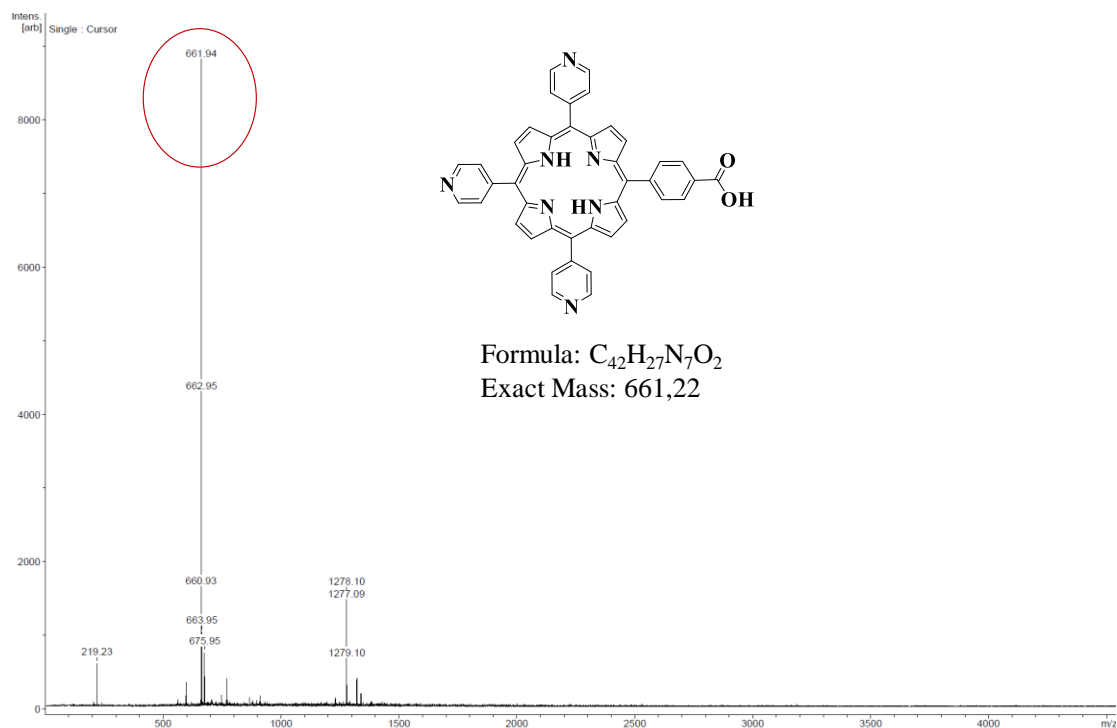


Figure 6.4.40 MALDI-TOF spectrum of compound **Py<sub>3</sub>P-COOH**.

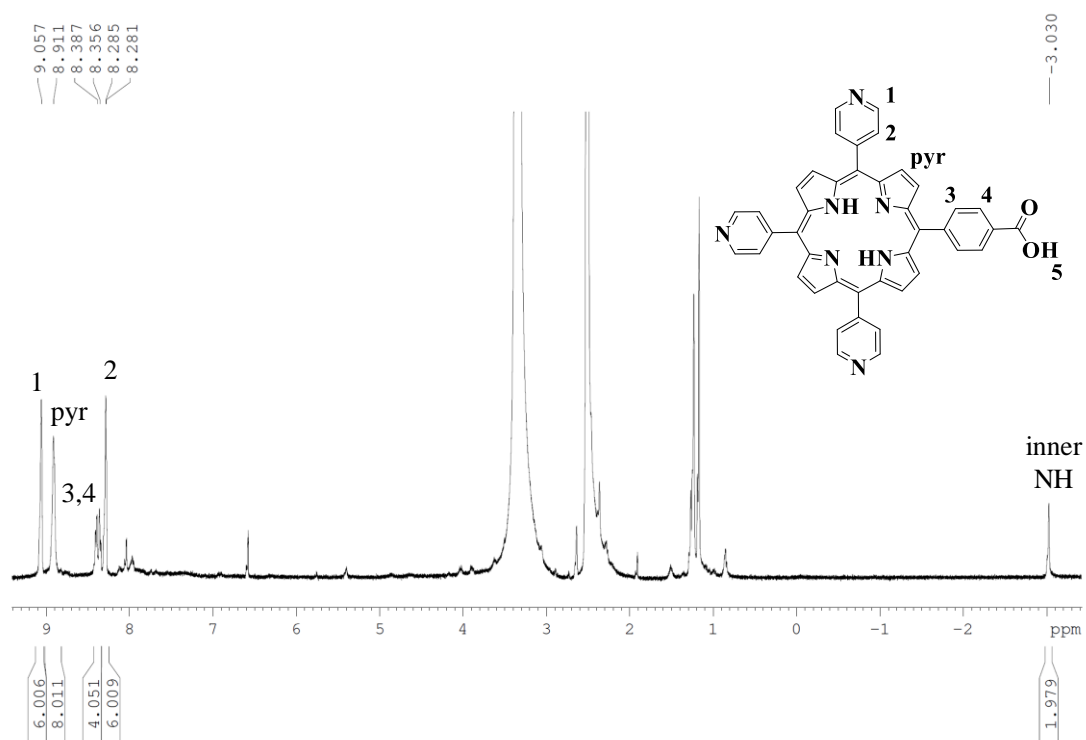
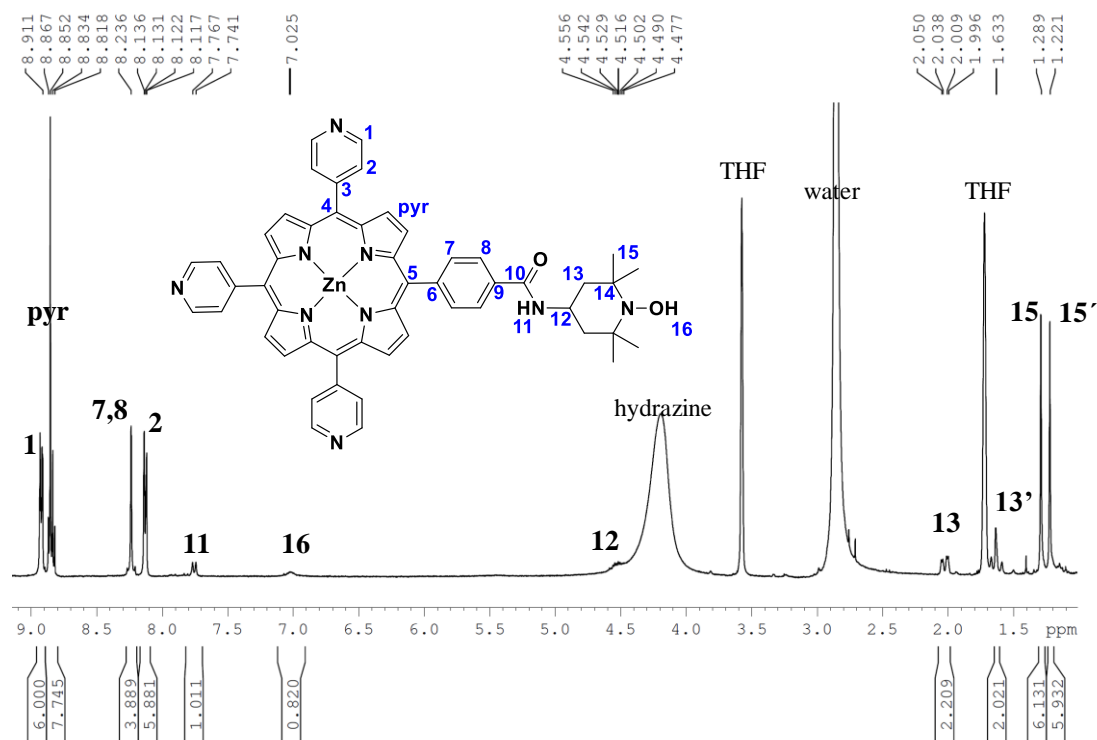
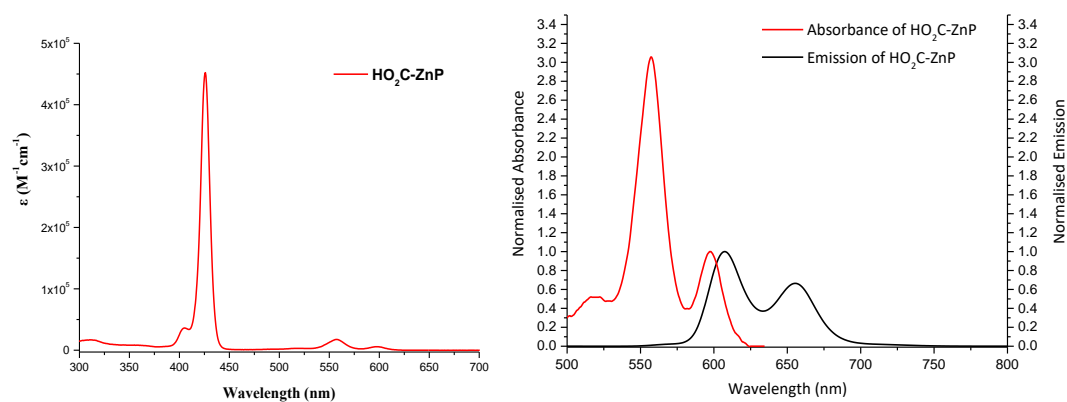


Figure 6.4.41  $^1H$  NMR spectrum of compound **Py<sub>3</sub>P-COOH** in  $DMSO-d_6$ .



**Figure 6.4.42**  $^1\text{H}$  NMR spectrum of compound  $\text{Py}_3\text{ZnP-TEMPO}$  in  $\text{THF-d}_4 + 10\%$  hydrazine.



**Figure 6.4.43** UV-Vis absorption spectrum of  $\text{HO}_2\text{C-ZnP}$  in THF (left). Overlay of the absorption and emission spectra of  $\text{HO}_2\text{C-ZnP}$  recorded in THF,  $\lambda_{\text{exc}} = 430$  nm (right).

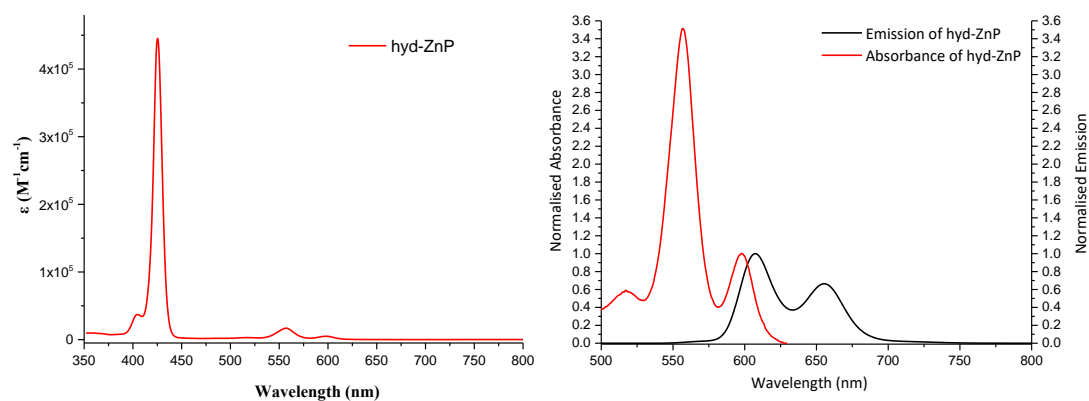


**Figure 6.4.44** UV-Vis absorption spectrum of **hyd-ZnP** in THF (left). Overlay of the absorption and emission spectra of **hyd-ZnP** recorded in THF,  $\lambda_{exc} = 430$  nm (right).

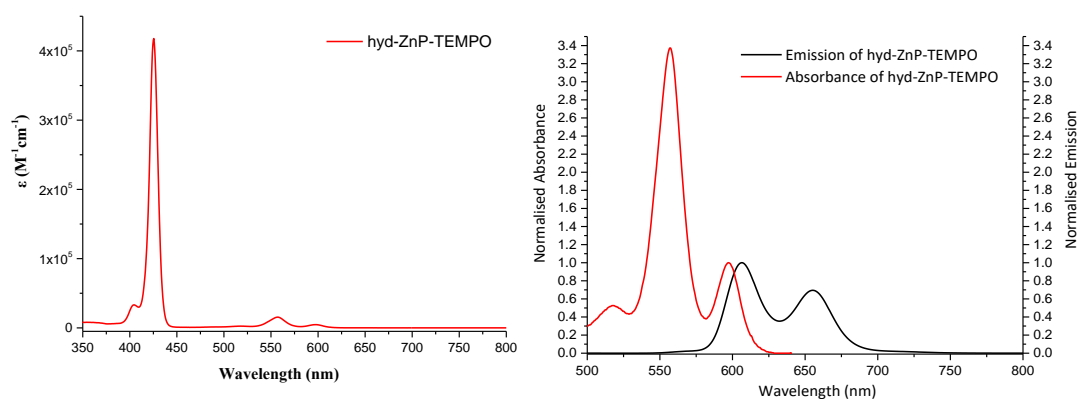


**Figure 6.4.45** UV-Vis absorption spectrum of **hyd-ZnP-TEMPO** in THF (left). Overlay of the absorption and emission spectra of **hyd-ZnP-TEMPO** recorded in THF,  $\lambda_{exc} = 430$  nm (right).

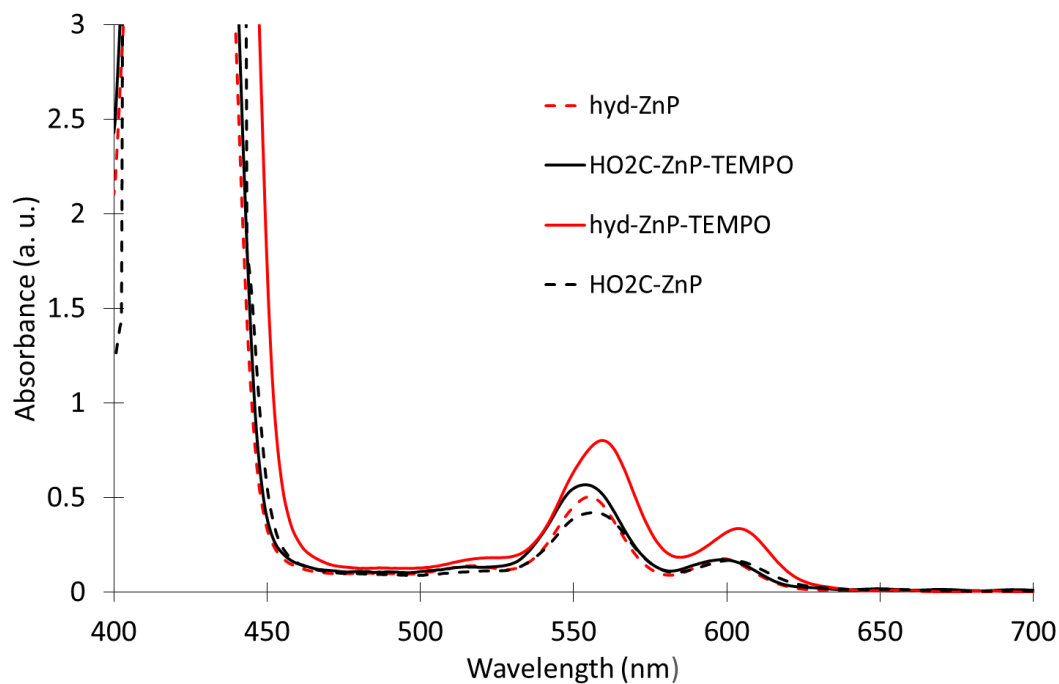


**Figure 6.4.46** Overlay of the absorption spectra recorded in thin  $\text{TiO}_2$  films ( $4 \mu\text{m}$ ).

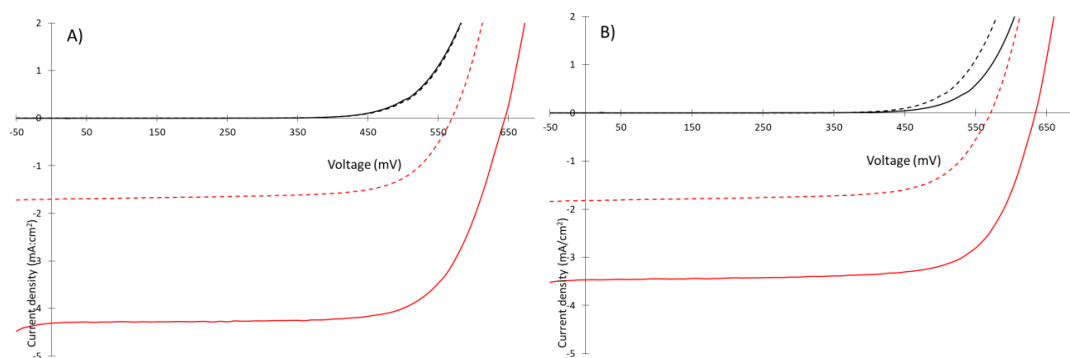


**Figure 6.4.47** Typical current/voltage characteristics of the DSSCs recorded under AM1.5 (red) and under the dark (black). A) **HO<sub>2</sub>C-ZnP** (dashed-line) and **HO<sub>2</sub>C-ZnP-TEMPO** (straight line). B) **hyd-ZnP** (dashed-line) and **hyd-ZnP-TEMPO** (straight line).

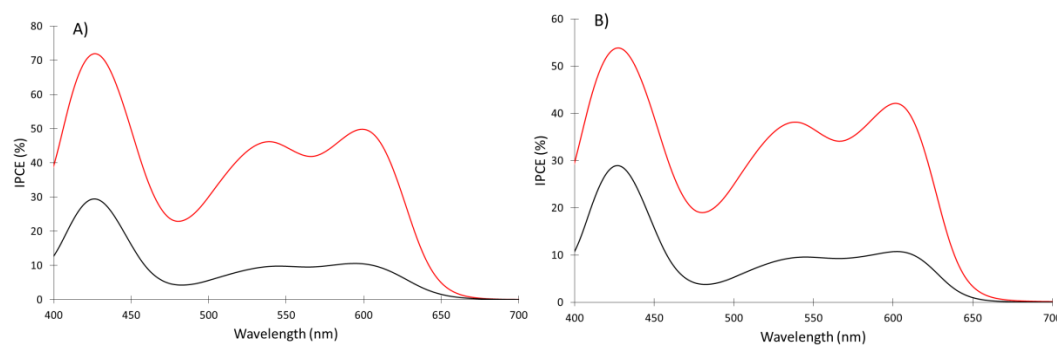


**Figure 6.4.48** IPCE spectra of the dyes in DSSC. A) **HO<sub>2</sub>C-ZnP** (black) and **HO<sub>2</sub>C-ZnP-TEMPO** (red). B) **hyd-ZnP** (black) and **hyd-ZnP-TEMPO** (red).



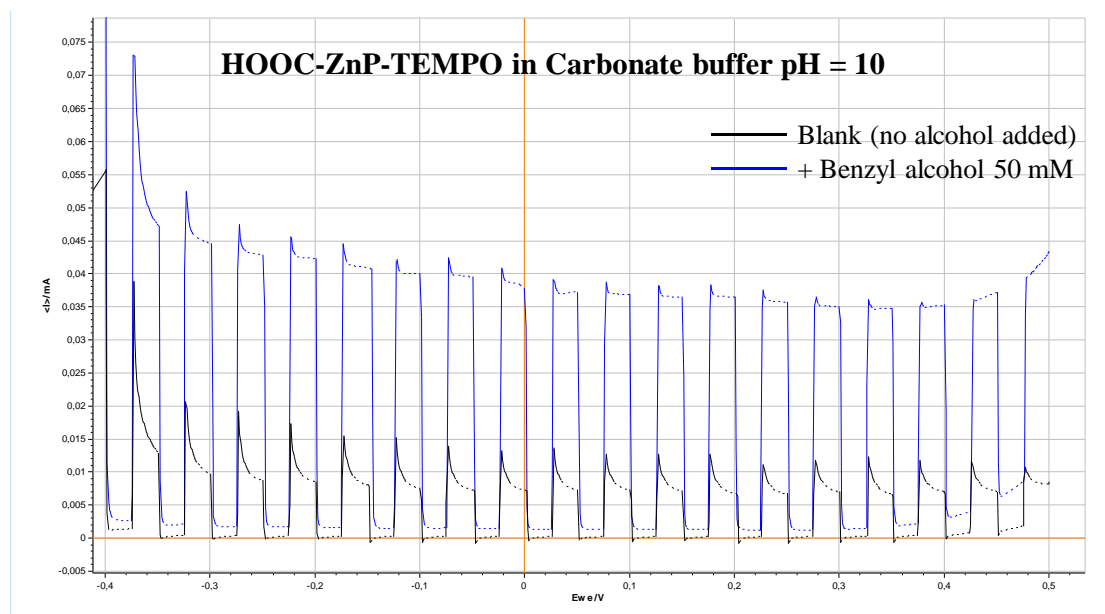


**Figure 6.4.49** Chopped light linear sweep voltammetry measurements recorded under white light irradiation of **HOOC-ZnP-TEMPO**, on  $\text{TiO}_2$  film with 0.1 M carbonate buffer at pH = 10 with [*para*-methoxybenzyl alcohol] = 50 mM (blue trace) and without (black trace).

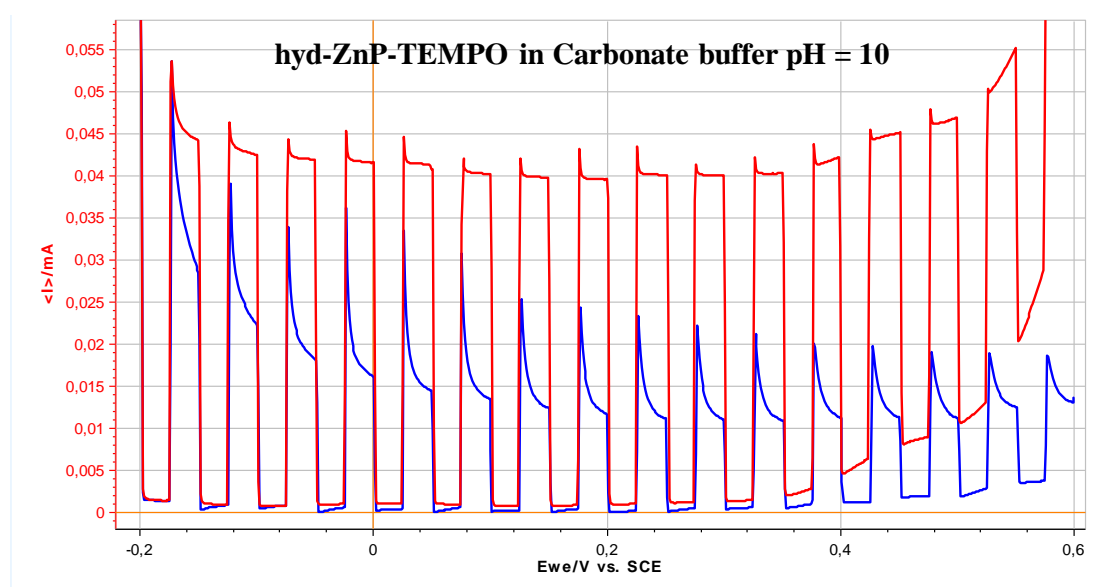


**Figure 6.4.50** Chopped light linear sweep voltammetry measurements recorded under white light irradiation of **hyd-ZnP-TEMPO** with 0.1 M carbonate buffer at pH = 10 with [*para*-methoxybenzyl alcohol] = 50 mM (red trace) and without (blue trace).

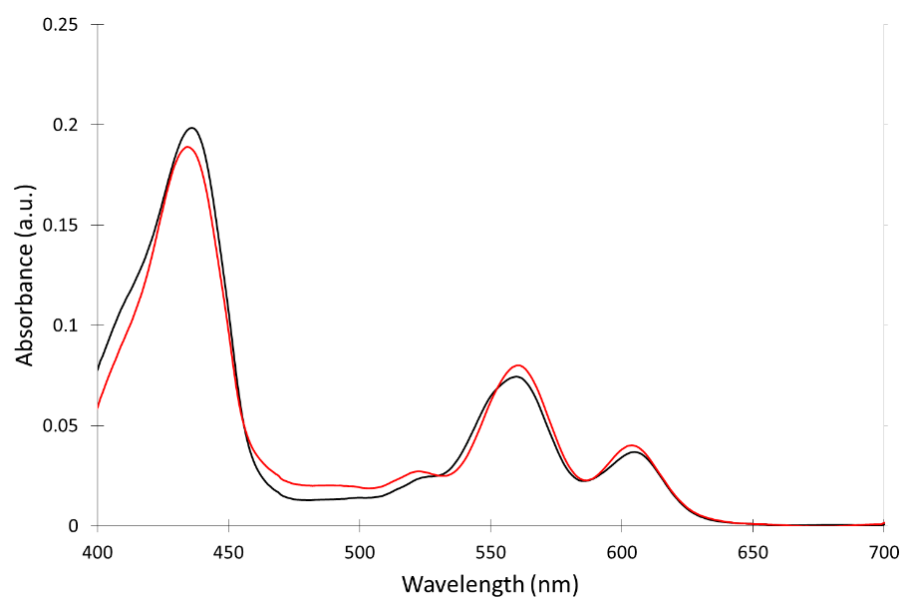


**Figure 6.4.51** Overlay of the absorption spectra of a thin TiO<sub>2</sub> film coated with **hyd-ZnP-TEMPO** before (black) and after 1 hour of photocatalysis in borate buffer at pH = 8 (red).

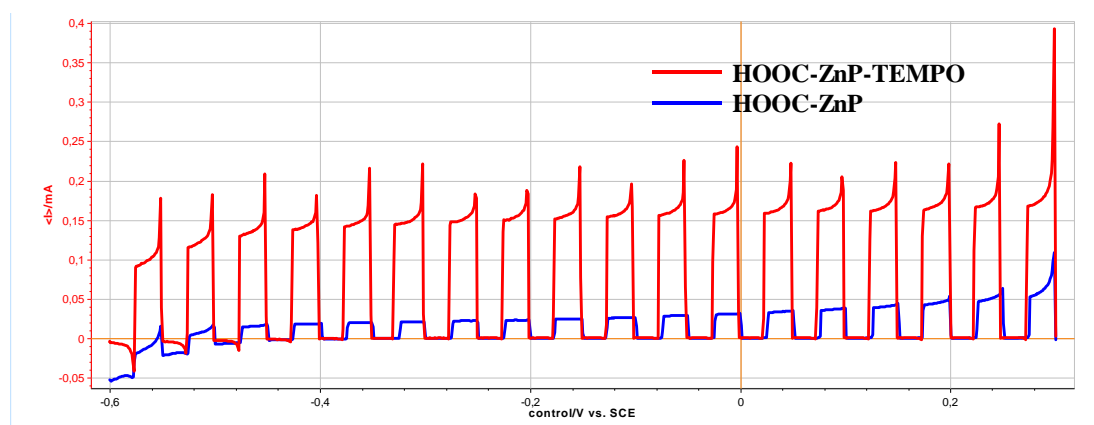


**Figure 6.4.52** Chopped light linear sweep voltammetry measurements recorded under white light irradiation of **HOOC-ZnP-TEMPO** and **HOOC-ZnP** on TiO<sub>2</sub> film with 0.1 M Me-Imd in acetonitrile with [*para*-methoxybenzyl alcohol] = 50 mM.

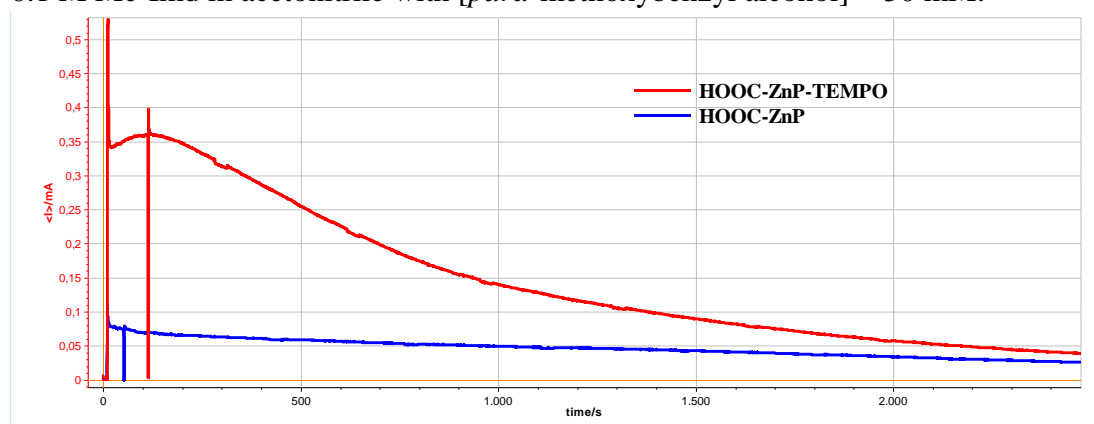


**Figure 6.4.53** Photocurrent density responses of **HOOC-ZnP-TEMPO** and **HOOC-ZnP** during long term photolysis experiments in acetonitrile in presence of 0.1 M of

Me-Imd with [*para*-methoxybenzyl alcohol] = 50 mM. Irradiation conditions: white light (about 100 mW/cm<sup>2</sup>).

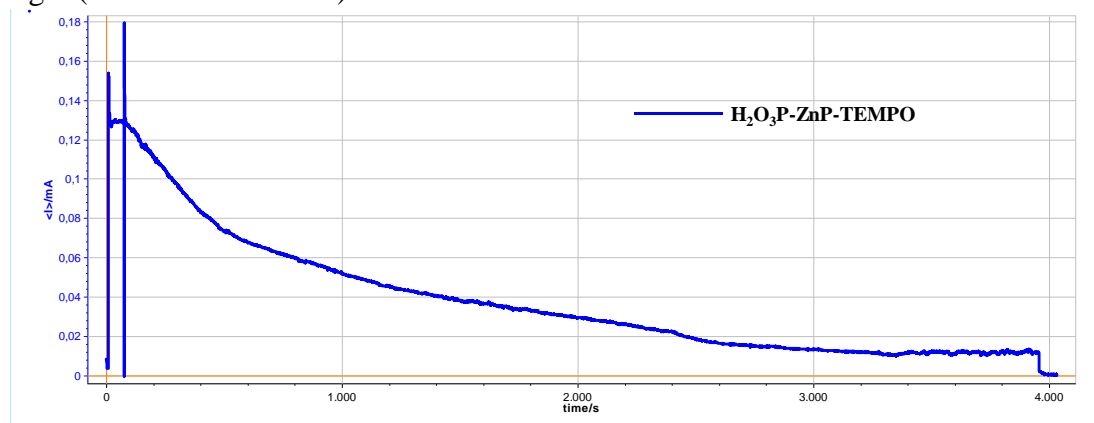


**Figure 6.4.54** Photocurrent density responses of **H<sub>2</sub>O<sub>3</sub>P-ZnP-TEMPO** during long term photolysis experiments in acetonitrile in presence of 0.1 M of Me-Imd with [*para*-methoxybenzyl alcohol] = 50 mM.

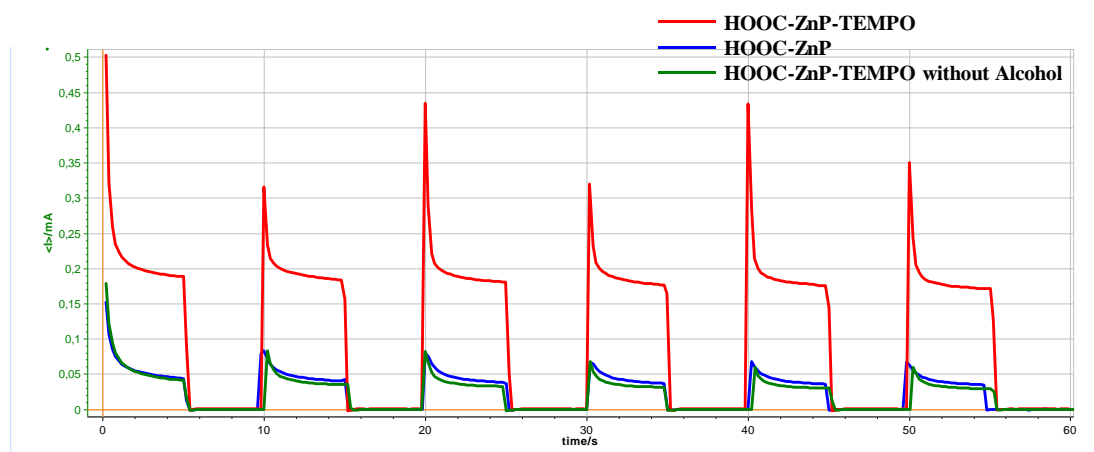


**Figure 6.4.55** Chopped light voltammetry measurements recorded at a constant potential of 0 V vs. SCE of TiO<sub>2</sub> photoelectrodes in acetonitrile in presence of 0.1 M of Me-Imd coated with **HOOC-ZnP-TEMPO** and **HOOC-ZnP** in presence of [*para*-methoxybenzyl alcohol] = 50 mM as well as **HOOC-ZnP-TEMPO** in the absence of *para*-methoxybenzyl alcohol.

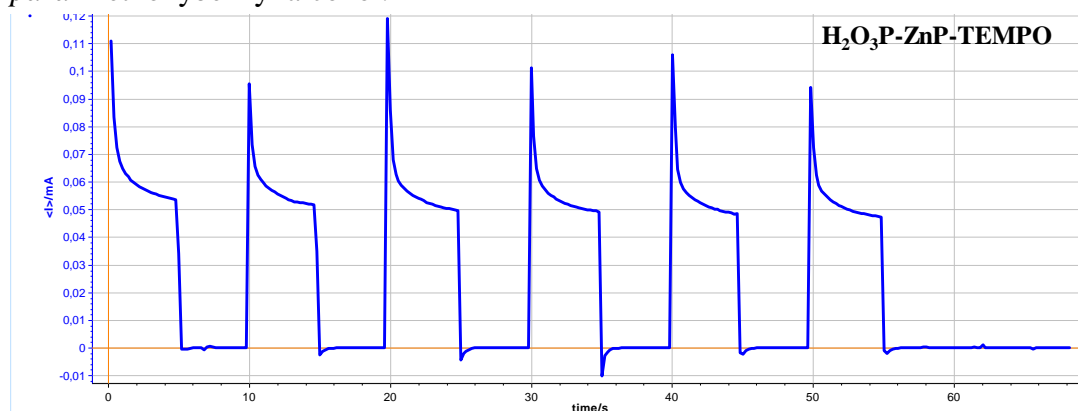


**Figure 6.4.56** Chopped light voltammetry measurements recorded at a constant potential of 0 V vs. SCE in acetonitrile in presence of 0.1 M of Me-Imd coated with **H<sub>2</sub>O<sub>3</sub>P-ZnP-TEMPO** in presence of [*para*-methoxybenzyl alcohol] = 50 mM.